Coupling of a Solid Oxide Fuel Cell with a Vapour Absorption Refrigeration System for refrigerated truck application

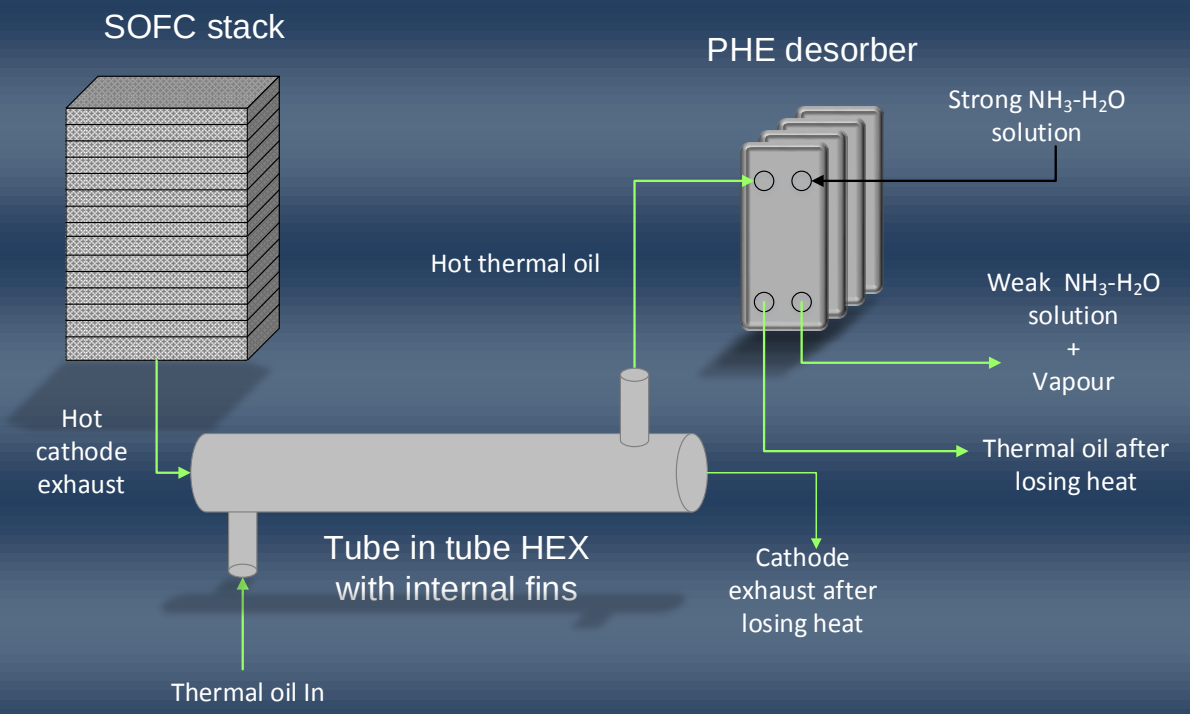

Vikrant Venkataraman
Doctoral thesis
University of Birmingham

UNIVERSITY OF BIRMINGHAM

Coupling of a Solid Oxide Fuel Cell with a Vapour Absorption Refrigeration System for refrigerated truck application

A modelling & simulation approach to understand system integration better

---

By

VIKRANT VENKATARAMAN

(Student ID: 1306674)

A thesis submitted to

The University of Birmingham

for the degree of

Doctor of Philosophy

Supervisor:
Prof. Dr. Robert Steinberger-Wilckens

Co-Supervisor:
Prof. Andrzej W Pacek

This work was performed at:

Centre for Fuel Cell and Hydrogen Research
School of Chemical Engineering
College of Engineering and Physical Sciences

University of Birmingham

March 2017

UNIVERSITY OF BIRMINGHAM

To see things in the seed, that is genius

Lao Tzu

Abstract

This PhD thesis presents a modelling and simulation approach for coupling a Solid Oxide Fuel Cell (SOFC) with a Vapour Absorption Refrigeration System (VARS) specifically for refrigerated trucks. This work lays the ground work for an ongoing project where the ultimate aim is to build a compact thermally driven refrigeration unit (with cooling load < 10 kW) which will replace the vapour compression (VC) system on-board the truck. Zero dimensional models were developed for the SOFC and VARS and detailed 1D and 3D models were developed for various components of the system.

A major challenge in this work was the thermal coupling of two systems working at entirely different temperature levels. The SOFC operates between 700 ^{o}C and 800 ^{o}C and the VARS between 150 ^{o}C and 200 ^{o}C. These two systems were successfully coupled to one another using two methods- indirect coupling and direct coupling. Indirect coupling involved the use of a coupling fluid which transfers the required amount of heat from the SOFC to the desorber of the VARS at the correct temperature level and direct coupling involved the use of heat pipes as the heat transport medium. The concept of using heat pipes has been explored for the first time in a desorber and hence that presents the biggest novelty of this work.

In order to develop a compact thermally driven refrigeration system it is extremely important to develop compact high performance components. Design and modelling of all the components in the VARS is a major project in itself hence in this thesis only the desorber of the VARS was designed and modelled. Two different compact desorbers were analysed, designed and modelled to cater to a 1 kW cooling load. The first one is a *plate heat exchanger desorber* and the second one is a *heat pipe integrated desorber*. It was found that both these desorbers produced enough refrigerant in order to cater to the 1 kW cooling load and were quite compact in volume. Hence, based on the modelling approach followed,

certain generalised design guidelines were developed for selection of SOFC stacks and VARS on-board different trucks for different cooling loads.

This work is the first one on the combined use of SOFC and VARS for a mobile application. Such a system, if developed, could also have wider implications in areas besides refrigerated transport. One example is in the air conditioning industry where heavy electricity consuming air conditioners could be replaced by compact thermally driven air conditioners.

Novelty/ Knowledge contribution

- System integration strategies for coupling of SOFC with Vapour Absorption Refrigeration System
    - Two devices working at entirely different temperature levels are thermally coupled.
- Thermal modelling of Plate Heat Exchanger desorber, leading to quantification of refrigerant generation inside flow channels.
    - A peak into the thermal processes occurring inside each flow channel of the plate heat exchanger desorber.
- Integration of SOFC and desorber of Vapour Absorption Refrigeration System via heat pipes. This is a novel concept and has not been tried before.
- Paving way for integration of fuel cells on heavy duty trucks and other vehicles.

Acknowledgements

A PhD journey is a unique experience in a researcher's life and it definitely is a long one where one requires three P's as I call it- *patience*, *perseverance* and *persistence*. I pursued this path even though I had a permanent job offer from a reputed firm back in India and one may wonder why did I do this? It's because I love research, the challenges that come along the way and the very fact of discovering new things on this path. The flexibility and freedom where one is allowed to work at one's own pace is something that can only be experienced at an academic institution. Doing the PhD has taught me a plethora of things such as to be totally independent, to be goal oriented and to learn and develop new ideas. These are things that cannot be learnt unless one pursues a PhD. Not only that, I met some really wonderful people along the way and have established contacts throughout the world. In short, I would say my journey so far has been wonderful, with moments of both ups and downs. It would have been boring if the PHD journey curve was flat, even the ECG (Electro cardiogram) is not flat ☺. I would like to take this opportunity to thank all the wonderful people who helped me through the thick and thins of my journey.

First of all I would like to express my heartfelt gratitude to Prof. Robert Steinberger-Wilckens who has not only been a great supervisor but also a great mentor and a friend. I must honestly say that one cannot find a better supervisor than him. His way of supervision is totally unorthodox which many people may not relish but I had a great time working with him. He gives you total freedom to explore and discover the things that you want to, provided you are self-driven and self-motivated. The trust that he placed in me with regards to the project and the specifics is something unique and wonderful. He is that kind of a supervisor who wants to be your friend and gives you enough room to marshal your thoughts and research ideas. I am still not sure as to why he chose me over other candidates but I would like to thank him from the bottom of my heart for his wonderful support through these years.

To Prof. Andrzej Pacek, my co-supervisor, who guided me through the intricate and specific details on heat transfer aspects. He has always been eager to give me a patient ear and listen to my ideas and work plan. His critical viewpoints has helped me fine tune my research ideas. He also provided me opportunities to help him with the course that he handles- *Heat Transfer* and *Advanced Transport Phenomena*. Being a teaching assistant for him provided me an opportunity to develop both my teaching and public speaking skills.

To Unilever, who not only supported my project but also provided funds for construction of a prototype based on the modelling and simulation work carried out by me. Without their support I don't think this project could even have existed. In my opinion, industry involvement with academic research could lead to better and fruitful results for the benefit of mankind. Thank you very much

When one is away from home especially in an entirely different country, one feels lonely. It is then that you find other people who become like family and you comingle with them. Sharing stuff and talking about things provides one a completely different viewpoint. You learn new things which you never even thought existed and you experience different things which you could never have done back in your own country. These people from different cultures, backgrounds and countries have taught me a lot and these years would have been tough without the support of these wonderful people. I will try not to miss anyone here.

First of all to my first housemate - Gaurav or G as I call him. He is one of the coolest persons I have seen. He never fritters under pressure and is calm as a cucumber and has always given me sensible advice on any topic. I owe him a great deal for all the help and support he has given me. He has been more than friend to me. Then I would like to thank Anwar who taught me not to believe in any story or news without analysing it completely from all angles. He has a controversial theory for almost every general topic in the world and my interactions with him have made me look at everything with a bit of critical thought.

Next I would like to show my appreciation to my dear housemates, Tanise, Armando, Daniel and Luca who have been like family. Some of them have already left the country but have left a deep impression inside me. Home here would not have been fun without you guys. Of course we had our differences on certain issues but we also had better and bigger moments. Love you fellows ☺.

My dearest office colleagues – Jong Eun, Yaxiang, Arvin, Nikkia, Surbhi, Kun, Yousif, Lina, Tsangi, Bernardo. Life in the office would have been very dull and boring without the support of you guys. One needs a little bit of spice during this long journey and you guys just provided that. I will definitely cherish all the small talk, pep talk, quarrels and big talk that we had.

My badminton buddies – Artur, Kannan, Halina and Tom. I needed this weekly dose to do something besides my lonely sport of running, swimming and cycling. Thank you Artur, for meticulously organising this every week.

To John Hooper & Lynn Draper, these two wonderful people in the graduate office make life as easy as possible for the students with regards to administration procedures. Kudos to you guys for always being there ready to help and that too with a smile on your faces.

At last but not the least, to my family back in Chennai India. Life is tough when one gets to go home only once every year. Without the strong support on my family I would not even have made it here let alone finish my PhD. My mom has always supported me in whatever I chose to do, thanks Ma for being their always and for providing your blessings. Your love, support and the confidence you have in me has provided me strength to carry on my activities here without having to worry about things happening back home. To my dad who feels proud of me but normally doesn't show off. To my brother with whom I can discuss anything and everything under the sun and is always there to pull my leg. Thanks dude for being a wonderful bro.

List of Publications and Awards

Journal Publications

'Coupling of a solid oxide fuel cell auxiliary power unit with a vapour absorption refrigeration system for refrigerated truck application'; **V Venkataraman**, A W Pacek, R Steinberger-Wilckens; **Fuel Cells** published by John Wiley & Sons; DOI: 10.1002/fuce.201500124; Vol 16, Issue 3, 273-293

Conference proceedings

'*Thermal integration of SOFC and Plate Heat Exchanger desorber*'; **Vikrant Venkataraman**, Andrzej W Pacek and Robert Steinberger- Wilckens; **ECS Transactions** 68 (1) 221-239 (2015)

Oral presentations

- *Thermal integration of SOFC and Plate Heat Exchanger desorber*; ECS conference on Electrochemical Energy Conversion & Storage with SOFC – XIV, **Glasgow Scotland**, July 2015
- *Coupling of an SOFC APU with a VARS for refrigerated truck application*, 8th Progress in Fuel Cell Systems workshop, **Bruges Belgium**, June 2015

Poster presentations

- *Coupling of SOFC and Vapour Absorption Refrigeration System for truck applications*, 11th European SOFC and SOE Forum, **Lucerne Switzerland**, July 2014

- *Modelling of SOFC heat driven Vapour Absorption Refrigeration System for trucks*, 10th International Hydrogen & Fuel Cell Technical Conference, Millennium point, **Birmingham UK**, May 2014
- Heat Transfer Modelling of Single High Temperature Polymer Electrolyte Fuel Cell, COMSOL conference, **Rotterdam The Netherlands**, Oct 2013

Awards

- First prize in Three Minute Thesis (3MT) competition at H2FC Supergen conference held at University of Bath; Dec 2015
- Finalist in Three Minute Thesis competition at the University of Birmingham; June 2016
- First prize in poster presentation at 10th International Hydrogen & Fuel Cell Technical conference, Millennium Point, Birmingham UK
- First Prize for best oral presentation among second years in Friday PhD seminar at the School of Chemical Engineering, June 2015

Table of Contents

3 CHAPTER 3

4 CHAPTER 4

5 CHAPTER 5

6 CHAPTER 6

7 CHAPTER 7

List of Figures

Chapter 1

Chapter 2

Chapter 3

Chapter 4

Chapter 5

Chapter 6

Chapter 7

List of Tables

Chapter 1

Chapter 2

Chapter 3

Chapter 4

Chapter 5

Chapter 6

Chapter 7

1

Introduction & Fundamentals

"*A journey of thousand miles begins with a single step*" **Lao – Tzu**

This chapter introduces the reader to the project, provides some necessary fundamentals required to understand the content in the forthcoming chapters and also touches on the scope and specific objectives of this thesis.

1.1 Introduction

There is renewed interest in using absorption refrigeration systems for small scale applications where thermal energy is freely available. The present day refrigeration and air conditioning systems are all based on Vapour Compression (VC) technology in which a compressor is employed to raise the pressure of the refrigerant. The compressor is a heavy consumer of electricity which is considered to be a precious form of energy when compared to mechanical or thermal energy. Energy forms are usually classified as either high quality or low quality depending on the amount of exergy (useful energy) that it possesses. Electrical and mechanical energy can easily be converted to other forms of energy, however, the usefulness of thermal energy depends on the temperature at which it is available, more of which can be explained using the second law of thermodynamics, ds = dQ/T and exergy. In short, higher the temperature, higher is the quality of heat.

Exergy of different energy forms is usually quantified by a term called *exergy index* and the exergy index of electrical and mechanical energy is almost 100% whereas for thermal energy it is 50% when the temperature at which it is available is 300 ^{o}C and a mere 20% [1] when the temperature at which it is available is 50 ^{o}C. Also between mechanical and electrical energy, the latter is freely available in nature only in the form of lightning and must therefore be generated and thus is more precious than the former. Hence any electrical equipment should be designed to attain the highest electrical efficiency possible. In places where electricity generation is in short supply, having a lot of heavy electrical energy consuming equipment can put a lot of strain on the electricity grid. It would be a lot more energy efficient, when considered on a systems basis, to use thermal energy (available freely or as residual heat) to drive an application which would otherwise be driven by electrical energy. One such application where thermal energy could be used to drive the

process is *Refrigeration,* and this will be one of the subject matters that will be discussed in the forthcoming chapters of this thesis, the others being fuel cells and heat exchangers pertaining to refrigeration.

There are alternatives available to the VC technology which could possibly be employed both in refrigeration and air conditioning applications. But the main drawback is that these technologies are not as efficient (considering the cooling system alone) as the VC technology. The VC system reaches COPs (Coefficient of Performance) between two and three whereas the COPs of other systems are all either below one or just above one. A listing of the alternate refrigeration technologies is given in *Appendix A*.

1.1.1 Application considered in this research work – Refrigerated Road Transportation

Refrigerated transportation plays a crucial role in transporting goods from manufacturing sites to primary storage centres and from primary storage centres to retail stores and secondary distribution centres. Most refrigerated trucks are fitted with one of the following systems to keep the refrigerated space at the desired temperature:

a) A Vapour Compression (VC) system
b) An Eutectic plate system

VC systems on refrigerated trucks are either powered by a separate auxiliary diesel engine or the main diesel engine itself. This is turn means

i) The main (or auxiliary) diesel engine needs to run continuously to power the refrigeration system, even when the truck is at a standstill and making deliveries (engine idling). The engine cannot be turned off because this will cause the

temperature to increase inside the refrigerated cabinet which will in turn harm or degrade the quality of foods being delivered/ transported [2].

ii) The noise generated by engines to power Truck Refrigeration Units (TRU's) may limit truck delivery to supermarkets and hotels situated in urban areas to specific times during the day [3].

iii) As the engine has to be kept in idle mode, emissions from the truck are increased and energy efficiency is extremely low.

Thus refrigerated trucks powered by internal combustion engines are noisy and emit considerable amounts of Green House Gases (GHGs). Also, the need for switching to alternate truck refrigeration systems or making refrigerated trucks more environment friendly arises because refrigerated trucks (>33 tons) deployed in the food industry comprise 80% of refrigerated food transportation and on a single vehicle, the conventional diesel engine powered vapour compression refrigeration system is responsible for 40% of the total vehicle GHG emissions [4].

The VC system as well as the Eutectic plate system mentioned above requires electrical energy. If a thermally driven refrigeration system could be used instead of an electrically powered one and if that thermal energy came from excess or waste energy sources, then it would be a lot more energy efficient to implement such a system.

This PhD thesis specifically looks into the possibility of driving the refrigeration system on-board the truck using residual heat available from a fuel cell.

1.2 Brief project description

In 2010 Unilever launched the Unilever Sustainability Living Program (USLP), which aims to halve the environmental footprint of its products by 2020, while at the same time growing its business. This plan applies across the whole value chain of Unilever's business, i.e. environmental impacts from suppliers, distributors and end users are included in time bound targets.

Within the USLP, targets are set for Unilever's global logistics organisation to maintain its 2020 CO_2 emissions at or below 2010 levels despite significant projected growth in business. This represents a 40% reduction in CO_2 emissions which is expected to be achieved by:

- Reducing truck mileage
- Using lower emission vehicles
- Employing alternative transport such as rail or ship instead of road transport
- Improving the energy efficiency of warehouses

It is estimated that 25% of the CO_2 emissions from Unilever's ice cream business, for instance, are due to transportation. To decrease these CO_2 emissions, and thus help meet the USLP target, Unilever R&D is keen on developing transportation systems that have low CO_2 emissions.

1.3 Synergies between fuel cells and refrigeration systems

Fuel Cells can in principle be coupled with refrigeration systems in one of the following configurations:

a) Fuel Cells as a source of electrical power – *Configuration 1*

In this case the fuel cell and the refrigeration system are connected as shown in Figure 1.1. The possible refrigeration systems that could be used with the fuel cell in this configuration are the **vapour compression (VC)** system, the **eutectic plate** refrigeration system and the **thermoelectric** refrigeration system. In the vapour compression system, the electrical power is used to run the compressor of the refrigeration system which then pressurises the refrigerant and supplies it to the condenser.

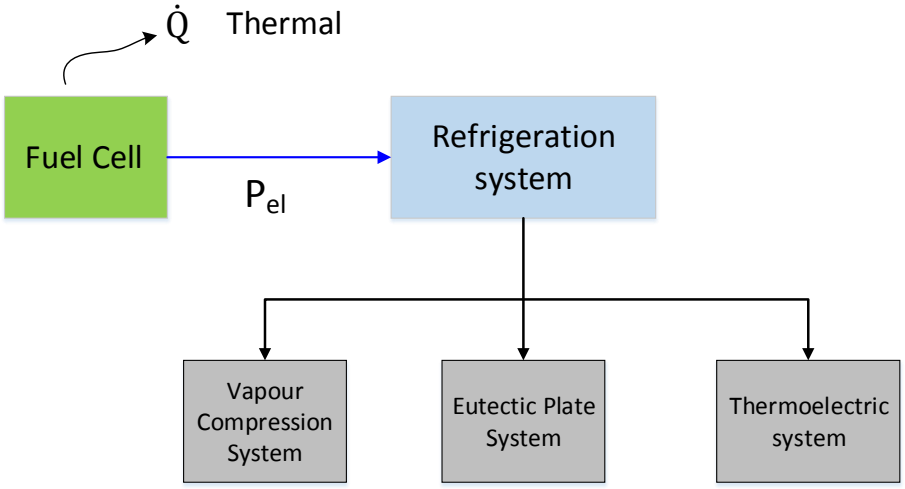

Figure 1.1: Possible refrigeration systems powered by electrical energy from fuel cell

In the eutectic plate system, electrical power is supplied to the moto-compressor, which then pumps Freon and circulates it around the cooling tubes to freeze the eutectic solution present inside it. The thermo-electric refrigeration system works on the principle of *thermoelectric effect* where electrical energy is converted to a temperature gradient, which is then used in refrigeration applications.

As only electrical power from the fuel cell is used in this configuration it is highly desirable to use a fuel cell system having the maximum electrical efficiency or power

efficiency. The heat produced by the fuel cell will be rejected via a radiator on the roof of the vehicle.

b) Fuel Cells as a source of heat – *Configuration 2*

In this configuration, the residual heat generated from the fuel cell is used to drive a thermally driven refrigeration system. As the electrical power from the fuel cell is not used for powering the refrigeration system, it is available for other purposes such as powering the auxiliary electrical/electronic loads on the truck or even for traction. The block diagram for this configuration is shown in Figure 1.2.

There are two possible refrigeration systems that fit this configuration. They are classified as 'Sorption' refrigeration systems and **Vapour Absorption** and **Adsorption** systems are the two subcategories. Both these systems are thermally driven and the amount of heat delivered to the system usually determines the efficiency or COP of the system.

The fuel cell in this configuration is used in the CCP (Combined Cooling & Power) mode. Hence, attention should be paid to maximise the utilisation of residual heat generated within the fuel cell, and at the same time the electrical power generated should also be put to use to the maximum extent possible. This means there might be a trade-off between the electrical efficiency and thermal efficiency obtained from the fuel cell and the operating point must be chosen accordingly.

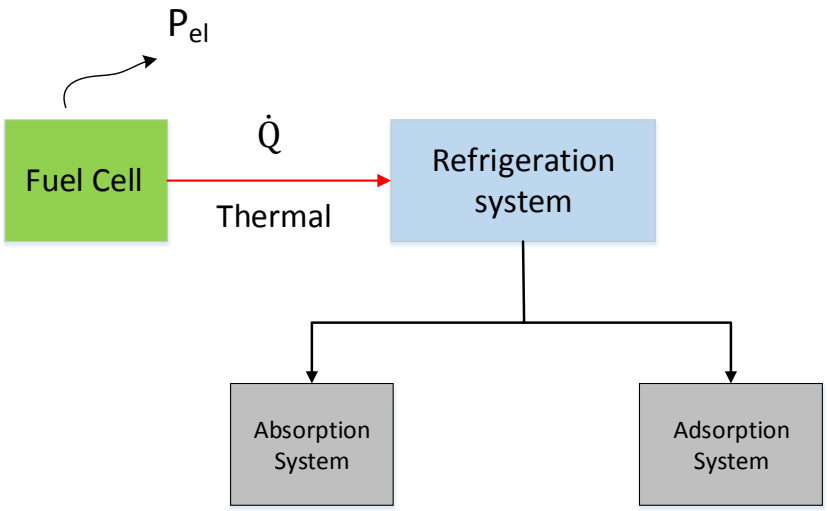

Figure 1.2: Refrigeration system powered by heat from fuel cell

c) Fuel Cells as a source of both heat and electrical power – *Configuration 3*

This configuration is basically a modification of Configuration 2 and incorporates a backup or safety aspect into the architecture. The waste heat from the fuel cell is used to drive the refrigeration system and the electrical power is used to power a heating element which is used as a backup. In case the residual thermal energy available from the fuel cell is insufficient to directly drive the refrigeration system, the heating element acts as a supplement to deliver the required amount of heat into the refrigeration system. Also, in an emergency situation where the transfer of residual heat from the fuel cell is not effective, the heating element takes over the role of the heat source. The block diagram of this configuration is shown in Figure 1.3.

The fuel cell in this configuration is also used in the CCP mode.

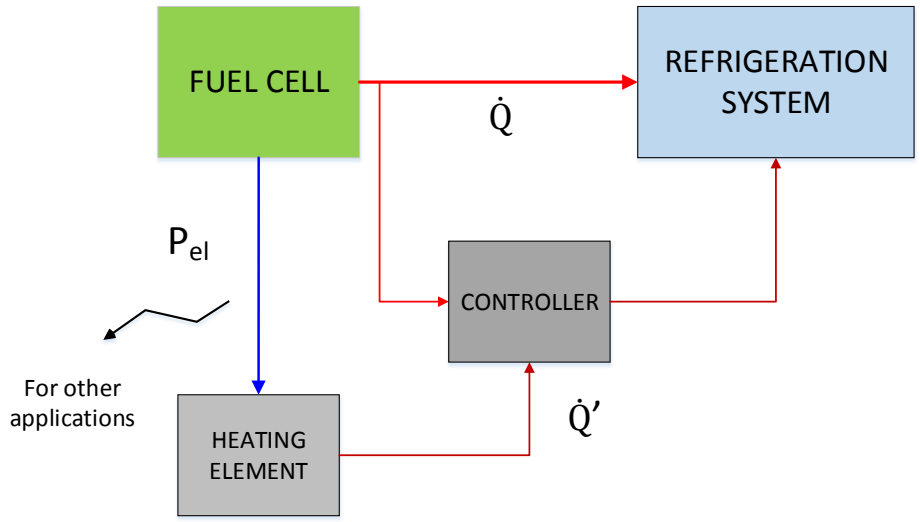

Figure 1.3: Refrigeration system powered by heat with a backup controller

Based on the configuration chosen for the final system design, the fuel cell and refrigeration system have to be chosen accordingly. In *Configuration 1*, the electrical power alone is used and residual heat generated is dissipated away. This amounts to not utilising the high quality waste heat, if produced, by the fuel cell, thereby compromising on total system efficiency. There is also considerable exergy loss from the system when the fuel cell is used in this configuration.

Configurations 2 & 3 present more holistic approaches of integrating the fuel cell with the refrigeration system. In *Configuration 2*, the heat from the fuel cell is utilised to run the sorption refrigeration system and the electrical power is available for use elsewhere. This presents a higher combined efficiency of up to 80% [5-7] when compared to the efficiency from *Configuration 1* which is limited to 40% if a PEFC is used [8] or up to 60% if an SOFC is used [9]. *Configuration 3* adds an element of safety to the system by incorporating a controller, which monitors the actual amount of heat required by the refrigeration system. If the heat supplied by the fuel cell is not sufficient or if for some reason the heat transferred is not effective then a backup heating element supplies the required amount of heat to the

refrigeration system. This in turn keeps the refrigeration system running and thereby prevents foods (kept in the refrigerated space) from getting spoilt or downgraded in quality.

1.4 Types of fuel cells

There are four types of fuel cells which in principle could be employed in the system analysed here and they are presented in the following sections. The discussion is limited to the critical characteristics that would help in making a conscious choice of the fuel cell for truck refrigeration applications. No material aspects or physico-chemical aspects are discussed in detail as the present project looks into system level studies where the electrical and thermal power produced from the fuel cell are of primary importance.

1.4.1 Solid polymer fuel cells

There are two types of fuel cells that fall under this category, they are:

a) PEFC

Polymer Electrolyte membrane Fuel Cells (PEFC) work in the temperature range of 40-100 ^{o}C (mostly around 80 ^{o}C) and are the best option to date for use in vehicles for traction power. There have been both prototypes and demonstration vehicles running on PEFC technology [10, 11]. But the projects demonstrated so far were limited to either passenger cars or buses. A full scale demonstration on a truck or trailer has been shown by very few manufacturers and '*Vision motor corp*' [12] is one such manufacturer who has built a zero emission fuel cell truck (curb weight being 7.65 tons). The main advantages of using PEFC technology are: *very quick start up*

times, *low temperatures of operation and use of a solid electrolyte* which is helpful in preventing electrolyte leakages and subsequent corrosion problems. As the operating temperature of this fuel cell is below 100 ^{o}C, the quality of residual heat available is not sufficient to drive a sorption refrigeration system (for transporting frozen food). Vilarinho et al [13] carried out a preliminary analysis of a '*Solar driven sorption refrigeration system*' and concluded that the minimum temperature of the coupling fluid needed to drive the sorption refrigeration system (for achieving refrigeration temperatures of -20 ^{o}C) is 150 ^{o}C. Hence PEFCs are not suitable for use with thermally driven refrigeration systems, however, electrical power from this fuel cell could still be used to power a refrigeration system that runs on electricity (configuration 1).

PEFCs have certain limitations that need to be addressed. Fuel flexibility is a big issue since the tolerance for CO poisoning is very low in these fuel cells (30 ppm being the upper limit and 1 ppm being the limit for sulphur). Thermal management of PEFC is quite challenging since both vapour and liquid phases of water need to be managed. Membrane hydration is another challenge because a specific amount of moisture needs to be maintained in the membrane in order to retain optimum performance of the fuel cell.

The maximum power density obtainable from a PEFC is around 0.7 W cm^{-2} [14] although a power density of 1.24 W cm^{-2} [15] has been reported by UTC power Ltd. PEFCs in general have a high electrical efficiency between 40-50% [16] and are best suited for integrating with systems that require only electrical power.

b) High temperature PEFC

High Temperature Polymer Electrolyte membrane Fuel Cells (HT-PEFC) are the other category of solid polymer fuel cell and operate at a higher temperature, in the range of 120-180 ^{o}C. These fuel cells are based on the same principle as standard PEFCs as far as electrochemical reactions are concerned but the materials involved in the construction of the fuel cell are drastically different. Operation at higher temperatures allows these cells to tolerate a larger percentage of carbon monoxide (3% being the limit for CO at 180 ^{o}C and 20 ppm being the limit for sulphur) as compared to low temperature PEFCs.

Higher temperature of operation facilitates faster electrochemical reactions and also allows utilization of waste heat for CHP (Combined Heat and Power) or CCHP (Combined Cooling Heat and Power) applications. This makes them a candidate for use with both types of refrigeration systems (electrical and thermal types).

When compared to standard PEFCs, these fuel cells have a slower start up time. The start-up time is in the order of few minutes in contrast to standard PEFCs which have a start-up time of few seconds. This might be a disadvantage as far as transport applications are concerned but in the case of stationary or large scale applications, which are operated with fixed time schedules, this does not present a major problem.

With regards to cooling of the fuel cell, a conscious choice needs to be made between air cooling and liquid cooling. This is because proper thermal management of the fuel cell is essential to maximise performance and transfer heat effectively away from the fuel cell. No water management is required since all water produced will be in the vapour state.

The maximum power density available from a HT-PEFC is currently in the order of 0.1-0.2 W cm^{-2} [17]. This power density is lower than what is possible from a low

temperature PEFC but there are other advantages such as reduced size of cooling system, higher fuel impurity tolerance, and higher temperature of useful heat extraction. All these tend to compensate for the disadvantages arising from lower power density.

1.4.2 Solid Oxide Fuel Cell

Solid Oxide Fuel Cells (SOFCs) are an entirely different class of fuel cells. They are classified as high temperature fuel cells and operate in the temperature range of 500-850 ^{o}C. High operating temperatures imply that these fuel cells are more tolerant to impurities in the fuel feed and also permit the use of alternate fuels (besides hydrogen) such as methane, ammonia, carbon monoxide etc.

SOFCs in general have been employed for stationary power, CHP and CCHP applications. They have also been employed as auxiliary power units (APUs) on ships and large trucks. They have the potential to act as a drivetrain for mobile or transport applications, however, their higher temperature of operation leads to longer start-up times which do not fit well with the quick start-up times desired for automobiles.

The quality of residual heat obtained from the SOFC is high. Nevertheless, using the SOFC in a system without harnessing the residual heat leads to reduction in overall efficiency when compared to a system operating with SOFC in a CHP or a CCHP mode. This means that SOFCs are a good choice for use with both electrically driven and thermally driven refrigeration systems.

The efficiency of a CHP system using an SOFC can be as high as 80-85 % [18]. Hence it is strongly recommended to use an SOFC in an application that requires both electrical power and heat.

Integrating these fuel cells with the other systems on the vehicle for transport application is quite a challenge considering the temperature levels and start-up times involved and hence needs to be researched further. The maximum obtainable power density from an SOFC (at 800 ^{o}C) can be as high as 1.2 W cm^{-2} [19] or even higher.

1.4.3 Direct Methanol Fuel Cell

Direct Methanol Fuel Cells (DMFCs) are a class of fuel cells that operate in the temperature range of 50-100 ^{o}C. They are the equivalent to a polymer electrolyte fuel cell but the fuel used here is a methanol/water mixture as opposed to gaseous fuels supplied to practically all other types of fuel cells. When compared to PEFCs, these fuel cells have a lower power density and lower efficiency. This is primarily due to the electrochemistry involved behind fuel oxidation. Slow oxidation kinetics of methanol coupled with methanol crossover from the anode side to the cathode side lead to increased losses and lower performance. However, the advantage of using a DMFC is that this fuel cell is compatible with liquid hydrocarbons as fuels and this perfectly fits with the present day fossil based fuel mix. This provides an opportunity for DMFCs to enter the transport market without any hindrances from a 'fuel infrastructure' point of view.

The cooling strategy (or thermal management) in a DMFC is a little simplified when compared to other fuel cells. By increasing the flow rate of methanol in the anode, waste heat can be effectively removed. But the quality of waste heat available and

the effective transfer of this waste heat for use in other applications warrants further investigation. Considering that the maximum operating temperature of this fuel cell is 100 ^{o}C, the quality of waste heat is the same as with the standard PEFC.

The power density from a DMFC varies between 0.2 and 0.4 W cm^{-2} [20]. Although these fuel cells perform poorly when compared to PEFCs, they fit in better for mobile/transport applications due to the liquid fuel used.

The essential characteristics of the four types of fuel cells discussed above are tabulated in Table 1.1.

Table 1.1: Comparison of characteristics of different types of fuel cells

	Low temperature PEFC	**High temperature PEFC**	**SOFC**	**DMFC**
PARAMETERS				
Max operating temperature	100 ^{o}C	180 ^{o}C	850 ^{o}C	100 ^{o}C
Operating temperature range	40-100 ^{o}C	120-180 ^{o}C	500-850 ^{o}C	50-100 ^{o}C
Suitability for automobile drive train applications	Yes	Yes	Yes	Yes
Suitability as an APU	Yes	Yes	Yes	Yes
Power Density (W/cm^2)	0.7	0.12	> 0.7	0.25
Fuel flexibility	No	To a certain extent	Yes	Different types of liquid hydrocarbons
Waste heat for applications	No	Yes	Yes	No
Quality of waste heat	Unsatisfactory	Very good	Excellent	Unsatisfactory
Start-up times	Quick	10-20 minutes	5-6 hours	Quick
Theoretical max open circuit cell voltage	1.23	1.15	1.1	1.21

Besides the four types of fuel cells mentioned above there are two more types *viz.* PAFC (Phosphoric Acid Fuel Cell) and MCFC (Molten Carbonate Fuel Cell). These fuel cells are mainly used for stationary applications and not usually employed on automobiles/ mobile applications. As these fuel cells do not fit the present context in which the possibility of employing fuel cells on-board the truck is explored, a detailed discussion of them is not given here.

Now that different types of fuel cells and their characteristics have been discussed, a reasonable decision can be made on what type of fuel cells and in which particular configuration do they fit with different truck refrigeration units. The matrix presented in Table 1.2 helps in choosing the right kind of fuel cell and refrigeration system.

Table 1.2: Matrix showing synergies between fuel cells and truck refrigeration systems

Type of fuel cell →	Low temperature PEFC	High temperature PEFC	SOFC	DMFC
Type of refrigeration system ↓				
VC system	*Configuration 1*	*Configuration 1*	*Configuration 1*	*Configuration 1*
Eutectic plate system	*Configuration 1*	*Configuration 1*	*Configuration 1*	*Configuration 1*
Thermoelectric system	*Configuration 1*	*Configuration 1*	*Configuration 1*	*Configuration 1*
Absorption system	*NA*	*Configuration 3*	*Configuration 2 & 3*	*NA*
Adsorption system	*NA*	*Configuration 3*	*Configuration 2 & 3*	*NA*

For thermally driven refrigeration systems either the HT-PEFC or the SOFC fit in well and even between these two types of fuel cells, there is more flexibility with SOFC because there is ample room to exploit the quality of heat and the temperature of the exhaust streams. Hence SOFC is chosen as the fuel cell in this study. The other three types of fuel cells are

ruled out because the quality of heat available will not be sufficient and considering there will be some thermal losses along the way, the quality of heat will be further reduced downstream.

1.5 Objective, scope and research framework

The broad objective of this project is to develop a compact thermal refrigeration unit powered by residual heat generated from a fuel cell. This unit will be used for mobile and transportation applications.

Within the broad objective, the scope of this thesis is to look into the following aspects:

a. Identify refrigeration systems that have potential synergies with fuel cell systems.
    - Preferably refrigeration systems that use thermal energy as the driving force.
b. Identify the right kind of fuel cell that would fit the intended application.
c. Modelling and simulation of the fuel cell system for electrical and thermal energy.
    - Characterize the operating point of the fuel cell.
d. Modelling and simulation of the refrigeration system to identify mass and energy flows into the system.
e. Coupling of the fuel cell system with the refrigeration system. Two different ways – direct and indirect, of transferring heat from the SOFC to the desorber are analysed.
    - Design and modelling of suitable heat exchangers.
f. Identify different compact desorber designs, model the desorber for heat transfer and evaluate the quantity and quality of refrigerant generated at the outlet.

This work mainly presents a simulation and modelling approach to understand system integration better and lays a firm groundwork for the prototype construction planned. Results

and data obtained from modelling and simulation studies will be used to build an experimental rig after which the design and performance of certain components will be optimized and improved further. Also, if a compact thermally driven refrigeration unit can be made for trucks, then future possibilities of drive train modification on trucks will emerge where the Internal Combustion Engine (ICE) will be completely eliminated and replaced by a combination of fuel cells and batteries, thereby making refrigerated road transportation completely green and environment friendly.

In this research, a bottom up approach has been adopted where end requirements are identified first, followed by upstream modelling and design calculations. A flow chart depicting the research methodology and the design process is shown in Figure 1.4 and Figure 1.5 respectively.

1.6 Research questions addressed

Although both the fuel cell system and the thermally driven refrigeration system are well established there are certain questions that need to be addressed and will be covered by this thesis:

- What should the operating point of the fuel cell be on the polarization curve?
- Should heat be taken directly from the inside of the fuel cell or from the exhaust streams?
- Will fuel utilization (anode gas utilisation) affect the exhaust flow rate from the fuel cell stack? If yes/no then how will the operating point on the polarization curve shift?
- The high temperature fuel cell and the thermally driven refrigeration system operate at different temperatures, how can they be thermally integrated? What are the issues if temperature incompatibility exists?

- The present day thermally driven refrigeration units are all of very large size. How can compact components be used and what will be the effect on performance?

Answers to the above questions will aid in the development of alternate truck refrigeration units and the implementation of fuel cells on board trucks. It will also allow one to make a comprehensive analysis on the technical feasibility of implementing a thermally driven refrigeration system on board the truck.

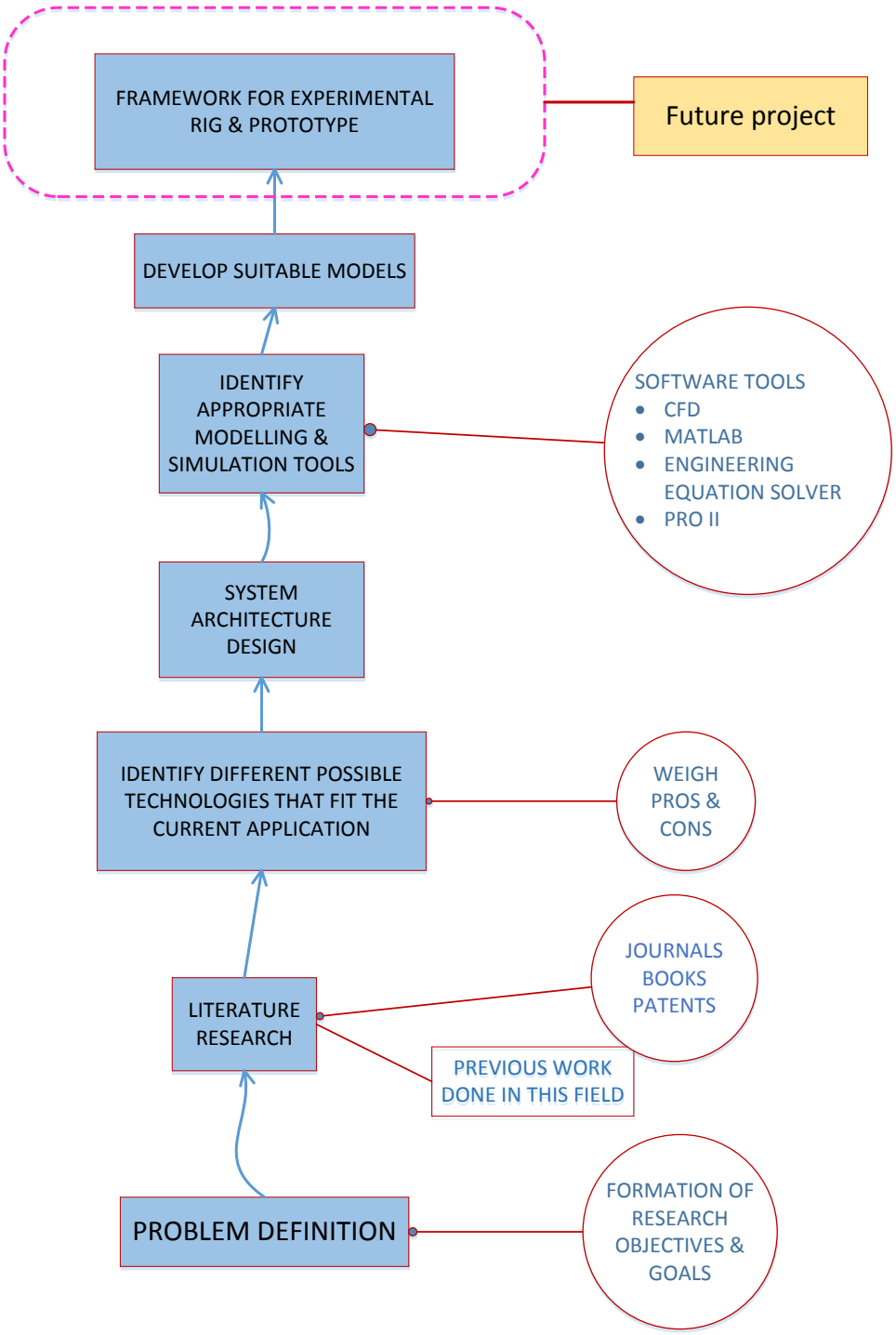

Figure 1.4: Research methodology

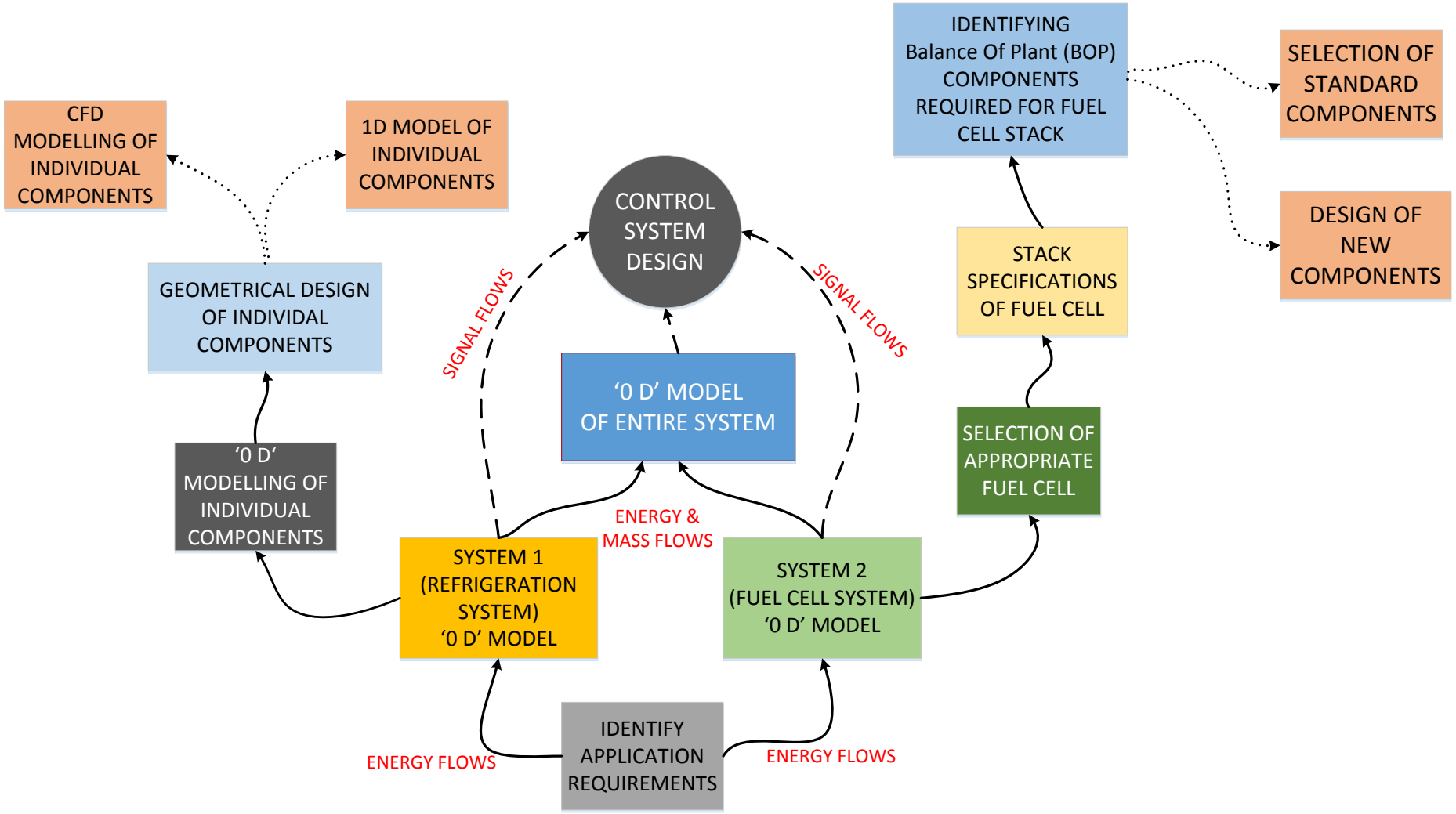

Figure 1.5: Flowchart depicting design process of the research work
(Control system not under the scope of the thesis)

1.7 Thesis organization

This doctoral thesis is organised in the following manner

Chapter 2 provides a comprehensive literature survey on the topics – '*Vehicle exhaust heat driven Vapour Absorption Refrigeration System'*, '*Coupling between fuel cells and thermally driven refrigeration units*' and '*Fuel Cell powered thermally driven refrigeration units on vehicles*'. This will give the reader a perspective of what has been done in this field so far, the shortcomings, and the technical challenges involved.

Chapter 3 is the start of the modelling and simulation work. The cooling load calculations needed on different kinds of trucks are presented first, followed by a '0D' model of the entire vapour absorption refrigeration system. The data and results obtained from this chapter serve as inputs for the next chapters.

Chapter 4 presents a detailed CFD model of the coupling heat exchanger which will be used between the SOFC and the Vapour Absorption Refrigeration System. CFD models are employed for detailed component level studies. The electrochemical and thermal model of the SOFC is also detailed.

Chapter 5 focuses on numerical modelling of the plate heat exchanger desorber. Detailed heat transfer modelling is carried out and the quantity and quality of refrigerant generated at the outlet is calculated. Optimisation studies have been carried out to size the plate heat exchanger to fit a small truck.

Chapter 6 touches upon a completely new concept where *heat pipes* are used for thermal integration between the SOFC and the desorber. The use of heat pipes is advantageous because the complexity of thermal integration between the two components is simplified and

a reduction in the total number of components to be used on-board the truck can be achieved.

Chapter 7 summarises the work and outlines areas for future research on this topic.

Bibliography

1. *Facts & Figures- Exergy; Concepts, Challenges and usage for industry*. 2013, ENEA consulting.
2. *Requirements document for demonstration of fuel cell based auxiliary power unit for refrigerated trucks*. Pacific Northwest National Laboratory Aug 2012, US Department of Energy.
3. Savin S, *New York Energy Highway Request for information- Plug Power*, Plug Power Inc.
4. Tassou S.A, De-Lille G, and Ge Y.T, *Food transport refrigeration – Approaches to reduce energy consumption and environmental impacts of road transport.* **Applied Thermal Engineering**, 2009. **29**(8–9): p. 1467-1477.
5. Freese H and Fennema E, *Higher efficiencies for micro CHP using fuel cells* in *Laboratory and field tests with micro combined heat and power based on fuel cell technology*. 2014, Rijksdienst voor Ondernemend, Nederland and Gas Terra B.V.
6. Gigliucci G et al, *Demonstration of a residential CHP system based on PEM fuel cells.* **Journal of Power Sources**, 2004. **131**(1–2): p. 62-68.
7. Najafi B et al, *Long-term performance analysis of an HT-PEM fuel cell based micro-CHP system: Operational strategies.* **Applied Energy**, 2015. **147**: p. 582-592.
8. Corbo P, Migliardini F, and Veneri O, *PEFC stacks as power sources for hybrid propulsion systems.* **International Journal of Hydrogen Energy**, 2009. **34**(10): p. 4635-4644.
9. Fang Q et al, *SOFC stack performance under high fuel utilization.* **International Journal of Hydrogen Energy**, 2015. **40**(2): p. 1128-1136.
10. Zaetta R and Madden B, *Hydrogen fuel cell bus technology state of the art review*. 2010-11, Element Energy.
11. Wipke K et al, *National Fuel Cell Electric vehicle Learning Demonstration Final Report*. July 2012, National Renewable Energy Laboratory (NREL), USA: Colorado.
12. http://www.visionmotorcorp.com. (last accessed May 2013)
13. Ines Vilarinho et al, *Evaluation of solar assisted sorption refrigeration for ice cream cabinets: I Absorption*. 2012, Unilever, Colworth UK
14. Millington B, Du S, and Pollet B.G, *The effect of materials on proton exchange membrane fuel cell electrode performance.* **Journal of Power Sources**, 2011. **196**(21): p. 9013-9017.
15. Skiba T, *Ultra high power density PEM fuel cell design- UTC power*.
16. http://energy.gov/eere/fuelcells/comparison-fuel-cell-technologies. (last accessed May 2013)

17. Taccani R and Zuliani N, *Effect of flow field design on performances of high temperature PEM fuel cells: Experimental analysis.* **International Journal of Hydrogen Energy**, 2011. **36**(16): p. 10282-10287.

18. Chan S.H, Ho H.K, and Tian Y, *Multi-level modeling of SOFC–gas turbine hybrid system.* **International Journal of Hydrogen Energy**, 2003. **28**(8): p. 889-900.

19. Zhou J, et al, *Influence of pore former on electrochemical performance of fuel-electrode supported SOFCs manufactured by aqueous-based tape-casting.* **Energy**, 2016. **115, Part 1**: p. 149-154.

20. Antonino Salvatore Arico, Baglio V, Antonucci V, *Electrocatalysis of Direct Methanol Fuel cells*, ed. Zhang J, Liu H; 2009: Wiley-VCH Verlag GmbH & Co. KGaA. Weinheim. 78.

2

Literature Survey

"*You don't write because you want to say something, you write because you have something to say*"
F. Scott Fitzgerald

A detailed literature survey is described in this chapter, on implementation of thermally driven refrigeration systems for mobile applications – what has been done in the past, how it was done, the efficiencies achieved, drawbacks involved etc. This chapter introduces the reader to the literature on the broader topic of this research work and does not delve into literature on specific components for reasons of brevity and clarity. The focus then shifts to the coupling of high temperature fuel cells with thermally driven refrigeration units, and finally an overview is provided on what specifically has been done in the field of fuel cell heat driven refrigeration systems for mobile/small scale applications.

2.1 Refrigerated road transportation – Energy consumption and emissions

With the increase in global population, it is predicted that by 2030 there will be major increases in demand in three major areas – food by 50%, energy by 45% and water by 30% [1]. With the increase in food demand there will also be a proportional increase in food transportation and this is expected across land, air and sea transportation. Among these modes, the majority of food transportation takes place via roads and this implies that the number of refrigerated vehicles on the roads is bound to increase.

As mentioned in *Chapter 1*, refrigerated transportation plays a vital link in the cold chain because there is a need for transporting foods (also certain goods like plants and pharmaceuticals) securely from the place where they are sourced to their ultimate destination - the consumers. Figure 2.1 shows a schematic of the cold chain process and the need for refrigerated transportation at different stages. As can be seen from this figure, refrigerated transportation takes centre stage. Without proper and adequate refrigerated transportation food and medicine supply chains would simply break down. Refrigerated transportation is also absolutely essential because distances between production areas and consumers are increasing and due to seasonal effects not all foods/products are available at one place at all time. It is only because of proper refrigerated transport that consumers are able to enjoy foods produced elsewhere in the world. Consumers are also becoming more aware about quality issues and demand foods of the highest quality which is again one of the driving factors for food companies to opt for refrigerated transport [2].

One of the greatest challenges facing refrigerated vehicles is their heavy dependence on oil for both refrigeration and traction purposes [3]. Most of the refrigerated vehicles are powered

by internal combustion engines and the refrigeration units on board are either directly or indirectly linked to them. This means, irrespective of the scenario whether the vehicle is moving or not, the diesel engine on-board the vehicle needs to be running at all times which leads to wasteful diesel consumption and increased emissions.

The most prominent refrigeration system used on trucks is the Vapour Compression (VC) refrigeration system and the refrigerant used in it is mainly R404A, R134A or R410A. These refrigerants have a high Global Warming Potential (GWP) and the annual refrigerant leakage rate from these units can be as high as 25 % [3, 4]. This is one of the reasons that has sparked increased interest in developing alternate refrigeration systems and more eco-friendly refrigerants.

The number of refrigerated road vehicles in operation around the world currently is close to 4 million [3] which includes all kinds of vehicles – vans, trucks, trailers and semi-trailers. This number is bound to increase by 2.5% every year until 2030. In addition to that there are around 1300 specialised refrigerated cargo ships, 80,000 refrigerated railcars and 650,000 refrigerated containers employed for food transportation worldwide [5]. Almost 44% of all goods in the EU are transported by road [3] which is quite a considerable figure and this is accomplished by 1 million freight vehicles which ply on its roads. In the UK, there are about 172,000 refrigerated vehicles plying across the country [2]. In comparison to refrigerated air and marine transport, refrigerated road transportation allows suppliers the flexibility and possibility of transporting goods even to the most remote places and also to provide door to door service as administered by a majority of the supermarkets.

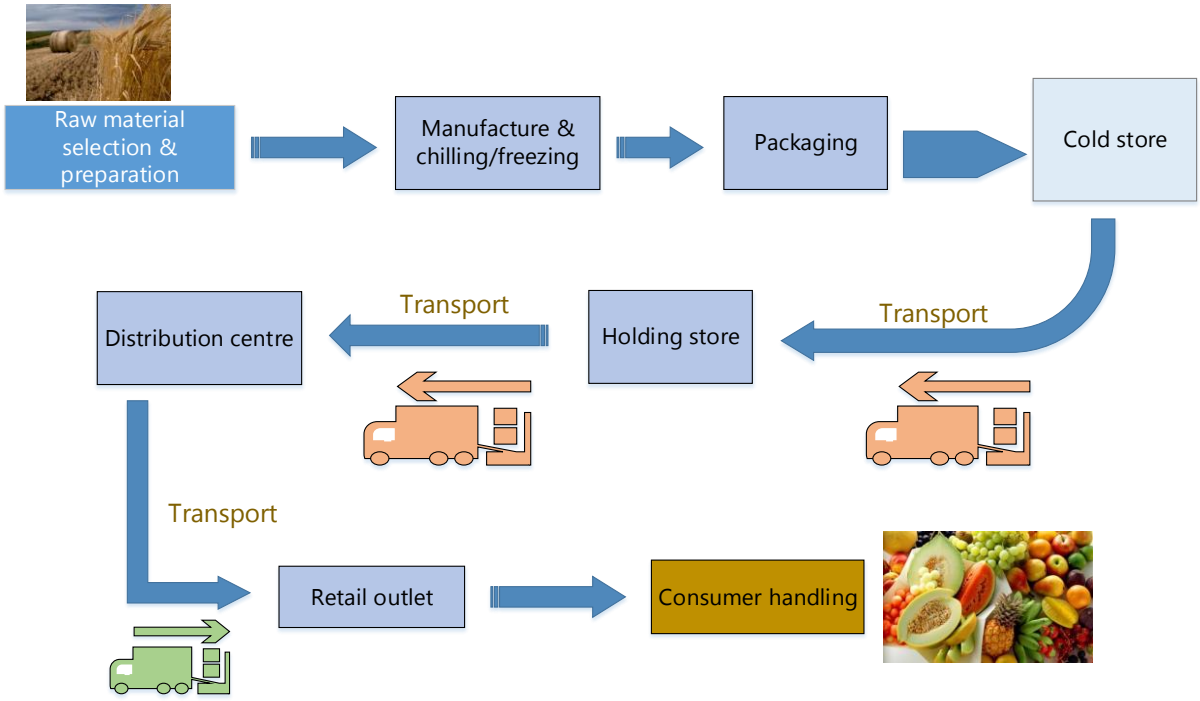

Figure 2.1: Block diagram representation of the cold chain process

Refrigerated trucks in many places are allowed to operate only during day time [6] and traffic jams are most prevalent during the day. Increase in the number of refrigerated trucks will mean they will have to spend more time stuck in traffic which will in turn increase energy consumption from these vehicles. At night, traffic levels are low and thus transport time can be reduced. This will in turn reduce energy consumption of these trucks but due to noise generated by refrigeration units and the truck itself, they are not allowed to operate during the night and there are regulations in place in major cities on truck delivery times into city limits [6-8]. Thus if alternate truck refrigeration units, which are less noisy, are developed and also modifications of truck drive trains are carried out then it could be a major breakthrough in refrigerated road transport and most of the refrigerated transportation can be carried out at night, thereby increasing energy efficiency and saving thousands of litres of diesel.

Table 2.1 shows the number of refrigerated vehicles in European countries.

Table 2.1: Refrigerated vehicle fleets across the EU [4]

Country	*ATP fleet	National fleet	Vans	Trucks	Trailers & semi - trailers
Belgium	3000	22000	12791	4589	4620
Czech Republic	4250	20000	13820	4400	1780
France	120000	150000	85500	33000	31500
Germany	25500	180000	78744	59886	41370
Italy	56700	115000	69888	35824	9288
Netherlands	5250	35000	13748	7720	13532
Poland	9500	80000	44132	17452	18416
Portugal	4150	22000	11215	4578	6207
Spain	112500	120000	73815	31964	14221
UK	N/A	84000	50000	16000	18000
EU 10	N/A	828000	453653	215413	158934
EU 28	N/A	1000000	530456	235210	234344

Truck refrigeration units operate in much harsher environments than stationary refrigeration units. This, along with other factors, reduces the efficiency of truck refrigeration units [9]. On-board refrigeration can account for up to 40% of the total vehicle fuel consumption [10, 11] and on-board air conditioning can increase fuel consumption by 20 % [12, 13] . This is because the compressor of the VC system increases the load on the engine which in turn increases the fuel consumption, emissions and operating temperature of the engine. The refrigerant R404A normally used in conventional TRUs (Truck Refrigeration Unit) has 4000 times greater global warming potential than CO_2 and hence refrigerant leaks are a major issue. Refrigeration is responsible for nearly 40% of the energy consumption during distribution [5]. If the refrigeration system could be driven by residual energy it would essentially run on no energetic cost and cause zero additional emissions.

The California Air Resources Board (CARB) [14] has carried out research to investigate emissions generated from TRUs. In California alone there are about 4000 TRU's operating at any given time. The diesel consumption from these units amounts to 75 million litres p.a. Besides increased diesel consumption TRU's cause particulate matter (PM) and nitrogen oxide (NOx) emissions of about 2 and 20 tons per day. This is projected to increase by 50%

by 2020. These figures are from actual measurement data on integrated diesel engine powered TRUs. Also in the USA, more than 50% of the states have anti-idling laws which prohibit trucks from keeping their diesel engines turned on during parking and deliveries.

The food chain in the UK is responsible for 18% of UK's total energy use and has emissions of approximately 176 Mt CO_2 [1]. Out of the total emissions from the food chain, commercial food transport is responsible for emissions of approximately 12 Mt CO_2; nearly half of this number is from food freight. Food transported through refrigerated transportation is responsible for 1.8% of the total greenhouse gas emissions in the UK [9]. In [9], it is claimed that CO_2 emissions from food transport in the UK, including all kinds of vehicles, amount to about 18 Mt per annum. This figure is the emissions from main diesel engines alone and does not cover emissions from auxiliary diesel engines. Besides CO_2 emissions there is also considerable PM (Particulate Matter) and NO_x (Nitrous Oxide) emissions which need to be accounted for. Hence the figures for CO_2 emissions from food transport range between 6 and 18 Mt p.a.

In the EU, road transportation is the biggest contributor to NO_x emissions, the percentage share being almost 40% of the total emissions. A report from the company Dearman [4] states that if no measures are taken to make refrigerated trucks more environmentally friendly, the environmental and health impacts from emissions from these trucks could cost the EU € 1.9 billion by 2015, increasing to about € 2.5 billion by 2025. In 2015, refrigerated transportation in the EU emitted around 13 million tonnes of CO_2 equivalent and 40k tonnes of NO_x which is more than 26 million Euro VI diesel cars combined, and around 5000 tonnes of PM which is equivalent to 56 million Euro VI diesel cars [4].

A TRU fitted on an articulated truck and powered by an auxiliary diesel engine emits more NO_x and PM over the course of a year than a Euro VI diesel engine used for propulsion. The reason for this is attributed to the strict regulations in place for diesel engines used for

traction but relatively lax regulation policies for auxiliary diesel engines. In the EU, TRUs are covered under the EU Non Road Mobile Machinery (NRMM) regulations. The current NRRM regulations [4] do not impose any kind of emission restrictions on engines rated less than 19 kW and most of the auxiliary diesel engines used for powering TRUs have a rating around this number. According to EU automotive regulations, the Euro VI engine used for traction is allowed to emit only 7% of the NO_x and just 2.5% of the PM for each kWh produced when compared to engines used for TRUs [4]. The TRU on an average small refrigerated van consumes about 900 litres of diesel per annum, on a medium refrigerated truck consumes about 6000 litres and on an average trailer around 9000 litres. Fuel consumption by the refrigeration unit is about 16 % higher for the urban/city driving cycle when compared to a highway driving cycle [9] due to the frequent stops and idling scenarios encountered in city driving. Fuel consumption per annum from running the refrigeration unit on-board refrigerated trucks, which are roughly 1 million in number in the United States, amounts to approximately 2×10^9 litres [11, 15].

Table 2.2, adapted from Tassou et al [9] shows the fuel consumption of different refrigerated vehicles based on the average distance travelled by each type of vehicle.

Table 2.2: Fuel consumption for refrigeration and traction [9]

Vehicle class	Distance travelled and fuel consumption (for traction)		Fuel consumption of refrigeration engine	Overall vehicle fuel efficiency (traction + refrigeration)	Percentage of refrigeration energy to traction energy
	Km/day	L/day	L/day	Km/L	%
Medium rigid	409	111.3	21	3.09	18.9
Large rigid	286	90.71	17.7	2.63	19.5
City articulated	335	112.33	26.1	2.42	23.2
32 ton articulated	419	140.8	34.1	2.4	24.2
38 ton articulated	486	159.62	24.9	2.52	15.6

In order to meet the consumer requirements and demands, there definitely will be an increase in refrigerated transportation but this expansion needs to be sustainable and should

not have a negative impact on the environment. Hence refrigerated transportation will need to meet several technical and scientific challenges, which should aim to minimise its impact on the environment.

A number of different approaches can be employed to reduce food transport emissions such as:

- Food chain optimisation
- Reduction in food transport intensity
- Modal shift
- Improved vehicle efficiency
- Alternative refrigeration technologies
- Electrification of transport with zero or low carbon electricity

Other than alternative refrigeration technologies, a detailed discussion on the above points is out of the scope of this thesis and will not be presented here. A discussion on alternative refrigeration technologies is given in *Appendix A*.

The above facts show that refrigerated vehicles powered by diesel engines and vapour compression systems are highly inefficient. The crux of the issue lies in the fact that diesel engines when operated in idle mode are extremely inefficient and the compressor of the VC system is noisy and has an efficiency of just 65% [16]

Considering the issues involved with refrigerated road transport, many research institutes and companies have been keen on developing sustainable/alternate ways of powering truck refrigeration units. One idea that is being actively pursued is the design and development of a compact thermally driven refrigeration unit that occupies a similar volume footprint as that of a conventional VC system. A compact vapour absorption refrigeration unit driven by

residual heat from a fuel cell is one such means to make refrigerated trucks greener by reducing diesel consumption. This is because fuel cells have a higher efficiency than internal combustion engines and are not limited by the Carnot efficiency [17]. Making refrigerated transport vehicles more environmentally friendly will be a small yet effective step towards making overall transportation more sustainable.

2.2 What is a VARS?

VARS is an acronym for Vapour Absorption Refrigeration System and is a thermally driven refrigeration system. The block diagram for a single stage VARS is shown in Figure 2.2.

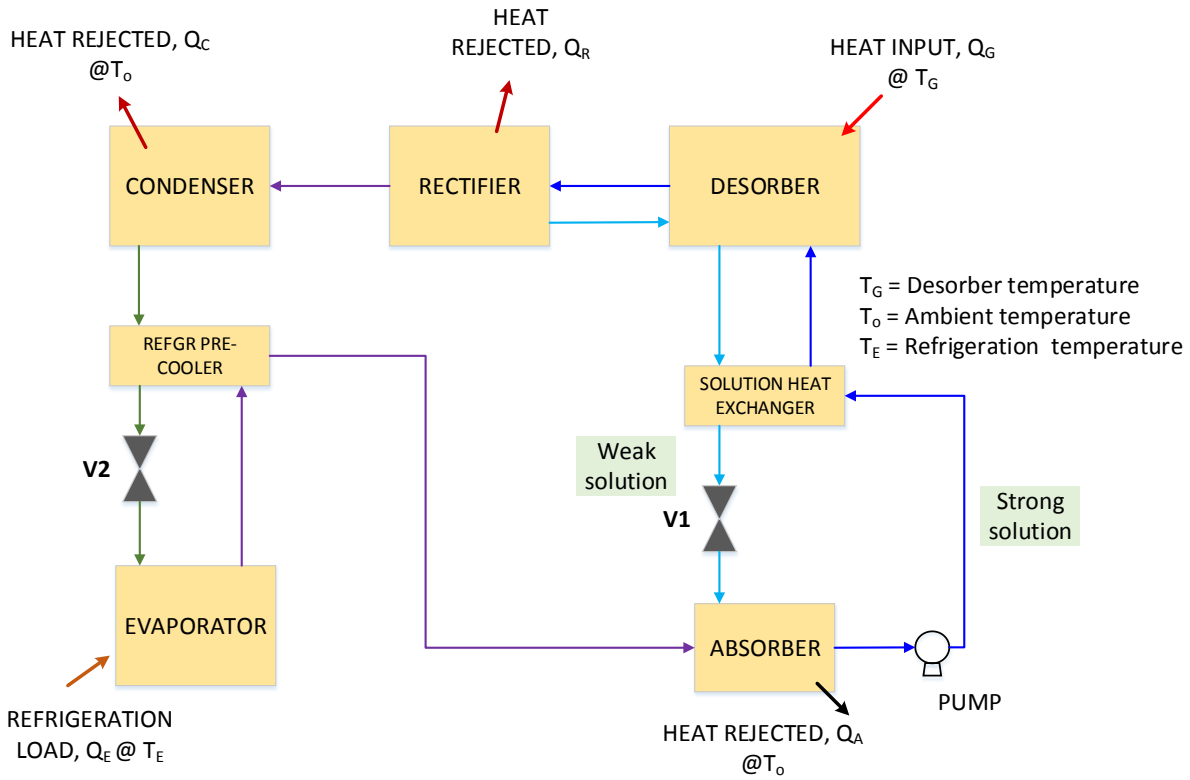

Figure 2.2: Block diagram of a single stage VARS

There are four main components in the system: *desorber (or generator)*, *condenser*, *evaporator* and *absorber*. On the whole the system can be divided into two parts, the *refrigerant part* and the *motive part*. The ***refrigerant part*** comprises of the condenser, evaporator, refrigerant expansion valve (V2) and the refrigerant heat exchanger (or refrigerant pre-cooler), while the ***motive part*** comprises of absorber, desorber, solution heat exchanger, solution pump and the solution expansion valve (V1). In the VAR system the refrigerant circulates throughout the system whereas the absorbent flows only between the desorber and absorber. NH_3-H_2O is a very common refrigerant-absorbent pair used in VARS and besides that H_2O-LiBr is another working pair that is often used. A lot of research is also being carried out on other kinds of working pairs [18-23] which are based on organic solvents and other environmentally friendly fluids. A brief description of the cycle is as follows:

In the *desorber*, the refrigerant-absorbent solution is heated to produce refrigerant vapour. The heat for this process is provided through an external means. This could either be a direct gas burner, heat from solar energy or any other means. In this case heat from the fuel cell exhaust is intended to be used to drive the absorption refrigeration system. The refrigerant separates from the absorbent in the *desorber* and flows through the rectification column, which purifies the vapour and removes any remaining water from it. The weak solution exiting the *desorber* goes to the absorber via a *solution heat exchanger*. The refrigerant vapour entering the *condenser* is almost 99% pure. The refrigerant then releases heat in the *condenser* and cools down to become a saturated liquid.

This refrigerant liquid is then passed through the refrigerant expansion valve V2 where the pressure is reduced before it enters the *evaporator*. In the *evaporator*, the liquid refrigerant turns into vapour again, drawing heat from the refrigerated space (to be cooled down) and in turn producing the refrigeration effect. The refrigerant vapour then passes through the refrigerant heat exchanger before entering the absorber. In the absorber it mixes with the

weak solution coming from the desorber, increasing it's concentration and making the resulting solution strong. The strong solution is then pumped through a solution heat exchanger back to the desorber for the cycle to repeat itself. The advantage of using the solution heat exchanger is that the strong solution is pre-heated to a certain extent before it enters the desorber, thereby minimizing the amount of heat required to boil (or heat) the strong solution. The advantage of using a refrigerant heat exchanger is that the liquid ammonia entering the evaporator is further cooled down, and this helps in enhancing the cooling capacity achieved at the evaporator.

The schematic presented in Figure 2.2 is for a single stage VARS. The same can be extended to a double stage and a triple stage VARS as seen in Figure 2.3. The COP of the double stage and triple stage VARS is higher than the single stage VARS however more components are used in those configurations and it is more complex than the single stage VARS. The COP is defined as *the ratio between the amount of cooling produced at the evaporator to the amount of heat added at the desorber*. With NH_3 as the refrigerant a double stage VARS cannot be realised because of very high pressures involved in the system [24] . Since the intended application is for trucks and other mobile units, a single stage VARS will be preferred.

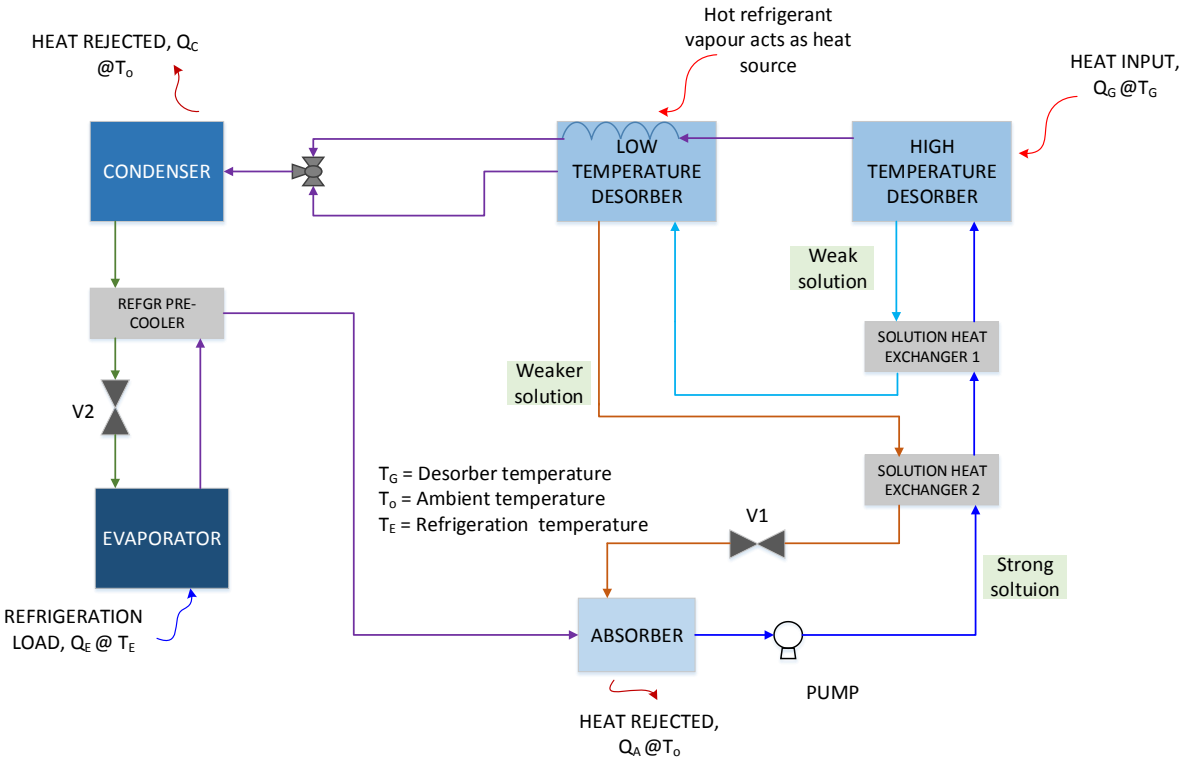

Figure 2.3: Block diagram of a double stage VARS

2.3 Absorption refrigeration system coupled to engine exhaust

The idea of using VARS for a refrigerated truck has already been explored by researchers albeit with less success. On a conventional truck, powered by a diesel engine, the source of residual thermal energy is mainly from two places – the **engine exhaust** and the **engine cooling loop**. The exhaust gas is in the temperature range between 250 ^{o}C and 490 ^{o}C depending on the engine RPM and engine torque.

Almost one third of chemical energy of the fuel is carried away by the exhaust stream [15, 25, 26] of the vehicle and another one third by the coolant loop and this has attracted considerable research in making use of the residual thermal energy available from the vehicle to drive the VARS. On the vehicle, the VARS can either be used for a refrigeration

system or for an air conditioning system. The evaporator temperature for air conditioning purposes will be between +10 and +15 ^{o}C and that for refrigeration purposes will be between -20 ^{o}C and +5 ^{o}C, depending on the product being transported [27].

The exhaust, however, is not a clean fluid and contains NO_x, SO_2 and hydrocarbons and is quite corrosive and harsh on metals that come in contact with it. With the flow rates and temperatures involved, a considerable amount of thermal energy can be tapped from it. The engine coolant on the other hand is usually a mixture of water and ethylene glycol or propylene glycol and its temperature is between 100 ^{o}C and 130^{o} C. The heat of the engine block is usually rejected in a radiator. The coolant flow rate is less compared to the engine exhaust flow rate [28] but the very fact that coolant is a liquid gives it a higher thermal capacity than the exhaust gas. The reason why engine coolant has not been used to drive the VARS on the vehicle is due to the low flow rates and small temperature change when coupled to heat exchangers of VARS thereby reducing the effectiveness of the heat exchanger below practical considerations.

In order to develop an alternate refrigeration system for trucks or other mobile applications there is a need to design and develop compact high performance components. Prototype development or table top demonstration is the way forward for adapting any new system for an application that is currently catered for by a conventional system. In light of that, very few research groups have carried out experimental investigation or prototype development of an engine exhaust heat driven VARS, and even among them very few have developed an integrated VARS which can be fitted on the vehicle. Most of them have focussed only on theoretical studies and modelling on proving the concept, where every component of the VARS was treated like a black box [29-32]. Although information on mass flows, energy flows and concentrations are crucial for design of individual components, the technology cannot be taken forward unless there is a working prototype or a comprehensive modelling study of each and every component along with the blueprint of its geometrical details. A brief

summary of the experimental and theoretical work carried out in this field to date is presented here.

2.3.1 Experimental /prototype work

For refrigeration

Koehler et al [15] developed a prototype of an absorption refrigeration unit, based on the NH_3 – H_2O working pair, for a truck trailer application, which utilised heat from the exhaust gases of the vehicle. They achieved COP values between 0.23 and 0.3 for the initial un-optimised system but suggested there was scope for increasing it by 25 %. Two more components in addition to the ones shown in Figure 2.2 were employed in their VARS unit viz. a mixing vessel and a sub cooler as seen from Figure 2.4.

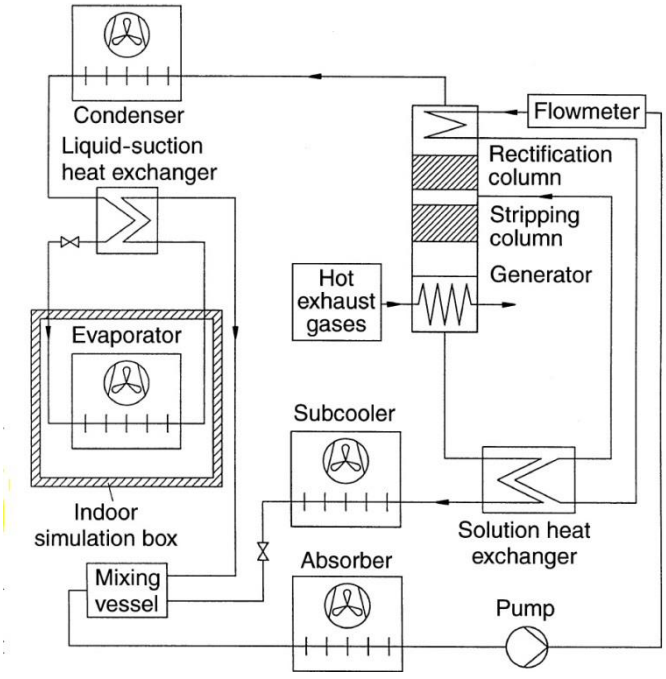

Figure 2.4: Schematic of VARS used by Koehler et al [15]

The mixing vessel was used to mix the weak solution with the refrigerant vapour coming from the evaporator and was fabricated as a column filled with pall rings, to increase the effective heat and mass transfer area. The sub cooler was designed as a fin and tube heat exchanger and was air cooled. They were able to achieve a cooling capacity of 6 kW at an ambient temperature of 30 ^{o}C and a cooling capacity of 8.5 kW at an ambient temperature of 20 ^{o}C for a refrigerated cabinet temperature of -20 ^{o}C. This was close to the German Industrial Standard (DIN 8959) which specifies a typical cooling load requirement of 5.7 kW for a truck trailer for an ambient temperature of 30 ^{o}C and a refrigerated temperature of -20 ^{o}C. They also stated that since in a VARS the concentrations of the solutions (weak and strong) are fixed, the COP cannot be varied much and it is extremely difficult to build a VARS with variable concentrations.

Horuz [33] integrated a VARS with the engine exhaust and proved that the concept is indeed feasible. He used a Robur Servel ACD – 3600, a commercially available VAR unit based on NH_3 – H_2O working pair which had a cooling capacity of 10 kW and integrated it with the exhaust of a Ford 150 (Dover) 6 litre turbo diesel engine. He however did not integrate the system on the vehicle but rather carried out the experiment on a test bench. In this paper he concentrated on two aspects - a plenum chamber design for exhaust flow around the desorber and engine performance when the VARS was connected to the exhaust.

The plenum chamber had a direct effect on the engine performance. When the chamber with a large flow area was connected to the exhaust; engine back pressure, fuel consumption and engine efficiency was not affected. On the other hand, when the chamber with a small flow area was connected to the exhaust, the engine back pressure was higher which resulted in higher fuel consumption and in turn lower engine efficiency. Hence the flow chamber for the exhaust gas around the desorber of the VARS had a major influence and was recommended to be designed in such a manner so as to have a similar pressure drop profile as that of a normal engine exhaust system.

Horuz and Callander [34] specified details of the type of heat exchangers used for major components on VARS. A major finding was that the VARS unit worked more efficiently when the condenser and absorber are cooled separately. They recommended maintaining the condenser cooling source temperature lower than the absorber cooling source temperature in order to increase the cooling capacity of the VARS.

Another experimental piece of work on integrating a VARS unit with the engine exhaust was performed by Manzela et al [35]. They used a 1.6 L, 8 valve 4 cylinder engine along with a domestic absorption refrigerator for their study. The engine was operated at 1500 rpm because they found that at higher engine RPMs excessive thermal energy was transferred to the refrigerant which prevented complete condensation in the condenser. They were able to achieve refrigeration temperatures between 5 ^{o}C and 13 ^{o}C and this was dependent on the percentage of valve opening between the engine exhaust and the desorber. The wider the opening, the lower the refrigeration temperature. The prototype developed had a maximum cooling capacity of 18.4 W when the valve was completely open. The COP and the cooling power behaved in a totally opposite manner with the percentage of valve opening. A higher percentage of the valve opening resulted in a higher cooling capacity but a lower COP because of increased thermal energy available from the exhaust. They concluded from their experiments that the percentage of valve opening need not be 100% and that keeping it at 25 % was more than sufficient to cater to the needs of the absorption refrigeration system. The maximum COP achieved was 0.049 which is way below than what can be theoretically achieved.

For air conditioning

Khaled et al [10] designed and fabricated a shell and tube heat exchanger as a desorber for use in an automobile air conditioning system where hot exhaust from the engine flowed

through the shell and the NH_3-H_2O solution flowed through the tubes. It had a heat load capacity of 4.6 kW, and could fit in a space of 50 cm x 25 cm x 15 cm. Besides specifying the mechanical design of the generator, the actual performance of the generator in terms of quantity of refrigerant desorbed and the heat and mass transfer aspects of the refrigerant absorbent solution were not specified. Hence it remains unclear if the desorber could actually cater to the required cooling load. In another study by Khaled [36], the entire air conditioning system was connected to the exhaust of a 4 cylinder engine. The size of the system designed was not suitable for automotive use due to space constraints on the vehicle.

Ismail Hilali [37] designed a VARS prototype based on H_2O-LiBr working pair with a cooling capacity between 2 and 2.5 kW. A 1.3 L internal combustion engine was employed whose exhaust was coupled to the desorber of the VARS. Like Koehler et al [15], he too used a mixing chamber prior to an air cooled absorber. He investigated the performance of the engine when it was coupled with the absorption refrigeration unit and also evaluated the performance of the absorption refrigeration unit as such. With such a custom built prototype, an evaporator temperature close to 11 ^oC was achieved at a COP of 0.78. The COP is a function of many different parameters viz. desorber temperature, evaporator temperature, condenser temperature and absorber temperature. Hence a delicate balance was required to maximise the COP of the absorption refrigeration unit.

Once again, with increase in engine RPM, the evaporator cooling capacity increased. This is because the heat recovered from the exhaust gases increased which in turn allowed the overall COP to increase. The waste heat available from the engine ranged from 3 kW at idling RPMs to a high value of 18 kW at full load conditions. However, for the engine used in this study, the efficiency decreased after an RPM value of 2750. Hence the maximum heat recoverable while maximising engine efficiency was around 9 kW. The engine suffered from back pressure effects when the desorber of the VARS was coupled to the engine exhaust

and because of this the fuel consumption of the engine increased and its efficiency decreased. Hilali [37] suggested designing the desorber with minimum pressure drop and maximum heat transfer efficiency which will lead to a greater cooling effect even at lower engine speeds. As the cooling capacity reduced when the vehicle was idling or when stationary, employing a backup gas burner at the desorber was recommended.

Talom and Beyene [11] coupled a 2.8 L V6 turbocharged internal combustion engine with a 10.55 kW Robur ACF-3600 absorption chiller and evaluated the system performance and responses both at part load and variable load conditions. The absorption chiller was modified; the original gas burner that supplied heat at the desorber was replaced by a plenum that channelled the hot engine exhaust. Under part load conditions and at an ambient temperature of 29.5 ^{o}C, the absorption chiller was able to produce chilled water down to a temperature of 12 ^{o}C when the engine RPM was 2400. A dynamic study was performed and the time taken by the absorption chiller to produce chilled water was calculated to be 14 minutes. At a higher engine RPM of 2800, the time taken by the absorption chiller to produce chilled water was almost half the previous. At variable load conditions, the chiller was able to produce chilled water as low as 6 ^{o}C at an ambient temperature of 18 ^{o}C. Other than specifying the temperature of the chilled water achieved, no further details on the coupling between the internal combustion engine and the absorption chiller were provided.

Sohail Bux and Tiwari [38] coupled the exhaust from a diesel engine directly into a plate heat exchanger desorber (using a H_2O-LiBr working pair). The remaining components of the VARS were not included in the test set up. Although the objective of the research was focussed towards developing an air conditioning system for a passenger vehicle based on VARS technology, no specific details of the cooling load or the plate heat exchanger desorber, nor the desorber's capability to produce sufficient refrigerant were specified. Critical data needed for the system design was missing in the article. Direct coupling of the

hot exhaust gases with the desorber, as carried out by these authors, is usually not recommended due to temperature incompatibility and possibility of corrosion.

Boatto et al [26, 39] discussed a more pragmatic approach for developing VARS as an alternate to the VC system for air conditioning. They stated that every part must be designed and manufactured with proper functional and geometrical characteristics owing to the limited space available on the vehicle and retrofitting commercially available VARS on the vehicle was not preferred. Their analysis was for a passenger vehicle and they recommended having storage vessels on board, for water and LiBr salt, to increase the system's capability to provide air conditioning at all times. Surplus thermal energy was available from the engine when it operated above 3700 rpm and there was a need for employing an auxiliary burner when the engine output was less than 10 kW, and if thermal energy storage was not provided. Their research work was split in two parts, the first part analysed the engine performance characteristics and the second discussed the layout and components involved in the VARS. Air cooled components (for condenser and absorber) were recommended due to space constraints. No detailed performance characteristics of the VARS were given, however, a self-support threshold of 6 kW as the minimum engine output was identified to sustain operation of the VARS using thermal energy recovered from the exhaust.

Details of the individual components used for the VARS prototype designed and built by the above experimental research groups are specified in Table 2.3.

Experimental research on the use of VARS as an alternative to the VC system is very scarce, with just a few research groups [10, 11, 15, 26, 33-38] carrying out prototype development or building a table top model. Even among these research groups half of them have concentrated on the refrigeration aspect and the other half on the air conditioning aspect for the vehicle. Only two research groups [15, 33] have actually tried constructing a

prototype from scratch and only Koehler et al [15] successfully integrated it on the vehicle but with very low efficiency. Other than Boatto et al no other experimental research group were able to design and develop a compact VARS for air conditioning applications. Hence there is a need for more experimental research in this field.

Most of these authors have recommended that further research needs to be carried out in the following areas:

i) Evaluation of effects of back pressure on the engine
ii) System scalability issues
iii) Sizing, compactness and packaging issues
iv) Regulatory use of NH_3 or LiBr in vehicles
v) Design of heat exchanger to extract sufficient heat from the exhaust
vi) Analysing corrosion effects on the desorber due to exhaust gases and subsequent effects on heat transfer performance.
vii) Refrigeration system performance at low engine speeds

Table 2.3: Details of components used in VARS for experimental prototypes

VARS components	Koehler et al [15]	Horuz et al [33]	Manzela et al [35]	Khaled et al [10]	Ismail Hilali [37]	Talom & Beyne [11]	Sohail Bux & Tiwari [38]	Boatto et al [26, 39]
Desorber	Plate fin	Closed steel cylinder with provisions for side heating from a natural gas burner and lower part being finned	Not specified	Shell and tube	Shell & tube	Not explicitly specified but absorption chiller model and manufacturer was given. Robur ACF-3600	Plate heat exchanger	Plate heat exchanger
Rectifier	Column filled with stainless steel pall rings	Coil in coil type	Not specified	Not specified	Not used		Not specified	Not used
Absorber	Fin and tube & air cooled	Plate & fin type with air cooling	Not specified	Not specified	Car radiator with aluminium tubes and fins & air cooled		Not specified	Finned tubes & air cooled.
Condenser	Fin and tube & air cooled	Plate & fin type with air cooling	Not specified	Not specified	Aluminium finned tube & air cooled		Not specified	Finned tube & air cooled
Evaporator	Fin and tube, with steel tubes and aluminium fins	Coiled tube type with ethylene glycol sprayed over it	Not specified	Not specified	Aluminium finned tube & air cooled		Not specified	Finned tube & air cooled
Solution Heat Exchanger	Plate fin made of stainless steel	Not used	Not specified	Not specified	Brazed plate heat exchanger		Not specified	Not specified
Refrigerant Heat Exchanger	Plate fin made of aluminium	Concentric tube in tube design	Not specified	Not specified	Not used		Not specified	Not specified
Mixing vessel	Column filled with pall rings	Not used	Not used	Not specified	Stainless steel column		Not used	Not specified
Sub cooler	Fin and tube & air cooled	Not used	Not used	Not used	Not used		Not used	Not specified
Solution cooled absorber	Not used	Simple pot with a coil inside	Not used	Not used	Not used		Not used	Not specified

2.3.2 Modelling work

When compared to experimental research there are a lot more research articles on modelling, simulation and theoretical aspect of coupling the VARS with the engine exhaust, micro-turbine exhaust and even coupling them with solar panels. Extensive design maps on how to operate the VARS and what conditions are most favourable to attain the highest system efficiency and VARS COP are outlined in these articles. In order to keep literature relevant to the use of VARS on vehicles, only the ones that employ engine exhaust heat are discussed here.

Fernandez-Seara et al [40] designed and modelled a heat recovery system to power an ammonia water based VARS on-board a trawler chiller fishing vessel. The heat recovery system consisted of two heat exchangers. The first one was an exhaust-gas to thermal-fluid heat exchanger and the second one a thermal-fluid to $NH_3 – H_2O$ solution heat exchanger. The former was made of a finned tube matrix which was arranged in series and fitted to the engine exhaust. The engine exhaust flowed on the outside of the finned tubes and the thermal fluid flowed inside the tubes. The latter acted as the desorber of the VARS and was made of a two-pass kettle type heat exchanger fitted to the bottom of the distillation column.

Two heat exchangers were used because the operating temperature of the engine and the VARS were entirely different, the engine operating between 350 ^oC and 420 ^oC and the VARS operating between 100 ^oC and 150 ^oC. A prototype based on the above designs was built. The remainder of the paper concentrated on modelling of these two heat exchangers and the design of a control system to regulate the flow of exhaust gases through the first heat exchanger which in turn controlled the heat input at the desorber. The control system designed worked by turning the baffle position in the first exchanger by a certain angle based on feedback from the desorber temperature. The entire heat recovery system

depended on the operating conditions required at the desorber, i.e the desorber pressure, temperature and heat load. The paper does not talk about the whole VARS but just the desorber and the heat recovery unit and states that VARS will be a good fit for the trawler chiller fishing vessel due to constant operation of the trawler engine during fishing periods and low refrigeration needs on-board the trawler.

Talbi and Agnew [29] carried out a theoretical study to combine a turbocharged diesel engine with an absorption refrigeration unit when operating in a high ambient temperature of 35 ^{o}C. The high ambient temperature condition was chosen because that would place the harshest constraints on operation of the engine. They used a caterpillar diesel engine for their simulation in four different modes – *non-cooled engine*, *engine with inter-cooler*, *engine with pre-cooler* and *engine with both pre and inter-cooler*. The use of an inter-cooler and a pre-cooler on an engine increases its brake thermal efficiency and also the power output when compared to a non-cooled engine. Their idea was to use the chilled water generated from the absorption refrigeration unit to cool the vehicle interior and also the inlet air entering the compressor of the diesel engine. Cooling of the inlet air in high ambient temperature conditions increases its density, thereby resulting in higher mass flow which in turn leads to high engine output and efficiency. They found that there was enough thermal energy in the exhaust to not only cater to the cooling load requirements of the absorption refrigeration unit but also that of the pre-cooler and the inter-cooler. High exhaust temperatures produced a higher amount of cooling in the absorption refrigeration system but at the expense of diesel cycle efficiency. The overall system efficiency of the configuration which had the engine fitted with both the inter-cooler and the pre-cooler was marginally lower than that of the configuration which had the engine with neither the pre-cooler nor the inter-cooler. No details of either the absorption refrigeration system or any of the heat exchangers used in the system were given.

Keinath et al [30] presented a modelling study on coupling a diesel engine with an absorption refrigeration system (with NH_3 – H_2O working pair) to produce chilled water. Their primary focus was to work with a single stage absorption refrigeration system, to optimize the operating conditions and to make it suitable for a small scale system catering to cooling loads up to 2 kW. Not only did they study the absorption refrigeration in the cooling mode but also in the heating mode. For the baseline study they achieved a COP of 0.69 for the cooling mode and a COP of 1.67 for the heating mode. They suggested controlling the chilled water inlet temperature to the evaporator in order for the system to achieve almost similar COPs over the entire ambient temperature range from -20 ^{o}C to +49 ^{o}C for the cooling mode. By employing such a control strategy, the system was able to cater to the required cooling load of 2 kW for the entire ambient temperature range and was able to achieve a higher system COP but at the cost of higher temperature of chilled water. The heat transfer between the exhaust gases and the desorber was achieved via a separate heat transfer fluid; direct coupling between the hot exhaust gases and the desorber was not done due to temperature incompatibility. No details of the diesel engine used or any of the heat exchangers employed in the absorption refrigeration system were given but a reference to another paper [41] in which these details were listed was provided.

Three groups [13, 31, 32] carried out theoretical modelling on integration of a VARS specifically for air conditioning on passenger vehicles.

Ramanathan and Gunasekaran [31] used VAR technology based on the H_2O-LiBr working pair for an air conditioning application. They focussed on gathering reference data for the scenario when the vehicle is idling because the cooling power of the VARS decreases when the engine is idling (due to reduced thermal energy input). Hence for the VARS to be considered as a replacement for the VC system this data was very crucial. They made use of experimental data of the engine from another research group [39] who stated that *only 30% of the chemical energy of the fuel is converted to useful engine power and the*

remaining is dissipated as heat- 40% via the exhaust and the rest via the engine coolant and that during idling about 5 kW of thermal energy was dissipated from the exhaust. The cooling load required for an air conditioning system on a mid-sized passenger vehicle is about 2 kW at both idle and cruise conditions. With a VARS based on a H_2O-LiBr working pair, a COP close to one can be achieved and hence it was envisaged that the cooling load requirement on the vehicle can be met even when the vehicle was idling. Fin and tube type heat exchangers were used for the evaporator, condenser and the absorber, and plate and tube heat exchangers were used for the desorber and the solution heat exchanger. A direct heat recovery mode where the engine exhaust was directly coupled to the desorber of the VARS was employed. From their simulation studies they found that at an idling RPM of 1300, the evaporator capacity was about 3.7 kW and this increased to 11 kW when the RPM was increased to 2000. This was attributed to the increased heat input into the desorber due to increased mass flow rate of the exhaust and also increased temperature. They also found that the evaporator capacity and the COP were linked to the desorber temperature. Increasing the desorber temperature reduced the evaporator capacity which in turn reduced the COP. Hence thermal coupling of the engine exhaust with the desorber has to be carefully designed in order to meet the required cooling capacity needed on the vehicle.

Vicatos et al [32] carried out a theoretical analysis of an air conditioning system for a Nissan 1400 mini truck powered by engine exhaust. They also verified their theoretical analysis with a laboratory prototype and concluded that a lot of improvements had to be made to their overall design due to the low COP values achieved, in the order of 0.08. The VARS unit used for the air conditioning system was based on an NH_3-H_2O working pair but taking into account the toxicity of NH_3, a direct expansion evaporator was not used but rather a secondary fluid (water glycol mixture) was used to cool the passenger space. Their designed system was able to generate a cooling load of 2 kW at 0 ^oC which was more than sufficient to cater to the needs of the vehicle chosen. Some photographs of the components used in

the VARS unit were presented and there was a mention of the condenser and absorber units being air cooled. Besides that no details of the heat exchangers or their design were given.

Javani et al [13] carried out a thermodynamic analysis, by performing energy and exergy analysis of waste heat recovery for cooling systems (mainly air conditioning for cabin) in hybrid (HEV) and electric vehicles (EV). They analysed two refrigeration cycles, the ejector cycle and the absorption cycle for cabin cooling. Only the results from the absorption cycle will be discussed here in order to keep literature relevant.

In HEVs, the heat for running the refrigeration system was obtained from the exhaust gases whereas in EVs the heat was obtained from the cooling loop used for thermal management of the battery. A thermal coupling fluid was used to extract heat from the exhaust gases and transfer it to the desorber rather than directly couple the desorber to the engine exhaust. The amount of heat dissipated through the exhaust for different vehicles is given in Table 2.4 [12]. The thermodynamic analysis was carried out for a mid-sized vehicle (average wheel base 2700 mm and average interior volume 3.2 m^3).

Table 2.4: Heat recovered through exhaust (kW) for different vehicles

Vehicle type driving mode	Subcompact	Compact	Mid-size
Highway driving	14.6	20.3	29.2
City driving	9.1	12.2	18.2

The minimum cooling capacity required for a mid-sized vehicle is around 5 kW. They found that in EVs, the cooling loop does not provide sufficient thermal energy input to the absorption system for achieving the desired cooling load required for air conditioning, the cooling achieved at the evaporator being around 2 kW. In comparison to EVs, the cooling achieved in HEV's at the evaporator was about 7.9 kW which is more than sufficient to cater to the needs of air conditioning on the vehicle. The heat recoverable from the exhaust gases in the HEV was around 15 kW and this meant a COP of 0.52 could be achieved. Other than

conducting a thermodynamic study, the authors did not specify any information on either the diesel engine used or the kind of heat exchangers employed in the absorption cooling system.

Sarabchi et al [42] carried out simulation studies for coupling a Homogenous Charge Compression Ignition (HCCI) engine with an Ammonia-Water Cogeneration Cycle (AWCC) which is basically a combination of the Rankine cycle and absorption refrigeration cycle, thereby providing both power and cooling. The exhaust gas from the HCCI engine was directly fed to the desorber of the AWCC after passing through a series of heat exchangers, resulting in desorber temperatures between 130^{o} and 180^{o} C. They found that the cooling capacity has an inverted 'U' shape, with a maximum value at a particular pressure ratio and desorber temperature. Their study was mainly focussed on showcasing the feasibility of the concept and exergy analysis of the whole system. They found that maximum exergy destruction occurred in the engine itself and at the absorber of the AWCC.

Another modelling work [43] incorporated the use of a three-fluid VARS coupled to the engine exhaust for air conditioning on a passenger vehicle. The amount of heat available at the desorber depended on the percentage of valve opening between the exhaust gas and the desorber and sufficient thermal energy was available to cater to the air conditioning needs of the vehicle, which was around 2.2 kW. Geometric and design specifications of the components were not given, however, some information on where the components can be packaged was stated. Ouadha and El-Gotni [44] carried out a thermodynamic analysis of the VARS coupled to the exhaust of a marine diesel engine and concluded that system COP increased with high desorber and evaporator temperature and low condenser and absorber temperature. Two papers by Mostafavi and Agnew [28, 45] discussed the thermodynamic aspects of coupling a supercharged diesel engine (with intercooling) and a naturally aspirated diesel engine with the absorption refrigeration unit. Their conclusion was that for a supercharged engine, the degree of intercooling affected the integration of the VARS on the

vehicle because the exhaust temperature was reduced due to intercooling and there might not be sufficient thermal power to drive the VARS. For a naturally aspirated engine there is sufficient thermal power in the exhaust gases and the cooling capacity depends on the pressure ratio and cycle temperature ratio of the engine.

Few other papers talk about coupling of engine exhaust with adsorption refrigeration systems [12, 46, 47] but adsorption systems as mentioned earlier are bulkier than absorption systems and hence are not considered as a viable alternative to VC systems.

As we can see, research on the modelling aspect of coupling the engine exhaust with VARS is not entirely focussed on one particular area but instead is spread over to different areas, ranging from studying the performance of the diesel engine, to control of VARS and also the operational characteristics for the VARS. Most of the modelling studies focussed on passenger vehicles and not on heavy duty trucks and in all the models only a system level '0D' model was presented. In order to consider VARS as a replacement for VC units, detailed component level modelling along with system level modelling is required in order to assess the component's ability to perform according to design specifications. Also, as Boatto [26, 39] mentioned, each and every component must be designed and developed separately for a particular class of vehicles due to space constraints.

A time line representing the experimental and modelling research carried out till date is presented in Figure 2.5 and Figure 2.6 and a summary of the research work carried out for coupling of the VARS with the engine exhaust is given in Table 2.5.

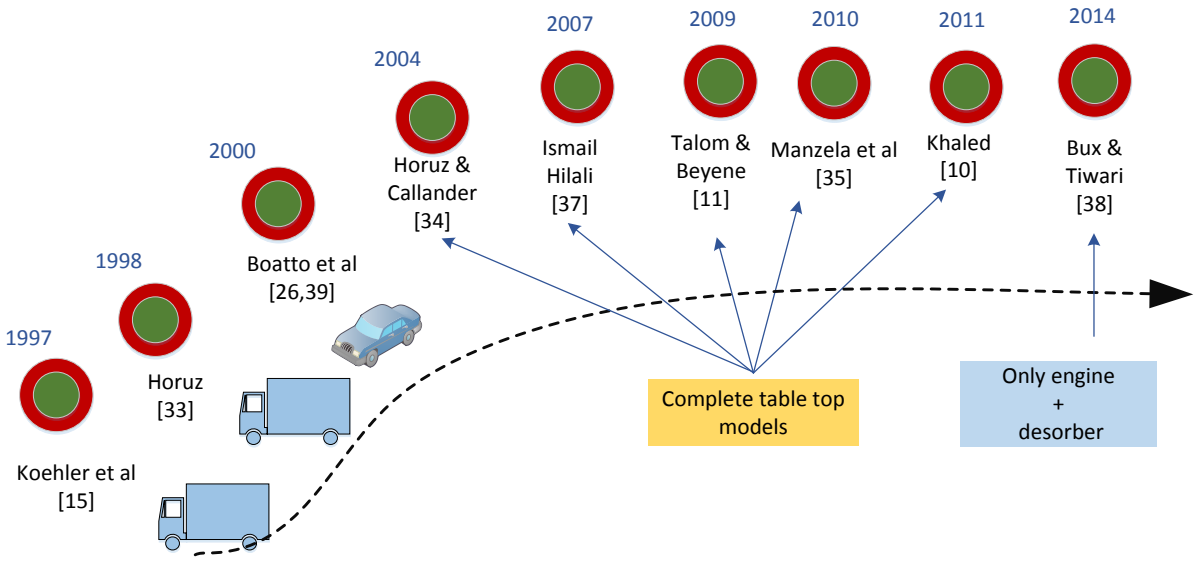

Figure 2.5: Timeline showing experimental research on VARS coupled to engine exhaust

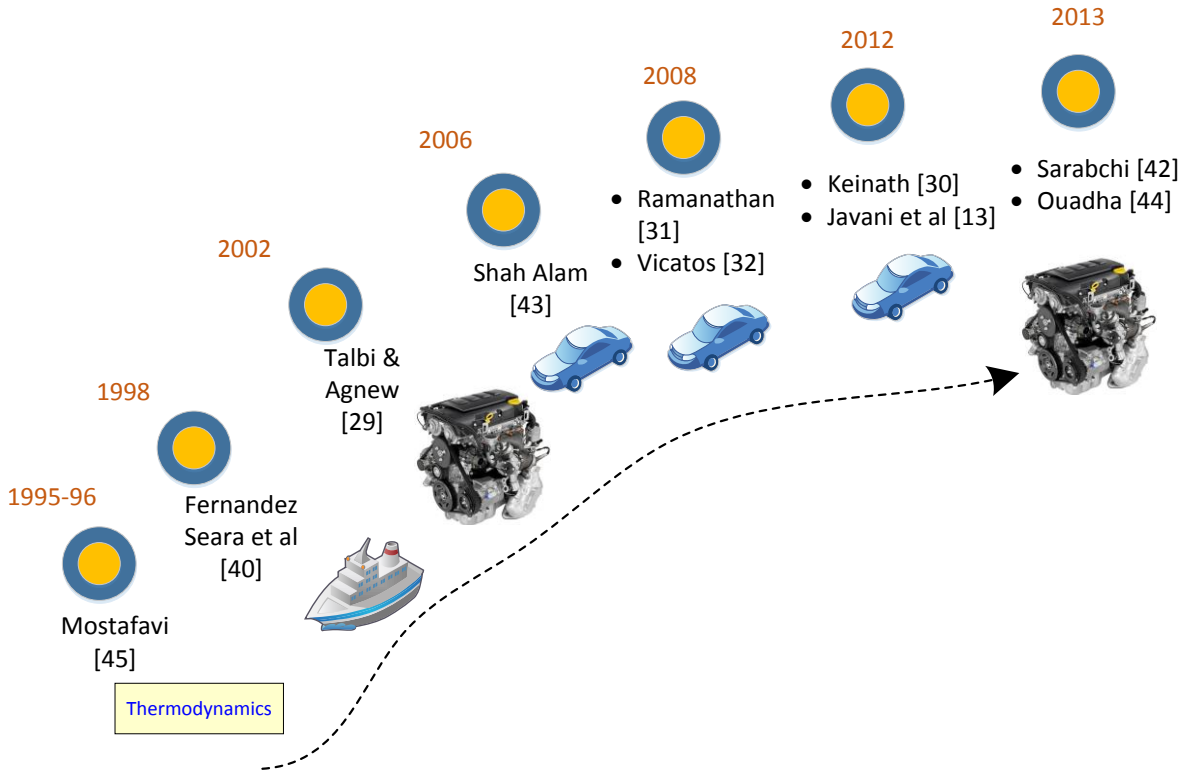

Figure 2.6: Timeline showing modelling research on VARS coupled to engine exhaust

Table 2.5: Summary of research activities carried out on coupling of engine exhaust with absorption refrigeration

Research group	Nature of work	Working pair	VARS unit details/ Application	Main focus points	Practical application on vehicle	Type of vehicle focused
Koehler et al [15]	Experimental	NH_3-H_2O	Complete unit / Refrigeration	Design of VARS components, coupling of engine exhaust with VARS, performance of VARS	Yes	Trucks
Horuz [33] Horuz & Callander [34]	Experimental	NH_3-H_2O	Complete unit/ Refrigeration	Integration of engine and VARS, effect on engine performance due to coupling with VARS	No	Trucks
Manzela et al [35]	Experimental	NH_3-H_2O	Complete unit / Refrigeration	Experimental integration of engine with commercially available VARS	No	Not specified
Khaled [36]	Experimental	NH_3-H_2O	Only desorber / air conditioning	Desorber design for automobile air conditioning	No	Not specified
Khaled et al [10]	Experimental	NH_3-H_2O	Complete unit / air conditioning	Prototype construction and study, Linkage of COP to other parameters	No	Not specified
Ismail Hilali [37]	Experimental	H_2O-LiBr	Complete unit/ air conditioning	Design of VARS components, coupling of engine exhaust with VARS, performance of VARS	Yes*	Trucks
Talom and Beyene [11]	Experimental	NH_3-H_2O	Complete unit / refrigeration or air conditioning	Integration of engine and VARS and system operation at part load and full load conditions	No	Not specified
Bux & Tiwari [38]	Experimental	H_2O-LiBr	Only desorber unit / air conditioning	Integration of diesel engine with plate heat exchanger desorber, engine performance study	No	Not specified
Boatto et al [26, 39]	Experimental	H_2O-LiBr	Complete unit / air conditioning	Engine performance characteristics, component layout on the vehicle	Yes	Passenger vehicle
Fernandez-Seara et al [40]	Modelling	NH_3-H_2O	Only desorber / Refrigeration	Heat recovery and desorber integration with trawler engine	No	Fishing trawlers

Talbi and Agnew [29]	Modelling	Not specified	Complete unit / Refrigeration	Heat recovery, availability of heat for VARS and also for engine pre-cooler and inter-cooler	No	Not specified
Keinath et al [30]	Modelling	NH_3-H_2O	Complete unit / air conditioning	Optimising operating conditions of the VARS, design of control system and modelling for small scale 2 kW cooling system	No	Not specified
Ramanathan and Gunasekaran [31]	Simulation	H_2O-LiBr	Complete unit / air conditioning	Use of engine exhaust heat to power VARS, specific consideration during engine idling	No	Mid-sized passenger car
Vicatos et al [32]	Theoretical analysis	NH_3-H_2O	Complete unit / air conditioning	Theoretical design of VARS components for automobile air conditioning system, verification of theoretical design with laboratory and road tests	Yes[#]	Mini truck
Javani et al [13]	Thermodynamic analysis	H_2O-LiBr	Complete unit / air conditioning	Air conditioning system based on VARS, comparison of thermal energy transfer from engine exhaust and cooling fluid used for battery cooling	No	Hybrid electric vehicles and pure electric vehicles
Sarabchi et al [42]	Modelling	NH_3-H_2O	Complete unit / Refrigeration	Coupling of Homogenous Charge Compression Ignition engine with AWCC, Exergy analysis	No	Not specified
Shah Alam [43]	Modelling	NH_3-H_2O	Complete unit / air conditioning	Integration of engine exhaust with three fluid vapour absorption system, availability of heat with throttle valve opening	No	Cars
Ouadha and El-Gotni [44]	Thermodynamic study	NH_3-H_2O	Complete unit / refrigeration and air conditioning	Integration of marine diesel engine with VARS, performance characteristics of VARS	No	Not specified
Mostafavi [28, 45]	Thermodynamic analysis	Not specified	Complete unit / air conditioning	Thermodynamic analysis of supercharged and naturally aspirated diesel engine with VARS, engine performance maps	No	Not specified

*Intended for truck applications but packaging on truck not carried out; [#] laboratory prototype developed

2.3.3 Discussion and analysis

From all these studies it is clear that the amount of thermal energy available from the engine exhaust, in most cases, is more than sufficient to cater to the cooling load requirements but only when the vehicle is cruising (above a certain speed), i.e between a certain minimum and maximum engine RPM (of that particular engine). In the idling scenario, the engine exhaust flow rate and temperature is low which results in insufficient heat input delivered to the VARS and a need for a back-up burner arises. Also the engine performance is greatly affected by coupling of the VARS to its exhaust; the back pressure generated at the engine exhaust has a negative effect on the engine performance. Another problem is the temperature incompatibility between the exhaust gas and the desorber and the corrosion effects on the desorber due to exhaust temperature level.

Hence, linking the absorption refrigeration unit with the internal combustion engine has its own set of problems. Every engine has a particular efficiency map and the highest efficiency is achieved at a particular RPM. Operation at RPMs and torque levels below this range will result in poor engine efficiency and increased fuel consumption. The absorption refrigeration system does not perform that well when the engine is idling and this might hinder the usage of thermally driven VARS for refrigerated trucks and automobile air conditioning based on engine exhaust heat

Two things also become clear from the work presented above with regards to application of VARS on vehicles. One, if the VARS is to be used for air conditioning then H_2O-LiBr is the preferred working fluid. If it is to be used for refrigeration then NH_3-H_2O is the working fluid to be employed. This is because sub-zero temperatures cannot be achieved when water is used as the refrigerant. Secondly, in many of the studies presented above, the coupling between the engine exhaust and the desorber is achieved via a separate fluid which then

delivers the required heat to the desorber at the right temperature. This mode of coupling will accomplish two things, one, reduce the back pressure effects on the engine and second, prevent corrosive effects of exhaust on the desorber. The use of an intermediate coupling fluid will result in additional components like pump and storage tank on the vehicle but the trade-off lies in better engine performance.

The throttle valve or the baffle position between the exhaust and the desorber plays a major role in the performance of the VARS. Most of the research papers recommend controlling the valve position in order to control the heat input to the desorber.

Koehler et al [15] made an assessment on the kind of terrain that will be best suited for a truck fitted with a VARS and concluded that it works best when driving on flat roads for long distances. This is because the engine RPM stays almost constant and the amount of heat supplied at the desorber also stays constant, thereby achieving a constant performance from the VARS. In city conditions as the engine has to idle a lot because of which the amount of heat delivered to the desorber is either not sufficient or is intermittent in nature which in turn affects the performance of the VARS. In mountainous terrain, once again the exhaust temperature varies a lot, reaching low values at some time and very high values at other times which affects the desorber performance and in turn the performance of the VARS as a whole. Hence, using engine exhaust heat to drive the VARS without back-up burners and adequate control mechanism can be quite challenging and unreliable.

Experimental research on prototype development of compact VARS on trucks has been virtually stagnant after 1998 as seen from Figure 2.5. Bespoke design and development stopped with Ismail Hilali's PhD thesis [37] and after that the research groups have just coupled commercially available products and evaluated their performance for suitability for implementation on automobiles. Hence individual component design, modelling and development for different types of vehicles for both air conditioning and refrigeration

applications is the way forward to qualify VARS as a replacement for VC units in areas where residual thermal energy is available.

2.4 Fuel Cells and VARS

Fuel Cells are devices that electrochemically convert fuel and generate both electricity and heat. In high temperature fuel cells, the heat generated is of high quality and by quality it means the amount of useful work that can be gleaned out of it is high. Heat generated as a by-product from fuel cells can be used as the driving force to operate VARS, thereby operating the fuel cell in a CCP (Combined Cooling and Power) and a CHCP (Combined Heating Cooling and Power) mode and this idea has been explored by many research groups. A summary of the activities carried out by different research groups in this field is outlined in this section. The literature on coupling of fuel cells with VARS is important to see if there are any key technological issues that need to be addressed when adapting fuel cell heat driven VAR technology to vehicles.

Zink et al [48] developed a concept for combining an SOFC system with a VARS based on the H_2O-LiBr working pair for providing heating, cooling and hot water for buildings. Their work mainly focussed on the modelling and simulation aspect of the whole system and comprised of three parts - an internal reformer model, an SOFC model and an absorption chiller model. They chose internal reforming over external reforming due to the fact that the former has higher efficiencies and faster load responses when compared to the latter. The SOFC model developed was based on a pre-commercial 110 kW tubular SOFC stack developed by Siemens-Westinghouse and the VARS model developed was based on a commercial H_2O-LiBr gas fired VARS unit available from Dalian Sanyo Refrigeration Co. Ltd.

All three models were developed and implemented using FORTRAN and the system architecture developed is shown in Figure 2.7.

The exhaust from the after burner unit (combustor) was used as the heat source in the desorber of the VARS. Their model had the capability to cater to the needs of space heating, cooling and providing hot water to a building of 9500 m^2 floor space and had an overall efficiency of 87% if both electricity and heat from the SOFC were utilised. They also stated that conventional VC systems are highly efficient when considered as a standalone unit however thermally driven refrigeration systems when combined with a fuel cell offer a higher overall system efficiency. Their conclusion was that although the combined system as a whole is technically feasible, economic considerations might hinder their implementation practically.

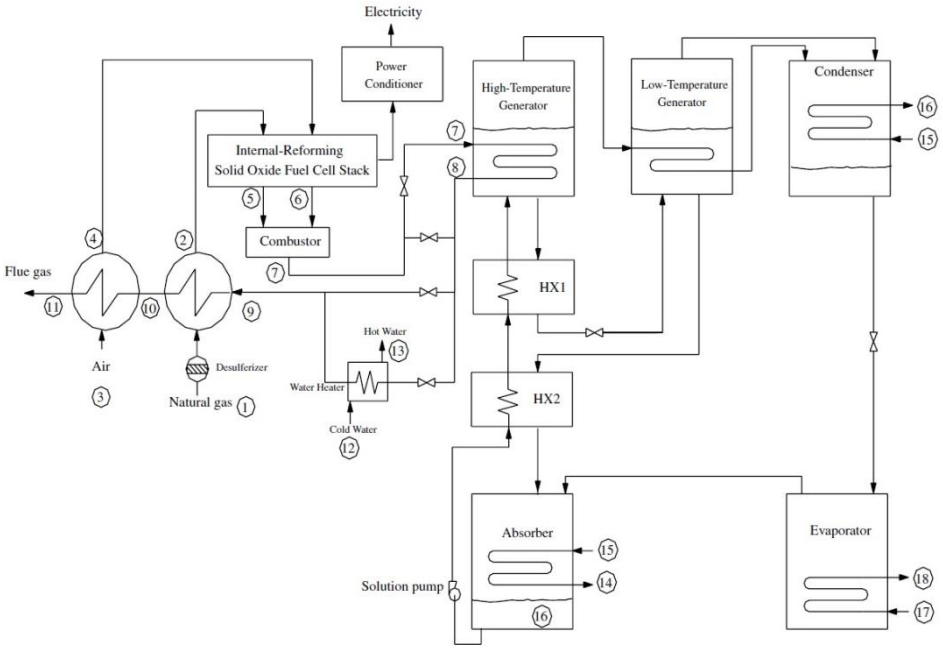

Figure 2.7: Combined SOFC-VAR system architecture [48]

Oshima et al [49] carried out a study on recovering FC exhaust to power a cooling system meant for telecommunication equipment. Their main focus was to look into different methods

of heat recovery from the fuel cell and draw appropriate conclusions on which heat recovery system was better.

The fuel cell used by them was a Phosphoric Acid Fuel Cell (PAFC) and they studied two different heat recovery methods - **mixed type heat recovery** and **separate type heat recovery**. The mixed heat recovery method involved combining the exhaust from the reformer and the cathode side of the PAFC and using the combined mixture in a heat exchanger to deliver the required quantity of heat to water which was then used as the coupling fluid in the desorber of the VARS. In the separate heat recovery method, the exhaust from the reformer and the cathode were used in separate heat exchangers to heat water and the heated water from these two separate heat exchangers was combined and then used in the desorber of the VARS. The total amount of heat recovered from the exhaust gases was calculated using sensible heat of the exhaust gas along with latent heat and sensible heat of the water vapour present in the exhaust gas. In both methods, the amount of heat recovered increased with decrease in exhaust gas temperature but the difference lay in the temperature of condensation of water vapour. The separate type heat recovery method had a higher temperature of condensation of water vapour due to increased partial pressure of water vapour. The reason for this was because the partial pressure of water vapour in the exhaust from the reformer was much higher than that in the exhaust from the cathode or, for that matter, in the combined reformer-cathode stream. So effectively a greater quantity of heat could be recovered at a higher temperature in the separate type heat recovery method. Based on the heat recovery data, the cooling capacity of the absorption refrigerator that used a separate type heat recovery method, at a source temperature between 65 and 85^{o} C, was about 2.5 times greater than the cooling capacity of the absorption refrigerator that used a fixed temperature heat source at 85^{o} C. No detailed information was provided by the authors on the type of absorption refrigerator or the components used in it.

Zeting Yu et al [50] developed a steady state mathematical model to simulate a TES (Total Energy System) comprising an SOFC and an absorption chiller in order to provide cooling, heating and power. The schematic developed by them for the total system is shown in Figure 2.8 and is akin to the system developed by Zink et al [48].

The mathematical model, developed on the Matlab platform simulates the performance of the TES and the SOFC under different operating conditions. Internal reforming was chosen over external reforming for the SOFC model because it has a higher efficiency and a faster load response. They validated their SOFC model with the data available for a tubular SOFC from Siemens Westinghouse. The developed model provided flexibility in varying certain operational parameters such as anode gas recirculation ratio, average current density, fuel utilization and SOFC cathode inlet gas temperature, however, the results presented discussed the effects of only current density and fuel utilisation.

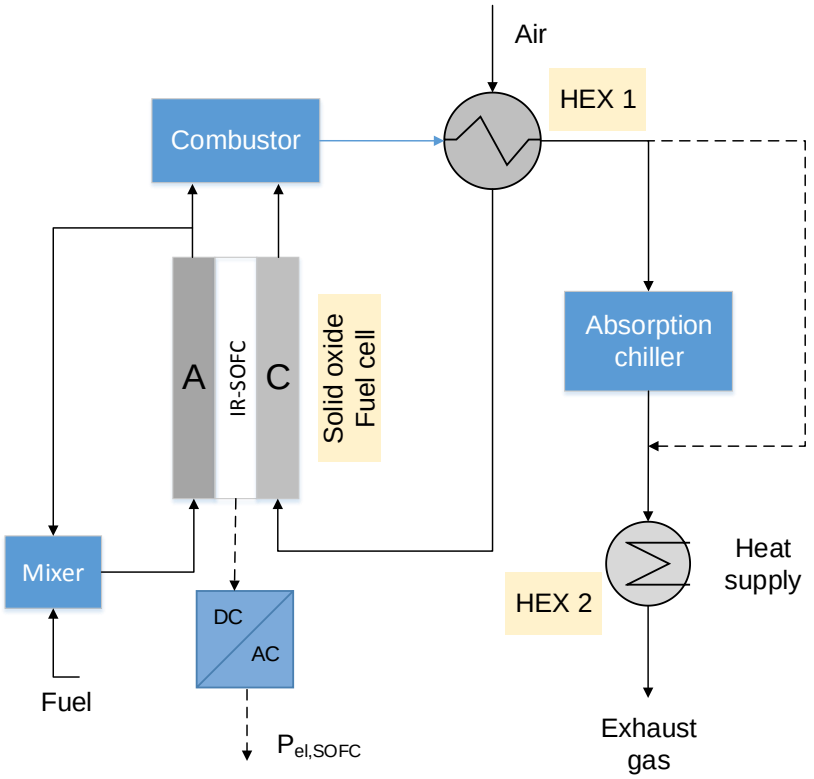

Figure 2.8: Schematic of TES comprising SOFC and absorption chiller [50]

With increase in current density, more heat is generated within the fuel cell and hence more heat has to be removed from it. This results in an increase in temperature of the exhaust stream and in turn increased heat input to the desorber of the VARS. Increased heat input to the desorber results in increased cooling output and thus increased cooling efficiency. However, the electrical efficiency of the fuel cell is reduced and this when combined with the cooling efficiency, reduces the total efficiency of the system. With an increase in fuel utilisation of the fuel cell, electrical efficiency and the total efficiency increase but the cooling efficiency decreases. This is because higher fuel utilisation results in lower combustion temperatures which lead to reduced heat input to the desorber and in turn reduced cooling output. A limit of 0.85 for the fuel utilisation was established beyond which the electrical efficiency did not increase but rather decreased.

As seen from the results above, electrical efficiency and cooling efficiency behave in a totally opposite manner when current density and fuel utilisation are varied. Hence a trade-off needs to be made between these two operational parameters of the SOFC depending on the application required. Once again no details were given about the absorption refrigeration unit or any of the heat exchangers used.

Another paper published by Zeting Yu et al [51] talks about a tri-generation system comprising an SOFC and a double stage absorption chiller, to provide combined cooling, heating and power. Their combined system could produce an electrical power of 339 kW along with 303.6 kW of cooling and 267 kW of heating, consuming about 40.2 g s^{-1} of fuel and 672 g s^{-1} of air. The fuel for the SOFC was derived from a gasification process and was internally reformed although external reforming is also possible. Through their simulations they showed that a CCP (Combined Cooling and Power) efficiency of 89 % and a CHP (Combined Heating and Power) efficiency of 84 % could be achieved. Similar to their previous paper, this paper also talks about the effect of different SOFC parameters on the performance of the whole system. The coupling between the SOFC stack and the absorption

chiller was achieved via HRSG (Heat Recovery Steam Generator) where saturated steam is generated and used to drive the high temperature desorber of the double stage VAR unit.

Darwish [52] proposed using a Phosphoric Acid Fuel Cell (PAFC) in combination with both VC system and VARS unit, to cater to air conditioning needs of buildings in Kuwait. They also proposed having a cold storage system as a buffer so that air conditioning needs during peak times can be met however they stated that there was no current expertise in the field of cold storage systems in Kuwait and hence the air conditioning needs had to be met by the VC and VARS units working together. This kind of integrated system was proposed to reduce the dependence on grid electricity for large buildings and instead employ small distributed generation units for each building. The PAFC chosen was a commercially available ONSI P24 with a nominal capacity of 200 kW_e. This came with a standard heat exchanger in the BoP (Balance of Plant) capable of supplying hot water at a temperature of 70 ^oC, but to integrate the VARS another high temperature heat exchanger had to be added to the system architecture. The chosen VC system had a maximum cooling capacity of 500 kW and the VARS unit had a maximum cooling capacity of 73.5 kW, hence put together they were able to cater to a cooling load of 573.5 kW. For the reference building of 1557 m^2, the maximum cooling load required during the hottest month of the year and during the hottest time of the day was around 569.5 kW. Hence the integrated PAFC-VC-VAR system was able to cater to the maximum cooling load at any time.

Waragai et al [53] studied the characteristics of an absorption refrigerator driven by PAFC exhaust heat. The application of the absorption refrigerator was specifically for telecommunication equipment cooling which requires a cooling system working continuously. Two different ways of heat recovery from the PAFC stack were proposed. One from the exhaust gases of the PAFC and the second from the coolant that is circulated through the stack. If the stack is operated at a specific rating then the amount of heat recovered from the coolant stays constant. In recovering heat from the PAFC's exhaust gases, the temperature

at which water condenses plays a crucial role. A brief discussion of this was presented above in Oshima et al's work [49]. The VARS employed was a combination of single stage and double stage configurations (based on H_2O-LiBr working pair) where a high temperature desorber and a low temperature desorber were employed and a working prototype was built. Steam generated by recovering heat from the coolant was supplied to the high temperature desorber (~160 ^oC) and hot water generated by recovering heat from the PAFC's exhaust gases was supplied to the low temperature desorber (65-85 ^oC).

For year round operation of the VARS, the cooling water temperature at the absorber and condenser was set to 15 ^oC. This value was derived considering the effect that cooling water has on both COP and the concentration of solution. Reduction in cooling water temperature increased the COP but decreased the concentration of the solution. Also, from the design map it was found that a low temperature heat source can be used for the VARS if the cooling water temperature is reduced. The other parameters affected by cooling water temperature are cooling performance, desorber/condenser pressure and absorber/evaporator pressure. Cooling performance increases whereas desorber and absorber pressure decreases with decrease in cooling water temperature.

They also tested the absorption refrigerator in two modes. In the first only steam was used as the heat source in the desorber and in the second both steam and hot water were used as heat source. Operation in both modes was successful, the only difference being in the amount of cooling generated, the latter generating more cooling than former due to the use of two heat sources (50 kW from the former and 65 kW from the latter). Also, the COP was around 1.5 for the double stage cycle and just 0.5 for a single stage cycle. The hot water used in the low temperature desorber was heated by the fuel cell's exhaust stream. Technically, its temperature should depend only on the quantity of heat that the fuel cell exhaust can transfer but in reality the cooling water temperature used in the VARS also affected the temperature of the hot water. A decrease in the cooling water temperature

decreased the temperature of the hot water and in turn the heat transfer capacity to the low temperature desorber, the graph obtained by them for the above statement is shown in . It was concluded that it is best to operate the VARS unit as a double stage unit with both steam and hot water as heat sources. This increases the cooling performance by 50% when compared to a single stage single heat source VARS unit.

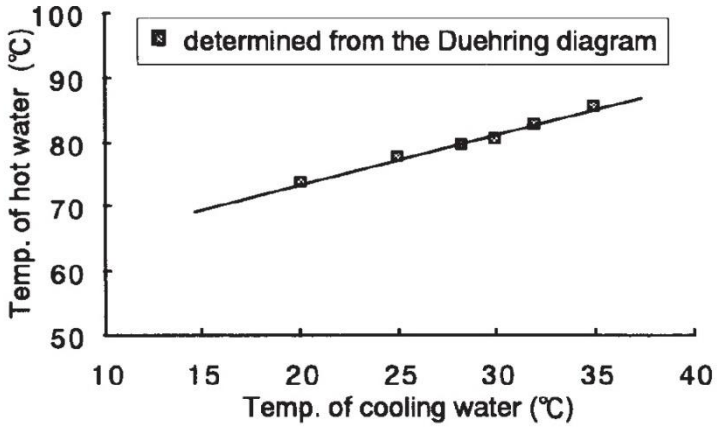

Figure 2.9: Temperature of hot water supplied to low temperature desorber [53]

Ishizawa et al [54] just like Waragai et al [53], integrated a 200 kW PAFC with an absorption chiller and the application of this combined system was to provide electricity for powering telecommunication equipment and to cool the room where it was kept. They tested the combined system in the field at two locations - the NTT Yokohama branch and the NTT Kansai centre in Japan.

The main focus of their study was recovery of heat in the temperature range of 80-85 ^{o}C from FC exhaust gases using suitable heat exchangers and also recovery of water from the exhaust gases in order to supply water to the cooling system of the PAFC. For heat recovery from the PAFC exhaust gases they employed a shell and tube heat exchanger (the coupling fluid being water) and for water recovery from the exhaust gases they used a DCC (Direct Contact Cooler). They employed a double stage absorption chiller and guessing by the application, it is believed that a H_2O-LiBr working pair was used. The heat recovered from

the PAFC coolant was transferred to the high temperature desorber and the heat recovered from the exhaust gases (through the coupling fluid) was transferred to the low temperature desorber. Recovery of heat from the FC exhaust gases was critical during winter time because a higher input temperature was needed at the low temperature desorber.

Their main conclusions were that the amount of heat recovered and the amount of water condensed from the exhaust gases increased if the inlet temperature of the water supplied at the shell and tube heat exchanger was reduced and this in turn depended on the ambient temperature where the cooling towers of the absorption chiller were placed. On the whole, they were able to achieve a heat recovery between 26-38 % combined, from both the PAFC coolant and the PAFC exhaust gases, and were able to operate the absorption chiller all year round even during peak summer.

Sevencan et al [55] carried out an economic study on the use of an MCFC coupled with a VARS for data centre cooling and concluded that the system was not economically feasible due to high capital and Operational & Maintenance costs and also that the lifetime of the current MCFC stacks is too short. This was a pure economical study and no technical details besides the type of the MCFC (DFC300 from Fuel Cell Energy) were provided.

Yang et al [56] modelled a hybrid system that comprised of a PAFC and an absorption refrigerator and mapped out general performance characteristics and optimum design criteria for the hybrid system.

The power density from the hybrid system reached its maximum at a higher current density than the individual systems. Also, the hybrid system's power density was higher than the individual PAFC system's power density by 2.6 % which implied that it was better to operate the PAFC in a hybrid configuration rather than as a standalone fuel cell unit. In the above context they defined power density as the amount of power produced per bi-polar plate area of the fuel cell. The power was pure electrical if the PAFC alone was operated and was a

combination of electrical and thermal if the PAFC was operated in a hybrid mode. They also identified a critical minimum current density of 0.05 A cm^{-2} for the PAFC above which the absorption refrigerator started to cool the refrigerated space and a maximum current density of 0.88 A m^{-2} above which the power density of the hybrid system began to drop. The efficiency of the hybrid system decreased continuously with current density although for the entire current density range it was higher than the individual PAFC unit. Besides specifying the current density, parametric studies were carried out for the operation of the hybrid system with variations in operating and functional parameters of the PAFC such as temperature, pressure, thermodynamic losses, and phosphoric acid concentration. They concluded that temperature and pressure of the PAFC had the highest influence on the operation of the hybrid system. No details on PAFC sizing, the method of heat recovery, thermal coupling with the absorption refrigerator or the components of the absorption refrigerator were provided.

Weber et al [57] focussed on decentralised energy generation for buildings in Tokyo, Japan, using an SOFC and coupling it to an absorption chiller for providing cooling/heating for buildings. They chose a double stage absorption chiller based on a H_2O-LiBr working pair because the main purpose of the absorption chiller was to provide air conditioning and not refrigeration, and the absorption chiller was powered by the exhaust gas coming from the combustor employed in the SOFC BoP (Balance of Plant). Their main findings were that a 30 % reduction in CO_2 emissions can be achieved when employing an SOFC-VARS system when compared to the conventional case but with a cost increase of almost 70%. They also found that a completely decentralised system with a VARS alone was not possible and an electric chiller needed to be incorporated to cater to the deficiency in cooling/heating load because the sized SOFC for the building could not supply enough exhaust gas to the absorption chiller.

Margalef and Samuelsen [58] integrated an MCFC (Molten Carbonate Fuel Cell) with an absorption chiller for a commercial building and stated that a high value market exists for such hybrid configurations in the distributed generation and CHCP (Combined Heating Cooling and Power) market. They modelled the MCFC based on the data available from a commercially available product, the *DFC300MA* manufactured by *FuelCell Energy* and also a commercially available absorption chiller from *Yazaki CH4040-KE*. Their integrated system could produce 300 kW of electrical power and 40 ton (140.7 kW) of refrigeration. The desorber in the refrigeration unit utilised the high temperature exhaust from the MCFC but also had provisions for another high temperature desorber which burned natural gas in case the thermal energy supplied by the MCFC exhaust was not sufficient. The VARS had a dual fired desorber, powered by exhaust and natural gas burner and employed H_2O-LiBr as the working pair.

They identified two critical issues that might pose problems when integrating the two systems. One issue was the '*cold end corrosion*' when acid and water vapour in the hot flue gases coming from the combustor of the fuel cell BoP might condense on the cooler end of the desorber of the absorption chiller and lead to its corrosion and eventually failure. The second issue was the crystallisation of the LiBr solution when the mass fraction of LiBr exceeded its solubility limit in water. In order to cater to the above issues, they employed the following three strategies to integrate the MCFC exhaust with the absorption chiller. The first strategy was to use the MCFC exhaust directly, the second was to blend it with ambient air at 25 ^{o}C, and the third was to blend it with the chiller exhaust gas (which is approximately 120 ^{o}C). Their main findings were that although the first strategy produced satisfactory results it is better not to employ it because when the MCFC exhaust is used directly as the heat source, there might be some temperature mismatch thereby leading to ineffective operation of the absorption chiller. Also, the absorption chiller manufacturer did not recommend using the MCFC exhaust at such high temperatures directly. In the second

strategy, the exhaust mass flow rate was increased but the temperature of the exhaust was reduced due to mixing in of air at 25 ^{o}C. This affected the chiller performance, nevertheless it was still higher than the first strategy. The last strategy was the best amongst the three because blending the MCFC exhaust with the chiller exhaust not only increased the mass flow rate but also did not allow the exhaust temperature to drop too much which led to increased chiller performance.

Arsalis [59] carried out modelling and simulation studies to integrate a 100 kWe HT-PEFC (with cell active area of 605 cm^2) subsystem with an absorption chiller for a commercial ship/container vessel. They employed a special thermal oil to cool the HT-PEFC stack and routed this to the desorber section of the VARS. A total of 107 kW of heat could be recovered from the fuel cell. They modelled two kinds of absorption chiller for system integration - a double stage type with H_2O-LiBr as the working pair and a single stage type with NH_3-H_2O as the working pair. The former could satisfy a cooling load requirement of 128.2 kW and the latter a cooling load requirement of 64.5 kW. Their proposed design was very simple where the coolant from the fuel cell was circulated to the desorber of the VARS and then back to the fuel cell. No specifics were given on the heat exchangers/ equipment used between the HT-PEFC and the VARS.

Pilatowsky et al [60] carried out simulation studies to work out the optimum operating conditions needed to run an air conditioning system based on an absorption refrigeration cycle using heat from a PEFC. The working pair employed in the absorption refrigeration cycle was monomethlyamine-water (MMA-WS). They found that COP values rose with an increase in desorber temperature, reached a maximum, and then dropped with further increase in desorber temperature. This trend in COP variation was replicated for different evaporator temperatures as well. The highest COP that could be achieved was 0.57 at a desorber temperature of 60^{o} C and an evaporator temperature of 10 ^{o}C, and the lowest COP was 0.23 at a desorber temperature of 80^{o} C and an evaporator temperature of -10 ^{o}C. It was

also found that the COP of the VARS decreased with increase in electrical power of the PEFC although the cooling power increased with increase in electrical power. With 1500 W of electrical power produced from the PEFC stack, 536 W of cooling could be generated when the desorber temperature was 60 ^{o}C, and 401 W of cooling when the desorber temperature was 80 ^{o}C. In order to operate the VARS with a high COP, desorber temperatures between 60 and 65 ^{o}C and evaporator temperatures between 5 and 10 ^{o}C were recommended. Evaporator temperatures in this range are quite sufficient for air conditioning purposes. Although not specified explicitly, it could be inferred from their block diagram that the thermal coupling between the PEFC and the VAR unit was achieved via a thermal storage tank, the heat being supplied by the coolant used in the PEFC and the hot water generated as a result was used as the heat transfer fluid in the desorber. Details or sizes of the heat exchangers employed in the system were not specified.

A peculiar aspect of their design with regards to the absorption chiller was that the temperature needed for driving the desorber was in the range of 60-80 ^{o}C. This could be attributed to the different refrigerant-absorbent working pair used in this VARS.

Frimodt and Mygind [61] studied '*Integration of Solid Oxide Fuel Cells and Absorption Cooling Units*'. They first carried out a market study for implementing such a system and narrowed down on two areas where it can be effectively used viz. APUs for ships (providing both power and cooling) and distributed generation units for hotels. Among the two applications they chose the latter. They developed a thermodynamic model for the whole system using Engineering Equation Solver and the absorption unit was designed as a double stage chiller with H_2O-LiBr as the working pair. All components were modelled as black boxes or as '0D' models where the energy and mass flows entering and leaving the system were identified. They also found that the SOFC-VARS unit was able to run effectively in very hot climates only if the humidity was low (dry climates). If the humidity was very high then the system was not able to run effectively at high ambient temperatures, the ambient

temperature being restricted to 33 ^{o}C. They also found a relation between the desorber temperature and ambient temperature. If the ambient temperature was below 20 ^{o}C then temperature at the desorber could be restricted to 150 ^{o}C and a dry cooling tower can be employed. If the ambient temperature exceeded 20 ^{o}C then either a wet cooling tower was necessary or the desorber temperature had to be increased to 190 ^{o}C. A final statement was that a complete market and economic study was essential before implementing an SOFC-VARS unit at any place.

Another piece of research on modelling and simulation of a high temperature fuel cell with an absorption chiller was carried out by Sarah Marie Martz [62]. Once again the combined system was designed to cater to the cooling and electrical load requirements of a commercial/institutional building. The fuel cell used was an MCFC and the absorption chiller modelled was based on the H_2O-LiBr working pair. A steady state and a dynamic model of the absorption chiller were established. Aspen Plus was used as a platform for carrying out the steady state simulations and Matlab/Simulink was used as a platform for carrying out dynamic simulations. No modelling of the MCFC was carried out but a detailed system integration strategy with the building and a thermal load following model was designed.

Two pieces of modelling work [63, 64] focussed on integration of SOFC-CHP systems into existing power plants to increase the overall efficiency of the power plant and at the same time also cater to the cooling and heating needs of the power plant. In the former, a combined SOFC gas turbine power plant-VARS-Rankine cycle was analysed both from an energy and exergy point of view and the optimal design conditions were established by carrying out a sensitivity analysis by varying key variables of the system. An economic study was also carried out for optimal design of the whole process. More emphasis was placed on the process itself rather than individual component design. In the latter, an SOFC-VARS system was integrated with a coke generating power plant whose residual fuel COG (Coke Oven Gas) was reformed and used in the SOFC. Once again the performance criteria and

the main factors influencing system performances were analysed. Both these papers provide insights into power plant design and system evaluation but give very little information on the kind of heat exchangers used for the VARS.

Table 2.6 summarises the research work done on coupling of fuel cells with VARS and lists the main application of VARS in system integration.

Table 2.6: Summary of research on coupling of fuel cells and VARS

Research group	Type of fuel cell used	Nature of work	VARS details/working pair	Main focus points of the paper	Application of VARS	Area considered for system implementation
Zink et al [48]	SOFC	Modelling	Double stage complete unit/ H_2O-LiBr	System integration studies, economic and environmental issues related to the system implementation	Space cooling/ heating	Buildings
Kazua Oshima et al [49]	PAFC	Simulation	Not specified	Types of heat recovery from the fuel cell for integration with VARS	Space cooling	Telecommunication equipment cooling
Zeting Yu et al [50]	SOFC	Modelling	Double stage Complete unit/ H_2O-LiBr	Study of effect of different SOFC operational parameters on the absorption chiller	Space cooling	Tri-generation for buildings
Darwish [52]	PAFC	Modelling	Single stage Complete unit/ H_2O-LiBr	Feasibility study of coupling fuel cell unit with VARS, idea of VARS supplementing the current VC system for buildings, distributed power generation for buildings	Space cooling	Buildings
Waragai et al [53]	PAFC	Working prototype	Single stage & double stage Complete unit/ H_2O-LiBr	System integration, heat recovery from PAFC, evaluation of cooling water temperature on VARS and the fuel cell	Space cooling	Telecommunication equipment cooling
Ishizawa et al [54]	PAFC	Working prototype	Double stage Complete unit/ H_2O-LiBr	Heat recovery from PAFC, operation of VARS for the whole year	Space cooling	Telecommunication equipment cooling
Sevencan et al [55]	MCFC	Economic analysis	Double stage Complete unit / H_2O-LiBr	Economic feasibility study for system implementation	Space cooling	Data centres

Yang et al [56]	PAFC	Modelling	Single stage Complete unit/ H_2O-LiBr	Operation of fuel cell with VARS in hybrid mode, effect of operational and functional fuel cell parameters on system performance	Not specified, but should be for space cooling	Stationary application
Weber et al [57]	SOFC	Modelling and socio economic studies	Double stage Complete unit/ H_2O-LiBr	Decentralised system for buildings based on SOFC, calculation & comparison of emissions from conventional and SOFC based systems	Air conditioning	Buildings
Margalef & Samuelsen [58]	MCFC	Modelling	Double stage Complete unit/ H_2O-LiBr	Coupling of MCFC exhaust with absorption chiller, Thermal integration strategies between the two systems	Cooling and heating	Buildings
Arsalis [59]	HT- PEFC	Modelling	Single stage Complete unit with both H_2O-LiBr and NH_3-H_2O	System integration, system matching, comparison to conventional systems	Cooling	Ship
Pilatowsky et al [60]	PEFC	Simulation	Single stage Complete unit/ monomethlyamine-water	Feasibility of using PEFC for cogeneration process, system integration	Air conditioning	Not specified
Frimodt & Mygind [61]	SOFC	Modelling	Double stage Complete unit/ H_2O-LiBr	Market study, system integration, system modelling, economic studies	Air conditioning	Buildings
Sarah Marie Martz [62]	MCFC	Modelling	Double stage Complete unit/ H_2O-LiBr	Steady state and dynamic modelling of VARS, system integration with MCFC, system operation and control	Air conditioning	Buildings
Mehrpooya et al [63]	SOFC	Modelling	Single stage Complete unit/ NH_3-H_2O	Power plant design optimization, incorporation of VARS and rankine cycle for additional benefits	Not specified	Power plant
Zhao et al [64]	SOFC	Modelling	Single stage Complete unit/ H_2O-LiBr	Use of Coke Oven Gas to run SOFC, system integration of SOFC & VARS, optimal design parameter evaluation	Power plant cooling needs	Power plant

2.4.1 Discussion and analysis

The following general observations can be made from the summary of the research work presented above:

i) Almost all the work related to coupling of fuel cells with VARS pertains to using the system for stationary applications either in buildings or for telecommunication equipment data centres. Only one paper [59] has talked about using it for mobile applications. This implies that most of the systems are designed for distributed generation, having additional features of providing cooling and heat. This is totally understandable because high temperature fuel cells are mainly used for stationary applications.

ii) The VARS in most of the cases is based on the H_2O-LiBr working pair and is designed as a double stage unit. As mentioned earlier, double stage VAR units have a higher COP than single stage VAR units but use more components, thereby increasing system complexity and weight. For stationary applications this is not much of a problem as the volume footprint is not too much of an issue.

iii) The use of NH_3-H_2O as the working fluid is not considered and this could be due to two reasons. The first being the impossibility of building a double stage VARS due to the need for extremely high system pressures and the second reason being the need for relatively high evaporator temperatures between 15 and 20^o C for air conditioning purposes which can easily be met by the H_2O-LiBr working pair.

iv) The preferred choice of fuel cell turns out to be either PAFC or SOFC in the literature presented above although an MCFC would also be equally suitable. An MCFC is generally not used on vehicles because for two reasons: first they have a molten carbonate electrolyte which is prone to leaching due to vibrations and second they are not manufactured in small kW ranges. Between the SOFC and PAFC, an SOFC

works at very high temperature (700-800 ^{o}C) and PAFC works between 150 and 200 ^{o}C. As seen from Table 2.6, all VAR systems that are integrated with a PAFC are used for air conditioning purposes; hence the temperature at which thermal energy is supplied from the PAFC is sufficient to run an air conditioning system. On the other hand, in an SOFC the quality of residual heat available is excellent and thus provides sufficient thermal energy to drive the VARS for both air conditioning and refrigeration purposes. Also scaling down the quantity and quality of heat is easy when high temperature fuel cells are involved although care must be taken in choosing suitable materials for heat exchangers employed for high temperature operation. From the literature presented on coupling of fuel cells with VARS, the bar chart in Figure 2.10 shows the number of research groups who have employed different kinds of fuel cells for integration with VARS.

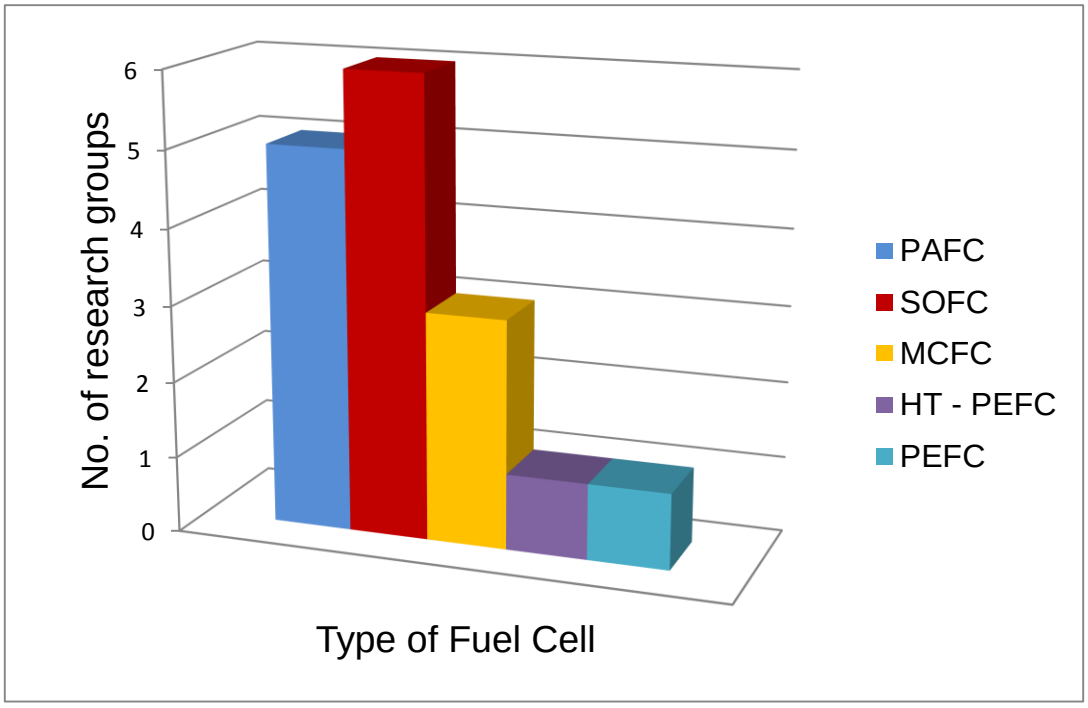

Figure 2.10: Fuel cell used by different research groups for integration with VARS

v) The method of heat recovery is crucial for system integration. Some of the research groups like Zink et al [48] and Pere Margalef [58] have employed direct exhaust gas coupling at the desorber. This method of thermal coupling might pose some challenges: first it might lead to corrosion at the cold end of the desorber and second the desorber design itself might be too large in terms of volume, warranting more heat transfer area because the exhaust gas has a low thermal capacity. Other research groups have used a thermal coupling fluid, mainly water [49, 52, 59, 60] which is heated either by the fuel cell exhaust gas or by the fuel cell coolant loop.

vi) Design maps for operation of the fuel cell in terms of current density and other parameters are not presented in the literature except for Zeting Yu [50] and Puquing Yang [56] . These two groups mention some details but the data presented is not sufficient. Hence there is need to further identify the operating point of the fuel cell on the polarisation curve for optimal thermal energy generation in a CHP or CHCP application.

vii) When compared to the heat available from the engine exhaust, which is intermittent in nature depending on the engine RPM, the heat available from the fuel cell is constant and thus the VARS operation can be relatively constant as well. This gives fuel cells an advantage over the internal combustion engine. Also by varying the operating point of the fuel cell, the amount of heat generated can be either increased or decreased.

viii) None of the systems discussed above have employed VARS for refrigeration purposes. Refrigeration sometimes requires sub-zero temperatures and space cooling in buildings does not. The cooling load is directly proportional to the evaporator temperature, hence sub-zero temperatures require a higher cooling load.

2.5 Fuel cells with VARS on vehicles

In the recent decade there has been an increasing interest on adoption of fuel cells in automobiles in order to make them more environmental friendly and to replace the conventional diesel engines. Fuel cells on board the vehicle have been used both as part of the power train and as an APU (Auxiliary Power Unit). Increasing electrical demand especially on large trucks has necessitated the implementation of APUs in order to reduce the load on the main diesel engine. SOFCs fit into this category because they can run on reformed diesel and are much more efficient than the diesel engine operating in idle mode. Some of the major players involved in developing SOFC APU's especially for heavy duty trucks include Delphi, AVL, Cummins Power Generation, and Eberspacher. Besides the activity carried out by major players other researchers have also looked into the prospect of using fuel cell auxiliary power units for trucks. Their research activity and findings can be accessed through the following references [65-70] and is not summarised here for reasons of brevity.

Other than a few patents [71-74] there is no published literature available on the use of heat from a fuel cell to drive the VARS on vehicles for either air conditioning or for refrigeration. Also in these patents, only the concept and block diagram of a fuel cell heat driven refrigeration system is presented. No specifics on the system size, component design or other vital design information are presented. Hence it remains unclear if such a system exists only on paper as a concept or can it be practically realised.

One may argue that replacing the engine exhaust with the exhaust from a high temperature fuel cell will solve the issue but the lack of literature on this specific topic shows that nobody has studied in detail the integration of a fuel cell with a vapour absorption refrigeration unit on trucks or for that matter on any vehicle. Sizing of the fuel cell, effect of functional and

operational parameters of the fuel cell on the VARS and on the fuel cell itself are some of the design criteria that need deeper analysis. If the fuel cell is employed on the vehicle, design consideration should be given towards the operating point of the fuel cell i.e. should the fuel cell be operated for maximum electrical efficiency or should a balance be achieved between the thermal and electrical energy generated within it. Also the fuel cell exhaust flow strongly depends on the fuel utilisation factor and the fuel utilisation factor also affects the performance of the fuel cell, hence some design maps would be vital in deciding the operating point of the fuel cell.

System integration of SOFCs with VARS on trucks and development of compact VARS could be an entirely new research area where more information is needed. This thesis provides the starting point for looking into this by taking possible cues and learnings from *sections 2.4* and *2.5*.

2.6 Outlook

As seen from the literature presented above, commercially available small scale VAR systems for mobile/automotive applications are very scarce. The idea of having a compact heat driven refrigeration system for trucks and other mobile applications is fascinating but in order to develop and implement it an altogether different approach needs to be taken. The problem is most research groups either try to use the off-the-shelf available VARS units or try to scale down design of large components meant for stationary applications to the required size. Both of these approaches will not work because for a mobile application a compact VARS with a volume foot print akin to the VC system is required and that requires bespoke design of compact high performance components.

Modelling and simulation followed by prototype construction is the way forward but the modelling aspect needs to be extended a bit further other than mass and energy flows. The overall system model for any application provides critical insights however it must be supplemented by detailed component level modelling and design as well. The modelling approach without design specification of the VARS components creates a void with respect to the technical feasibility of the concept. A grey area is created especially where small scale systems are involved and this warrants more research.

If absorption refrigeration systems have to be mounted and integrated on the vehicle then each part of it must be designed with proper geometrical and functional characteristics. This is because space is a major constraint on vehicles. Another important aspect is the presence of acceleration and vibration. Instability problems should be taken into due consideration with regards to those components such as the absorber and the desorber in which fundamental processes take place. Also appropriate operational maps for the fuel cell and effective heat recovery methods need to be designed.

Development of small scale VARS units that could run effectively using heat from the SOFC exhaust or any high temperature fuel cell exhaust could potentially find use in a wide variety of applications. Replacement of VC units with VARS units running off residual thermal energy available from the vehicle will aid in the use of refrigerants that have lower Global Warming Potential (GWP) and also pave the way for using valuable electrical energy needed for the compressor today for other purposes.

Bibliography

1. Tassou S.A, et al., *Erratum: Energy demand and reduction opportunities in the UK food chain.* Proceedings of the Institution of Civil Engineers - **Energy**, 2015. **168**(1): p. 74-74.
2. *Global cold chain news- UK temperature controlled-transport market booms*, Dean Stiles and S. Nash, Editors. 2011.
3. Gerald Cavalier and Savaas Tassou, *Sustainable Refrigerated Road Transport*. 2011, International Institute of Refrigeration: Paris, France.
4. Zoe Bengherbi, et al., *Liquid Air on the European Highway- The economic and environmental impact of zero-emission transport refrigeration*. 2015, Dearman.
5. James S.J and James C, *The food cold-chain and climate change.* **Food Research International**, 2010. **43**(7): p. 1944-1956.
6. van den Engel A.W, *Driving restrictions for heavy goods vehicles in the European Union*. July 2010, European Commission: Zoetermeer.
7. www.epa.vic.gov.au, *Noise control guidelines*. October 2008: Melbourne.
8. *http://about-france.com/hgv.htm (last accessed 13 July 2007)*.
9. Tassou S.A, De-Lille G, and Ge Y.T, *Food transport refrigeration – Approaches to reduce energy consumption and environmental impacts of road transport.* **Applied Thermal Engineering**, 2009. **29**(8–9): p. 1467-1477.
10. Khaled A, Alsaqoor S, and Al-Jarrah A, *Design and Fabrication of Auto Air Conditioner Generator Utilizing Exhaust Waste Energy from a Diesel Engine.* **International Journal of Thermal and Environmental Engineering**, 2011. **3**(2): p. 87-93.
11. Talom H.L and Beyene A, *Heat recovery from automotive engine.* **Applied Thermal Engineering**, 2009. **29**(2–3): p. 439-444.
12. Lambert M.A and Jones B.J, *Automotive Adsorption Air Conditioner Powered by Exhaust Heat. Part 1: Conceptual and Embodiment Design.* Proceedings of the Institution of Mechanical Engineers, **Part D: Journal of Automobile Engineering**, 2006. **220**(7): p. 959-972.
13. Javani N, Dincer I, and Naterer G.F, *Thermodynamic analysis of waste heat recovery for cooling systems in hybrid and electric vehicles.* **Energy**, 2012. **46**(1): p. 109-116.
14. Barnitt R.A, et al., *Emissions of Transport Refrigeration Units with CARB Diesel, Gas-to-Liquid Diesel and Emissions Control Devices*. 2009, **SAE Technical Paper**.
15. Koehler J, et al., *Absorption refrigeration system for mobile applications utilizing exhaust gases.* **Heat and Mass Transfer**, 1997. **32**(5): p. 333-340.

16. Mei V.C, Chen F.C, and Kyle D.M, *Alternative Non-CFC mobile air conditioning*. 1992, Oak Ridge National Laboratory - Energy Division.
17. Ryan O' Hayre, Suk Won Cha, Whitney Colella, Fritz B. Prinz, *Fuel Cell Fundamentals*. Second Edition ed. 2009: John Wiley & Sons.
18. He Z, et al., *Thermodynamic properties of new heat pump working pairs: 1,3-Dimethylimidazolium dimethylphosphate and water, ethanol and methanol.* **Fluid Phase Equilibria**, 2010. **298**(1): p. 83-91.
19. She X, et al., *A novel low-grade heat-driven absorption refrigeration system with LiCl–H2O and LiBr–H2O working pairs.* **International Journal of Refrigeration**, 2015. **58**: p. 219-234.
20. Tora E.A.H., *Computer-aided design and simulation of working fluid pairs for absorption refrigerators.* **International Journal of Scientific & Engineering Research**, 2013. **4**(4): p. 1306-1310.
21. Zohar A, et al., *Performance of diffusion absorption refrigeration cycle with organic working fluids.* **International Journal of Refrigeration**, 2009. **32**(6): p. 1241-1246.
22. Flores V.H, Roman J.C;, and Alpirez G.M, *Performance analysis of different working fluids for an absorption refrigeration cycle.* **American Journal of Environmental Engineering**, 2014. **4**(4A): p. 1-10.
23. Vijayaraghavan S. and Goswami D.Y, *Organic Working Fluids for a Combined Power and Cooling Cycle.* **Journal of Energy Resources Technology**, 2005. **127**(2): p. 125-130.
24. Labus J., *Modelling of small capacity absorption chillers driven by solar thermal energy or waste heat*, in *Mechanical Engineering*. 2011, Universitat Rovira I Virgili: Tarragona.
25. Kang H, Ahn H, and Min K, *Smart cooling system of the double loop coolant structure with engine thermal management modeling.* **Applied Thermal Engineering**, 2015. **79**: p. 124-131.
26. Boatto P, et al., *Internal combustion engine waste heat potential for an automotive absorption system of air conditioning Part 2: The automotive absorption system.* Proceedings of the Institution of Mechanical Engineers, **Part D: Journal of Automobile Engineering**, 2000. **214**(8): p. 983-989.
27. Ashby B.H, *Protecting perishable foods during transport by truck*. 2008, United States Department of Agriculture, Agricultural Marketing Service.
28. Mostafavi M and Agnew B, *Thermodynamic analysis of combined diesel engine and absorption refrigeration unit—naturally aspirated diesel engine.* **Applied Thermal Engineering**, 1997. **17**(5): p. 471-478.

29. Talbi M and Agnew B, *Energy recovery from diesel engine exhaust gases for performance enhancement and air conditioning.* **Applied Thermal Engineering**, 2002. **22**(6): p. 693-702.
30. Keinath C.M, et al. *Diesel Engine Waste-Heat Driven Ammonia-Water Absorption System for Space-Conditioning Applications*. in *International Refrigeration and Air Conditioning Conference*. 2012. Purdue, USA.
31. Ramanathan A and Gunasekaran P, *Simulation of Absorption Refrigeration System for Automobile Application.* **Thermal Science**, 2008. **12**(3): p. 5-13.
32. Vicatos G, Gryzagoridis J, and Wang S, *A car air-conditioning system based on an absorption refrigeration cycle using energy from exhaust gas of an internal combustion engine.* **Journal of Energy in Southern Africa**, 2008. **19**: p. 6-11.
33. Horuz I, *An Alternative Road Transport Refrigeration.* **Turkish journal of Engineering and Environmental Sciences**, 1998. **22**(3): p. 211-222.
34. Horuz I and Callander T.M.S, *Experimental investigation of a vapor absorption refrigeration system.* **International Journal of Refrigeration**, 2004. **27**(1): p. 10-16.
35. Manzela A.A, et al., *Using engine exhaust gas as energy source for an absorption refrigeration system.* **Applied Energy**, 2010. **87**(4): p. 1141-1148.
36. AlQdah K.S, *Performance and Evaluation of Aqua Ammonia Auto Air Conditioner System Using Exhaust Waste Energy.* **Energy Procedia**, 2011. **6**: p. 467-476.
37. Hilali I, *An Experimental Study on Absorption Refrigeration System driven by Engine Exhaust Gas for Vehicles*, in *Mechanical Engineering*. 2007, University of Gaziantep
38. Bux S and Tiwari A.C, *Vapour absorption based automobile air conditioning using exhaust waste heat of diesel engine through plate and frame heat exchanger.* **VSRD International Journal of Mechanical, Civil, Automobile and Production Engineering**, 2014. **IV**(III): p. 25-35.
39. Boatto P, et al., *Internal combustion engine waste heat potential for an automotive absorption system of air conditioning Part 1: Tests on the exhaust system of a spark-ignition engine.* Proceedings of the Institution of Mechanical Engineers, **Part D: Journal of Automobile Engineering**, 2000. **214**(8): p. 979-982.
40. Fernández-Seara J, Vales A, and Vázquez M, *Heat recovery system to power an onboard NH3-H2O absorption refrigeration plant in trawler chiller fishing vessels.* **Applied Thermal Engineering**, 1998. **18**(12): p. 1189-1205.
41. Determan M.D and Garimella S, *Ammonia–water desorption heat and mass transfer in microchannel devices.* **International Journal of Refrigeration**, 2011. **34**(5): p. 1197-1208.

42. Sarabchi N, Khoshbakhti Saray R, and Mahmoudi S.M.S, *Utilization of waste heat from a HCCI (homogeneous charge compression ignition) engine in a tri-generation system.* **Energy**, 2013. **55**: p. 965-976.

43. Alam S. *A proposed model for utilising exhaust heat to run automobile air conditioner*. in *The 2nd Joint International Conference on "Sustainable Energy and Environment (SEE2006)"*. 2006. Bangkok, Thailand.

44. Ouadha A. and El-Gotni Y, *Integration of an Ammonia-water Absorption Refrigeration System with a Marine Diesel Engine: A Thermodynamic Study.* **Procedia Computer Science**, 2013. **19**: p. 754-761.

45. Mostafavi M and Agnew B, *Thermodynamic analysis of combined diesel engine and absorption refrigeration unit—supercharged engine with intercooling.* **Applied Thermal Engineering**, 1996. **16**(11): p. 921-930.

46. Zhong Y, *Size Reduction of an Engine Waste-Heat Driven Air- Conditioner for Passenger Cars and Light-Duty Trucks.* **Energy Procedia**, 2012. **14**: p. 351-357.

47. Lambert M.A and Jones B.J, *Automotive Adsorption Air Conditioner Powered by Exhaust Heat. Part 2: Detailed Design and Analysis.* Proceedings of the Institution of Mechanical Engineers, **Part D: Journal of Automobile Engineering**, 2006. **220**(7): p. 973-989.

48. Zink F, Lu Y, and Schaefer L, *A solid oxide fuel cell system for buildings.* **Energy Conversion and Management**, 2007. **48**(3): p. 809-818.

49. Oshima K, et al. *A study of heat recovery from fuel cell exhaust gas for telecommunications equipment cooling*. in *Telecommunications Energy Conference, 1991. INTELEC '91., 13th International*. 1991.

50. Yu Z, et al., *Analysis of total energy system based on solid oxide fuel cell for combined cooling and power applications.* **International Journal of Hydrogen Energy**, 2010. **35**(7): p. 2703-2707.

51. Yu Z, Han J, and Cao X, *Investigation on performance of an integrated solid oxide fuel cell and absorption chiller tri-generation system.* **International Journal of Hydrogen Energy**, 2011. **36**(19): p. 12561-12573.

52. Darwish M.A, *Building air conditioning system using fuel cell: Case study for Kuwait.* **Applied Thermal Engineering**, 2007. **27**(17–18): p. 2869-2876.

53. Waragai S, Uekusa T, and Oshima K. *Characteristics of an absorption refrigerator driven by fuel cell exhaust heat and used for telecommunications equipment cooling*. in *Telecommunications Energy Conference, 1994. INTELEC '94., 16th International*. 1994.

54. Ishizawa M, Okada S, and Yamashita T, *Highly efficient heat recovery system for phosphoric acid fuel cells used for cooling telecommunication equipment.* **Journal of Power Sources**, 2000. **86**(1–2): p. 294-297.
55. Sevencan S, et al., *Economic feasibility study of a fuel cell-based combined cooling, heating and power system for a data centre.* **Energy and Buildings**, 2016. **111**: p. 218-223.
56. Yang P, Zhang H, and Hu Z, *Parametric study of a hybrid system integrating a phosphoric acid fuel cell with an absorption refrigerator for cooling purposes.* **International Journal of Hydrogen Energy**, 2016. **41**(5): p. 3579-3590.
57. Weber C, Koyama M, and Kraines S, *CO2-emissions reduction potential and costs of a decentralized energy system for providing electricity, cooling and heating in an office-building in Tokyo.* **Energy**, 2006. **31**(14): p. 3041-3061.
58. Margalef P and Samuelsen S, *Integration of a molten carbonate fuel cell with a direct exhaust absorption chiller.* **Journal of Power Sources**, 2010. **195**(17): p. 5674-5685.
59. Arsalis A, *Modeling and simulation of a 100 kWe HT-PEMFC subsystem integrated with an absorption chiller subsystem.* **International Journal of Hydrogen Energy**, 2012. **37**(18): p. 13484-13490.
60. Pilatowsky I, et al., *Simulation of an air conditioning absorption refrigeration system in a co-generation process combining a proton exchange membrane fuel cell.* **International Journal of Hydrogen Energy**, 2007. **32**(15): p. 3174-3182.
61. Frimodt C and Mygind K F, *Integration of Solid Oxide Fuel Cell and absorption cooling units*, in *Mechanical Engineering*. 2010, Denmark Technical University.
62. Martz S.M, *Modelling and integration of a combined cooling, hetaing and power system with a high temperature fuel cell and absorption chiller*, in *Mechanical and Aerospace engineering*. 2011, University of California, Irvine: Irvine.
63. Mehrpooya M, Dehghani H, and Ali Moosavian S.M, *Optimal design of solid oxide fuel cell, ammonia-water single effect absorption cycle and Rankine steam cycle hybrid system.* **Journal of Power Sources**, 2016. **306**: p. 107-123.
64. Zhao H, Jiang T, and Hou H, *Performance analysis of the SOFC–CCHP system based on H2O/Li–Br absorption refrigeration cycle fueled by coke oven gas.* **Energy**, 2015. **91**: p. 983-993.
65. *www.desta-project.eu*. (last accessed November 2015)
66. *Solid Oxide Fuel Cell and Power System Development at PNNL*. 2011.

67. Jain S, Chen H.Y, and Schwank J, *Techno-economic analysis of fuel cell auxiliary power units as alternative to idling.* **Journal of Power Sources**, 2006. **160**(1): p. 474-484.

68. Rechberger J, et al., *Development of a Methanol SOFC APU Demonstration System*, in *ECS conference*, **ECS transactions** 25 (2) 1085-1092.

69. Draper R and DiGiuseppe G, *High Power Density Solid Oxide Fuel Cells for Auxiliary Power Unit Applications.* **Journal of Fuel Cell Science and Technology**, 2008. **5**(3): p. 035001-035001.

70. Rechberger J et al, *Fuel Cell Auxiliary Power Units for Heavy Duty Truck Anti-Idling.* SAE, **International Journal of Commercial Vehicles**. **6**: p. 555-562.

71. Wessells K. D and Kaido P. F, *Electrically powered trailer refrigeration unit*, E.P. Office, Editor. 2003, Carrier Corporation.

72. Daniel Augusto Betts, et al., *Fuel Cell coupled heating and refrigeration system*, U.S.P. office, Editor. 2012, Enerfuel Inc.: USA.

73. Justin Yee, et al., *Vehicle power system with fuel cell auxiliary power unit*, U.S.P. office, Editor. 2013, Daimler Trucks North America LLC: USA.

74. Betts D.A, *Integrated energy management system including a fuel cell coupled refrigeration system*, U.S.P. office, Editor. 2012, Enerfuel Inc.: USA.

3

Cooling load calculation & thermodynamic modelling of VARS

"*All truths are easy to understand once they are discovered; the point is to discover them*"
Galileo Galilei

A bottom up modelling approach has been carried out where end requirements were identified first, followed by upstream modelling and simulation. In this chapter the amount of cooling required on different kinds of refrigerated trucks is presented followed by a fundamental thermodynamic model of the Vapour Absorption Refrigeration System. The cooling load values serve as inputs for the thermodynamic model of the VARS and the resulting outputs from the VARS model serve as inputs for further modelling and simulation. Modelling the VARS unit will give information on the energy and mass flows into and out of the unit which is critical for component development.

3.1 Mathematical modelling of cooling load

The amount of cooling load (or heat to be removed) needed inside a refrigerated space is to be calculated as accurately as possible because the sizing of the refrigeration system will depend on the cooling load calculations. For refrigerated transport there are primarily four heat loads that need to be accounted for viz. *Transmission Heat Load (THL)*, *Service Heat Load (SHL)*, *Product Heat Load (PHL)* and *Solar heat Load (SL)*. Thus the total heat load can be summarized as the sum of the four individual heat loads.

$$Q_{Total} = Q_{THL} + Q_{SHL} + Q_{SL} + Q_{PHL} \quad \textbf{Eq. 3.1}$$

Transmission Heat Load (Q_{THL}), is defined as the heat penetrating (or leaking) the refrigerated space from the ambient via conduction and convection. A simple diagrammatic representation of the same is shown in Figure 3.1. This heat load is the steady state heat load getting into the refrigerated space from the ambient. The THL is modelled by the mathematical equation based on Fourier's law for any given temperature difference.

$$Q_{THL} = k_b * A_{mean} * \Delta T \quad \textbf{Eq. 3.2}$$

Where,

k_b	Body 'K' factor, the heat flow per m^2 per ^oC (W m^{-2} $^oC^{-1}$)
A_{mean}	Mean surface area of the refrigerated space (m^2)
ΔT	Temperature difference between the refrigerated space and the ambient (^oC)

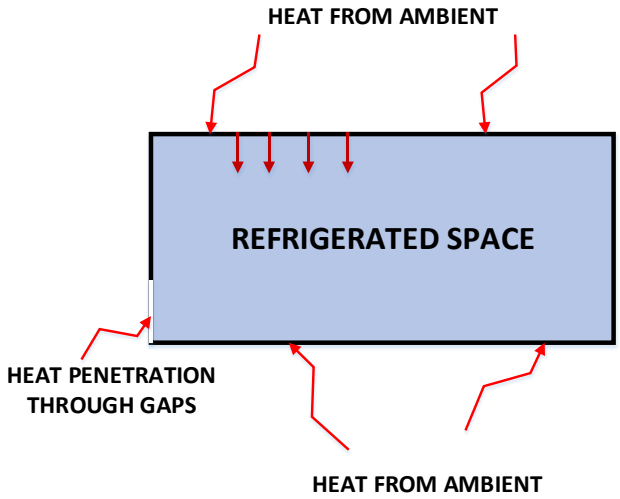

Figure 3.1: Heat load penetrating refrigerated space via conduction and convection

Service Heat Load (Q_{SHL}) is the heat load entering the refrigerated space whenever the doors of the refrigerated cabinet are opened. The service heat load not only depends on the position and size (and shape) of the doors but also on the door opening frequency and on the door opening times. The Service Heat Load is modelled by Eq. 3.3 [1]. This particular equation was derived based on tests carried out on refrigerated truck bodies in a controlled environment by the United States Department of Agriculture.

$$Q_{SHL} = K\, A_c\, V_t \left(\frac{h_a}{v_a} - \frac{h_r}{v_r}\right) * \left(\frac{60}{t_{avg}}\right) * 0.2931 \qquad \textbf{Eq. 3.3}$$

Where,

K Ratio of actual enthalpy change to maximum theoretical enthalpy change. The value ranges from 0.53 to 0.91, the lower value corresponding to the refrigerated cabinet being completely empty and the higher value corresponding to the refrigerated cabinet being half full.

A_c	Number of air changes inside the refrigerated space resulting from door openings
V_t	Volume inside the refrigerated space not occupied by cargo (ft^3)
h_a	Enthalpy of ambient air (Btu/ pound of dry air)
h_r	Initial enthalpy of air inside refrigerated space (Btu/ pound of dry air)
v_a	Specific volume of ambient air (ft^3/ pound of dry air)
v_r	Initial specific volume of air inside refrigerated space (ft^3/ pound of dry air)
t_{avg}	Average time between door openings (minutes)

The number of air changes resulting from door openings is modelled by Eq. 3.4

$$A_c = 2\ln(1 + X) \qquad \textbf{Eq. 3.4}$$

Where, X is given by the following expression

$$X = \frac{1}{2}\ 3700\ A_d C\ \sqrt{H}\sqrt{(T_a - T_r)}\ \frac{\theta}{V_t\ T_m} \qquad \textbf{Eq. 3.5}$$

and

A_d	Effective door area (ft^2)
C	Discharge coefficient for a rectangular opening, 0.7
H	One half of effective door height (ft)
V_t	Volume inside the refrigerated space not occupied by cargo (ft^3)
T_m	Mean temperature of refrigerated space and ambient air (^{o} Rankine)
T_a	Temperature of ambient (^{o}F)
T_r	Temperature of refrigerated space (^{o}F)
θ	Door opening time (minutes)

The enthalpy and specific volume required in Eq. 3.3 are calculated from Eq. 3.6 and Eq. 3.7

$$h_i = \left(0.24 * (T_i * \frac{9}{5} + 32)\right) + x\ \left(\ 0.444\ * (T_i * \frac{9}{5} + 32) + 970\right) \qquad \textbf{Eq. 3.6}$$

Where, subscript i = a (ambient) or r (refrigerated)

$$v_i = \left(1 + \frac{R_w}{R_a} * x\right) R_a \frac{(273 + T_i)}{P} * 16.0185 \qquad \textbf{Eq. 3.7}$$

Where,

R_w	455, Individual gas constant for water vapour (J kg^{-1} K^{-1})
R_a	286.9, Universal gas constant (J kg^{-1} K^{-1})
P	Pressure of air (Pa)
x	Humidity ratio
T_i	Temperature of ambient or refrigerated space (^{o}C)

Note that Eq. 3.3 to Eq. 3.7 are based on imperial units and conversion to SI units is not straightforward due to the fact that some of the coefficients were experimentally fitted while recording data in imperial units. Hence, these equations are used as such and the final conversion from BTU hr^{-1} to Watts is done in Eq. 3.3.

The humidity ratio x in Eq. 3.6 and Eq. 3.7 is given by Eqs. 3.8 to 3.10

$$x = 0.622 \left(\frac{\varepsilon_w}{P - \varepsilon_w}\right) \qquad \textbf{Eq. 3.8}$$

$$\varepsilon_{ws} = (1.007 + 3.46 * 10^{-6} * P) * \left(6.1121 * e^{\frac{17.502 * T_a}{240.97 + T_a}}\right) \qquad \textbf{Eq. 3.9}$$

$$\varepsilon_w = RH * \varepsilon_{ws} \qquad \textbf{Eq. 3.10}$$

Where,

ε_{ws}	Saturated vapour pressure (Pa)
ε_w	Partial pressure of water vapour (Pa)
RH	Relative humidity (%)

Product Heat Load (Q_{PHL}) is the heat given off by the goods (products) present in the refrigerated space. Heat is generally given off by agricultural products such as fruits and vegetables and also from certain animal products. When compared to *Transmission Heat Load* and *Service Heat Load*, the heat given off by the goods present inside the refrigerated space is minimal and can safely be neglected.

The effect of solar radiation (Solar Load) needs to be considered as well while calculating the cooling load requirements for a refrigerated vehicle. The equation for *Transmission Heat Load* (THL) assumes the exterior body temperature to be the same as that of the ambient but in practice this might not be the case. The roof skin temperatures of the external body can reach a temperature anywhere between 15 and 20 ^{o}C higher than the ambient temperature [2]. The effect of solar load will be the highest when trucks are stationary (parked) for a very long time and the effect will be even higher when it is parked with its longitudinal axis along the North-South direction. In this case, both the sides as well as the roof will receive maximum solar radiation throughout the day.

The amount of heat received by the refrigerated truck parked in the sun can be described by Eq. 3.11.

$$Q_{Solar} = U\ A\ (T_{em} - T_r + E) \qquad \textbf{Eq. 3.11}$$

Where,

U	Overall heat transfer coefficient of the refrigerated truck body (W m^{-2} K^{-1})
A	Area of the exterior surface of the truck exposed to solar radiation at any given point of time (m^2)
T_{em}	Mean solar air temperature (K)
T_r	Temperature of refrigerated space (K)
E	Heat sink characteristic factor, representing the resistance to change in heat flow through a particular material per unit watt of heat flowing (K)

The mean solar air temperature is given by Eq. 3.12

$$T_{em} = T_a + \frac{\phi \alpha}{h_o} \qquad \textbf{Eq. 3.12}$$

Where,

T_a	Temperature of ambient (K)
ϕ	Solar insolation impinging on the vehicle (W m^{-2})
α	Surface absorptivity
h_o	Outside heat transfer coefficient (W m^{-2} K^{-1})

For detailed calculations of cooling load including '*Solar Load*', the solar insolation data of a particular place needs to be obtained from meteorological data. This data is then to be used in conjunction with Eq. 3.11 to obtain the heat entering the vehicle due to solar load. The United States Department of Agriculture has carried out detailed testing on refrigerated vehicles for interior refrigeration temperatures of -17 ^{o}C and concluded that a factor of 1.22 when multiplied to the THL is sufficient to take into consideration the effect of '*Solar Load*'.

3.1.1 Assumptions made

The following assumptions were made when calculating the total heat load to be removed from the refrigerated space:

i) There is only one door present on the refrigerated truck and this door is located at the back of the refrigerated cabinet. This is a valid assumption since most of the large trucks and medium sized trucks have just one door at the rear of the refrigerated cabinet.

ii) The refrigerated cabinet is considered to be a perfect cuboid and the door is of rectangular shape.

iii) The effective door area is 88% of the total surface area of the rear face. This value was derived from analysis of door dimensions and external refrigerated body dimensions available from standard refrigerated cabinet manufacturers for trucks. The ratio of door area to the external surface area of the face (comprising the width and height) fell in the range 85-91%, hence an average value of 88% was used in the calculation.

iv) The height of the door is assumed to be 96 % of the total external height of the refrigerated cabinet. This value was calculated based on the ratio of door height to external refrigerated body height and most values fell around 96 %.

v) The value of 'K' in the equation for *Service Heat Load* is assumed to be 0.6 for all cooling load calculations. This is because of two reasons. First, there is no realistic formula to calculate its value and only a range for the parameter was determined through extensive tests conducted by United States Department of Agriculture [1] and second, lower values of 'K' correspond to higher cooling loads, which aids in designing the refrigeration system for the worst case possible. In order to be realistic, the lowest value of 0.53 has not been assumed because the lowest value corresponds to the refrigerated cabinet being empty and no truck will keep the refrigeration unit running when the cabinet is empty.

vi) Heat load from lights present inside the refrigerated cabinet are not considered and it is assumed that products are loaded into the refrigerated space at the right temperature meant for that product.

3.2 Results from cooling load calculations

The total cooling load calculated based on the mathematical relations presented in the previous section is discussed here. Three kinds of trucks are considered in this study – a large tractor trailer (40 ton gross weight) which is used for primary distribution, a medium sized truck (12 ton gross weight) which is used for secondary distribution and a small delivery van (~ 1 ton gross weight) which is used for tertiary distribution.

Variation with k_b (body 'K' factor)

The body '*K*' factor, k_b, is the inherent property of the insulation and is usually specified by the manufacturer. Typical insulation materials used in refrigerated truck bodies are high density *Styrofoam* or high density *Polyurethane* [3]. The ATP agreement [4], which is an agreement drawn in the year 1970-71 by the Inland Transport Committee of the United Nations Economic Committee for Europe, lays down common international standards for mobile refrigerated vehicles such as trucks, trains and ships. The ATP agreement states that a normally insulated refrigerated space needs to have a k_b of 0.7 W m^{-2} K^{-1} and a heavily insulated refrigerated space needs to have a k_b of 0.4 W m^{-2} K^{-1} [4]. Refrigerated trucks (especially the ones transporting frozen goods) fall in the category of heavily insulated refrigerated spaces and it is essential to insulate the refrigerated space with good quality insulation, having an insulation factor matching that of k_b.

The variation of total cooling load with k_b is shown in Figure 3.2.

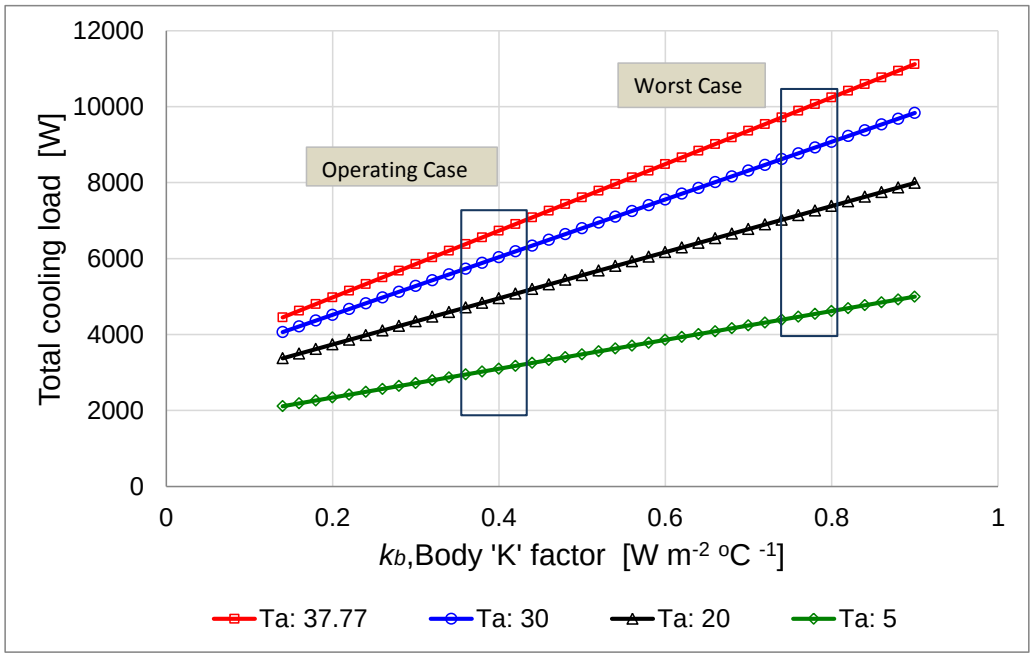

Figure 3.2: Variation of total cooling load with body 'K' factor

The better the insulation, the lower the k_b and hence lower the cooling load requirements. One can see that along with k_b, the ambient temperature also plays a vital role in deciding the total cooling load requirements. A refrigerated space with superior insulation operating at a higher ambient temperature will have the same cooling load requirements as that of a refrigerated space operating with a slightly inferior insulation at a lower ambient temperature provided other operational and functional parameters remain the same. The insulation used will degrade in quality after a certain period of time hence the refrigeration unit needs to be sized allowing room for certain tolerance when the insulation degrades. Figure 3.2 also shows the operating case when the insulation is good and a worst case where the insulation degrades after prolonged use.

Variation with 'External' dimensions

The variation of total cooling load with external dimensions of the refrigerated space is shown in Figure 3.3. The larger the size of the refrigerated cabinet, the larger will be the

cooling load. The dimensions of the refrigerated cabinet used on large, medium and small sized trucks are given in Table 3.1.

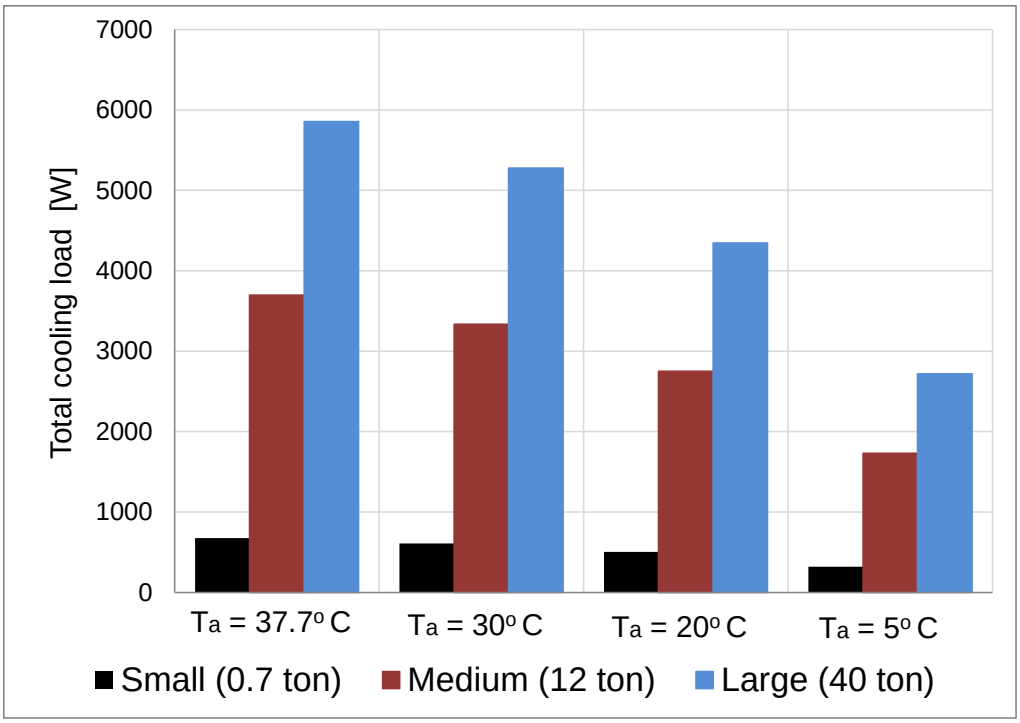

Figure 3.3: Variation of total cooling load with external dimensions

Table 3.1: Size of different types of trucks used in this study

Type of truck	External Length (m)	External Width (m)	External Height (m)
Large (40 tons)	13.6	2.6	2.4
Medium (12 tons)	9.4	2.5	2.4
Small (0.7 ton)	2.48	1.88	1.57

(Based on standard truck sizes available in the market)

The cooling load requirements for a small refrigerated truck is under a kilowatt whereas it ranges from 2.5 kW to almost 6 kW for a large 40 ton refrigerated truck and from 1.6 kW to 3.6 kW for a medium 12 ton truck.

Variation with percentage of cargo

Another factor that affects the cooling load is the amount of cargo/goods present inside the refrigerated space. It is always better to load the refrigerated space up to the maximum extent possible in order to reduce the cooling load requirements. Unlike the case where the cooling load varied linearly with k_b, the variation of cooling load with percentage of cargo is not linear as shown in Figure 3.4.

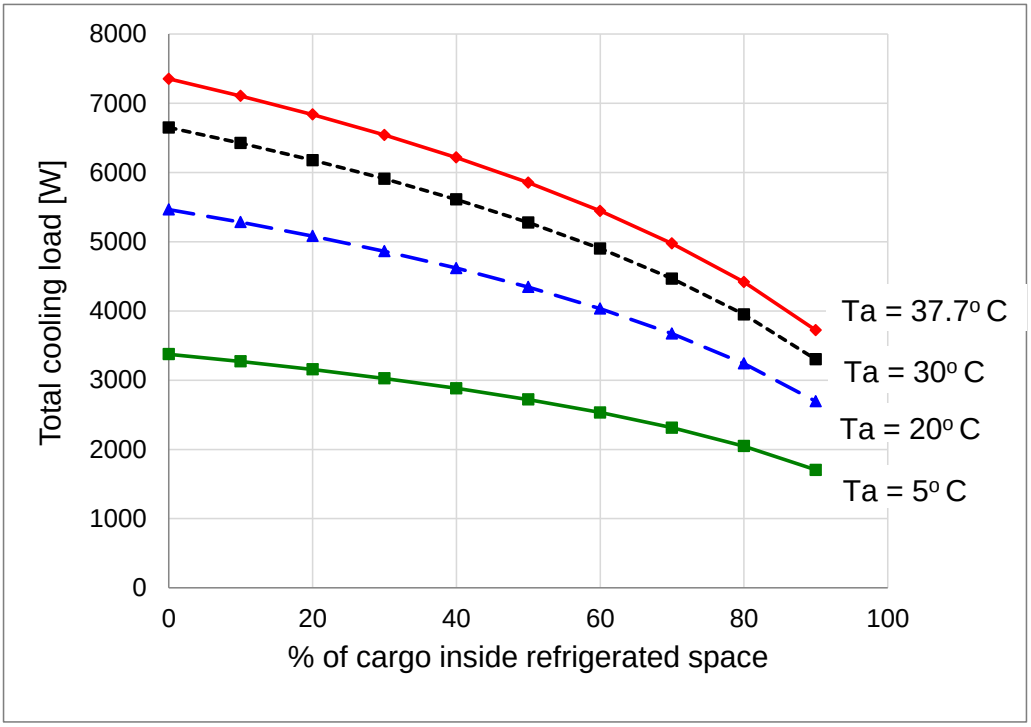

Figure 3.4: Variation of total cooling load with % of cargo inside refrigerated space (For large truck)

This factor will be critical for small delivery vans rather than for large and medium trucks. This is because the delivery cycle of small refrigerated vans is vastly different from that of large and medium trucks. The volume of cargo decreases after each delivery for a small van and hence the refrigeration unit must be able to cater to the cooling load required at the end

of the driving cycle. This will of course mean the refrigeration unit will be oversized initially but eventually as the cooling load increases the refrigeration unit will be able to cater to the increased demand. Large and medium trucks unlike small delivery vans deliver goods from point to point which means throughout the delivery cycle no doors are opened and hence the percentage of cargo stays the same.

The reason why percentage of cargo plays an important role in determining the cooling load calculations is that it directly affects the number of air changes that occur each time the door is opened. More hot air will tend to get in each time the door is opened if the refrigerated space is not completely filled with cargo, thereby increasing the service load and thus the total cooling load.

Variation with temperature of refrigerated space

Another factor that influences the total cooling load is the temperature at which the cabinet has to be maintained at. The lower the temperature required inside the refrigerated space, the higher will be the cooling load requirement. The variation of cooling load with refrigeration temperature is again linear as shown in Figure 3.5. The type of foods being transported determines the refrigerated cabinet temperature and hence the total cooling load requirement. Chilled foods which need to be maintained between +1 and +10 ^{o}C demand a lower cooling load when compared to frozen foods which need to be maintained between - 5 and - 20 ^{o}C. This is shown in Figure 3.6.

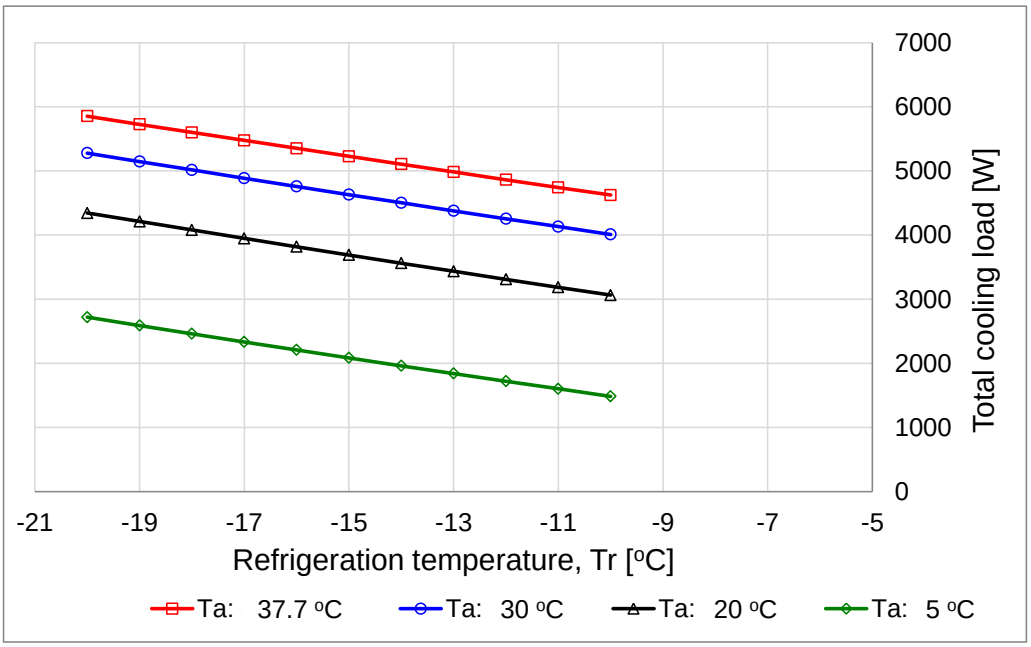

Figure 3.5: Variation of cooling load with refrigeration temperature
(For large truck)

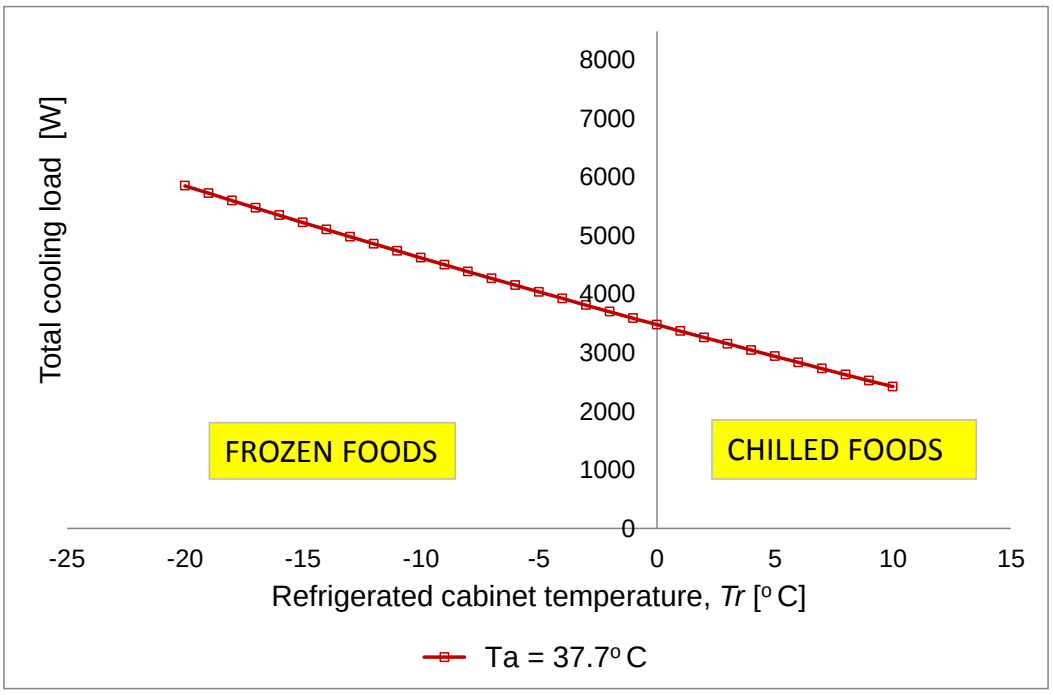

Figure 3.6: Cooling load requirements for frozen and chilled foods
(For a large truck)

Variation with door opening time

The final parameter that affects cooling load calculations is the amount of time the door of the refrigerated cabinet is kept open while unloading goods. This is a crucial parameter because it affects the Service Heat Load and thereby the total cooling load requirement. The number of air changes that occur depends directly on the door opening time and the longer the doors are kept open, the harder the refrigeration unit has to work in order to cool down the refrigerated space to the desired temperature because more hot air tends to enter. Hence it is desirable to unload the goods in the shortest time possible, to prevent heat from getting into the refrigerated space.

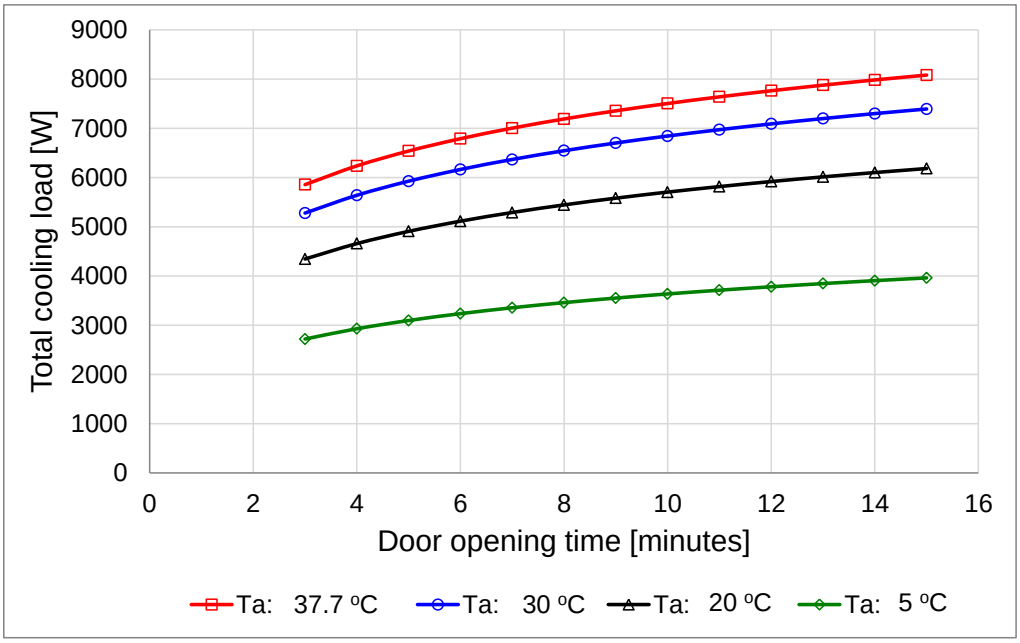

Figure 3.7: Variation of cooling load with door opening time
(For large truck)

The parameters that were kept constant when varying each of the above factors, is tabulated and given in *Appendix B*.

Heat addition due to solar load

As described in *Section 3.1*, detailed calculations of the effect of solar load would necessitate calculation of instantaneous solar insolation and meteorological parameters. A typical solar insolation curve is shown in Figure 3.8. The solar insolation values can be obtained at different times of the day for typical weather conditions from this curve.

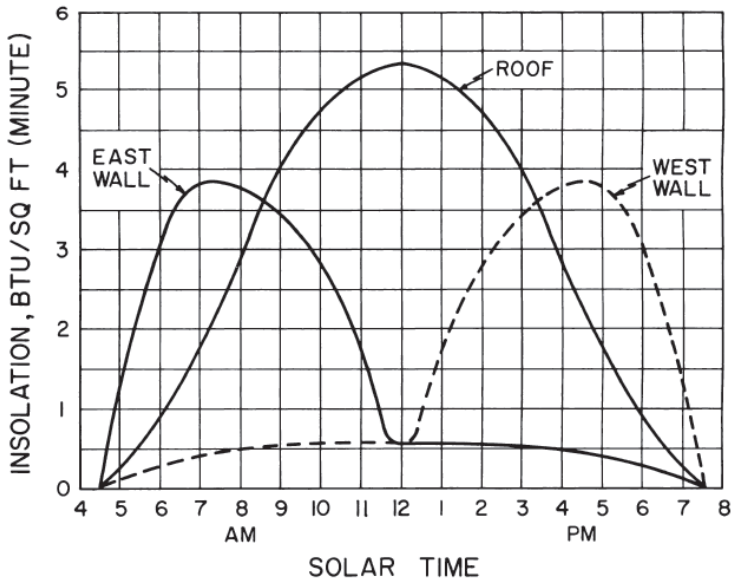

Figure 3.8: Typical solar insolation curve on a cloudless day in summer [2]
(For 21 June at latitude 40 ^{o}N)

The overall heat transfer coefficient for the vehicle is calculated using Eq. 3.13

$$\frac{1}{U} = \frac{1}{h_1} + \sum_{i=1}^{n} \frac{dx_i}{k_i} \qquad \textbf{Eq. 3.13}$$

Where,

h_1	Heat transfer coefficient of outside air at standstill (W m^{-2} K^{-1})
dx_i	Thickness of wall (m), part *i*
k_i	Thermal conductivity of wall (W m^{-1} K^{-1})

The overall heat transfer coefficient is calculated for the geometry shown in Figure 3.9 and is tabulated in Table 3.2. These are the typical dimensions for the wall of the truck body.

As an approximation and to use an estimate of maximum solar load, the surface area of the truck body is taken as the vertical truck body surface area when the solar load impinges on the truck during morning and evening and as the top surface area when the solar load impinges on the truck at noon. From Figure 3.8, it can be deduced that maximum solar insolation in the morning occurs at 7:30 hrs, for noon it occurs at 12:00 hrs and in the evening it occurs at 16:30 hrs. The corresponding value for maximum insolation can be deduced which is 738 W m^{-2} for morning and evening and 1003 W m^{-2} for noon. Using Eq. 3.11 along with the solar insolation values, the amount of solar load on the vehicle can be calculated. These values along with the truck surface area are presented in Table 3.3.

Note: The heat sink characteristic factor has been ignored in the calculations.

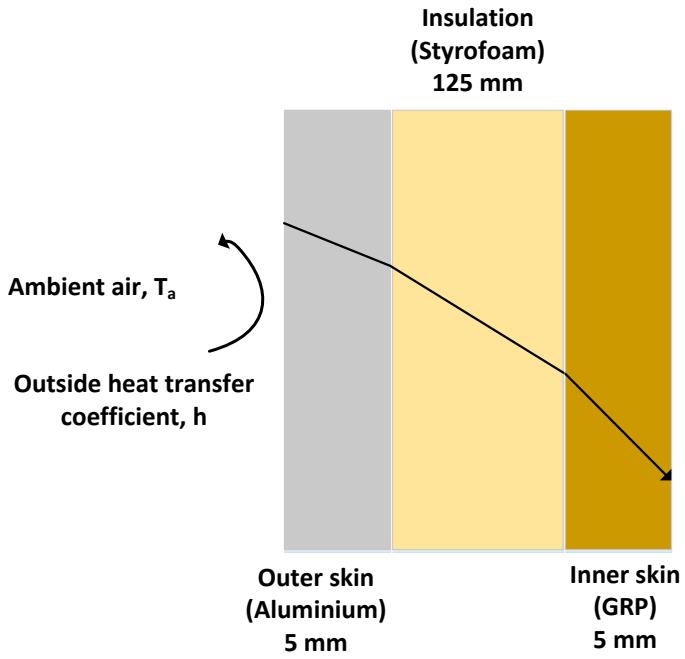

Figure 3.9: Cross section of refrigerated cabinet body showing different layers

Table 3.2: Material properties of typical truck body layers

	Outside heat transfer coefficient, h (W m^{-2} K^{-1})	25
Aluminium	Thickness of outer skin (m)	0.005
	Thermal conductivity of material of outer skin (W m^{-1} K^{-1})	205
Styrofoam	Thickness of insulation (m)	0.125
	Thermal conductivity of insulation (W m^{-1} K^{-1})	0.027
GRP	Thickness of inner skin (m)	0.005
	Thermal conductivity of material of inner skin (W m^{-1} K^{-1})	0.25
	Overall heat transfer coefficient (W m^{-2} K^{-1})	0.213

Table 3.3: Surface area exposed to maximum solar radiation and corresponding solar load

Surface area of truck exposed to direct solar radiation during morning (L x H)	38.08 m^2	Solar load during morning	625 W
Surface area of truck exposed to direct solar radiation during noon (L x W)	35.36 m^2	Solar load during noon	632.3 W
Surface area of truck exposed to direct solar radiation during evening (L x H)	38.08 m^2	Solar load during evening	625 W

Calculated for T_a = 37.77 ^oC and surface absorptivity of 0.65 (for rough aluminium), large truck considered

3.3 Thermodynamic modelling of VARS

A thermodynamic model of the NH_3-H_2O based Vapour Absorption Refrigeration System based on first law of thermodynamics is presented here to analyse the amount of thermal energy that would be needed to drive it. This thermal energy data will then be used to size the SOFC stack. The cooling load to be achieved inside the refrigerated space was

calculated and presented in *Sections 3.1* and *3.2* respectively. This serves as input for modelling of the VARS.

The VAR unit analysed here is a single stage system based on NH_3-H_2O working pair. The reason for choosing NH_3-H_2O based absorption chillers is as follows [5]:

i) The freezing point of NH_3 is -77.7 ^oC which implies that this working pair is suitable as a refrigerant in systems to be employed for both chilled and frozen products.
ii) This working pair is free from crystallisation problems normally encountered with H_2O-LiBr working pair.
iii) A VAR system with the NH_3–H_2O working pair does not require an air purge system because it works under positive pressure (above atmospheric pressure)
iv) The high pressure refrigerant with low specific volume means that the VAR system based on NH_3-H_2O can be relatively compact when compared to a VAR system with H_2O-LiBr as the working pair.

The thermodynamic steady state model of the VARS was built using EES (Engineering Equation Solver). EES was chosen as the preferred platform because EES has built in thermodynamic functions for different refrigerants. EES solves a set of linear and non-linear equations (both algebraic and differential) as long as the number of equations and unknown variables are the same. Since it solves the system of equations automatically it is more convenient to use and does not warrant complex iterative loops, thereby providing the user a greater amount of flexibility.

In the present model, each block is treated as a control volume and mass and energy balances are applied to it. The general mass and energy balance applied to each control volume is given by Eq. 3.14 and Eq. 3.15.

$$\sum \dot{m}_{in} - \sum \dot{m}_{out} = 0 \qquad \textbf{Eq. 3.14}$$

$$\sum \dot{m}_{in} h_{in} - \sum \dot{m}_{out}\, h_{out} + \dot{Q}_{CV} - \dot{W}_{CV} = 0 \qquad \textbf{Eq. 3.15}$$

Where,

$\dot{m}_{in}$	Mass flow into the control volume (kg s^{-1})
$\dot{m}_{out}$	Mass flow out of the control volume (kg s^{-1})
h_{in}	Enthalpy of the fluid into the control volume (kJ kg^{-1})
h_{out}	Enthalpy of the fluid out of the control volume (kJ kg^{-1})
$\dot{Q}_{CV}$	Heat input into the control volume (W)
$\dot{W}_{CV}$	Work done by the control volume (W)

The detailed set of equations for each component of the VARS is given in Table 3.4 and the corresponding block diagram with all the state points mentioned is shown in Figure 3.10

There are two COP (Coefficient of Performance) terms used in this model, they are $COP_{Thermal}$ and $COP_{Overall}$ and are given by Eq. 3.16 and Eq. 3.17.

$$COP_{Thermal} = \frac{Q_E}{Q_G} \qquad \textbf{Eq. 3.16}$$

$$COP_{Overall} = \frac{Q_E}{Q_G + W_P} \qquad \textbf{Eq. 3.17}$$

Where,

Q_E	Cooling load or heat taken out from the refrigerated space (kW)
Q_G	Heat supplied to the desorber (kW)
W_P	Work done by the pump (kW)

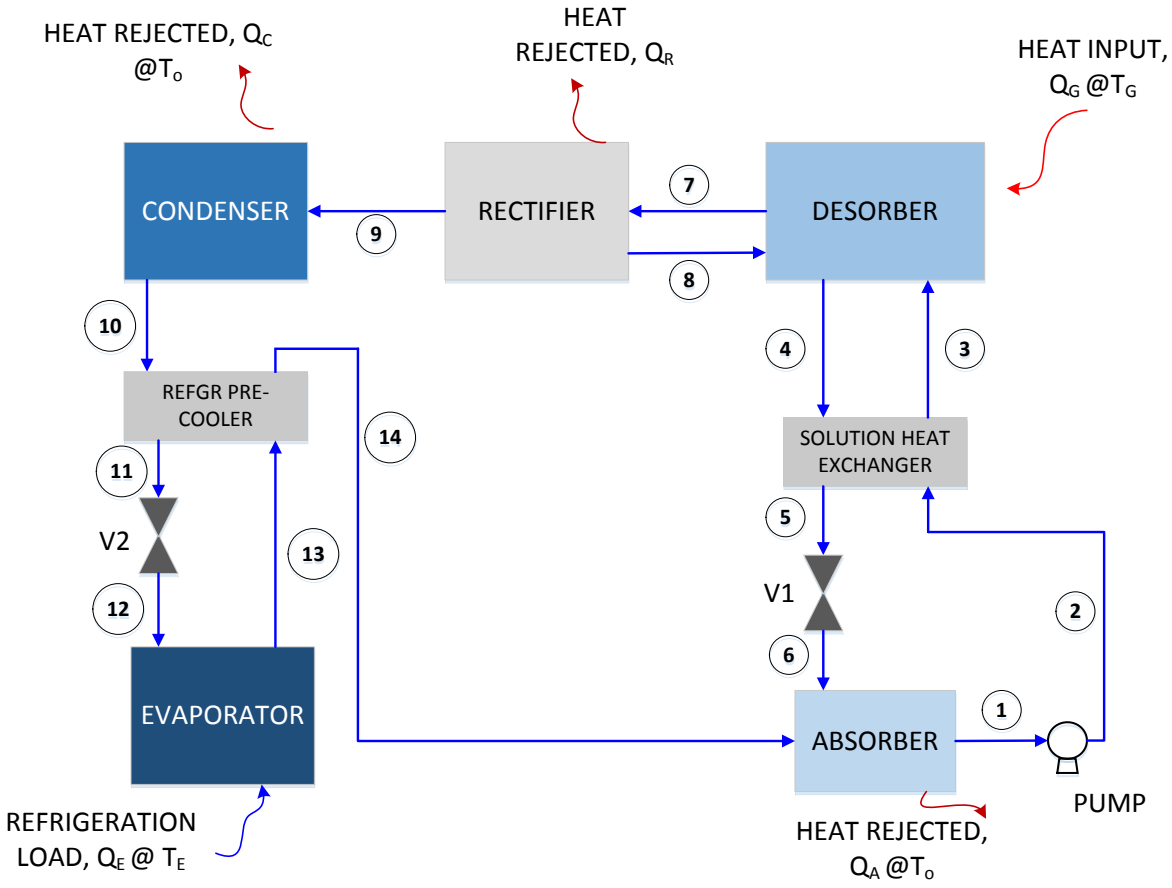

Figure 3.10: Block diagram of VARS with state points labelled

Table 3.4: Mass and energy balance at each component of VARS

Mass balance at Absorber	*For total mixture* $\dot{m}_1 = \dot{m}_{14} + \dot{m}_6$
	For ammonia $\dot{m}_1 x_1 = \dot{m}_{14} x_{14} + \dot{m}_6 x_6$
Energy balance at Absorber	$\dot{m}_6 h_6 + \dot{m}_{14} h_{14} = Q_a + \dot{m}_1 h_1$
Mass balance for Pump	$\dot{m}_1 = \dot{m}_2$
Energy balance for Pump	$\dot{m}_1 h_1 + W_P = \dot{m}_2 h_2$
Pump Work	$W_P = \dot{m}_1 v_1 \left(\frac{P_2 - P_1}{\eta_P}\right)$
Mass balance for Solution Heat Exchanger	$\dot{m}_4 = \dot{m}_5$ $\dot{m}_3 = \dot{m}_2$
Energy balance for Solution Heat Exchanger*	$\dot{m}_4 h_4 + \dot{m}_2 h_2 = \dot{m}_5 h_5 + \dot{m}_3 h_3$
Mass balance at Desorber	*For total mixture* $\dot{m}_8 + \dot{m}_3 = \dot{m}_7 + \dot{m}_4$
	For ammonia $\dot{m}_8 x_8 + \dot{m}_3 x_3 = \dot{m}_7 x_7 + \dot{m}_4 x_4$
Energy balance at Desorber	$\dot{m}_8 h_8 + \dot{m}_3 h_3 + Q_G = \dot{m}_7 h_7 + \dot{m}_4 h_4$
Mass balance at throttle valve V1	$\dot{m}_6 = \dot{m}_5$
Energy balance at throttle valve V1	$\dot{m}_6 h_6 = \dot{m}_5 h_5$
Mass balance at Condenser	$\dot{m}_9 = \dot{m}_{10}$
Energy balance at Condenser	$\dot{m}_9 h_9 = \dot{m}_{10} h_{10} + Q_C$
Mass balance at Refrigerant pre-cooler	$\dot{m}_{10} + \dot{m}_{13} = \dot{m}_{11} + \dot{m}_{14}$
Energy balance at Refrigerant pre-cooler*	$\dot{m}_{10} h_{10} + \dot{m}_{13} h_{13} = \dot{m}_{11} h_{11} + \dot{m}_{14} h_{14}$
Mass balance at throttle valve V2	$\dot{m}_{11} = \dot{m}_{12}$
Energy balance at throttle valve V2	$\dot{m}_{11} h_{11} = \dot{m}_{12} h_{12}$
Mass balance at Evaporator	$\dot{m}_{12} = \dot{m}_{13}$
Energy balance at Evaporator	$\dot{m}_{13} h_{13} = \dot{m}_{12} h_{12} + Q_E$
Mass balance at Rectifier	*For total mixture* $\dot{m}_7 = \dot{m}_9 + \dot{m}_8$
	For ammonia $\dot{m}_7 x_7 = \dot{m}_9 x_9 + \dot{m}_8 x_8$
Energy balance at Rectifier	$\dot{m}_7 h_7 = \dot{m}_9 h_9 + \dot{m}_8 h_8 + Q_R$

(* Represents equation for ideal case; v = specific volume of solution, η_P = pump efficiency)

3.3.1 Model input parameters

The base case input parameters to the EES model are listed in Table 3.5. Since a temperature of at least -20 ^{o}C is needed for storing and preserving frozen foods (such as ice creams, certain kinds of meat etc.), this temperature was set to be the evaporator exit temperature.

Table 3.5: Base case operating parameters for VARS running on NH_3-H_2O

Evaporator/ Absorber pressure	1 bar
Condenser/ Desorber pressure	15 bar
Temperature of saturated liquid leaving the condenser	40 ^{o}C
Temperature of saturated strong solution leaving the absorber	40 ^{o}C
Evaporator temperature	-20 ^{o}C
Effectiveness of solution heat exchanger (SHX)	0.8
Effectiveness of the refrigerant heat exchanger (RHX)	0.8
Efficiency of the pump	70 %
Mass fraction of ammonia at state 9	0.99
Mass fraction of ammonia at state 11	0.99
Mass fraction of ammonia at state 12	0.99
Mass fraction of ammonia at state 14	0.99
Quality of vapour at state point 4	0
Quality of vapour at state point 7	1
Quality of vapour at state point 8	0
Quality of vapour at state point 9	1
Quality of vapour at state point 10	0
Quality of vapour at state point 13	0.998
Mass flow rate of strong solution	0.036 kg/s

(Effectiveness refers to efficiency of heat exchanger)

The concentration of ammonia in the strong solution exiting the absorber can be determined if the pressure and rejection temperature of the absorber are fixed [6]. The equation

describing the relation between saturation pressure, solution temperature and ammonia concentration of a NH_3-H_2O mixture is given by Eq. 3.18 to 3.20 [6].

$$\log P = A - \frac{B}{T} \quad \textbf{Eq. 3.18}$$

$$A = 7.44 - 1.767\,X + 0.9823\,X^2 + 0.3627\,X^3 \quad \textbf{Eq. 3.19}$$

$$B = 2013.8 - 2155.7\,X + 1540.9\,X^2 - 194.7\,X^3 \quad \textbf{Eq. 3.20}$$

Where,

P	Operating pressure of the absorber in (kPa)
T	Rejection temperature of absorber (K)
X	Ammonia concentration (wt %)

3.3.2 Assumptions made in the model

The following assumptions are made in the model

i) The system works under steady state conditions.

ii) Heat exchange occurs only at the five components indicated and nowhere else in the system.

iii) The solution heat exchanger and refrigerant heat exchanger are not ideal; hence not 100% of heat is transferred from the hot solution to the cold solution.

iv) The pressure drops in the pipes and across components is negligible.

v) The concentration of the strong solution remains the same at state points 1, 2 & 3.

vi) The concentration of the weak solution remains the same at state points 4, 5 & 6.

vii) The pump and expansion valves were considered friction-less or generating minimum heat so that boiling of solution due to flashing does not occur.

viii) The concentration difference (of NH_3) between the strong solution and the weak solution was set to 10 wt%. A minimum of 5 wt% difference is needed to guarantee separation of ammonia from water in the desorber [7]

The flows at different state points are as follows:

i) Pure NH_3 vapour flows at state points 9, 13 & 14.

ii) Strong solution (rich in NH_3) flows at state points 1, 2 & 3.

iii) Weak solution (poor in NH_3) flows at state points 4, 5 & 6.

iv) Pure ammonia liquid (saturated liquid) flows at state points 10, 11 & 12.

v) Ammonia vapour mixed with water vapour flows at state point 7.

vi) Condensed water with a minute fraction of NH_3 flows at state point 8 (from rectifier) and returns to desorber.

3.4 Results from thermodynamic modelling of VARS

The thermodynamic model is solved for the initial pre-set operating conditions and the thermal and fluid flow parameters needed to operate the VARS for different cooling loads is obtained and tabulated in Table 3.6. The range of cooling loads presented represents the cooling needs on different types of trucks. The cooling load desired inside the refrigerated space can be achieved by varying the mass flow rate of the strong solution alone. The $COP_{Thermal}$ and $COP_{Overall}$ do not change with the mass flow rate of the strong solution. With the base case, the COP of the system is around 42 %.

Table 3.6: System operating parameters needed for different cooling load

	Cooling Load				
System parameters	1 kW	5 kW	6 kW	8 kW	10 kW
Actual cooling load (kW) (from model)	1.013	5.065	6.05	8.02	10.06
Heat Input at Desorber (kW)	2.39	11.95	14.27	18.92	23.73
Heat rejected at Condenser (kW)	1.047	5.235	6.253	8.289	10.4
Heat rejected at Absorber (kW)	1.759	8.796	10.51	13.93	17.47
Heat rejected at Rectifier (kW)	0.6125	3.063	3.658	4.85	6.083
Work done by pump (kW)	0.0158	0.0794	0.095	0.126	0.158
Mass flow rate of refrigerant (g/s)	0.84	4.2	5	6.6	8.3
Mass flow rate of strong solution (g/s)	7.2	36	43	57	71.5
Mass flow rate of weak solution (g/s)	6.36	31.8	38	50	63.16
$COP_{THERMAL}$	0.4239	0.4239	0.4239	0.4239	0.4239
$COP_{OVERALL}$	0.4211	0.4211	0.4211	0.4211	0.4211
Concentration of strong solution (wt %)	23.3	23.3	23.3	23.3	23.3
Concentration of weak solution (wt %)	13.3	13.3	13.3	13.3	13.3

3.4.1 Strategies to improve COP

With the base case COP being just 42 % it is envisaged that there is scope for improving the COP of the single stage VARS unit. In this section, ways to improve the COP are discussed for a 5 kW cooling load. The same improvements can then be adapted for other cooling loads.

Variation of Solution Heat Exchanger effectiveness (ε_{SHX})

Figure 3.11 shows the improvement in COP (overall and thermal) as the effectiveness of the solution heat exchanger is increased.

The cooling load remains constant because the refrigeration temperature is fixed and other flow rates to and from the evaporator are not altered. However the thermal energy needed to drive the desorber to achieve that particular cooling load is reduced. This is because as the effectiveness of the solution heat exchanger is increased more heat is transferred from the hot (weak) solution to the cold (strong) solution. Basically, preheating of the solution takes place before it enters the desorber. For a 5 kW cooling load designed for a refrigeration temperature of -20 ^{o}C, a thermal energy input of just 7.6 kW is needed at the desorber at a solution heat exchanger effectiveness value of 0.86 as compared to 11.95 kW needed for the base case where the solution heat exchanger effectiveness is 0.8.

Not having a solution heat exchanger between the desorber and the absorber would warrant more heat input at the desorber to achieve the same performance out of the VAR system. Thus a 6 % increase in solution heat exchanger effectiveness results in about 36 % less heat input and an almost 55 % increase in COP.

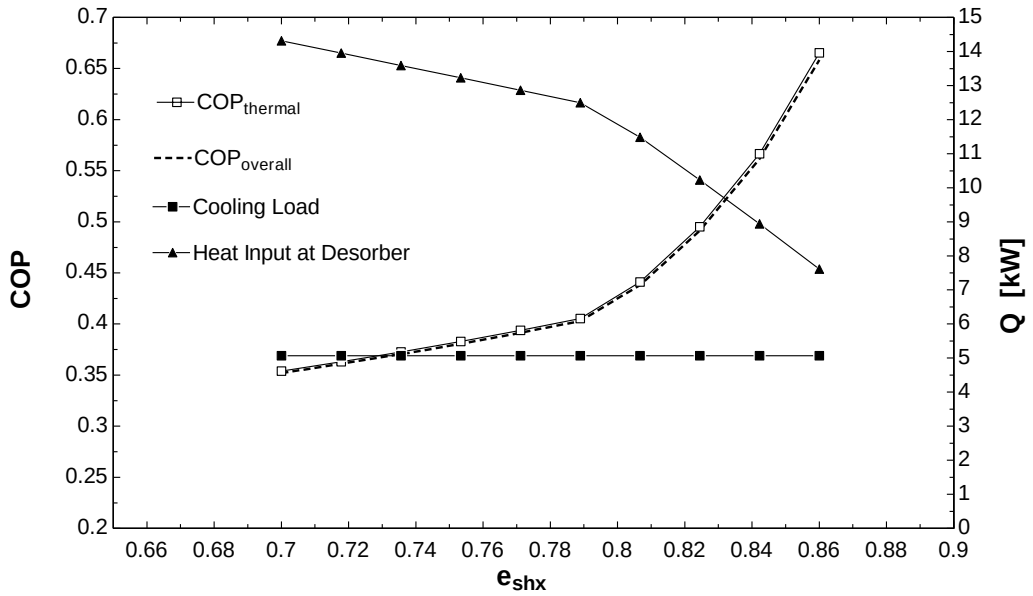

Figure 3.11: Variation of COP with Solution Heat Exchanger effectiveness

As the present application of the VARS is for a refrigerated truck, compactness of components is very important. Hence in this case a realistic limit of 86% is imposed on the heat exchanger effectiveness.

Variation of absorber rejection temperature

Figure 3.12 shows the variation in COP with the absorber rejection temperature. The lower the absorber rejection temperature, the higher is the system COP. However the absorber rejection temperature depends on the type of cooling employed to maintain the absorber temperature within limits without affecting its performance. If the absorber is air cooled then the absorber rejection temperature is limited by the temperature of the ambient air. For example, if the temperature of the ambient air is 30 ^{o}C then the absorber rejection temperature has to be greater than 30 ^{o}C to allow enough room for heat exchange. A temperature difference of 10 ^{o}C is considered practical. Hence the absorber rejection temperature in this case has to be at least 40 ^{o}C. However if the absorber is water cooled then perhaps a lower absorber rejection temperature can be achieved but the challenge in this case would be in removing the heat away from the cooling water and bringing it back to its original state.

The variation in absorber rejection temperature also leads to a variation in the concentration of the strong solution. This is depicted in Figure 3.13. Higher concentration of strong solution means that more ammonia can be vapourised in the desorber, leading to more refrigerant production. This explains the improved COP of the system with reduction in absorber temperature.

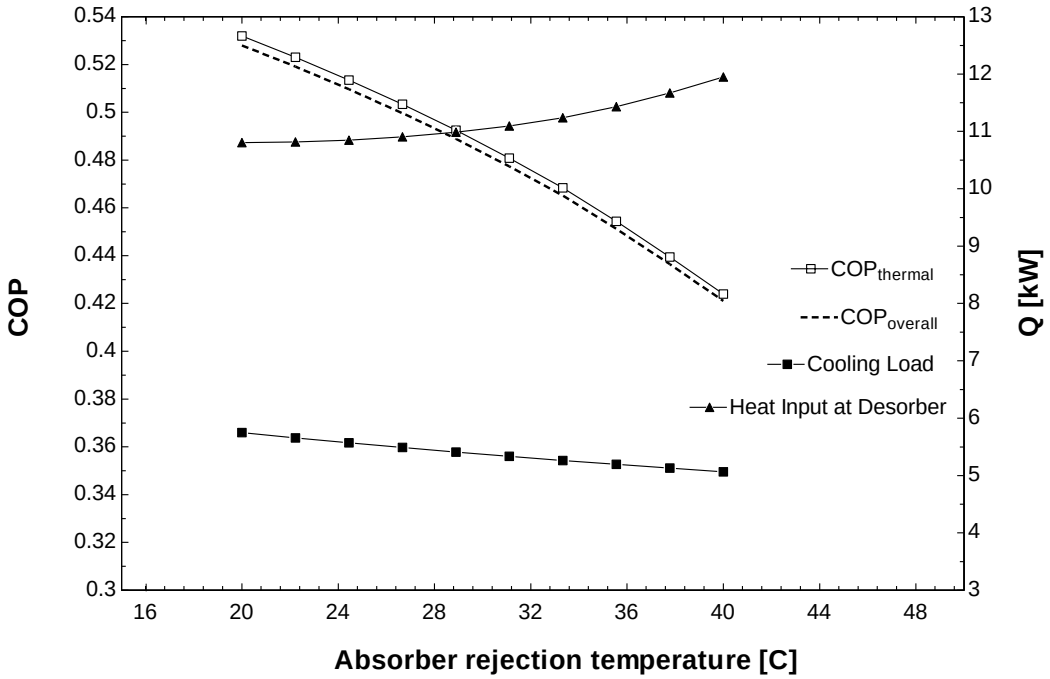

Figure 3.12: Variation of COP with absorber rejection temperature

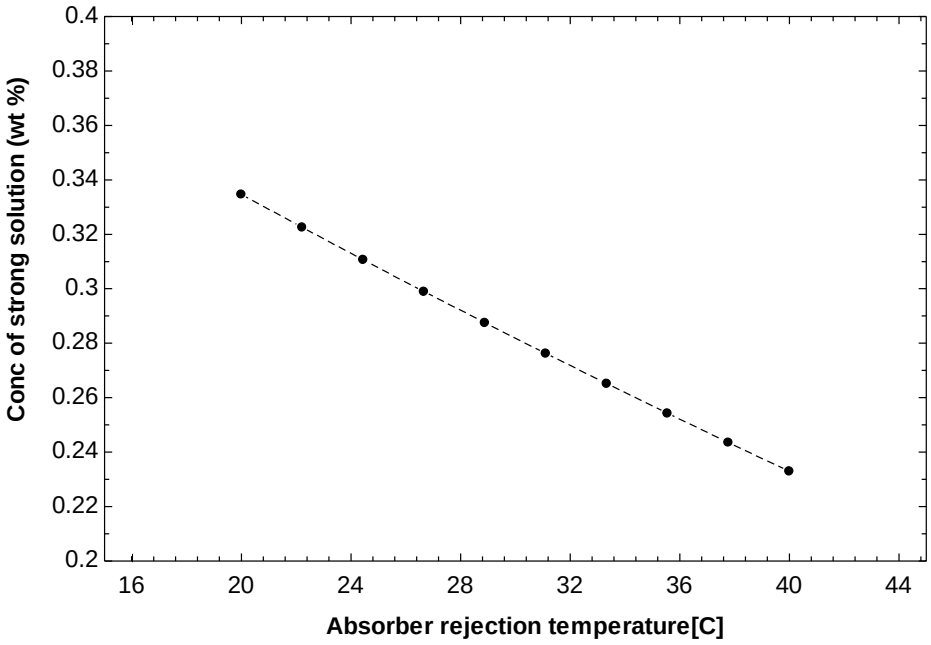

Figure 3.13: Variation of concentration of strong solution with absorber rejection temperature

Variation in concentration difference between strong and weak solution

As mentioned before a minimum of 5 wt% difference is needed between the strong and weak solution to ensure separation of ammonia from the solution. Hongxi Yin [8] found out that the larger the difference in concentration between the strong and the weak solution, the higher the COP. This feature was also incorporated in the model and it was found that the COP increases with increase in concentration difference as seen from Figure 3.14. There is of course a theoretical limit on the maximum concentration difference that can be achieved from the system and that limit is also investigated here.

The concentration of the strong solution (χ_{ss}) is determined by the exit temperature of the absorber and operating pressure of the absorber. The theoretical concentration of the weak solution can then range from $(\chi_{ss} - 5)wt\% \geq \chi_{ws} \geq 0$. The concentration of the weak solution cannot be zero because ammonia will never be 100% removed from the weak solution.

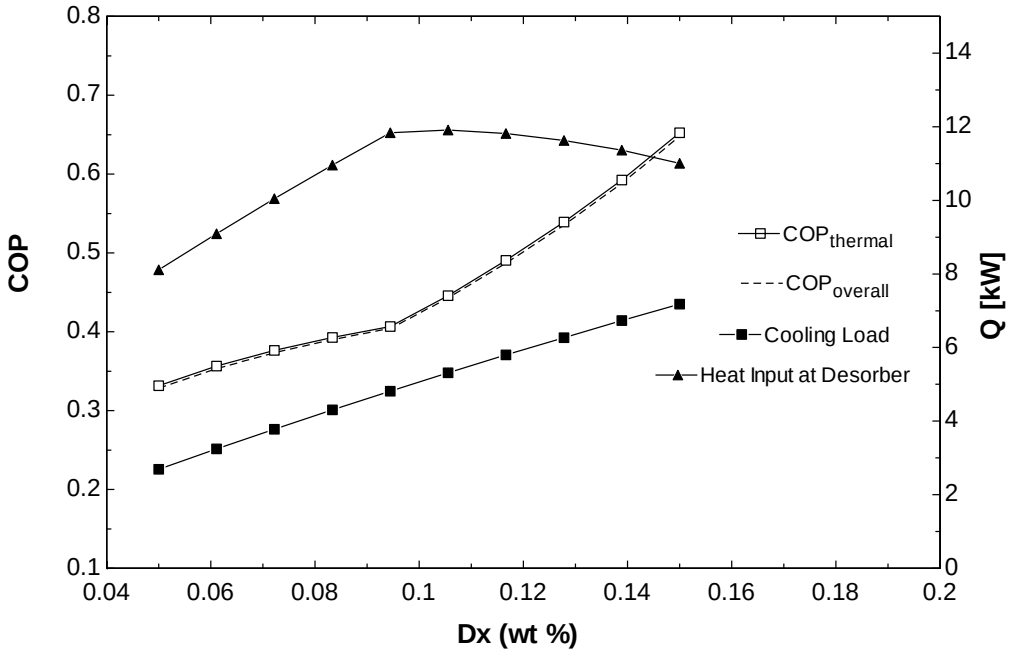

Figure 3.14: Variation of COP with concentration difference

Simulations revealed that for an absorber operating pressure of 1 bar and absorber exit temperature of 40 ^{o}C, the concentration of the strong solution is 23.3 wt%. A concentration difference greater than 15 wt% between the strong and weak solution, results in negative temperatures at state points 5 & 6. This means that the weak solution would actually freeze at points 5 & 6 and hinder the flow between the desorber and absorber. The temperature at which ammonia-water solution freezes is taken from the standard tables available [9]. Hence a maximum concentration difference of only 15 wt% can be achieved for this particular combination of absorber pressure, absorber rejection temperature and strong solution concentration.

Further limits on the concentration difference between the strong and weak solution for different absorber pressures and absorber rejection temperatures is investigated after the design limits on the absorber/evaporator pressures are investigated.

3.4.2 Design limits on absorber/evaporator pressure

The limits to the pressure level that can be maintained in the absorber/evaporator will be investigated in this section.

i) Increasing the absorber/evaporator pressure while maintaining other parameters constant (as listed in Table 3.5) results in an increase in COP. But there is a limit to the value that can be achieved.

ii) If the condenser/desorber pressure is maintained at 1500 kPa (15 bar) then the maximum absorber/evaporator pressure that can be achieved is 493 kPa (4.93 bar). Beyond this value the model does not converge. This indicates that there is a limit on the absorber/evaporator pressure. The same holds true at other condenser/desorber

pressures. EES automatically calculates the thermodynamic properties of the refrigerant-absorbent solution at different state points. For a fixed desorber pressure, if the absorber pressure is exceeded beyond what is theoretically possible then EES gives out an error stating that the thermodynamic properties at that particular state point could not be calculated and this is the reason for non-convergence of the model.

iii) The *temperature glide* across the evaporator, which is defined as the difference between the evaporator inlet temperature and evaporator outlet temperature, decreases with increase in absorber/evaporator pressure. Increasing the pressure beyond 175 kPa (at a condenser/desorber pressure of 1500 kPa) makes the temperature at the inlet of the evaporator higher than the temperature at the outlet of evaporator (which is at the evaporator pressure), which is not feasible. This is because an evaporator is a device that absorbs heat from its surroundings hence the inlet temperature at the evaporator has to be lower than its outlet temperature. At a value of 175 kPa (1.75 bar) the temperature glide is minimum around 1.62 ^{o}C.

On the whole for a particular condenser/desorber pressure, the maximum absorber/evaporator pressure was chosen according to the following criteria:

i) A minimum temperature glide of at least 1.6 ^{o}C should be maintained.
ii) The COP of the system cannot be greater than 1 as practically it is impossible to achieve a COP greater than 1 for a single stage NH_3-H_2O system.

The reason for the COP being less than 1 can be explained with the help of the first and second laws of thermodynamics. The VARS operates between three temperature levels *viz.* desorber temperature, evaporator temperature and external heat sink temperature (assuming that the condenser and absorber heat rejection takes place at the same heat sink temperature).

From the first law of thermodynamics we can write

$$Q_e + Q_d - Q_{c+a} + W_p = 0$$

Where,

Q_e	Cooling load (W)
Q_d	Heat supplied at desorber (W)
Q_{c+a}	Heat rejected by condenser and absorber (W)
W_p	Work input to the solution pump (W)

The second law of thermodynamics is about entropy and for the VARS we can write

$$\Delta S_{total} = \Delta S_{system} + \Delta S_{surroundings} \geq 0$$

Where,

ΔS_{total}	Total entropy change
ΔS_{system}	Entropy change of the system
$\Delta S_{surroundings}$	Entropy change of surroundings

As the VARS operates in a closed cycle, ΔS_{system} is equal to zero. The change in entropy of the surroundings is given by

$$\Delta S_{surroundings} = -\frac{Q_e}{T_e} - \frac{Q_d}{T_d} + \frac{Q_{a+c}}{T_o} \geq 0$$

By substituting the first law into the above equation we get

$$Q_d \left(\frac{T_d - T_o}{T_d}\right) \geq Q_e \left(\frac{T_o - T_e}{T_e}\right) - W_p$$

The COP of the VARS is given by

$$COP_{VARS} = \frac{Q_e}{Q_d} \leq \left(\frac{T_e}{T_o - T_e}\right)\left(\frac{T_d - T_o}{T_d}\right)$$

In an ideal system, the processes are totally reversible and hence the total entropy change is equal to zero. Thus $\Delta S_{total} = \Delta S_{surroundings} = 0$ and

$$COP_{ideal,VARS} = \frac{Q_e}{Q_d} = \left(\frac{T_e}{T_o - T_e}\right)\left(\frac{T_d - T_o}{T_d}\right)$$

In a real world VARS, there are various irreversible effects such as *viscous friction*, *thermal mixing*, *heat transfer*, *mass mixing* and many more. Irreversibilities occur between the absorption cycle and the surroundings and that is the main reason for the actual COP to be lesser than the ideal COP. Also with increase in temperature, the irreversibilities associated with heat transfer increase significantly.

The graphs shown in Figure 3.15 depict the maximum absorber/evaporator pressure for a particular condenser/desorber pressure. The following information can be inferred from these graphs.

i) When the desorber pressure is 1500 kPa (15 bar), all the criteria mentioned above are met and a maximum COP of 0.6 can be achieved from the system.
ii) As the desorber pressure is lowered, the maximum COP that can be achieved at the maximum allowable absorber pressure is increased and reaches values up to 0.95. This is because the temperature glide at the evaporator reduces thereby maximizing the heat transfer at the evaporator and thus increasing the cooling capacity.
iii) At very low desorber pressures of 900 kPa, the temperature glide tends to remain more or less constant after a certain absorber pressure.
iv) The NH_3 mass fraction at state point 10 decreases as the desorber pressure is lowered and does not vary with absorber pressure. This could be attributed to the reduced desorption capability at the desorber at lower pressures.

v) The COP increases with increase in absorber/evaporator pressure. This is because with increase in absorber/evaporator pressure (provided absorber rejection temperature is constant), the concentration of the strong solution coming out of the absorber and entering the desorber increases which provides for more refrigerant desorption in the desorber thereby translating to increased COP.

The limits on the absorber/evaporator pressure for a given condenser/desorber pressure and the COP at that value is listed in Table 3.7.

Table 3.7: Maximum limit on the Absorber/Evaporator pressure at fixed desorber pressure

Desorber pressure (bar)	Maximum absorber pressure (bar)	COP at max absorber pressure
15	1.75	0.6
13	1.8	0.7
11	2.5	0.95
9	2	0.95
7	1.5	0.95

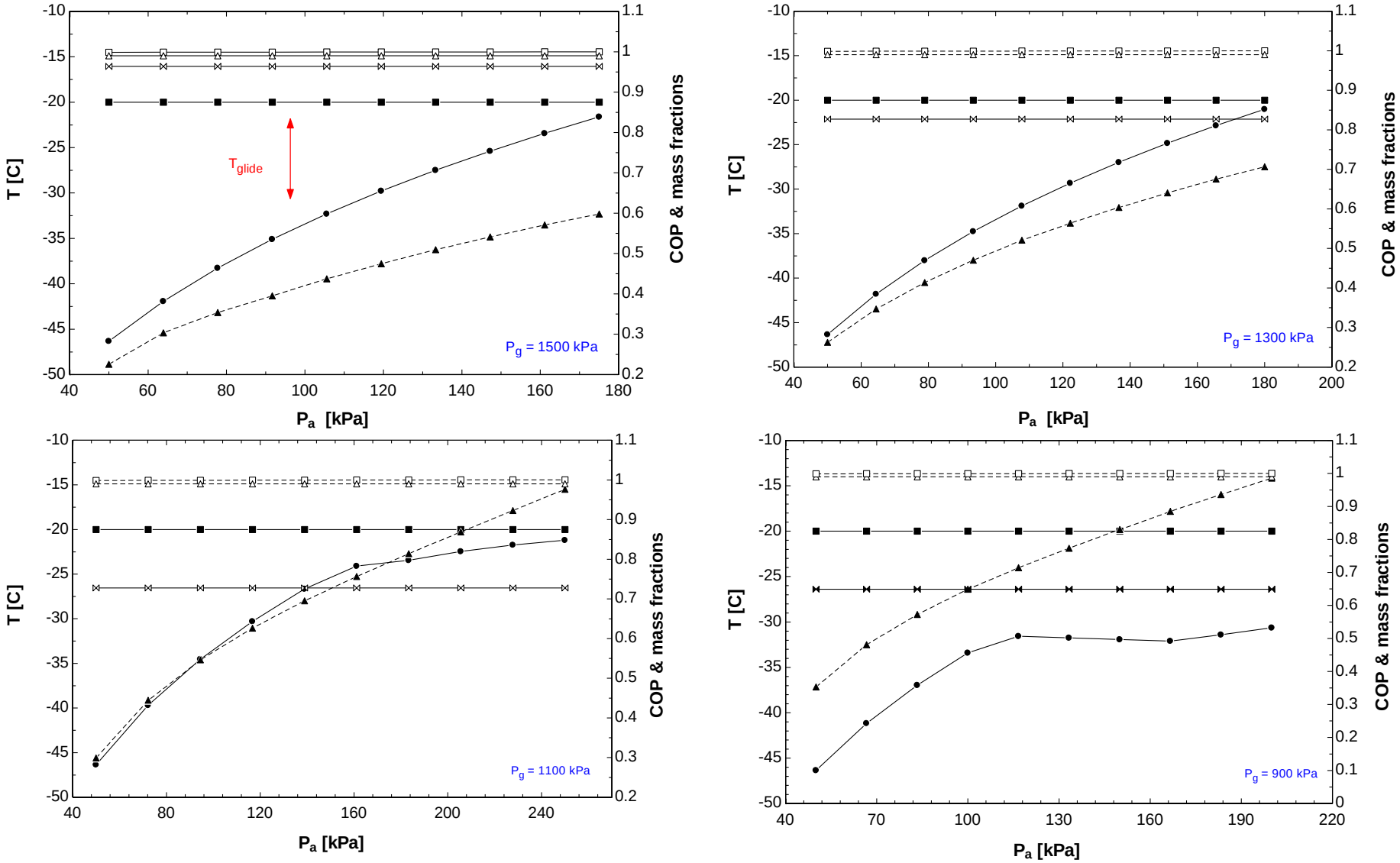

Figure 3.15: Temperature, concentration and COP as a function of Absorber/Evaporator pressure at different Condenser/Desorber pressure

3.4.3 Design limits on condenser / desorber pressure

As with the case of absorber/evaporator pressure, there are certain limits on the condenser/desorber pressure levels for a particular value of absorber/evaporator pressure and this is analysed in this section. The criteria for selecting the minimum condenser/desorber limit for a particular absorber/evaporator pressure is as follows:

i) The COP of the system cannot be greater than 1 as it is practically impossible to achieve a COP greater than 1 for a single stage NH_3-H_2O system.
ii) A minimum temperature glide of at least 2 ^oC must be maintained at the condenser and the condenser inlet temperature must not be less than the condenser outlet temperature. This is because condenser is a device that rejects heat to its surroundings.

The graphs depicted in Figure 3.16 to 3.18 show the minimum condenser/desorber pressure for a particular absorber/evaporator pressure. The following inferences can be made based on these graphs:

i) The condenser inlet temperature decreases with decrease in desorber pressure.
ii) The temperature glide becomes wider with increase in absorber pressure.
iii) The COP increases with decrease in condenser/desorber pressure and increase in absorber/evaporator pressure. This is because with increase in absorber/evaporator pressure, the concentration of the strong solution coming out of the absorber is increased. A solution with a higher concentration, when undergoes boiling (in the desorber) produces more refrigerant thereby translating to increased cooling capacity and thus higher COP.
iv) The NH_3 mass fraction at state point 10 reduces if the condenser/desorber pressure is reduced. This could be attributed to the decreased desorption at lower pressures in the desorber.

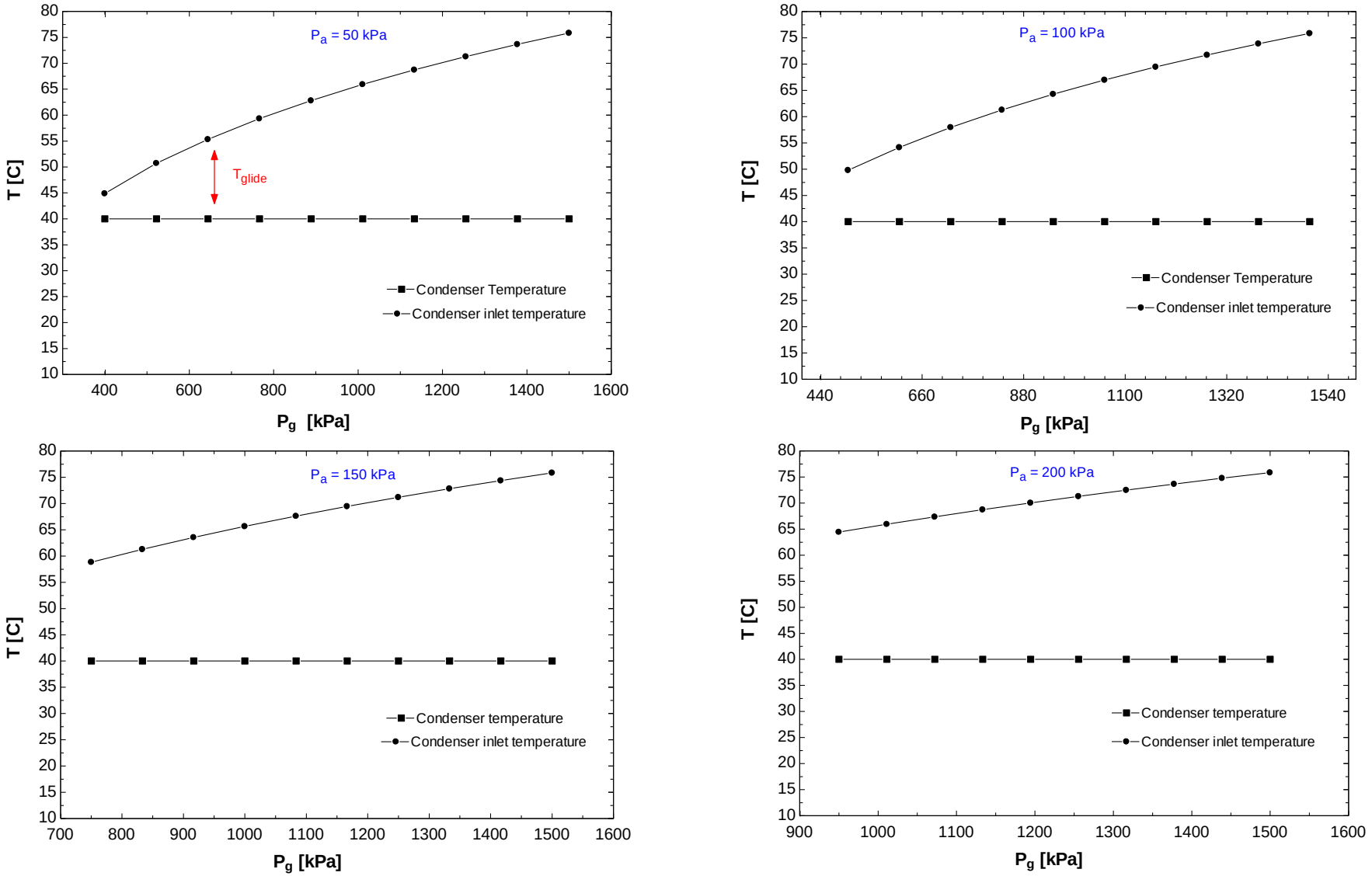

Figure 3.16: Condenser inlet & outlet temperatures vs desorber pressure at different absorber pressures (P_a at state points 1, 6, 12, 13 and14; P_g at state points 2, 3, 4, 5, 7, 8, 9, 10 and 11)

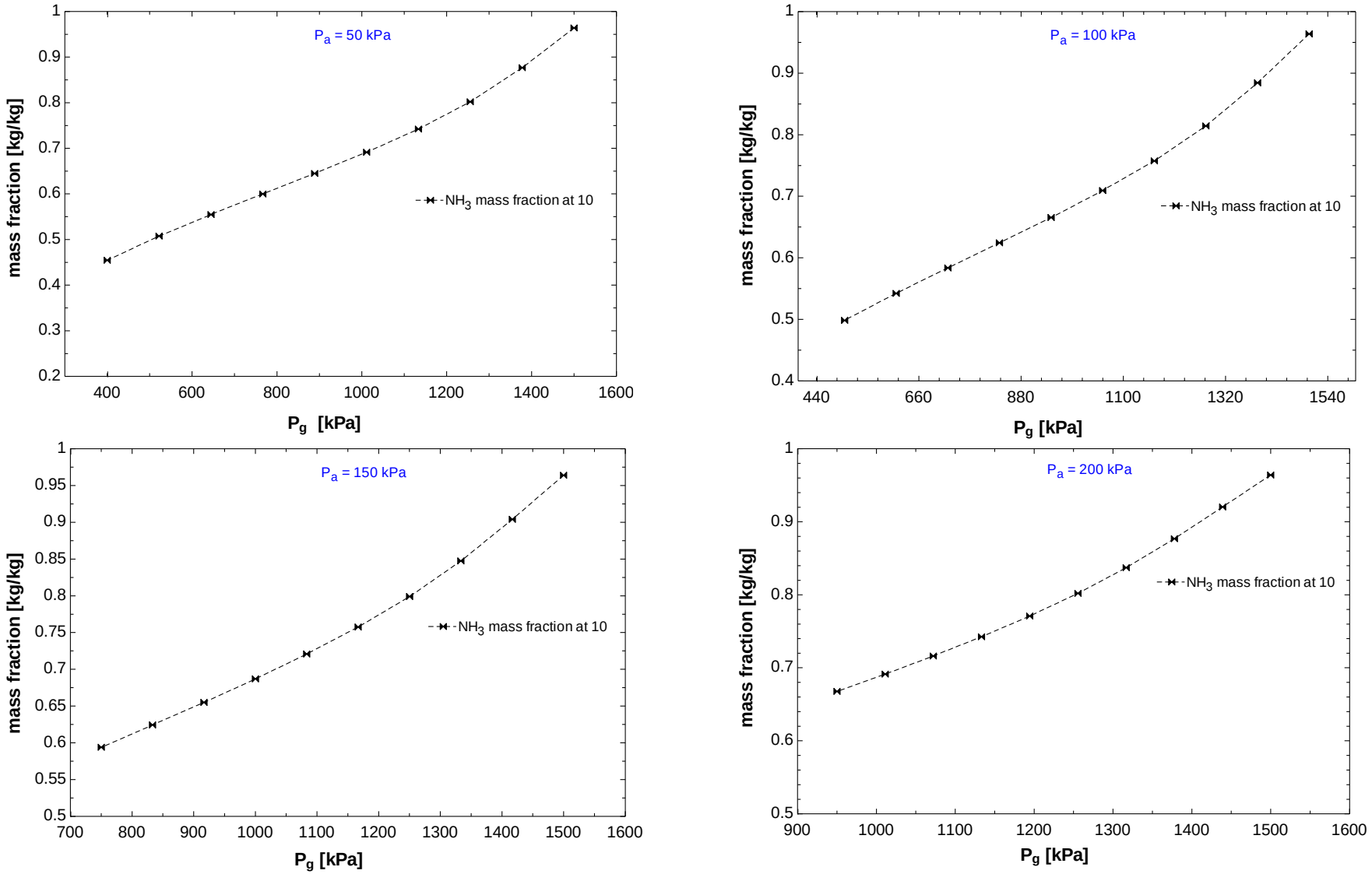

Figure 3.17: NH_3 mass fraction at state point 10 vs desorber pressure at different absorber pressures (P_a at state points 1, 6, 12, 13 and14; P_g at state points 2, 3, 4, 5, 7, 8, 9, 10 and 11)

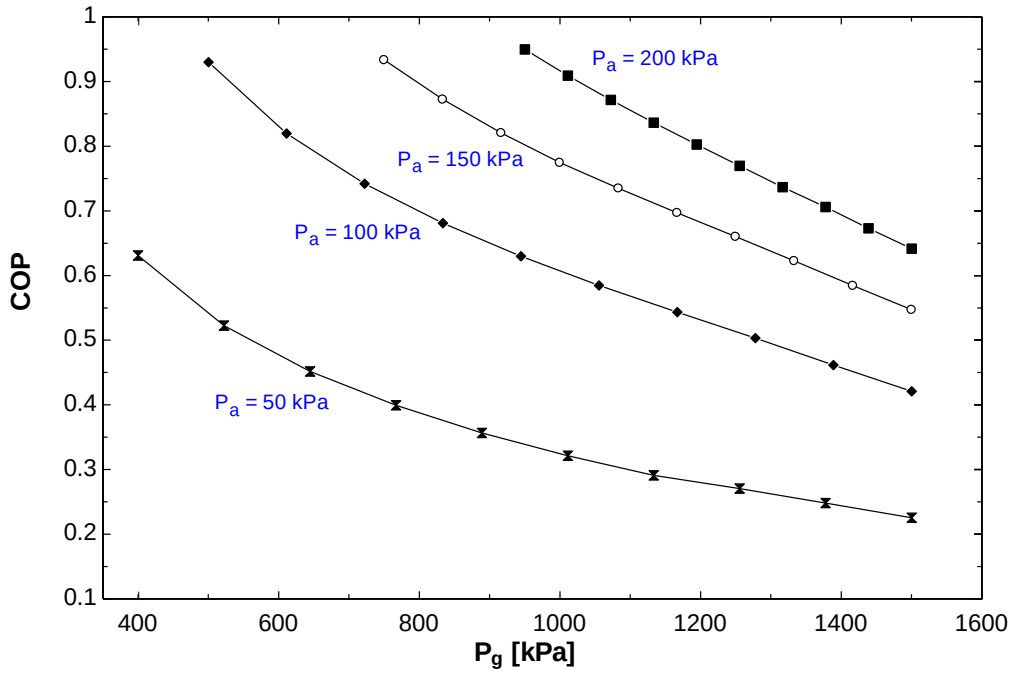

Figure 3.18: Variation of COP with desorber pressure at different absorber pressures (P_a at state points 1, 6, 12, 13 and14; P_g at state points 2, 3, 4, 5, 7, 8, 9, 10 and 11)

The limits on condenser/desorber pressure for a given absorber/evaporator pressure along with the COP value is shown in Table 3.8.

Table 3.8: Limit on minimum desorber pressure at a fixed absorber pressure

Absorber pressure (bar)	Minimum desorber pressure (bar)	COP at minimum desorber pressure
0.5	4	0.65
1	5	0.93
1.5	7.5	0.93
2	9.5	0.93

The limit imposed on the COP (in the thermodynamic model) is that it cannot be greater than 1 and because of this the COP reaches the highest possible value as obtained in Table 3.7 and Table 3.8.

3.4.4 Variation of condenser rejection temperature, solution pump efficiency and refrigerant heat exchanger effectiveness (ε_{RHX})

The variation of COP with condenser rejection temperature, solution pump efficiency and refrigerant heat exchanger effectiveness is shown in Figure 3.19. There is only a marginal increase in COP with decrease in condenser rejection temperature. When compared to the absorber rejection temperature, the condenser rejection temperature has a negligible effect on the system performance. The energy needed to drive the pump is as such very low as compared to the energy needed to drive the desorber. Increasing the pump efficiency does not make a significant difference to the overall COP of the system; however the pump work is reduced. The inference that can be made out of this is that it is not necessary to use a very high efficiency solution pump between the absorber and desorber. A pump with reasonable efficiency gives the same performance as a pump with very high efficiency. The main purpose of the refrigerant heat exchanger is to sub-cool the condensed refrigerant before it enters the evaporator. Increasing the effectiveness of the refrigerant heat exchanger has a very little effect on the overall COP of the system.

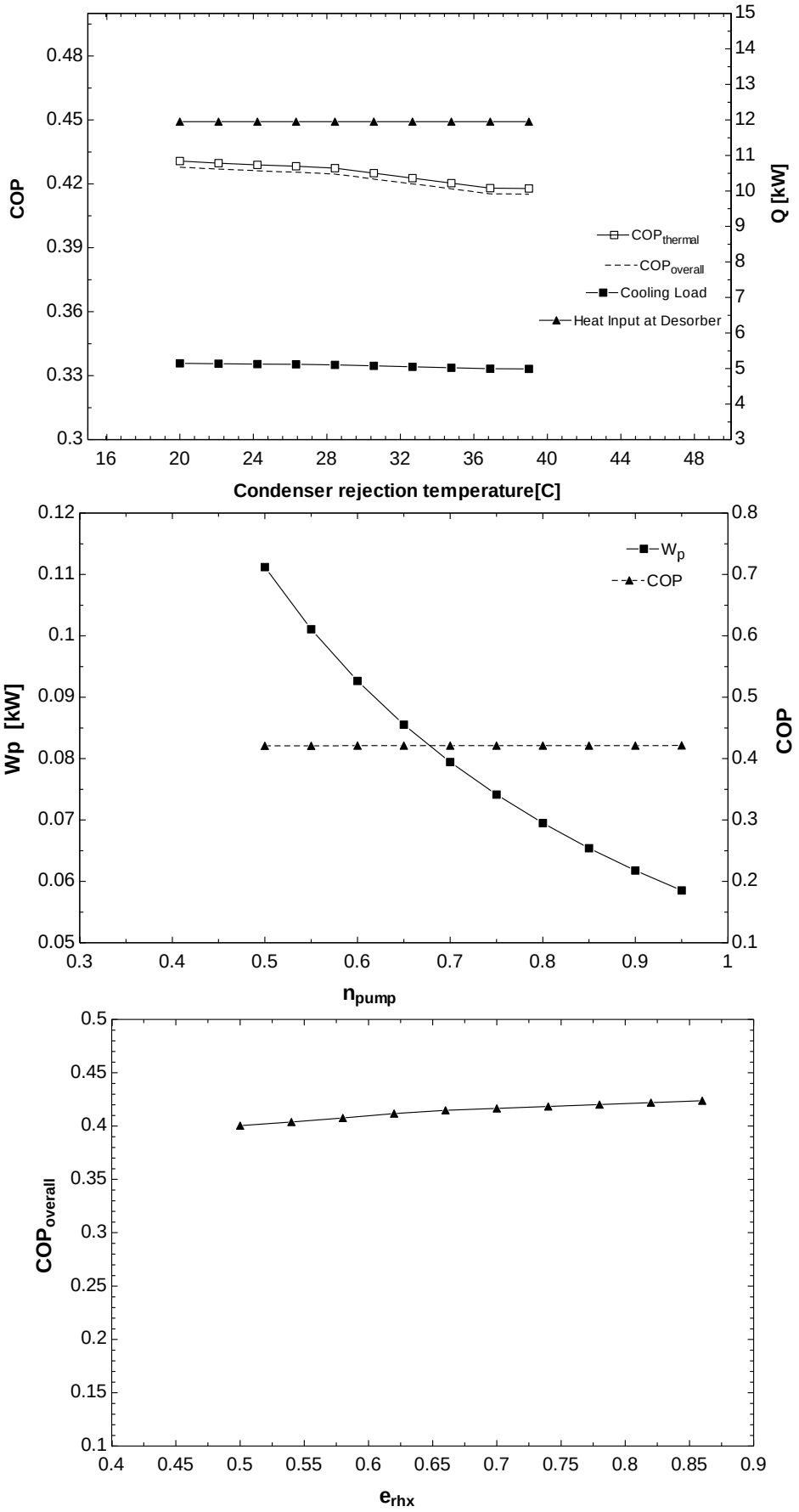

Figure 3.19: Variation of $COP_{OVERALL}$ with condenser rejection temperature, efficiency of solution pump & refrigerant heat exchanger effectiveness

3.5 Discussion

Sections 3.4.2 and 3.4.3 provided insights into the maximum absorber pressure for a fixed desorber pressure and the minimum desorber pressure for a fixed absorber pressure. This aids in choosing the practical limits on the operating pressures for both the absorber and the desorber. Further criteria to choose the absorber and desorber operating pressures are listed down.

i) The COP of the system should be as high as possible but not greater than 1.

ii) The ammonia mass fraction at state point 10 should not be less than 80 wt%. This is because the mass fraction of NH_3 vapour at the condenser input (state point 9) is 99 wt% and this cannot fall to a very low value when the vapour is condensed. In the condenser phase change of the refrigerant occurs along with heat transfer.

iii) A minimum temperature glide of 5 ^{o}C is needed for the evaporator and 25 ^{o}C for the condenser. These numbers for the temperature glides were chosen to allow enough room for heat exchange at these components. A very small temperature glide at the evaporator will result in incomplete conversion of liquid ammonia into vapour, thereby not utilizing the full capacity of the refrigerant in providing cooling to the refrigerated space. Similarly a very small temperature glide at the condenser might result in incomplete conversion of ammonia vapour to ammonia liquid.

Considering all the criteria mentioned above very few combinations exist for the absorber/evaporator pressure and the condenser/desorber pressure and these are listed in Table 3.9.

The possible absorber pressure ranges between 1 and 1.75 bar and the desorber pressure ranges between 12.5 and 15 bar. These values give the highest COP possible from the system. These values are for the base case operating conditions mentioned in Table 3.5.

Now that the pressure limits on the system are known, the maximum possible concentration difference can be calculated.

Table 3.9: Best absorber and desorber pressures for highest COP

Desorber pressure (bar) (Fixed)	Absorber pressure (bar)	COP	NH_3 mass fraction at state point 10 (kg/kg)
15	1.42	0.55	0.97
13	1.50	0.65	0.82
Absorber pressure (bar) (Fixed)	Desorber pressure (bar)	COP	NH_3 mass fraction at state point 10 (kg/kg)
0.5	12.5	0.27	0.8
1.0	12.5	0.52	0.8
1.5	12.5	0.66	0.8
2.0	12.5	0.76	0.8
0.5	15	0.23	0.8
1.0	15	0.42	0.97
1.5	15	0.56	0.97
2.0	15	0.66	0.97

Design limits for maximum concentration difference between strong and weak solution:

The maximum possible concentration difference that could be maintained between the strong and weak solution is found out for different absorber pressures and tabulated in Table 3.10. The higher the concentration difference, the higher is the system COP; hence this is a critical parameter that decides the system performance.

It can be seen that the maximum possible concentration difference between the strong and weak solution is around 15 wt%. Beyond this limit either the COP of the system is greater than 1 or the temperature at state point 5 is below the freezing point of the $NH_3 – H_2O$ solution for that particular concentration. To also ensure that the results obtained above were correct, the temperatures at the evaporator inlet and condenser inlet were analysed to check if they fell within reasonable limits.

Table 3.10: Maximum conc. difference between strong and weak soln. at different absorber pressures

Absorber pressure (bar)	Absorber rejection temperature (^oC)	Concentration of strong solution (wt%)	Maximum concentration difference between strong and weak solution (wt%)
1	40	23.3	15
1.25	40	26.2	16
1.5	40	28.68	16
1.75	40	30.9	15

(Strong solution – State point 3; Weak solution – State point 4)

Finalized system parameters for 5 kW & 1 kW cooling load

The final system operating parameters can now be decided based on the data presented in the previous sections. The major factors that influence the COP of the system are

i) Solution heat exchanger effectiveness

ii) Absorber rejection temperature

iii) Concentration difference between strong and weak solution

iv) Absorber & desorber operating pressures

The ranges of these parameters are shown in Table 3.11

Table 3.11: Finalized system operating parameters

Effectiveness of Solution Heat Exchanger	0.86
Effectiveness of Refrigerant Heat Exchanger	0.86
Efficiency of solution pump	0.7
Absorber rejection temperature range	30 - 40 ^oC
Evaporator/Absorber pressure range	1 – 1.75 bar
Condenser/Desorber pressure range	12.5 – 15 bar
Condenser rejection temperature range	30- 40^oC
Concentration difference range	5-15 wt%

The limit on each parameter in the above table to achieve the highest COP was obtained whilst keeping other parameters listed in Table 3.5 constant. Through simulations in EES it was found that if the limit of different parameters that give the maximum COP is implemented in the model then it gives unrealistic values of COP, giving values close to 2.

As it is impossible to get COP values greater than 1 for single stage systems, a further investigation into the system parameters is necessary to achieve a high COP.

Figure 3.20 shows the operating band for the absorber pressure when

- The condenser and absorber rejection temperature are varied.
- When the concentration difference between the strong and weak solution is varied
- The desorber pressure is varied

If the absorber and condenser rejection temperature is lowered, a higher COP is achieved but the operating band of the absorber/evaporator pressure becomes narrower. The COP is definitely higher than the base case COP of 42 %. Similarly a higher concentration difference gives a higher COP value but to limit COP values around 0.7 the operating band has to be restricted. Again with desorber pressures, a realistic band for the absorber/evaporator pressures is chalked out.

The operating system parameters for achieving a 5 kW and 1 kW cooling load with the highest COP possible are listed in Table 3.12

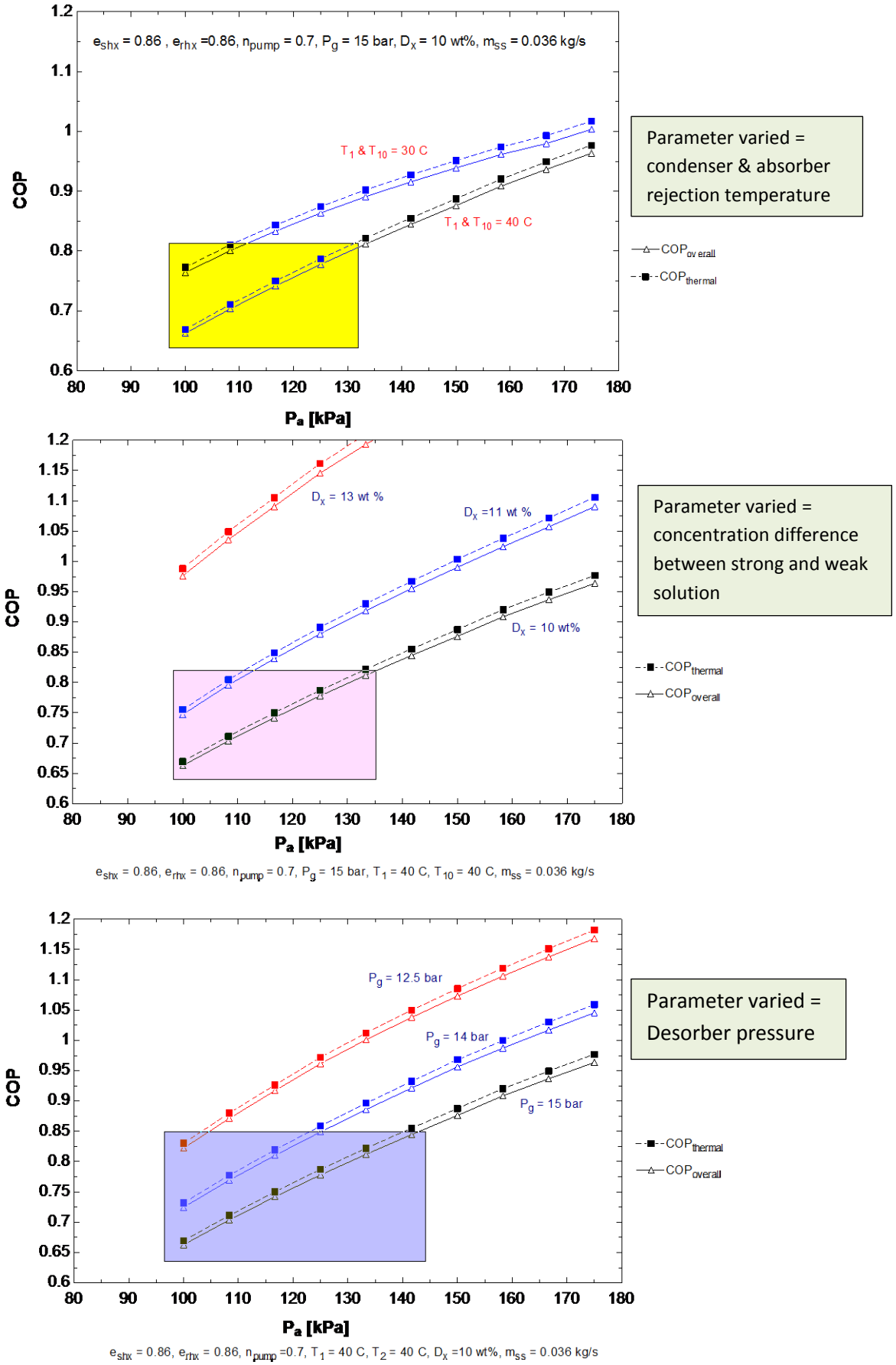

Figure 3.20: Operating band for absorber/evaporator pressure when other parameters are varied

Table 3.12: Operating parameters of VARS system for a 5 kW & 1 kW cooling load

	5 kW cooling load	1 kW cooling load
Operating system parameters		
Actual cooling load (kW) (from model)	5.01	1.031
Heat Input at Desorber (kW)	6.196	1.276
Heat rejected at Condenser (kW)	5.15	1.06
Heat rejected at Absorber (kW)	4.117	0.847
Heat rejected at Rectifier (kW)	2.01	0.4139
Work done by pump (kW)	0.0743	0.0153
Mass flow rate of refrigerant (kg s^{-1})	0.00413	0.000851
Mass flow rate of strong solution (kg s^{-1})	0.034	0.007
Mass flow rate of weak solution (kg s^{-1})	0.0298	0.0061
$COP_{Thermal}$	0.808	0.808
$COP_{Overall}$	0.7986	0.7986
Concentration of strong solution (wt %)	26.72	26.72
Concentration of weak solution (wt %)	16.72	16.72

The thermodynamic properties at each state point for a 5 kW cooling load is given in Table 3.13. Similar tables can be made for other cooling loads.

Table 3.13: Thermodynamic properties at different state points for 5 kW cooling load

State Point	$\dot{m}$ (kg s^{-1})	T (^oC)	p (bar)	h (kJ/kg)	x (kg/kg)
1	0.034	40	1.3	-1.997	0.2672
2	0.034	40.23	15	0.1885	0.2672
3	0.034	138.6	15	536.2	0.2672
4	0.0298	154.6	15	555.4	0.1672
5	0.0298	13.54	15	-54.78	0.1672
6	0.02987	13.85	1.3	-54.78	0.1672
7	0.00488	129.5	15	1696	0.8588
8	0.000755	161.3	15	599.4	0.1412
9	0.00413	75.84	15	1410	0.99
10	0.00413	40	15	164.2	0.9639
11	0.00413	9.167	15	35.76	0.99
12	0.00413	-28.02	1.3	35.76	0.99
13	0.00413	-20	1.3	1248	0.99
14	0.00413	31.6	1.3	1376	0.99

3.6 Conclusions

Cooling load requirements for different types of trucks under different ambient temperature conditions and with variations in different parameters were calculated. The cooling load calculations were based on *Transmission Heat Load*, *Service Heat Load* and *Solar Load*. The effect of solar load is quite significant and cannot be ignored and this becomes more important when such a system is designed for hot climates, especially when the truck is parked directly under the sun. Nevertheless due to lack of precise geographical specifications at this point in time, an upper limit estimate for solar load calculation was used here. The cooling load requirements for a larger truck fell in the range between 3 kW and 6 kW and for a small truck it was less than 1 kW. These values were calculated for a refrigeration temperature of -20 ^{o}C.

The cooling load data for different types of trucks served as one of the main inputs for developing the thermodynamic model of the VARS. Since the end application of the VARS is for a truck it was decided to model it as a single stage unit rather than go for a double stage one. This was done to reduce both the system size and complexity considering the limited amount of space available on the truck. Also considering sub-zero refrigeration temperatures required inside the cabinet, the working pair for the VARS was chosen to be NH_3-H_2O. The thermodynamic model of the VARS was developed for a range of cooling loads. With the initial base case parameters an overall system COP of 0.42 could be achieved. However, with implementation of a few strategies, the COP of the system could be improved close to 0.7. The major parameters that had an influence on the COP included the **solution heat exchanger effectiveness**, **absorber rejection temperature**, **concentration difference between the strong and weak solution** and the **desorber and absorber pressures**. Appropriate design maps were drawn to show the ranges of desorber and absorber pressures and also the maximum concentration difference that needs to be maintained

between the strong and weak solution. Through these design maps, limits were placed on the above mentioned parameters so that the results obtained were realistic.

The above modelling results are crucial because they provide vital information on the energy and mass flows into and out of the system which aids in design and development of each and every component of the VARS.

Bibliography

1. *"Refrigeration Requirements for Truck Bodies- Effects of Door Usage" by United States Department of Agriculture & National Bureau of Standards United States Department of Commerce (1967)*, US Goverment Printing Office: Washington DC.
2. *"Development of a method for testing and rating refrigerated truck bodies" by United States Department of Agriculture & National Bureau of Standards United States Department of Commerce (1967)*, US Government Printing Office: Washington DC.
3. www.hubbard.co.uk, *A Guide to Transport Refrigeration*. (last accessed Dec 2013)
4. Tassou S.A, De-Lille G, and Ge Y.T, *Food transport refrigeration – Approaches to reduce energy consumption and environmental impacts of road transport.* **Applied Thermal Engineering**, 2009. **29**(8–9): p. 1467-1477.
5. Deng J, Wang R.Z, and Han G.Y, *A review of thermally activated cooling technologies for combined cooling, heating and power systems.* **Progress in Energy and Combustion Science**, 2011. **37**(2): p. 172-203.
6. Sun D-W, *Thermodynamic design data and optimum design maps for absorption refrigeration systems.* **Applied Thermal Engineering**, 1997. **17**(3): p. 211-221.
7. Ines Vilarinho, Damiano Rossetti, and Critoph R, *Evaluation of Solar Assisted Sorption Refrigeration for Ice Cream Cabinets: I Absorption*. April 2012, Unilever, Colworth UK
8. Yin H, *An Absorption Chiller in a Micro BCHP Application: Model based Design and Perfromance Analysis*, PhD thesis, *School of Architecture* 2006, Carnegie Mellon University.
9. Burgess H Jennings and Shannon F.P, *Tables of the properties of aqua ammonia solutions - Part 1 of the thermodynamics of Absorption Refrigeration*. 1938, Lehigh University studies: Bethlehem, Pennsylvania.

4

CFD modelling of coupling heat exchanger & thermal energy available from SOFC stack

"*Science never solves a problem without creating ten more*" **George Bernard Shaw**

---

*The chapter presents the reader with detailed CFD modelling of the coupling heat exchanger used between the SOFC and VARS. Design maps for heating of the thermal oil using the cathode exhaust from the SOFC stack is presented as well. The thermal energy available from the SOFC stack and the point on the j-V curve at which it needs to be operated is also detailed out. Certain portions of this chapter has been taken from the paper (DOE:10.1002/fuce.201500124) published by the author in the journal '**Fuel Cells**' (Wiley)*

4.1 SOFC – VAR integration strategies

The SOFC-VAR concept hinges on the idea of harnessing heat from the exhaust stream of the SOFC to run the refrigeration system, thereby making the refrigeration system run on residual thermal energy which would otherwise be dissipated away. When using the SOFC-VAR system on the truck, the configuration and design of the main system remains the same, however the method of coupling at the desorber end varies. There are two ways to couple the SOFC with the desorber viz:

i) Indirect coupling – Using thermal oil

In this concept, the coupling between the SOFC and the desorber is achieved via a thermal oil circuit. The following components are thus required to establish the coupling:

- Intermediate gas-liquid heat exchanger
- Thermal oil pump
- Thermal oil storage tank

The thermal oil circuit is required because the SOFC and the desorber work at different ends of the temperature spectrum, the former between 700-800 ^{o}C and the latter between 150-200 ^{o}C. The thermal oil circuit thus acts as a medium to transfer heat from the exhaust of the SOFC to the desorber at a compatible temperature.

The advantage of indirect coupling is that the desorber can be designed in a very compact way and will permit the use of a plate heat exchanger as the desorber. Plate heat exchangers have been proposed for desorbers because they are extremely

compact and fit small scale applications. Plate heat exchanger desorbers will be discussed in detail in *Chapter 5*.

ii) Direct coupling – Using heat pipes

In this method, thermal energy from the cathode exhaust is supplied to the desorber via a heat pipe heat exchanger network. One end of the heat pipe is inside the desorber and the other end is exposed to the cathode exhaust. This mode of coupling eliminates the thermal oil circuit completely and needs just one component between the SOFC and the desorber as compared to three in the previous case. The crucial bit is the design of the heat pipe itself and the heat transport capability of the heat pipe. Also, since one end of the heat pipe is inside the desorber, a completely new custom made desorber design is required. Heat pipe integrated desorber and heat pipe design will be detailed in *Chapter 6*.

Direct coupling of the exhaust with the desorber (without a heat pipe heat exchanger network) will lead to a desorber design which will not be compact. This is due to two reasons: first in such a design, heat transfer will rely entirely on the sensible heat that can be transferred from the exhaust to the NH_3-H_2O solution and second the thermal capacity of the exhaust is much lower than a thermal coupling liquid thereby necessitating higher exhaust volume flow rates. Another problem is the incompatibility between the exhaust temperature and the desorber temperature as mentioned earlier, which prevents direct coupling without a heat pipe.

In the following sections, the design of the coupling heat exchanger for indirect coupling is discussed.

4.2 Coupling heat exchanger design

The 3D schematic of the coupling heat exchanger along with the different domains is shown in Figure 4.1 and the detailed geometric dimensions are shown in Figure 4.2. This is a simple tube in tube heat exchanger with fins (on the inside) where hot cathode exhaust is passed through the interior of the heat exchanger and thermal oil is passed through the annulus. This design was obtained after a number of parametric and optimisation studies in order to meet two criteria – smaller volume footprint and effective heat transfer characteristics during steady state operation.

4.3 CFD modelling of coupling heat exchanger

The coupling heat exchanger was modelled using COMSOL Multiphysics®, a commercial software package. The software package is useful for detailed component level modelling and for analysing the respective processes in detail. The physics employed in various domains are as follows:

Heat transfer in solids – Stainless steel tube

Heat transfer in fluids – Thermal oil & Air

Laminar fluid flow – Thermal oil & Air

The thermal oil selected is Paratherm HR® available from Paratherm Heat Transfer fluids [1]. This particular thermal oil can withstand a high temperature, up to 623 K without undergoing thermal degradation.

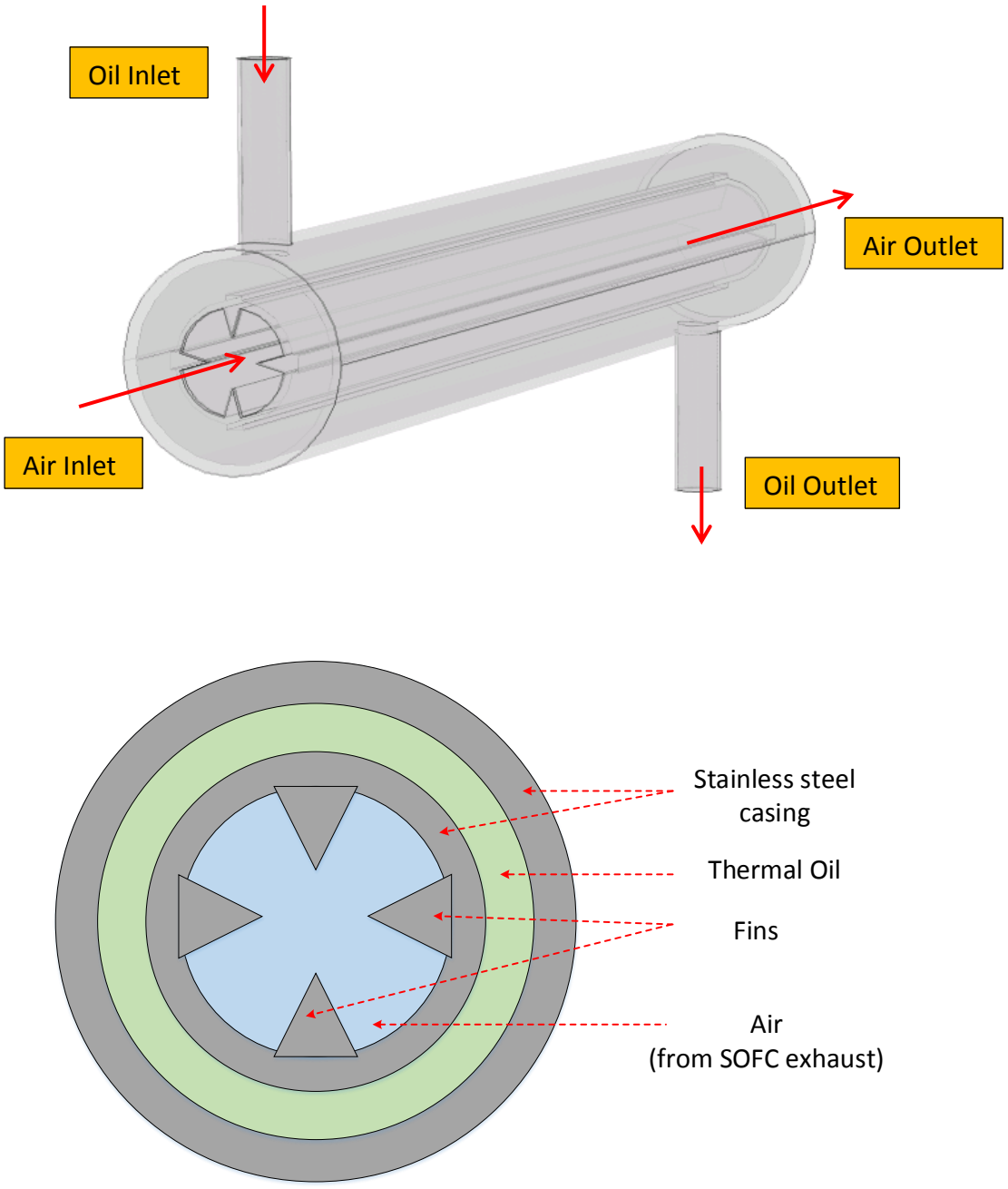

Figure 4.1: 3D schematic and different domains of coupling heat exchanger

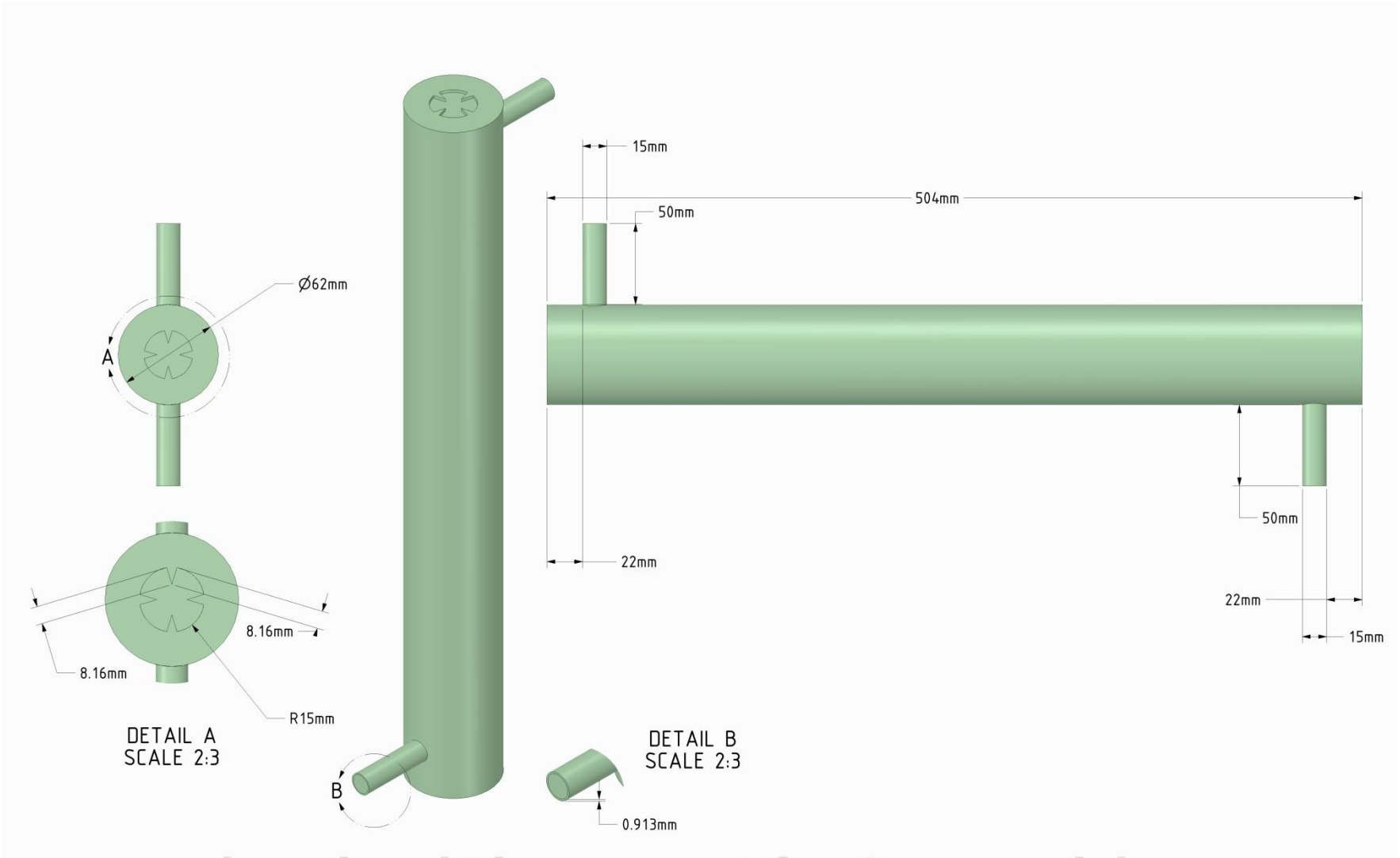

Figure 4.2: Engineering drawing of coupling heat exchanger

The governing equations for the different physics employed are as follows:

Heat transfer in solids

$$\rho C_p \nabla T = \nabla.(k\nabla T) + Q \qquad \textbf{Eq. 4.1}$$

Where,

k	Thermal conductivity of material (W m^{-1} K^{-1})
∇T	Temperature gradient (K m^{-1})
ρ	Density of material (kg m^{-3})
C_p	Specific heat capacity of material at constant pressure (J kg^{-1} K^{-1})
Q	Total volumetric heat transferred (W m^{-3})

Heat transfer in fluids

$$\rho C_p u.\nabla T = \nabla.(k\nabla T) + Q + Q_{vh} + W_P \qquad \textbf{Eq. 4.2}$$

Where,

k	Thermal conductivity of fluid (W m^{-1} K^{-1})
∇T	Temperature gradient (K m^{-1})
ρ	Density of the fluid (kg m^{-3})
u	Velocity vector (m s^{-1})
C_p	Specific heat capacity of the fluid at constant pressure (J kg^{-1} K^{-1})
Q	Total volumetric heat transferred (W m^{-3})
Q_{vh}	Viscous heating term
W_P	Pressure work term

Navier Stokes Equation

$$\rho(u.\nabla)u = \nabla.\left[-pl + \mu(\nabla u + (\nabla u)^T) - \frac{2}{3}\mu(\nabla.u)l\right] + F \qquad \textbf{Eq. 4.3}$$

Continuity Equation

$$\nabla.(\rho u) = 0 \qquad \textbf{Eq. 4.4}$$

Where,

u Fluid velocity (m s^{-1})

ρ Fluid density (kg m^{-3})

p Fluid pressure (Pa)

F External force applied to fluid (N)

The equation for heat transfer in solids is basically the 3D form of the Fouriers Law and is used to solve for the variable 'T'. In a fluid, an additional two terms are required in the heat equation. The viscosity of the fluid produces fluid heating and this term is represented as Q_{vh} in Eq. 4.2. The density of the fluid is temperature dependent, hence a pressure work term, W_P is added to the heat equation. The Navier Stokes equation and the continuity equation are used to solve for variables related to fluid flow viz. velocity and pressure and the equation for heat transfer in fluids is used for solving the temperature profiles in the fluid. The terms inside the brackets of the Navier Stokes equation represent the pressure forces and viscous forces and the term on the left hand side represents the inertial forces.

The boundary conditions applied to the geometry are:

i) Thermal insulation on the outer surface of the tube.

ii) Initial temperature for the whole geometry set to 300.15 K.

iii) Inlet temperature of air and thermal oil specified.

iv) Inlet flow rates of air and thermal oil specified.

v) The outlet boundary condition for both fluid streams was fixed at ambient pressure.

4.4 Electrochemical and thermal modelling of SOFC

The thermal energy from the SOFC stack will be used to drive the VARS and in order to assess the amount of thermal energy generated within the stack it is essential to develop both an electrochemical model and a thermal model. The electrochemical model provides the polarization curve for the SOFC at different operating temperatures which helps in deciding the operating point. Using the data from the electrochemical model, the thermal model calculates the amount of thermal energy generated within the stack. This thermal energy is then carried away by the exhaust streams exiting the stack.

Electrochemical model

The electrochemical model is developed based on the Nernst equation and the polarisation loss equations.

The theoretical open circuit voltage is given by Eq. 4.5 [2]

$$E = E_{rev} + \frac{RT}{nF}\ln\left(p_{H_2}.\frac{p_{O_2}^{0.5}}{p_{H_2O}}\right) \qquad \textbf{Eq. 4.5}$$

Where,

E_{rev}	Reversible potential (V)
R	Gas constant (J mol^{-1} K^{-1})
T	Operating temperature of SOFC (K)
n	Number of electrons involved in the electrochemical reaction
F	Faraday's constant 96485 (C mol^{-1})
p_{H_2}	Partial pressure of hydrogen (bar)
p_{O_2}	Partial pressure of oxygen (bar)
p_{H_2O}	Partial pressure of water vapour (bar)

The reversible potential is given by Eq. 4.6 [3]

$$E_{rev} = 1.253 - 2.4516 * 10^{-4} * T \quad \textbf{Eq. 4.6}$$

The actual fuel cell voltage V_{cell} is obtained by subtracting the losses from the open circuit voltage.

$$V_{cell} = E - \eta_{act} - \eta_{ohmic} - \eta_{conc} \quad \textbf{Eq. 4.7}$$

Where,

η_{act}	Activation overpotential (V)
η_{ohmic}	Ohmic overpotential (V)
η_{conc}	Concentration overpotential (V)

4.4.1 Electrochemical losses

Activation overpotential:

The activation overpotential is related to the kinetics of the reactions occurring at the respective electrodes. It is usually distinguished in two parts – the overpotential at the anode and the overpotential at the cathode. The Butler Volmer equation, which is the main equation describing the overpotential is given by Eq. 4.8 [3]

$$j = j_0 \left\{ \exp\left(\frac{\alpha z F \eta_{act}}{RT}\right) - \exp\left(-\frac{(1-\alpha) z F \eta_{act}}{RT}\right) \right\} \quad \textbf{Eq. 4.8}$$

Where,

j_0	Exchange current density (A cm^{-2})
z	Number of electrons involved in the reaction
α	Symmetry factor (usually taken as 0.5)
F	Faraday constant 96485 (C mol^{-1})

The activation overpotential is given by Eq. 4.9

$$\eta_{act,i} = \frac{RT}{F} \ln\left(\left(\frac{j}{2j_{0,i}}\right) + \left(\left(\frac{j}{2j_{0,i}}\right)^2 + 1\right)^{0.5}\right) \quad \textbf{Eq. 4.9}$$

Where,

i = a, c (anode, cathode). The anode and cathode exchange current densities are then calculated from the following expressions

$$j_{0a} = K_a \left(\frac{p_{H2}}{P_{ref}}\right)\left(\frac{p_{H2O}}{P_{ref}}\right)\exp(-E_{act,a}/RT) \quad \textbf{Eq. 4.10}$$

$$j_{oc} = K_c \left(p_{O2}/P_{ref}\right)^{0.25} \exp(-E_{act,c}/RT) \quad \textbf{Eq. 4.11}$$

Where,

p_{H2}	Partial pressure of hydrogen
p_{H2O}	Partial pressure of water vapour
p_{O2}	Partial pressure of oxygen
P_{ref}	Reference pressure (bar)
$E_{act,a}$	Activation energy needed for electrochemical process at anode (J mol^{-1})
$E_{act,c}$	Activation energy needed for electrochemical process at cathode (J mol^{-1})
K_a	Anode proportionality constant (mA cm^{-2})
K_c	Cathode proportionality constant (mA cm^{-2})

By entering the appropriate values of the corresponding parameters, the anode and cathode exchange current densities can be determined, which in turn allows the calculation of the corresponding overpotential terms. The total activation overpotential is then a sum of the two individual overpotentials.

$$\eta_{act,Total} = \eta_{act,a} + \eta_{act,c} \qquad \textbf{Eq. 4.12}$$

Ohmic overpotential:

Ohmic overpotential is mainly attributed to the losses occurring in the electrolyte of the fuel cell and is modelled by Eq. 4.13 [4]

$$\eta_{ohmic} = j\,(ASR_{ohmic}) = j\frac{d_{Ely}}{\sigma} \qquad \textbf{Eq. 4.13}$$

Where, σ is the temperature dependent conductivity of the electrolyte and is given by

$$\sigma = \frac{A_{Ely} \cdot e^{\frac{-\Delta G_{act}}{RT}}}{T} \qquad \textbf{Eq. 4.14}$$

Where,

d_{Ely}	Thickness of the electrolyte (m)
A_{Ely}	Electrolyte constant (S K m^{-1})
ΔG_{act}	Electrolyte activation energy (J mol^{-1})

Concentration overpotential:

Concentration overpotential is related to the mass transport and diffusion limitations of the reactants trying to reach the active sites on the respective electrodes and is also

distinguished in two parts – overpotential at the anode and the overpotential at the cathode [3].

$$\eta_{conc,a} = \frac{RT}{2F}\ln\left(\frac{1+\left(\frac{RTd_aj}{2FD_a^{eff}p_{H2O}}\right)}{1-\left(\frac{RTd_aj}{2FD_a^{eff}p_{H2}}\right)}\right) \quad \textbf{Eq. 4.15}$$

$$\eta_{conc,c} = \frac{RT}{4F}\ln\left(\frac{p_{O2}}{\left\{\left(\frac{P_c}{\delta_{O2}}\right)-\left(\frac{P_c}{\delta_{O2}}-p_{O2}\right)exp\left(RTd_c\frac{j\delta_{O2}}{4FD_c^{eff}P_c}\right)\right\}}\right) \quad \textbf{Eq. 4.16}$$

$$\delta_{O2} = \frac{D_{O2,k}}{D_{O2,k}+D_c^{eff}} \quad \textbf{Eq. 4.17}$$

Where,

P_c	Operating pressure (bar)
d_a, d_c	Thickness of anode and cathode electrodes (m)
$D_{O2,k}^{eff}$	Effective Knudsen coefficient ($cm^2\ s^{-1}$)
D_a^{eff}	Effective anode diffusion coefficient ($cm^2\ s^{-1}$)
D_c^{eff}	Effective cathode diffusion coefficient ($cm^2\ s^{-1}$)
p_{O2}	Partial pressure of oxygen

$D_a^{eff} = \frac{\varepsilon}{\tau}\left(\frac{1}{D_{H_2-H_2O}}+\frac{1}{D_{H_{2,k}}}\right)^{-1}$, ε & τ are the porosity and tortuosity of the anode electrode

$D_{H_2-H_2O}$ and $D_{H_{2,k}}$ are the binary diffusion coefficient and Knudsen diffusion coefficient of hydrogen.

$D_c^{eff} = \frac{\varepsilon'}{\tau'}\left(\frac{1}{D_{O_2-N_2}}+\frac{1}{D_{O_{2,k}}}\right)^{-1}$, ε' & τ' are the porosity and tortuosity of the cathode electrode

$D_{O_2-N_2}$ and $D_{O_{2,k}}$ are the binary diffusion coefficient and Knudsen diffusion coefficient of oxygen.

The total concentration overpotential is then given by the sum of anodic and cathodic overpotentials.

$$\eta_{conc} = \eta_{conc,a} + \eta_{conc,c} \qquad \textbf{Eq. 4.18}$$

The functional parameters of an SOFC single cell used in the model along with the equations related to diffusion of species are given in *Appendix C*.

4.4.2 Thermal model

MATLAB was used to model the amount of thermal energy generated within an SOFC stack. In doing so the SOFC stack was treated as a black box where only the flows into and out of the stack were of primary interest. A schematic for the same is presented in Figure 4.3.

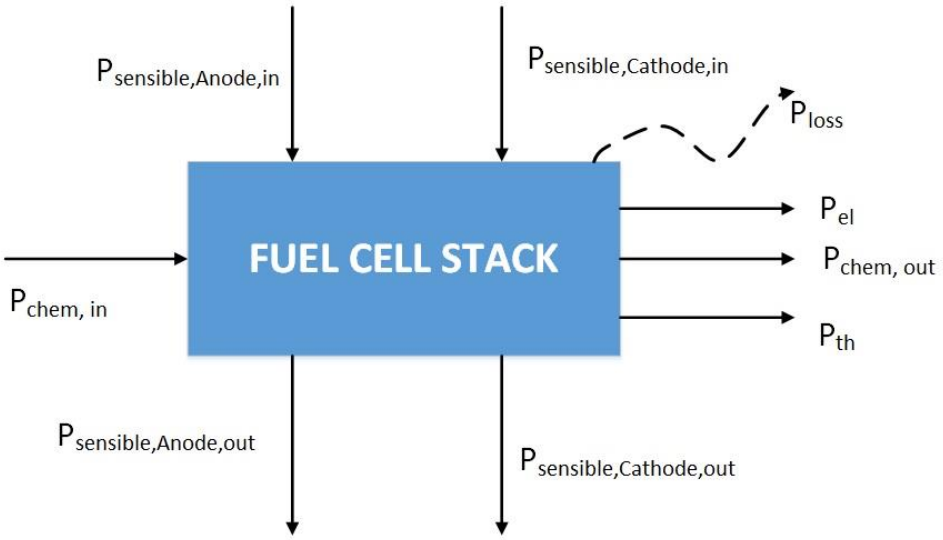

Figure 4.3: Energy balance on SOFC stack

The thermal energy generated within the stack is carried out by the exhaust streams exiting the stack because unlike other types of fuel cells, in an SOFC no separate cooling loop is employed. For proper thermal management, the fuel and the air stream flow rates need to be chosen accordingly. The model calculates the thermal energy produced in the stack as a function of operating current density of the SOFC by way of an energy balance for which the set of equations is given in Eqs. 4.19 to 4.22 [5]. The model assumes pure hydrogen as the operating fuel however other fuel types can be incorporated by easily changing the thermodynamic properties of the fuel in the model.

$$P_{chem,in} + \Sigma P_{sensible,in} = P_{el} + P_{th} + P_{chem,out} + \Sigma P_{sensible,out} + P_{loss} \quad \textbf{Eq. 4.19}$$

$$P_{chem} = \dot{m}_{H_2} * U_{f,H_2} * HHV \quad \textbf{Eq. 4.20}$$

$$P_{loss} = h_{cr} * A_{stack} * (T_{ins} - T_a) \quad \textbf{Eq. 4.21}$$

$$P_{Sensible} = \dot{m}_{H_2} * U_{f,H_2} * H_{H_2} + \dot{m}_{Air} * U_{f,oxygen} H_{air} \quad \textbf{Eq. 4.22}$$

Where,

$P_{chem,in}$	Chemical energy of fuel fed into the stack (kW)
$P_{chem,out}$	Chemical energy of fuel going out of the stack (kW)
$P_{Sensible}$	Sensible heating of the species (kW)
P_{el}	Electrical power produced by the stack (kW)
P_{th}	Thermal power generated in the stack (kW)
P_{loss}	Energy lost from the fuel cell stack to ambient via convection and radiation (kW)
$\dot{m}_{H_2}$	Mass flow rate of hydrogen (kg s^{-1})
$\dot{m}_{Air}$	Mass flow rate of air (kg s^{-1})
U_{f,H_2}	Fuel utilisation
$U_{f,oxygen}$	Oxygen utilisation

h_{cr}	Heat transfer coefficient taking into account both convective and radiative losses to the environment (W m^{-2} K^{-1})
H_{H_2}	Enthalpy of hydrogen (kJ kg^{-1})
H_{air}	Enthalpy of air (kJ kg^{-1})
T_{ins}	Temperature of insulation (K)
T_a	Temperature of ambient (K)

Latent heat was not considered in the equations described above because water is generated as a by-product in the vapour phase. The $P_{chem,out}$ and $P_{chem,in}$ terms are connected by the fuel utilisation (anode gas utilisation) factor and calculated by Eq. 4.20. $P_{chem,out}$ is nothing but the chemical energy of the unused fuel which depends on the fuel utilisation factor. The code written in MATLAB is flexible enough in allowing the user to vary not only the SOFC functional layer parameters but also the operating conditions of the SOFC stack.

The algorithm followed by the MATLAB code and the equations related to the fluid properties for the SOFC thermal model are given in *Appendix C*.

4.5 Results

As mentioned in *Chapter 1*, a bottom up modelling approach is followed where upstream component modelling and design is carried out based on the inputs derived from downstream components or systems. Hence for the coupling heat exchanger it is essential to know the SOFC cathode exhaust volumetric flow rates and temperature because these serve as inputs for modelling the performance of the heat exchanger.

4.5.1 SOFC thermal energy and flow rate of exhaust streams

The amount of thermal energy generated within an SOFC single cell when operating at 700 ^{o}C (973 K), 750 ^{o}C (1023 K) and 800 ^{o}C (1073 K) is shown in Figure 4.4. The SOFC thermal energy refers to the heat generated in the stack as a result of electrochemical reactions occurring at both the electrodes (in the individual cells within the stack) and ohmic heating. This heat is then carried out by the exhaust streams. As can be seen from the figure, the thermal energy generated is a direct function of operating current density. Electrical power is also a direct function of current density but unlike thermal power, electrical power begins to decrease after about 50% of the OCV (Open Circuit Voltage) is reached. The thermal power and electrical power cross-over at different values of current densities depending on the operating temperature of the fuel cell. The cross-over occurs at a larger value of current density if the operating temperature is higher as shown in Figure 4.4. This means that up to the cross-over point the fuel cell has a higher electrical power.

The thermal energy available from the stack decreases with increase in temperature for a fixed current density. This is because at higher temperatures, the individual cell voltage is higher as depicted in the j-V curves shown in Figure 4.5 which in turn translates to less overpotential losses and thereby higher electrical efficiency.

An SOFC stack comprising cells of a fixed size and rated for a given electrical power operates at a set operating point along the j-V curve, depending on the load current. The higher the voltage, the higher the electrical efficiency which in turn means the stack is being operated at low current densities. Usually stack manufacturers choose an operating point along the j-V curve where the cell voltage is high and current density is low. The reason for this is to achieve high electrical efficiencies [6] and also allow enough room for the fuel cell to be used for a longer duration, taking voltage degradation into account. The actual geometrical design and number of cells in a stack then follows from various design choices

on total voltage, rated electrical power, efficiency and desired lifetime. Table 4.1 lists the SOFC stack specifications for operation at three different temperatures when an electrical power of 1 kW is desired.

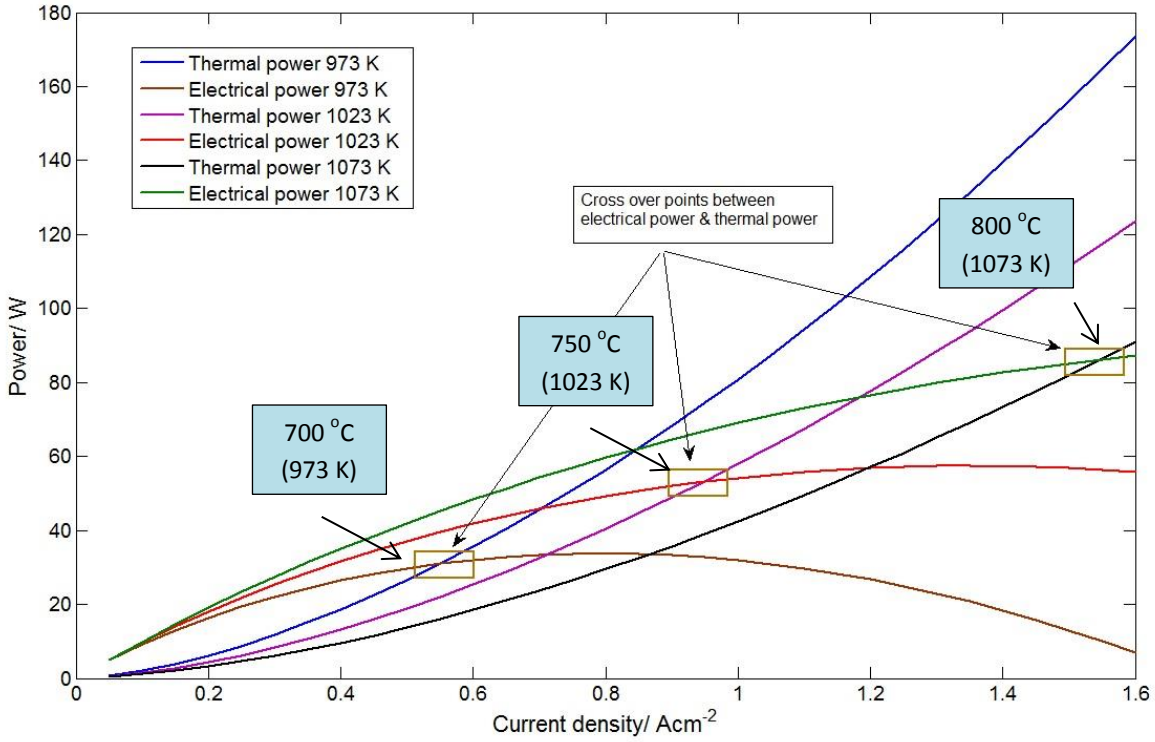

Figure 4.4: Electrical and thermal energy from SOFC single cell

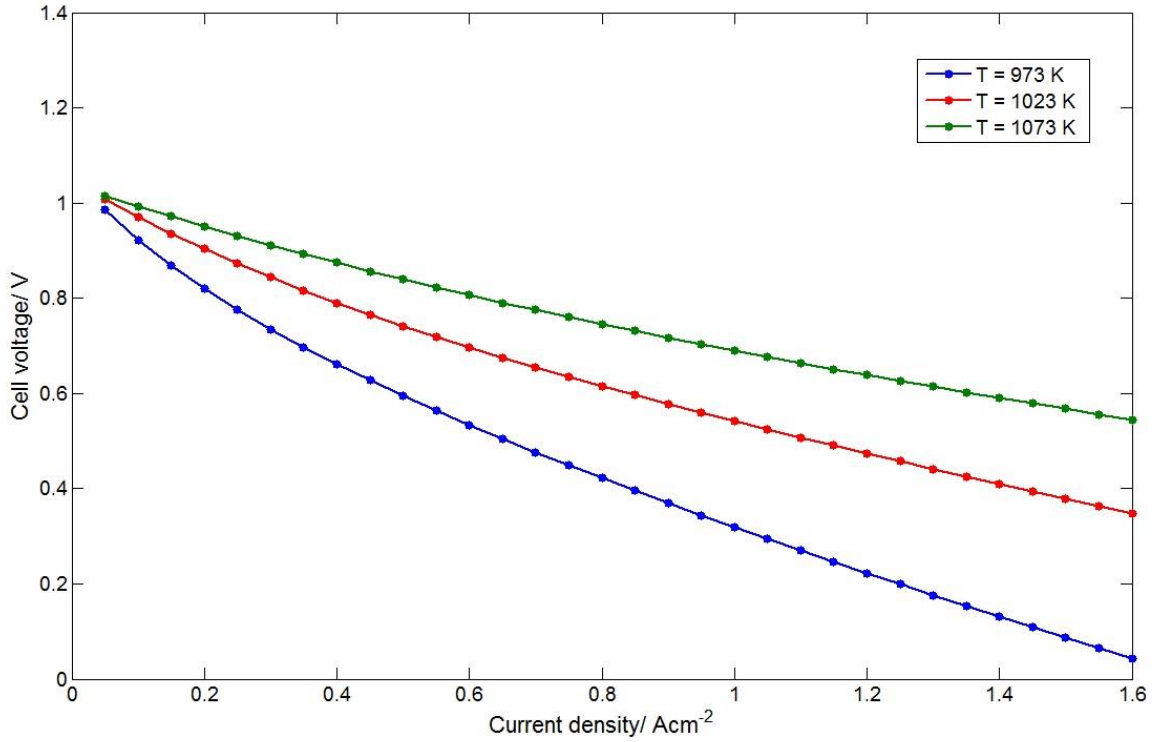

Figure 4.5: j-V curves of SOFC single cells
(T = 1073 K, P = 1 bar, pH_2 = 0.97, pO_2 = 0.21, pH_2O = 0.03)

Table 4.1: SOFC stack specifications for a desired electrical power of 1 kW

	T = 973 K	**T = 1023 K**	**T = 1073 K**
Operating current density (A cm^{-2})	0.35	0.6	1.0
Operating voltage (V)	0.7	0.7	0.7
Power density (W cm^{-2})	0.245	0.42	0.7
Active area of each cell (cm^2)	100	100	100
Desired electrical power (kW)	1	1	1
No. of cells	41	24	15
Thermal power generated per cell (W)	12	22	40
Total thermal power generated in stack (W)	492	528	600

As can be seen from this table, operation of the stack at 800 ^oC (1073 K) generates the most heat because the operating current density of the stack is also higher. The amount of thermal energy generated in a stack at a particular operating temperature can be increased

by operation at a higher current density which eventually leads to a drop in cell voltage. Hence the operating current density needs to be chosen in such a way as to balance the electrical power and thermal energy desired from the stack. The thermal energy generated within the stack will be carried out by the exhaust streams. This is so far the only way to capture the high quality heat from an SOFC [7]. As the coupling between the SOFC and VARS unit is established via a thermal oil circuit it is important to determine the exhaust flow rates. Both the anode and the cathode exhaust streams will be in the temperature range 700-800 ^{o}C, depending on the SOFC operating temperature. The exhaust flow rates will depend on the fuel utilisation of the stack (and each single cell within the stack) and follows the operating set point of the stack. The oxygen used is generally half the fuel used because one mole of hydrogen requires half a mole of oxygen in the electrochemical reaction. The molar consumption rate of the reactants is calculated from Eq. 4.23 to 4.25.

$$\dot{N}_{H_2} = \frac{I}{2F} \qquad \textbf{Eq. 4.23}$$

$$\dot{N}_{O_2} = \frac{I}{4F} \qquad \textbf{Eq. 4.24}$$

$$\frac{V}{\dot{N}_i} = \frac{R.T}{P} \qquad \textbf{Eq. 4.25}$$

Where,

$\dot{N}_{H_2}$	Molar consumption rate of hydrogen (mol s^{-1})
$\dot{N}_{O_2}$	Molar consumption rate of oxygen (mol s^{-1})
F	Faraday constant 96485 (C mol^{-1})
V	Volume flow rate (m^3 s^{-1} or L s^{-1})
$\dot{N}_i$	Molar consumption rate of species (mol s^{-1})

Depending on the fuel utilisation (anode gas utilisation), the inlet flow rate of the reactants to be supplied to the stack will vary. The exhaust flow rate will then be the difference between the inlet flow rate and that consumed in the electrochemical reaction. Figure 4.6 shows the anode and cathode exhaust flow rates for two different SOFC stacks. The stack specifications for the same are given in Table 4.2. The exhaust flow rates and temperature serve as inputs for modelling and simulating the tube in tube heat exchanger (with fins) which couples the SOFC stack and the VARS unit.

Table 4.2: SOFC stack specifications for different power ratings

	SOFC 1 kW stack	**SOFC 5 kW stack**
Single cell voltage (V)	0.6	0.6
Single cell current density (A cm^{-2})	1.26	1.26
Power density of single cell (W cm^{-2})	0.756	0.756
Active area of single cell (cm^2)	100	100
No. of cells needed for desired power	14	67
Stack current (A)	126	126
Stack voltage (V)	8.4	40.2

(Operating temperature = 800 ^oC)

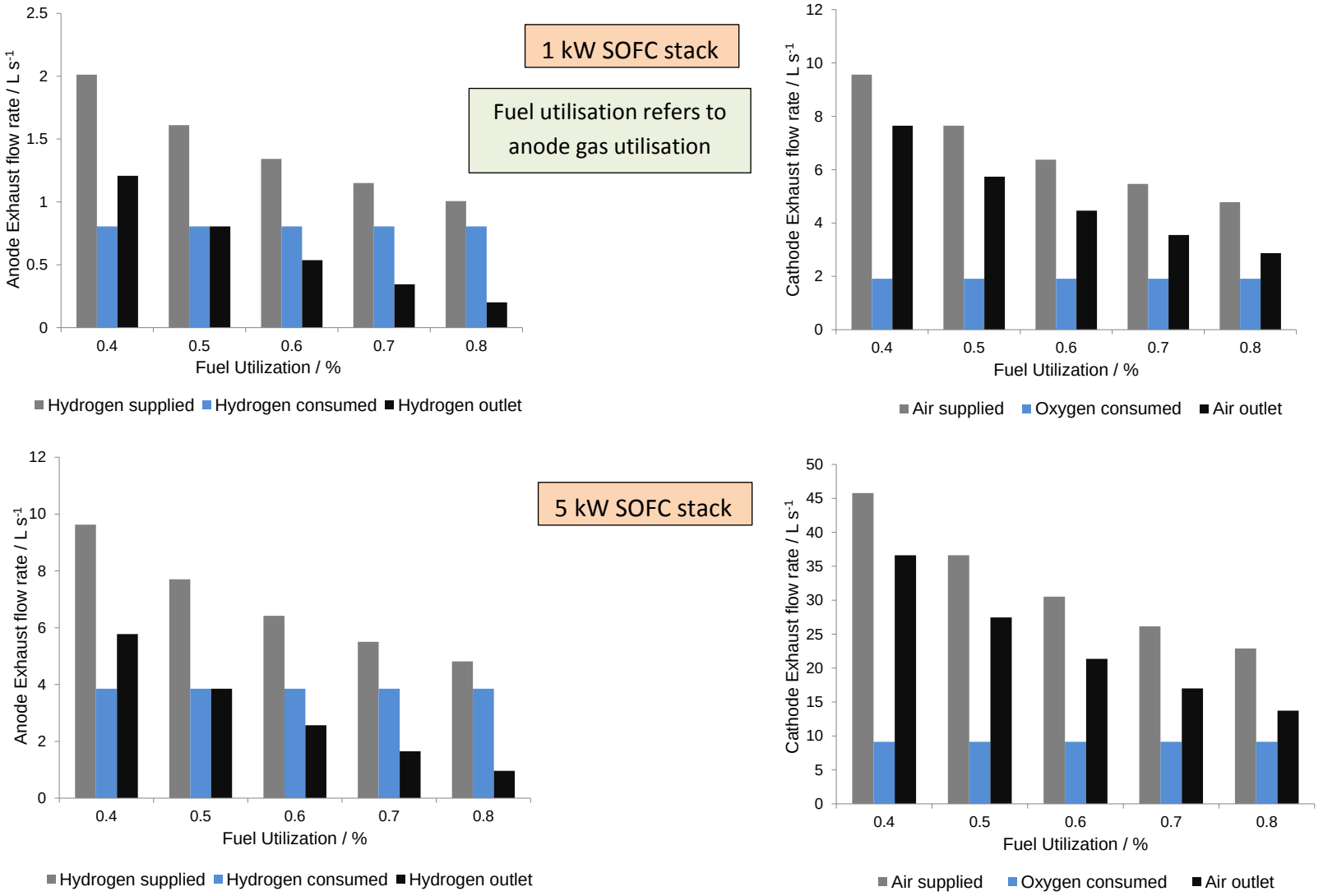

Figure 4.6: Anode and cathode exhaust flow rates from a 1kW and 5 kW SOFC stack

4.5.2 Temperature, pressure and flow visualizations – Coupling heat exchanger

Meshing plays a crucial role in CFD simulations. COMSOL Multiphysics® numerically solves the mathematical equations pertaining to the respective physics applied based on a finite element method rather than a finite volume method. This is because the finite element method is more suitable for solving multiphysics problems. The geometry of the coupling heat exchanger that was meshed for CFD simulations is shown in Figure 4.7. The corresponding mesh statistics are given in Table 4.3.

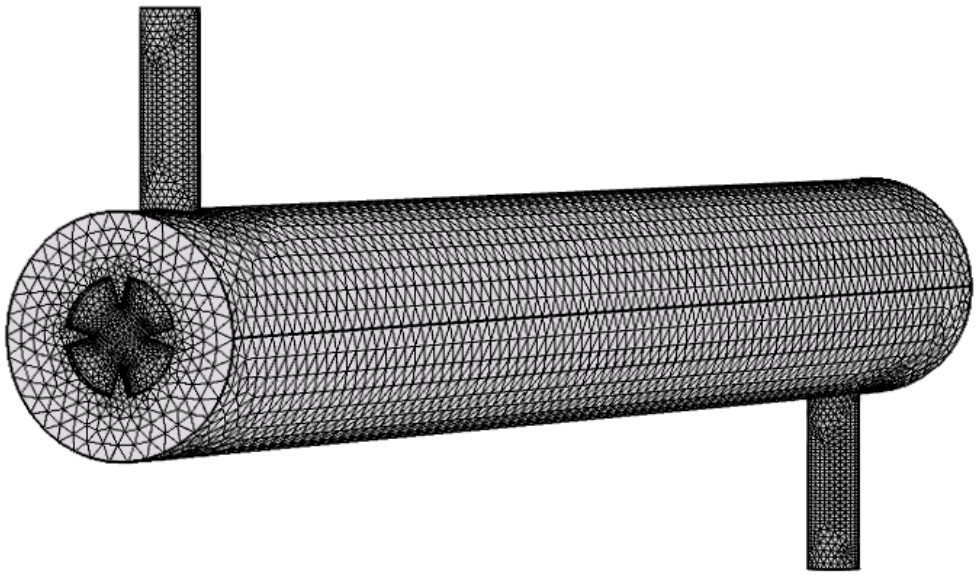

Figure 4.7: Meshing of the coupling heat exchanger geometry

The quality of the elements in the mesh is very important in order to achieve accurate results from CFD and also for convergence of the solvers. As seen from Table 4.3, the average element quality is 0.64 which is good and the number of elements is more than 2 million

which is sufficient enough to guarantee meaningful and accurate CFD results. The computer used for running simulations places an additional constraint on meshing. This is because if the computer is not powerful enough in terms of memory and processing speed, then generating a dense mesh will result in a very long computational time or even failure to solve. Hence a suitable compromise needs to be achieved based on the results desired and the computational resource available.

All CFD simulations for this work were carried out on a Windows 7 computer with Intel ® Xenon ® CPU E5-2660 v2 2.2 GHz processor and 128 GB RAM.

Table 4.3: Detailed mesh statistics for heat exchanger geometry

Tetrahedral elements	2185242
Pyramid elements	20820
Prism elements	201076
Triangular elements	133770
Quadrilateral elements	320
Edge elements	11284
Vertex elements	120
Domain element statistics	
Number of elements	2407138
Minimum element quality	0.005047
Average element quality	0.6441
Element volume ratio	3.298 E-4
Mesh volume	0.00153 m^3
Maximum growth rate	8.535
Average growth rate	1.893

The temperature, pressure and velocity profiles of the fluids through the heat exchanger when using the cathode exhaust flow rate from a 1 kWe SOFC stack at a fuel utilisation of 0.5 and a thermal oil mass flow rate of 0.02 kg s^{-1} is shown in Figure 4.8 to 4.12.

As can be seen from Figure 4.8, the temperature distribution from the hot air to thermal oil is quite uniform. This means that thermal energy is being transferred almost uniformly to heat the oil to the required temperature. The heat transfer between air and thermal oil is enhanced due to the presence of internal fins.

For the hot fluid (air), the pressure gradient is almost uniform along the length of the flow passage. This is due to the almost smooth passage present for the air flow. It is essential that the pressure drop of air when passing through the heat exchanger is not too much else the air blower, which is one of the components in the SOFC BoP (Balance of Plant), will use more energy. The pressure drop for the thermal oil side is about 60 Pa and for the air side varies from 5 Pa to 271 Pa, depending on the flow rate of air. The pressure drops for a fixed flow rate of oil with different flow rates of air are tabulated in Table 4.4.

Table 4.4: Pressure drops and heat gained by thermal oil

SOFC stack size	Cathode exhaust flow rate (L s^{-1})	ΔP (Pa) air side	ΔP (Pa) oil side	Heat gained by thermal oil (kW)
1 kWe	5.74	11.75	59.83	1.84
	4.46	07.47	62.00	1.63
	3.55	05.05	63.38	1.48
2 kWe	11.06	41.88	61.74	2.29
	8.61	25.50	62.14	2.07
	6.85	16.40	62.49	1.89
5 kWe	27.45	271.10	58.06	3.28
	21.35	159.65	59.06	2.98
	17.00	98.55	59.44	2.72

(Mass flow rate oil is kept constant at 0.02 kg s^{-1})

The velocity streamlines for the thermal oil indicate that there is some turbulence (which increases heat transfer) present where the oil enters and leaves the heat exchanger but otherwise the flow is quite laminar in the middle section of the heat exchanger.

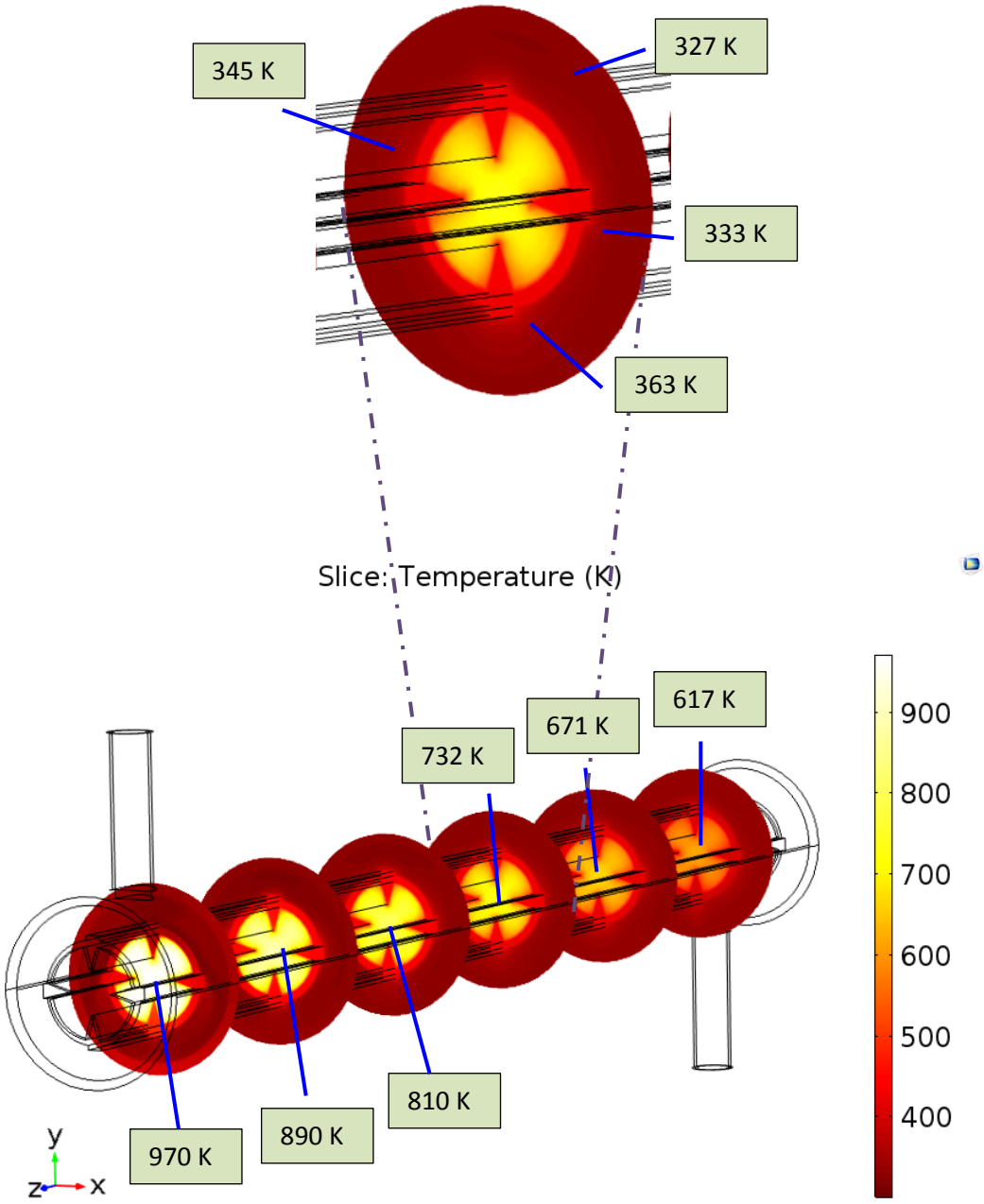

Figure 4.8: Temperature profile development through the oil and air domains ($T_{Air,In}$ = 973.15 K, $T_{Oil,In}$ = 300.15 K, v_{Air} = 5.74 L s^{-1}, m_{Oil} = 0.02 kg s^{-1})

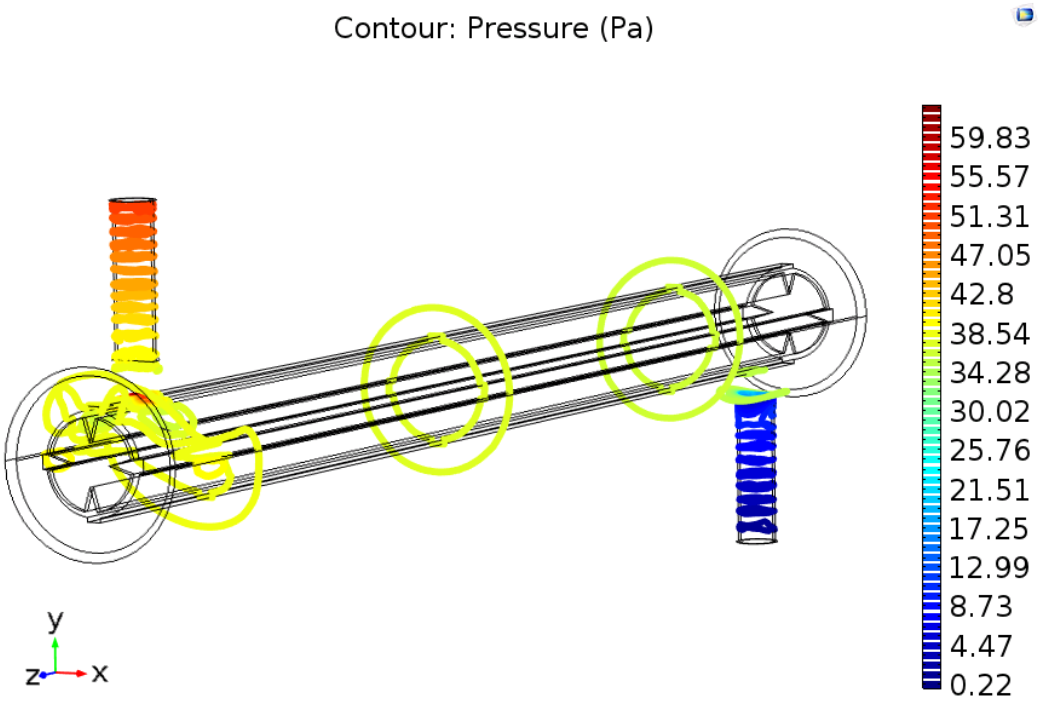

Figure 4.9: Pressure drop for thermal oil
($T_{Air,In}$ = 973.15 K, $T_{Oil,In}$ = 300.15 K, v_{Air} = 5.74 L s^{-1}, m_{Oil} = 0.02 kg s^{-1})

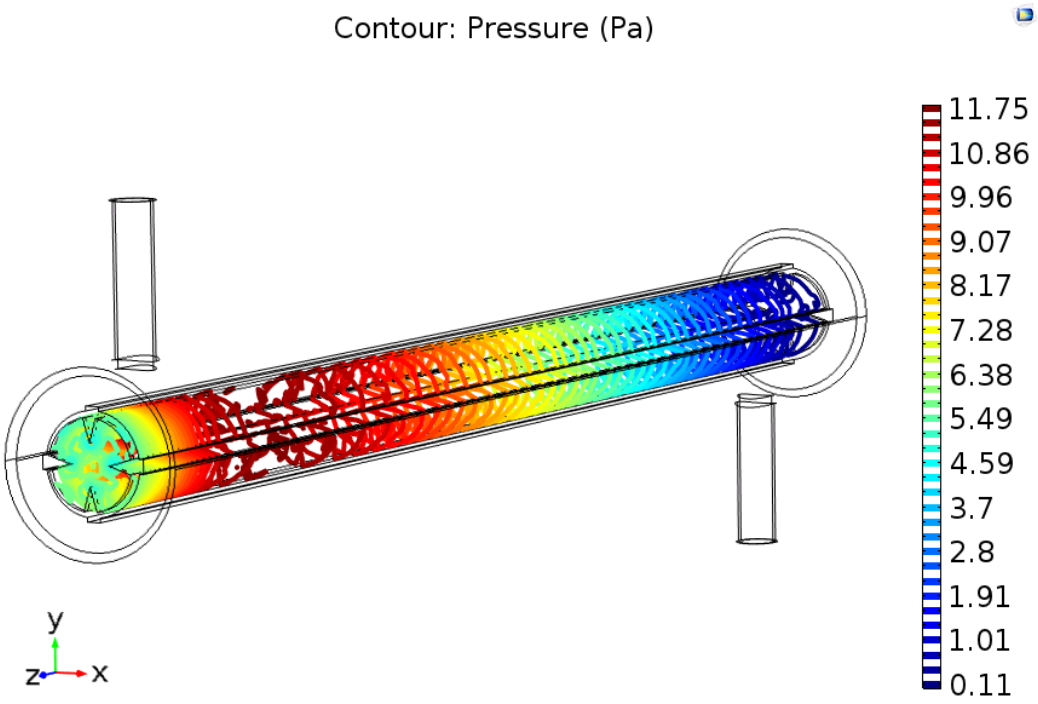

Figure 4.10: Pressure drop for air side
($T_{Air,In}$ = 973.15 K, $T_{Oil,In}$ = 300.15 K, v_{Air} = 5.74 L s^{-1}, m_{Oil} = 0.02 kg s^{-1})

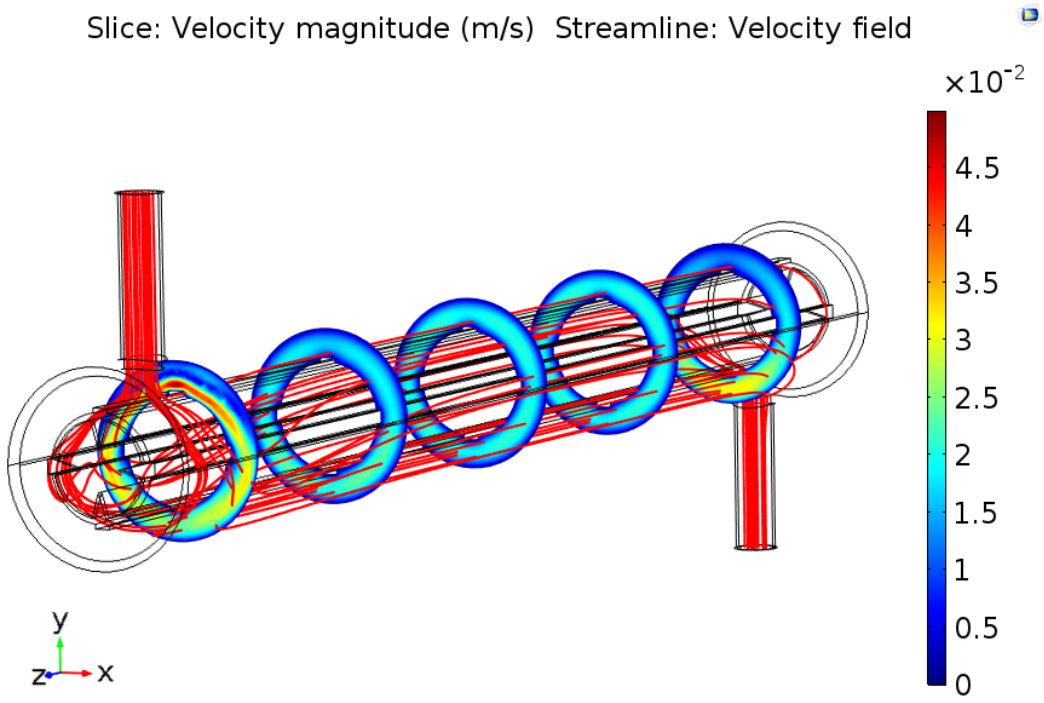

Figure 4.11: Velocity stream lines and velocity profile for thermal oil
($T_{Air,In}$ = 973.15 K, $T_{Oil,In}$ = 300.15 K, v_{Air} = 5.74 L s^{-1}, m_{Oil} = 0.02 kg s^{-1})

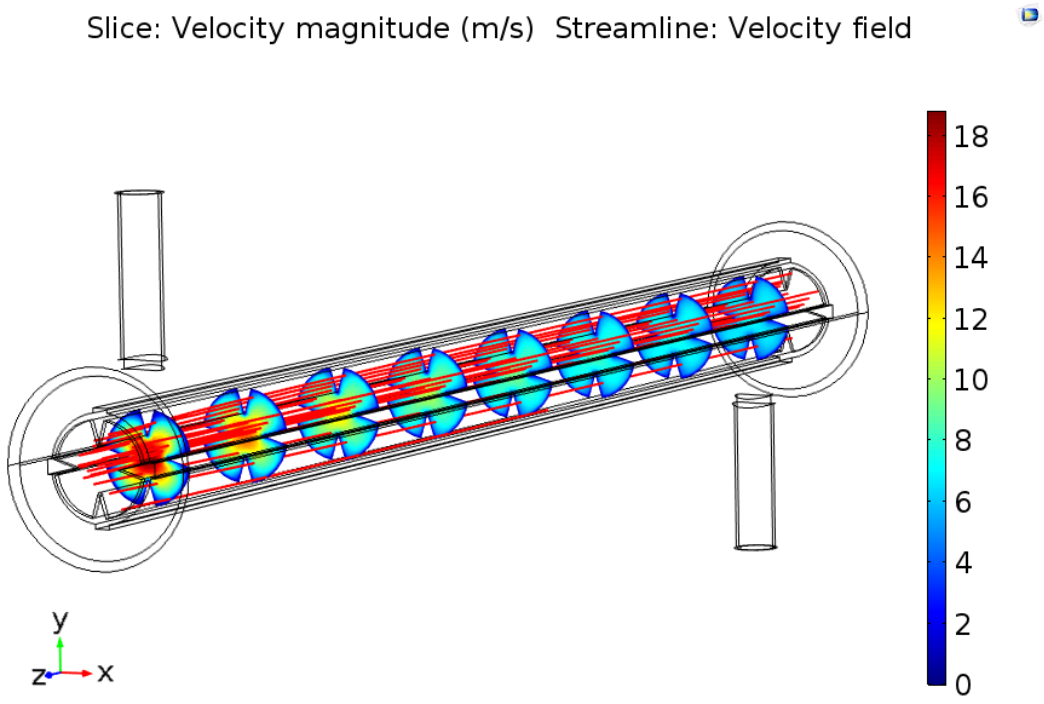

Figure 4.12: Velocity stream lines and velocity profile for air
($T_{Air,In}$ = 973.15 K, $T_{Oil,In}$ = 300.15 K, v_{Air} = 5.74 L s^{-1}, m_{Oil} = 0.02 kg s^{-1})

Similar CFD plots can be obtained for other combinations of cathode exhaust flow rates and thermal oil flow rates and a few of the combinations are shown in *Appendix D*. The pressure drops experienced by the fluids and the thermal energy gained by the oil are summarised in Table 4.4.

Thermal performance of the coupling heat exchanger - Using Effectiveness NTU method

Based on the data obtained from CFD modelling, the thermal performance of the coupling heat exchanger has been assessed using the effectiveness NTU method. A brief description of the method is outlined below:

$$C_{cold} = \dot{m}_{cold} * c_{p,cold} \quad \textbf{Eq. 4.26}$$

C_{cold} is the product of mass flow rate of the cold stream and the specific heat capacity of the cold stream.

$$C_{hot} = \dot{m}_{hot} * c_{p,hot} = C_{cold} \frac{(T_{cold,o} - T_{cold,i})}{(T_{hot,i} - T_{hot,o})} \quad \textbf{Eq. 4.27}$$

C_{hot} is the product of mass flow rate of the hot stream and the specific heat capacity of the hot stream and can be written in terms of C_{cold} and the temperatures of the streams involved as shown in Eq. 4.27.

The maximum heat that could possibly be transferred between the two streams is given by

$$q_{max} = C_{min} (T_{hot,i} - T_{cold,i}) \quad \textbf{Eq. 4.28}$$

$$C_{min} = \min\ (C_{cold}, C_{hot}) \quad \textbf{Eq. 4.29}$$

The actual heat transferred between the two streams is given by

$$q_{actual} = C_{cold}\left(T_{cold,o} - T_{cold,i}\right) \quad \textbf{Eq. 4.30}$$

The effectiveness of the heat exchanger is given by

$$\varepsilon = \frac{q_{actual}}{q_{max}} \quad \textbf{Eq. 4.31}$$

Where,

$\dot{m}_{cold}$	Mass flow rate of the cooler fluid which will gain heat (kg s^{-1})
$c_{p,cold}$	Specific heat capacity of the cooler fluid (J kg K^{-1})
$\dot{m}_{hot}$	Mass flow rate of the hot fluid which will transfer heat (kg s^{-1})
$c_{p,hot}$	Specific heat capacity of the hotter fluid (J kg K^{-1})
$T_{cold,i}$	Inlet temperature of the cooler fluid (K)
$T_{cold,o}$	Outlet temperature of the cooler fluid (K)
$T_{hot,i}$	Inlet temperature of the hotter fluid (K)
$T_{hot,o}$	Outlet temperature of the hotter fluid (K)
q_{max}	Maximum heat transferrable (W)
q_{actual}	Actual heat transferred (W)
ε	Heat exchanger effectiveness

Figure 4.13 to 4.15 shows the effectiveness of the heat exchanger for heating different oil flow rates when using the cathode exhaust from different SOFC stacks.

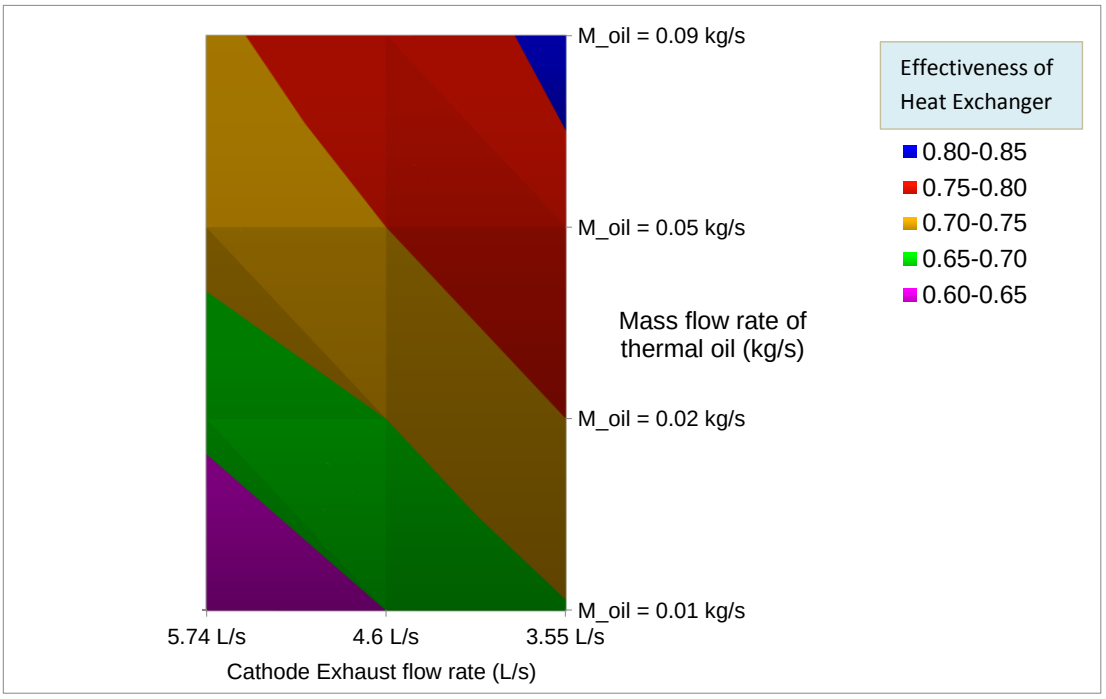

Figure 4.13: Effectiveness of heat exchanger using cathode exhaust from 1 kWe SOFC stack

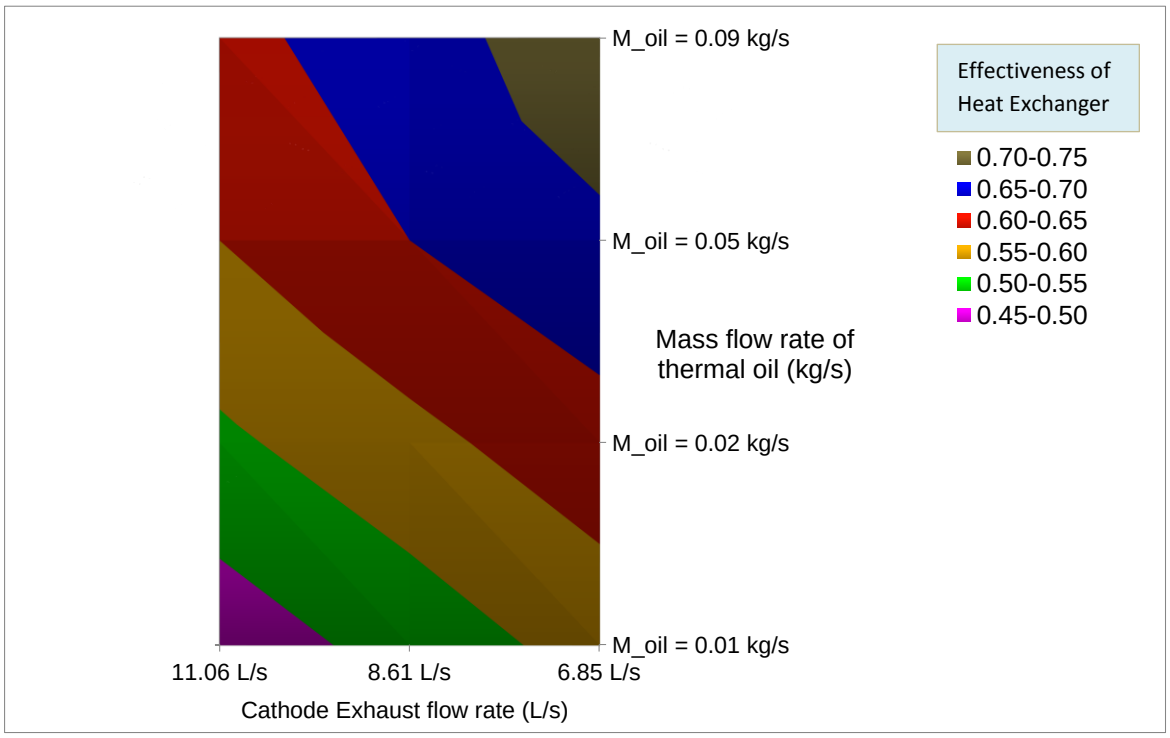

Figure 4.14: Effectiveness of heat exchanger using cathode exhaust from 2 kWe SOFC stack

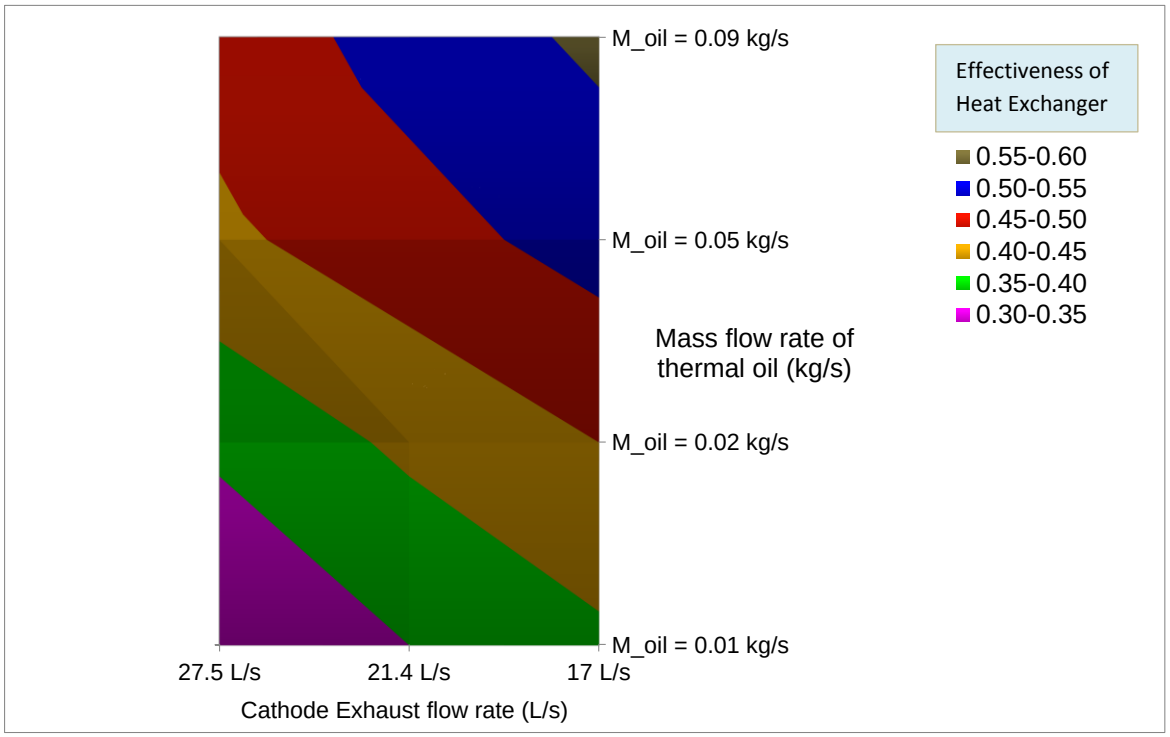

Figure 4.15: Effectiveness of heat exchanger using cathode exhaust from 5 kWe SOFC stack

An ideal heat exchanger has an effectiveness of 1 but in reality this is not possible because then the heat exchanger will have to be infinitely long. Practical heat exchangers always have an effectiveness less than 1. The higher the effectiveness, the better the heat exchanger; typical values ranging anywhere between 0.6 and 0.9. When the coupling heat exchanger is used with the cathode exhaust from a 1 kWe stack, the effectiveness of the heat exchanger ranges between 0.6 and 0.85, the higher values being attributed to low cathode exhaust flow rates and high thermal oil mass flow rates. The same heat exchanger when used with cathode exhaust flow rates from a 2 kWe and 5 kWe stack has a lower effectiveness although the trends observed in the effectiveness contour map are similar to the ones observed on the effectiveness contour map when cathode exhaust from a 1 kWe SOFC stack is used. The reason for this is because with increase in cathode exhaust flow rate at a fixed temperature, although the thermal energy gained by oil is greater, the maximum heat that could potentially be transferred is even higher. The heat exchanger

being of a fixed size is not able to capture this entire heat and the effectiveness reduces as a result. Although in all cases the thermal oil gains sufficient heat to transfer it at the desorber, the heat exchanger is not used to its full capacity when the cathode exhaust flow rates are increased to values greater than 6 L s^{-1} and oil flow rates reduced below 0.02 kg s^{-1}. This doesn't present any inherent problems as such although having a heat exchanger with maximum heat exchanger effectiveness is desired. One of the goals is also to standardise components that can be used across a range of trucks and this heat exchanger is one of the components.

Since this is a parallel flow heat exchanger, the NTU (Number of Transfer Units) can be calculated for the different flow combinations using the correlation given in Eq. 4.32 [8]

$$\varepsilon = \frac{1 - \exp[-NTU\ (1 + \ C_r)]}{1 + C_r} \qquad \textbf{Eq. 4.32}$$

Where,

$C_r = \ C_{min}/C_{max}$

C_{min} & C_{max} are the product of the mass flow rate and specific heat capacity of the respective fluids.

The plot of the effectiveness vs NTU for the designed heat exchanger when coupled with exhaust flow rates from different sized stacks for different thermal oil flow rates is shown in Figure 4.16.

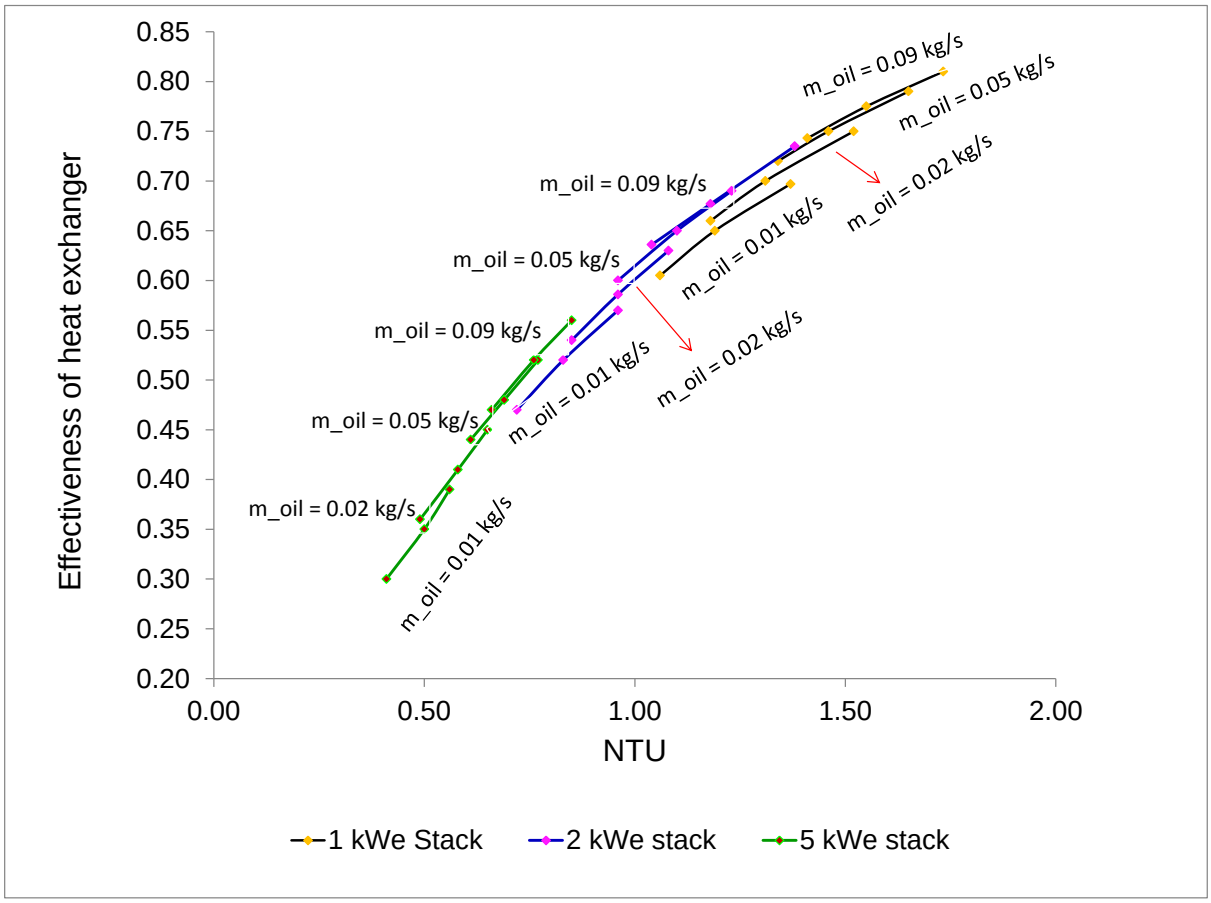

Figure 4.16: Effectiveness vs NTU plot for coupling heat exchanger

4.5.3 Design maps for heating of thermal oil

When using indirect coupling between the SOFC and VARS, a plate heat exchanger desorber is the most compact component that can be used as a desorber [9]. The coupling fluid temperature needed at the desorber is around 200 ^{o}C. During steady state operation of the whole system, the thermal oil needs to attain a temperature around 200 ^{o}C as it exits the coupling heat exchanger. The temperature gained by the thermal oil in the coupling heat exchanger and the temperature drop that it would undergo at the desorber must closely

match in order for the process to be continuous. The mass flow rate of thermal oil needed to supply the required quantity of heat at the desorber for different types of trucks at that inlet temperature is shown in Figure 4.17. These flow rates have been calculated based on the temperature gained and lost by the thermal oil when passing through the coupling heat exchanger and plate heat exchanger desorber.

Using the multi-physics model of the coupling heat exchanger, the temperature gained by the thermal oil (with different mass flow rates) in one pass through the heat exchanger when heated by different cathode exhaust flow rates from the SOFC stack can be plotted into a contour map and this is shown in Figure 4.18 to 4.20. These cathode exhaust flow rates correspond to operation of the SOFC stack at different fuel utilisations. Practical fuel utilisation factors for operating an SOFC stack range between 0.5 and 0.7 and the cathode exhaust flow rates pertaining to these values have been used in generation of the contour maps.

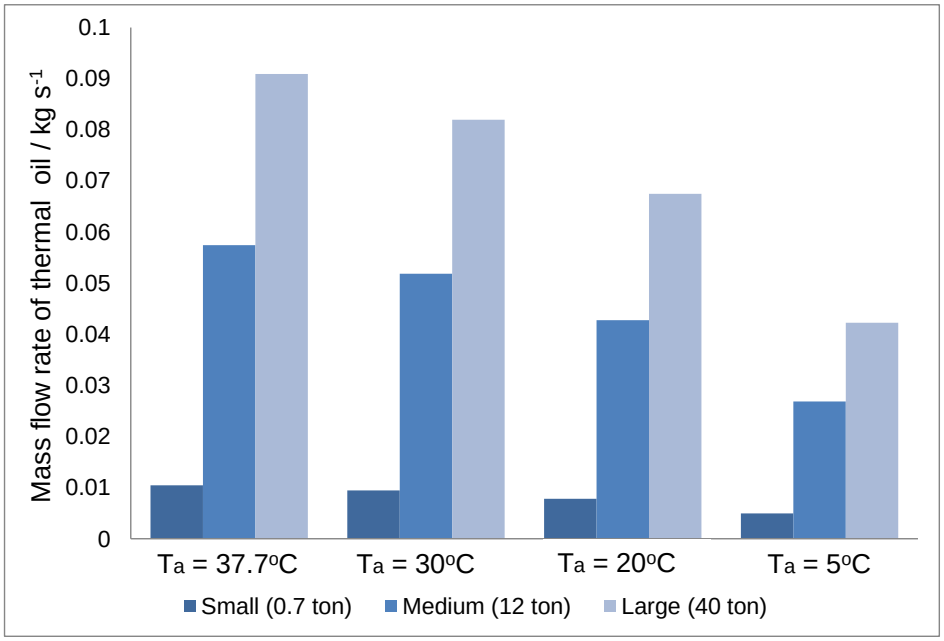

Figure 4.17: Mass flow rate of thermal oil needed at the desorber
(C_P = 2300 J kg^{-1} K^{-1}, $T_{Oil,in}$ = 200 ^oC, $T_{Oil,out}$ = 160 ^oC)

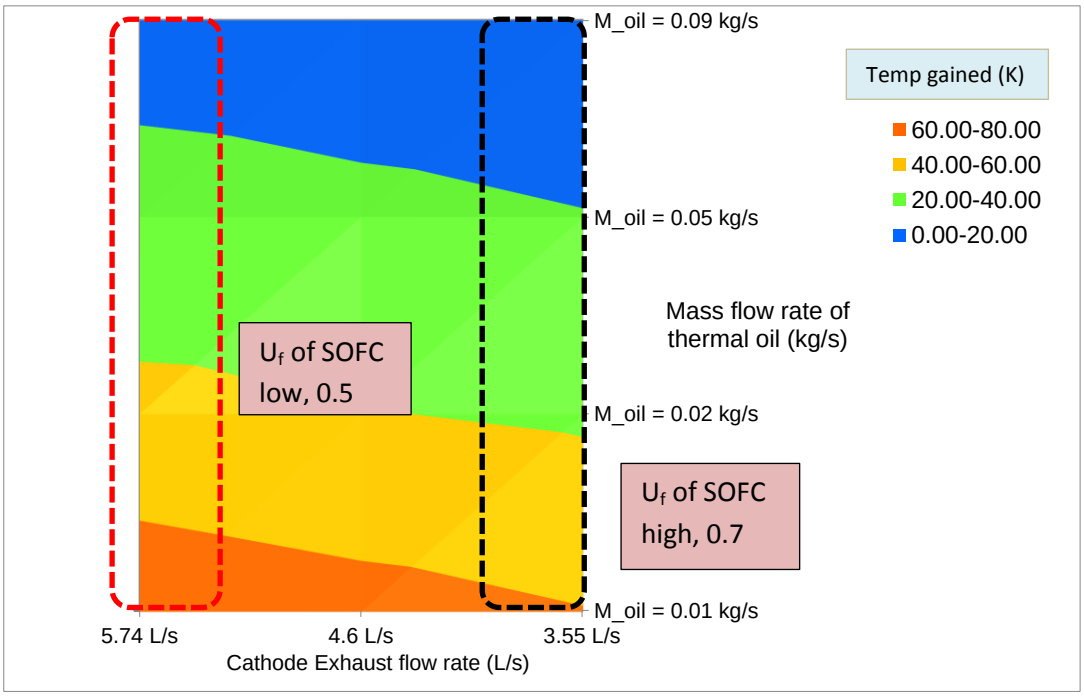

Figure 4.18: Heating of thermal oil using cathode exhaust from a 1 kW_e SOFC stack (Design map)

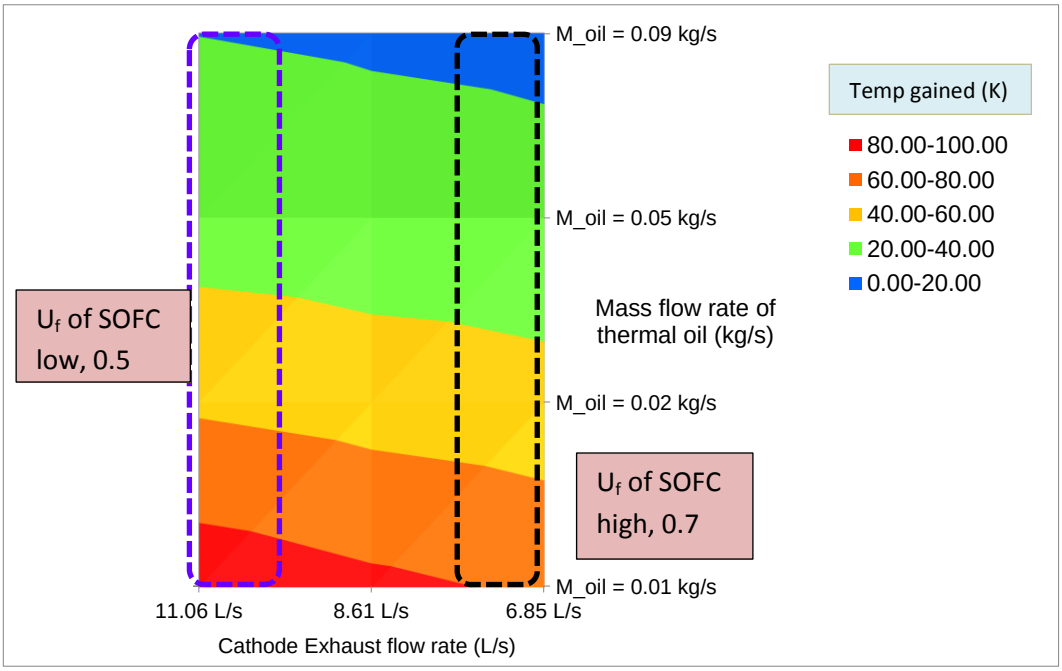

Figure 4.19: Heating of thermal oil using cathode exhaust from a 2 kW_e SOFC stack (Design map)

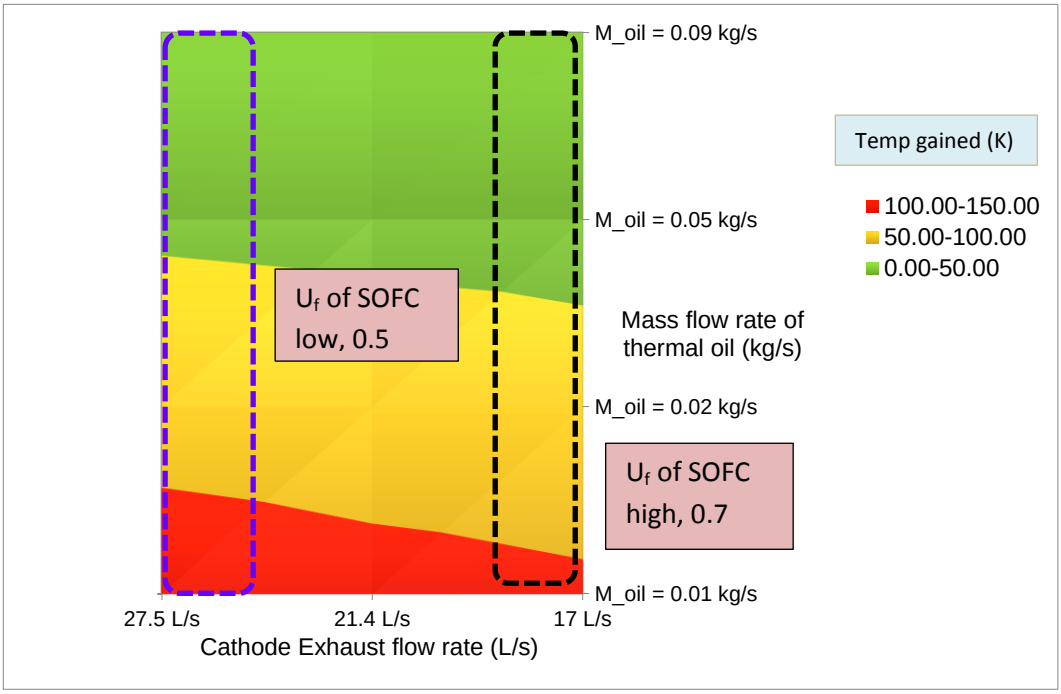

Figure 4.20: Heating of thermal oil using cathode exhaust from a 5 kW_e SOFC stack (Design map)

Operation of the SOFC stack at low fuel utilisations leads to higher cathode exhaust flow rates and in turn higher ΔT gained by the thermal oil in one pass through the heat exchanger. A higher ΔT attained by the thermal oil is preferred because that allows enough room to play with the heat transfer aspect at the desorber end. These contour maps provide information for development of another design table which provides information on the SOFC stack size, the fuel utilisation at which it is to be operated, the mass flow rate of thermal oil needed and the ambient temperature range in which such a system can be used on board different types of trucks and the same is shown in Table 4.5. The values in Table 4.5 were obtained based on the thermal energy requirement needed at the desorber for different cooling loads.

Different permutation and combination for selection of an appropriate SOFC stack and thermal oil flow rate can be done depending on the cooling load requirement and the type of truck onto which such a system is to be fitted.

Table 4.5: Design table for choosing SOFC stack size and thermal oil flow rate

SOFC stack size →		1 kWe stack	2 kWe stack	5 kWe stack	8 kWe stack
Thermal oil flow rate ↓					
Small Truck	0.01 kg/s	$U_f = 0.7$ $T_a = 38^oC$ to 5^oC	**Oversized**	**Oversized**	**Oversized**
Medium truck	0.05 kg/s	$U_f = 0.6$ $T_a = 5^oC$	$U_f = 0.5$ $T_a = 15^oC$ to 5^oC	$U_f = 0.5$ $T_a = 30^oC$ to 5^oC	**Oversized**
	0.09 kg/s	$U_f = 0.5$ $T_a = 15^oC$ to 5^oC	$U_f = 0.5$ $T_a = 25^oC$ to 5^oC	$U_f = 0.6$ $T_a = 38^oC$ to 5^oC	**Oversized**
Large truck	0.05 kg/s	**Undersized**	**Undersized**	$U_f = 0.5$ $T_a = 10^oC$ to 5^oC	$U_f = 0.6$ $T_a = 18^oC$ to 5^oC
	0.09 kg/s	**Undersized**	$U_f = 0.5$ $T_a = 7^oC$ to 5^oC	$U_f = 0.5$ $T_a = 15^oC$ to 5^oC	$U_f = 0.6$ $T_a = 25^oC$ to 5^oC
	0.11 kg/s	**Undersized**	$U_f = 0.5$ $T_a = 10^oC$ to 5^oC	$U_f = 0.5$ $T_a = 20^oC$ to 5^oC	$U_f = 0.6$ $T_a = 28^oC$ to 5^oC

(T_a = ambient temperature, U_f = fuel utilisation)

The ambient temperature of operation for the truck is linked to the operational capability of the VARS unit. Although the refrigerated truck can be driven at any ambient temperature, the VARS (if fitted) will work only for the ambient temperature range specified because it is a thermally driven refrigeration system where the performance is closely coupled with the ambient temperature (as the heat rejection sink).

On a small truck, which has a cooling load requirement of about 1 kW, it is sufficient to have an oil mass flow rate of 0.01 kg s^{-1} and a 1 kWe stack operating at a fuel utilisation of 0.7. This will be sufficient to cater to the cooling load requirements across the ambient temperature spectrum of 5 ^oC to 38 ^oC. The same 1 kWe stack can be used on a medium

truck but only when the ambient temperature is 5 ^{o}C and here the oil flow rate has to be increased to 0.05 kg s^{-1} in order to meet a greater cooling demand. However, a 5 kWe SOFC stack operating at a fuel utilisation of 0.6 along with a mass flow rate of thermal oil of 0.09 kg s^{-1} will be sufficient to cater to the cooling load requirements across the temperature spectrum of 5 ^{o}C to 38 ^{o}C. Other combinations for different trucks and different sizes of SOFC stacks can be read out from this table.

4.5.4 Design maps for selection of SOFC stacks

Design maps can be chalked out for integration of SOFC stacks with VARS units based on the results obtained in previous sections. Table 4.6 specifies the SOFC stack size in terms of electrical power in order to meet the desired cooling load needed at a refrigeration temperature of -20 ^{o}C. This is the rating of the stack at an operating temperature of 800 ^{o}C.

Table 4.6: Rating of SOFC stack based on amount of thermal energy generated within the stack

Cooling load desired at T_R = -20 ^{o}C (kW)	Heat input at desorber at COP 0.7 (kW)	Electrical power from SOFC stack (kW)	Corresponding thermal energy generated inside stack (kW)	Corresponding operating current density (A cm^{-2})
1	1.43	2	2	1.55
3	4.28	5	5	1.55
6	8.57	9	9	1.55

(At SOFC operating temperature of 800 ^{o}C)

The following inferences can be drawn from this table:

i) From the results presented in Chapter 3, the average cooling load needed for a small, medium and large truck at a refrigeration temperature of -20 ^{o}C is about 1 kW, 3 kW and 6 kW respectively.

ii) The preferred SOFC stack size in terms of electrical power to meet these cooling loads is 2 kW, 5 kW and 9 kW respectively. The amount of thermal energy generated inside the SOFC stack at an operating current density of 1.55 A cm^{-2} is almost the same as the amount of electrical power as seen from Figure 4.4.

iii) As mentioned earlier, a conscious choice needs to be made about the operating point of the SOFC. Operation of the stack at higher current densities beyond the cross over point implies more thermal energy generation and less electrical energy generation from the stack. This will mean the fuel cell is being used as a heat generating machine with low electrical efficiency. Operation at high current densities also leads to faster stack degradation [6, 10], for instance due to excessive heat generation and crack development within SOFC functional layers. Operation at lower current densities implies a greater electrical energy output than thermal energy, and to meet a particular cooling load a very large stack (in terms of electrical power) will be needed.

iv) Although the SOFC stack meets the cooling load requirements in terms of thermal energy, there is an excessive amount of electrical power available which needs to be put to good use. If the electrical energy from the SOFC is not used or is too much in surplus then it does not make sense to use a thermally driven refrigeration system. One possibility is the use of electricity generated to constantly charge the batteries in a hybrid truck configuration which then opens up opportunities for future drive train configurations.

v) If the refrigeration temperature is lowered say for chilled foods application (between 0 and 5 ^{o}C) then the cooling load required will be drastically reduced and so will the size of the SOFC stack. For example on a large truck, the cooling load requirement at a refrigeration temperature of 5 ^{o}C is about 3 kW. So rather than use an 8 kWe stack it will be sufficient to use a 5 kWe stack. This way the electrical power available from the SOFC stack will be sufficient to meet the truck

electrical loads and will only be slightly in surplus unlike the case where the SOFC stack is used to meet the cooling load requirements for a refrigeration temperature of -20 ^{o}C.

Figure 4.21 to 4.23 show the design maps for integration of an SOFC stack on board different trucks and the different ranges of cooling load catered by the SOFC-VAR system. Besides the rating of the stack, the mass flow rate of thermal oil plays a very important role in delivering the required quantity of heat and in turn the amount of cooling produced. Simulations were carried out with different mass flow rates of thermal oil and the following phenomena were observed:

i) With a higher mass flow rate of thermal oil, a larger quantity of heat can be delivered, thereby resulting in catering to a higher cooling load on a particular kind of truck. The start-up time however will be greater because the temperature gained by the oil during one pass through the heat exchanger is reduced.

ii) If the mass flow rate of thermal oil is reduced then the temperature gained by the thermal oil in one pass through the heat exchanger is increased but the amount of heat that can be delivered to the desorber is reduced.

Thus along with mass flow rate of thermal oil, the maximum temperature gained by thermal oil in one pass and the exit temperature of weak solution from the desorber determines the quantity of heat delivered at the desorber. Simulations from VARS modelling presented in *Chapter 3* indicated that the temperature of the strong solution entering the desorber is about 130 ^{o}C and the exit temperature of the weak solution from the desorber is about 150 ^{o}C. Hence the exit temperature of thermal oil from the desorber is fixed at 433 K (160 ^{o}C)

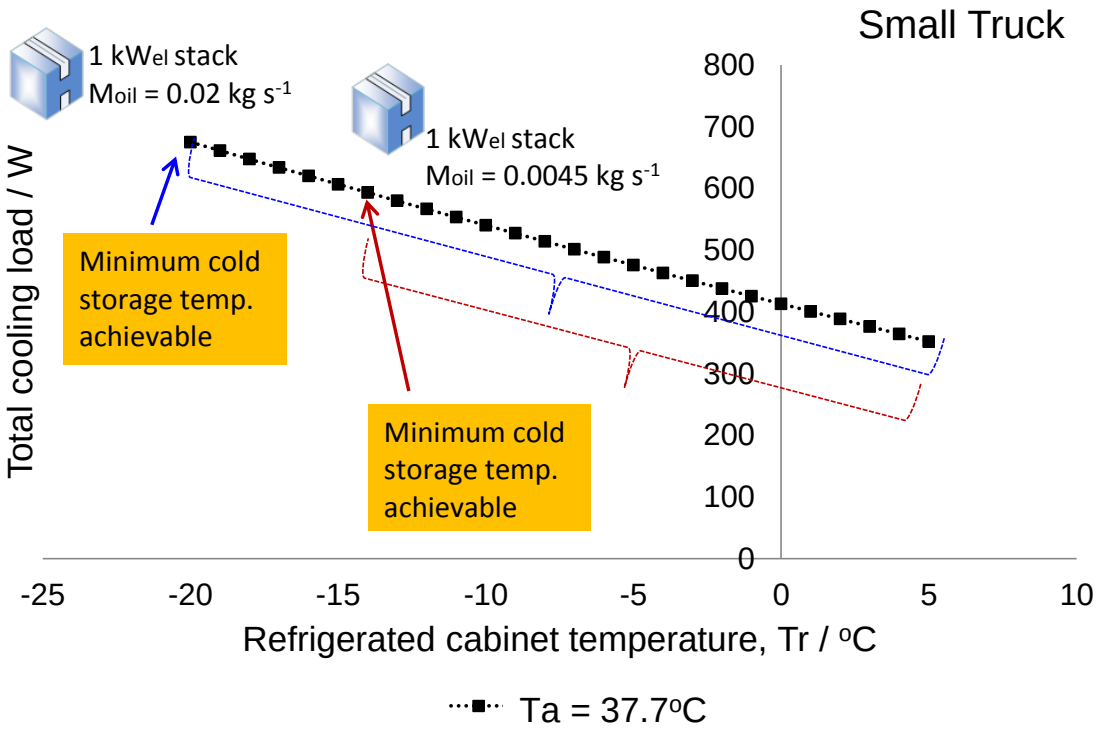

Figure 4.21: Design map for using 1 kWe SOFC stack on small truck

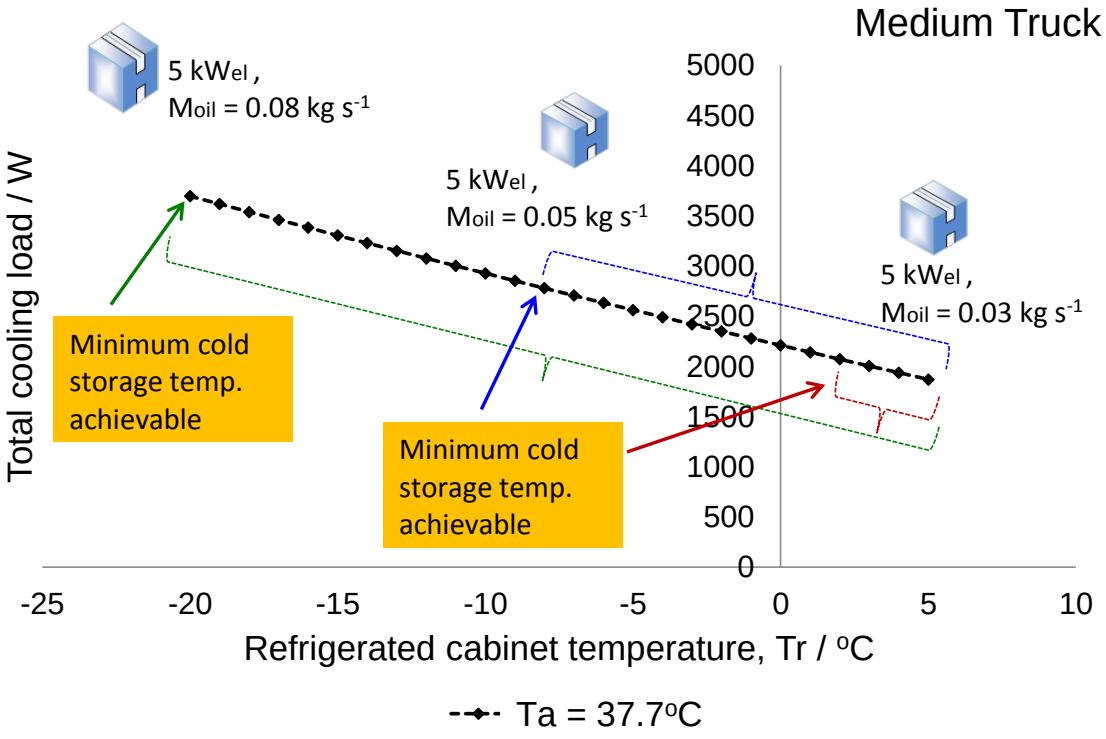

Figure 4.22: Design map for using 5 kWe SOFC stack for medium truck

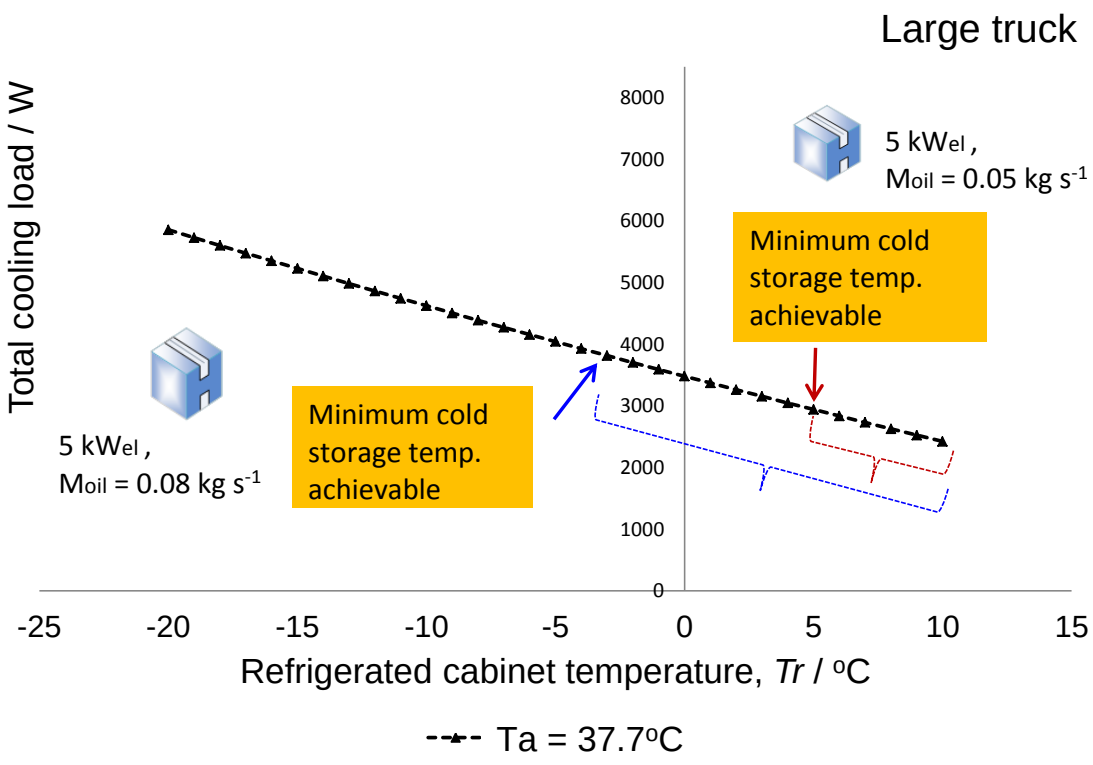

Figure 4.23: Design map for using 5 kWe SOFC stack for large truck

4.6 Conclusions

This chapter focussed on two key issues- the first being the design and performance of the coupling heat exchanger and the second being thermal energy generation within the SOFC stack. The need for the coupling heat exchanger arose due to temperature incompatibility between the two components viz. SOFC & desorber. A suitable coupling fluid, Paratherm HR, was chosen to transfer the required quantity of heat at the desorber at the appropriate desorber temperature.

The use of SOFC for a CHP (Combined Heat & Power) or a CCP (Combined Cooling & Power) application depends on how one operates the fuel cell along the polarization curve.

Operation of the SOFC at low current densities makes it electrically efficient and the residual thermal energy generated will be less. Operation at the cross over point generates equal amount of electrical and thermal energy and operation at high current densities results in more thermal energy generation than electrical energy. Hence depending on the application, the SOFC can either be used as an extremely efficient electricity generator or as a thermal machine. In either case the total efficiency will be high due to use of both electricity and heat, the only difference being in the electrical efficiency which will be high when the operating point is on the left and low when the operating point is on the right of the polarization curve.

Design maps for selection of SOFC stacks and contour maps for heating of the thermal oil from the cathode exhaust of the SOFC stack were drawn to provide a holistic picture of the range of cooling loads that can be catered to by the SOFC-VAR system on different refrigerated trucks.

Bibliography

1. http://www.paratherm.com/heat-transfer-fluids/. (last accessed Oct 2014)
2. Boaventura M, Sousa J M, and Mendes A, *A dynamic model for high temperature polymer electrolyte membrane fuel cells.* **International Journal of Hydrogen Energy**, 2011. **36**(16): p. 9842-9854.
3. Ni M, Leung M.K.H, and Leung D.Y.C, *Parametric study of solid oxide fuel cell performance.* **Energy Conversion and Management**, 2007. **48**(5): p. 1525-1535.
4. Ryan O' Hayre, Suk Won Cha, Whitney Colella, Fritz B. Prinz, *Fuel Cell Fundamentals*. Second Edition ed. 2009: John Wiley & Sons.
5. Cozzolino R et al., *Theoretical and experimental investigations on thermal management of a PEMFC stack.* **International Journal of Hydrogen Energy**, 2011. **36**(13): p. 8030-8037.
6. Axel Muller; Andre Weber; Hans Jurgen Beie; Albert Krugel; Dagmar Gerthsen; Ellen Ivers-Tiffee. *Influence of current density and fuel utilization on the degradation of the anode*. in *3rd European Solid Oxide Fuel Cell Forum*. 1998. Nantes,France.
7. Dillig M and Karl J, *Thermal Management of High Temperature Solid Oxide Electrolyser Cell/Fuel Cell Systems.* **Energy Procedia**, 2012. **28**: p. 37-47.
8. Incropera F.P, et al., *Principles of heat and mass transfer*. 7th ed. 2013.
9. Balamurugan P. and Mani A, *Heat and mass transfer studies on compact generator of R134a/DMF vapour absorption refrigeration system.* **International Journal of Refrigeration**, 2012. **35**(3): p. 506-517.
10. Hagen A, Johnson G.B, and Hjalmarsson P, *Electrochemical evaluation of sulfur poisoning in a methane-fuelled solid oxide fuel cell: Effect of current density and sulfur concentration.* **Journal of Power Sources**, 2014. **272**: p. 776-785.

5

Thermal modelling and sizing of plate heat exchanger desorber

"*To accomplish great things we must not only act but also dream*" **Anatole France**

In this chapter, thermal modelling of a plate heat exchanger (PHE) desorber has been carried out for an ammonia-water based Vapour Absorption Refrigeration System (VARS), using MATLAB & EES (Engineering Equation Solver). The modelling work focusses on determining the amount and mass fraction of the refrigerant produced at the outlet of the PHE desorber for a given mass flow rate of strong solution and applied heat flux. A sensitivity analysis has also been performed to identify the parameters that have a profound effect on refrigerant desorption. Based on the results obtained, the optimum geometrical dimensions of the PHE desorber are specified to cater to a 1 kW cooling load at a refrigeration temperature of -20 ^{o}C on-board a refrigerated truck.

Note: This chapter is being prepared for a journal submission. Certain sections of this chapter were published in ECS transactions 68 (1) 221-239; July 2015

5.1 Introduction

The desorber is one of the vital components of the VARS unit. The boiling of the refrigerant-absorbent pair takes place in the desorber where the refrigerant is separated from the absorbent. This boiling process involves two phenomena that occur simultaneously- heat transfer and mass transfer.

The desorber is designed in such a way that it produces refrigerant of high purity. The amount of heat supplied to the desorber accomplishes two tasks. One, it raises the temperature of the refrigerant-absorbent solution to the saturation temperature, characterized as *sensible heat transfer*. Second, it desorbs the refrigerant out of the solution, characterized by *latent heat transfer*. This is possible due to the different boiling points of the refrigerant and the absorbent. In the present case, ammonia is used as the refrigerant which has a boiling point of -33 ^{o}C at STP and water is used as the absorbent which has a boiling point of 100 ^{o}C.

Desorbers can be broadly classified into two categories viz.

a) Directly fired desorbers
b) Indirectly fired desorbers

A directly fired desorber employs a gas burner to supply heat whereas an indirectly fired desorber employs a coupling fluid to transfer heat to the desorber.

5.1.1 Compact desorber designs

The first step towards realising a compact VARS unit for the refrigerated truck application is to identify different compact designs for different components. The possible designs for the desorber are shown in Figure 5.1.

A compact flooded column desorber is one where pool boiling of the refrigerant-absorbent solution takes place. The refrigerant is collected from the top of the column. The desorber with a fractal like flow structure consists of many such plates. Here flow boiling of the refrigerant-absorbent solution takes place rather than pool boiling. The solution flows through the centre and spreads across the plate, undergoing boiling in the process. The weak solution and refrigerant vapour are collected from the sides of the plate. A plate heat exchanger desorber is also one where flow boiling of the refrigerant-absorbent solution takes place. Scaling up is possible in all three configurations by addition/stacking of similar units.

Additionally, the concept of the desorber design with fractal like flow structure and the PHE desorber is similar except for the geometry and flow patterns.

Of the different compact designs for desorbers only the plate heat exchanger type is not protected by patents and is available as a commercial product. The flooded column desorber design is patented by Georgia Institute of Technology [1] and the desorber with fractal like flow structure is patented by Oregon State University [2]. Of the available plate heat exchangers, a brazed plate heat exchanger is considered for the design. This is because a brazed PHE can withstand higher pressure and is vacuum tight when compared to a gasketed PHE. The gasketed PHE has operational pressure constraints and is also subjected to leaks due to fouling of the gasket material.

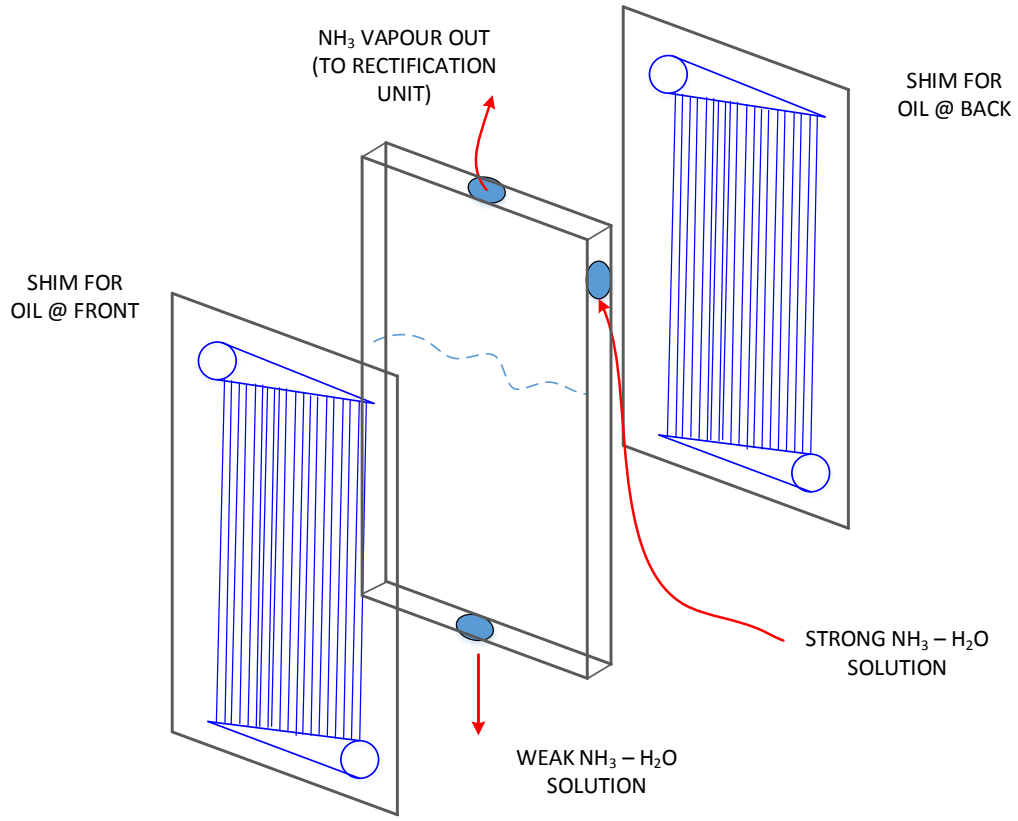

Compact flooded column desorber

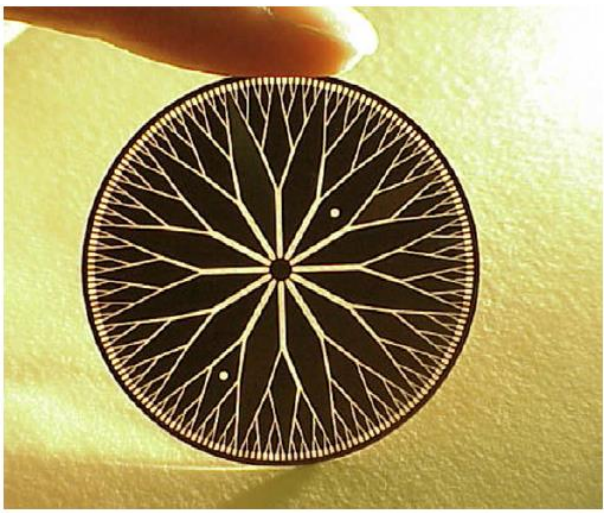

Desorber with Fractal like flow structure

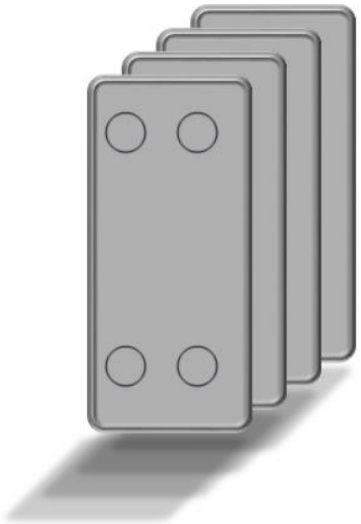

Plate heat exchanger desorber

Figure 5.1: Different designs of compact desorber
(Image of fractal desorber [3])

Figure 5.2 shows the schematic layout of a plate heat exchanger desorber as it will be used in the context of the system analysed here.

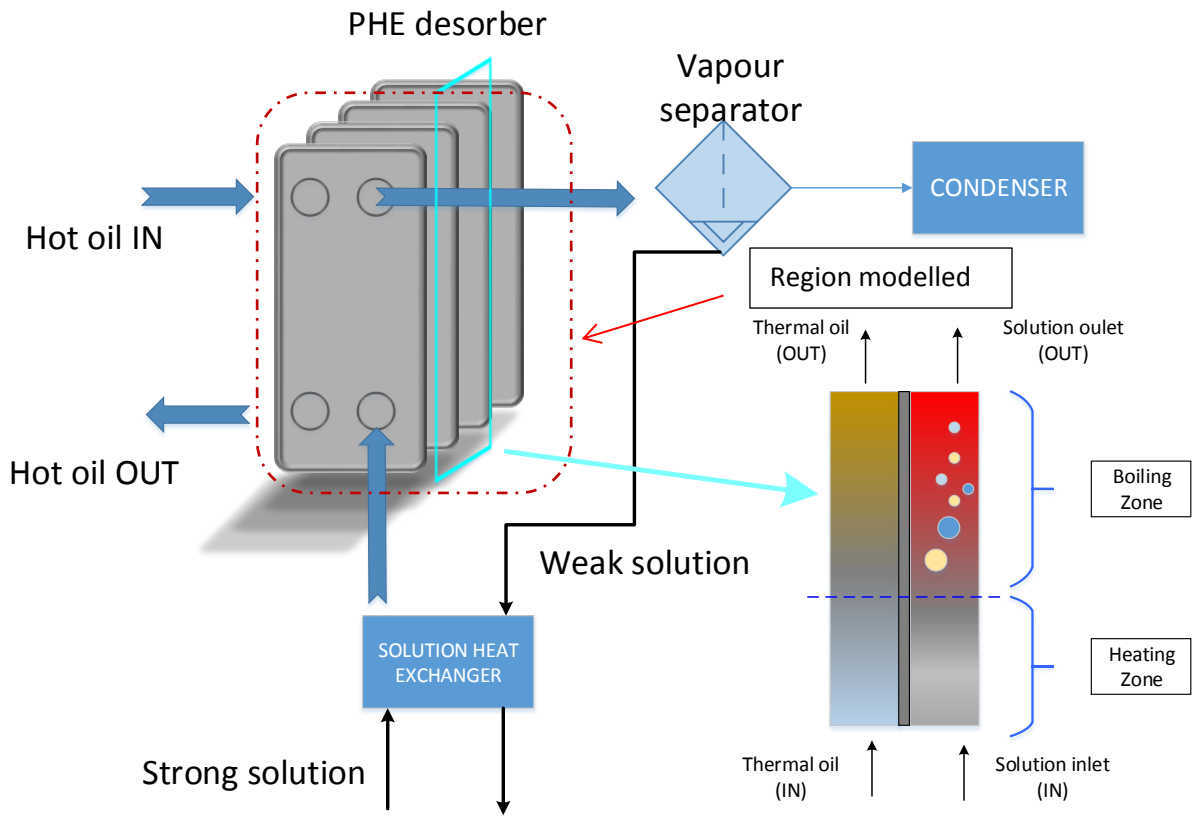

Figure 5.2: Layout of a plate heat exchanger desorber for use in VARS

5.2 Literature study on use of PHE desorbers

There is renewed interest in the use of absorption refrigeration systems of late and small scale VARS in particular, especially in areas where residual thermal energy is freely available. Scaling down large components to suit small applications works only to some extent, hence there is a need for compact heat exchangers that deliver high performance and at the same time can be packaged into the required volume space, to suit a particular

application. Plate heat exchangers (PHEs) have been proposed as possible candidates for use as desorbers due to reasons of compactness and high thermal performance.

So far only a few research groups have carried out experimental testing with a PHE as a desorber although a large amount of work has been carried out on use of plate heat exchangers as evaporators and condensers by various research groups worldwide [4-7]. Even though two-phase flow is present in both cases, the fact that the fluid involved is a binary mixture complicates the study when the PHE is used as a desorber.

Four research groups have carried out extensive experimental research focussing on the use of the PHE as a desorber. Among the four groups, each has dealt with a different refrigerant-absorbent pair. Only one group has conducted experiments with ammonia-water solution in a PHE [8]. The experimental findings of different research groups are briefly summarized here.

Taboas et al [8] used a brazed PHE to study the flow boiling of ammonia water solution. They focussed particularly on the saturated flow boiling heat transfer coefficient and associated frictional pressure drop in a vertical plate heat exchanger. In their study, different parameters such as the mass flux of the refrigerant absorbent solution, applied heat flux and ammonia mass fraction were varied and their effect on the flow boiling heat transfer coefficient was analysed. The overall operating conditions were chosen to mimic actual conditions encountered in an ammonia-water VARS driven by low temperature heat sources in the range of 80 to 100 ^{o}C. They concluded that the mass flux of the solution affects the boiling heat transfer coefficient more than the heat flux. The heat flux affects the boiling heat transfer coefficient only for vapour qualities less than 0.1. Another finding was that frictional pressure drop in the PHE desorber increases with increase in mass flux of the solution and with increase in vapour quality.

The same authors [9] also studied the boiling heat transfer and two phase pressure drop in the same plate heat exchanger but with NH_3 - $LiNO_3$ and NH_3 - $LiNO_3$ + H_2O as working pairs. The reason for choosing these working pairs was because the absorption refrigeration system could be driven with lower desorber temperatures and these working pairs would eliminate the need for the rectifier. They concluded that the solution mass flux plays a major role in the flow boiling process and these working pairs performed poorer than traditional NH_3 – H_2O working pair because of higher viscosity of these fluid mixtures.

Zacarias et al [10] studied the boiling heat transfer coefficient and pressure drop of ammonia lithium nitrate solution in a fusion PHE. They concluded from their experiments that both mass flux of the solution and applied heat flux have a significant role in influencing the boiling heat transfer coefficient and that nucleate boiling is the dominant phenomenon during the boiling process. They also obtained a correlation for the boiling heat transfer which offered a better fit for their experimental data when compared to correlations suggested by other research groups mentioned in their literature.

Balamurugan and Mani [11] used a R134a/DMF mixture to study heat and mass transfer in a compact brazed PHE used as a desorber. Not only did they use a PHE for the desorber but also for other components in the VARS. Their main experimental findings were that the Nusselt number (which represents the boiling heat transfer coefficient), Sherwood number (which represents mass transfer) and desorption ratio increase with increase in driving temperature ratio, R134a mass fraction, and two-phase Reynolds number but decreases with increase in driving pressure ratio. The driving temperature ratio was defined as $T_{Desorber}/T_{Absorber}$ and the driving pressure ratio was defined as $P_{Desorber}/P_{Absorber}$. They concluded that increased driving temperature ratio and decreased driving pressure ratio contributed to higher system COP and necessitated less circulation of the solution. Empirical correlations for the Nusselt number, and the Sherwood number were obtained from their experimental studies.

Marcos et al [12] studied the boiling heat transfer coefficient of water-lithium bromide solution in a brazed PHE desorber. All the research groups mentioned previously used a single effect system but Marcos et al carried out experiments with a double effect system. Also, all previous research groups had used hot water as the coupling fluid to supply heat to the desorber which indirectly meant that the coupling fluid temperature was less than 373 K (boiling point of water), representing a low grade heat source. Marcos et al used thermal oil as the coupling fluid to supply heat to the desorber. This correlates more to what is being done in this study although the refrigerant-absorbent solution is different. Their main experimental findings were that within the desorber there are two zones, viz. a liquid/liquid heat transfer zone and a liquid/liquid-vapour heat transfer zone. The liquid/liquid heat transfer zone is dominated by sensible heating and the liquid/liquid-vapour heat transfer zone is dominated by latent heating. The heat transfer coefficients on the solution side were obtained for both zones and it was found that the heat transfer coefficient in zone two (liquid/liquid-vapour) was three times higher than that in zone one. Finally they state that most of the heat supplied to the desorber goes into desorbing the refrigerant which means that more heat is needed in zone two.

All four research groups mentioned above have selected a plate heat exchanger which is commercially available in the market. The geometric specifications of the PHE used by each research group are different, details of which are shown in Table 5.1

Table 5.1: Dimensions of plate heat exchangers used as desorbers by various research groups

	Taboas et al G1	Zacarias et al G2	Balamurugan et al G3	Marcos et al G4
PHE specifications				
Refrigerant-absorbent tested	$NH_3 – H_2O$	$NH_3 – LiNO3$	R134a-DMF	H_2O - LiBr
Heating medium	Water	Water	Water	Thermal oil
Height of plate	466 mm	519 mm	172 mm	250 mm
Width of plate	112 mm	175 mm	77 mm	112 mm
Thickness of plate	0.4 mm	0.4 mm	0.3 mm	0.5 mm
Hydraulic diameter	4 mm	3.9 mm	4 mm	5.2 mm
Corrugation type	Chevron	Not mentioned	Chevron H type	Chevron
Corrugation angle	60^o from vertical	58.5^o from vertical	60^o from vertical	30^o from vertical
Amplitude of corrugation	2 mm	2.4 mm	1.5 mm	2.6 mm
Pitch of corrugation	9.6 mm	9.85 mm	2.5 mm	8 mm
Surface area of a single plate (H x W)	0.0522 m^2	0.091 m^2	0.0132 m^2	0.028 m^2
Number of plates	4	20	14	30
Number of flow channels	3	19	13	29

(Height and width of plate correspond to actual heat transfer surface area)

Figure 5.3 shows the front view of a single plate of a plate heat exchanger with the corresponding geometric details.

Besides the four research groups mentioned above few others have made use of PHEs as components in VARS. Garcia Hernando et al [13] studied the pressure drop in a PHE when used as a desorber. They used both working fluids NH_3-H_2O and LiBr-H_2O and concluded that the pressure drop plays a major role in determining the desorption temperature when LiBr-H_2O is used as the working fluid because the VARS based on LiBr-H_2O operates at a lower pressure when compared to the VARS based on NH_3-H_2O.

de Vega et al [14] studied the performance of a LiBr-H_2O absorption chiller with PHEs. They particularly replaced the heat exchangers used in the desorber and the condenser with PHEs and carried out modelling of the whole system. They found that use of PHEs

considerably reduced the volume footprint of the absorption chiller although a number was not given. Appropriate design maps for desorber heat transfer, COP, cooling water temperature and evaporation temperature were also presented in their research article.

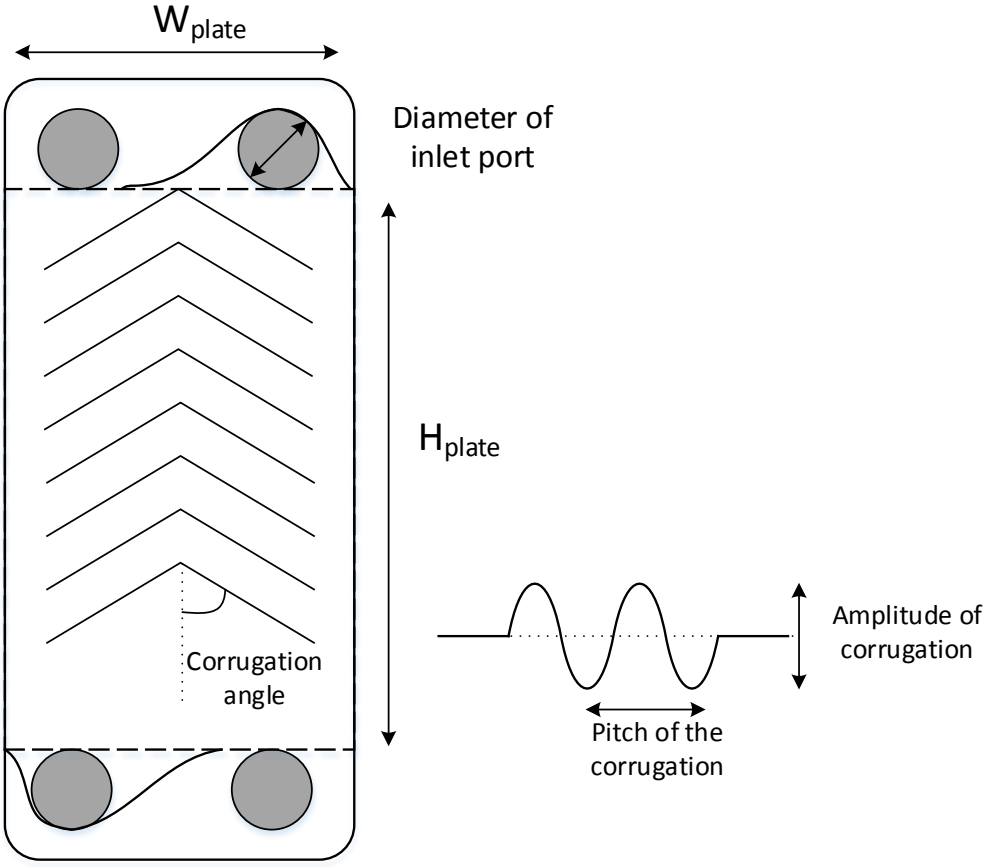

Figure 5.3: Front view of a plate heat exchanger and geometric details

Venegas et al [15] experimentally analysed the heat transfer during subcooled and saturated boiling of ammonia-lithium nitrate solution in a plate heat exchanger desorber and found that subcooled boiling is present in the desorber and that the initial boiling temperature is 3.1 ^{o}C lower than the saturation temperature.

Research on plate heat exchanger desorbers has been purely experimental and most of the research groups were interested in gaining deeper insights into the boiling heat transfer coefficient and how it gets affected by the applied heat flux of the coupling fluid and mass

flux of the solution under study. None of them discuss the effect of geometric dimensions on the desorber performance nor do they quantify the amount of refrigerant desorbed. Also, all these studies used a global equation to determine the average boiling heat transfer coefficient which will only be an approximation.

There is a lack of a model that describes the performance of a PHE desorber with regards to refrigerant desorbed and its relation to the geometry and number of plates. A generalized model for heat and mass transfer is available from Kang et al [16] for designing different components of the VARS but it does not specifically talk about the amount of refrigerant desorbed.

This chapter is purely focussed on studying the correlation between the amount and mass fraction of refrigerant generated/desorbed with the heat supplied and the geometry of the PHE. The amount of refrigerant and the mass fraction of ammonia in the refrigerant along each channel cannot be identified from experiments but can easily be found from numerical modelling, which in turn will help identify the exact number of plates required in the PHE desorber for a particular application. This will aid in reducing the volume footprint of desorbers used in absorption chillers thereby allowing the chiller unit itself to be more compact.

5.3 Thermal modelling of PHE desorber

The thermal model developed for the PHE desorber is described in detail in this section. Results from *Chapter 4*, thermal oil flow rate and temperature serve as input for modelling the PHE desorber.

5.3.1 Approach & methodology

Two platforms - MATLAB and EES (Engineering Equation Solver) were used in the modelling work reported here. The two platforms are not linked automatically hence the user has to manually feed the outputs from one platform into the other. The interlinking of the two platforms for information exchange is shown in Figure 5.4. The reason for using two platforms is because most of the modelling on SOFC has been carried out in MATLAB and the heat to drive the PHE desorber also comes from the SOFC. Hence to keep all modelling on the same platform, MATLAB was chosen. The reason for using EES is because MATLAB does not have built in thermodynamic functions to calculate the thermodynamic properties of refrigerants.

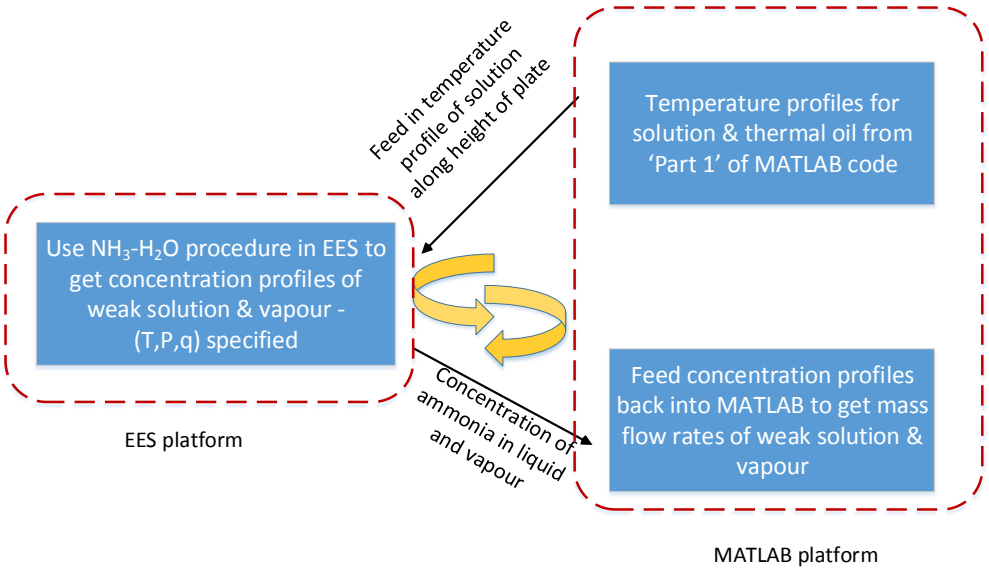

Figure 5.4: Block diagram showing interlinking of MATLAB and EES platforms

5.3.2 Model development

As shown in Figure 5.2, hot thermal oil [17] serves as the coupling fluid to transfer heat to the ammonia water solution in the PHE desorber. Since high temperatures are involved it is essential that the thermal oil selected does not undergo degradation. For this reason Paratherm HR from Paratherm Heat Transfer fluids was selected as the coupling fluid.

A PHE is made up of a number of plates N; and the number of flow channels is N-1. The heat flux experienced by the flow channels will be different. The channels in the middle will receive more heat flux than those at the end as seen from Figure 5.5. This information is important for quantifying the refrigerant desorbed from different channels.

A Control Volume Method (CVM) is used here for modelling the PHE desorber as shown in Figure 5.6. The numerical modelling process is split into two parts

i) Determination of temperature profiles along the plate

   This is essential because if the temperature profile along the channel is known then a reasonable estimate on where exactly the boiling process begins can be made.

ii) Determination of mass flow rates of weak solution and vapour along the plate

   This information is necessary to size the PHE to be used as desorber, to suit different cooling loads.

A single flow channel is modelled first and results from this are extended to the whole PHE. A simple co-flow configuration was used in the PHE as a starting point for modelling of the complete PHE desorber.

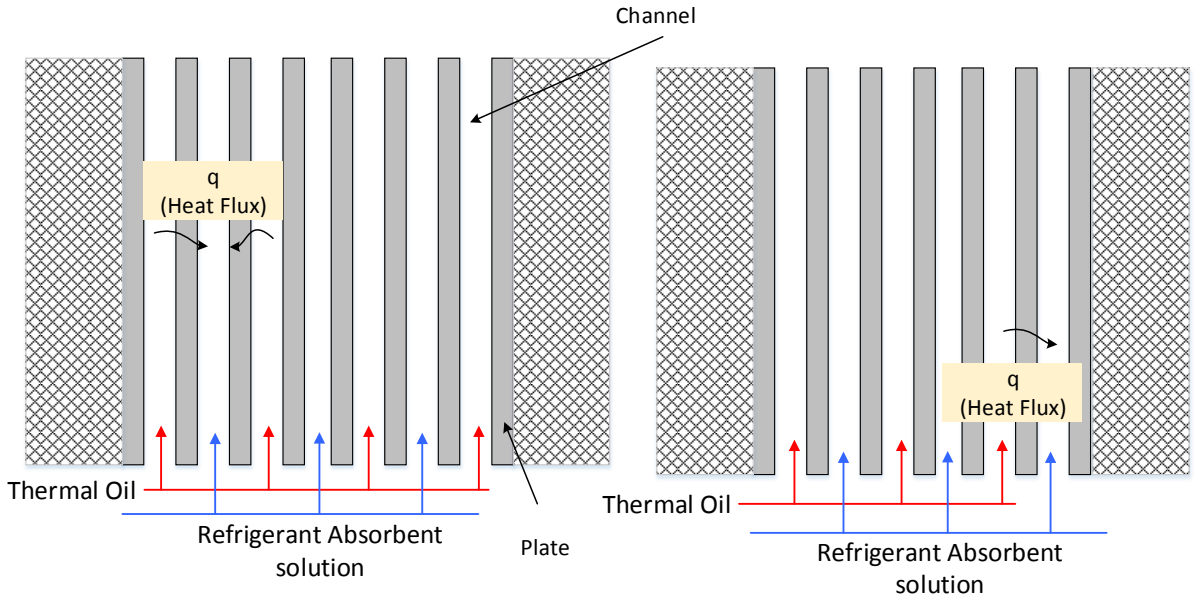

Figure 5.5: Cross section of PHE showing heat flux for the middle channel and end channel

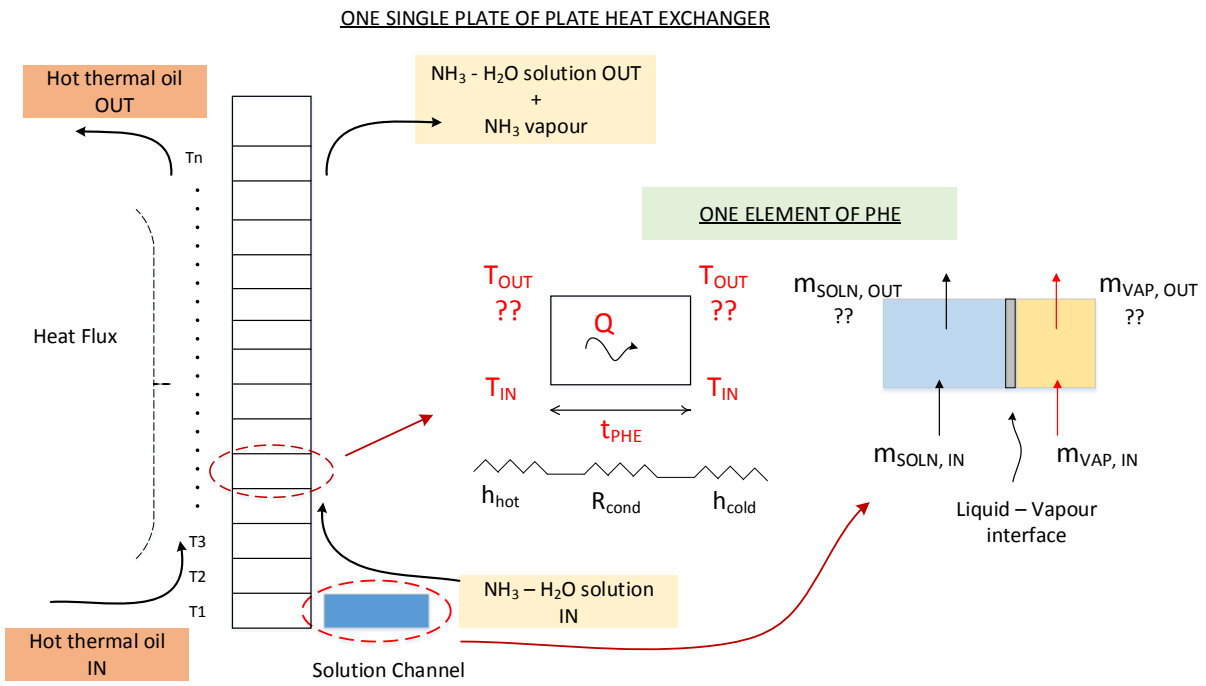

Figure 5.6: CVM analysis to determine temperature and mass flow rate profiles along the plate

Determination of temperature profiles

The first element of any plate in the PHE is the starting point for the analysis. The approach followed here is as follows:

1. Determine the local heat transfer coefficient for both fluids (thermal oil & NH_3 – H_2O solution) using correlations available in literature suitable for corrugated plate heat exchangers. The local heat transfer coefficients for the particular element are calculated at the inlet temperature into that element.
2. Depending on the number of plates, the mass flow rate in each flow channel for each fluid is calculated.
3. The thermal conductivity and thickness of the plate are known. An energy balance is then performed on the first element to determine the local heat transfer rate and the outlet temperatures from the first element.
4. Steps 1 to 3 are continued along the direction of flow until the height of the plate heat exchanger is reached.

The outlet temperature from the first element for both fluids can be calculated using Eq. 5.1 to 5.3.

$$Q_{element} = m_{oil,ch} * C_{p,Oil} * (T_{1,oil\,IN} - T_{1,oil\,OUT}) \quad \textbf{Eq. 5.1}$$

$$Q_{element} = m_{soln,ch} * C_{p,soln} * (T_{1,soln\,IN} - T_{1,soln\,OUT}) \quad \textbf{Eq. 5.2}$$

$$Q_{element} = U_{element} * A_{element} * LMTD_{element} \quad \textbf{Eq. 5.3}$$

Figure 5.6 also shows the schematic of an element and the input and output quantities involved.

The overall heat transfer coefficient for each element is calculated from Eq. 5.4

$$\frac{1}{U_{element}} = \frac{1}{h_{oil}} + \frac{t}{k} + \frac{1}{h_{soln}} \qquad \textbf{Eq. 5.4}$$

To predict the approximate point where boiling of the NH_3 – H_2O solution starts, the following method was applied

1. PHE specific heat transfer correlations (specific to flow in corrugated plate HEX) for single phase flow for both fluids were used. The dynamic viscosity term and Prandtl number take care of the difference in fluids along with the thermal conductivity.
2. The temperature at which the solution reaches the saturation temperature marks the end of the heating zone and beginning of the boiling zone. This temperature is also called the *bubble point temperature*. Once the solution temperature reaches the bubble point temperature, the two-phase heat transfer correlation is used for the solution. Although subcooled boiling may be present it is neglected because the difference between subcooled boiling temperature and saturation temperature is very small [15].
3. For the boiling zone, the two-phase heat transfer coefficient as mentioned by Taboas et al [18] was used for the solution.
4. Further CVM analysis was carried out based on the two phase heat transfer correlation on the solution side and single phase heat transfer correlation on the oil side. Doing so enables determination of exact outlet temperature of the fluids from one flow channel and also the mass fraction of refrigerant produced.

The single phase heat transfer correlation was calculated from Eq. 5.5 to 5.7

$$h_{SP,i} = (Nu_i * k_i)/D_h \qquad \textbf{Eq. 5.5}$$

i = thermal oil or NH_3-H_2O solution

Numerous correlations are available in literature for calculating the heat transfer coefficient in a plate heat exchanger and all these relations can be found in [19]. However, the most widely suggested correlation is that of Muley & Manglik [20] and that is used in the present modelling study. The Nusselt number is given by Eq. 5.6 and Eq. 5.7 for low and high Reynolds number.

For $30^o \leq \beta \leq 60^o$ and $30 \leq Re \leq 400$

$$Nu = 0.44 * \left(\frac{\beta}{30}\right)^{0.38} * Re^{0.5} * Pr^{\left(\frac{1}{3}\right)} * \left(\frac{\mu}{\mu_w}\right)^{0.14} \quad \textbf{Eq. 5.6}$$

For $30^o \leq \beta \leq 60^o$ and $Re \geq 1000$

$$Nu = \left[(0.2668 - 0.006967 * \beta + 7.244 * 10^{-5} * \beta^2) * (20.7803 - 50.9372 * \phi + 41.1585 * \phi^2 - 10.1507 * \phi^3) * Re^p * Pr^{\frac{1}{3}} * \left(\frac{\mu}{\mu_w}\right)^{0.14}\right] \quad \textbf{Eq. 5.7}$$

The exponent of Re in Eq. 5.7 is given by

$$p = 0.728 + 0.0543 \sin\left(\frac{2 * \pi * \beta}{90} + 3.7\right) \quad \textbf{Eq. 5.8}$$

Where,

Nu	Local Nusselt number
β	Corrugation angle of the plate wrt vertical (degrees)
Re	Reynolds number
Pr	Prandtl number
μ	Temperature dependent dynamic viscosity of the fluid (Pa.s)
μ_w	Temperature dependent dynamic viscosity of the fluid at the wall (Pa.s)
ϕ	Area enlargement factor

The correlation suggested by Taboas et al [18] is applied for the two phase flow on the solution side. This correlation is used because it was derived from experiments carried out on NH_3-H_2O desorption in a PHE by the same research group.

The two-phase heat transfer correlation is given by Eq. 5.9

$$h_{TP} = 5 * Bo^{0.15} * h_{SP} \qquad \textbf{Eq. 5.9}$$

Where Bo is the boiling number, incorporated to represent two-phase flow and is given by

$$Bo = \frac{q}{\dot{m}_{soln} * H_{fg}} \qquad \textbf{Eq. 5.10}$$

The above relations for the Nusselt number ensure that the fluid flow is coupled to the geometric dimensions of the PHE.

Determination of boiling temperature

In order to identify the boiling zone, the boiling temperature of NH_3-H_2O solution at the desorber pressure and ammonia concentration needs to be determined. For the base case scenario, the operating pressure of the desorber is taken to be 15 bar and the concentration of the NH_3-H_2O solution is taken to be 30 wt%, corresponding to an ammonia mass fraction of 0.3.

The bubble point temperature is given by Eq. 5.11 [21]. This gives a good indication of the beginning of the boiling process because at the bubble point temperature the first vapour bubble is formed.

$$T_b(P.x) = T_o \sum a_i (1 - X)^{m_i} \left[\ln\left(\frac{P_o}{P}\right)\right]^{n_i} \qquad \textbf{Eq. 5.11}$$

X, which is the ammonia mole fraction, is given by Eq. 5.12

$$X = \frac{17.03 * x}{17.03 * x + 18.015 * (1 - x)} \qquad \textbf{Eq. 5.12}$$

Where, x is the ammonia mass fraction in the inlet solution.

The values of the constants used in Eq. 5.11 are given in Table 5.2.

Table 5.2: Values of constants used in Eq. 5.11

i	m	n	a
1	0	0	3.22
2	0	1	-0.384
3	0	2	0.046
4	0	3	-0.00378
5	0	4	0.000135
6	1	0	0.488
7	1	1	-0.12
8	1	2	0.0106
9	2	3	-0.000533
10	4	0	7.85
11	5	0	-11.59
12	5	1	-0.0523
13	6	0	4.89
14	13	1	0.0421

(T_o = 100 K and P_o = 20 bar)

The bubble point temperature is a function of pressure and ammonia concentration and was developed as a polynomial function with minimum standard deviation to best represent the experimental data literature presented in [21].

Determination of mass flow rates of weak solution and vapour

The approach followed here to determine the mass flow rates of weak solution and vapour is as follows:

1. An overall mass balance and an ammonia mass fraction mass balance for each element is obtained from

$$m_{SOLN,IN} + m_{VAP,IN} = m_{SOLN,OUT} + m_{VAP,OUT} \quad \textbf{Eq. 5.13}$$

$$m_{SOLN,IN} * x_{SOLN,IN} + m_{VAP,IN} * x_{VAP,IN} = m_{SOLN,OUT} * x_{SOLN,OUT} + m_{VAP,OUT} * x_{VAP,OUT} \quad \textbf{Eq. 5.14}$$

Where,

$m_{SOLN,IN}$	Mass flow rate of solution into the control volume (kg s^{-1})
$m_{SOLN,OUT}$	Mass flow rate of solution out of the control volume (kg s^{-1})
$m_{VAP,IN}$	Mass flow rate of vapour into the control volume (kg s^{-1})
$m_{VAP,OUT}$	Mass flow rate of vapour out of the control volume (kg s^{-1})
$x_{SOLN,IN}$	Concentration of solution into the control volume
$x_{VAP,IN}$	Concentration of vapour into the control volume
$x_{SOLN,OUT}$	Concentration of solution out of the control volume
$x_{VAP,OUT}$	Concentration of vapour out of the control volume

2. The following boundary conditions were applied:
    a. For the first segment, $m_{VAP,IN}$ = 0 and $\chi_{VAP,IN}$ = 0 since there is no vapour present.
    b. $m_{SOLN,IN}$ is known from the knowledge of total mass flow rate of solution and number of channels present. The inlet concentration $x_{SOLN,IN}$ is also known (which in this case is fixed at 0.3).
    c. $x_{SOLN,OUT}$ from each segment can be determined by writing a simple code in EES (*Engineering Equation Solver*) by specifying outlet temperature from that segment, pressure and vapour mass fraction in the stream. The outlet temperature from the segment is derived from the steps outlined before.
    d. $x_{VAP,OUT}$ for the first segment is determined by drawing a horizontal line from the initial point on the bubble point line to the corresponding point on the dew

point line. Similarly $x_{VAP,OUT}$ for subsequent segments can be determined by drawing horizontal lines from the corresponding points on the 'bubble point line' to the corresponding points on the 'dew point line'. This is the procedure followed by the EES code.

As mentioned earlier, the bubble point temperature is the temperature at which the first vapour bubble is formed and the dew point temperature is the temperature at which the last vapour bubble is formed. The solution between the bubble point and dew point line is in the two phase region.

3. Once the concentration profiles of both streams are known, Eq. 5.13 and Eq. 5.14 are solved simultaneously to give the mass flow rate of the weak solution and refrigerant.
4. For element 2, the outputs from element 1 serve as inputs. This process is repeated until the height of the plate heat exchanger is reached.

5.3.3 Assumptions made in the model

The following assumptions are made in the model

1. The weak solution coming out from each segment is at saturated condition.
2. The quality of the weak solution is taken as 'zero' at the outlet of each segment for the sake of convenience in calculations.
3. Both the vapour and the weak solution are at desorber pressure throughout the height of the plate. Pressure drop in PHE is neglected.
4. The quality of vapour generated is taken as 'one' at the outlet of each segment.
5. Entrainment of liquid in vapour is neglected. This assumption is reasonable because the vapour is generated as a result of desorption and not supplied externally.

6. Heat losses from the end plates are neglected when solving for temperature profiles and heat transfer across each element.
7. Effect of subcooled boiling is not considered.

Assuming a value of vapour fraction for each of the streams is important for calculating the quantity of refrigerant generated (desorbed) because the thermodynamic state of the stream can be predicted if any three of the following parameters are specified, temperature, pressure, ammonia mass fraction, enthalpy, entropy, internal energy, specific volume and vapour mass fraction. There will of course be some entrainment of the liquid with the vapour but that is not considered in the model, in order to keep the model simple.

5.3.4 Operating conditions

The operating conditions at the PHE desorber are those encountered when catering to a cooling load requirement of 1 kW at a refrigeration temperature of -20 ^{o}C. The respective parameters are tabulated in Table 5.3.

Table 5.3: Operating parameters of the PHE desorber

Parameter	Value
Total mass flow rate of thermal oil	0.02 kg s^{-1}
Total mass flow rate of solution	7 g s^{-1}
Inlet temperature of thermal oil	473 K
Inlet temperature of solution	383 K

A ‘0D’ model of the VARS unit developed and presented in *Chapter 3* revealed that COP values can reach up to 0.7 with certain improvements in the whole system and that for a 1 kW cooling load the mass flow rate of strong solution needed is 7 g s^{-1}. This value is used as the input in the model.

5.3.5 Outputs desired from modelling

The desired outputs from modelling the PHE desorber are as follows:

- Mass flow rate of refrigerant produced at the outlet of one plate.
- Mass fraction of refrigerant produced at the outlet of one plate.
- Outlet temperature of solution.
- Determination of number of plates required in the PHE.
- Identification of boiling and heating zones within the PHE.
- Heat flux distribution along the plate of the PHE.
- Local heat transfer coefficients along the plate.

5.4 Results and discussion

The PHE geometry of all four research groups mentioned earlier is taken into consideration for the modelling study and a comparison between them is drawn for the different output parameters desired. A sensitivity analysis is also performed to study the effect of different geometrical and operational parameters on PHE desorber performance.

5.4.1 Bubble point and dew point line

Using Eq. 5.11 and 5.12, the bubble point line and the dew point line are plotted in Figure 5.7 for an ammonia mass fraction ranging from 0.1 to 1. For the given ammonia mass fraction of 0.3, the bubble point temperature is 394.1 K (121 ^{o}C). Hence, it is safe to assume that if the solution enters the desorber at this or a higher temperature, some vapour fraction will already be available in the stream and the whole channel will contribute only to boiling of

the refrigerant-absorbent solution or in other words the heat transfer is characterised as latent heat transfer.

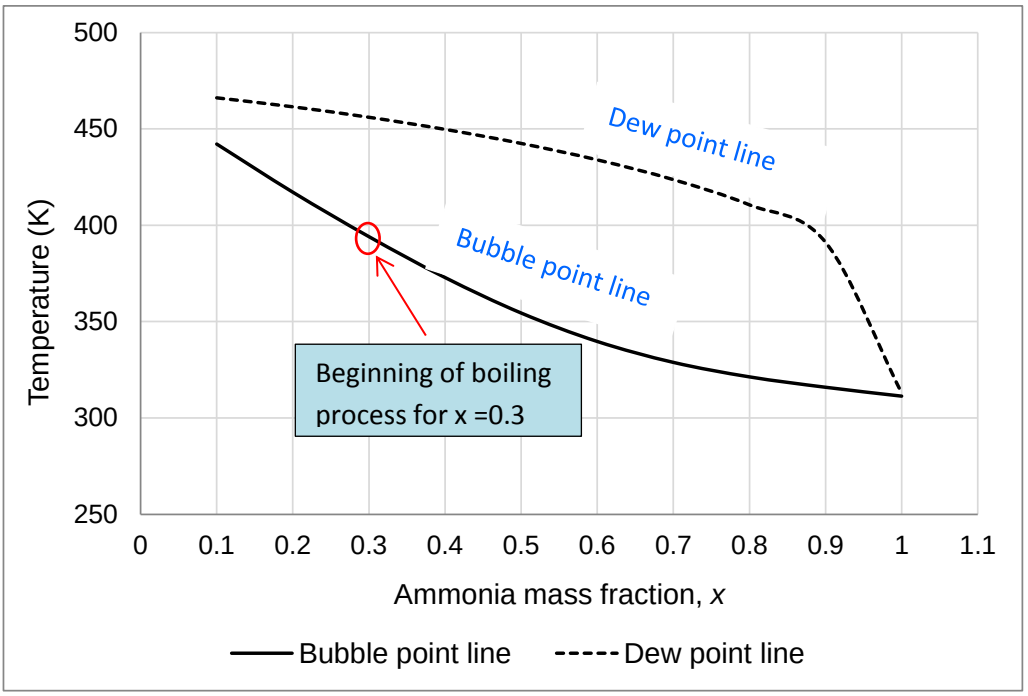

Figure 5.7: Bubble point and dew point line for NH_3-H_2O solution at P = 15 bar

If on the other hand, the solution enters at a lower temperature, then some amount of heat is needed to raise the temperature of the solution to the bubble point temperature and this is characterised as sensible heat required.

5.4.2 Determination of temperature profiles

The temperature profile along the flow channel (in the direction of fluid flow) for all four geometries is shown in Figure 5.8. Except for geometry G1, the bubble point temperature is reached almost instantaneously in other cases. This is the temperature profile for the end flow channel where the heat flux impinges only from one side. The temperature profile of the

solution flowing in the middle flow channel for geometry G1 is also shown in Figure 5.8. Due to higher flux impinging, the bubble point temperature is reached earlier for the middle channel when compared to the solution flowing in the end channel. The temperature profile in the middle channel for other geometries can be obtained in a similar fashion and are not shown in order not to clutter the graph with too many curves.

The temperature data is useful in identifying the heating and boiling zones within individual channels. As one example, a 2D schematic of where the boiling and heating zones lie for geometry G1 is shown in Figure 5.9.

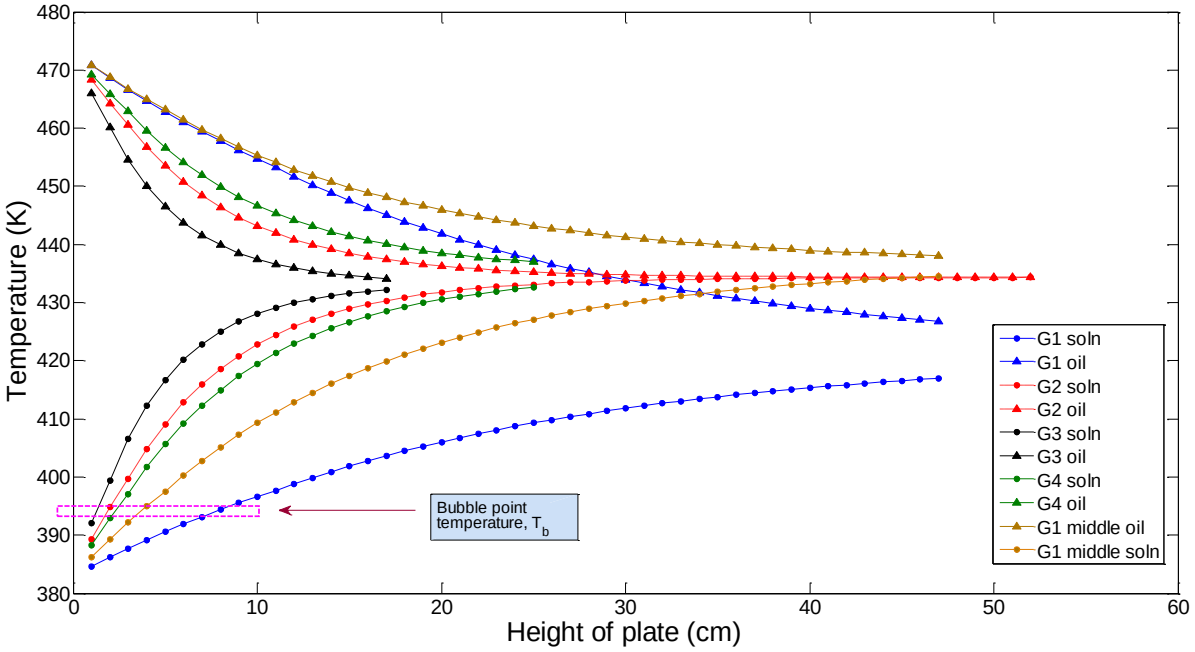

Figure 5.8: Temperature profile along the height of plate for different PHE geometries

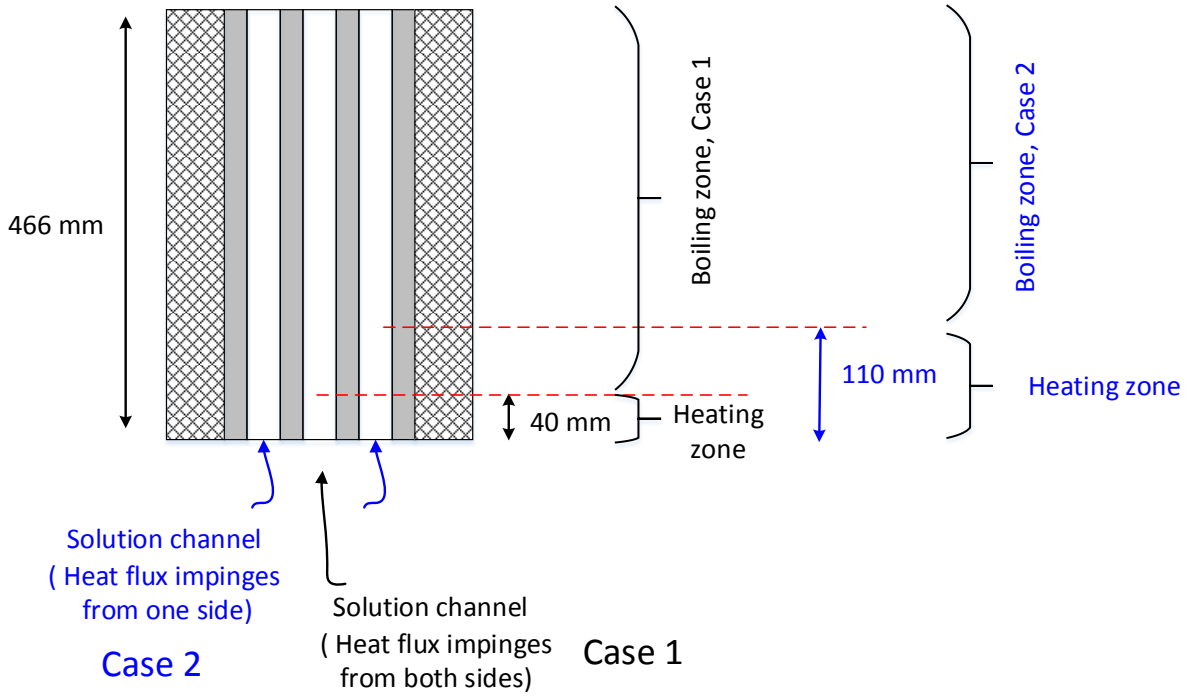

Figure 5.9: Identification of heating & boiling zones within solution channels for Geometry G1

5.4.3 Mass flow rate and mass fraction of weak solution and refrigerant

Before delving further into the results, it is important to elucidate the number of flow channels available for the solution and thermal oil within the PHE. A PHE can have an odd number of plates with an even number of flow channels or vice versa. In case of a PHE with an odd number of flow channels, either the solution or the thermal oil could have an extra channel. As all four geometries mentioned above have an even number of plates they all have an odd number of channels. Hence with regards to mass flow rate and mass fraction, two scenarios are analysed

- Case 1 – Thermal oil having an extra flow channel
- Case 2 – Solution having an extra flow channel

If oil has an extra channel then solution always flows through the middle channels in the PHE desorber. The middle channels (for the solution) in this case are classified as central middle channels (CMC) and peripheral middle channels (PMC). If the solution has an extra channel in the PHE desorber then the solution flows through middle channels (MC) and end channels (EC). This is explained in Figure 5.10.

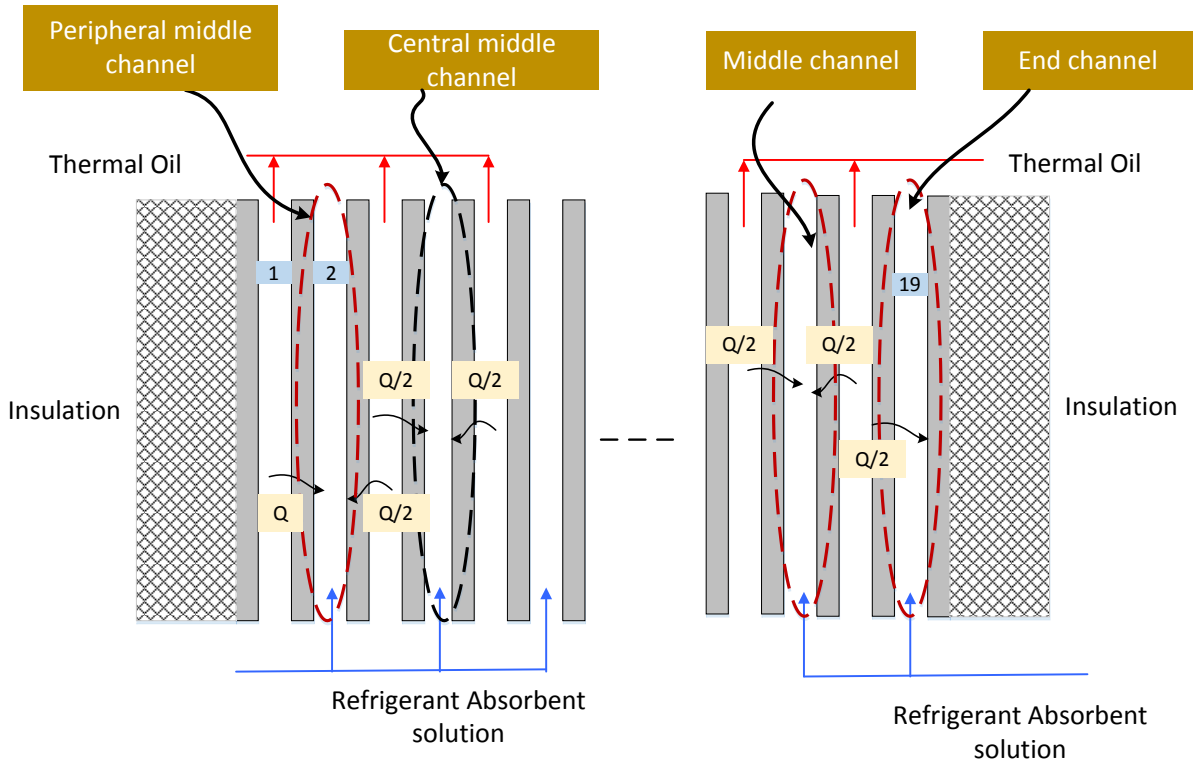

Figure 5.10: Classification of different channels within the PHE desorber

Mass flow rate and concentration

The variation in ammonia concentration and mass flow rate of weak solution and vapour for geometries G1 and G2 along the height of the channel is shown in Figure 5.11 and Figure 5.12 respectively.

Case 1, geometry G1

Geometry G1 has four plates, which translates to three flow channels. In case 1, there is one solution flow channel and two thermal oil flow channels. The total amount of refrigerant produced from the desorber will be the amount generated from that flow channel alone. The concentration of the weak solution drops from an initial value of 0.3 to 0.141 indicating that ammonia has been desorbed from the solution. The concentration of ammonia in the vapour stream is initially high but gradually reduces to a lower value as it proceeds along the channel. This is because as the temperature of the solution increases not only does ammonia boil off but also water. Hence the vapour stream exiting the PHE desorber will be a two phase mixture thereby necessitating the need for a rectifier.

The total refrigerant (vapour) production is 2.415 g s^{-1} with an average ammonia concentration of 0.6 as seen from Figure 5.11.

Case 2, geometry G1

In this case there are two solution channels hence the total refrigerant produced will be the sum of refrigerant produced from each channel. The concentration of the weak solution passing through each of those channels reduces from 0.3 to 0.136 while the concentration of vapour decreases from 0.87 to 0.59. The amount of refrigerant generated from each channel is 1.26 g s^{-1} with an ammonia concentration of 0.59. The total refrigerant production from both the channels combined is thus 2.52 g s^{-1}.

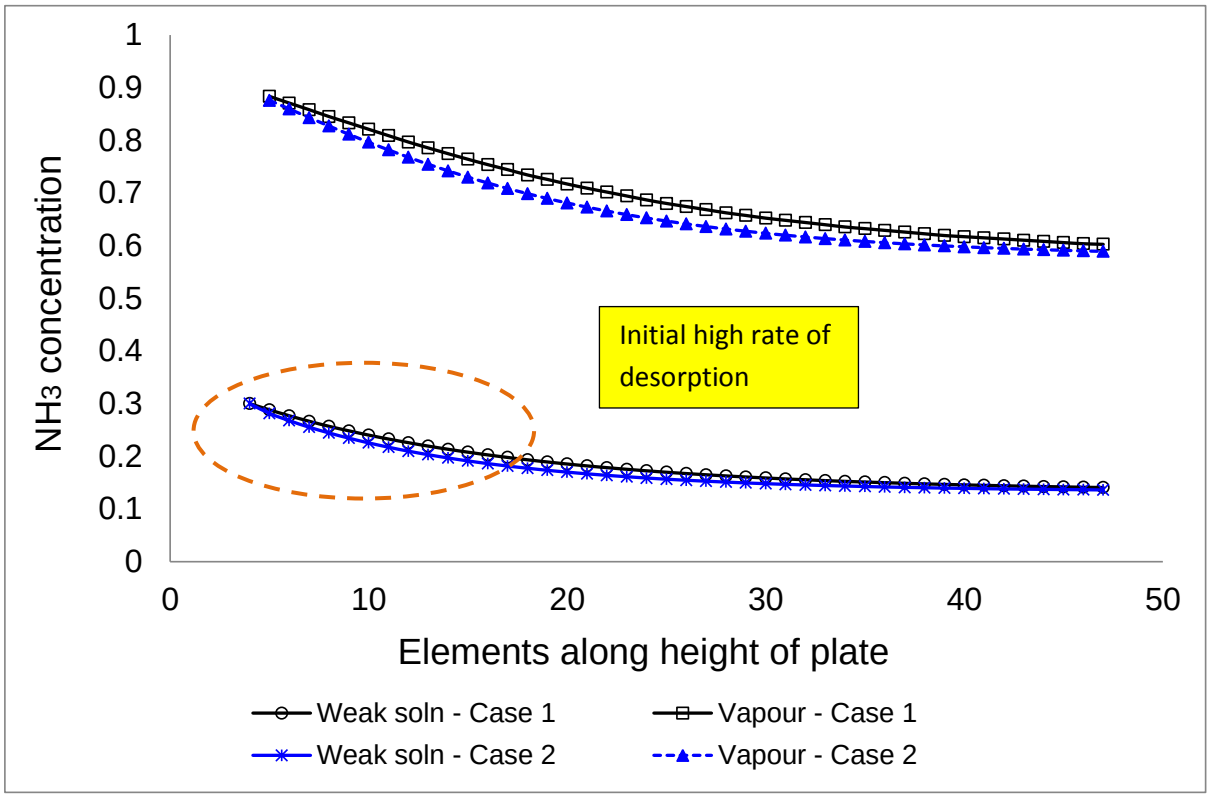

a) Concentration profiles

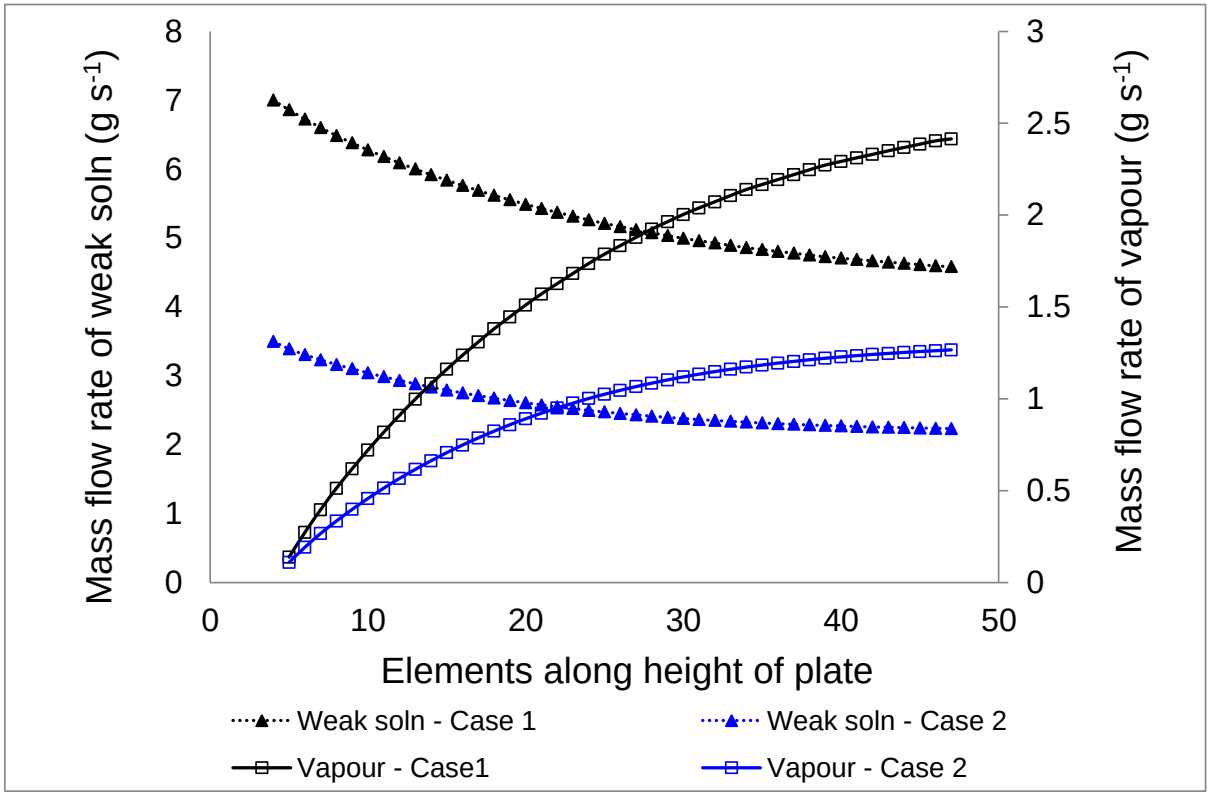

b) Mass flow rate profiles

Figure 5.11: Concentration and mass flow rate of weak solution and vapour along middle and end channels – Geometry G1

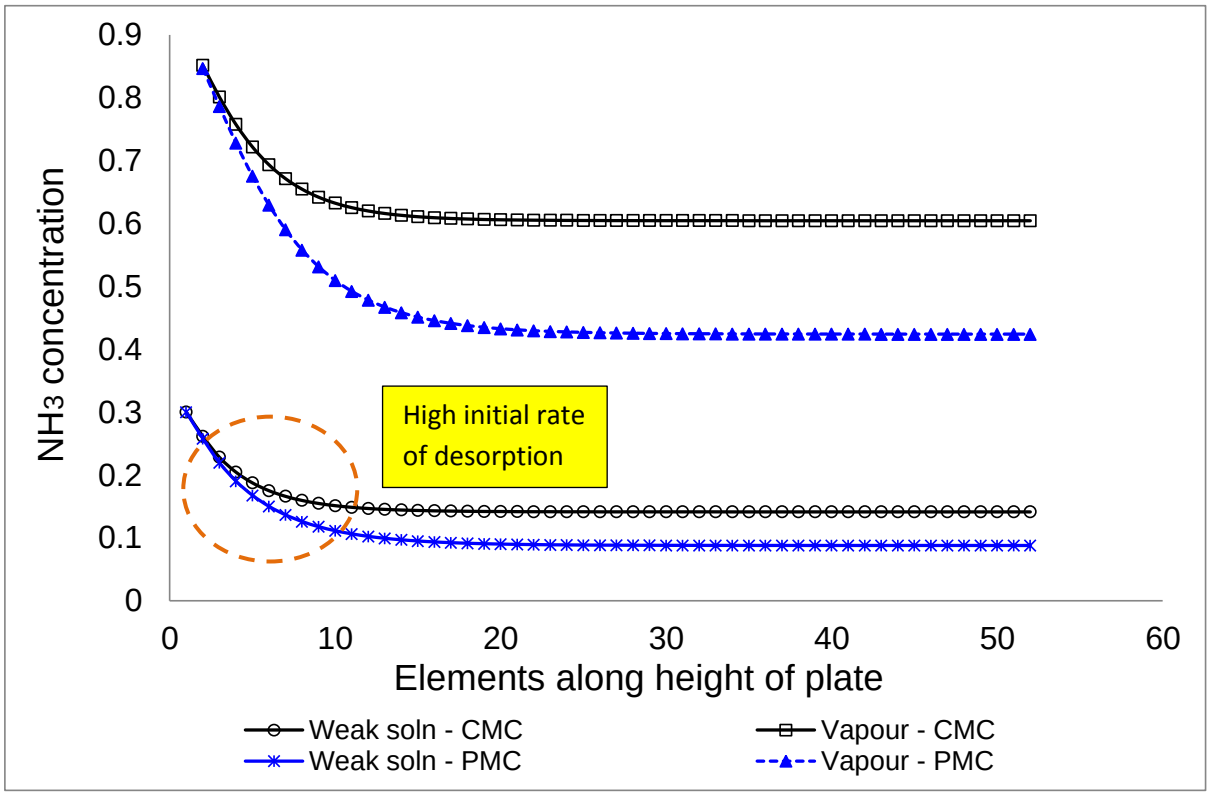

a) Concentration profiles

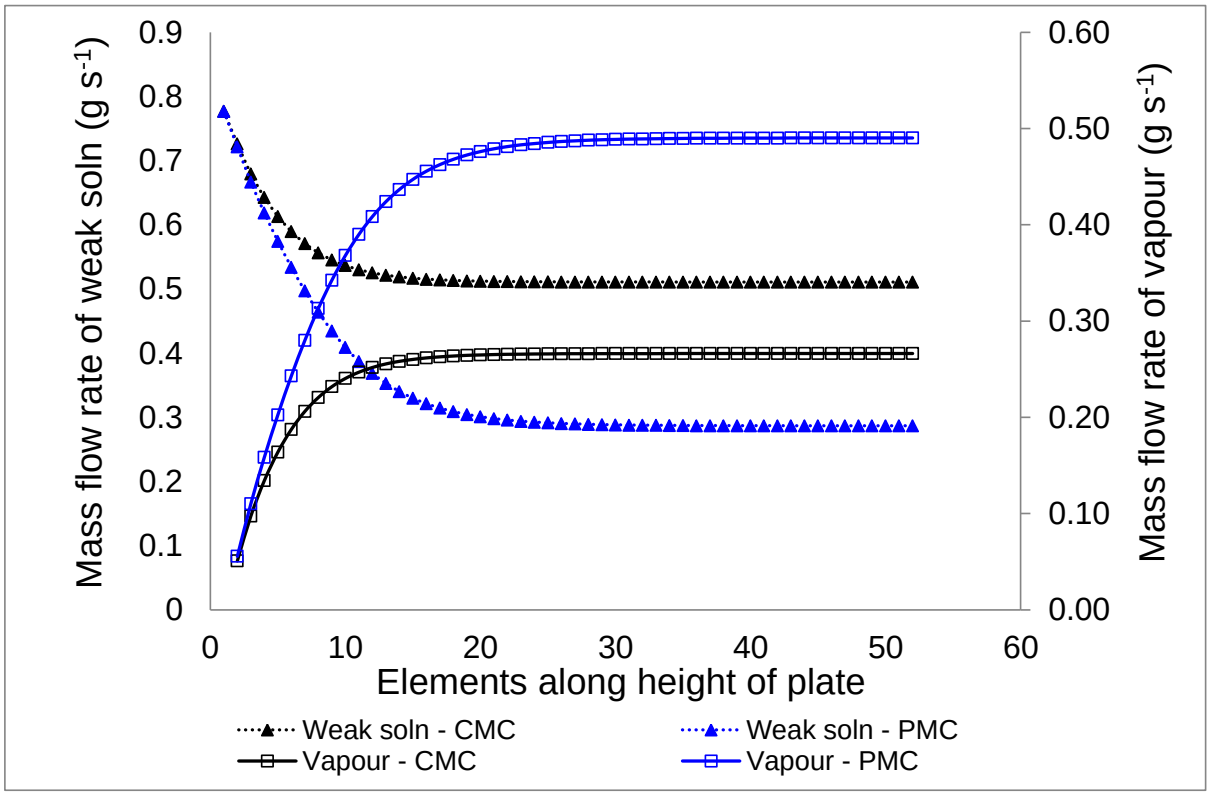

b) Mass flow rate profiles

Figure 5.12: Concentration and mass flow rates of weak solution and vapour along central middle channels (CMC) and peripheral middle channels (PMC) – Case 1, geometry G2

From both cases presented for geometry G1, the following inferences can be drawn

- The amount of vapour generated for case 2 is 5% greater than that from case 1.
- The concentration of ammonia in the vapour is slightly higher for case 1 than case 2 but the difference is not very pronounced.
- When the NH_3-H_2O solution flows through the end flow channels, the amount of vapour generated is almost 50% less per channel than when the solution flows through the middle flow channel. This is due to less heat flux available for desorption at the end channel which increases the percentage of heating zone for the end flow channel when compared to the middle flow channel. However, since there are two end flow channels for case 2, the cumulative effect is greater than that of case 1 which explains the slightly higher quantity of vapour generation.

Case 1, geometry G2

Geometry G2 has 20 plates, translating to 19 flow channels – 10 oil channels and 9 solution channels. In this case, the solution flows only in the middle channels, receiving heat flux from both sides. The peripheral middle channels (PMC) receive 50% more heat flux than central middle channels (CMC). This is because the entire heat from the end oil flow channel (thermal losses from end plates are neglected) is transferred to the peripheral middle channel.

Hence out of 9 solution flow channels, 7 of them will generate almost similar refrigerant volumes and the remaining two will generate slightly higher refrigerant volume. The NH_3 concentration of weak solution and vapour along the peripheral middle channel and central middle channel is shown in Figure 5.12 a) respectively. Once again it is evident that the rate of desorption is high initially and gradually reduces thereafter, thus indicating that most of desorption occurs in the initial part of the channel. The concentration of NH_3 in the vapour is

0.6 for the central middle channels and 0.42 for the peripheral middle channels, leading to an average concentration of 0.51 in the outlet stream of the desorber which is 15 % lower than the concentration in the outlet stream from G1. This is attributed to a low solution flow rate in the flow channels of G2, which is an order of magnitude lower than that in the flow channels of G1.

The central middle channel generates a mass flow rate of 0.266 g s^{-1} and the peripheral middle channel generates a mass flow rate of 0.49 g s^{-1}, leading to a total refrigerant generation of 2.842 g s^{-1} (7 times CMC + 2 times PMC).

Case 2, geometry G2

In this case there are 10 solution flow channels and 9 oil flow channels. Of the 10 solution channels, eight solution flow channels will experience heat flux from both sides and the remaining two solution flow channels will experience heat flux from one side only as seen from Figure 5.10. The profiles of NH_3 concentration and the mass flow rates for the middle channel (MC) and end channel (EC) have a similar shape as that of case 1 of geometry G2 and are not shown here for reasons of brevity. The vapour concentration is 0.55 for the middle channels and 0.714 for the end channels, leading to an average concentration of 0.63 at the outlet of the desorber. The middle channels generate a vapour mass flow rate of 0.29 g s^{-1} and the end channels generate a mass flow rate of 0.153 g s^{-1}. The total refrigerant generation (8 times MC + 2 times EC) is thus 2.626 g s^{-1}.

From both cases presented for geometry G2, the following inferences can be drawn

- The amount of vapour generated in case 1 is about 8 % higher than that from case 2 but the concentration of ammonia in the vapour in case 2 is 23.5 % higher than in case 1.

- In case 1, although PMCs generate a higher volume of vapour than CMCs, the concentration of vapour is lower in PMCs. This is due to higher heat flux experienced by PMCs that eventually leads to boiling of water along with ammonia.
- Similarly in case 2, middle channels generate higher vapour flow when compared to end channels however the concentration of vapour is lower.

The slope of the ammonia concentration curve and weak solution mass flow rate curve is quite steep in the initial part of the channel and tends to plateau later, indicating that in the plateau part both ammonia and water boil off at the same rate, thus preventing further increase in ammonia concentration. This data will be crucial in sizing PHE desorbers to meet small scale applications because if there is no profound increase in mass flow rate or concentration along the height of the channel, it can be rigorously reduced to meet the required value/capacity.

Graphs for geometries G3 & G4 show very similar behaviour and have been included in *Appendix E*.

5.4.4 Comparison of results from all geometries

The total amount of refrigerant generated from all four geometries for both Case 1 and Case 2 is shown in Figure 5.13. Except for geometry G1, the remaining geometries generate more refrigerant when oil has an extra flow channel (Case 1). The amount of refrigerant generated in Case 1 is 8 % more for G2, 10% more for G3 and 5 % more for G4 than that generated in Case 2 for the respective geometries. The trend observed in G1 can be explained by the fact that G1 employs only 4 plates, leading to 3 flow channels. Although the amount of refrigerant generated from the middle channel is greater than that of an end channel, the cumulative

sum of the refrigerant generated from the end channels is greater than that generated from the middle channel alone.

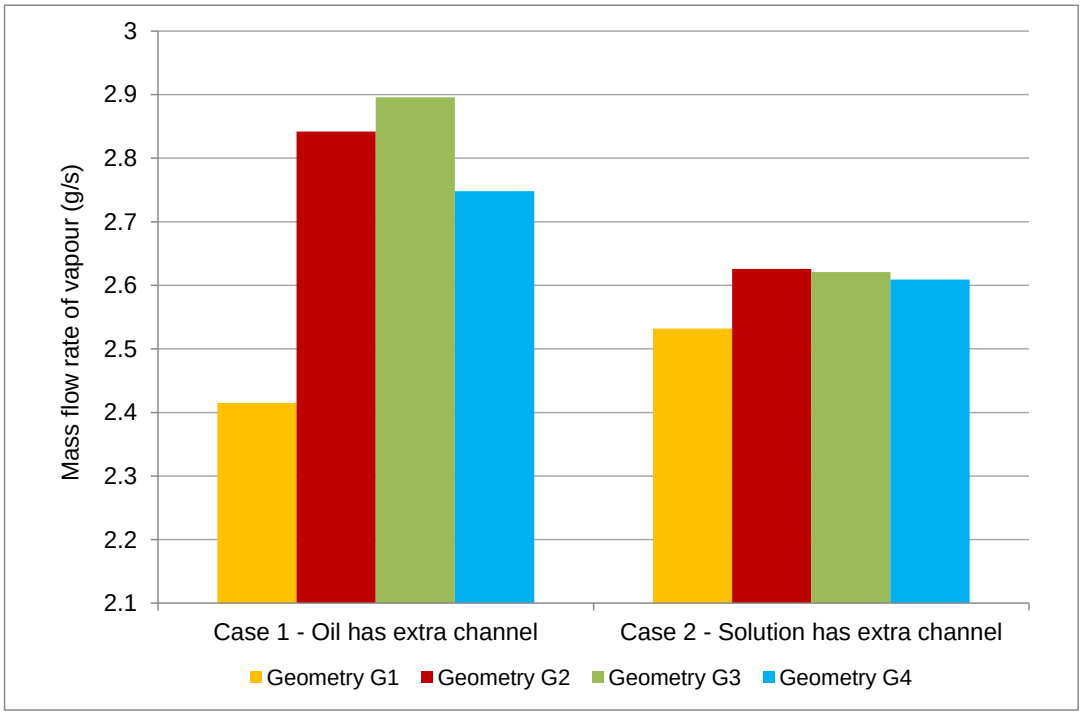

Figure 5.13: Comparison of total mass flow rate of vapour from different geometries

Figure 5.14 shows the mass flow rate and NH_3 mass fraction in the refrigerant generated along different channels for Case 1 and Case 2. It is evident that channels with higher heat flux generate more vapour but the mass fraction of NH_3 in the vapour is lower. This is because higher heat flux also causes water to boil off thus diluting the initial ammonia rich vapour. The number of flow channels in a PHE also plays a crucial role in determining the NH_3 mass fraction in the vapour. Geometry G1 has only 3 flow channels hence the NH_3 mass fraction in the middle channels and end channels is almost the same. The other geometries have more than 10 flow channels in the PHE and hence display almost similar trends in terms of NH_3 mass fraction obtained from different flow channels.

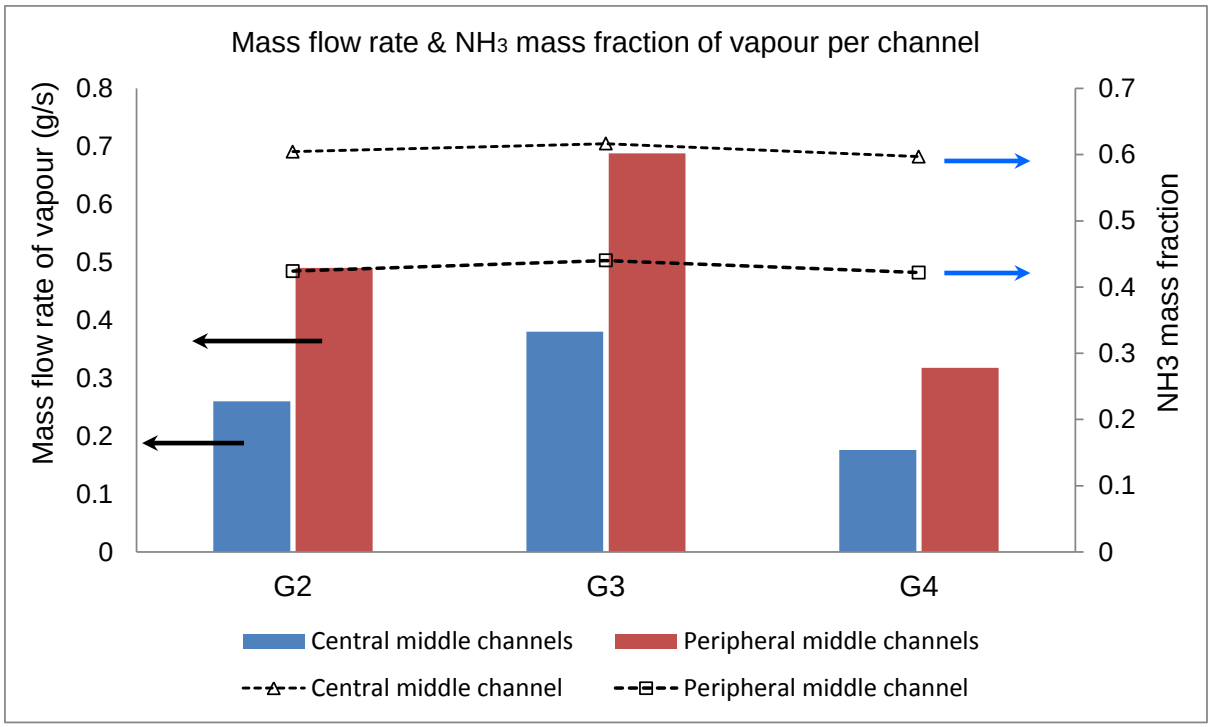

A)

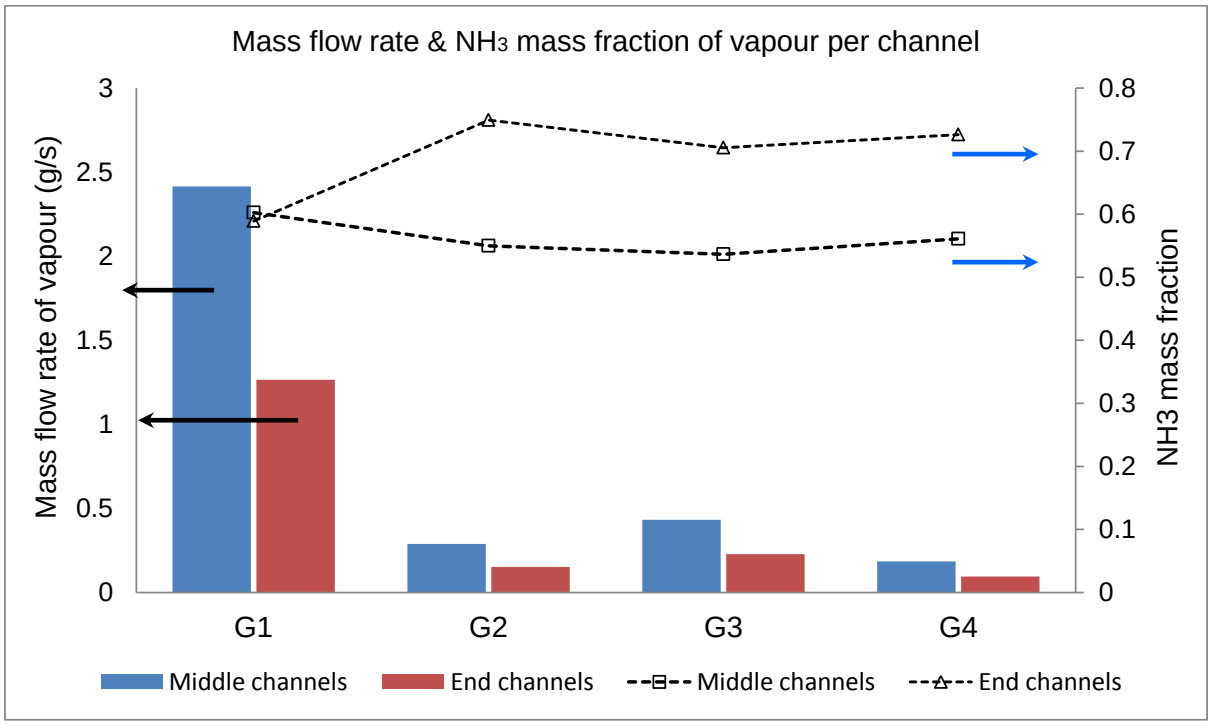

B)

Figure 5.14: Mass flow rate & NH_3 mass fraction in vapour from different channels
A) Case 1 B) Case 2

5.4.5 Desorption ratio

Based on the above data, desorption ratios for different geometries can be calculated. Desorption ratio is defined as the amount of refrigerant vapour generated divided by the total mass flow rate of the strong solution. Desorption ratio for different geometries for both cases is shown in Figure 5.15. It lies in the range of 0.34 to 0.41 across all geometries. A higher desorption ratio is favourable because that indirectly means more refrigerant has been released from the solution.

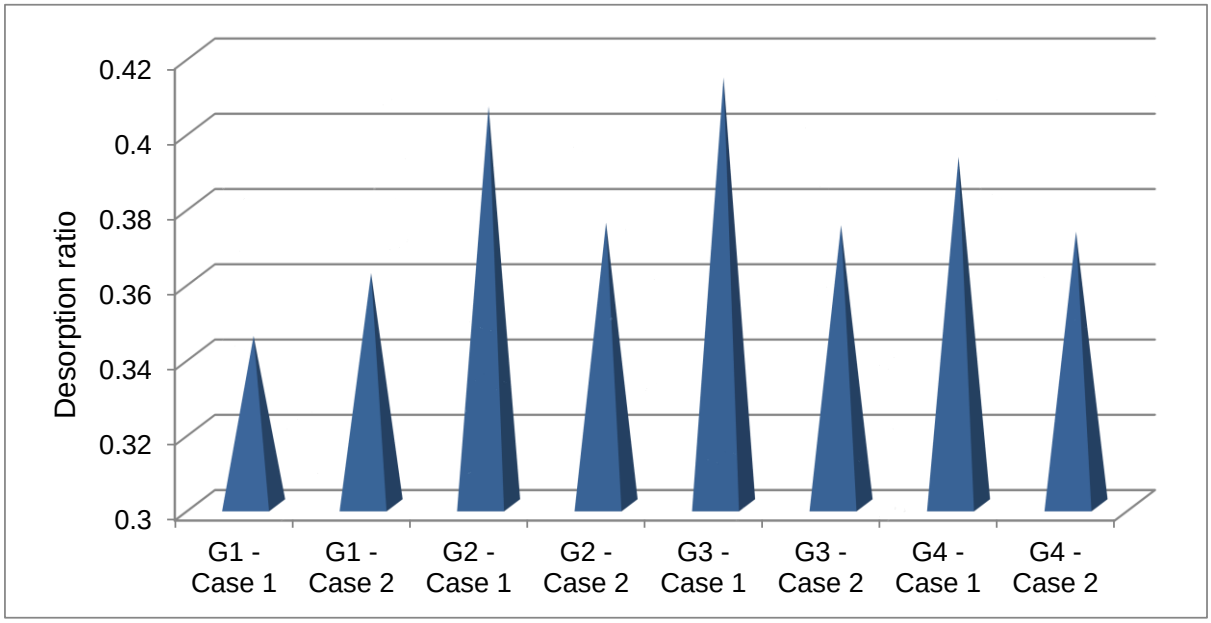

Figure 5.15: Desorption ratio for different geometries

5.4.6 Heat flux variation

Since the amount of vapour generated in Case 1 (oil having extra flow channel) is higher than Case 2 for most of the geometries, further analysis will concentrate on Case 1 arrangements.

The heat flux variation along the height of the solution flow channel for different channels for all four geometries is shown in Figure 5.16. The height of each element is 10 mm. As can be seen from the figure, the heat flux values along the solution flow channel is highest for geometry G1 followed by geometry G3. For geometry G2 and G4, the heat flux values are almost 4 times smaller when compared to geometry G1. This is because the number of flow channels in G2 & G4 is 19 and 29 when compared to G1 & G3 where the number of flow channels is 3 and 13 respectively. As higher heat flux leads to more refrigerant production it is desirable that the solution channels experience as high heat flux as possible. Having a lesser number of flow channels in the PHE can lead to higher heat flux values along the solution channel. This directly indicates that there is a threshold for the number of flow channels and in turn for the number of plates above which there is no appreciable effect.

The Nusselt number is an indication of the mode of heat transfer. It is the ratio of convective heat transfer to conductive heat transfer. If the Nusselt number is close to one then heat transfer via convection and conduction is almost of similar magnitude. On the other hand a larger Nusselt number indicates convective heat transfer as a dominant factor. Table 5.4 shows the average Nusselt number along the height of the solution flow channel for different channels of different geometries. The Nusselt number for geometry G1 is almost 4 times higher when compared to the Nusselt number from other geometries. This clearly indicates that the dominant mode of heat transfer is via convection for geometry G1. This result is also supported by a fluid flow analysis presented in the next section.

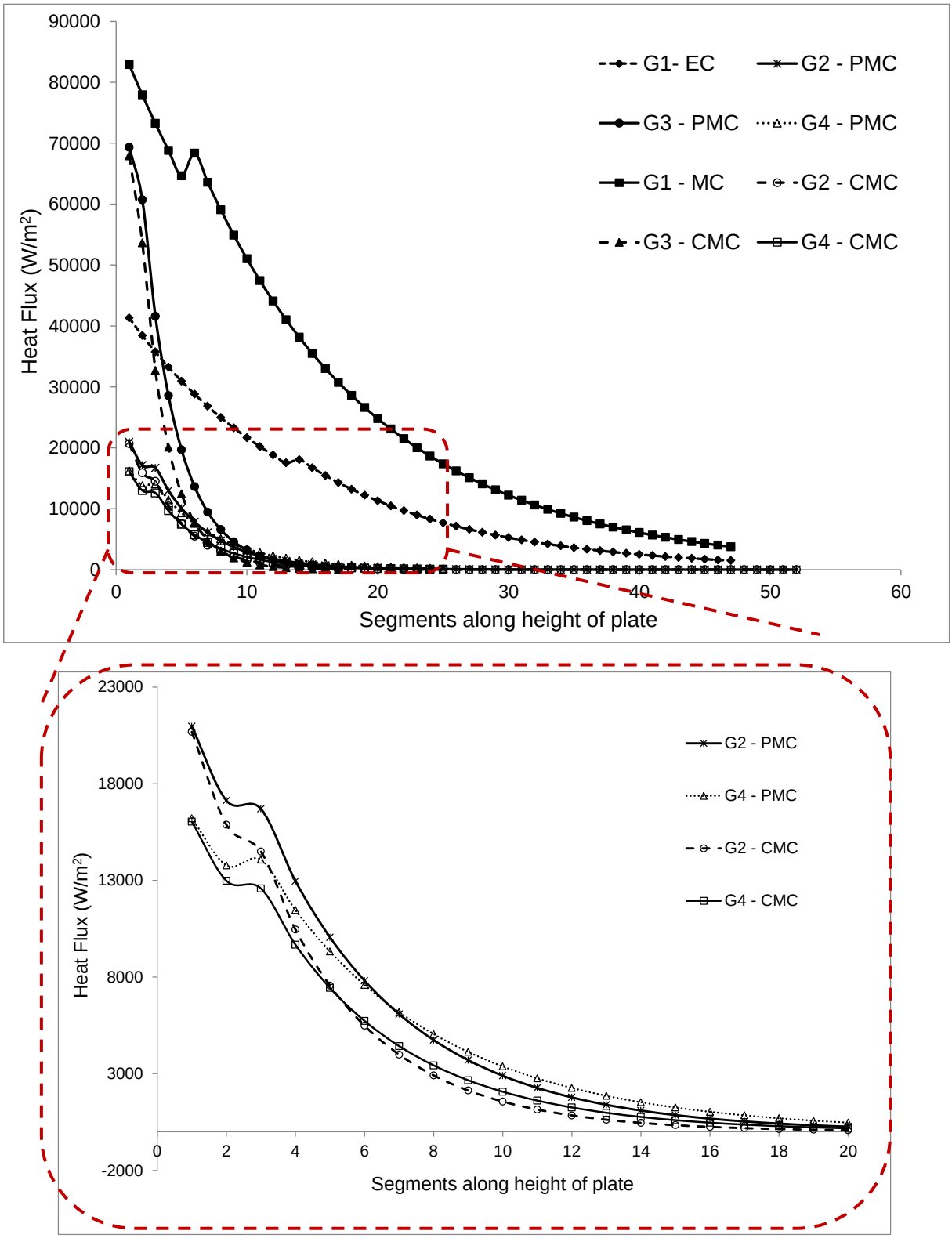

Figure 5.16: Heat flux along the height of the solution channel
(PMC = Peripheral Middle Channel, CMC = Central Middle Channel,
MC = Middle Channel, EC = End Channel)

Table 5.4: Nusselt number for different channels of different geometries

Geometry	Nusselt number
G1 – EC	19.6
G1 – MC	20.5
G2 – CMC	4.3
G2 – PMC	4.32
G3 – CMC	6.65
G3 – PMC	6.8
G4 – CMC	3.22
G4 – PMC	3.27

(EC = End Channel, MC = Middle Channel, CMC = Central Middle Channel, PMC = Peripheral Middle Channel)

5.4.7 Fluid flow analysis

The Reynolds number for the solution flowing through different flow channels for the geometries discussed here is plotted in Figure 5.17. Except for geometry G1, the flow is completely laminar through other flow channels for other geometries because of a very low Reynolds number. The velocity profiles for a single flow channel for different geometries are shown in Figure 5.18. Higher velocities of the solution occur in the flow channels that experience higher heat flux, as seen in the middle channel of G1 and peripheral middle channels (PMC) of G2, G3 and G4. This is because channels that receive a higher heat flux generate more vapour and this combined two phase flow has a higher velocity.

5.4.8 Heat transfer coefficient variation

The variation in heat transfer coefficient along the height of the channel for different geometries is shown in Figure 5.19. The kink observed in the curves indicates the transition from sensible heating of solution to latent heating which is also the point where boiling starts to occur. Heat transfer coefficients are higher when the flow changes to two-phase flow than when the flow is single phase.

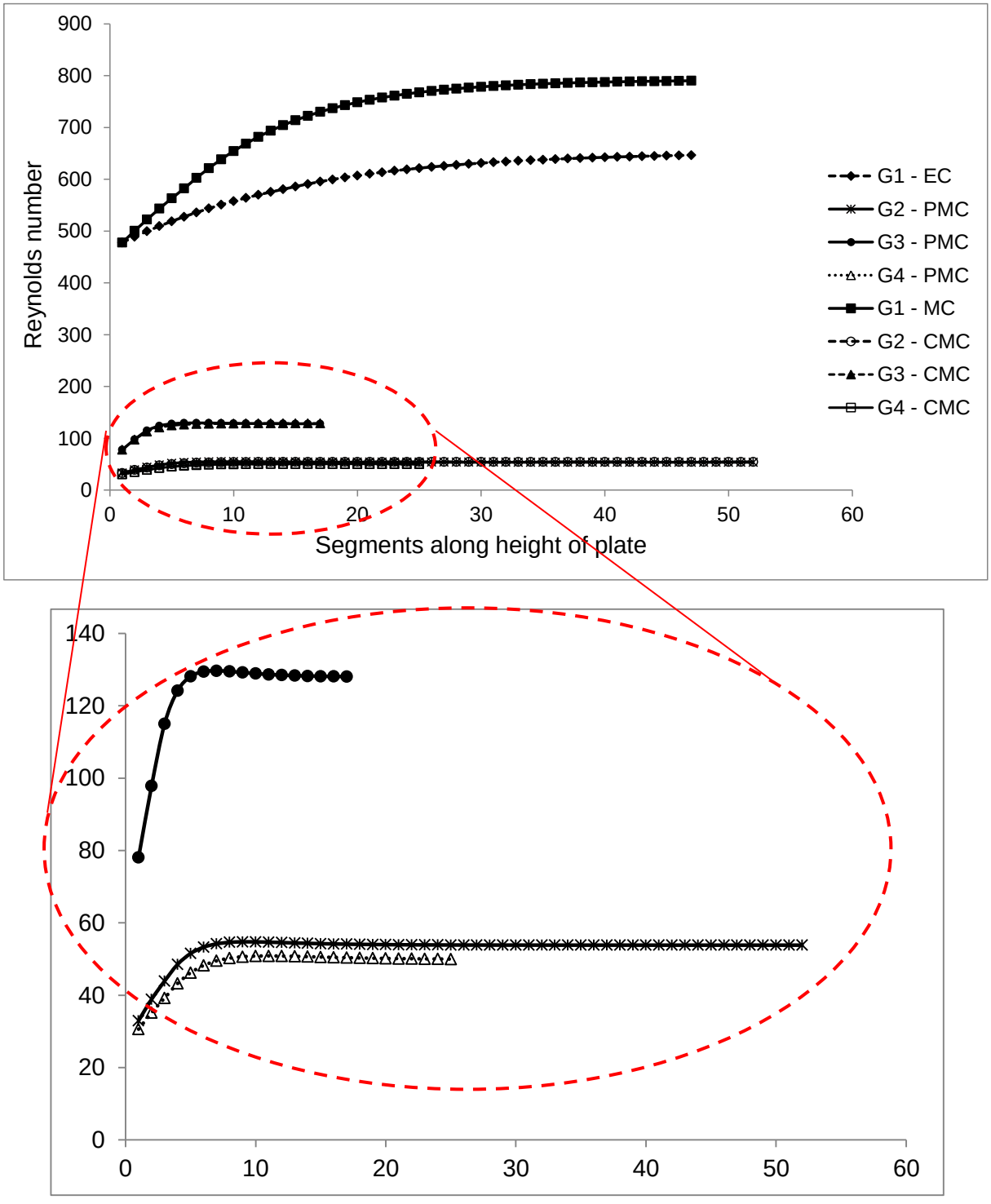

Figure 5.17: Reynolds number of solution through different channels for different geometries

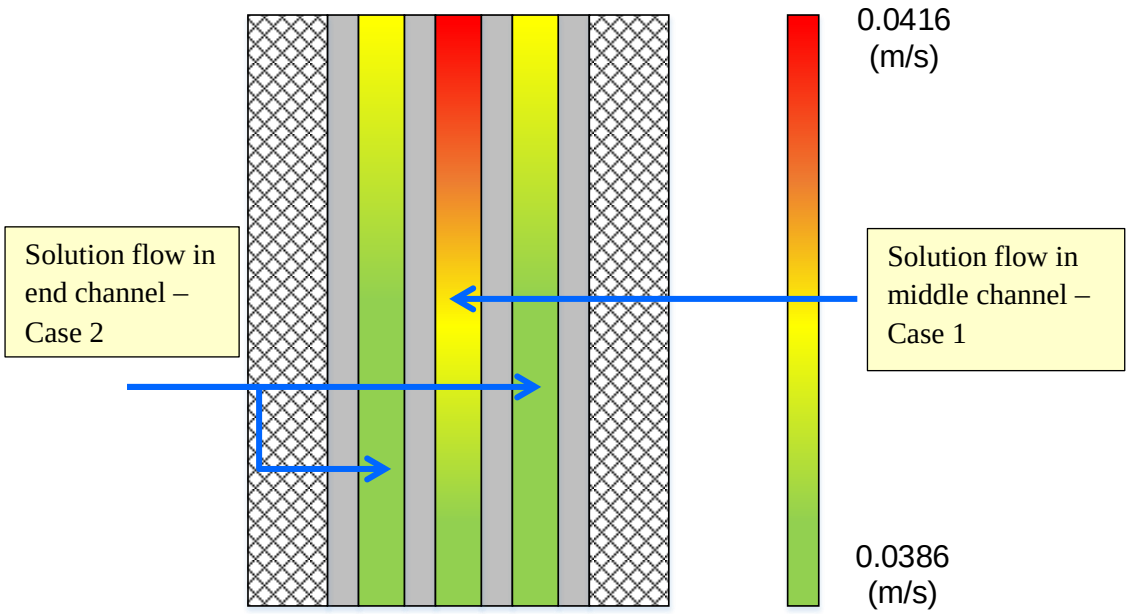

a) Velocity profile illustration for individual channels in G1

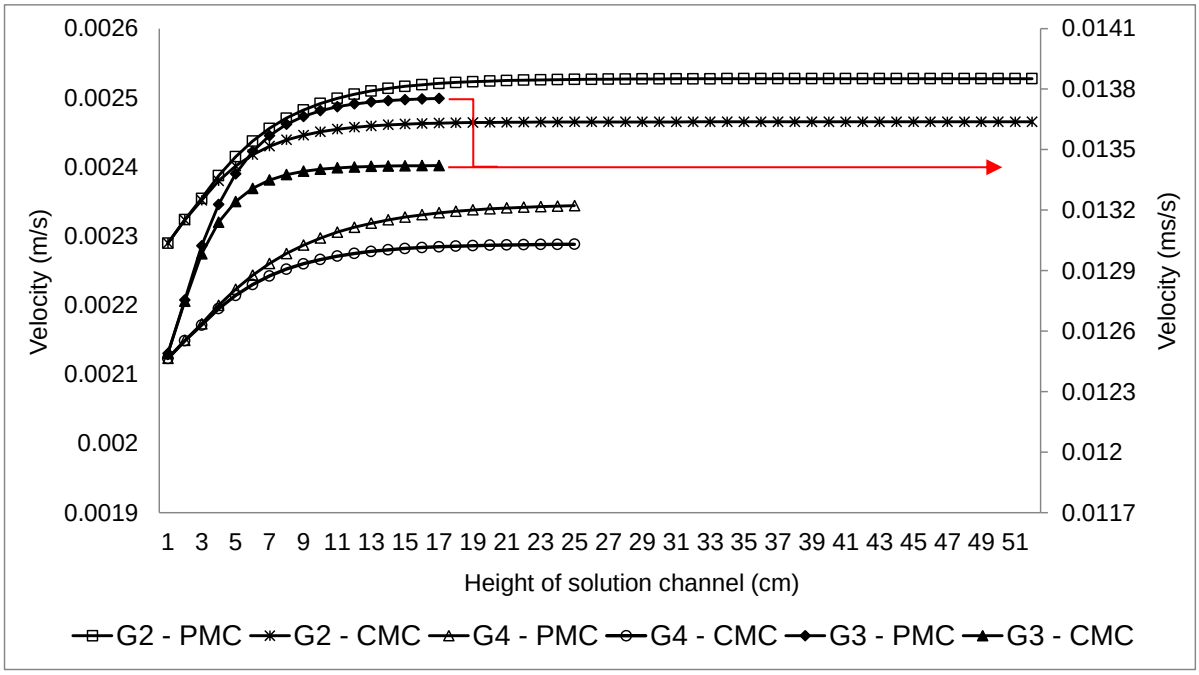

b) Velocity plots for different channels in G2, G3 & G4

Figure 5.18: Velocity profile along height of solution channel

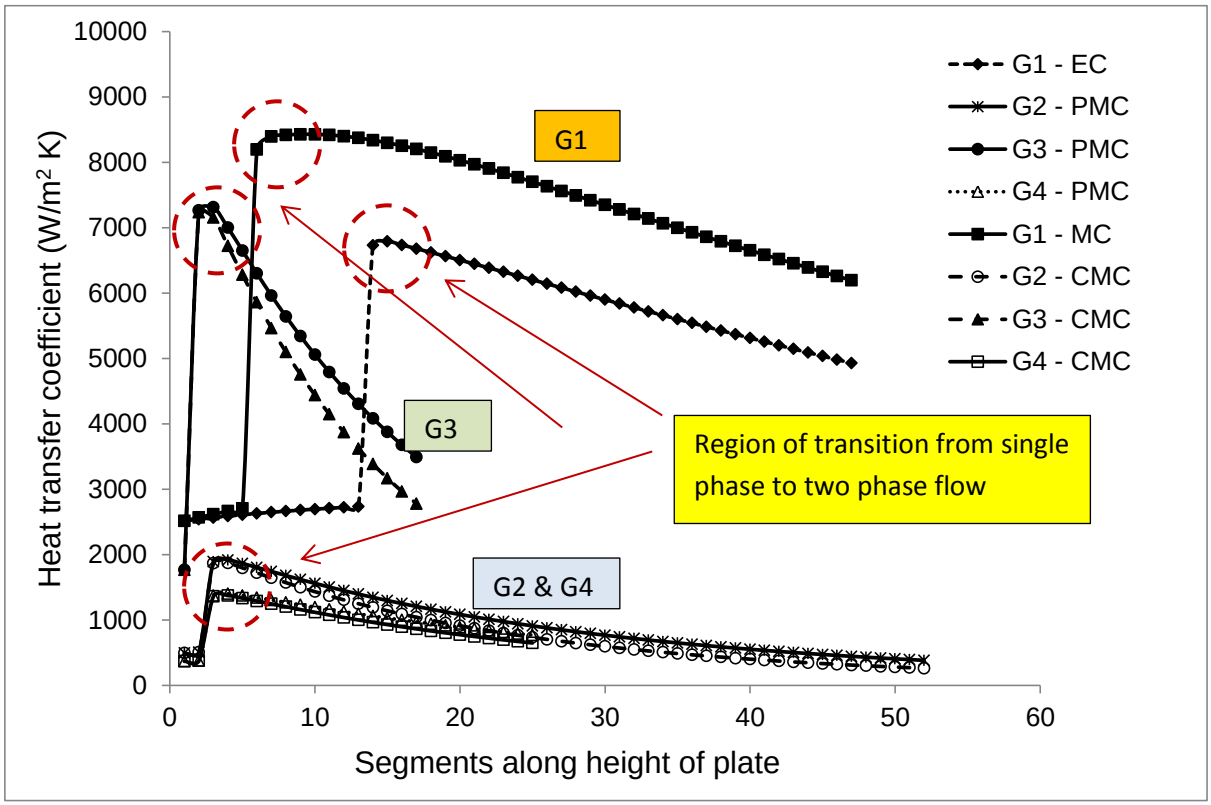

Figure 5.19: Heat transfer coefficient variation along height of plate
(PMC = Peripheral Middle Channel, CMC = Central Middle Channel)

5.5 Sensitivity Analysis

Performing a sensitivity analysis will help in understanding the influence of a variety of parameters on PHE desorber performance. In the present study geometry G2 is taken as the base case because it has 20 channels and allows one to look at either end of the spectrum for less and more number of channels and also because it has the highest plate height. The different parameters that were varied are:

a) Number of plates
b) Height of plate
c) Width of plate
d) Corrugation angle of the plate
e) Pitch of corrugation
f) Inlet temperature of thermal oil
g) Mass flow rate of solution
h) Mass flow rate of thermal oil

When each parameter is varied, the other parameters are kept constant as the base case parameter for geometry G2. The base case geometrical parameters of G2 were compiled in Table 5.1.

a) Number of plates

For an even number of plates, the extra flow channel is assigned to oil because it leads to a higher vapour mass flow rate. The variation in mass flow rate of vapour and NH_3 mass fraction with the number of plates is shown in Figure 5.20. The mass flow rate of vapour increases with the number of plates up to a certain number, after which adding plates does not make much of a difference. This limit is reached around 10 plates. The ammonia mass fraction, on the other hand, decreases with the number of plates and then levels off.

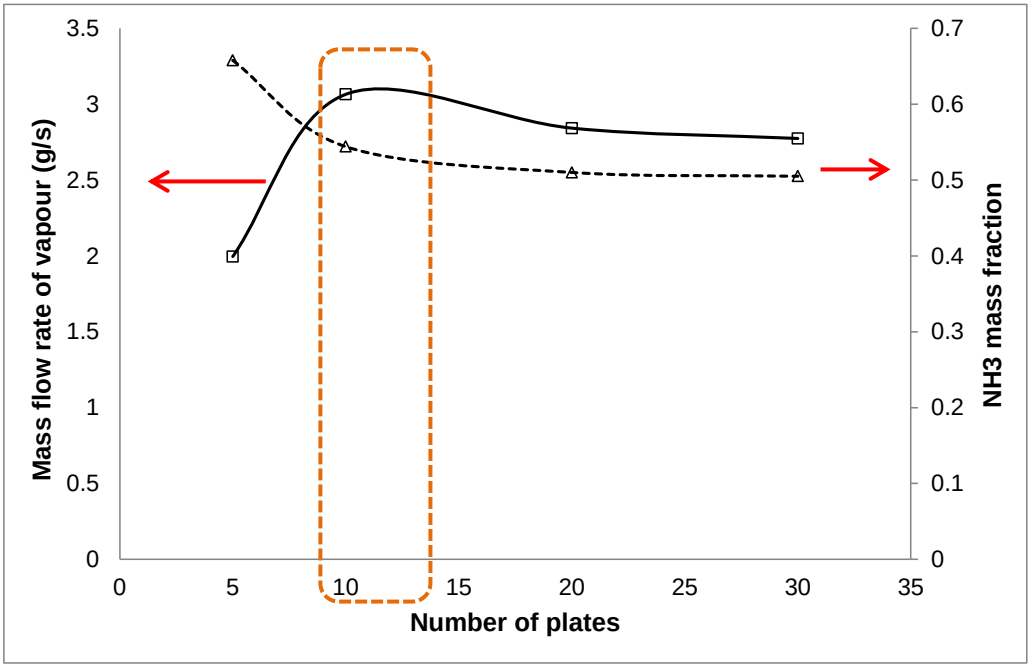

Figure 5.20: Variation of total mass flow rate & NH_3 mass fraction of vapour with No.of plates

The increase in mass flow rate of vapour with increase in number of plates can be explained from the fact that the total heat transfer area increases, which effectively leads to more desorption of the ammonia-water solution. However after a certain number of plates is reached, the increase in heat transfer area is offset by the transition to laminar flow which leads to a lower heat transfer coefficient and thus reduced heat flux. This is evident from Figure 5.19 where G2 & G4 have a very low heat transfer coefficient due to a large number of channels.

b) Height of plate

The height of the PHE desorber was varied to check if it has any influence on the amount of vapour generated. This is shown in Figure 5.21. The total amount of vapour generated increases with increase in height of the plate however the increase is not very pronounced. Hence it can be concluded that the height of the plate does not have a major influence on the total amount of vapour generated.

The height of the plate indeed does not have a major role as evident from Figure 5.13 where geometry G3 produces more vapour than geometry G2 even though geometry G2 has a higher plate dimension. This is because G3 has 14 plates when compared to G2 which has 20 plates and as explained above the mass flow rate of vapour decreases after a certain number of plates are reached.

The temperature profiles of the solution and thermal oil tend to converge after a height of 300 mm and hence there is no effective heat transfer from the oil to the solution which in turn leads to no appreciable generation of vapour.

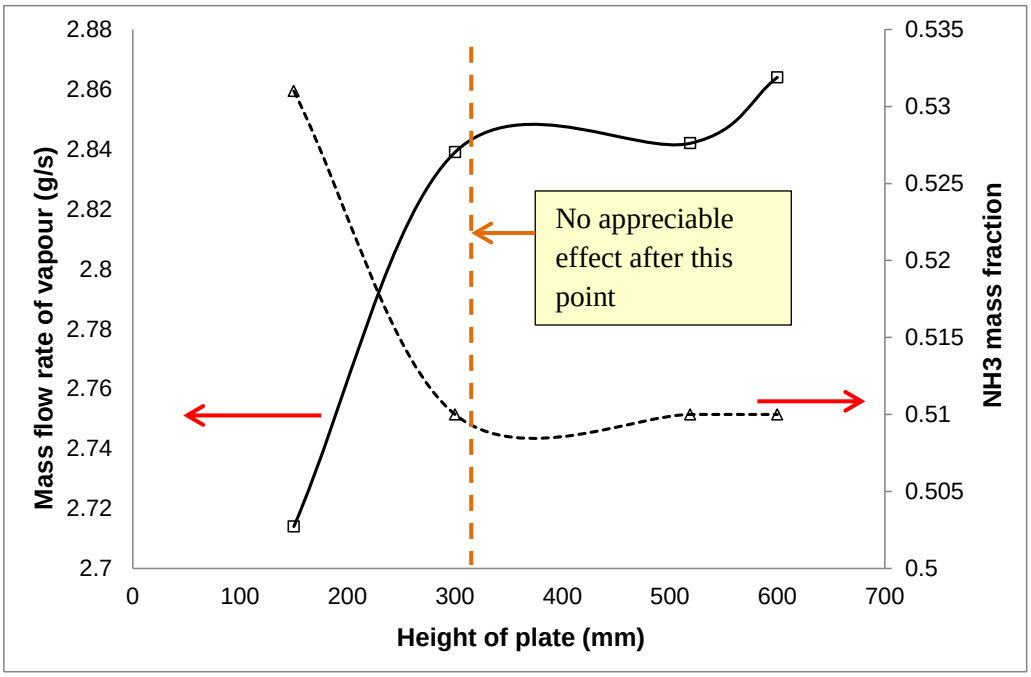

Figure 5.21: Variation of total mass flow rate & NH_3 mass fraction of vapour with height of plate

c) Width of plate

There is no appreciable increase in either mass flow rate of vapour or NH_3 concentration with increase in width of the plate. This is because with increase in width of the plate, the area of each element increases which in turn increases the total heat transferred. However, the amount of heat flux does not increase by a great amount and because of which the amount of vapour generated was less pronounced. Hence the width of the plate can be kept to the minimum possible to reduce the size of the desorber.

d) Pitch and Corrugation angle of plate

The pitch of corrugation was varied from 2 mm to 10 mm and the effect on mass flow rate of vapour and NH_3 mass fraction is negligible.

The corrugation angle of the plate was varied from 30^o to 60^o. The effect of corrugation angle on the mass flow rate of vapour and NH_3 concentration was not significant. Hence the corrugation angle of the plate as designed by the manufacturer can be retained.

e) Inlet temperature of thermal oil

With decrease in inlet temperature of the thermal oil, the total mass flow rate of vapour generated in the PHE desorber decreases as seen from Figure 5.22. This is because with decrease in temperature of the coupling fluid (thermal oil in this case), there is a corresponding decrease in heat transfer to the NH_3-H_2O solution. However, the ammonia mass fraction in the vapour is higher with decrease in inlet temperature of thermal oil. This is because the amount of water being boiled off is also less, resulting in a higher concentration of ammonia in the vapour.

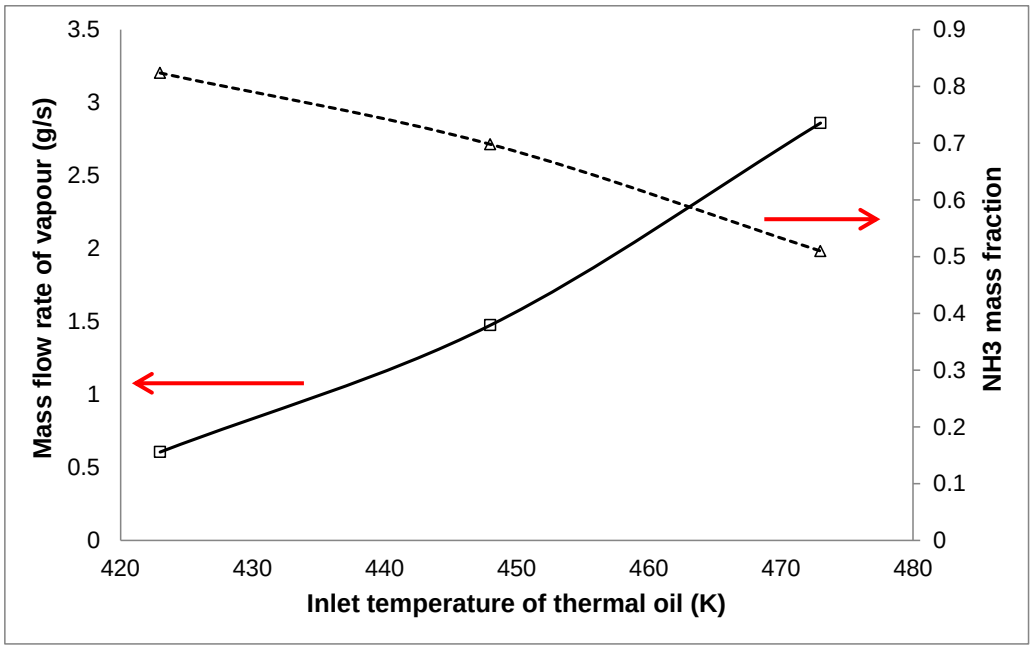

Figure 5.22: Variation of total mass flow rate & NH_3 mass fraction with T_{Inlet} of thermal oil

f) Mass flow rate of strong solution

The variation of mass flow rate of vapour and NH_3 mass fraction with the mass flow rate of strong solution is shown in Figure 5.23. The mass flow rate of vapour produced is lower when the mass flow rate of strong solution is reduced and also the fraction of ammonia in the vapour is a mere 36%. The concentration of ammonia in the vapour is greatly increased when the flow rate of strong solution is increased. Higher mass flow rates of strong solution ensure higher concentration of ammonia in the vapour and also higher mass flow rate of vapour and hence the mass flow rate of the strong solution can be optimised to meet the cooling requirements. Also increasing the mass flow rate changes the flow regime from laminar to turbulent thereby enhancing the heat transfer.

One interesting phenomena that was observed when solving the model for very low mass flow rates of strong solution is that in the peripheral middle channels (PMCs), the solution turns to vapour immediately, within a certain height of the channel. This is because of the high heat flux present in the peripheral middle channels. Hence reducing the mass flow rate of the strong solution below 5 g s^{-1} is not feasible for this particular PHE desorber when all other parameters/conditions were kept constant.

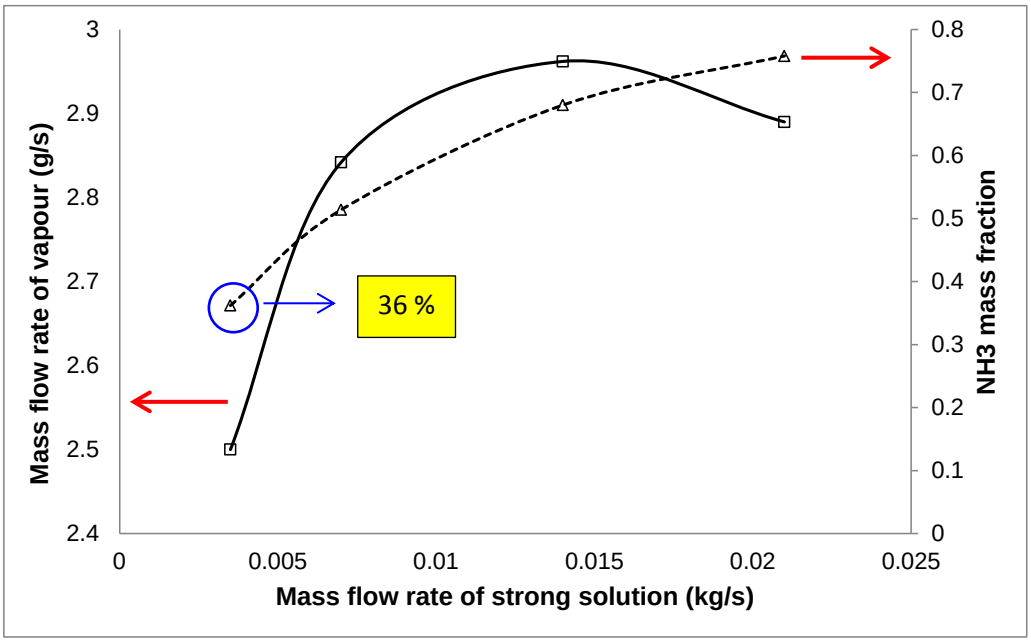

Figure 5.23: Variation of mass flow rate & NH_3 mass fraction of vapour with $m_{Strong\ soln}$

g) Mass flow rate of thermal oil

Higher mass flow rate of thermal oil results in a higher mass flow rate of vapour for the same base case operating conditions but leads to lower NH_3 mass fraction. This is because with increase in mass flow rate there is a larger heat addition and this causes water to boil off from the solution as well, thereby diluting the NH_3 mass fraction in the vapour. This variation is shown in Figure 5.24.

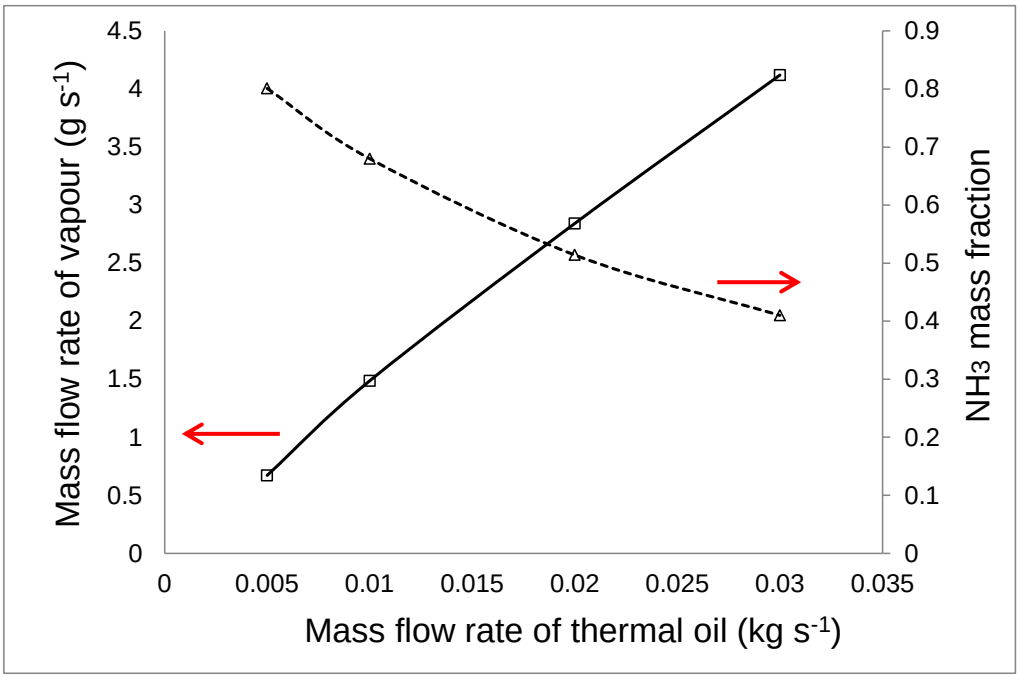

Figure 5.24: Variation of mass flow rate & NH_3 mass fraction of vapour with $m_{thermal\ oil}$

Based on the modelling and sensitivity analysis carried out, a general set of geometrical and operating parameters can be defined for generation of NH_3 vapour in a PHE desorber.

Number of plates: The number of plates can be restricted to about 15 in order to reduce the size and volume of the PHE desorber. The reason for the same has been explained before.

Inlet temperature of thermal oil: Inlet temperature of thermal oil plays a major role in the vapour generation and vapour concentration in the PHE desorber. Ideally the temperature should be between 450 and 500 K (177 ^oC to 227 ^oC). This will ensure that sufficient heat is transferred to the NH_3-H_2O solution. The designer has the choice of lowering the thermal oil temperature if the refrigeration temperature required is low (0 to 5 ^oC). The minimum inlet temperature for the thermal oil is 440 K if the desorber is to be

used in the VARS catering to sub-zero refrigeration temperatures and 400 K if the VARS is going to cater to chilled food (0 to 5 ^{o}C) temperatures.

Mass flow rate of solution: Depending on the cooling load required, the mass flow rate of solution should be varied. It is more or less a fixed parameter for a particular cooling load however some reserve capacity should be available in case the cooling demand suddenly increases. Having a solution flow rate between 7 to 10 g s^{-1} will be sufficient for a 1 kW cooling load.

Mass flow rate of thermal oil: The mass flow rate of thermal oil has to be delicately balanced in order to provide just enough heat to boil NH_3 from the refrigerant-absorbent solution. This will ensure that the NH_3 concentration in the vapour also stays high. High mass flow rates will no doubt deliver the required quantity of heat at the desorber but this will be totally unwarranted. Having the correct mass flow rate of thermal oil will also ensure that the thermal oil pump and the rectifier (component after desorber) are sized correctly. The mass flow rate is linked to the temperature of the thermal oil and the quantity of heat required at the desorber.

Height of plate: With the operating conditions mentioned in Table 5.3, the height of the plate can be limited between 300 and 400 mm. The height can be reduced further if the inlet temperature of the solution is increased which leads to a reduction in heating zone in the solution flow channel.

5.6 Design maps

Design maps can be drawn to relate the size of the PHE desorber for different cooling loads. From the '0D' model performed on VARS, mentioned in *Chapter 3*, the flow rates of strong solution and corresponding vapour needed for a 1 kW and 5 kW cooling load were identified and the same is given in Table 5.5.

Table 5.5: Operating parameters needed for 5 kW & 1 kW cooling load

Operating system parameter	5 kW cooling load	1 kW cooling load
Mass flow rate of strong solution (g s^{-1})	36	7.2
Mass flow rate of refrigerant (g s^{-1})	4.2	0.84
NH_3 mass fraction in refrigerant	0.99	0.99

The PHE desorbers of all four geometries generate vapour (refrigerant) in the range of 2.4 g s^{-1} to 2.8 g s^{-1} with an average NH_3 mass fraction of about 0.6. This in turn means the actual refrigerant flow rate (after rectification) is around 1.62 g s^{-1} with an ammonia concentration of 99%. This quantity of refrigerant is more than sufficient to cater to a 1 kW cooling load. In fact this quantity of refrigerant is sufficient to cater to cooling loads up to 1.9 kW. The optimised dimensions of the PHE desorber which can meet cooling loads up to 1.9 kW are listed below

Number of plates	10
Height of plate	300 mm
Width of plate	50 mm
Thickness of plate	0.4 mm
Corrugation angle	60^o
Pitch of corrugation	5 mm
Amplitude of corrugation	2 mm

Taking into account the height, width and overall thickness of this PHE desorber, the volume space needed to house it is just a mere 60 cm^3 which is extremely compact for a desorber. The cooling load requirements at different refrigeration temperatures for a small and medium truck are shown in Figure 5.25 and the appropriate area covered by the compact PHE desorber design is also highlighted.

5.7 Data for other component modelling

The results obtained from PHE desorber modelling provide useful data for modelling components both upstream and downstream. The mass flow rate and NH_3 concentration produced at the outlet of the PHE desorber serve as input for rectifier component modelling. The rectifier is the next component in series after the desorber and is used to purify the refrigerant and remove any water vapour present in it. The inlet temperature of the strong solution gives information on how the solution heat exchanger must be designed and what should be its effectiveness. The inlet temperature of the thermal oil provides information on the design of the heat exchanger that has to be coupled with the heat source. Thus numerical modelling of the PHE desorber is also crucial to determine the performance and sizing of other upstream and downstream components.

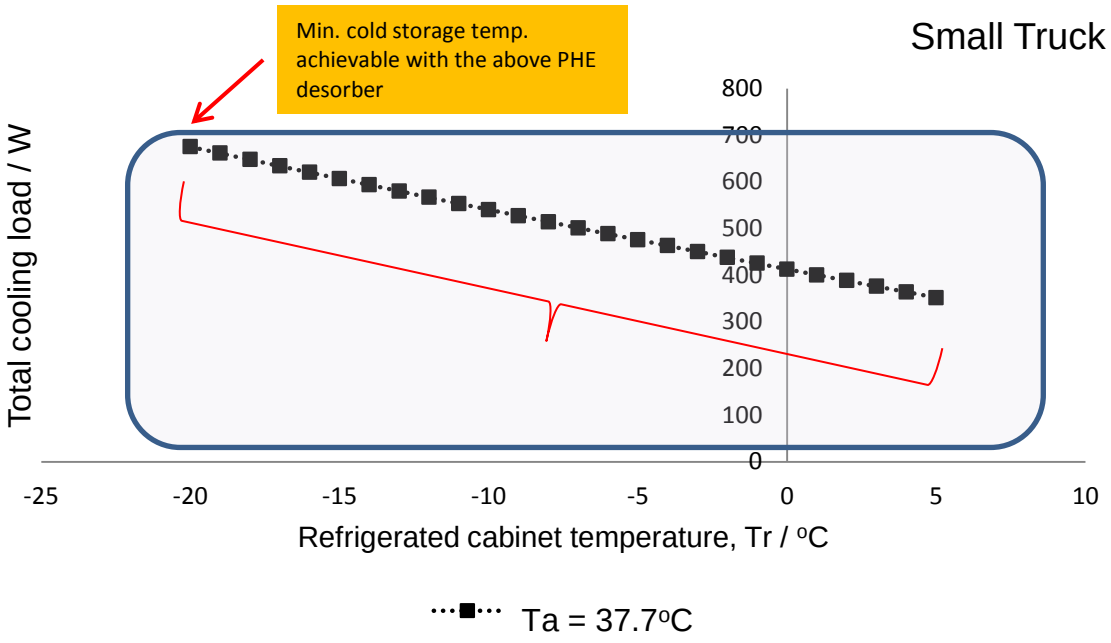

a) Cooling loads covered on a small truck of refrigerated volume 7.3 m^3

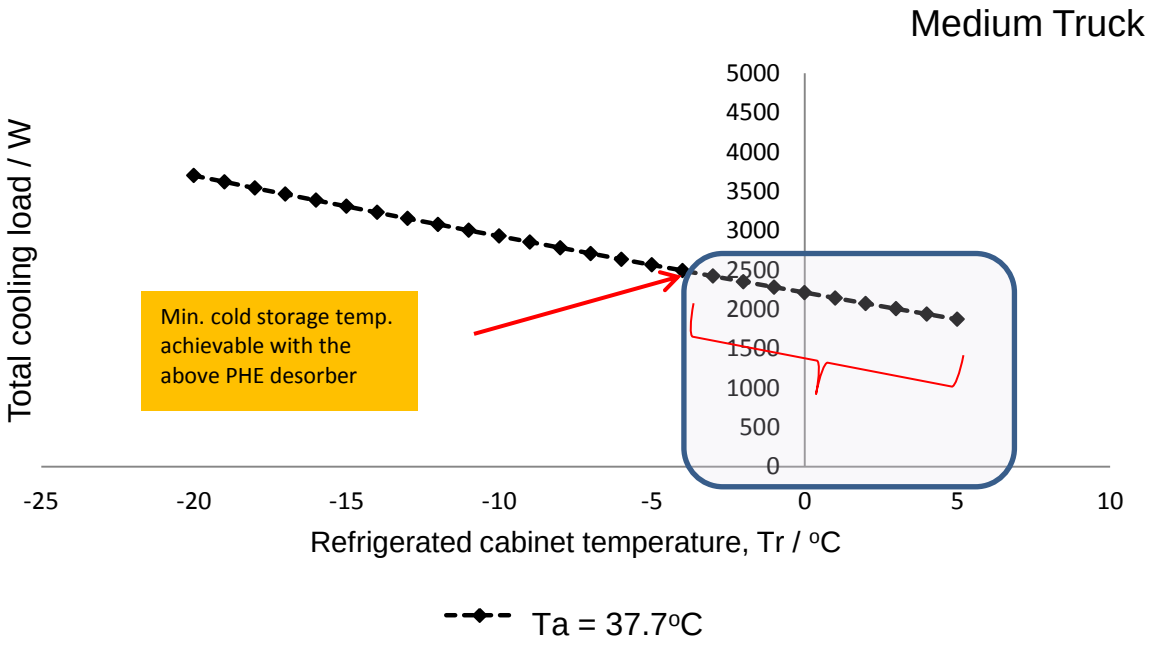

b) Cooling loads covered on a medium truck of refrigerated volume 56.4 m^3

Figure 5.25: Design maps showing the cooling loads covered by the compact PHE desorber

5.8 Conclusions

A numerical thermal model of the PHE desorber for an NH_3-H_2O system was developed and critical data such as temperature profiles, heat transfer coefficient, mass flow rate of refrigerant and NH_3 mass fraction in the refrigerant were plotted along the height of the flow channel. As the PHE consists of different flow channels and the type of channels varies depending on the number of plates used, the numerical model provides valuable insights into the heat transfer and refrigerant production aspects of what actually happens within these channels. These effects cannot otherwise be captured via experiments.

It was found that flow channels that received a higher heat flux generated more vapour but the NH_3 concentration in the vapour was less when compared to flow channels that received relatively lower heat flux. Also, in cases where there were an odd number of flow channels, it was better to allocate the extra channel to the hot coupling fluid rather than the refrigerant-absorbent solution because that results in generation of more vapour. The numerical model also helps in identifying the heating and boiling zones within the desorber based on the point where the solution reaches the bubble point temperature.

The dimensions of the PHE used by several experimental research groups were taken as input for the numerical model in order to keep dimensions realistic. All four geometries produced sufficient quantity of refrigerant needed for a 1 kW cooling load with a desorption ratio between 0.34 and 0.41. A sensitivity analysis was performed by varying different geometrical and operational parameters of the PHE and the desorber performance was analysed in terms of mass flow rate and NH_3 mass fraction produced at the outlet. It was found that the number of plates, mass flow rate of the fluids and inlet temperature of the oil had the greatest influence on the desorber performance.

Based on the results obtained, the PHE dimensions were optimised to cater to a cooling load from 1 kW to 1.9 kW. Such a compact PHE desorber (with volume space of 60 cm^3) can be used on board a small and medium truck as seen from Figure 5.25. This PHE desorber is able to cover the entire cooling load across a wide refrigeration temperature range on a small truck being driven at 38 ^oC ambient temperature however is only able to cover a refrigeration temperature range from -5 ^oC to +5 ^oC on a medium truck being driven at 38 ^oC ambient temperature.

Bibliography

1. Garimella S, Delahanty J.C, and Nagavarapu A.K, *Vapour-liquid heat and/or mass exchange device*, U.S.P. Office, Editor. 2013, Georgia Tech Research Corporation: USA.
2. Drost K.M, Narayanan V, and Pence D.V, *Droplet desorption process and system*, United States Patent Office, Editor. 2008: USA.
3. Pence D, *The simplicity of fractal-like flow networks for effective heat and mass transport.* **Experimental Thermal and Fluid Science**, 2010. **34**(4): p. 474-486.
4. Wellsandt S and Vamling L, *Heat transfer and pressure drop in a plate-type evaporator.* **International Journal of Refrigeration**, 2003. **26**(2): p. 180-188.
5. Würfel R. and Ostrowski N, *Experimental investigations of heat transfer and pressure drop during the condensation process within plate heat exchangers of the herringbone-type.* **International Journal of Thermal Sciences**, 2004. **43**(1): p. 59-68.
6. Hsieh Y.Y and Lin T.F, *Saturated flow boiling heat transfer and pressure drop of refrigerant R-410A in a vertical plate heat exchanger.* **International Journal of Heat and Mass Transfer**, 2002. **45**(5): p. 1033-1044.
7. Yan Y.Y, Lio H.C, and Lin T.F, *Condensation heat transfer and pressure drop of refrigerant R-134a in a plate heat exchanger.* **International Journal of Heat and Mass Transfer**, 1999. **42**(6): p. 993-1006.
8. Táboas F, et al., *Flow boiling heat transfer of ammonia/water mixture in a plate heat exchanger.* **International Journal of Refrigeration**, 2010. **33**(4): p. 695-705.
9. Táboas F, Bourouis M, and Vallès M, *Boiling heat transfer and pressure drop of NH3/LiNO3 and NH3/(LiNO3 + H2O) in a plate heat exchanger.* **International Journal of Thermal Sciences**, 2016. **105**: p. 182-194.
10. Zacarías A, et al., *Boiling heat transfer and pressure drop of ammonia-lithium nitrate solution in a plate generator.* I**nternational Journal of Heat and Mass Transfer**, 2010. **53**(21–22): p. 4768-4779.
11. Balamurugan P and Mani A, *Heat and mass transfer studies on compact generator of R134a/DMF vapour absorption refrigeration system.* **International Journal of Refrigeration**, 2012. **35**(3): p. 506-517.
12. Marcos J.D, et al., *Experimental boiling heat transfer coefficients in the high temperature generator of a double effect absorption machine for the lithium bromide/water mixture.* **International Journal of Refrigeration**, 2009. **32**(4): p. 627-637.

13. García-Hernando N, et al., *On the pressure drop in Plate Heat Exchangers used as desorbers in absorption chillers.* **Energy Conversion and Management**, 2011. **52**(2): p. 1520-1525.
14. de Vega M, Almendros-Ibañez J.A, and Ruiz G, *Performance of a LiBr–water absorption chiller operating with plate heat exchangers.* **Energy Conversion and Management**, 2006. **47**(18–19): p. 3393-3407.
15. Venegas M, et al., *Subcooled and saturated boiling of ammonia–lithium nitrate solution in a plate-type generator for absorption machines.* **International Journal of Heat and Mass Transfer**, 2012. **55**(17–18): p. 4914-4922.
16. Kang Y.T, Chen W, and Christensen R.N, *A generalized component design model by combined heat and mass transfer analysis in NH3-H2O absorption heta pump systems*, in ***ASHRAE Transactions*** *103*. 1997.
17. http://www.paratherm.com/heat-transfer-fluids/. (last accessed June 2016)
18. Táboas F, et al., *Assessment of boiling heat transfer and pressure drop correlations of ammonia/water mixture in a plate heat exchanger.* **International Journal of Refrigeration**, 2012. **35**(3): p. 633-644.
19. Ayub Z.H, *Plate heat exchanger literature survey and new heat transfer and pressure drop correlations for refrigerant evaporators.* **Heat Transfer Engineering**, 2003. **24**(5): p. 3-16.
20. Palm B and Claesson J, *Plate Heat Exchangers: Calculation Methods for Singleand Two-Phase Flow.* **Heat Transfer Engineering**, 2006. **27**(4): p. 88-98.
21. Pátek J and Klomfar J, *Simple functions for fast calculations of selected thermodynamic properties of the ammonia-water system.* **International Journal of Refrigeration**, 1995. **18**(4): p. 228-234.

6

Coupling of SOFC and desorber *via* heat pipes

"*If we knew what it was we were doing it would not be called research, would it?*" **Albert Einstein**

This chapter presents a new way of coupling the SOFC with the desorber of the VARS unit. This coupling is via a bank of heat pipes. Different designs for coupling the SOFC, desorber and heat pipes are presented. A complete system level model for integrating the SOFC and the desorber via the heat pipe is also presented. Besides the system level model, a fundamental heat pipe model is also developed where the heat pipe is designed to meet a certain heat transport requirement. This enables in choosing the number of heat pipes required at the desorber. Different working fluids within the heat pipe are analysed and appropriate conclusions are drawn.

6.1 What is a heat pipe?

Heat pipes are isothermal devices that can transport large quantities of heat from one end to another (at well-defined temperature levels) by making use of the latent heat capacity of the working fluid present inside it.

The basic schematic of a heat pipe is shown in Figure 6.1

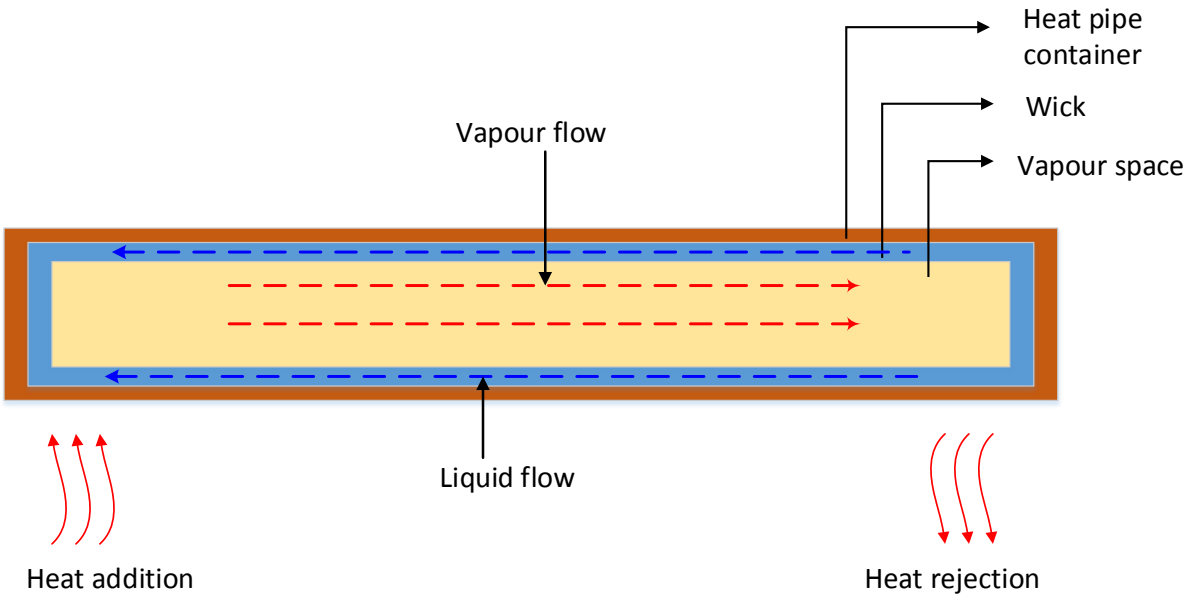

Figure 6.1: 2D schematic of a heat pipe

A heat pipe consists of three sections viz. evaporator section, adiabatic section and the condenser section. The heat pipe as such is made up of a metal container and a wick material placed inside the container. The wick is usually saturated with liquid. Heat addition occurs at the evaporator section which results in boiling of the liquid and generation of vapour. The vapour then travels through the vapour space to the other end of the heat pipe

where it loses heat (at the condenser section) and turns back to liquid. The liquid is then returned back to the evaporator via the porous wick structure.

Some of the advantages of heat pipes are [1]:

a) Very high thermal conduction
b) Fast response to thermal loading
c) Quiet operation
d) Reliability
e) Absence of moving parts
f) Well defined temperature of delivery

6.2 Literature on use of heat pipes with fuel cells

An overview on the use of heat pipes with fuel cells is presented in this section. As such the use of heat pipe technology in the field of fuel cells is very rare. Very few research groups have looked into this concept and even fewer have conducted experiments.

Dillig et al [2, 3] carried out experimental studies using planar sodium heat pipes for thermal management of an SOFC/SOEC stack thereby reducing the size of the air blower needed in the BoP (Balance of Plant) and also achieving near uniform temperature distribution in the stack. In a European project titled ‘Biocellus’ [4], heat pipes were used for thermal management of a planar SOFC stack. The use of heat pipes in a planar SOFC stack resulted in translating the horizontal temperature gradients to vertical temperature gradients, thereby making the stack temperature more uniform. Figure 6.2 shows the way heat pipes were integrated into the stack for this project.

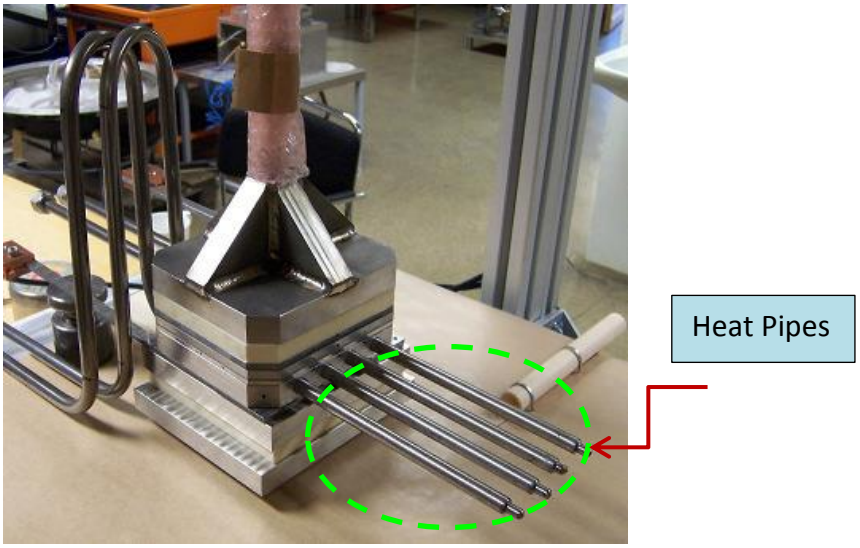

Figure 6.2: Integration of heat pipes into SOFC stack – Biocellus project

Niemasz et al [5] employed heat pipes with water as the working fluid for thermal management of a HT-PEFC (High Temperature Polymer Electrolyte Fuel Cell) stack in order to maintain a homogenous and uniform heat distribution in the stack. They performed experimental studies by embedding the heat pipe into the bipolar plate of the fuel cell. The use of heat pipes in the HT-PEFC stack design enabled assembly of a stack with fewer components and elimination of the oil cooling loop.

Firat et al [6] carried out CFD modelling studies on thermal management of a HT PEFC stack by embedding heat pipes into the bipolar plate of the stack. They modelled the heat pipe using the thermal resistance model and performed the modelling and simulation using COMSOL multi-physics. The stack modelled consisted of twenty four cells, each with an active area of 300 cm^2. They performed two studies, one with four heat pipes per cell and another with six heat pipes per cell. The study with six heat pipes per cell produced a more uniform temperature distribution throughout the stack.

Supra et al [7] conducted experiments with heat pipes incorporated into a HT PEFC stack for effective thermal management. Their main hypothesis was if oil is used as a coolant directly

in the stack then there is a high probability of oil leaking into the MEA and degrading the cell and eventually the whole stack. Hence the evaporator end of the heat pipe was embedded in a separate cooling cell which was placed at regular intervals between individual fuel cells. The condenser end of the heat pipe was exposed to an oil bath. So the heat transfer was from the interior of the stack to the evaporator, along the heat pipe and then out of the condenser and into the oil. This study is slightly different from that of Niemasz et al [5] in that the condenser end of the heat pipe was exposed to an oil bath rather than being exposed to air. Hence heat is taken away at a potentially higher rate.

Fryda et al [8] carried out an exergy analysis of an SOFC-biomass gasifier system. They used high temperature sodium heat pipes for coupling the SOFC stack with an allothermal biomass gasification system. By employing heat pipes two tasks *viz*. supply of heat to the gasification system and cooling of the SOFC stack were accomplished in one step. The transfer of heat from the SOFC stack to the gasification unit resulted in a significantly reduced amount of air needed to cool the stack and thereby a reduced size for the blower. They concluded that the system as a whole had a very high electrical efficiency but low thermal efficiency primarily because the high quality heat was consumed to do three processes *viz*. drive the gasification unit, pre-heat the SOFC air and generate steam required for SOFC operation. The resulting flue gases were thus low in temperature which could be used only to produce hot water at around 350 K.

Vinicio Oro and Bazzo [9] carried out modelling studies to design a stainless steel flat heat pipe for thermal management of PEFC's in order to maintain the temperature of PEFC's between 70 and 90 ^{o}C. The heat pipe designed was able to dissipate 12 W with a heat flux of 1.8 W cm^{-2} at the evaporator section. Their proposed model could replace the conventional water cooled thermal management system of PEFC's.

Santhanam et al [10] carried out thermodynamic modelling of a combined system which comprised of a heat pipe integrated gasifier, two SOFC stacks and a gas turbine. In their study, heat pipes were proposed to be placed in between the SOFC stacks rather than integrating them within the SOFC stacks. This was done to reduce the complexity of stack design. The heat from the SOFC stack was directly transferred to the gasifier and hence high temperature heat pipes with sodium as the working fluid were used. A total of 33 kW could be removed from the SOFC stack and the same was transferred to the gasifier at a temperature of 800 ^{o}C. In their paper, the heat pipe was not modelled in detail but rather taken as a heat transport medium with a particular parameter set.

Tetuko et al [11] developed a mathematical model to thermally couple a PEFC and a metal hydride storage tank using heat pipes. Metal hydrides are an alternate way to store hydrogen and require external heat to desorb hydrogen. The authors found that for their system, the PEFC was generating almost five times more heat than that required by the metal hydride canisters. Hence, in addition to the heat pipe integrated in the fuel cell stack, an external cooling mechanism was needed to remove all the heat generated from the fuel cell.

6.3 Different designs for coupling of SOFC with desorber via heat pipes

The desorber and the SOFC can be coupled with one another via heat pipes in one of the following ways:

a) Design 1: Direct plugging at both ends:

In this design, shown in Figure 6.3, the heat pipe(s) is directly embedded into the SOFC stack at one end and into the desorber at the other end. The pros and cons of this design are summarized in the table below

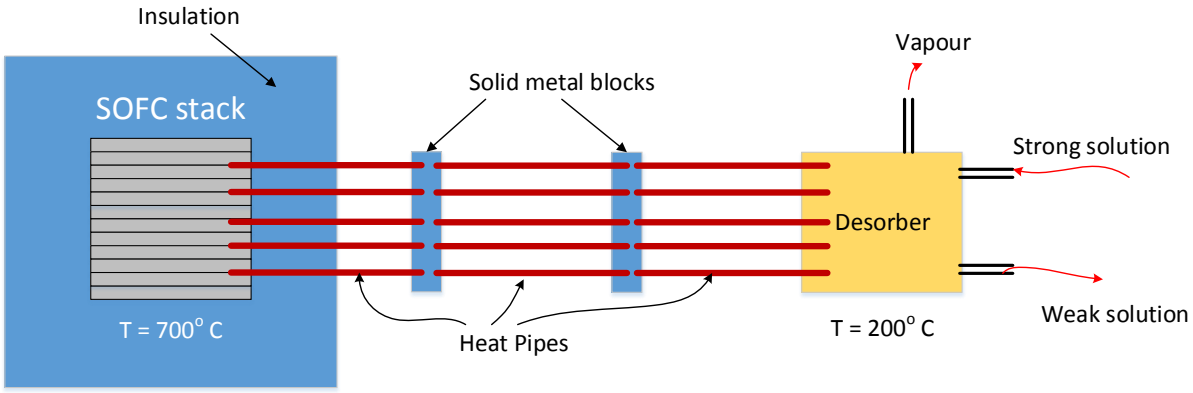

Figure 6.3: Design 1 – Direct plugging of heat pipes at both SOFC and desorber ends

Pros	Cons
Easy concept	Mechanical integrity of the whole structure
	Temperature drop along the heat pipe is small. Hence the temperature at the desorber end might be too high.
	Issues with plugging in heat pipes into SOFC stack
	Issues with plugging heat pipes into desorber
	Warrants a new desorber design

As the temperature at the SOFC end is around 700 ^{o}C and the temperature at the desorber end is around 200 ^{o}C, there needs to be some metal blocks placed between the SOFC & desorber in order to achieve temperature compatibility at both ends. This is because the heat pipe is an isothermal device. Design of the individual heat pipes between different blocks needs to be carefully made in order to transfer heat efficiently. Through this design, not only is thermal energy transferred to the desorber but also the SOFC stack temperature is maintained at the desired value which is critical for stack operation.

Direct plugging of the heat pipe into the SOFC stack can result in hydrogen permeation into the heat pipe container and thereby affect its performance. Hence this option needs careful evaluation.

b) Design 2: Direct plugging at one end

In this design, the heat pipe is embedded only at the desorber end and the other end is either

- Placed adjacent to the SOFC stack within the insulation – Option 1

  (or)

- Exposed to hot cathode exhaust – Option 2

Both options give flexibility as far as heat transfer to the heat pipe(s) is concerned. In the former, the heat pipe can be moved around in the space between the stack and insulation, to vary the heat transfer rate while in the latter, the cathode exhaust flow rate and temperature can be varied. The pros & cons of this design are summarized in the table below

Pros	Cons
Easy concept	Mechanical integrity of the whole structure
Laboratory scale prototype construction possible	Issues with plugging in heat pipes into desorber
Heat input at the evaporator section can be controlled by varying the temperature & mass flow rate of exhaust flow	New desorber design required
Option 2 provides flexibility in terms of packaging because the hot cathode exhaust can be channeled easily to the evaporator section.	In option 1, the desorber has to always be in close proximity with the SOFC stack. This might place some constraints in packaging.

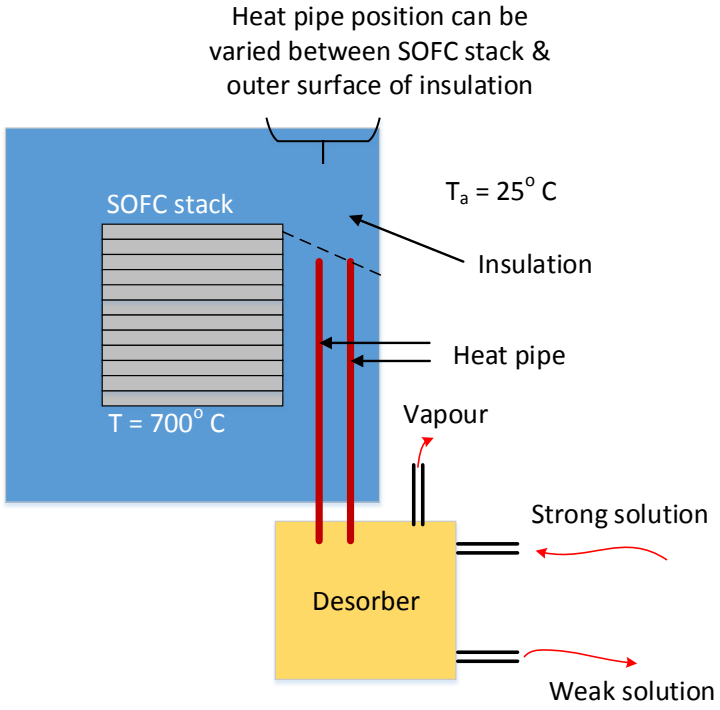

Figure 6.4: Design 2 – Direct plugging only at desorber end, Option 1

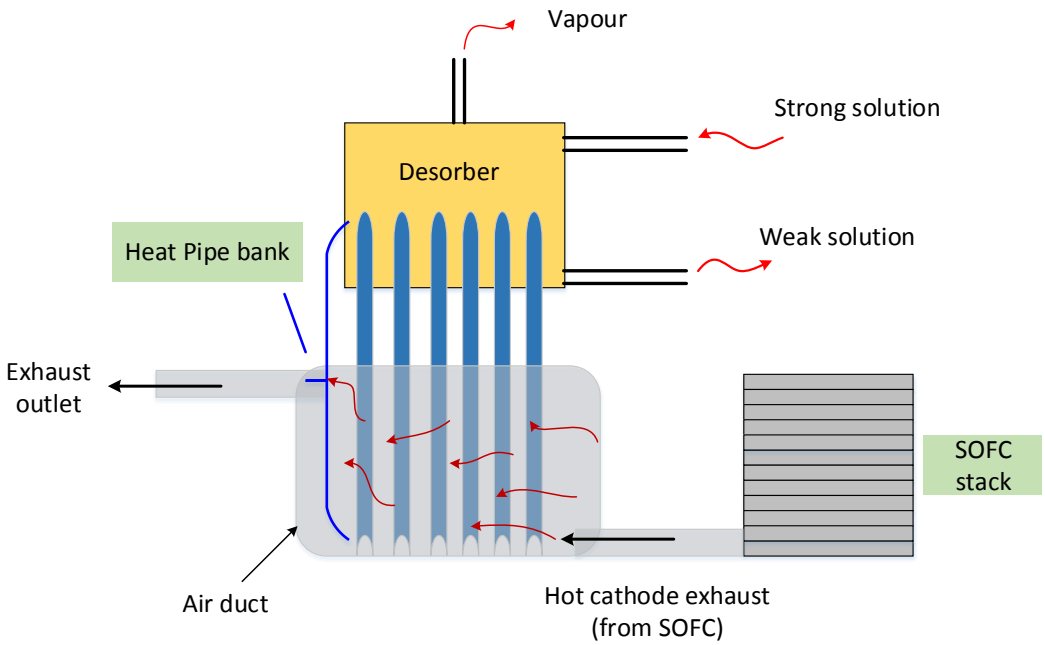

Figure 6.5: Design 2 – Direct plugging only at desorber end, Option 2

c) Design 3: Use as heat exchanger

In this design there is no plugging of the heat pipe either at the desorber end or the SOFC end instead it is used as a heat exchanger in which thermal oil is heated by the hot cathode exhaust to the required temperature. The hot thermal oil is then used as a coupling fluid in a plate heat exchanger desorber. The schematic for the same is shown in Figure 6.6.

Pros	Cons
Simple heat exchanger design	High temperature heat pipes need to be used
Advantage over the tube in tube heat exchanger in terms of heat transfer capability	Thermal oil (selected for this purpose) degrades at 644 K; hence care should be taken to avoid temperatures exceeding the degradation temperature of thermal oil.
Desorber is a plate heat exchanger which in turn is a standard component available in the market.	Coupling fluid circuitry and other associated components are still required

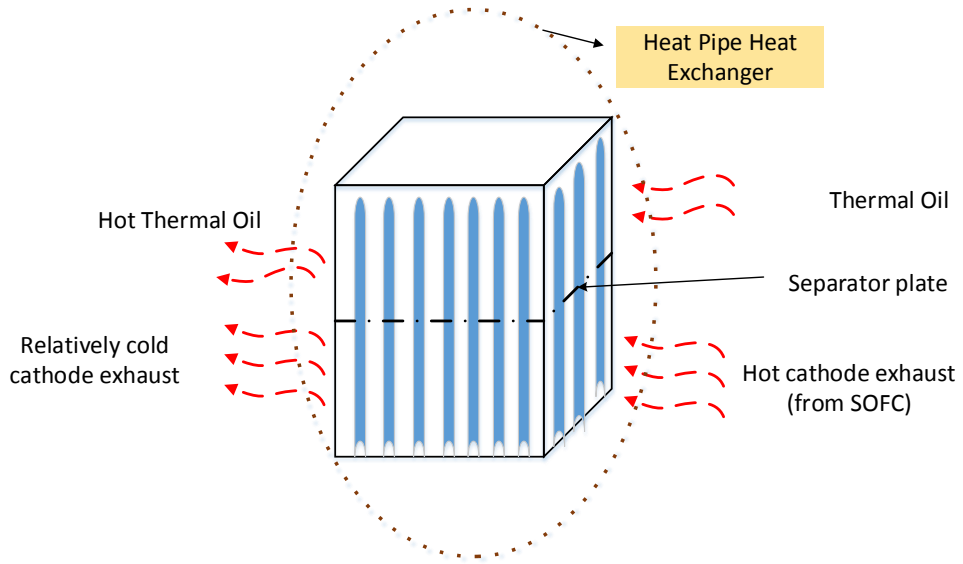

Figure 6.6: Design 3 – Use of heat pipes in a heat exchanger configuration to heat thermal oil

6.4 Modelling

Modelling of the whole heat pipe integrated desorber is divided into three parts

i) **Transfer of heat from SOFC cathode exhaust to evaporator**

The heat flux impinging at the evaporator section of the heat pipe is from the hot cathode exhaust stream. Modelling of this part will provide data on how much heat is actually getting into the heat pipe.

ii) **Modelling & design of the heat pipe for heat transport capability**

The heat transferred at the evaporator section needs to be transported via the heat pipe and hence the heat pipe has to be designed to meet the required heat transport capability.

iii) **Transfer of heat at the condenser end to NH_3-H_2O solution**

The heat transported by the heat pipe will be dissipated from the condenser section and will cause boiling of the refrigerant-absorbent solution. Modelling this part is more complex because it involves many intricate processes and phenomena.

Option #2 of design 2 is chosen for coupling the SOFC stack with the desorber via heat pipes. This is because the heat pipe is a near isothermal device and direct plugging of one end of the heat pipe into the SOFC stack and the other end into the desorber will technically not be feasible due to the simple reason that both these devices operate at different temperature levels.

For the current application, the first step involved is the design of the heat pipe itself in order to meet a particular (range of) heat transport capacity. The heat pipe design itself is an iterative process. Hence some initial design parameters need to be fixed which are given in Table 6.1. The goal of the design process is to use a minimum number of heat pipes in the

desorber, in order to keep the desorber design as compact as possible. Therefore the heat transport capability per heat pipe has to be maximized.

Table 6.1: Initial design specifications of a single heat pipe

Amount of heat to be transferred	300 W
Vapour temperature	200^{o}C
Diameter of vapour space	20 mm
Length of heat pipe	20 cm
Length of Evaporator section	8 cm
Length of Condenser section	8 cm
Wick type	Wrapped screen wick
Mesh size	400 inch^{-1}
Wire diameter of mesh	0.02 mm
Nucleation site radius	0.254 μm

(The wick used is a wire screen wick and the mesh size refers to the size of the screen)

NOTE: *The wick used in the heat pipe can be of different types [1] and wick design and fluid flow characteristics within it is a subject that needs to be dealt separately. In this study a simple* ***single layer wrapped screen wick*** *is used for heat pipe design.*

The picture of a wrapped screen wick is shown in Figure 6.7

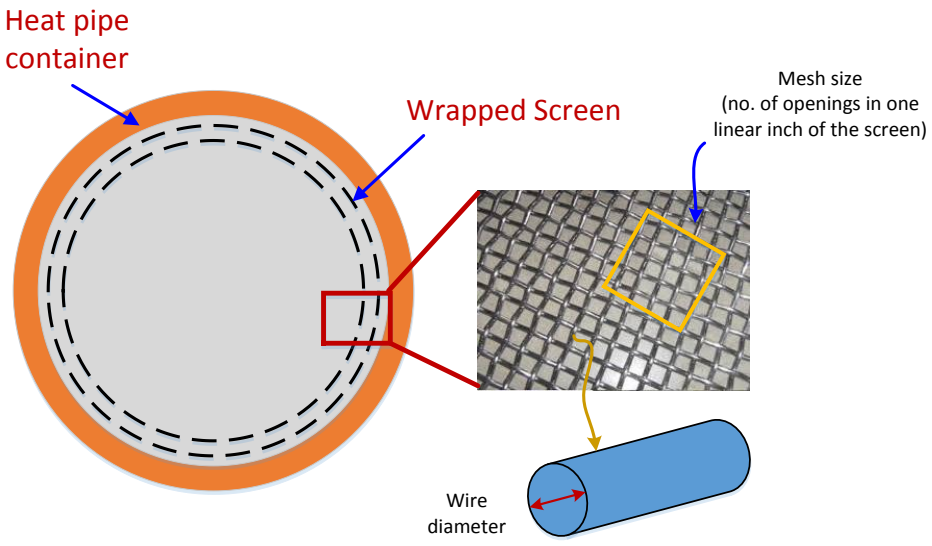

Figure 6.7: Schematic of wrapped screen wick in a heat pipe

6.4.1 Fundamental model of heat pipe

The steps involved in developing a fundamental model of the heat pipe are as follows:

Determination of mass flow rate of working fluid

The mass flow rate of the working fluid which will be used inside the heat pipe needs to be determined first and can be calculated from Eq. 6.1

$$\dot{m} = \frac{Q_{max}}{h_{fg}} \qquad \textbf{Eq. 6.1}$$

Where,

Q_{max} Maximum heat transport capability of the heat pipe (W)

h_{fg} Latent heat of vapourisation of the fluid at the particular vapour temperature at which the heat pipe needs to operate (J kg^{-1})

Calculation of different heat transport limits

The next step in modelling the heat pipe is to identify the heat transport capability of the heat pipe. There are four main limitations to heat transport in a heat pipe *viz*.:

- Capillary limitation
- Sonic limitation
- Entrainment limitation
- Boiling limitation

The sonic limit is dependent on temperature alone but the other parameters depend on the geometry of the heat pipe as well.

Capillary limitation occurs when there is insufficient capillary pressure in the wick to pump the liquid back to the evaporator end. For the heat pipe to function properly, the net capillary pressure should be greater than the sum of all pressure drops occurring in the liquid and vapour flow paths. The capillary pressure difference is given by Eq. 6.2

$$\Delta P_c = \Delta P_v + \Delta P_l + \Delta P_{norm} + \Delta P_{axial} \quad \textbf{Eq. 6.2}$$

Where,

ΔP_c	Capillary pressure difference between evaporator and condenser (Pa)
ΔP_v	Vapour pressure drop (Pa)
ΔP_l	Liquid pressure drop (Pa)
ΔP_{norm}	Normal hydrostatic pressure drop (Pa)
ΔP_{axial}	Axial hydrostatic pressure drop (Pa)

Each of the above terms is given by Eq. 6.3 to Eq. 6.7

$$\Delta P_c = \frac{2\sigma \cos\theta}{r_{ce}} \quad \textbf{Eq. 6.3}$$

$$\Delta P_v = \frac{C\,(f_v\,Re_v)\,\mu_v}{2\,r_v^2\,A_v\,\rho_v\,h_{fg}}\,.L_{eff}\,Q \quad \textbf{Eq. 6.4}$$

$$\Delta P_l = \frac{\mu_l}{K A_w\,h_{fg}\,\rho_l}.L_{eff}\,Q \quad \textbf{Eq. 6.5}$$

$$\Delta P_{norm} = \rho_l g d_v\,.\cos\psi \quad \textbf{Eq. 6.6}$$

$$\Delta P_{axial} = \rho_l g L\,.\sin\psi \quad \textbf{Eq. 6.7}$$

Where,

σ	Surface tension of the liquid (N m^{-1})
θ	Contact angle between the liquid interface and solid interface (degrees)
r_{ce}	Effective capillary radius (m) {If screen wick is used}
μ_v	Dynamic viscosity of vapour (Ns m^{-2})
L_{eff}	Effective length of the heat pipe (m), this is given by $\left(\frac{L_e + L_c}{2} + L_a\right)$, L_e is the length of the evaporator section, L_c is the length of the condenser section and L_a is the length of the adiabatic section
Q	Capillary heat transport limit (W)
r_v	Radius of vapour space (m)
A_v	Cross sectional area of the vapour space (m^2)
ρ_v	Density of vapour (kg m^{-3})
h_{fg}	Latent heat of vapourisation (J kg^{-1})
μ_l	Dynamic viscosity of liquid (Ns m^{-2})
K	Permeability of the wick (m^2)
A_w	Cross sectional area of the wick (m^2)
ρ_l	Density of the liquid (kg m^{-3})
g	Acceleration due to gravity (m s^{-2})
d_v	Diameter of the vapour space (m)
ψ	Angle of inclination of the heat pipe wrt horizontal (degrees)
L	Total length of the heat pipe (m)

The vapour pressure drop is negligible when compared to the liquid pressure drop. Hence the above equations can be written as

$$\frac{2\sigma\, cos\theta}{r_{ce}} = \frac{\mu_l}{K A_w h_{fg} \rho_l} . L_{eff}\, Q + \rho_l g d_v . cos\psi + \rho_l g L . sin\, \psi \qquad \textbf{Eq. 6.8}$$

Taking Q to be the maximum heat transport capacity, which in this case is the capillary limitation and assuming that the working fluid completely wets the wick surface, the $K.A_w$ factor (product of wick permeability and wick cross section area) for the heat pipe can be calculated and is given in Eq. 6.9.

$$K.A_w = \frac{\left(\dot{m} * \mu_l * L_{eff}\right)}{\left(\rho_l * \left(\left(\frac{2\sigma}{r_{ce}}\right) - \rho_l g L \sin\psi - \rho_l g d_v \cos\psi\right)\right)} \quad \textbf{Eq. 6.9}$$

The *sonic limitation* occurs in a heat pipe when the velocity of vapour exceeds the sonic limit and as a result there is choked flow of vapour inside the heat pipe. The sonic heat transport limitation is given by Eq. 6.10

$$Q_{sonic} = 0.474 * h_{fg} A_v \sqrt{\rho_v P_v} \quad \textbf{Eq. 6.10}$$

Where, P_v is the vapour pressure (N m^{-2}). The remaining terms have the usual meaning as mentioned earlier.

The *entrainment limitation* occurs due to entrainment of liquid drops at the evaporator end with the vapour. This leads to insufficient mass of liquid at the evaporator which in turn affects the heat transport capability of the heat pipe. The entrainment limit is given by

$$Q_{ent} = A_v h_{fg} * \sqrt{\frac{\sigma \rho_v}{2 r_{hw}}} \quad \textbf{Eq. 6.11}$$

Where r_{hw} is the hydraulic radius (m) and is given by Eq. 6.12

$$r_{hw} = \frac{2A_w}{P} \quad \textbf{Eq. 6.12}$$

The *boiling limit* occurs in the heat pipe due to excessive heat flux at the evaporator which causes boiling of the working fluid. The bubbles generated as a result get trapped in the wick and block the flow of liquid back to the evaporator. The boiling limit is given by Eq. 6.13

$$Q_{boil} = \frac{4\,\pi\, L_e\, \kappa_{eff}\, T_v\, \sigma}{h_{fg}\, \rho_v \ln\left(\frac{r_i}{r_v}\right)} * \left(\frac{1}{r_n} - \frac{1}{r_{ce}}\right) \quad \textbf{Eq. 6.13}$$

Where,

κ_{eff}	Effective thermal conductivity of the wrapped screen wick (W m^{-1} K^{-1})
T_v	Vapour temperature (K)
r_i	Internal radius of heat pipe (m)
r_n	Nucleation site radius (m)

In order to avoid very high temperature and pressure drops in the heat pipe, the actual heat transport rate should not exceed 30-50 % of the sonic limit. Calculation of the heat transport limitations is critical in determining the operating temperature and heat transport rate of the heat pipe.

Calculation of wick porosity, wick effective thermal conductivity and wick permeability

The porosity of the screen wick is given by Eq. 6.14

$$\varepsilon = 1 - \frac{(1.05\,\pi\,N\,d_w)}{4} \qquad \textbf{Eq. 6.14}$$

The effective thermal conductivity κ and permeability K of the screen wick is given by Eq. 6.15 and Eq. 6.16

$$\kappa = \kappa_l \frac{\left((\kappa_l + \kappa_w) - (1-\varepsilon)(\kappa_l - \kappa_w)\right)}{(\kappa_l + \kappa_w) + (1-\varepsilon)(\kappa_l - \kappa_w)} \qquad \textbf{Eq. 6.15}$$

$$K = \frac{(d_w^2\,\varepsilon^3)}{122(1-\varepsilon)^2} \qquad \textbf{Eq. 6.16}$$

The above mentioned properties completely define the characteristics of the screen wick.

The modelling procedure followed to formulate the fundamental model of the heat pipe is as follows:

i) One of the heat transport limits is fixed as the maximum heat transport capability of the heat pipe. The capillary heat transport limit is usually the limiting factor amongst all four heat transport limits and is thus fixed as the heat transport capability of the heat pipe.

ii) The initial design specifications for the heat pipe, as mentioned in Table 6.1, are fixed and the various heat transport limits are calculated.

iii) The actual heat transport capability of the heat pipe is determined by the lowest value among all four heat transport limits.

$$Q_{heat\ pipe} = minimum\ (Q_{capillary}, Q_{sonic}, Q_{entrainment}, Q_{boil})$$

iv) A sensitivity analysis is then carried out by varying each of the design parameters while keeping the rest of the parameters constant, to assess if the heat transport capability of the heat pipe can be improved.

v) The optimal design parameters are achieved when the actual heat transport capability is as close to the initial specified heat transport limit of 300 W.

6.4.1.1 Results for heat pipe design

The heat pipe working fluid determines the operating temperature range of the heat pipe. Since the maximum operating temperature required at the desorber is 200 ^{o}C, the possible working fluids that can be used in the heat pipe are listed in Table 6.2.

One way to choose a suitable working fluid is to assess its heat transport capability over a wide temperature range. The heat transport capability is calculated using the liquid heat transport parameter (also known as figure of merit) whose definition is given below.

Table 6.2: List of suitable working fluids in the temperature range of 150-200 ^{o}C

Working fluid	Useful temperature range (^{o}C)	Boiling point at atmospheric pressure (^{o}C)
Water	30 – 200	100
Toluene	50 – 200	110
Flutec PP9	0 – 225	160
Heptane	0 – 150	98
Thermex	150 - 350	257
Flutec PP2	10 - 160	76

$$N_l = \frac{\left(\rho_l \, \sigma \, h_{fg}\right)}{\mu_l} \qquad \textbf{Eq. 6.17}$$

Where,

ρ_l Temperature dependent density of the working fluid (kg m^{-3})

σ Temperature dependent surface tension of the working fluid (N m^{-1})

h_{fg} Latent heat of vapourisation of the working fluid (J kg^{-1})

μ_l Temperature dependent dynamic viscosity of the working fluid (N s m^{-2})

The figure of merit plotted as a function of temperature for the fluids mentioned above is shown in Figure 6.8.

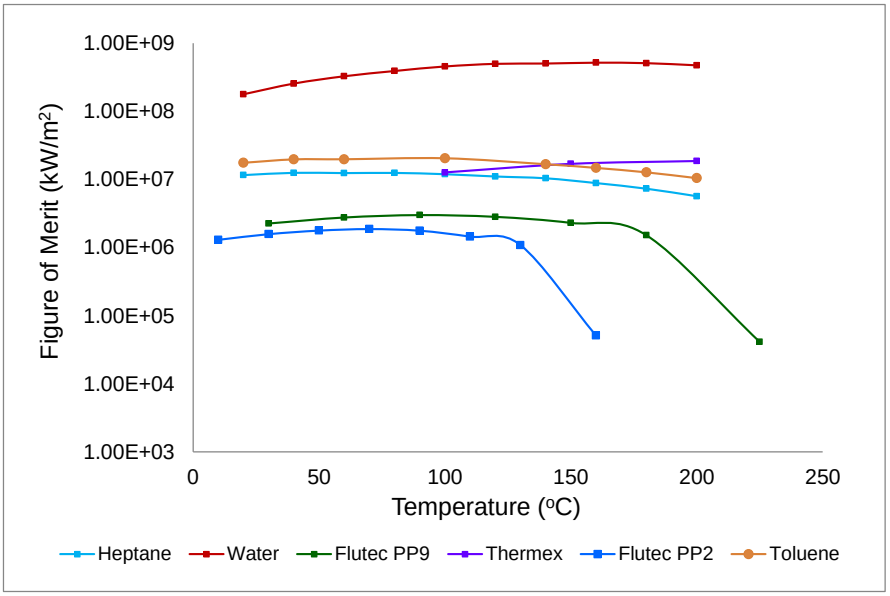

Figure 6.8: Figure of merit for different working fluids

Among the working fluids, water is superior to all other working fluids by an order of magnitude. Besides water, Thermex and Toluene are the next best candidates for the working fluid for the heat pipe. Hence in the temperature range desired, water has got the best combination of surface tension, latent heat and vapour density. The general rule of thumb in heat pipe design is that the fluid with a higher merit number is more desirable.

The working fluid to be used is determined from two criteria:

a) Figure of merit

b) KA_w factor

Based on the figure of merit values, water had the highest heat transport capability and since water can be used in the useful temperature range between 30-200 ^oC, it is selected as the ideal working fluid for this application.

The KA_w factor is another criterion which is used for selecting the working fluid. Among all the working fluids, only water and Thermex have positive values when the heat pipe is positioned at an angle of 90^o wrt horizontal. This is shown in Figure 6.9.

The KA_w factor for water as the working fluid at a vapour temperature of 200 ^oC for two different tilt angles of the heat pipe is shown in Figure 6.9. When the heat pipe is at an inclination angle of 90^o, the KA_w factor remains negative till a screen mesh size of 350 $inch^{-1}$ (Note: the heat pipe is designed with a wrapped screen wick) hence the minimum screen mesh size which can be used is 375 $inch^{-1}$. However when the heat pipe is tilted to an angle of 10^o wrt horizontal it is possible to use any mesh size. This is because as the tilt angle reduces, the axial pressure drop decreases thereby enabling the use of a mesh screen in a wider range of sizes. Also with reduction in axial pressure drop, the capillary pressure increases thus transporting the liquid back to the evaporator section.

Similarly when Thermex (at a vapour temperature of 200 ^oC) is used as the working fluid in the heat pipe kept at an inclination angle of 90^o, the KA_w factor remains negative till a mesh size of 550 $inch^{-1}$. Hence the minimum mesh size needed is about 575 $inch^{-1}$. However when the heat pipe is tilted to an angle of 10^o then it is possible to use a mesh size starting from 150 $inch^{-1}$. Thermex is to be selected only as the next best candidate.

The variation of KA_w factors with the mesh size for other working fluids is shown in Figure 6.10 and Figure 6.11. Both Heptane and Toluene cannot be used when the heat pipe is positioned at an angle of 90^o because the KA_w is negative but if the heat pipe is tilted to an angle of 10^o wrt the horizontal then they can be used. For heptane, the KA_w factor is positive only after a mesh size of 275 $inch^{-1}$ and for toluene the KA_w is positive after a mesh size of 225 $inch^{-1}$.

Flutec PP2 and Flutec PP9 are definitely ruled out as working fluids because the KA_w factor is negative irrespective of the tilt angle of the heat pipe. This is because the combined effect of both axial and hydrostatic pressure drop is greater than the other pressure drops for these two fluids thereby making KA_w factor negative. Also the figure of merit value for both these fluids is an order of magnitude below other fluids.

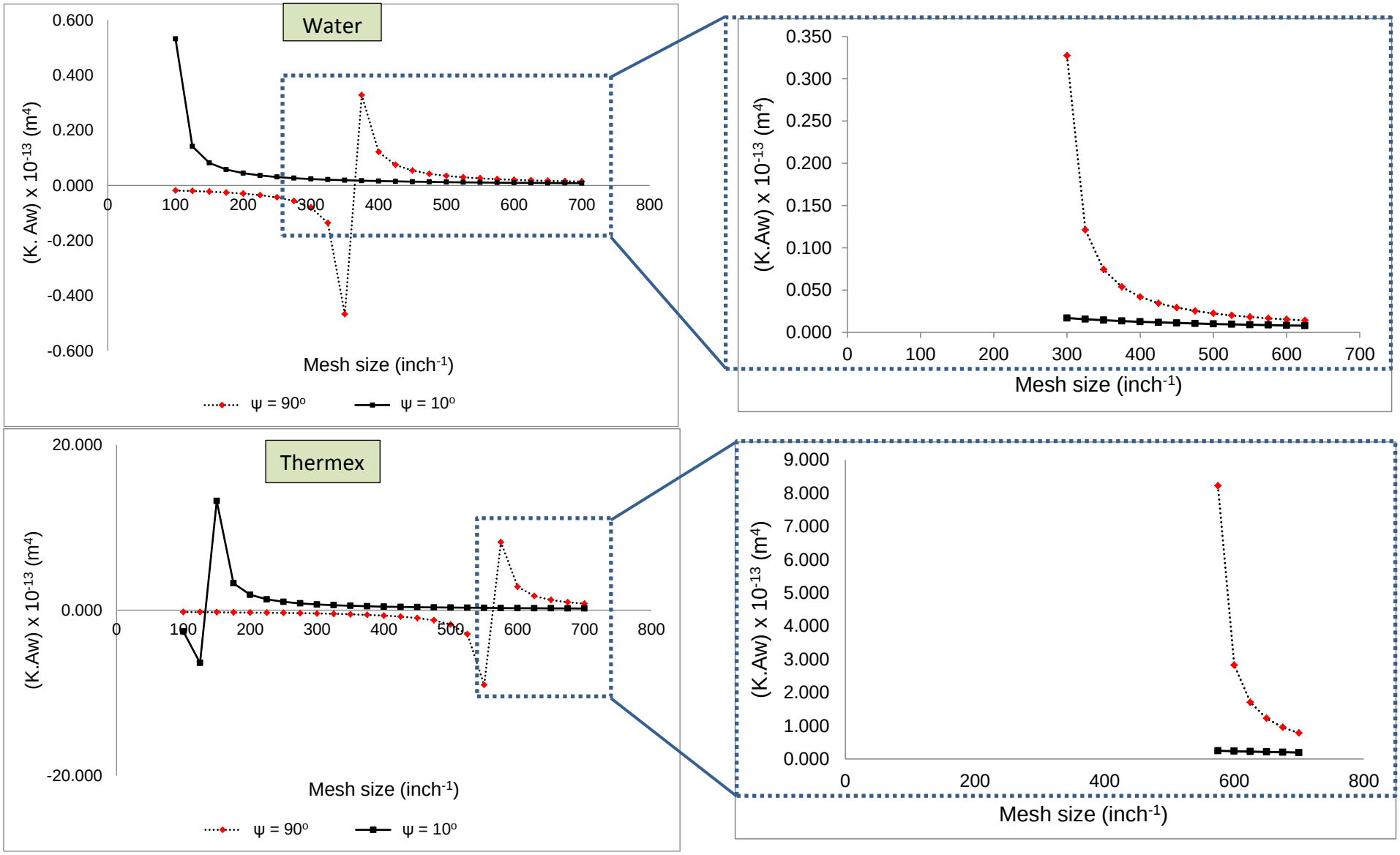

Figure 6.9: Variation of KA_w factor with screen mesh size for Water and Thermex

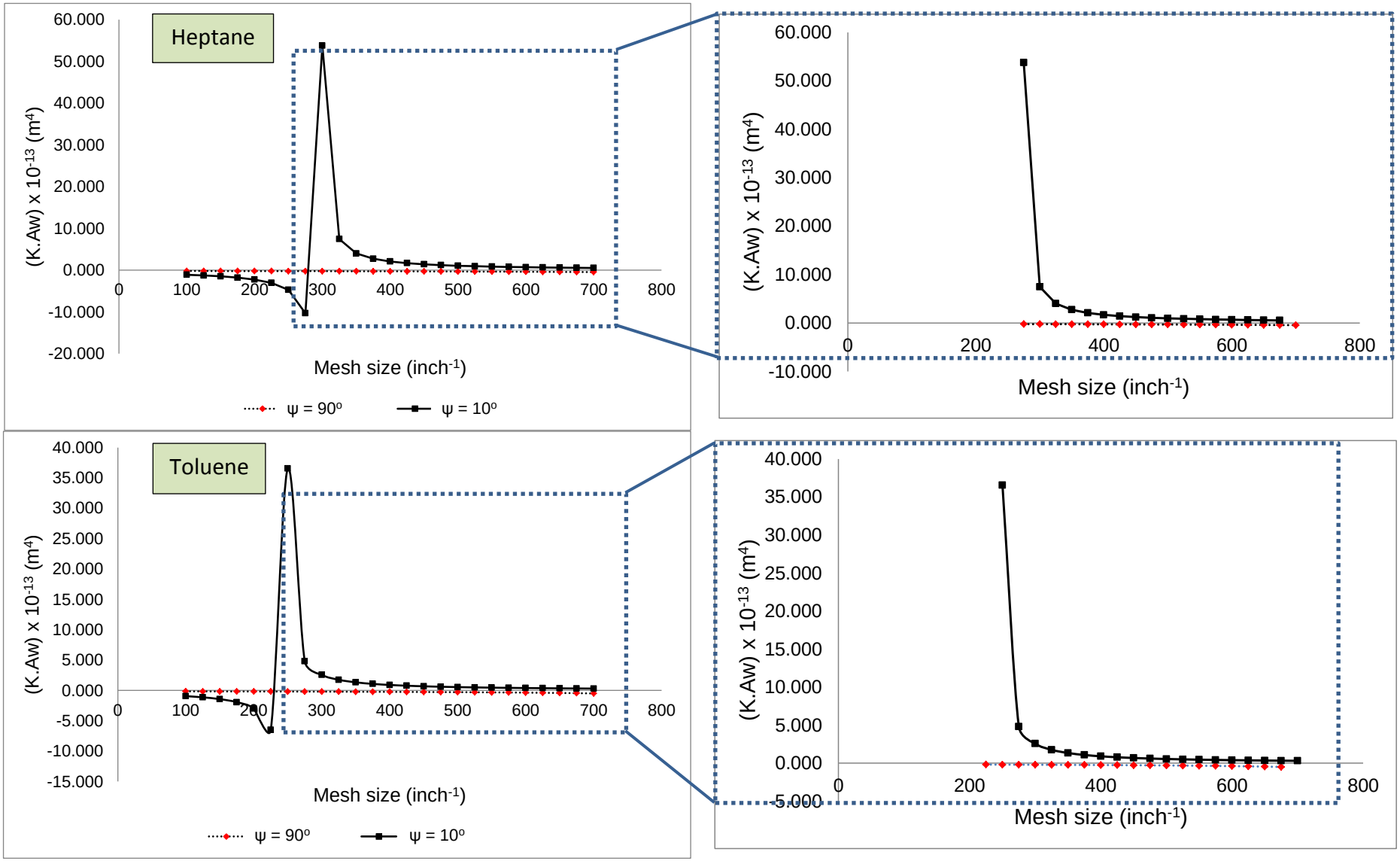

Figure 6.10: Variation of KA_w factor with screen mesh size for Heptane and Toluene

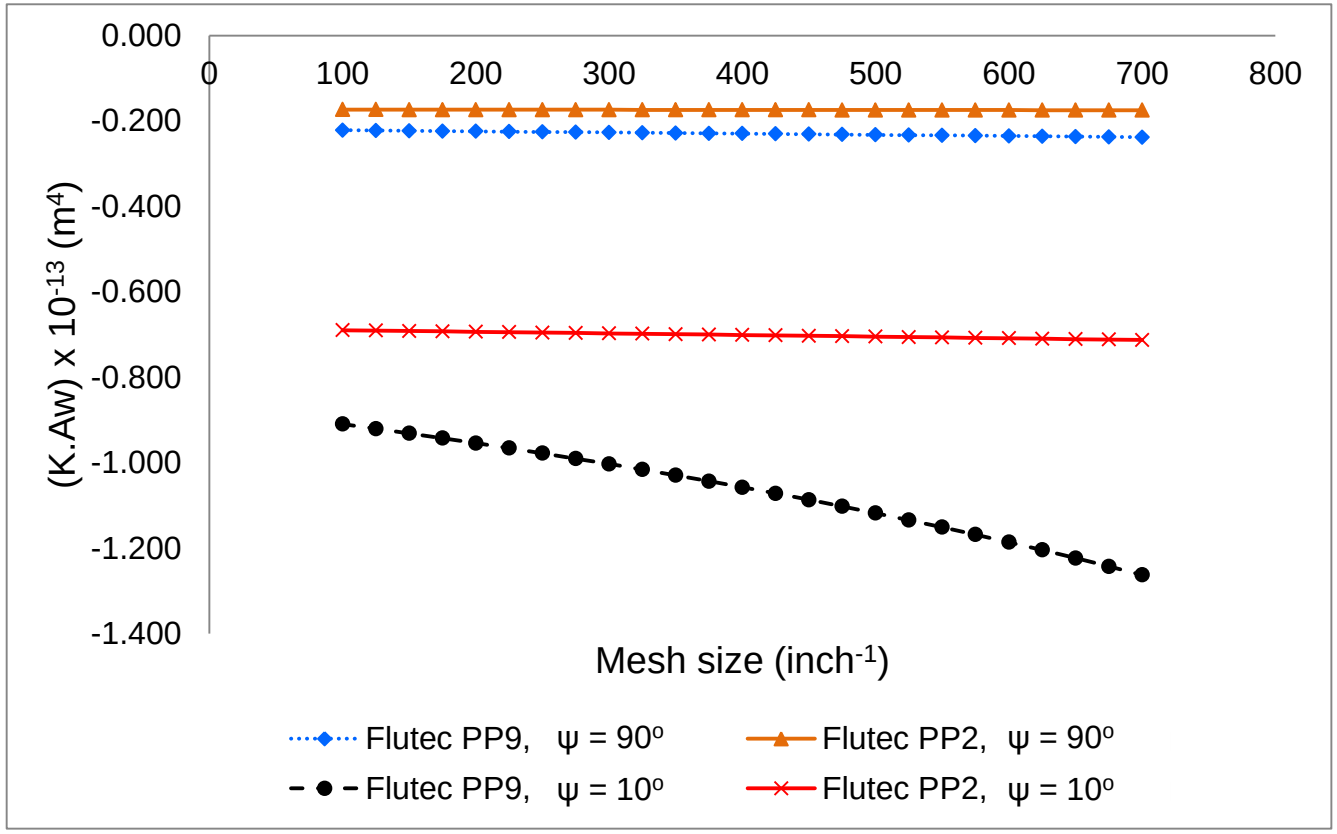

Figure 6.11: Variation of KA_w factor with screen mesh size for Flutec PP9 & Flutec PP2

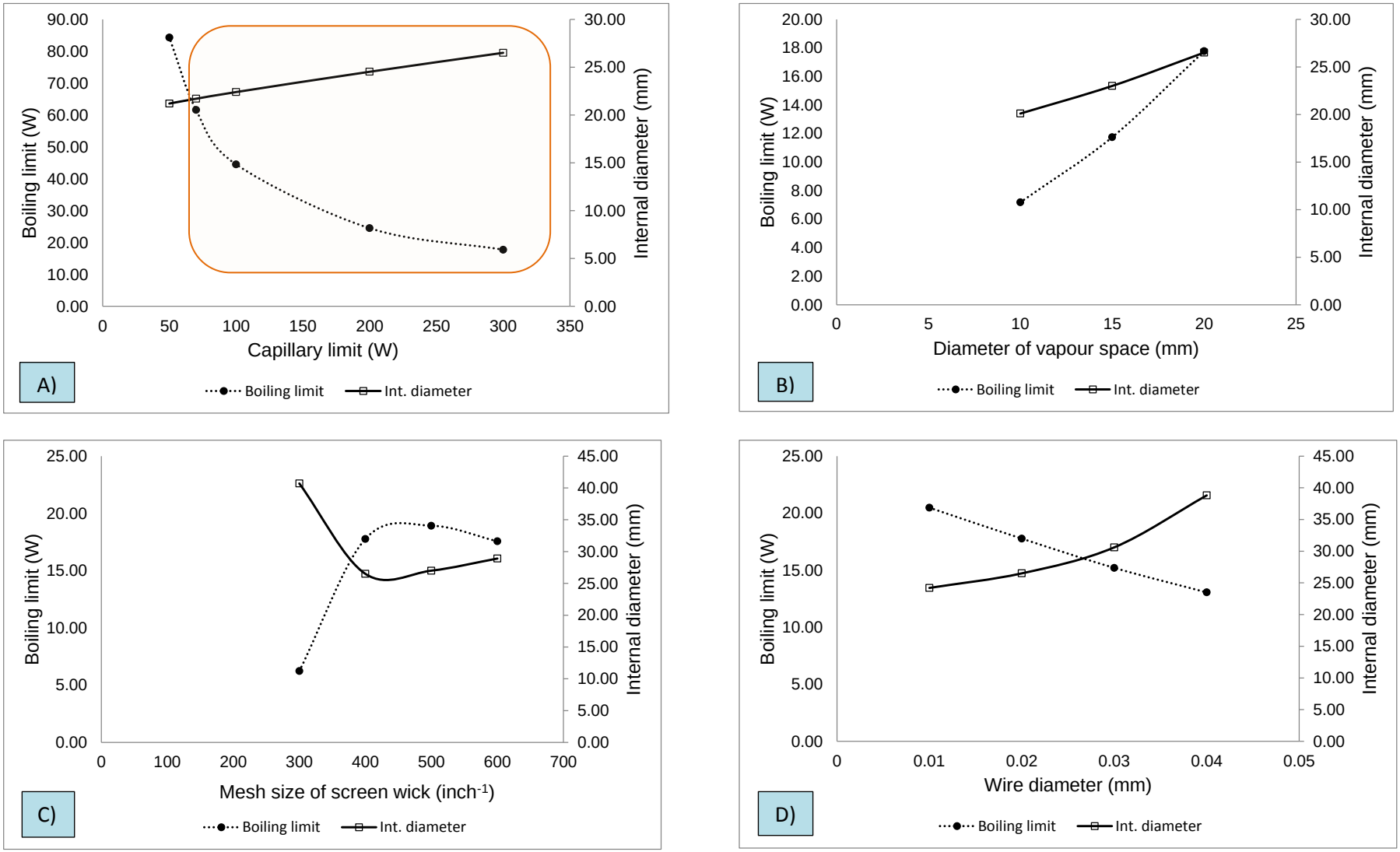

Figure 6.12: Sensitivity analysis with different heat pipe parameters – Part 1
(With water as the working fluid)

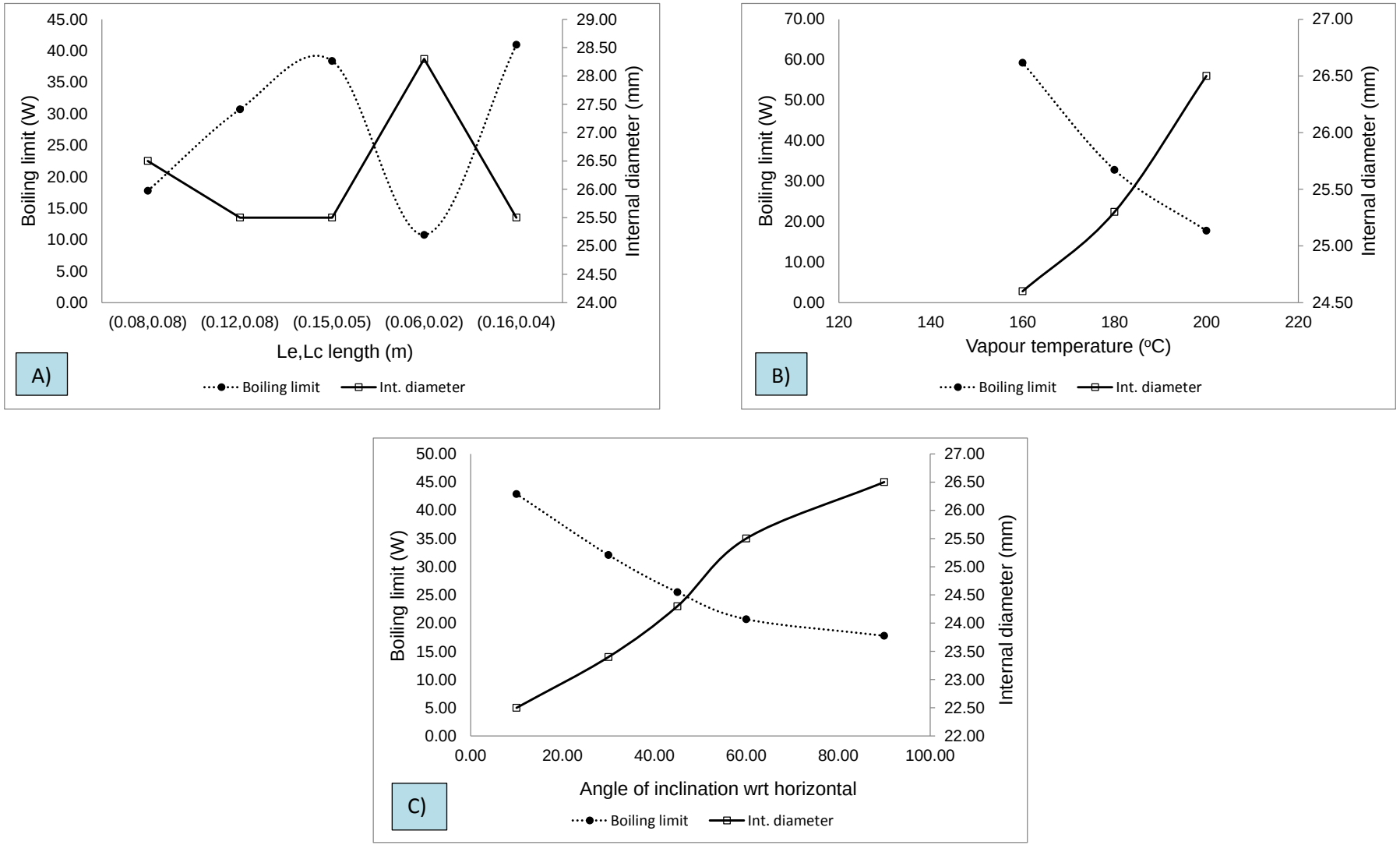

Figure 6.13: Sensitivity analysis with different heat pipe parameters – Part 2
(With water as the working fluid)

Sensitivity analysis

A complete sensitivity analysis with water as the working fluid was carried out to assess which parameters affected the heat transport (within the heat pipe) the most and the least. When varying each parameter, the other parameters were kept constant at values mentioned in Table 6.1. Sonic and entrainment limits do not pose any limitation due to very high values and the main heat transport limitation is either from the capillary limit or from the boiling limit. The following parameters were varied:

- Capillary heat transport limit

  Even though the capillary limit has been set as the total heat transport capability of the heat pipe, the actual heat transport capability is limited by the boiling limit. The variation in the boiling limit and the internal diameter of the heat pipe with the capillary limit is shown in Figure 6.12 A). The heat transport capability of the heat pipe is determined by the boiling limit in the boxed portion of the graph after which the heat transport capability is determined by the capillary limit.

  Reducing the capillary limit also results in reduced internal diameter of the heat pipe which is preferred in order to design a compact heat pipe desorber.

- Diameter of vapour space

  Larger vapour space diameter results in greater heat transport capability of the heat pipe. This is evident from the increase in boiling limit achieved by increasing the diameter of the vapour space. Caution must be exercised to limit the diameter of the vapour space to reasonable values in order to avoid very thick heat pipes.

  The variation in boiling limit and internal diameter with diameter of vapour space is shown in Figure 6.12 B).

- Screen mesh size

  The higher the mesh screen size, the finer the mesh. Increasing the mesh screen size also increases the boiling limit but the increase tends to plateau after a screen size of 400 $inch^{-1}$ because the finer the mesh the greater is the pressure drop of the liquid and the capillary limit becomes the limiting factor. This variation is shown in Figure 6.12 C).

- Wire diameter

  The wire diameter refers to the diameter of the wire used in the screen wick. Making the wire diameter larger makes the pores in the screen narrower and also increases the internal diameter of the heat pipe, thereby decreasing the boiling limit. But again there are some limits on how small or large the diameter can be. It is usually not recommended to increase the wire diameter beyond 0.03 mm in order to keep the heat pipe radius compact and to decrease it below 0.01 mm due to manufacturing constraints. The decrease in boiling limit is however not that pronounced and this parameter has a negligible effect when compared to other parameters, as seen in Figure 6.12 D)

- Length of evaporator and condenser sections

  The Le/Lc ratio of each heat pipe (of a fixed length) can be varied to alter the heat transport capability of the heat pipe. As can be seen from Figure 6.13 A), the smaller the condenser length and larger the evaporator length, higher is the boiling limit and eventually the heat transport capability of the heat pipe. Hence it is desired to make the evaporator section longer to enhance the heat transport capability of the heat pipe.

- Vapour temperature

  With increase in vapour temperature, the boiling limit and hence the heat transport capability of the heat pipe is reduced. This is because the latent heat of vapourisation/condensation decreases with increase in vapour temperature. Also most of the fluid properties have a negative function with temperature and that also results in reduced heat transport capability of the heat pipe. The variation of the heat transport capability with vapour temperature is shown in Figure 6.13 B).

- Tilt angle wrt horizontal

  As described in the previous section, when the tilt angle of the heat pipe is reduced, the axial hydrostatic pressure drop is also reduced which in turn reduces the overall capillary pressure drop between the condenser and the evaporator section thereby enhancing the heat transport capability of the heat pipe. The internal diameter of the heat pipe can also be made smaller with reduction in tilt angle thereby making the heat pipe compact. This variation is shown in Figure 6.13 C).

A summary of the effect of different parameters on the heat transport capability of the heat pipe is given in Table 6.3.

Table 6.3: Summary of effect of different parameters on heat pipe heat transport limit

Parameter	Effect
Capillary limit	Very strong effect
Diameter of vapour space	Strong effect
Screen mesh size	Negligible effect
Wire diameter	Negligible effect
Le,Lc length	Strong effect
Vapour temperature	Very strong effect
Angle of inclination (wrt horizontal)	Very strong effect

Discussion and final design parameters

The final geometrical parameters for the individual heat pipe with and without the adiabatic section are given in Table 6.4.

Table 6.4: Optimised dimensions of the heat pipe with no adiabatic section

	Without adiabatic section	With adiabatic section
Vapour temperature	160 ^{o}C	160 ^{o}C
Diameter of vapour space	20 mm	20 mm
Length of heat pipe	25 cm	25 cm
Length of Evaporator section	16 cm	14.5 cm
Length of Condenser section	9 cm	9 cm
Length of adiabatic section	0 cm	1.5 cm
Wick type	Screen wick	Screen wick
Mesh size	400 inch^{-1}	400 inch^{-1}
Wire diameter of mesh	0.01 mm	0.01 mm
Nucleation site radius	0.254 μm	0.254 μm
Angle of inclination wrt horizontal	10^{o}	10^{o}

Without the adiabatic section, the heat pipe is able to transport 250 W of heat which is quite close to the initial design specification of 300 W. The main heat transport limitation in this case is from the capillary limit. The boiling limit was calculated to be 318 W.

If a 1.5 cm adiabatic section is provided by reducing the length of the evaporator section from 16 cm to 14.5 cm then the heat transport capability per heat pipe is still maintained at 250 W however the boiling limit reduces to 273 W.

The reason for having an adiabatic section is to provide some leeway between the heat source side which is the cathode exhaust and the heat sink side which is the NH_3-H_2O solution in the desorber. If there is no adiabatic section then the two chambers viz the evaporator chamber and the condenser chamber will be in thermal contact and this might pose some problems due to temperature incompatibility. Hence from a safety point of view, it is desirable to have some gap between these two sections. This is depicted in Figure 6.14.

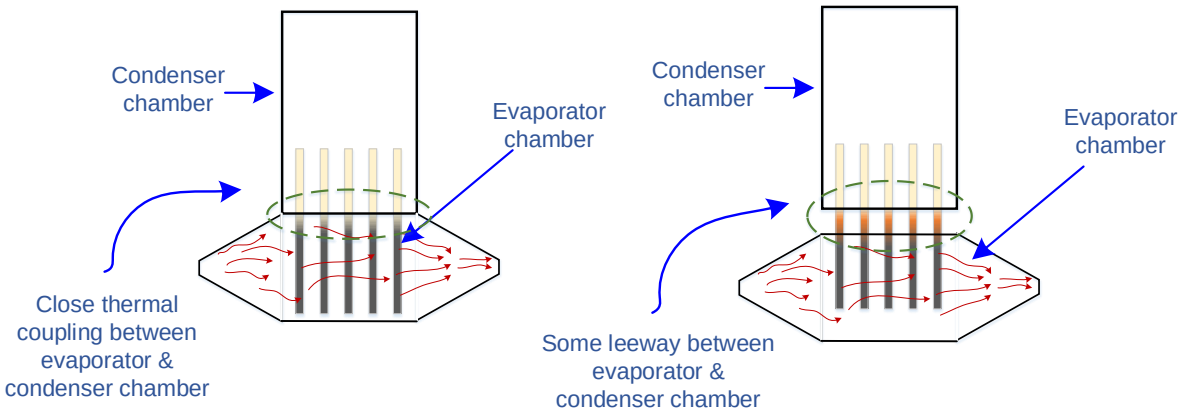

Figure 6.14: Schematic showing contact between evaporator and condenser chamber

The variation of different heat transport limits with vapour temperature are shown in Figure 6.15 for the optimised dimensions of heat pipe (with adiabatic section) mentioned in Table 6.4. As can be seen from this figure, the sonic and entrainment limits are quite high and the main limitation comes from either the boiling limit or the capillary limit. In the present case, the capillary limit is fixed to 250 W. The capillary limit is the limiting factor when the vapour temperature is below 165 ^{o}C and the boiling limit becomes the limiting factor when the vapour temperature is above 165 ^{o}C. This is because the boiling limit decreases with increase in vapour temperature. So if the heat pipe is operated at higher vapour temperatures then the heat transport capability of the heat pipe is reduced and more heat pipes need to be employed in the desorber in order to maintain the same heat input.

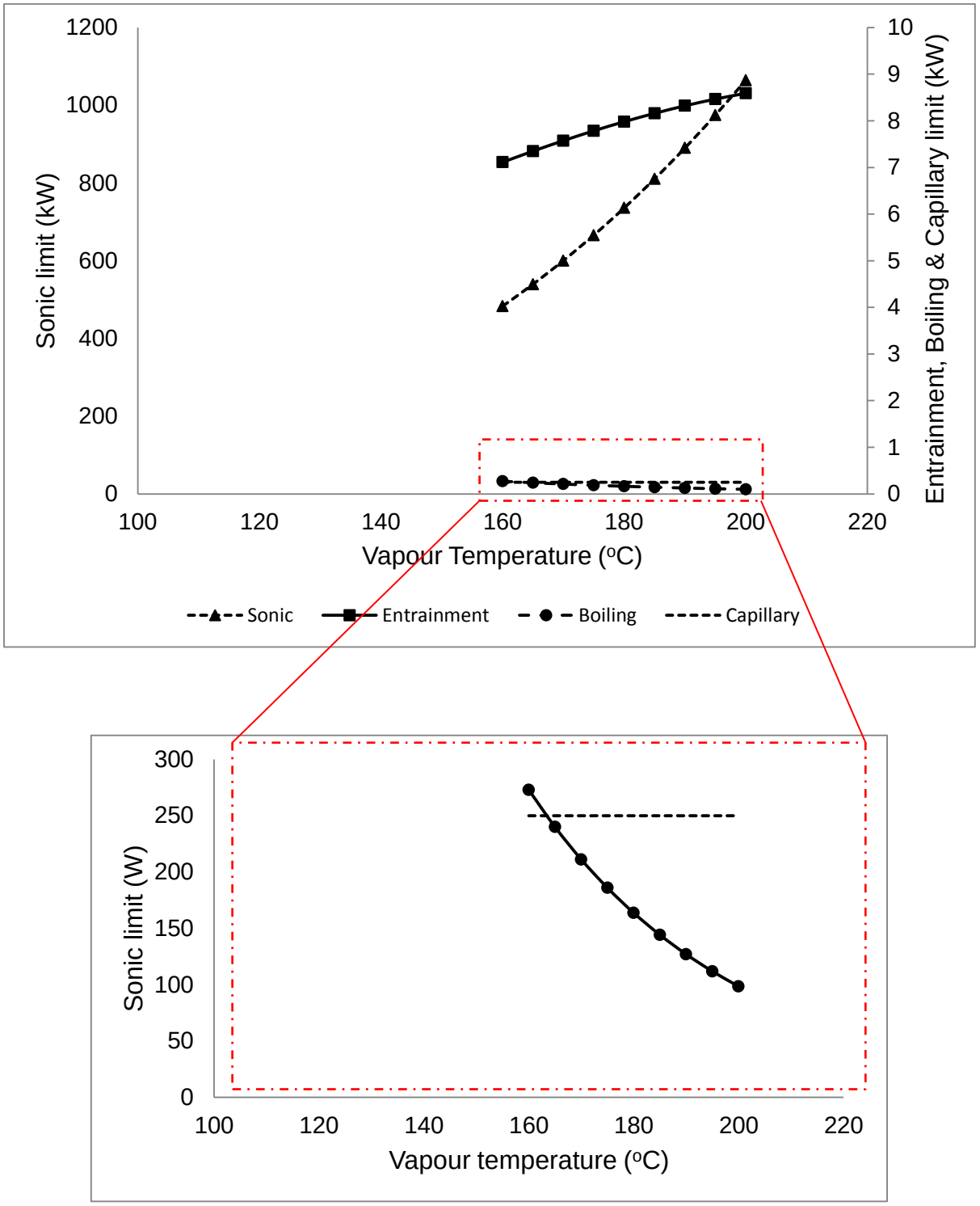

Figure 6.15: Variation of different heat transport limits with vapour temperature
(For optimised dimensions of heat pipe with adiabatic section as stated in Table 6.4)

Wick and heat pipe container characteristics

The other intricate details of the heat pipe can now be listed out based on the modelling results. The wick to be used is a wrapped screen (single layer) whose characteristics are mentioned in Table 6.5.

Table 6.5: Wick characteristics for the heat pipe designed

Wick parameter	Without adiabatic section	With 1.5 cm adiabatic section
Material	Stainless steel	Stainless steel
Porosity	0.87	0.87
Permeability	3.2017×10^{-11} (m^2)	3.2017×10^{-11} (m^2)
Effective thermal conductivity	0.8768 (W/m K)	0.8768 (W/m K)
Thickness of the wick	0.6176 (mm)	0.6535 (mm)
Cross sectional area of the wick	4.0×10^{-5} (m^2)	4.24×10^{-5} (m^2)
Hydraulic radius of the wick	0.6176 (mm)	0.6535 (mm)

The internal diameter of the heat pipe is 21.3 mm, calculated from optimised dimensions of the heat pipe with adiabatic section. This means the wall of the heat pipe container can be made thin enough ~ 1 to 1.5 mm. The external diameter of the heat pipe is then between 23.3 mm and 24.3 mm. This information is important because it will affect the heat transport into and out of the heat pipe at either ends of the heat pipe.

6.4.2 Transfer of heat from SOFC cathode exhaust to evaporator of heat pipe

The evaporator section of the heat pipe is exposed to the cathode exhaust from the SOFC stack. The cathode exhaust does not contain any water vapour. The schematic of how this arrangement might look is shown in Figure 6.16. The amount of heat flux impinging the evaporator surface for each heat pipe can be calculated from

$$\dot{Q} = \frac{(T_{Outer} - T_{Inner})}{R_{Total}} \qquad \textbf{Eq. 6.18}$$

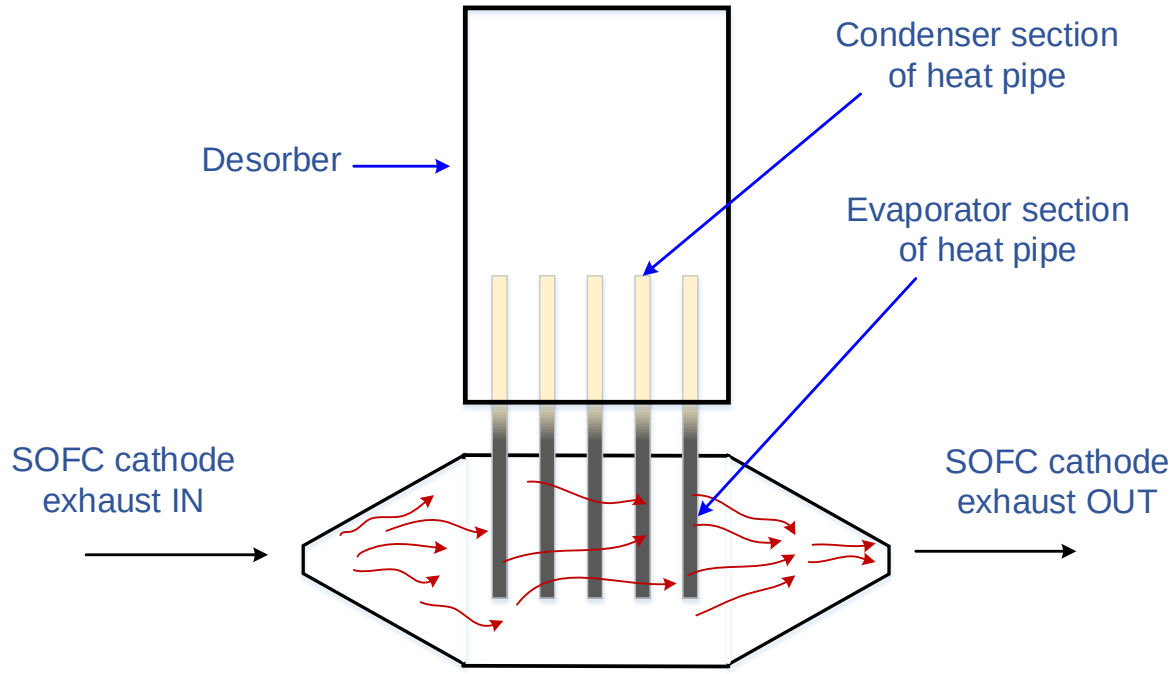

Figure 6.16: Evaporator section of heat pipe exposed to hot cathode exhaust from SOFC stack

Where

R_{Total}	Total radial thermal resistance of the evaporator section
T_{Outer}	Temperature on the outside surface of the heat pipe container
T_{Inner}	Temperature on the inside surface of the heat pipe (on the surface of the wick)

The detailed thermal resistance network of the heat pipe is given in *Appendix F*.

The thermal resistance for the hollow cylinder is given by

$$R = \frac{\ln\left({}^{r_o}/_{r_i}\right)}{2\pi\, L\, k} \qquad \textbf{Eq. 6.19}$$

Where,

L	Length of the cylindrical section (m)
k	Thermal conductivity of the material (W m^{-1} K^{-1})
r_o	Outer radius of the cylinder (m)
r_i	Inner radius of the cylinder (m)

The total thermal resistance is split into two parts viz. thermal resistance of the heat pipe container and thermal resistance of the wick. While calculating the radial resistance of the container and wick, the parameter 'L' is taken as the length of the evaporator section.

$$R_{Total} = R_{Container} + R_{Wick}$$

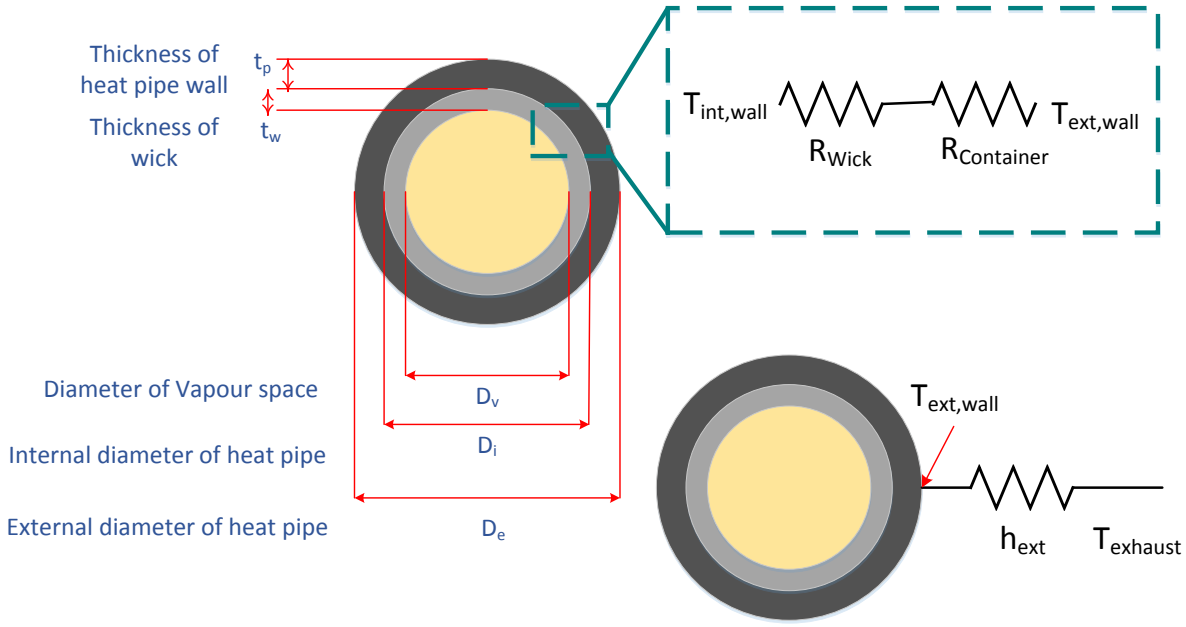

Figure 6.17: Thermal resistance network in radial direction

The thermal resistance network in the radial direction is depicted in Figure 6.17.

The heat transport capability of the heat pipe has been previously calculated and can be fixed as the heat supplied to each heat pipe based on the assumption that the heat absorbed at the evaporator is in turn transported via the heat pipe. The geometrical and thermal parameters of the heat pipe container material and wick are known so the temperature drop and in turn the cathode exhaust temperature needed on the outside of the heat pipe can be calculated. The results are summarized in Table 6.6.

Table 6.6: Calculation of ΔT for desired heat transport through the heat pipe

	Heat Pipe with no adiabatic section	Heat Pipe with 1.5 cm adiabatic section
Heat transport capability (W)	250	250
Length of Evaporator (cm)	16	14.5
Outer diameter of heat pipe (mm)	23.2	23.3
Inner diameter of heat pipe (mm)	21.2	21.3
Radial thermal resistance of Container (K/W)	5.468×10^{-3}	6.01×10^{-3}
Radial thermal resistance of Wick (K/W)	0.0662	0.0789
Total radial thermal resistance (K/W)	0.0716	0.0849
ΔT between inside surface and outside surface of heat pipe (K)	17.9	21.23

It was previously determined that a vapour temperature of 160 ^{o}C inside the heat pipe is sufficient to transport the required quantity of heat. Based on the ΔT values calculated in Table 6.6, the temperature on the outer surface of the heat pipe container can be calculated which is found to be around 180 ^{o}C. The wall thickness (difference between outer and inner diameters) of the designed heat pipe is 1 mm and this value is close to the wall thickness of copper based low temperature heat pipes designed in [12]. Hence from a design aspect it looks correct. A mechanical strength analysis is definitely required for the heat pipe designed but it is not under the scope of the current work as this chapter deals only with the heat transfer aspect both within and outside the heat pipe. However a quick calculation for thickness of the heat pipe is given below

$$t = \frac{P\,r}{\sigma_n} \qquad \textbf{Eq. 6.20}$$

Where,

t Thickness of the heat pipe needed (mm)

P Vapour pressure of the working fluid inside the heat pipe (MPa)

r Inner radius of the heat pipe

σ_n Normal stress (MPa)

The working fluid pressure (water in this case) at 160 ^{o}C is 6.6 bar (0.6 MPa) and taking the normal stress to be 10% of the maximum tensile strength of the heat pipe container (titanium is assumed in this case, which has a maximum tensile strength of 434 MPa), the thickness of the heat pipe turns out to be 0.15 mm whereas the designed heat pipe has a thickness of 1 mm. Hence a quick conclusion can be drawn on the mechanical integrity of the heat pipe.

A suitable air duct for near uniform distribution of the cathode exhaust was designed and the same is shown in *Appendix F*.

Modelling of the evaporator chamber

It was found that the outer surface of the heat pipe needs to be at a temperature of 180 ^{o}C if 250 W of heat needs to be transported through each heat pipe. The temperature of the cathode exhaust and the external heat transfer coefficient needs to be calculated to ensure that the cathode exhaust transfers sufficient thermal energy into the heat pipe. The amount of thermal energy transferred will depend on the thermal resistance between the exhaust bulk temperature and the outer wall temperature of the heat pipe and this thermal resistance is mainly governed by the heat transfer coefficient h_{ext} of air as shown in Figure 6.17.

The total amount of heat transferred by the cathode exhaust to a heat pipe can be calculated using Eq. 6.21

$$Q = h_{ext}\, A_{evap} \left(T_{exhaust} - T_{ext,wall}\right) \qquad \textbf{Eq. 6.21}$$

Where,

A_{evap}	Area of the evaporator section (m^2)
h_{ext}	External heat transfer coefficient (W m^{-2} K^{-1})
$T_{exhaust}$	Bulk temperature of the exhaust (K)
$T_{ext,wall}$	External wall temperature of the heat pipe (K)

The external heat transfer coefficient (HTC) depends both on the fluid properties and the geometry around which the fluid flows. In this case since the heat pipes are cylindrical, the HTC is calculated for flow around cylinders by using the Churchill and Bernstein equation for Nusselt number, Eq. 6.22, and then using Eq. 6.23

$$Nu = 0.3 + \frac{0.62\, Re^{\frac{1}{2}} Pr^{\frac{1}{3}}}{\left(\left(1 + \left(\frac{0.4}{Pr}\right)^{\frac{2}{3}}\right)\right)^{\frac{1}{4}}} \left[1 + \left(\frac{Re}{282000}\right)^{\frac{5}{8}}\right]^{\frac{4}{5}} \qquad \textbf{Eq. 6.22}$$

$$Nu = \frac{h_{ext}\, d}{k} \qquad \textbf{Eq. 6.23}$$

Where,

Nu	Nusselt number
Re	Reynolds number
Pr	Prandtl number
d	Outer diameter of heat pipe (m)
k	Thermal conductivity of air (W m^{-1} K^{-1})
h_{ext}	External heat transfer coefficient (W m^{-2} K^{-1})

Certain assumptions need to be made for modelling the evaporator chamber and they are:

1) All heat pipes experience the same velocity of air.
2) The bulk temperature of the exhaust remains the same for all heat pipes.

3) The outer wall temperature of the heat pipe is fixed as 180 ^{o}C as calculated previously.
4) Steady state conditions prevail.

The exhaust from a 1 kWe SOFC stack has the following parameters:

Exhaust temperature	550 ^{o}C
Pressure	1.2 bar
Exhaust flow rate	0.00574 m^3 s^{-1}
Fuel utilisation (corresponding to the flow rate)	0.5

Now that the external HTC, evaporator surface area, outer wall temperature and bulk fluid temperature are known, the heat transferred by the cathode exhaust into the heat pipe can be calculated. It is found, though, that the geometry given by Table 6.6 is insufficient to transfer the required heat flux. As one solution, the surface area of the heat pipe can be increased by adding fins.

The area of the evaporator is calculated from

$$A_{evap} = X * (2\pi r_o L_e) + \pi r_o^2 \qquad \textbf{Eq. 6.24}$$

Where,

X	Increase in evaporator surface area required (by addition of fins)
r_o	External heat pipe radius
L_e	Length of the evaporator section

After a number of iterations it was found that the evaporator surface area needs to be increased by 7.5 times to achieve the required heat input of 250 W per heat pipe. Hence for

further analysis, the factor X is fixed at 7.5 to calculate the total evaporator surface area. For the time being it is assumed that heat transfer in the fins is ideal.

The geometrical dimensions of the evaporator section of the heat pipe are shown in *Appendix F*.

The variation in heat transferred into the heat pipe with the following parameters is analysed here and resulting graphs are shown in Figure 6.18.

- **With bulk temperature of cathode exhaust**

  The bulk fluid temperature plays a vital role in the amount of heat transferred into the heat pipe. Increasing the bulk exhaust temperature does not increase the heat transfer coefficient however the driving temperature difference is increased which causes more heat to enter the heat pipe. Having the bulk exhaust temperature around 550 ^{o}C ensures 250 W of heat is supplied.

- **With pressure of cathode exhaust**

  If the SOFC stack is operated under pressure (slightly above atmospheric pressure) then the amount of heat transferred into the heat pipe is increased. This is because pressurized operation increases the density of air which in turn affects the Reynolds number and the Nusselt number.

- **With length of evaporator**

  The length of the evaporator section of the heat pipe also plays a major role in the amount of heat absorbed at the evaporator. The longer the evaporator section, the larger will be the surface area and hence more heat will be absorbed. The ultimate length of the evaporator section is decided by the application intended and the quantity of heat desired to be transported.

- **With cathode exhaust flow rate**

  The way the SOFC stack is operated also affects the amount of heat absorbed by the heat pipe. SOFC stacks operated with low fuel utilisation will have higher cathode exhaust flow rates and vice versa. Larger flow rates will deliver more heat due to the fact that the velocity of flow is increased and this in turn increases the Reynolds number and the Nusselt number.

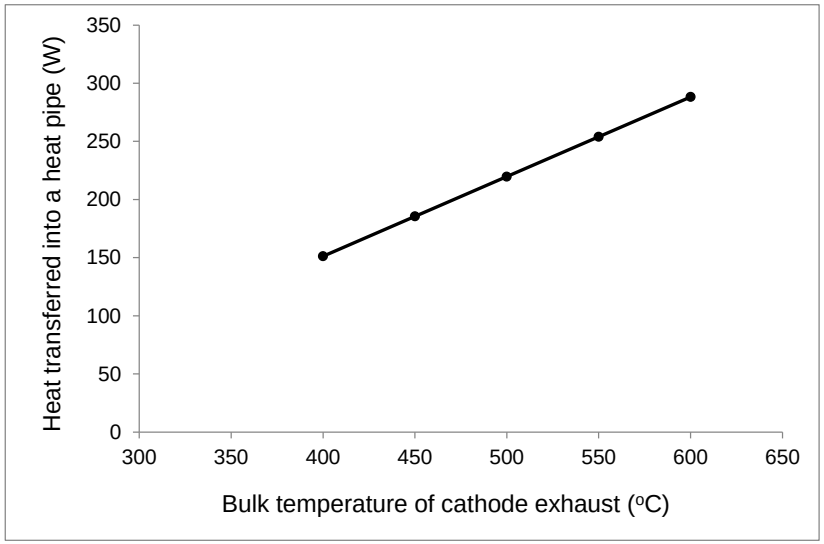

a) Bulk temperature of cathode exhaust

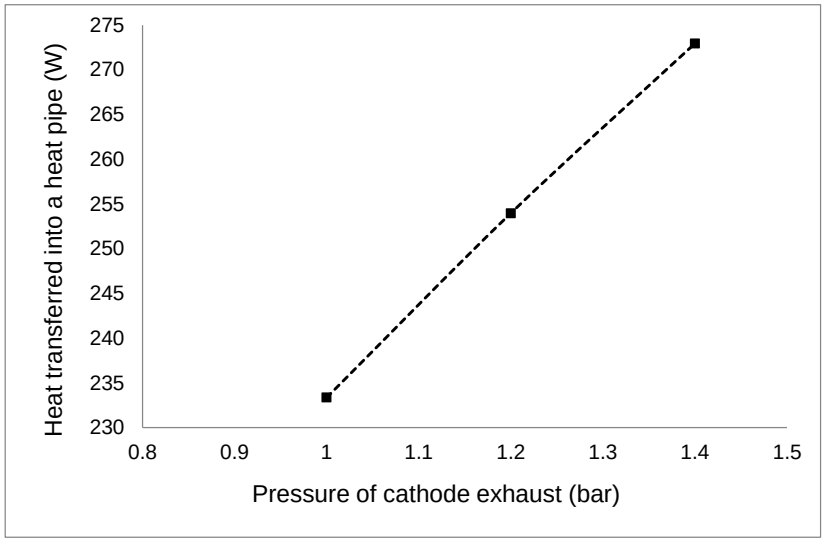

b) Pressure of cathode exhaust

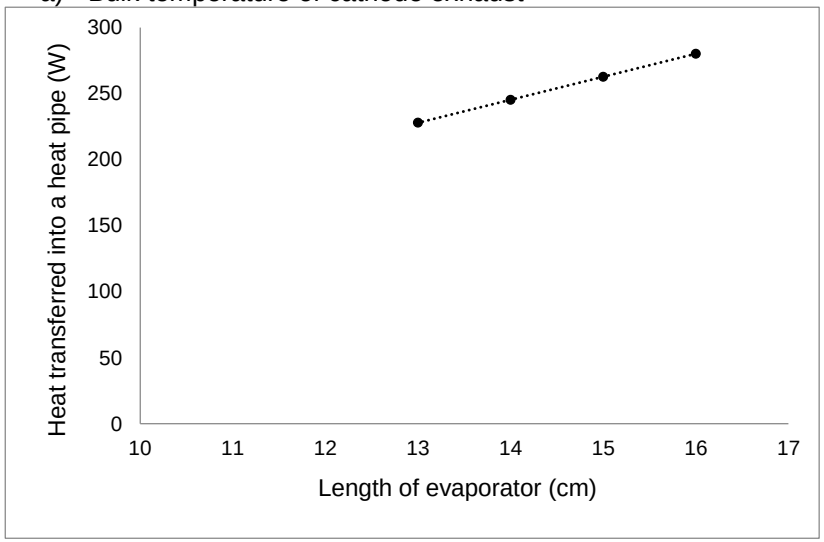

c) Length of evaporator

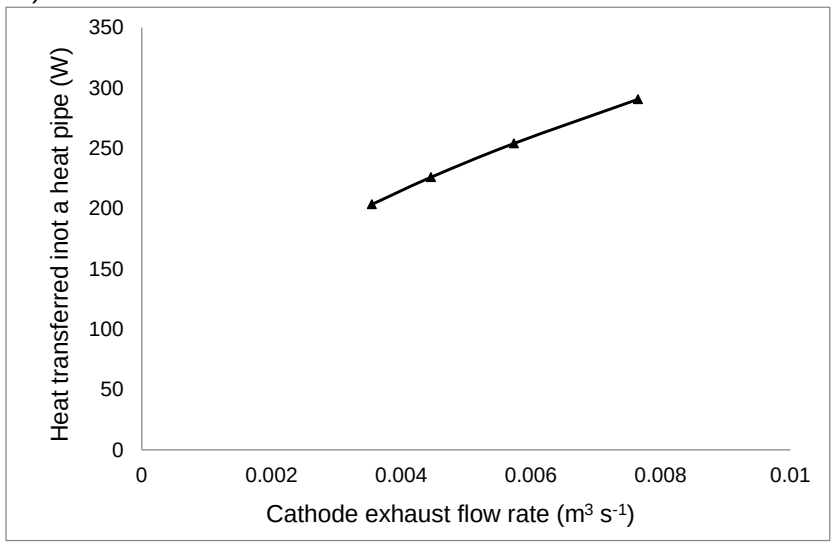

d) Cathode exhaust flow rate

Figure 6.18: Variation in heat transferred into the heat pipe with different parameters
(For dimensions of heat pipe given in Table 6.4 and Table 6.5)

6.4.3 Transfer of heat from condenser to NH_3-H_2O solution

The heat transported by each heat pipe will be dissipated out from the condenser side into the NH_3-H_2O solution. This heat will be used to raise the temperature of the solution if its temperature is below the saturation temperature and also be used to boil the solution to generate NH_3 vapour.

The heat supplied will cause pool boiling of NH_3-H_2O solution. Modelling the entire heat transfer aspect at the condenser end is quite complex because of the different complex phenomena involved with boiling of binary mixtures. Hence in this section only heat transfer modelling of the NH_3- H_2O solution is carried out and based on the temperature reached by the solution appropriate conclusions are drawn as to whether the solution remains in saturated phase, two phase or gets completely vapourised. The entire boiling modelling process is summarized in Figure 6.19.

The amount of heat flux at the condenser end can once again be calculated from the total heat transferred out and the condenser surface area. If the condenser section does not have any fins then the total heat transfer surface area is 7.014 x 10^{-3} m^2 and considering that the entire heat supplied at the evaporator is transferred out from the condenser, the heat flux value is 35.64 kW m^{-2} or ~ 36 kW m^{-2}. There are no losses from each heat pipe at the condenser end because each heat pipe is completely immersed in the NH_3-H_2O solution and the entire heat that is transported out of the heat pipe is used to boil the NH_3-H_2O solution.

6.4.3.1 Model development

The model developed to determine the solution temperature and the state of the solution in the desorber is outlined in the flowchart shown in Figure 6.20.

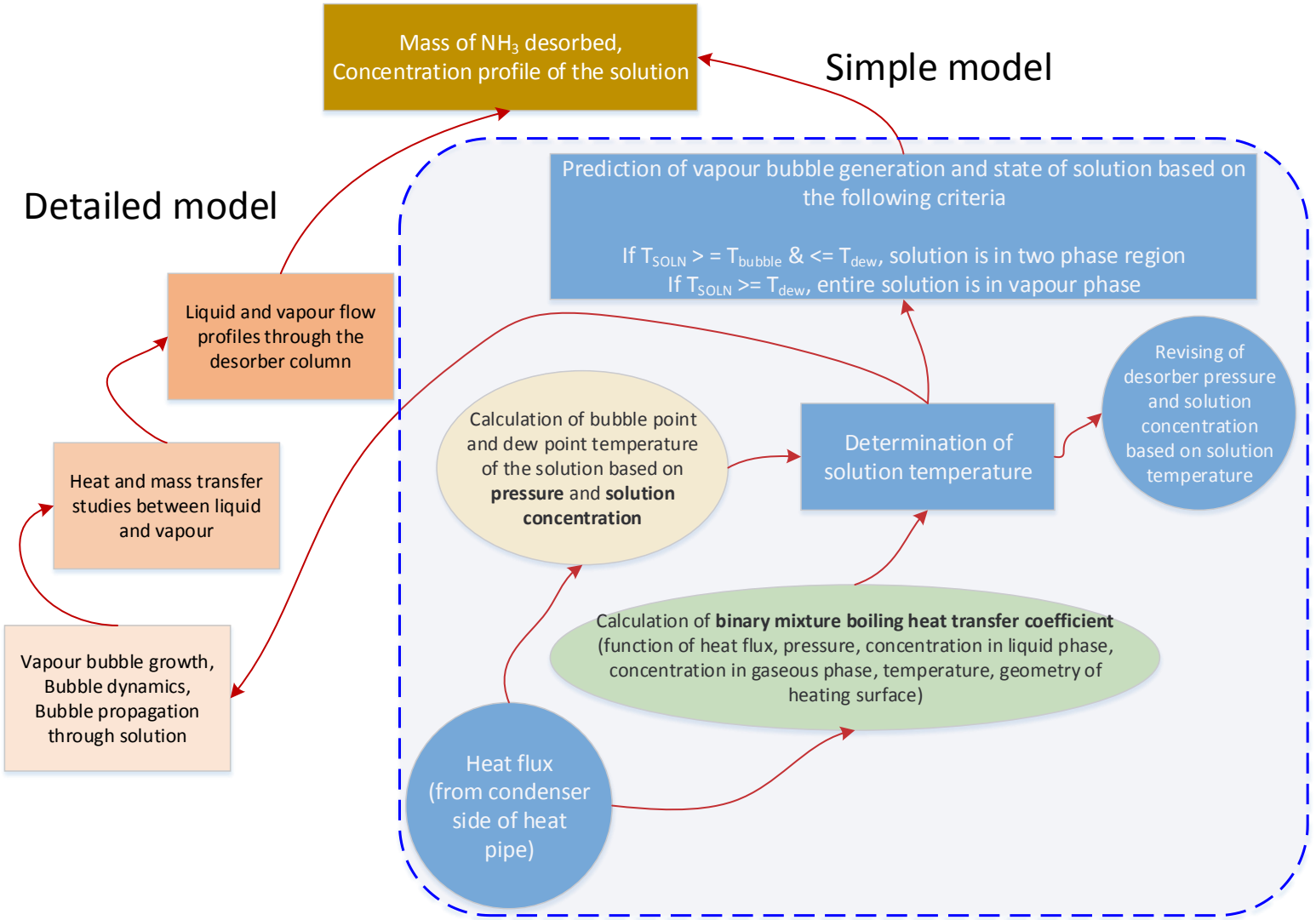

Figure 6.19: Flow chart for modelling the complex boiling process at the condenser end

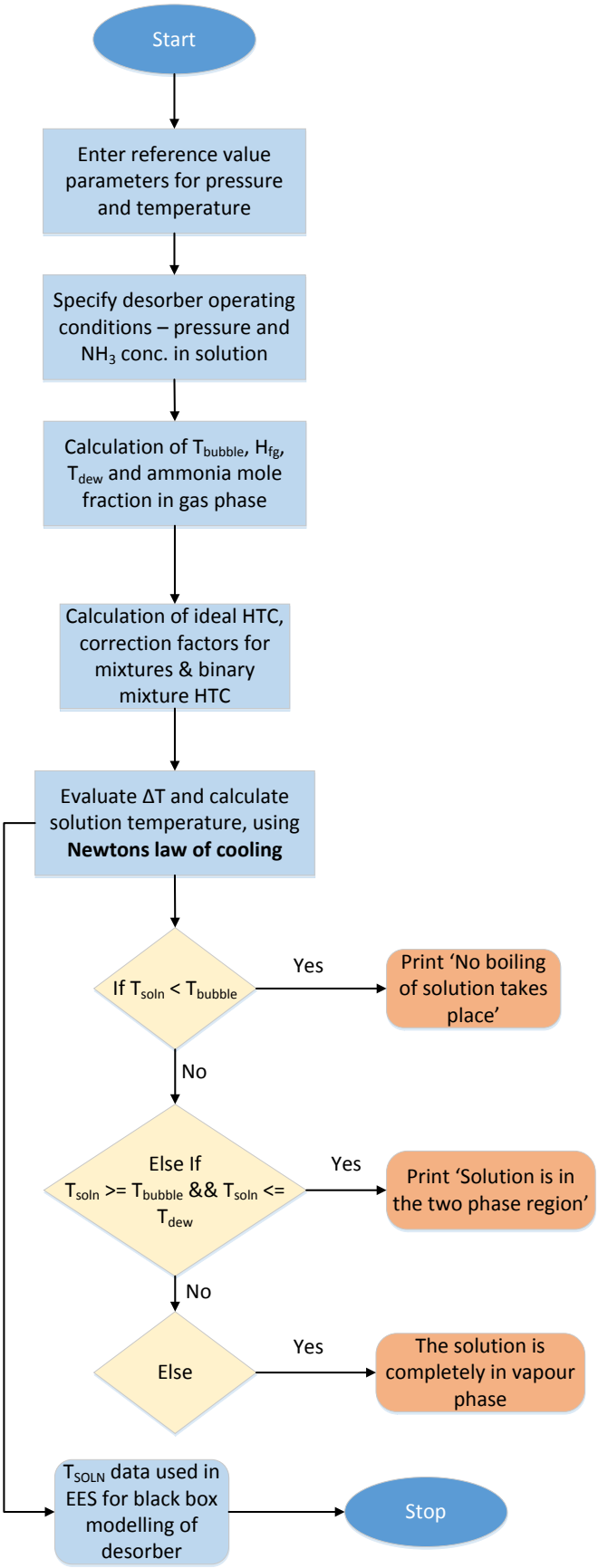

Figure 6.20: Modelling methodology for heat transfer at condenser end of heat pipe

The part of the heat pipe (condenser end which is in contact with NH_3-H_2O solution) that is modelled is shown in Figure 6.21.

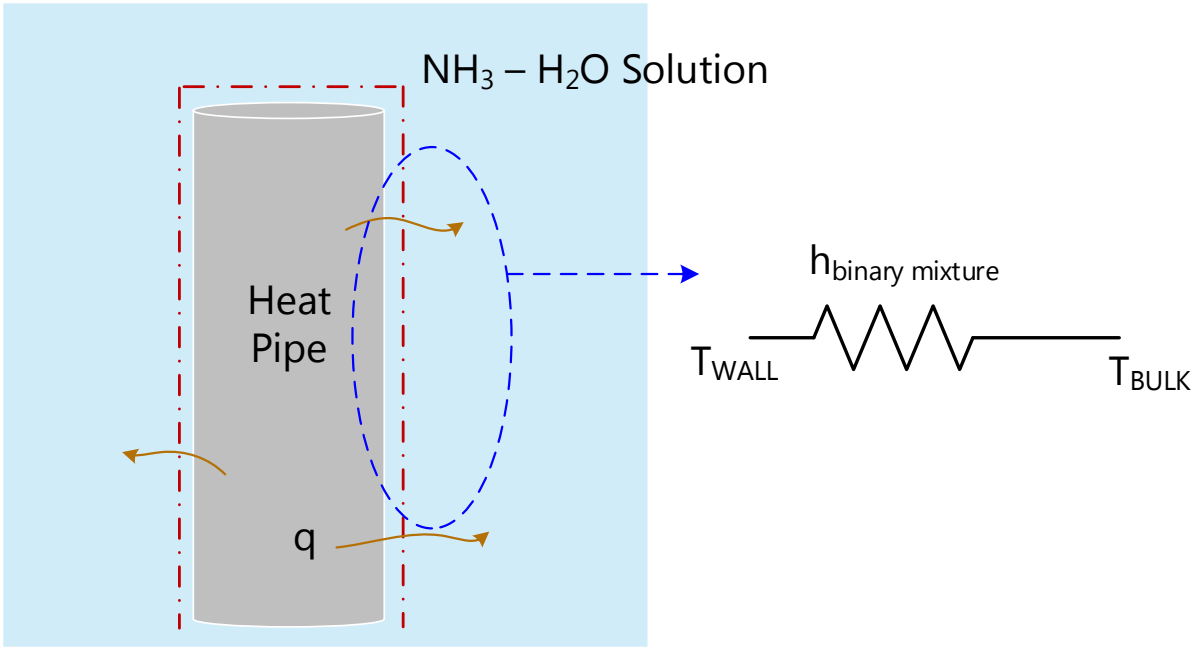

Figure 6.21: Modelling of condenser end of the heat pipe

The Heat Transfer Coefficient (HTC) plays a key role in boiling of NH_3-H_2O solution and is a complex function of pressure, temperature, heat flux, concentration, fluid properties and characteristics of heating surface. Dedicated experimental studies are needed to determine the exact value of it and generally correlations developed from one experiment might not be applicable to another experiment due to differences in experimental conditions, equipment used, geometry of the heating surface and other factors. Very few research groups have worked on determining the experimental values of boiling heat transfer coefficient for NH_3-H_2O solution [13-15] and have fitted their experimental data with theoretical correlations. However, there is still no complete consensus on which theoretical correlation to use in general that will satisfactorily predict all experimental data from different authors.

The heat transfer coefficient of a binary mixture is always lower than the heat transfer coefficient of the individual components [16]. This is because the physical and

thermodynamic properties of the mixture are different from that of the single components. Some of the other reasons for lower HTC of mixtures as outlined in [16] are:

i) Localized increase in temperature of the liquid (mixture/solution) close to the wall of the heating surface, due to preferential evaporation of the component that is more volatile.

ii) Presence of a mass transfer resistance which hinders the volatile component from moving up towards the bubble interface.

iii) Need for a higher energy for generating a bubble nucleus in mixtures.

iv) Decrease in bubble nucleation sites.

v) Departure from linear behaviour of mixture properties with composition.

The heat transfer coefficient for the binary mixture is defined by Eq. 6.25

$$h_{binary} = \frac{h_{id}}{1 + E} \qquad \textbf{Eq. 6.25}$$

Where,

h_{id} Ideal heat transfer coefficient (W m^{-2} K^{-1})

E Correction factor

h_{binary} Actual heat transfer coefficient of the binary mixture (W m^{-2} K^{-1})

The ideal heat transfer coefficient for the binary mixture is given by Eq. 6.26 [14]

$$h_{id} = \frac{\left(\frac{P}{P_o}\right)^a \left(f_\zeta q\right)^b}{\left(\left(\frac{x_1}{c_1}\right) + \left(\frac{x_2}{c_2}\right)\right) R^c} \qquad \textbf{Eq. 6.26}$$

Where,

P Operating pressure, in this case it is the desorber operating pressure (Pa)

P_o Standard atmospheric pressure (Pa)

f_ζ Nucleation factor

R Characteristic length of the heating surface, which in this case is the height

	of the condenser section of the heat pipe (m)
q	Heat flux (W m^{-2}), this quantity is known from heat pipe modelling
x_1	Mole fraction of liquid (low boiling point component) NH_3
x_2	Mole fraction of liquid (high boiling point component) H_2O
a	0.23
b	0.8
c	0.2
c_1	0.3073
c_2	0.3233

There are umpteen numbers of mixture correction coefficients available in literature, a comprehensive list of equations are mentioned in [17]. In this modelling study the modified Stephan & Korner relation as mentioned in Sathyabama et al [17] is made use of because the use of heat pipes to boil NH_3-H_2O solution closely matches their experimental set-up where they used a cylindrical heating surface to evaluate the boiling heat transfer coefficient of the NH_3-H_2O solution. The Stephan & Korner correlation for the correction factor is given by Eq. 6.27

$$E = A_o\,(0.88 + 0.12P)(y - x) \qquad \textbf{Eq. 6.27}$$

Where,

A_o	1.6631, coefficient value suggested by [17] to match experimental data
P	Operating pressure in the desorber (Pa)
y	Ammonia mole fraction in gas phase
x	Ammonia mole fraction in liquid phase

Once the heat transfer coefficient of the mixture is known, it is possible to calculate the temperature difference between the outer wall temperature and the bulk solution temperature and in turn the actual bulk solution temperature can be determined.

$$\Delta T = \frac{q}{h_{binary}};\ \Delta T = T_{wall} - T_{soln} \qquad \textbf{Eq. 6.28}$$

If the outer wall temperature of the heat pipe is greater than the saturation temperature or the bubble point temperature then phase change can be expected and there will be some refrigerant generation. The solution temperature may or may not reach the bubble point temperature and this entirely depends on three factors viz.

- Heat transfer coefficient of the solution
- Outer wall temperature of the heating surface (heat pipe in this case)
- Heat flux

The desorber pressure and the inlet solution concentration also play a key role in determining the bubble point temperature. The bubble point temperature increases with increase in desorber pressure and decrease in NH_3 concentration in the solution. Hence the desorber pressure and solution concentration need to be chosen in such a way that the solution temperature reaches a value greater than the bubble point temperature else there will be no boiling of the solution. Ideally, a solution temperature between the bubble point and dew point temperature will be preferred. This will ensure that the solution will be in the two phase region thereby leading to sufficient refrigerant production.

The bubble point and dew point temperatures are given by Eq. 6.29 and Eq. 6.30 [18]

$$T_{Bubble} = T_o \sum a_i \, (1-x)^{m_i} \left[\ln\left(\frac{P_o}{P}\right)\right]^{n_i} \qquad \textbf{Eq. 6.29}$$

$$T_{Dew} = T_o \sum a_i \, (1-y)^{m_i/4} \left[\ln\left(\frac{P_o}{P}\right)\right]^{n_i} \qquad \textbf{Eq. 6.30}$$

The coefficients of a, m and n in Eq. 6.29 and Eq. 6.30 are given in Table 6.7 and Table 6.8 respectively.

Table 6.7: Coefficients for a, m and n for Eq. 6.29

i	m_i	n_i	a_i
1	0	0	3.22
2	0	1	-0.384
3	0	2	0.046
4	0	3	-0.00378
5	0	4	0.000135
6	1	0	0.488
7	1	1	-0.12
8	1	2	0.0106
9	2	3	-0.000533
10	4	0	7.85
11	5	0	-11.59
12	5	1	-0.0523
13	6	0	4.89
14	13	0	0.0421

Table 6.8: Coefficients for a, m and n for Eq. 6.30

i	m_i	n_i	a_i
1	0	0	3.24
2	0	1	-0.3959
3	0	2	0.04356
4	0	3	-0.002189
5	1	0	-1.43526
6	1	1	1.05256
7	1	2	-0.071928
8	2	0	12.236
9	2	1	-2.2436
10	3	0	-20.178
11	3	1	1.1083
12	4	0	14.539
13	4	2	0.6443
14	5	0	-2.2125
15	5	2	-0.75626
16	6	0	-1.3553
17	7	2	0.18354

T_o and P_o in Eq. 6.29 and Eq. 6.30 are respectively 100 K and 20 bar.

A correction factor ΔT mentioned in Eq. 6.31 is needed for the dew point temperature

$$\Delta T = -233.9\, x^2 + 307.5\, x - 9.368 \qquad \textbf{Eq. 6.31}$$

The need for a correction factor in the dew point temperature arises because Eq. 6.30 under-predicts the dew point temperature for NH_3 mass fractions between 0.1 and 0.9. This correction factor was obtained after comparing the dew point temperature values obtained from EES and those calculated from Eq. 6.30 and then fitting them via the curve fitting toolbox in MATLAB to a polynomial function which gave an R square value of 0.99.

The NH_3 vapour mole fraction needed in Eq. 6.30 is given by Eq. 6.32

$$y = 1 - exp\left(\ln(1-x)\sum a_i \left(\frac{P}{P_o}\right)^{mi} x^{\frac{n_i}{3}}\right) \qquad \textbf{Eq. 6.32}$$

The coefficients of a, m and n for Eq. 6.32 are given in Table 6.9.

Table 6.9: Coefficients for a, m and n for Eq. 6.32

i	m_i	n_i	a_i
1	0	0	19.8022
2	0	1	-11.8093
3	0	6	27.748
4	0	7	-28.8634
5	1	0	-59.162
6	2	1	578.0913
7	2	2	-6.2174
8	3	2	-3421.984
9	4	3	11940.3127
10	5	4	-24541.377
11	6	5	29159.1865
12	7	6	-18478.229
13	7	7	23.482
14	8	7	4803.106

6.4.3.2 Results

The heat transfer from the condenser end of the heat pipe into the NH_3-H_2O solution depends on many factors such as temperature of the heat pipe, heat transported by the heat pipe, desorber pressure, concentration of NH_3 in the solution and many more. In this section some of the parameters that have an influence on the heat transfer are discussed.

a) **Role of desorber pressure and solution concentration in determining bubble point temperature**

The operating pressure of the desorber and the solution concentration play a decisive role in determining the bubble point temperature of the solution as seen from Figure 6.22. The bubble point temperature is the minimum temperature required for the solution to boil and there can be no vapour generation from the desorber without the solution reaching this value. Hence the first goal is to create some design maps for each operating pressure of the desorber and identify if the solution will boil or not. These design maps are created for an outer heat pipe wall temperature of 124.5 ^{o}C (at the condenser end), a heat transport capability of 250 W through the heat pipe (with the dimensions of the heat pipe as mentioned before) and assuming at this stage that only one heat pipe is employed.

Note: *The temperature drop along the heat pipe and the temperature at the condenser end is calculated in Appendix F*.

The operating pressure of the desorber and the mass fraction of NH_3 needed in the solution, for the solution to reach bubble point temperature are specified in the design map shown in Figure 6.23. However it would be better if the solution is completely in the two phase region rather than just hovering around the bubble point curve. Hence a minimum ΔT of 10 K above the bubble point temperature is fixed as the desired temperature. The revised desorber pressure and NH_3 mass fraction in the solution are also specified in the design map.

From the design map one can make an inference that it is sufficient to operate the desorber at a pressure of 10 bar. There is no specific need to go for higher pressures and the ammonia mass fraction needed in the solution is 0.4 or 40 wt%.

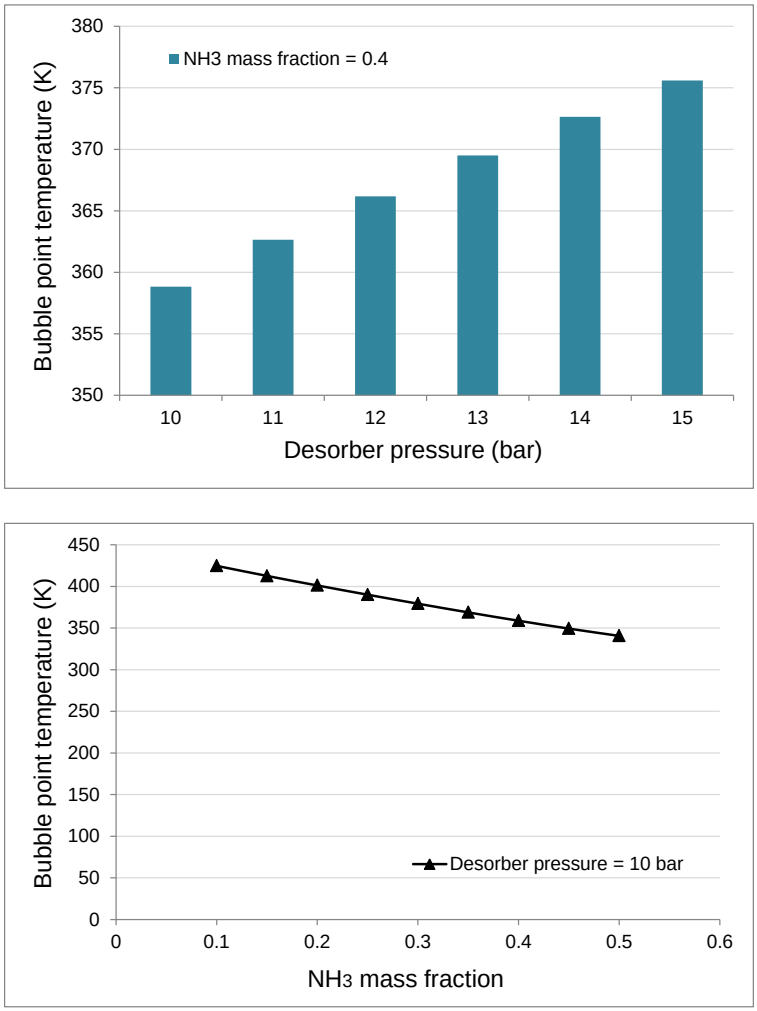

Figure 6.22: Variation of bubble point temperature with desorber pressure and NH_3 mass fraction

b) **Role of heat flux in different liquid sections**

The solution in the desorber can be divided into different liquid layers as shown in Figure 6.24. The heat flux has a major role to play in determining the heat transfer coefficient which in turn determines the ΔT between the condenser wall temperature and the bulk solution temperature.

The end liquid sections will experience heat flux from only one side (of the heat pipe) whereas the middle sections will experience heat flux from both sides (from the end of the heat pipe on the left and from the end of the heat pipe on the right).

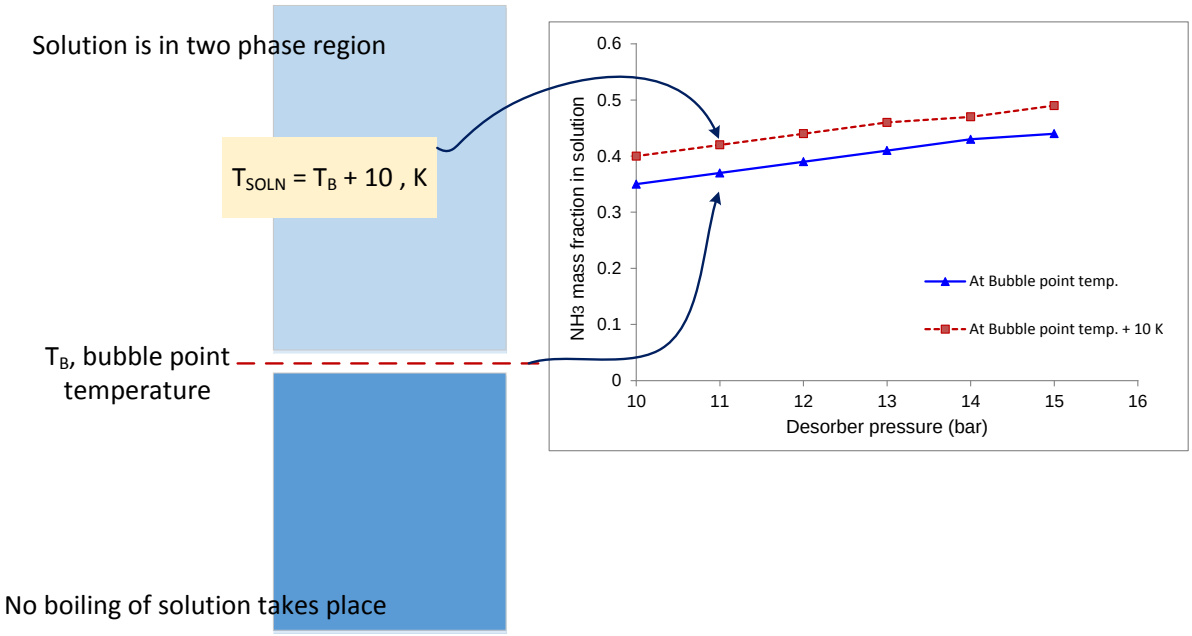

Figure 6.23: Design map for choosing desorber pressure and NH_3 mass fraction in the solution

This view point is taken for understanding the model development although in the real scenario there will be mixing between different liquid sections. Hence just to provide a 2D perspective, the whole solution is divided into different sections and the temperature and HTCs in each section are analysed.

The heat transfer coefficient (HTC) in the end liquid section is calculated to be 1.29 kW m^{-2} K^{-1}. The heat flux for the middle section is nearly doubled because there is simultaneous heat addition from two heat pipes also resulting in increased heat transfer surface area. Hence the heat transfer coefficient for the middle section is 2.246 kW m^{-2} K^{-1}. The HTC increases with increase in heat flux which matches the correlation between heat flux and HTC described in literature for binary mixtures [17, 19-21]. The variation in HTC with heat flux is shown in Figure 6.25.

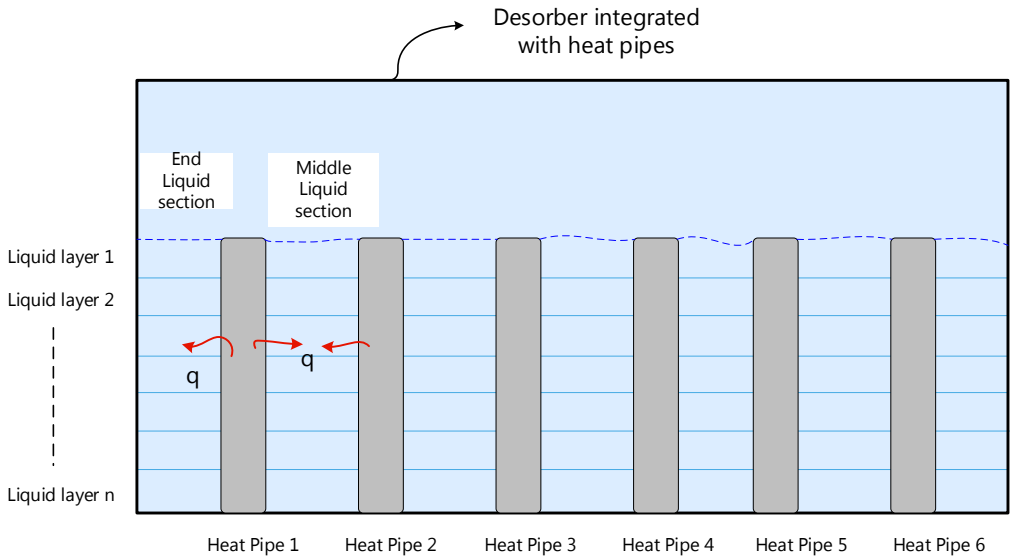

Figure 6.24: Schematic of different liquid layers & sections in a heat pipe integrated desorber

Due to increased HTC, the temperature difference between the wall of the heat pipe and the solution is also increased in spite of them being inversely related. This is because the temperature difference is also directly proportional to heat flux applied which for the middle section is doubled. The increase in ΔT in turn reduces the solution temperature. Thus a variation in HTC will cause the solution temperature to be different in different parts of the desorber. The localised temperature distribution and the HTC in different parts of the desorber are shown in Figure 6.26.

The bubble point temperature at a pressure of 10 bar and an ammonia mass fraction of 0.4 is 358.8 K. As seen from Figure 6.26, the temperature of all sections is greater than the bubble point temperature; hence the solution is definitely in the two phase region. Vapour generation will usually begin from the liquid layers in contact with the heat pipe surface, forming tiny bubbles initially and later propagating upwards along the solution. Modelling of the bubble generation process and its propagation is not within the scope of this work.

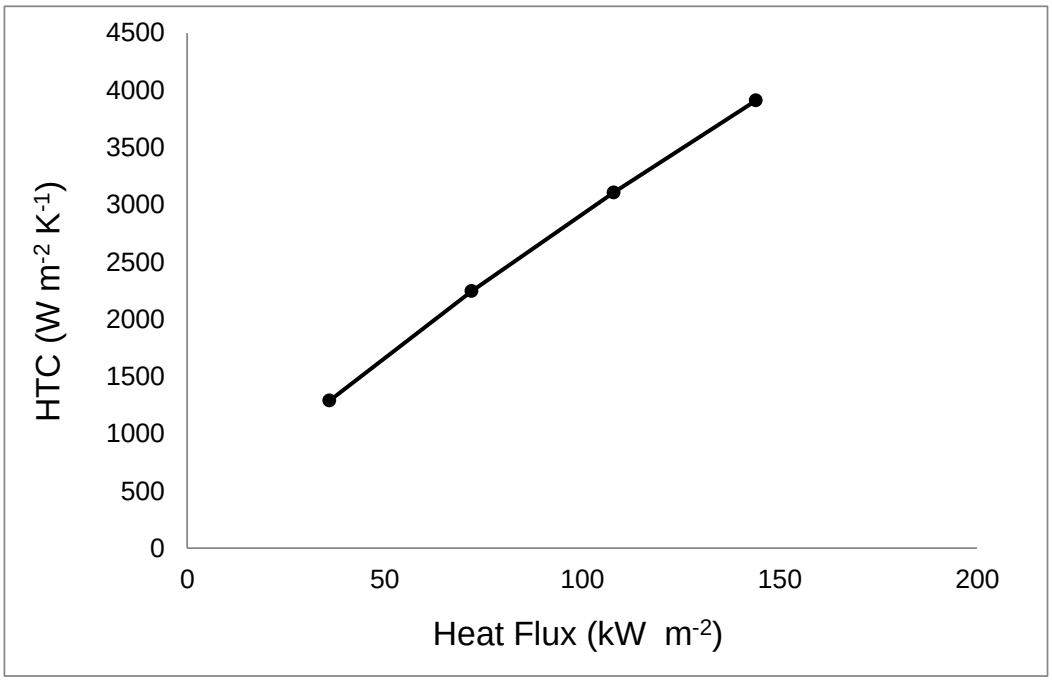

Figure 6.25: Variation of HTC with heat flux

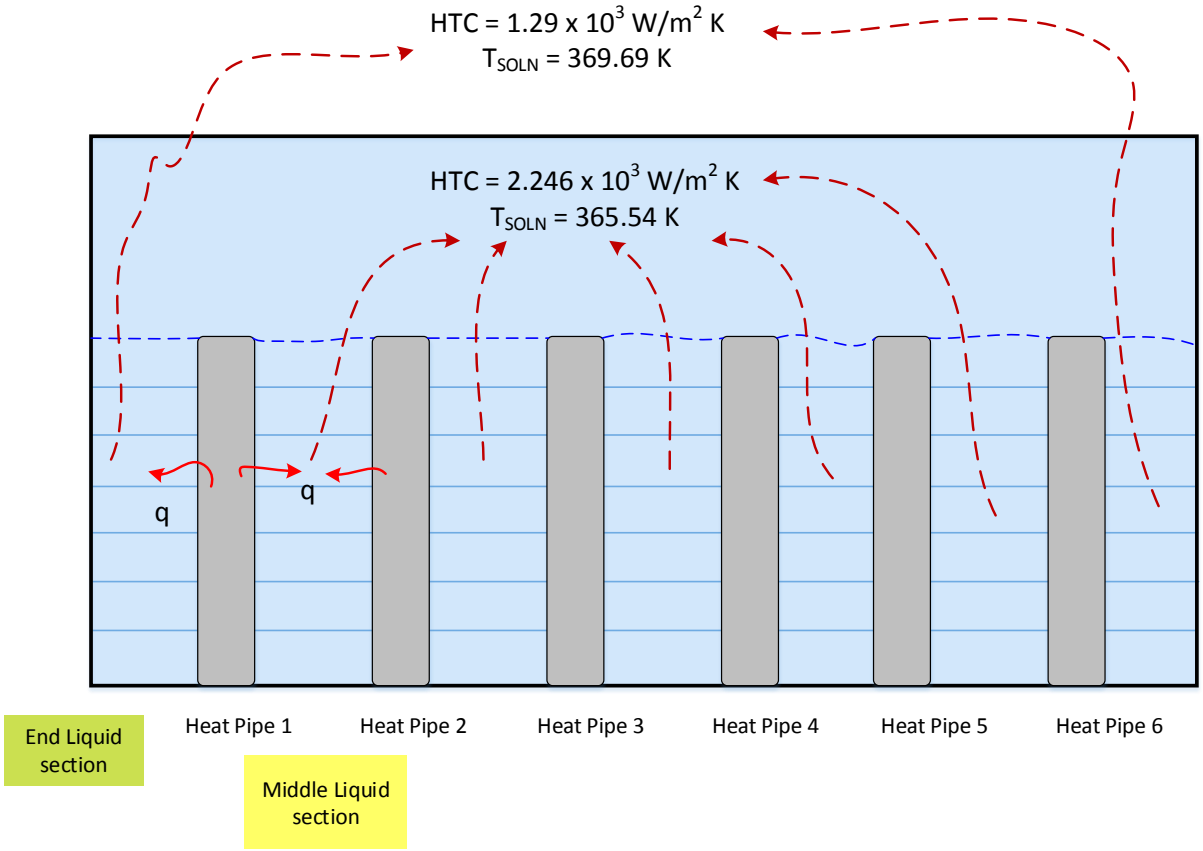

Figure 6.26: Local temperature and HTC distribution in heat pipe integrated desorber
P = 10 bar, x = 0.4

c) **Role of heat flux in determining HTC and data verification with Sathyabama et al [17]**

The HTC values (for the conditions in the heat pipe desorber) are quite small, between 1.2 and 2.2 kW m^{-2} K^{-1}. This is because the heat flux applied to the solution is also small which in this case is just 36 kW m^{-2} (per heat pipe). A comparison of the HTC values with that of Sathyabama et al [17] will provide more credibility to the modelling studies carried out.

Figure 6.27 shows the variation of HTC with heat flux for different solution concentrations and different desorber pressures as adapted from [17]. As can be seen from the figure, the HTC decreases with increase in NH_3 concentration in the solution and decrease in heat flux. Sathyabama et al [17] used a cylindrical heating element to measure the pool boiling HTC of NH_3-H_2O solution. The cylindrical heating element was 6 mm in diameter and 20 mm in length and had a heating capacity of 1 kW. In comparison, the heating element in this work is the heat pipe embedded in the desorber, each having a length of 90 mm (condenser section alone) and an outer diameter of 23.3 mm with a maximum heat transfer capacity of 250 W.

Direct one to one comparison with Sathyabama's work cannot be done because of differences in experimental set up and conditions however certain inferences can be drawn due to similarity in shape of the heating element and the code can be modified to incorporate the geometrical dimensions of the heating element. For low applied heat fluxes, the heat transfer coefficient of the mixture is very low and if the concentration of NH_3 is increased then the heat transfer coefficient is lowered even further.

The comparison of HTC values obtained from the modelling work and that of Sathyabama et al [17] is shown in Figure 6.28. The geometrical parameters of the

condenser end of the heat pipe were tweaked to match the dimensions of the heating element used in Sathyabama's work. The model does a good job in closely predicting the HTC values for higher pressures but fails to predict the HTC values close enough at lower pressures. This could be attributed to the fact that the model uses a theoretical correlation for predicting the binary mixture heat transfer coefficient and till date there is no theoretical correlation available that can be easily adapted to predict the actual values obtained from experiments.

d) **How the desorber pressure can be reduced by using heat pipe integration**

By using a heat pipe integrated desorber, the operating pressure of the desorber in the VARS unit can be reduced. From modelling studies carried out in previous chapters it was found that the operating pressure needed in the desorber is around 15 bar and the NH_3 concentration in the solution is 0.3. However in this new design of the desorber, the operating pressure can be reduced to around 10 bar. This is because the mechanism of heat transfer is totally different in this new kind of desorber. Rather than flow boiling, pool boiling of NH_3-H_2O solution takes place. Higher desorber pressures will lead to higher bubble point temperature in the pool and if the solution doesn't reach the bubble point temperature, no boiling can take place, thereby resulting in zero refrigerant generation. Hence by lowering the desorber pressure and increasing the NH_3 concentration in the solution, the bubble point temperature is also lowered. Lower system pressures are also preferred from a safety point of view.

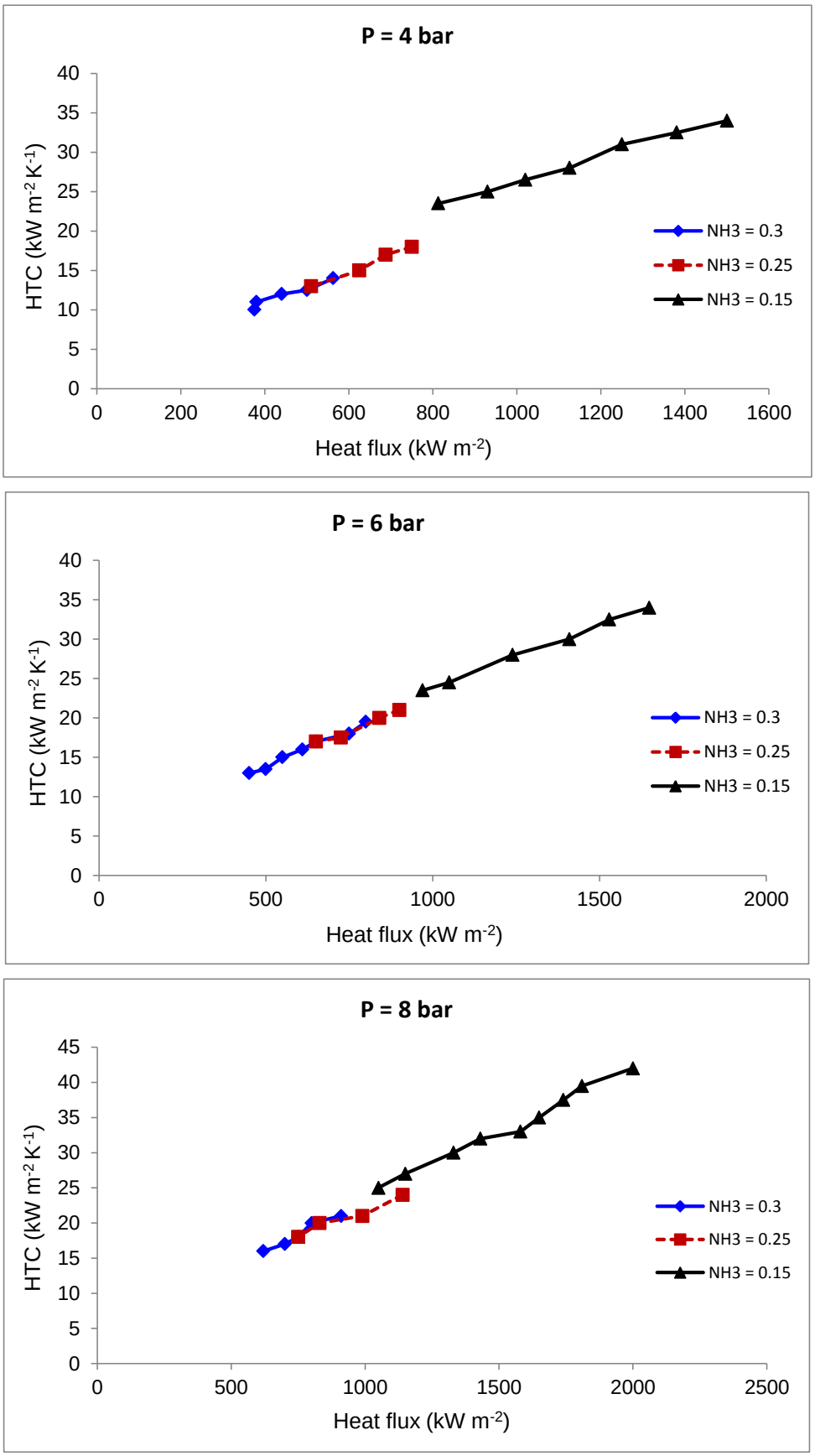

Figure 6.27: Variation of HTC with heat flux at different desorber pressures & NH_3 conc. (Adapted from Sathyabama et al [17])

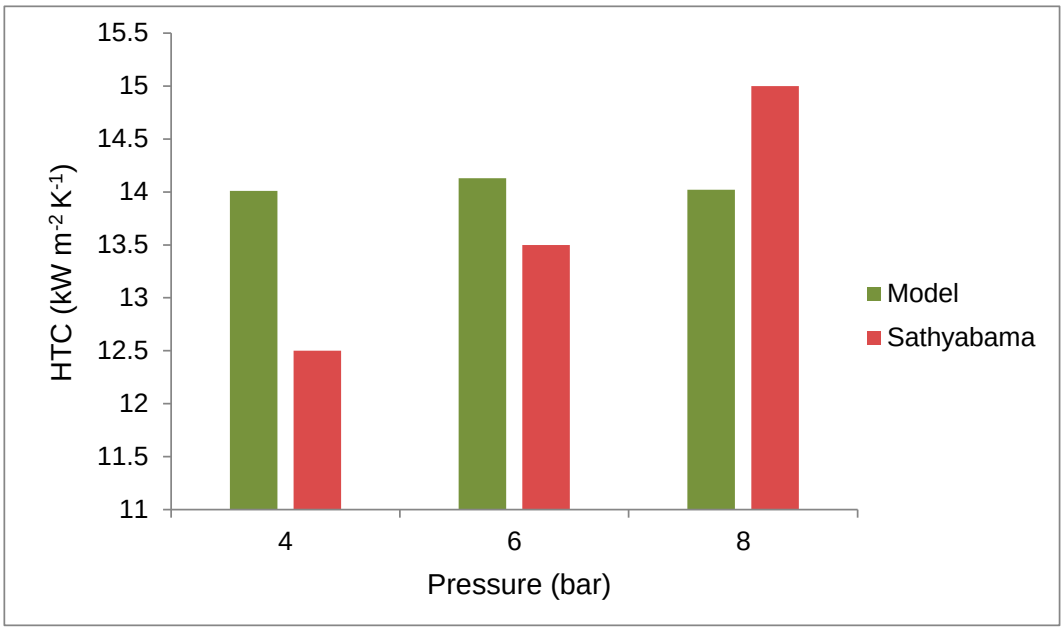

Figure 6.28: Comparison between HTC values obtained from Model and Sathyabama [17]

Since the temperature of the solution is below 100 ^{o}C, boiling of water might not occur and the vapour generated might be greater than or equal to 90% pure in NH_3. This will eliminate the need for a rectifier or a very simple rectifier will be needed to purify the refrigerant. This is an added advantage of using the heat pipe integrated desorber. At a pressure of 10 bar, the boiling temperature of water is around 180 ^{o}C so only preferential evaporation of NH_3 will take place. The bubble point and dew point curves for the NH_3-H_2O solution at a pressure of 10 bar are shown in Figure 6.29. The NH_3 mass fraction in the vapour phase will be around 0.9 and this data is used in the EES model outlined in the section below.

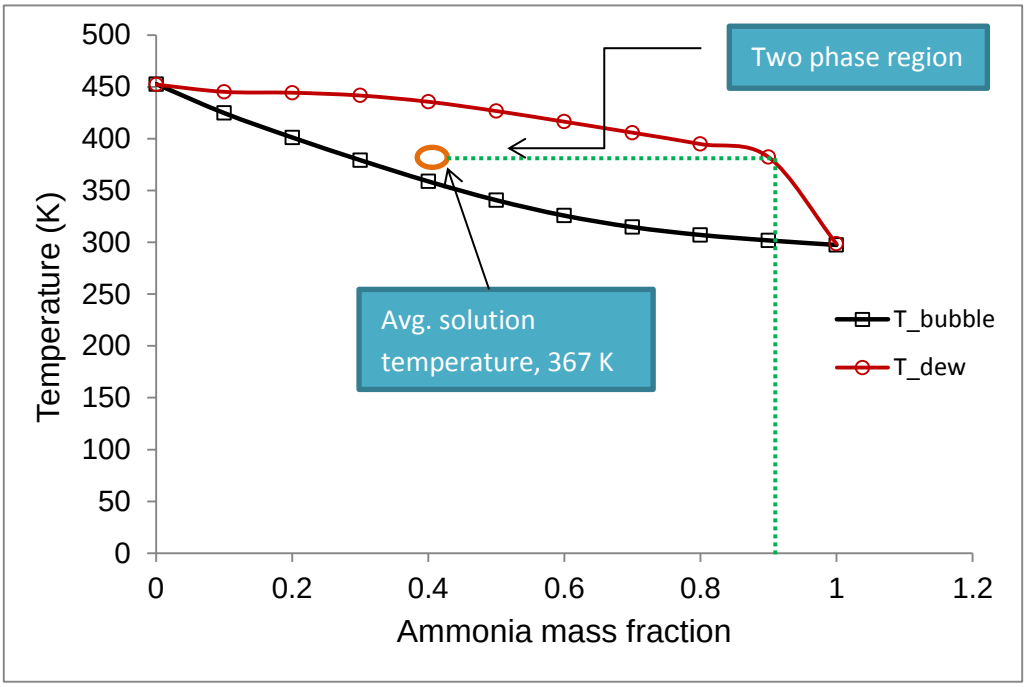

Figure 6.29: Bubble point and dew point curves for NH_3-H_2O solution at P = 10 bar

6.4.3.3 EES modelling of the complete desorber

The quantity and mass fraction of the vapour (refrigerant) generated from the heat pipe integrated desorber can be found by developing a black box model of the desorber in EES, using the data obtained in the previous sections. The black box model is developed by writing energy and mass balance equations for the flows entering and leaving the desorber.

Overall mass balance

$$m_1 = m_2 + m_3 \qquad \textbf{Eq. 6.33}$$

NH_3 mass balance

$$m_1 x_1 = m_2 x_2 + m_3 x_3 \qquad \textbf{Eq. 6.34}$$

Overall energy balance

$$m_1 h_1 + Q_G = m_2 h_2 + m_3 h_3 \qquad \textbf{Eq. 6.35}$$

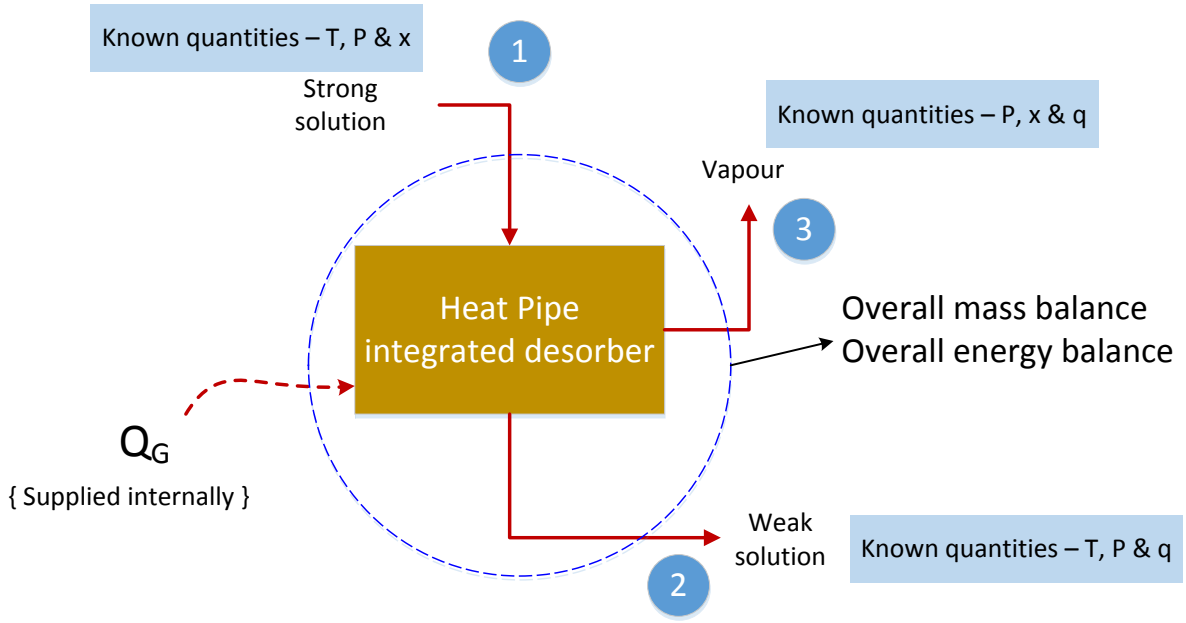

Figure 6.30: Black box approach to model the heat pipe integrated desorber (Respective state points mentioned)

Where,

m_1	Mass flow rate of strong solution, at state point 1 (kg s^{-1})
m_2	Mass flow rate of weak solution after desorption of refrigerant, at state point 2 (kg s^{-1})
m_3	Mass flow rate of vapour desorbed, at state point 3 (kg s^{-1})
x_1	Mass fraction of NH_3 in the strong solution, at state point 1
x_2	Mass fraction of NH_3 in the weak solution, at state point 2
x_3	Mass fraction of NH_3 in the vapour desorbed, at state point 3
h_1	Enthalpy of strong solution entering the desorber (kJ kg^{-1})
h_2	Enthalpy of weak solution leaving the desorber (kJ kg^{-1})
h_3	Enthalpy of vapour generated (kJ kg^{-1})
Q_G	Heat supplied to the desorber by heat pipes (kW)

The following input conditions mentioned in Table 6.10 are applied to the model

Table 6.10: Input conditions to the EES model

Parameter	State point	Value
Mass flow rate of strong solution	1	7 g s^{-1}
Inlet temperature of strong solution	1	80 ^{o}C
Outlet temperature of weak solution (same as the steady state solution temperature)	2	96.55 ^{o}C
Operating pressure of desorber	1,2,3	10 bar
NH_3 mass fraction in the solution	1	0.4
NH_3 mass fraction in the vapour	3	0.9
Quality of solution	2	0
Quality of vapour	3	0.99

(Quality refers to state of the fluid, a value of 0 indicates complete liquid and a value of 1 indicates complete vapour)

At each state point if three thermodynamic properties are known, the remaining thermodynamic properties can easily be calculated because EES has built-in functions to calculate them. Thermodynamic properties known at different state points are also shown in Figure 6.30.

For the initial input conditions, the thermodynamic properties calculated at different state points are mentioned in Table 6.11.

Table 6.11: Thermodynamic properties at different state points for initial input conditions

State point	$\dot{m}$ (g s^{-1})	T (^{o} C)	p (bar)	h (kJ/kg)	x (kg/kg)
1	7	80	10	128.1	0.4
2	6.15	96.55	10	219.8	0.3314
3	0.845	106.5	10	1592	0.9

For the initial input conditions, the heat input required at the desorber is 1.8 kW and the amount of refrigerant generated is around 0.85 g s^{-1}. This is exactly the amount of refrigerant required to generate 1 kW of cooling load as mentioned in *Chapter 3*. With the given initial conditions, the desorber requires more heat input than what can be transported by the bank of heat pipes. Hence two more heat pipes need to be added or the conditions at the

desorber need to be altered. A parametric analysis is thus required where different parameters are varied one at a time in order to evaluate the best inlet conditions required at the desorber.

Variation in inlet solution temperature:

If the inlet solution temperature is increased then the amount of heat to be supplied at the desorber is reduced. This is shown in Figure 6.31.

The ideal temperature of the solution is between 84 ^{o}C and 87 ^{o}C for which the heat input to the desorber varies between 1.5 kW and 1.1 kW (boxed area in the figure). The inlet solution temperature cannot be greater than this because the heat input required will drop below 1 kW and the COP will tend to become greater than 1 for a 1 kW cooling load which is both theoretically and practically not possible in a single stage VARS (with NH_3-H_2O).

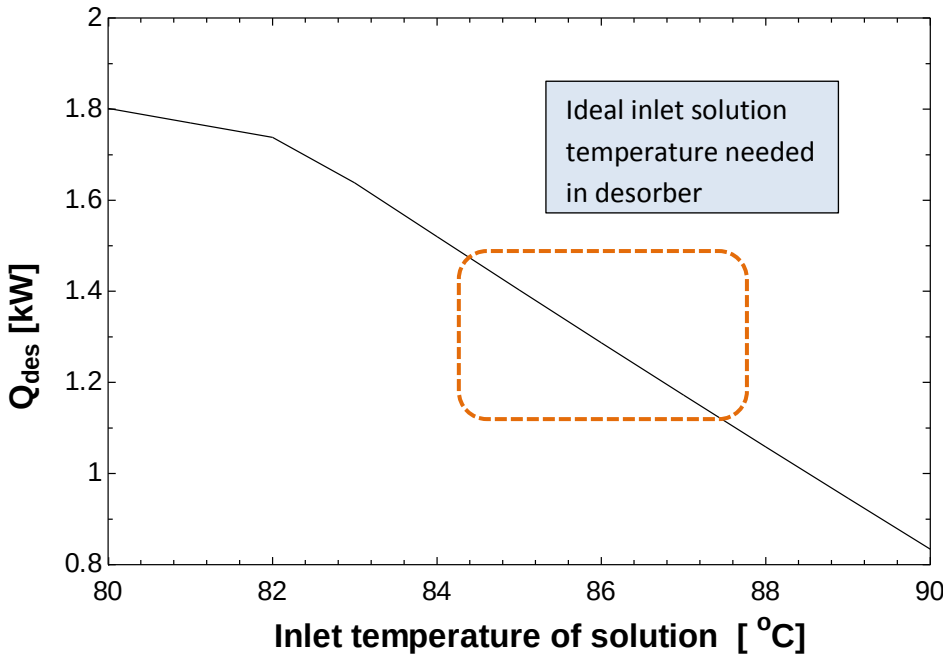

Figure 6.31: Variation of desorber heat input with inlet solution temperature

Variation in desorber pressure

The role of the desorber pressure in determining the bubble point temperature of the solution was mentioned in the previous section. The desorber pressure could also play a role in determining the amount of heat required at the desorber as seen from Figure 6.32.

The temperature of the weak solution (state point 2) is determined by the combination of the desorber pressure and the solution concentration. Hence, if the desorber pressure is varied then the temperature at state point 2 also needs to be changed in the input conditions in the EES model.

For the base case ammonia fraction of 0.4, the desorber pressure can be increased from 10 bars to 12 bars, beyond which the bubble point temperature becomes greater than the solution temperature and no boiling of the solution would take place. With increase in pressure, the heat input required at the desorber is reduced however the difference between the bubble point temperature and the actual solution temperature becomes smaller. Although the solution still stays in the two phase region, the solution temperature just hovers close to the bubble point temperature which can be quite tricky because any slight change in other parameters might affect the solution temperature from reaching the bubble point temperature and in turn prevent the solution from boiling and generating any refrigerant.

Hence the desorber pressure needs to be fixed giving more weight to the fact that the solution temperature must be greater than the bubble point temperature. The difference in temperature (ΔT) between the bubble point temperature and the actual solution temperature vs desorber pressure is plotted in Figure 6.33.

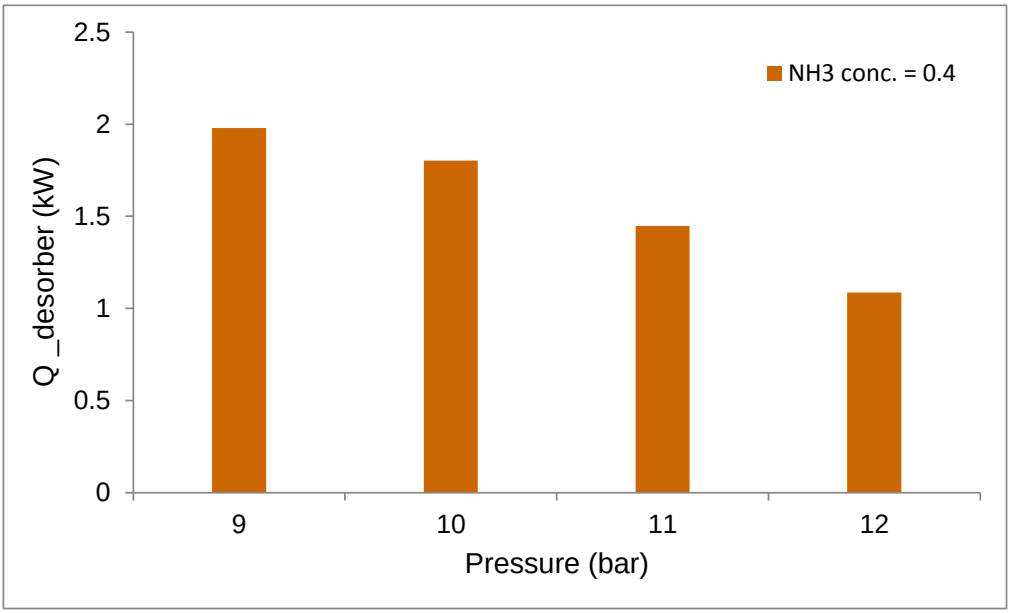

Figure 6.32: Variation of desorber heat input with pressure

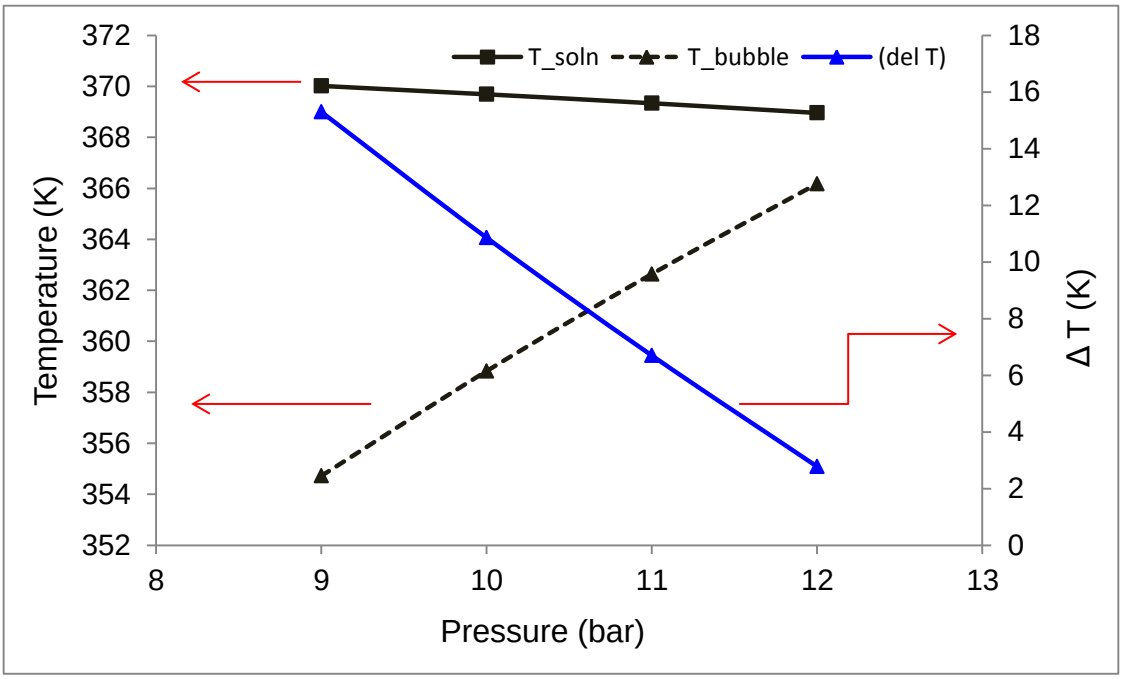

Figure 6.33: Variation of T_{SOLN}, T_{BUBBLE} and ΔT with desorber pressure

Variation in NH_3 mass fraction in the strong solution

The ammonia mass fraction in the solution also plays a key role in determining the amount of heat input required at the desorber. Increasing the NH_3 mass fraction warrants higher heat input at the desorber because more heat will be needed to desorb ammonia out of the solution for the same conditions desired of the vapour at the outlet of the desorber. The variation in heat needed at the desorber with NH_3 mass fraction is shown in Figure 6.34.

Once again in the present case each heat pipe can supply only 250 W of heat and a bank of six heat pipes can supply a total of 1.5 kW of heat. So the ammonia concentration needs to be restricted between 0.36 and 0.4. Having a lower ammonia concentration is also good from a toxicity point of view. But lower mass fractions will increase the bubble point temperature. A balance thus needs to be achieved between the heat input required at the desorber and the bubble point temperature of the solution.

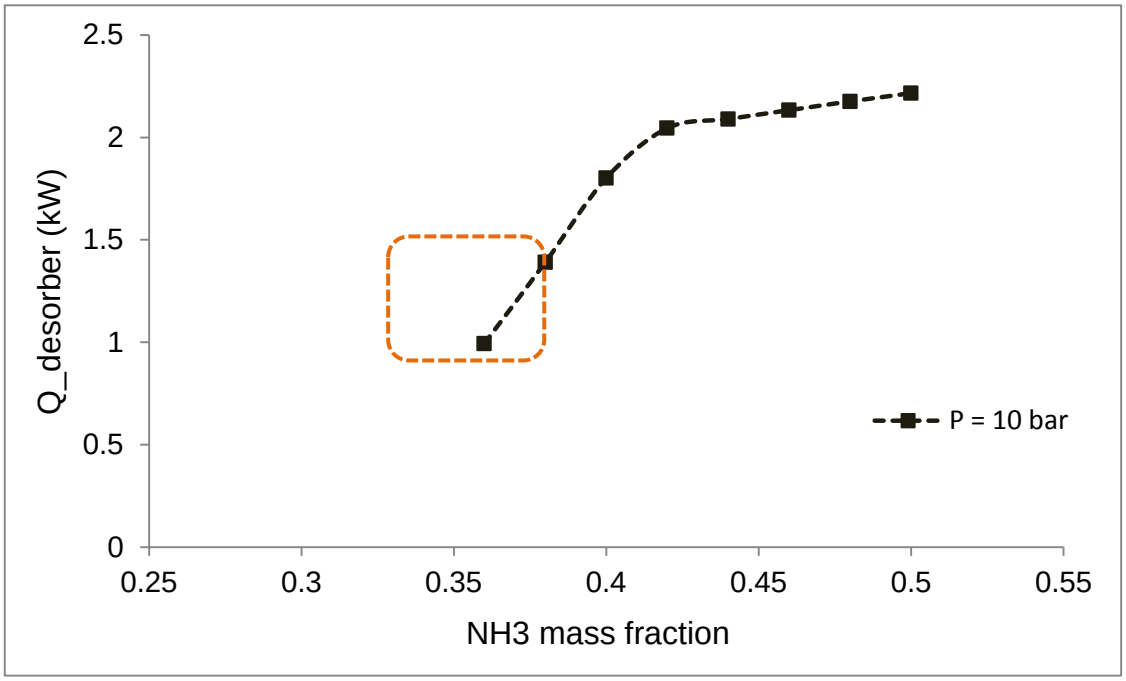

Figure 6.34: Variation of desorber heat input with NH_3 mass fraction

Amount of refrigerant generated

The ultimate goal of the EES model is to calculate the following quantities:

- Mass flow rate of vapour
- Mass flow rate of weak solution
- Desorption ratio
- Outlet temperature of vapour
- Outlet temperature of weak solution
- Heat required at desorber and heat supplied by heat pipes

The above quantities are calculated for three different desorber pressures and the results are tabulated in Table 6.12. For a fixed amount of strong solution, the amount of vapour generated and desorption ratio increases with decrease in desorber pressure. This could be attributed to the fact that with decrease in pressure, the solution tends to be more in the two phase region (at the fixed operating conditions mentioned earlier) thereby generating more refrigerant.

Table 6.12: Output quantities from heat pipe desorber at different pressures ($T_{SOLN,IN}$ = 85 ^{o}C)

Output Quantities	P = 9 bar	P = 10 bar	P = 11 bar
$\dot{m}_{strong}$ **(g s^{-1})**	7	7	7
$\dot{m}_{vapour}$ **(g s^{-1})**	1.06	0.845	0.62
$\dot{m}_{weak}$ **(g s^{-1})**	5.93	6.16	6.38
Desorption ratio	0.15	0.12	0.00885
Outlet temperature of vapour (^{o} C)	103.3	106.5	109.4
Outlet temperature of weak solution (^{o} C)	96.87	96.54	96.19
Heat required at desorber (kW)	1.401	1.402	1.289
Heat supplied by heat pipes (kW)	1.5	1.5	1.5

The outlet vapour temperature increases with increase in desorber pressure which means the enthalpy of the vapour is increased. This is because both the bubble point and dew point temperature increase with increase in pressure which in turn causes the vapour temperature to rise.

Depending on the amount of cooling load required (at a refrigeration temperature of -20 ^{o}C), the heat pipe integrated desorber can be operated at any of the above pressures. Also the heat input required is below the maximum limit that can be supplied by the heat pipe bank. For a 1 kW cooling load, the mass flow rate of refrigerant needed is 0.85 g s^{-1}. Hence, the heat pipe integrated desorber needs to be operated at either 9 bar or 10 bar, with a strong solution mass flow rate of 7 g s^{-1}.

6.5 Conclusions

The concept of a heat pipe integrated desorber was developed and three different designs for coupling it to an SOFC stack were presented. Among the three designs, the one that harnesses heat from the cathode exhaust was found to be most flexible and feasible and hence was chosen as the design to proceed with. An analysis was also performed on finding a suitable working fluid for the heat pipe at the required heat pipe operating temperature which in turn is governed by the vapour temperature inside the heat pipe.

Water was found to be the best candidate for use as the heat pipe fluid and thermex was the next best candidate. It was also found that the ideal positioning of the heat pipe is not 90^{o} wrt the horizontal but 10^{o} wrt horizontal because keeping the heat pipe vertical to the ground increases the axial hydrostatic pressure drop which in turn hinders the heat transport capability of the heat pipe.

The main advantage of using a heat pipe integrated desorber design is the complete elimination of the coupling fluid circuitry and its associated components. The required heat transfer needed at the desorber now takes place via heat pipes. Besides that, the desorber also serves as a storage tank thereby eliminating the need for a separate storage tank within the VARS unit. The desorber along with the heat pipes is completely modular which helps if the heat pipe or the casing or both are to be replaced.

A complete model was developed right from coupling the evaporator end of the heat pipe with the cathode exhaust of SOFC to coupling the condenser end of the heat pipe with NH_3-H_2O solution. A fundamental model of the heat pipe from basic principles was generated and design parameters for both the heat pipe and the desorber were specified to cater to a 1 kW cooling load at a refrigeration temperature of -20 ^{o}C.

Bibliography

1. Silverstein C.C, *Design and technology of heat pipes for cooling and heat exchange*. 1992: Hemisphere publishing corporation.
2. Dillig M, Leimert J, and Karl J, *Planar High Temperature Heat Pipes for SOFC/SOEC Stack Applications.* **Fuel Cells**, 2014. **14**(3): p. 479-488.
3. Dillig M, Meyer T, and Karl J, *Integration of Planar Heat Pipes to Solid Oxide Cell Short Stacks.* **Fuel Cells**, 2015. **15**(5): p. 742-748.
4. http://cordis.europa.eu/result/rcn/47851_en.html. (Last accessed Sept 2016)
5. Niemasz J, et al. *High temperature membrane fuel cell with integrated heat pipe*. in *PowerMEMS workshop*. 2007. Freiburg, Germany.
6. Firat E, et al. *Heat Pipe Assisted Thermal management of a HT PEMFC stack*. in *COMSOL conference*. 2012. Milan.
7. Supra J, et al., *Design and Experimental Investigation of a Heat Pipe Supported External Cooling System for HT-PEFC Stacks.* **Journal of Fuel Cell Science and Technology**, 2013. **10**(5): p. 051002-051002.
8. Fryda L, et al., *Exergetic analysis of solid oxide fuel cell and biomass gasification integration with heat pipes.* **Energy**, 2008. **33**(2): p. 292-299.
9. Oro M.V and Bazzo E, *Flat heat pipes for potential application in fuel cell cooling.* **Applied Thermal Engineering**, 2015. **90**: p. 848-857.
10. Santhanam S, et al., *Thermodynamic modeling and evaluation of high efficiency heat pipe integrated biomass Gasifier–Solid Oxide Fuel Cells–Gas Turbine systems.* **Energy**, 2016. **109**: p. 751-764.
11. Tetuko A.P, Shabani B, and Andrews J, *Thermal coupling of PEM fuel cell and metal hydride hydrogen storage using heat pipes.* **International Journal of Hydrogen Energy**, 2016. **41**(7): p. 4264-4277.
12. Lee H.S, *Thermal Design: Heat Sinks, Thermoelectrics, heat Pipes, Compact Heat Exchangers and Solar cells*. 2010: **Wiley**. 180-237.
13. Inoue T and Monde M, *Prediction of pool boiling heat transfer coefficient in ammonia/water mixtures.* **Heat Transfer—Asian Research**, 2009. **38**(2): p. 65-72.
14. Arima H, Monde M, and Mitsutake Y, *Heat transfer in pool boiling of ammonia/water mixture.* **Heat and Mass Transfer**, 2003. **39**(7): p. 535-543.

15. Inoue T, Monde M, and Teruya Y, *Pool boiling heat transfer in binary mixtures of ammonia/water.* **International Journal of Heat and Mass Transfer**, 2002. **45**(22): p. 4409-4415.

16. Táboas F, et al., *Pool boiling of ammonia/water and its pure components: Comparison of experimental data in the literature with the predictions of standard correlations.* **International Journal of Refrigeration**, 2007. **30**(5): p. 778-788.

17. Sathyabhama A and Ashok Babu T.P, *Experimental investigation in pool boiling heat transfer of ammonia/water mixture and heat transfer correlations.* **International Journal of Heat and Fluid Flow**, 2011. **32**(3): p. 719-729.

18. Pátek J and Klomfar J, *Simple functions for fast calculations of selected thermodynamic properties of the ammonia-water system.* **International Journal of Refrigeration**, 1995. **18**(4): p. 228-234.

19. Inoue T, et al., *Pool boiling heat transfer in binary mixtures of ammonia/water: Effect of heat of dilution and dissolution on heat transfer coefficient.* **Heat Transfer—Asian Research**, 2002. **31**(4): p. 272-283.

20. Peyghambarzadeh S.M, et al., *Experimental and theoretical study of pool boiling heat transfer to amine solutions.* **Brazilian Journal of Chemical Engineering**, 2009. **26**: p. 33-43.

21. Sathyabhama A. and Ashok Babu T.P, *Experimental study of nucleate pool boiling heat transfer to ammonia–water–lithium bromide solution.* **Experimental Thermal and Fluid Science**, 2011. **35**(6): p. 1046-1054.

7

Conclusions, perspective & scope for future work

"*It always seems impossible until it's done*" **Nelson Mandela**

Based on the results presented in the previous chapters, appropriate conclusions are drawn and presented in this chapter. In short, a holistic picture is provided on how different results can be combined to achieve the desired objective. A generalised design guideline and some generalised graphs are presented in this chapter.

7.1 Overview

This thesis explored the facets of integrating a Solid Oxide Fuel Cell (SOFC) with a Vapour Absorption Refrigeration System (VARS) for a refrigerated truck application and identified the system integration and design strategy which, if employed, will make application of such systems feasible on trucks. Besides system integration, detailed component level modelling of two different kinds of desorbers was also carried out.

Refrigerated trucks powered by diesel engines and fitted with vapour compression systems have their own set of problems such as engine idling, increased levels of noise, low efficiency and increased emissions. A lot of research is being carried out on alternate truck refrigeration and air conditioning systems not only at the system level but also at the fundamental level, as mentioned in *Chapter 2*. Among fuel cells, Solid Oxide Fuel Cells in particular have been used as APUs (Auxiliary Power Units) on trucks in order to reduce the load on the main diesel engine. SOFCs not only generate electricity but also high quality heat. Harnessing and utilising this high quality heat to drive a thermally driven refrigeration system on-board the truck has been the core idea of this thesis.

Through the results and discussion provided in the previous chapters, it is possible to say with confidence that it is indeed feasible to develop a compact thermally driven refrigeration system, provided heat exchangers and other heat transfer devices are custom designed for the specific application(s).

Absorption refrigeration technology is not something new and has been employed for large scale systems already but absorption refrigeration technology for vehicles (<20 kW cooling) is something that the research community needs to explore further. The technical challenges involved with design and development of absorption refrigeration technology at a small scale

are not that straight-forward because the respective devices need to have the required thermal performance at a small scale [1] and this warrants research both at the fundamental and design level. One example is the reduction in surface area available for heat transfer at a small scale and scaling down a particular design of a large scale component to a smaller size will not lead to a similar scaling down in performance. Also if a compact component has to achieve the same performance as a large scale component then design changes are a must.

The desorber and the absorber are the key components in an absorption refrigeration system and in order to develop a compact thermally driven refrigeration unit it is absolutely necessary to have these two components as compact as possible and at the same time not compromise on thermal performance. If both these components can be packaged in a volume space otherwise occupied by the compressor of a vapour compression system, then realisation of thermally driven refrigeration systems for trucks is not far away.

7.2 Research questions addressed

The ongoing project involves development of transportation systems that have low CO_2 emissions, preferably with fuel cells. Within the broad objective (of the ongoing project) which is to develop a complete compact thermal refrigeration unit for a truck, this study sought out to answer the following research questions stated in the introductory chapter.

i) What should the operating point of the fuel cell be on the polarisation curve for such an application?

ii) Should heat be taken directly from the inside of the fuel cell or from the exhaust streams?

iii) *Will fuel utilisation affect the exhaust flow rate from the fuel cell stack? If yes/no then how will the operating point on the polarisation curve shift?*

iv) *The high temperature fuel cell and the thermally driven refrigeration system operate at different temperatures, how can they be thermally integrated?*

v) *The present day thermally driven refrigeration units are all of very large size. How can compact components be used and what will be the effect on performance?*

Answers to the above questions obtained from the modelling and simulation studies carried out lay the foundations for development of a working prototype which would be the next step of the project.

The operating point on the fuel cell polarisation curve provides information on three things – the ***electrical efficiency*** of the fuel cell, the ***voltage*** at which the fuel cell is operated and the ***electrical power*** of the fuel cell. If the heat from the SOFC is to be used for a particular application then in order to have enough thermal energy, the SOFC has to be operated at a particular point on the polarisation curve. Operation of the fuel cell at a higher current density will generate more heat and vice versa. As shown in Figure 7.1, there is a certain crossover point at which the amount of electrical and thermal power generated within the SOFC is equal.

For a thermally driven refrigeration system, the SOFC needs to be operated at a said current density which would generate sufficient thermal energy which can then be extracted by the exhaust streams. The polarisation curve of an SOFC single cell is shown in Figure 7.2. The high thermal energy generation region and the high electrical efficiency region are clearly marked for the practical window of operation of the SOFC.

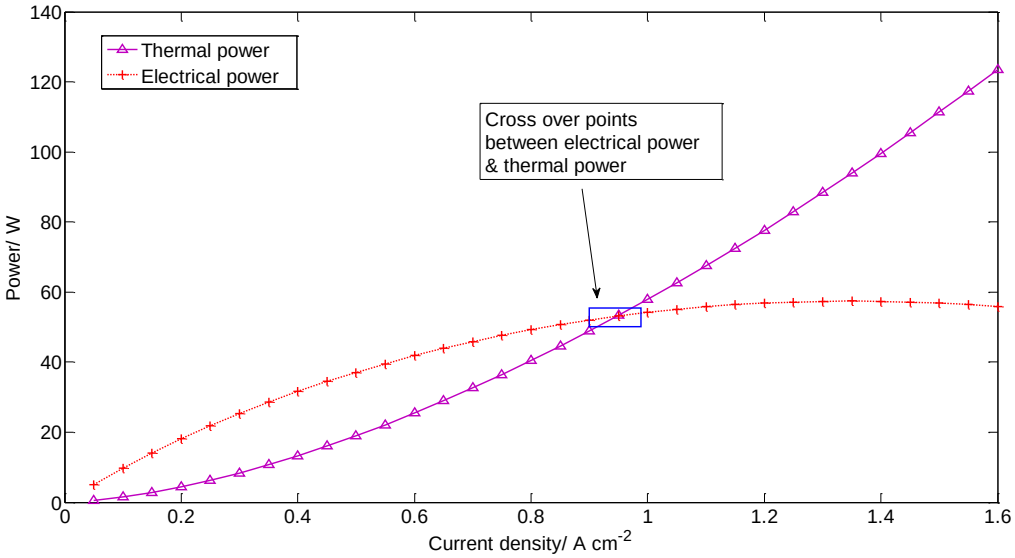

Figure 7.1: Electrical and thermal energy generated in an SOFC single cell
(Operating temperature 1023 K)

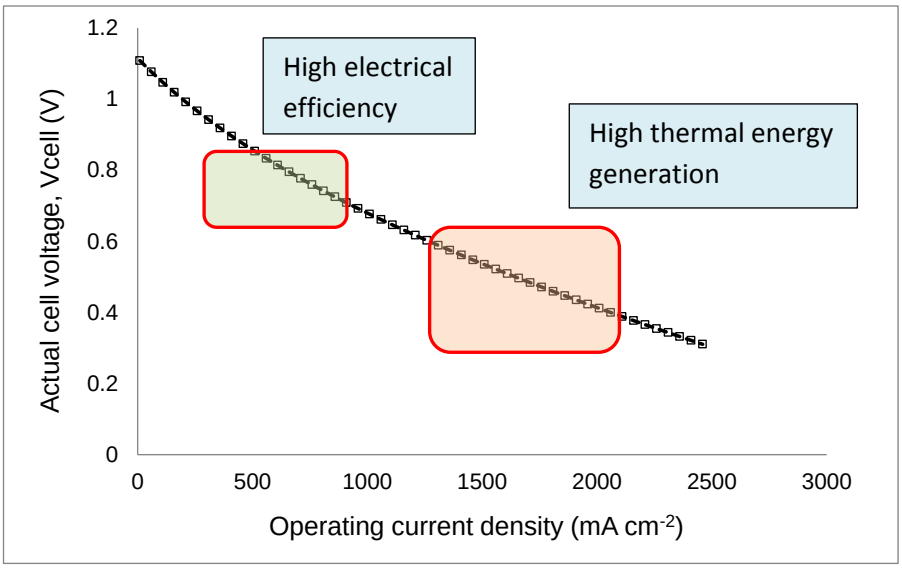

Figure 7.2: Polarisation curve of an SOFC single cell
(The region marked is the practical windows of operation)

The size of the SOFC stack needed in order to cater to the thermal input requirements of the VARS ranged from a 1 kWe stack for a small truck (1 ton gross weight) that needed 700 W

of cooling at a refrigeration temperature of -20 ^{o}C to an 8 kWe stack for a large truck (40 ton gross weight) that needed about 6 kW of cooling at a refrigeration temperature of -20 ^{o}C. These details were mentioned in *Chapter 4*.

The second research question was about the method of extraction of heat. For a CHCP (Combined Heating Cooling & Power) application, the heat generated within the SOFC needs to be made use of and efficiently extracted. There are two ways in doing this – first by using heat pipes directly embedded into the stack, and the second by employing forced air cooling through the cathode manifold. The second method is the most widely used one but necessitates the need for a more powerful air blower. The first method is still in its nascent stage as seen from the limited literature available on it as mentioned in *Chapter 6*.

It is more convenient to extract heat from the exhaust streams of the SOFC rather than tap into the fuel cell stack itself. Employing methods to extract heat directly from inside the SOFC has its own set of challenges such as mechanical connection of the stack and the heat pipe, hydrogen permeation in the heat pipe due to being embedded in the SOFC stack and many more issues [2, 3]. Use of heat pipes should be done only for applications that require similar temperature levels as that of the SOFC. This is because the heat pipe itself is almost an isothermal device. Extracting heat from the exhaust streams provides a greater flexibility in the amount of heat that can be transferred as both the mass flow rate and temperature of the exhaust streams can be varied. However, the heat exchanger should be carefully designed if indirect coupling to the VARS is employed in order to maximize the amount of heat transferred because the exhaust has a low thermal heat capacity.

The next research question was about the correlation between fuel utilisation and exhaust flow rates. If the operating point on the polarisation curve is fixed, then the fuel utilisation directly affected the flow rate of the exhaust streams. This particular approach was taken because residual heat utilisation from the SOFC was of primary interest. Higher fuel

utilisation resulted in lower exhaust flow rates and vice versa. An analogy can be drawn here between the exhaust from the diesel engine and the exhaust from an SOFC. The temperature and mass flow rate of the exhaust coming from a diesel engine depends on the engine RPM. In a similar way, the exhaust flow rate from the SOFC stack depends on the fuel utilisation (anode gas) in the stack if the operating point is fixed.

To find an alternate to the conventional system on-board refrigerated trucks, two new systems *viz* the SOFC and the VARS had to be integrated. The SOFC and the VARS operate at two different temperature levels, the former operating between 700 ^{o}C and 800 ^{o}C and the latter at 200 ^{o}C. Hence it is a challenge from a heat transfer aspect to thermally connect these two systems. One way is to indirectly couple them using a coupling fluid and the other way is to directly couple them using heat pipes. Heat pipes, if used, have to be placed in the exhaust stream and not be directly embedded in the stack due to reasons explained above. It is advantageous to operate the SOFC at lower fuel utilisations when employing a coupling fluid to transfer heat to the VARS due to resulting higher exhaust flow rates and thereby increased heat transfer to the coupling fluid, details of which were elaborated in *Chapter 4*.

Volume space available on trucks:

So does the VARS unit occupy a similar volume as a VC unit? The VARS definitely employs more components than the VC system but the volume occupied by the whole VARS unit can be almost the same as a VC unit if a compact desorber and absorber are developed. The desorber and the absorber together serve as the thermal compressor and take over the role of the electric compressor (in a VC system). The list of main components for each system is given in Table 7.1. The packaging space available on different types of trucks for the integrated SOFC-VARS box is as follows:

- Small truck – 0.44 m^3
- Medium truck – 0.9 m^3
- Large truck – 2.73 m^3

These volume spaces were calculated physically on different trucks, keeping in mind the position and volume space available for current VC systems on refrigerated trucks.

If the VARS with indirect coupling is employed then it is suitable for implementation only on large and medium sized trucks given the ample amount of space available. On a small truck, it is envisaged that it would occupy too much space. But if the VARS with direct coupling is employed then there is a possibility of employing it across all three kinds of trucks.

Table 7.1: Main components of different refrigeration systems

VC system	VARS - indirect coupling	VARS - direct coupling
Compressor	Gas- liquid heat exchanger	Heat pipe exchanger
Condenser	Thermal oil storage tank	Desorber
Evaporator	Thermal oil pump	Rectifier
	Desorber	Condenser
	Rectifier	Evaporator
	Condenser	Absorber
	Evaporator	Solution pump
	Absorber	
	Solution pump	

7.3 Coupling of SOFC with VARS - General design maps

The desorber of the VARS on-board the truck can be developed as a component that is powered either directly from the exhaust of the SOFC or indirectly by a coupling fluid. Both

these methods result in compact desorber designs. In the previous chapters '0D' models of the entire VAR system and SOFC stack along with component specific models of the desorber and coupling heat exchanger were presented. With the wealth of information and data available from the modelling and simulation studies, it is imperative to formulate some general design maps for coupling the SOFC stack with the VARS. Doing so for the specific application and/or for a range of cooling capacities will complete the design loop and will provide a coherent picture on how to go about the entire simulation, design and development process. This is important from a system development perspective.

The detailed design guidelines for indirectly coupled and directly coupled systems are shown in Figure 7.3 and Figure 7.4 respectively and the schematic for the entire design process is presented in Figure 7.5.

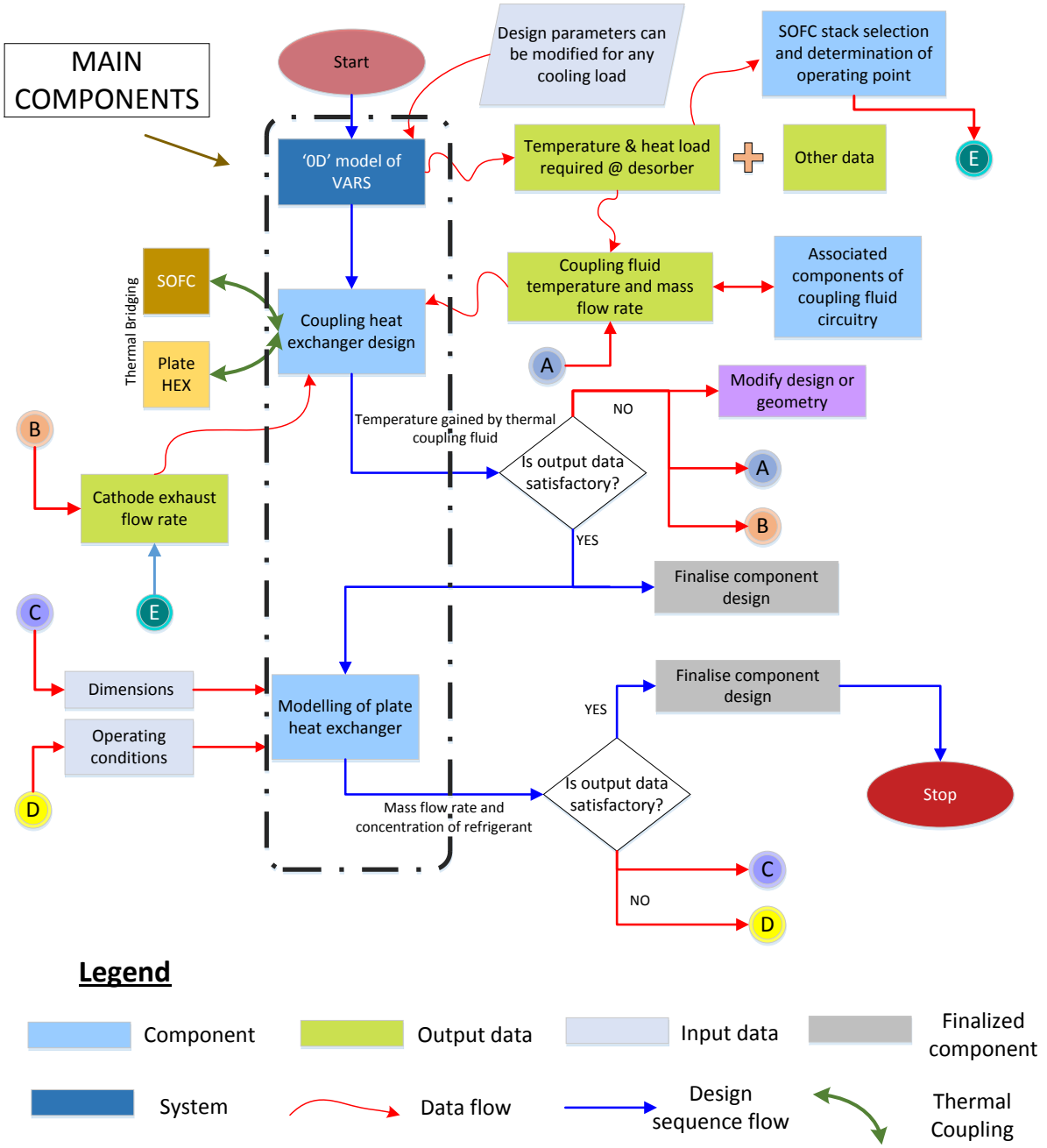

Figure 7.3: Flowchart for design of indirectly coupled SOFC-VAR system

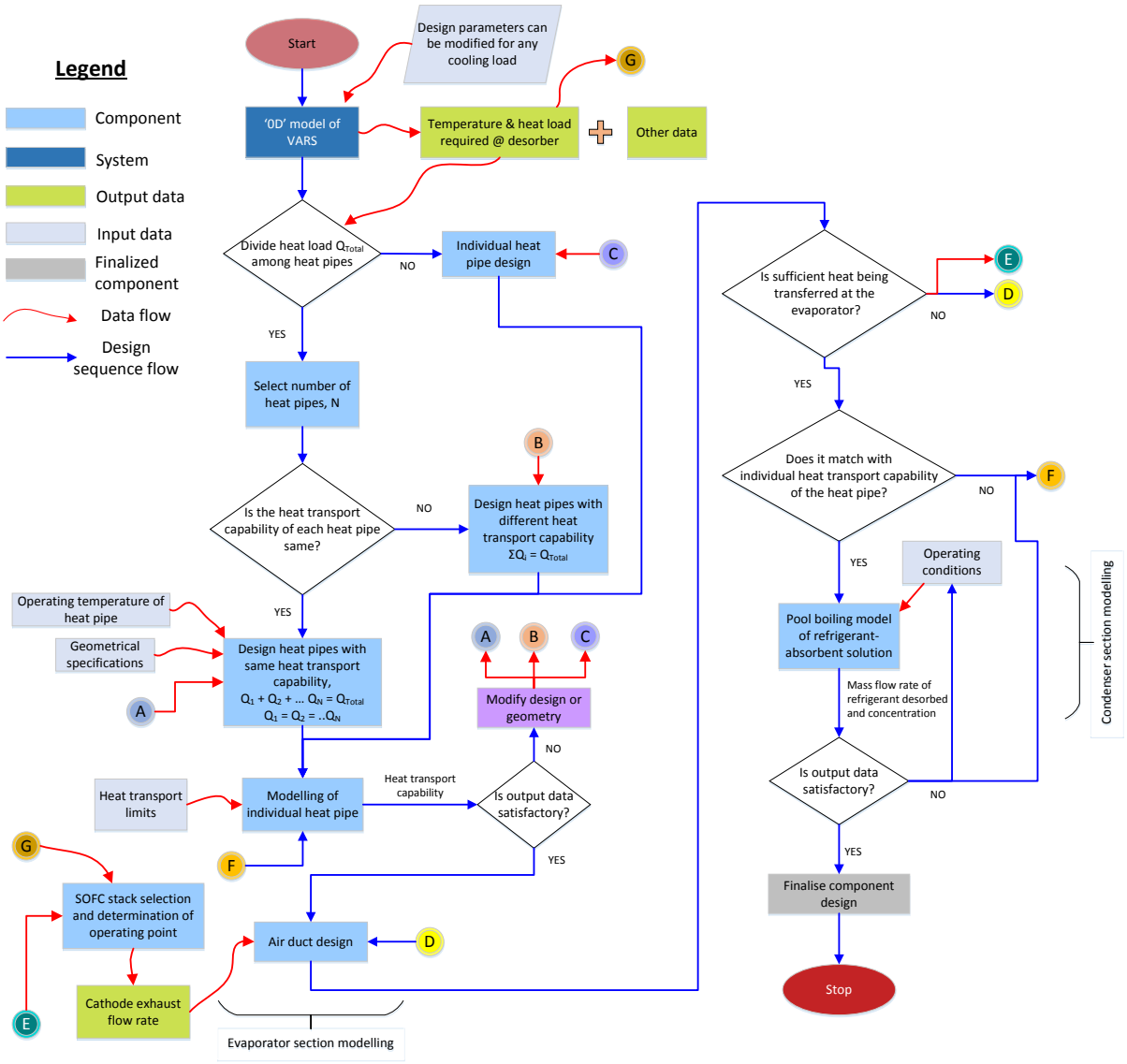

Figure 7.4: Flowchart for design of directly coupled SOFC-VAR system

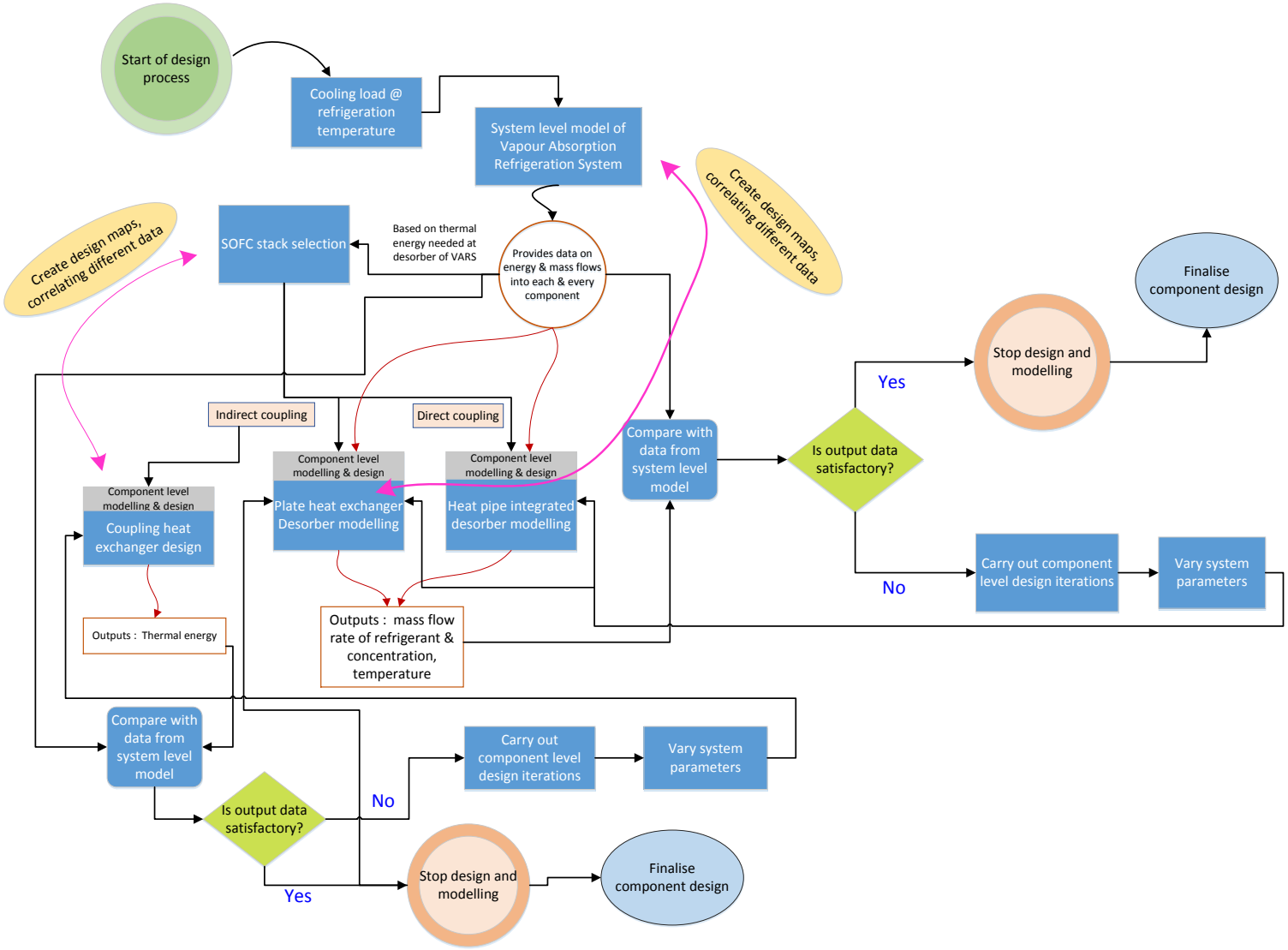

Figure 7.5: General design rules for development of compact thermally driven refrigeration systems coupled to SOFC

7.3.1 General design maps for indirectly coupled systems

It would be helpful to create some general design maps for the indirectly coupled SOFC-VAR system in order to provide information in a summary rather than go through the entire modelling and simulation work.

Figure 7.6 shows the cooling load requirements for different sizes of trucks as a function of refrigeration temperature and the respective SOFC stack size is also mentioned. This particular map is useful because it gives a first indication for the selection of the SOFC stack needed on-board the truck.

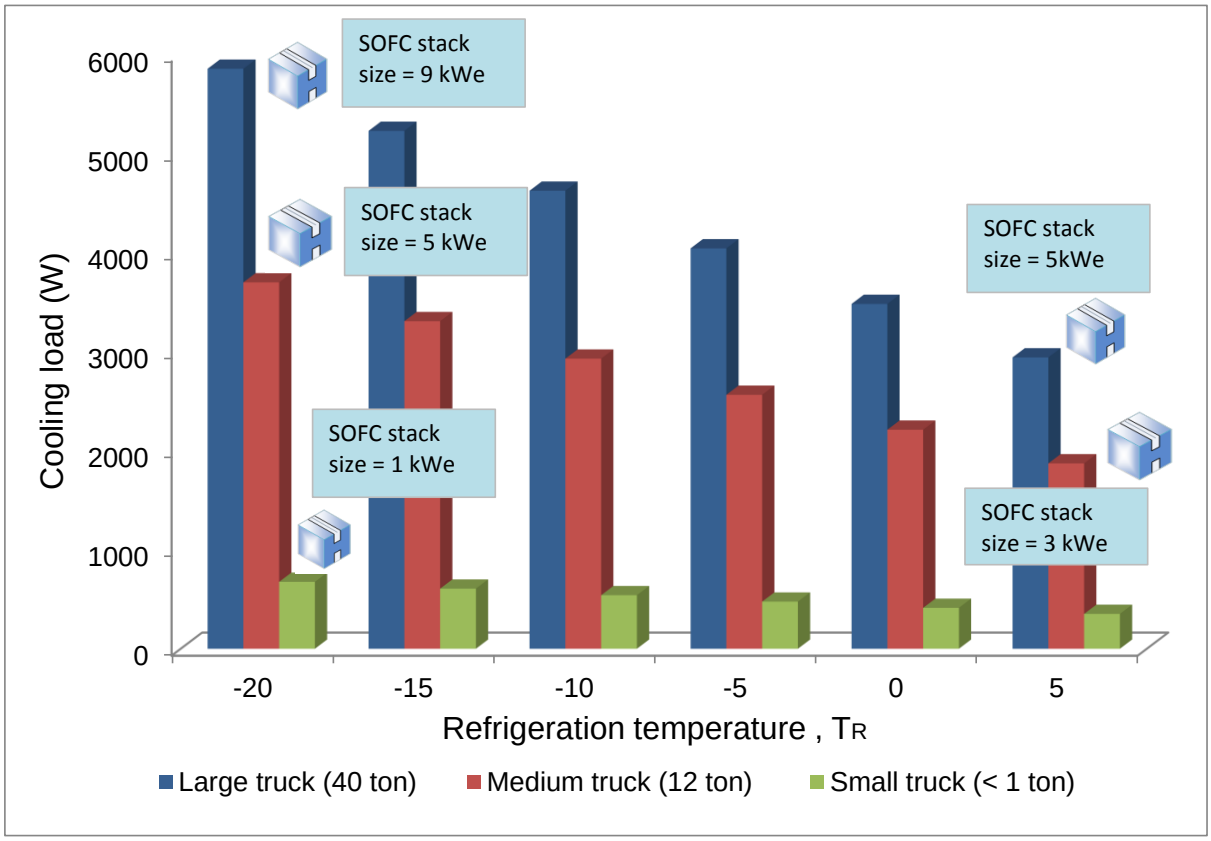

Figure 7.6: Cooling load and corresponding SOFC stack size needed for different truck sizes (This is the stack size when the SOFC is operated at the crossover point where $P_{el} = P_{thermal)}$

Figure 7.7 shows the variation of cathode exhaust flow rate with fuel utilisation for different SOFC stacks. Depending on how the stack is operated, the cathode exhaust flow rate varies and this data is useful for designing the coupling heat exchanger which thermally connects the SOFC and the desorber of the VARS.

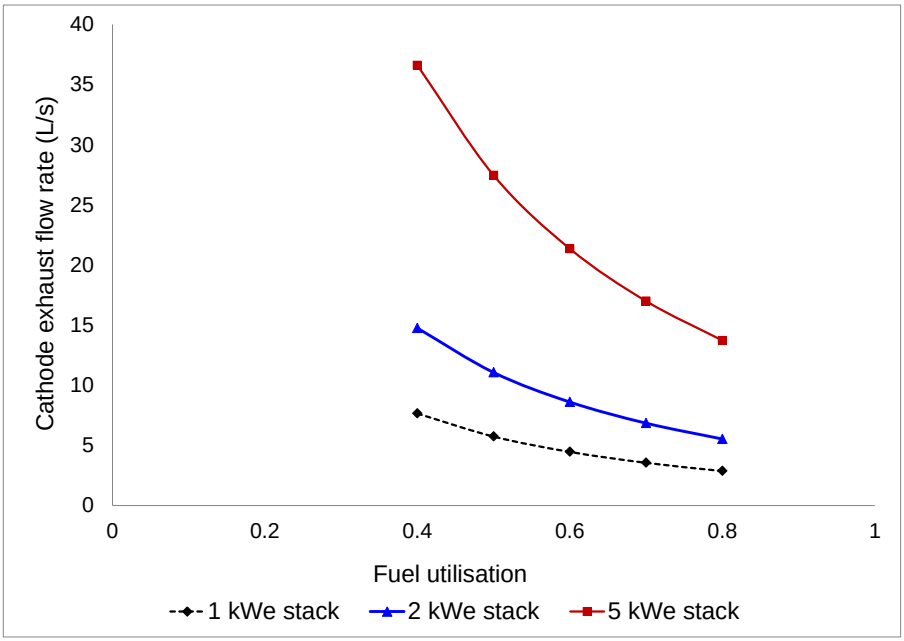

Figure 7.7: Cathode exhaust flow rate vs fuel utilisation – SOFC stacks

Detailed contour maps for heating of the thermal oil in the coupling heat exchanger (designed in this study) were presented in *Chapter 4*. It will be beneficial if the coupling heat exchanger is standardized for all three kinds of trucks and the design presented in this study has done that. The current design caters to the thermal input requirements of all three kinds of trucks just by varying the coupling fluid and SOFC exhaust flow rates. The designer has the option of making the heat exchanger even more compact provided a similar thermal performance is achieved.

The steady state cyclic operation of the coupling fluid that circulates between the coupling heat exchanger and PHE desorber should have a temperature gain and drop similar to the

graph shown in Figure 7.8. This is very essential from a steady state operational point of view.

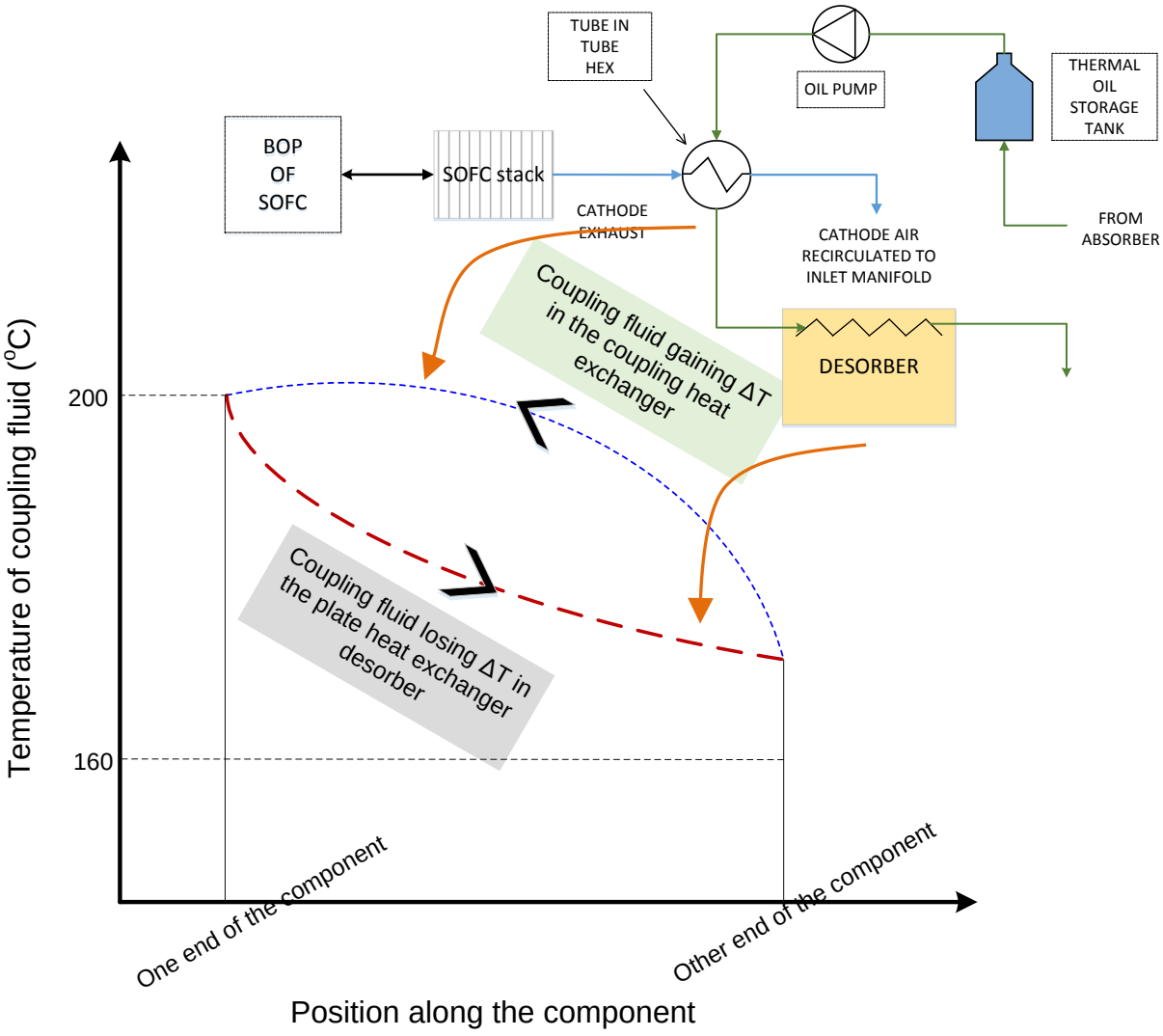

Figure 7.8: Temperature gained and lost by the coupling fluid in different components

The variation in NH_3 mass fraction with the applied heat flux in the flow channels of the PHE desorber follows the trend shown in Figure 7.9. It is desired that the NH_3 mass fraction in the vapour coming out from the desorber be 1 but this is not possible due to the thermodynamics of the refrigerant-absorbent solution. Hence the goal should be to get an NH_3 concentration as high as possible in order to reduce the rectification load (in the

rectifier). The desired NH_3 concentration in the vapour from PHE desorber is also shown in Figure 7.9. This information can also be used to size the PHE desorber.

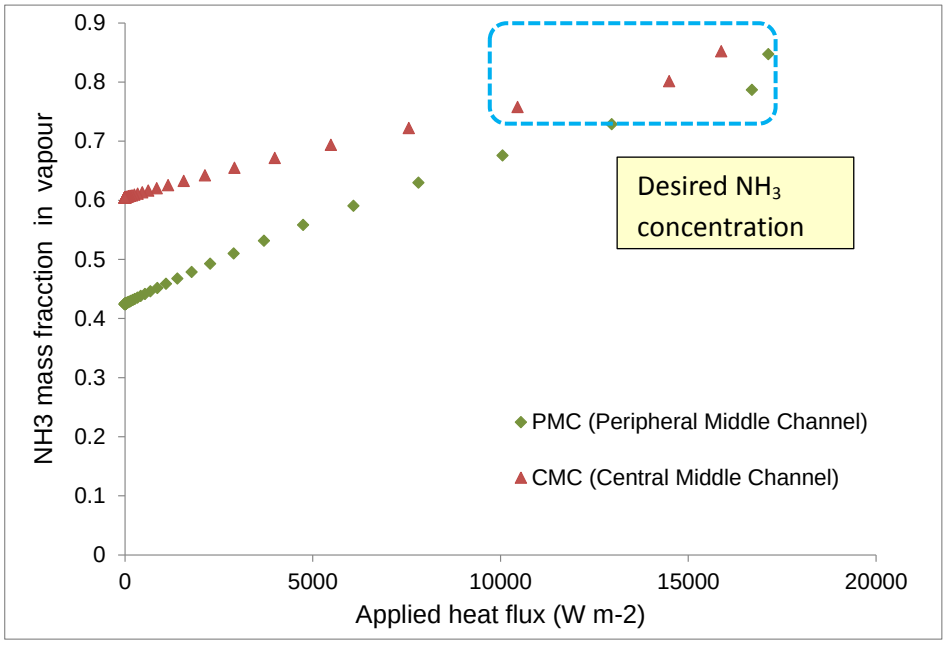

Figure 7.9: NH_3 mass fraction in vapour vs applied heat flux

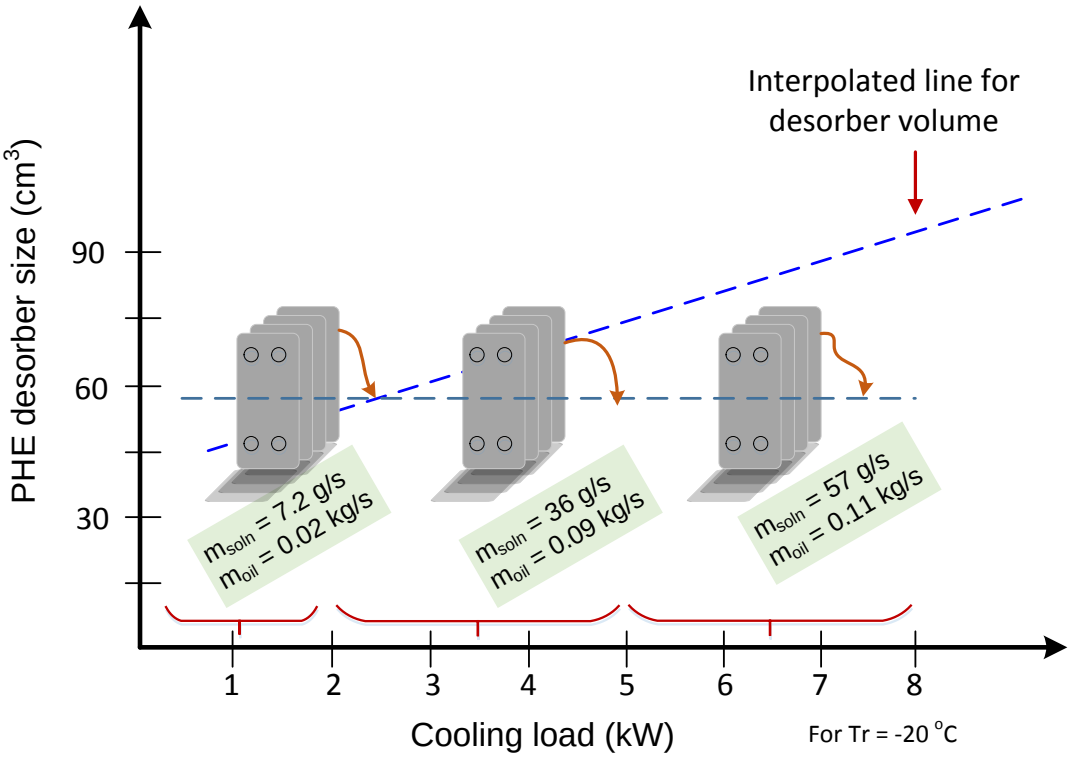

Figure 7.10: PHE desorber volume needed for different cooling loads

Figure 7.10 shows the PHE desorber volume that is needed to cater to different cooling loads. The plate heat exchanger desorber as a component can be standardized across different trucks if the mass flow rates are adjusted accordingly as seen from the horizontal line or could follow the interpolated desorber volume line for different cooling loads. The designer has absolute flexibility with regards to choosing the PHE desorber volume for different cooling loads.

7.3.2 General design maps for directly coupled systems

As with indirectly coupled systems, certain design maps can also be drawn for directly coupled systems. These will be helpful in choosing the right combinations of individual components for system integration.

Figure 7.11 shows the variation in external heat transfer coefficient (HTC) with cathode exhaust flow rate on the evaporator side of the heat pipe. This particular parameter is crucial as it governs the total heat that is absorbed by the heat pipe. The HTC values for exhaust temperatures in the range of 450-650 ^{o}C are close to the ones obtained for 550 ^{o}C and hence Figure 7.11 can be generalised for the temperature range 450-650 ^{o}C. The total heat absorbed by the heat pipe from the cathode exhaust for different exhaust temperatures is shown in Figure 7.12. This map is extremely useful in selecting both the number of heat pipes and the SOFC stack size for a particular cooling load.

Note: Both these design maps are specific to the air duct design presented in *Appendix F* and might vary slightly for other air duct designs. But nevertheless they provide useful information on the amount of heat absorbed by the heat pipes and provides a quick design guide. Also, these maps are valid only for designing heat pipes that operate at a vapour temperature of 160 ^{o}C.

The whole heat pipe desorber design process is iterative which involves many parameters. Hence providing a complete general design map is not possible.

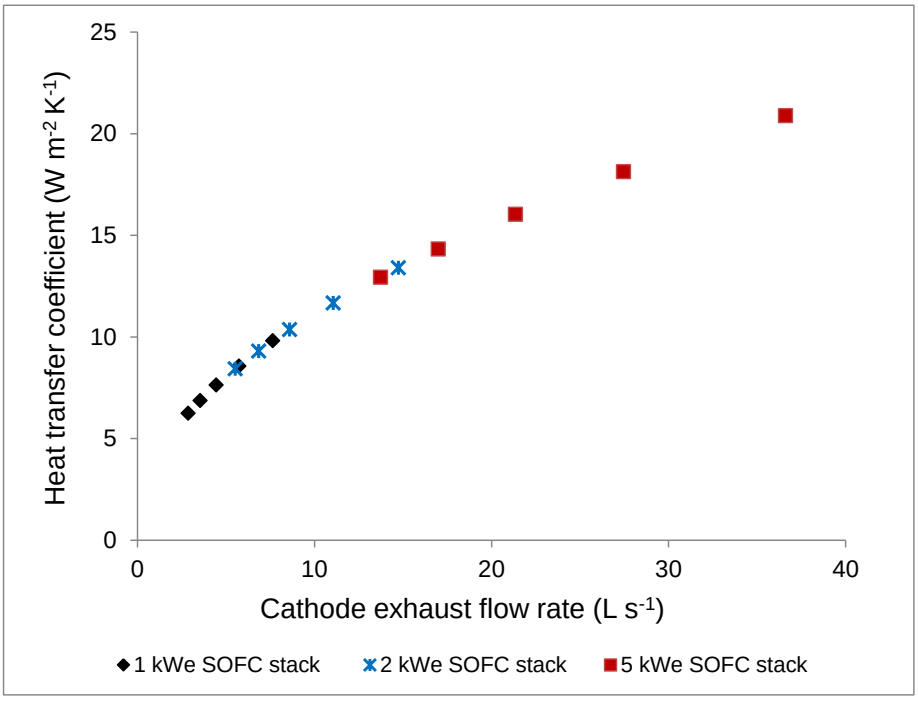

Figure 7.11: HTC vs cathode exhaust flow rate
(For cathode exhaust temperature range 450-650 ^{o}C and heat pipe operating temperature of 160 ^{o}C)

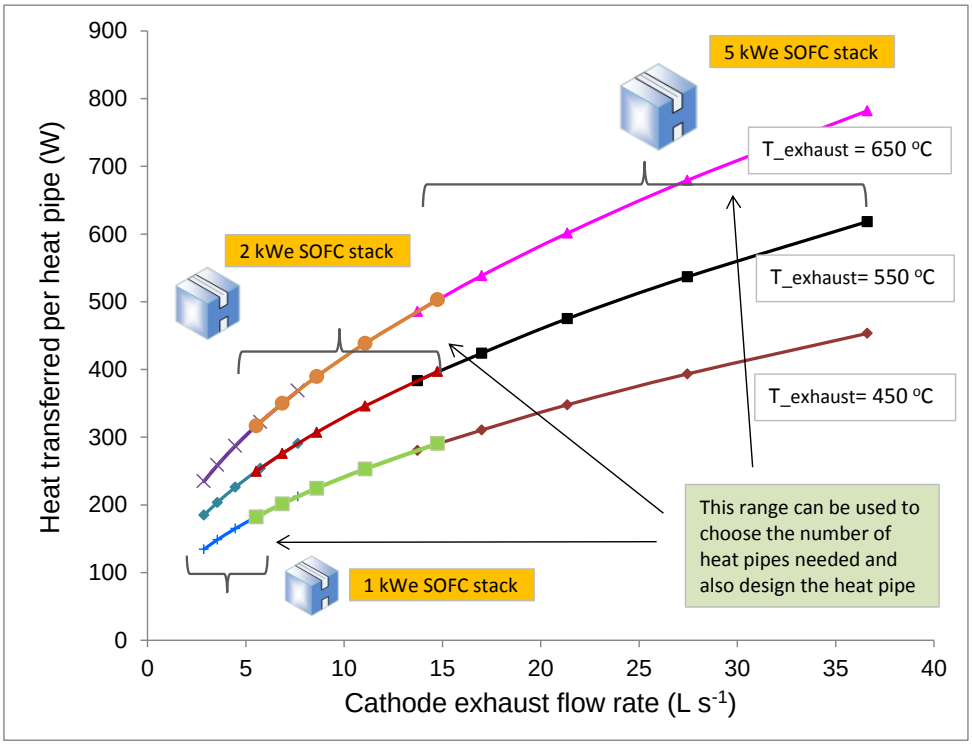

Figure 7.12: Design map for choosing SOFC stack and heat transferred per heat pipe

7.4 Key findings and Perspective

This is the first study carried out specifically for developing a compact vapour absorption refrigeration unit driven by heat from an SOFC for a refrigerated truck application. The key findings are as follows:

i) The size of the SOFC stack needed for catering to cooling loads at a particular refrigeration temperature is determined entirely from the thermal energy requirements needed at the desorber of the VARS. It was found that for a refrigeration temperature of -20 ^{o}C, the minimum size required of the SOFC stack is 1 kWe and 8 kWe in order to cater to the cooling load requirements on a small and large truck respectively.

   - The operating point along the polarisation curve of the fuel cell plays a very important role for such an application. The SOFC needs to be operated either at the crossover point or beyond it. Operation at low current densities results in insufficient heat generation. If the SOFC is operated below the cross over point, the fuel cell needs to be larger in terms of kWe rating.

ii) The amount of electrical energy generated from the stack is greater than the electrical energy requirement on the vehicle. Hence, unless the excess electrical energy is made use of, employing a thermally driven refrigeration system powered by heat from an SOFC does not make sense from an overall efficiency point of view.

iii) The desorber of the VARS can be made compact and two designs were described, as discussed in *Chapters 5* and *6*. The plate heat exchanger desorber and the heat pipe integrated desorber were both designed and modelled to cater to a 1 kW cooling load (at a refrigeration temperature of -20 ^{o}C) and it was found that they generate the required quantity of refrigerant. Although the plate heat exchanger was compact it

warranted additional components *viz.* coupling heat exchanger, pump and storage tank and this made the system bulkier.

- Heat transfer modelling of the plate heat exchanger desorber provided insights into the heat transfer process at every flow channel. The mass flow rate and concentration of the refrigerant desorbed were quantified. This is the first study carried out on the subject of modelling plate heat exchangers for refrigerant desorption and has not been reported in literature yet. Modelling at a fundamental level added to further understating of the desorption process than just using the black box approach.
- A co-flow configuration is needed in the plate heat exchanger desorber because boiling of the refrigerant-absorbent solution has to take place in the flow channels. A counter-flow arrangement will lead to superheating of the vapour at the outlet of the flow channel which is not desired.

iv) The heat pipe integrated desorber is a novel concept that has been developed in this thesis which has not been explored before. By use of a heat pipe integrated desorber, the three additional components (coupling fluid and associated circuitry) required with a plate heat exchanger desorber can be eliminated. The heat pipe integrated desorber also serves as storage tank for the NH_3-H_2O solution (or any other refrigerant-absorbent solution) which will lead to the whole VARS being more compact.

- The desorber can easily be scaled up by addition of more heat pipes.
- The working fluid and the tilt angle of the heat pipe play a major role in determining its heat transport capability.
- The heat pipe integrated desorber is a device where pool boiling of the refrigerant-absorbent solution takes place. A complete modelling scheme right from the design of the heat pipe to refrigerant desorption from the

desorber has been carried out and from the modelling results obtained it is indeed possible to develop this new kind of desorber.

Perspective

As mentioned in the literature survey chapter, besides a few patents there are almost no research papers that talk about coupling of an SOFC with a VARS for mobile/truck applications. Hence this thesis adds to the research base in this particular field.

Making use of both the residual heat and the electrical energy generated from the fuel cell on board the truck is one way to maximise the efficiency from the fuel cell. A compact thermally driven refrigeration system, when developed, will literally run on free residual thermal energy which would otherwise be dissipated away. The excess electricity generated by the SOFC can be used in hybrid powertrain configurations thereby making refrigerated trucks greener and cleaner.

In order to realise thermally driven refrigeration systems for trucks/mobile applications, it is highly desirable to develop heat exchangers that are compact. Besides that, the heat exchangers at the condenser and absorber end need to be air cooled and not water cooled because water cooling will lead to addition of extra components. Only if these two criteria can be met along with satisfactory thermal performance can small scale VARS be applied as an alternative to VC units. The air cooling of the components can be carried out in two ways:

a) With forced convection and/or
b) With heat pipes and natural/forced convection.

Using heat pipes to dissipate heat away at the condenser and absorber end is again something new that has not been explored yet.

A small scale thermally driven refrigeration unit, once developed, can be extended to the air conditioning sector where heavy electricity consuming vapour compression air conditioning units can be replaced by thermally driven cooling systems. In places with hot climates where air conditioning is a must but at the same time having the air-conditioner switched on all the while will incur a high energy cost, a compact thermally driven air-conditioning unit will certainly be of advantage. The driving force in this case can also be solar energy or any other sort of residual thermal energy with sufficient high-quality heat.

The concept of having a thermally driven refrigeration/cooling system powered by heat from an SOFC on-board a refrigerated truck seems exciting and feasible from a theoretical point of view but they come with their own set of challenges.

7.5 Scope for future work

This is an exciting project which, if taken forward, can have wider implications for reducing vehicle emissions. There are many more areas which need to be developed and requires in-depth research and analysis. If vapour absorption refrigeration technology is to replace vapour compression technology on refrigerated trucks, two key aspects need to be further analysed, namely:

- Heat transfer at the desorber without coupling fluid and
- Mini and microscale heat exchangers.

Some of the future areas in which work can be carried out are as follows:

a) Prototype construction and experimental testing of plate heat exchanger desorber and heat pipe integrated desorber and validation of results obtained from modelling.

b) Along with the desorber, the absorber is also a key component of the VARS. A compact bubble type desorber with air cooling will complete the whole package of the thermal compressor. The first step should be complete modelling and simulation of this component and comparison of results with the '0D' model of the VARS unit. This will be the 'Generation 1' absorbers.
    - The 'Generation 2' absorbers will focus on using heat pipes to dissipate the heat of absorption. This again will entail geometrical design, modelling and simulation.

c) System integration of desorber, absorber, condenser, and evaporator, and complete system testing. Identification of pitfalls and improvements on the same.

d) The SOFC stack size increases considerably when catering to larger cooling loads. More electrical energy is available from the SOFC stack on these trucks which needs to be put to good use. Decoupling the TRU (Truck Refrigeration Unit) from the main diesel engine is absolutely essential in order to
    - Reduce engine idling time
    - Reduce diesel consumption rate

    Along with compact component development there is a need to change the powertrain design on trucks if thermally driven refrigeration systems are to be used in conjunction with SOFCs. Simulation of alternate powertrain designs for trucks could possibly be a follow-up project. This way the excess electricity available from the SOFC is put to good use and will lead to hybrid powertrain concepts.

e) In this thesis, hydrogen was considered as the choice of fuel for the SOFC stack. However to be more realistic, hydrocarbon fuels such as natural gas, biogas and even reformed diesel need be considered. A complete well to wheel analysis of the fuel consumption of this concept (fuel cell heat driven VARS) and it's comparison with the conventional case will provide a complete understanding if it would be

advantageous to go ahead with thermally driven refrigeration systems on-board trucks.

f) Some studies on start-up and shutdown operations of SOFC and its effect on the VARS will be helpful in understanding the dynamics of such a system. Different cases such as planned shutdown, emergency shutdown and unplanned shutdown of the SOFC stack can be simulated and the corresponding response of the VARS can be analysed. Also some design and analysis of a backup heating element or heat storage source would be beneficial to consider the case where the SOFC breaks down completely.

Bibliography

1. Labus J, *Modelling of small capacity absorption chillers driven by solar thermal energy or waste heat*, in *Mechanical Engineering*. 2011, Universitat Rovira I Virgili: Tarragona.
2. Gorman J.K and Nardella W.R, *Hydrogen permeation through metals.* **Vacuum**, 1962. **12**(1): p. 19-24.
3. Lan L, et al., *Hydrogen permeation behavior in relation to microstructural evolution of low carbon bainitic steel weldments.* **Corrosion Science**, 2016. **112**: p. 180-193.

Appendix A

Overview of alternate refrigeration technologies

Vapour Compression (VC) technology is well established for food refrigeration but rising cost of electricity coupled with the need to reduce environmental impact and carbon footprint has prompted the use of alternate refrigeration technologies which have a lesser environmental impact. Besides vapour compression technology which is widely used in almost all refrigerating and air conditioning equipment, there exists a number of alternate technologies which can be employed in places wherever technically and economically feasible. A brief listing of these alternate refrigeration technologies is presented here along with their working principles [1]

Sorption refrigeration

There are two types of sorption refrigeration systems viz *adsorption refrigeration* and *absorption refrigeration*. Both these technologies employ heat as the driving force rather than electricity and employ a thermal compressor to pressurize the refrigerant.

The schematic of an adsorption refrigeration unit is shown in Figure A.1. In adsorption refrigeration, adsorbent beds of suitable material are made use of into which the refrigerant is either adsorbed or from which it is desorbed. The refrigerant is desorbed from the

desorbent bed by applying heat to it. This raises the pressure and temperature of the refrigerant; which is then subsequently passed on to the condenser where the high pressure high temperature refrigerant loses heat and is condensed to a saturated liquid which is then passed on to the evaporator at low pressure. At the evaporator, necessary cooling occurs by evaporating the refrigerant back to gaseous form which is then adsorbed in an adsorbent bed. When the adsorbent bed is saturated with refrigerant it is isolated from the evaporator and connected to the desorbent bed. The cycle is then repeated for continuous operation.

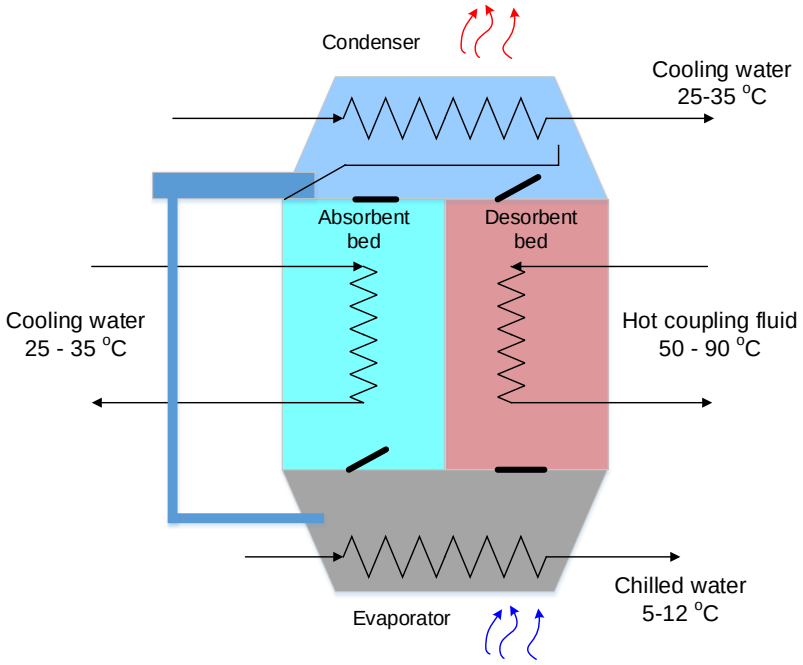

Figure A.1: Schematic of an adsorption refrigeration unit

The working of an absorption refrigeration system has already been explained in *section 2.2* of *Chapter 2* and hence not repeated here.

Even within the absorption refrigeration system, a large number of configurations exist. Srikhirin et al [2] carried out a detailed literature study on the different configurations and concluded that the single stage VARS is the most prominent with considerable commercial success. Besides the single stage VARS, the double stage VARS based on H_2O-LiBr

working pair is also commercially available and has a higher COP than a single stage VARS. Other configurations are either still at an experimental stage or require further research.

Ejector refrigeration

The block diagram of a simple ejector refrigeration system is shown in Figure A.2.

Unlike absorption refrigeration systems where a binary mixture – refrigerant and absorbent is used, the ejector refrigeration system uses only the refrigerant. It is usually characterized by two loops – viz. the power loop and the refrigeration loop. The ejector is a crucial component in the whole system and is internally comprised of a *motive nozzle*, *suction chamber*, a *mixing chamber* and *a diffuser*. In the power loop, heat is applied to the generator where high pressure high temperature refrigerant is generated and is then passed on to the motive nozzle in the ejector. The motive nozzle is of converging-diverging type and the flow accelerates through it, resulting in pressure reduction. At the exit of the nozzle, in the suction chamber, this high velocity refrigerant meets the low pressure refrigerant coming from the evaporator and transfers part of its momentum to it. The two streams mix in the mixing chamber where the pressure of the mixed stream rises but the flow velocity still remains high. Hence a diffuser section is used in which pressure recovery occurs and flow velocity is reduced. The mixed fluid is then passed on to the condenser where it loses heat and changes its state to a saturated liquid. Part of the liquid refrigerant is sent back to the power loop and the remaining to the evaporator for use in the refrigerant loop.

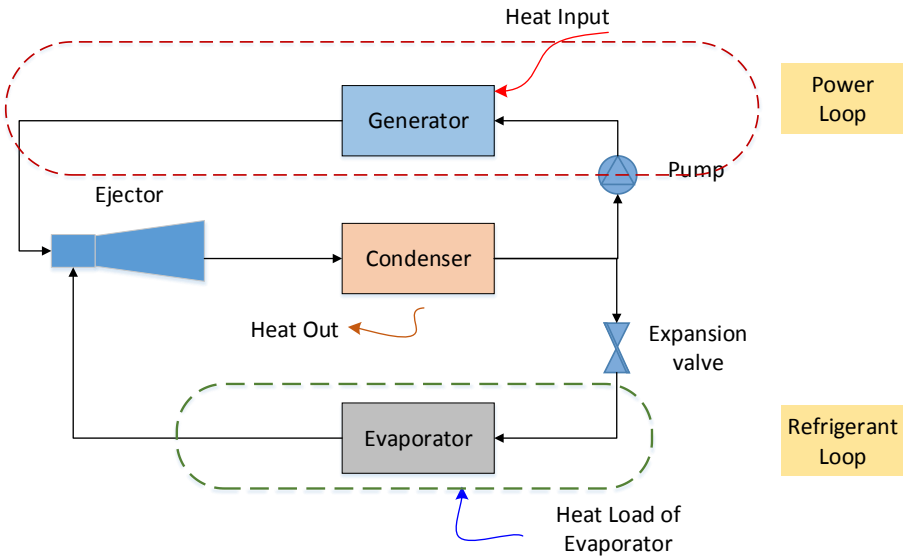

Figure A.2: Block diagram of Ejector refrigeration technology

Air cycle refrigeration

Technically air cycle refrigeration is not a heat driven refrigeration technology. It works on the principle of compression and expansion of air during which it gets heated and cooled. The block diagram for an air cycle refrigeration system is shown in Figure A.3.

Air is compressed using a compressor. This raises the temperature of the air. The air is then cooled at constant pressure and heat taken away from it. This is followed by expansion in a turbine where the temperature of the air is further reduced. The cool air can now be used as a refrigerant directly in an open system or indirectly through a heat exchanger in a closed system. Efficiencies of air cycle refrigeration are mainly limited by efficiencies of the compressor and turbine and the COP is usually in the range of 0.4 to 0.7. An advantage of this technology is that air temperature, after undergoing expansion in the turbine, can be as low as -100 ^{o}C so very low refrigeration temperatures can be achieved. Such low refrigeration temperatures are not feasible by VC systems so that gives air cycle refrigeration a very niche application. Besides cooling, air cycle refrigeration can also provide sufficient

heat, which is recovered after removing the heat from the air exiting the compressor. Thus air cycle refrigeration systems can be used in CCHP applications.

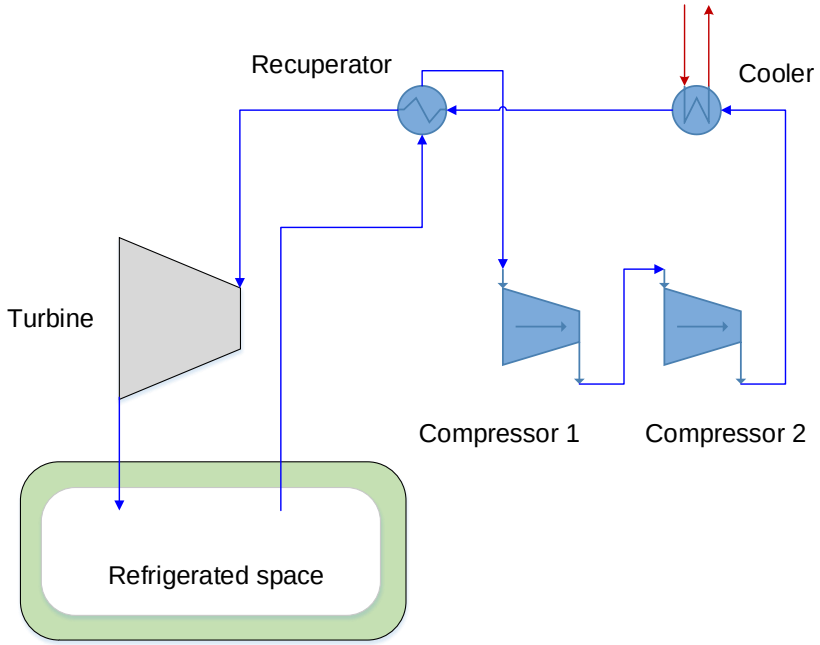

Figure A.3: Block diagram of air cycle refrigeration

Stirling cycle refrigeration

The Stirling cycle refrigerator is a closed cycle regenerative thermal machine, comprising of a piston and the displacer. The role of the piston is to compress and expand the working gas whereas the role of the displacer is to shuttle the working gas back and forth between the cold end from where heat is absorbed and the refrigeration effect takes place and the hot end where heat is rejected.

There are two designs of Stirling cycle refrigerator, one where the piston and the displacer are mechanically linked to the drive shaft and the other where the piston is linked to the

power supply by an AC linear motor and the displacer is driven by fluctuations in the gas pressure in the system.

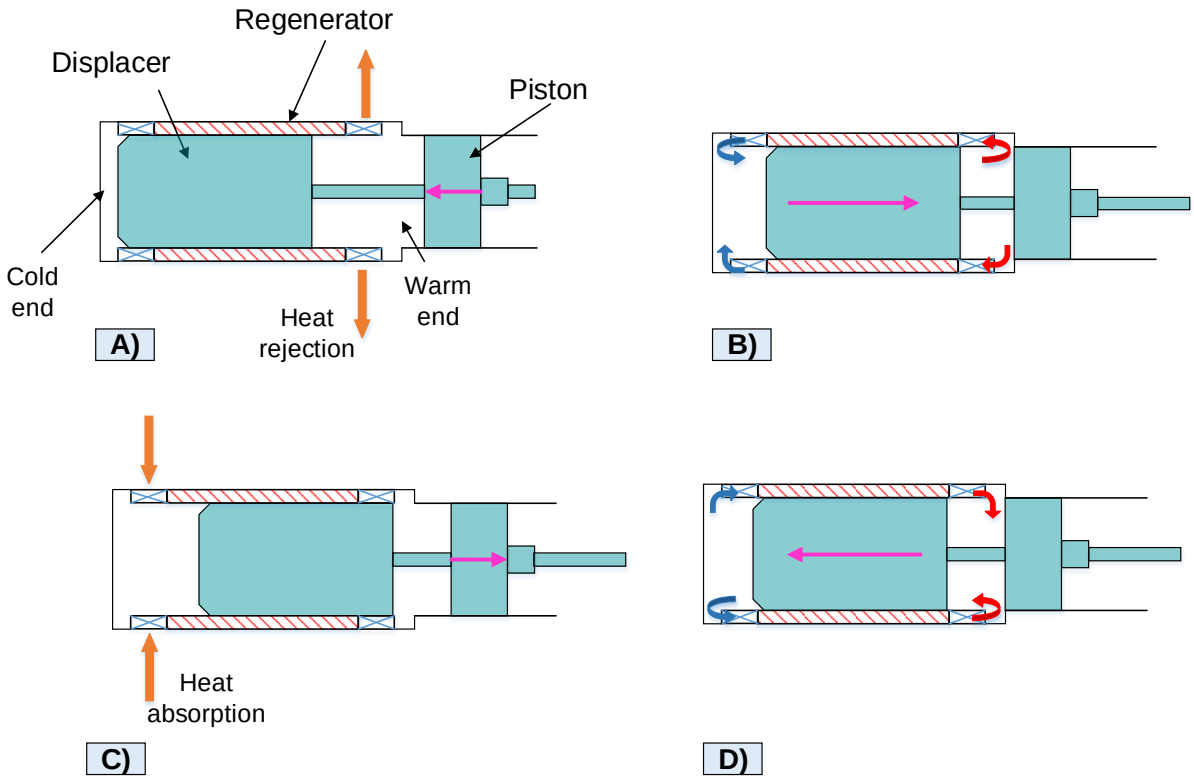

Figure A.4: Operating principle of Stirling cycle refrigeration
A) Piston moves in compressing gas. Heat rejection from warm end; B) Displacer moves gas to cold end space via regenerator; C) Piston moves out expanding gas. Heat absorption at cold end; D) Displacer moves gas to warm end space via regenerator

The working of the Stirling cycle refrigerator is displayed through a series of diagrams shown in Figure A.4. In short, the stirling cycle refrigeration is mainly a mechanical refrigeration system rather than a heat driven one.

Thermoelectric refrigeration

A thermoelectric refrigeration system works on the principle of '*Peltier effect*'. *Peltier effect* causes the junction of two dissimilar conducting materials to either warm up or cool down when direct current is passed through the junction. The schematic of such a thermoelectric device is shown in Figure A.5. This is the basic building block of a thermoelectric refrigeration unit which is comprised of many such blocks.

When the current flows from the n-type semiconductor to the p-type semiconductor, the junction experiences a temperature decrease and thermal energy is absorbed thereby producing a cooling effect at the junction. If on the other hand the direction of current is reversed, the junction will warm up.

The main advantages of thermoelectric refrigeration technology over conventional vapour compression technology is the lack of moving parts or circulating fluid, compact size, long life and flexible shape. The drawbacks however are poor efficiency and relatively high cost. The maximum temperature difference that can be achieved between the hot and cold ends in a single stage module is about 70 K so that limits thermoelectric cooling systems to a very specific temperature range.

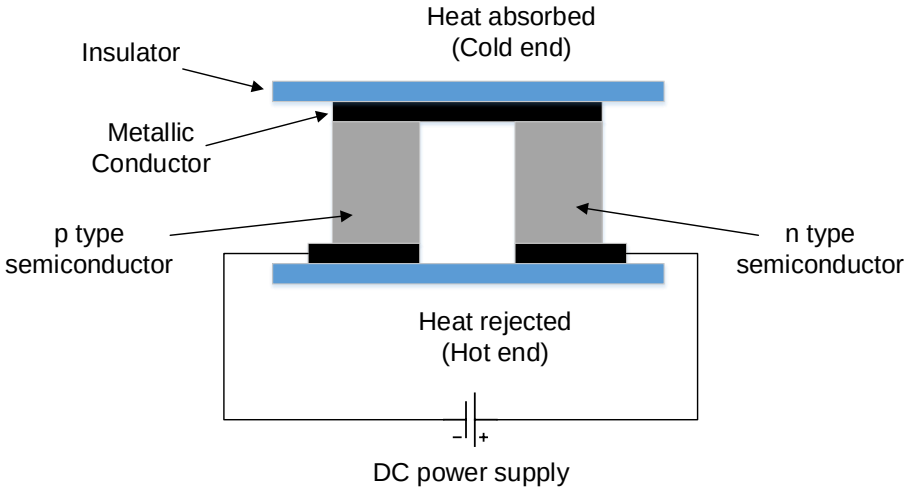

Figure A.5: A thermoelectric device

Thermo-acoustic refrigeration

Thermo-acoustic devices make use of high amplitude sound waves to transfer heat from one location to another. The ones used for refrigeration are of two types viz. standing wave devices and travelling wave devices. In a standing wave device, sound waves are generated using a loudspeaker whereas in a travelling wave device, pressure is generated using a moving piston which may be connected to either a motor or an engine. In order to move heat from one location to another work has to be done and this work is done by the sound waves. A brief explanation of the standing wave and travelling wave device is given here.

The schematic of a standing wave device is shown in Figure A.6. It consists of a closed tube (resonator) containing a sound wave generator (loud speaker), the hot end heat exchanger, a stack made of porous material, the cold end heat exchanger and a working gas. Interference occurs in the closed tube when two waves travel in the opposite direction and at certain frequencies (referred to as resonant frequencies). This interference causes resonance which in turn creates a standing wave and hence the name for this device. As the gas shuttles back and forth in the chamber it creates a temperature difference along the length of the porous stack. The temperature difference is generated mainly due to compression and expansion of the gas which in turn occurs due to sound pressure and by placing heat exchangers at either end of the stack this heat can be recovered.

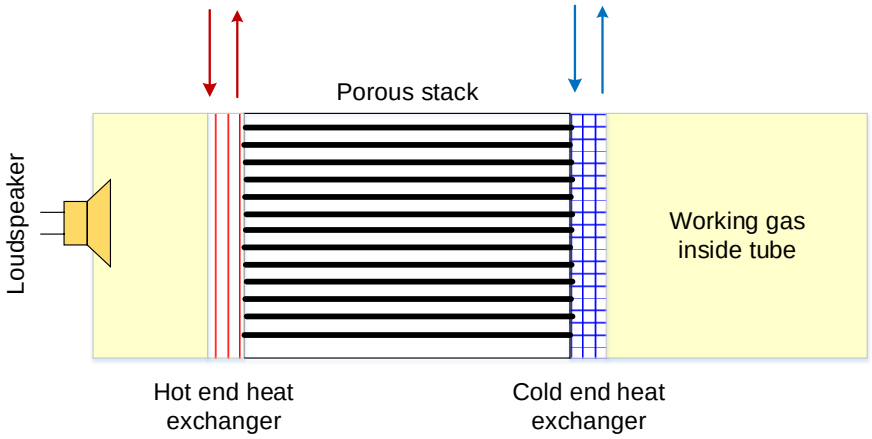

Figure A.6: 2D schematic of standing wave thermos-acoustic device

The schematic of a travelling wave device is shown in Figure A.7. Here in place of a porous stack, a regenerator is used to convert acoustic power to heat. The regenerator has a number of channels which are smaller than the ones used in the porous stack in the standing wave device and relies on good thermal contact between the gas and the channels. The design of the travelling wave device is in such a way that the gas moves to the cold heat exchanger when the pressure is low and moves to the hot heat exchanger when the pressure is high, thereby transferring heat between the two ends.

The drawbacks of thermo-acoustic refrigeration units are that they have a low COP and no commercial prototypes are currently available.

Both thermoelectric and thermo-acoustic refrigeration systems are actually not heat driven and the names are a misnomer for one to believe that thermal energy could be driving these systems. The word ‘thermo’ in these systems refer to the transfer of heat from the cold end to the warm end and hence cannot be classified as a thermally driven refrigeration system.

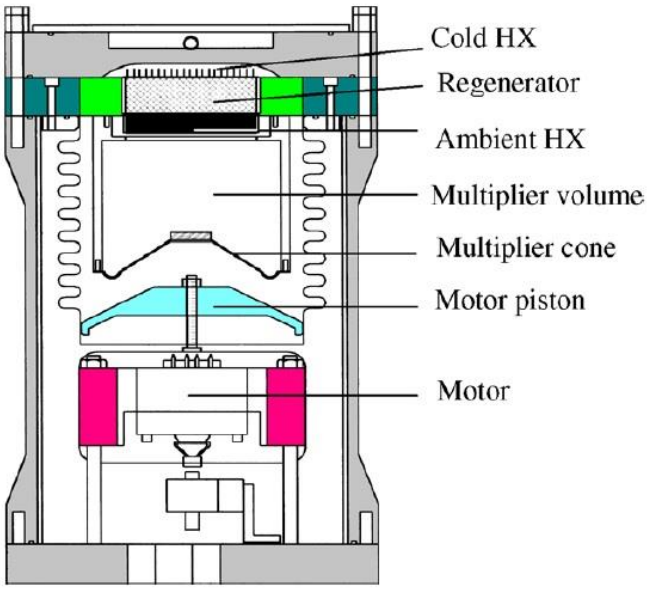

Figure A.7: A travelling wave thermo-acoustic device [1]

Magnetic refrigeration

Magnetic refrigeration works on the principle of Magneto-Caloric Effect (MCE) which is described as a phenomenon where a suitable material undergoes a reversible temperature change when exposed to a varying magnetic field. The MCE peaks more or less around the Curie temperature or the magnetic ordering temperature for that respective material.

The magnetic refrigeration cycle is similar to the vapour compression refrigeration cycle but rather than use variations in pressure, variations in magnetic field strength are used to generate cooling and move heat around. The working substance which is a magneto-caloric substance is also the refrigerant. A brief description of the working cycle which comprises of four main processes is given below.

a) Adiabatic magnetization:

   In this process, the working substance is placed in an insulated environment and the magnetic flux is gradually increased. Increasing the magnetic flux causes the magnetic dipoles of the atoms (of the working substance) to align which in turn leads

to a decrease in the working substance's magnetic entropy and heat capacity. As the working substance is placed in the insulated environment, the overall energy (and entropy) is not lost and it is heated up.

b) Isomagnetic enthalpic transfer:

In this process the magnetic field is held constant and the heat generated in the working substance is removed by using another coupling fluid or gas. The reason why the magnetic field needs to be held constant is to prevent the dipoles of the working substance from reabsorbing the heat. Once all the heat from the working substance is removed it is separated from the coupling fluid or gas.

c) Adiabatic demagnetization:

This process is the reverse of the first process. Magnetic flux is gradually reduced which causes magnetic entropy to increase or in other words the dipoles become unaligned. When the magnetic flux is reduced, the thermal energy aids the magnetic moments to overcome the field and in turn leads to cooling of the working substance.

d) Isomagnetic entropic transfer

The magnetic field is once again held constant to prevent the working substance from reheating. When the cool working substance is placed in contact with the space to be refrigerated, heat flows from that space into the working substance and thus the required refrigeration effect is produced.

The cycle repeats itself once thermal equilibrium is achieved between the refrigerated space and the working substance.

Some of the advantages of magnetic refrigeration units over conventional vapour compression refrigeration units are that they are safer, quieter, and more compact, have a

higher cooling efficiency and are more environmentally friendly because no ozone depleting refrigerants are used. Also this technique can be used to achieve very low temperatures.

Cryogenic refrigeration

Cryogenic refrigeration is used for those applications that require extremely low temperatures not usually achieved by conventional VC systems. The limit for conventional VC systems is around -50 ^{o}C below which the system gets complicated. Theoretically cryogenic refrigeration can provide refrigeration temperatures down to -150 ^{o}C.

The refrigerants used in cryogenic refrigeration are usually liquid helium, liquid hydrogen or liquid nitrogen and of late even liquid CO_2 but the most widely used refrigerant is liquid nitrogen. There are three modes in which cryogenic refrigeration units can be employed which are:

- Direct mode
- Semi-indirect mode
- Indirect mode

In the direct mode, liquid nitrogen is directly injected into the refrigerated space. This provides rapid cooling and achieves maximum efficiency but it causes foaming and localised freezing which is often not desired. Hence direct mode of cryogenic refrigeration is not used unless otherwise required.

In the semi-indirect mode, liquid nitrogen is passed through a heat exchanger or a coil with large surface area and a fan blows air across the coil (or heat exchanger). This allows accurate temperature control because both the flow rate of liquid nitrogen and the fan speed can be controlled. This design also allows the nitrogen to be reused. The main drawbacks are however reduced efficiency when compared to the direct mode, need for construction of

expensive storage vessels which should not only handle very low temperatures but should also be corrosion resistant.

In the indirect mode, liquid nitrogen is circulated in an external heat exchanger in which another coupling fluid is cooled down. This coupling fluid is then circulated through a heat exchanger placed inside the refrigerated space, across which a fan blows air and the required refrigeration effect is produced. This mode offers precise temperature control, great system flexibility because the respective heat exchangers can be sized accordingly, and can also accommodate large heat loads.

A schematic of the different cryogenic operation modes is depicted in Figure A.8.

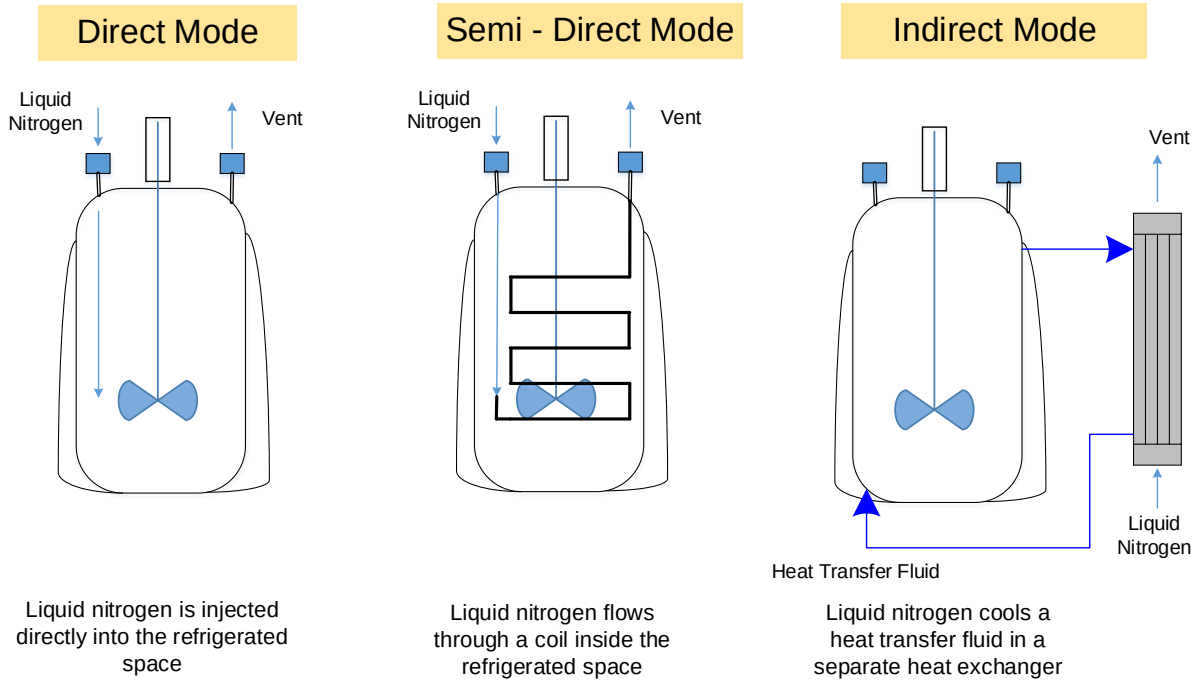

Figure A.8: Three modes of cryogenic refrigeration

Table A.1 summarizes the applicability of alternate refrigeration technologies towards the current research objective and if they can be coupled to high temperature fuel cells.

Table A.1: Applicability of alternate refgr. technologies towards the current research objective

Refrigeration technology	Thermally driven	Indicative theoretical COP/efficiency	Suitability of coupling with high temperature fuel cell	Current market application
Adsorption system	Yes	0.4-0.7	Yes	Food processing, retail cold storage
Absorption system	Yes	0.4-1.2	Yes	Stationary air conditioning, refrigeration
Ejector system	Yes	0.1-0.3	Yes	Refrigerated transport, food processing
Air cycle	No	0.4-0.7	No	Food processing
Stirling cycle	No	1.0-3.0	No	Refrigerated cabinets, domestic refrigerators
Thermo-electric	No	0.6 at 0 ^{o}C	Yes but using DC current from the fuel cell	Recreational vehicles, portable coolers
Thermo-acoustic	No	Up to 1	No	Domestic and commercial refrigerators, freezers and cabinets
Magnetic	No	1.8 at room temperature	No	Low capacity mobile/stationary systems
Cryogenic	No	0.15-0.2	No	Stationary systems, refrigerated transport

(refgr. = Refrigeration)

Summary overview

As mentioned in *Chapter 1*, the goal of the current research is to use the residual heat from the Solid Oxide Fuel Cell to power a refrigeration system on-board the truck. The advantage in doing so is that the refrigeration system will literally be run on free thermal energy which would otherwise be dissipated. The only thermally driven refrigeration technologies are **sorption refrigeration systems** and **ejector refrigeration systems**. Hence only these two refrigeration technologies will be suitable when coupled to the fuel cell. Also among the three heat driven refrigeration technologies, vapour absorption refrigeration system has the highest COP [1]. Ejector refrigeration technologies are not commercially available and

refrigeration temperatures achieved are above 0 ^{o}C. Adsorption refrigeration systems need complex adsorbent beds which are not only bulky but also more expensive than VARS components and the refrigeration temperatures achieved are above 0 ^{o}C. Taking all these factors into consideration, VARS technology will be most suitable for powering refrigerated trucks provided the thermal energy input is generated as a by-product.

References

1. Tassou S.A, et al., *A review of emerging technologies for food refrigeration applications.* **Applied Thermal Engineering**, 2010. **30**(4): p. 263-276.
2. Srikhirin P, Aphornratana S, and Chungpaibulpatana S, *A review of absorption refrigeration technologies.* **Renewable and Sustainable Energy Reviews**, 2001. **5**(4): p. 343-372.

Appendix B

Parameters fixed during cooling load calculations

The parameters that were fixed when varying other parameters one at a time is shown in Tables B.1 to B.5

Table B.1: Parameters that were fixed while varying body 'K' factor

External Length	13.6 m
External Width	2.6 m
External height	2.8 m
Temperature of refrigerated space	-20 ^{o}C
Insulation thickness	125 mm
Percentage of cargo inside refrigerated space	50%
Door opening time	3 minutes
Average time between door openings	30 minutes
Relative humidity	0.5

Table B.2: Parameters that were fixed while varying external dimensions

Body 'K' factor	0.3 (W m^{-2} ^{o}C^{-1})
Temperature of refrigerated space	-20 ^{o}C
Insulation thickness	125 mm
Percentage of cargo inside refrigerated space	50%
Door opening time	3 minutes
Average time between door openings	30 minutes
Relative humidity	0.5

Table B.3: Parameters that were fixed while varying percentage of cargo

Body 'K' factor	0.3 (W m^{-2} $^{o}C^{-1}$)
External height	2.8 m
External width	2.6 m
External length	13.6 m
Temperature of refrigerated space	-20 ^{o}C
Insulation thickness	125 mm
Door opening time	3 minutes
Average time between door openings	30 minutes
Relative humidity	0.5

Table B.4: Parameters that were fixed whilst varying refrigerated cabinet temperature

Body 'K' factor	0.3 (W m^{-2} $^{o}C^{-1}$)
External height	2.8 m
External width	2.6 m
External length	13.6 m
Percentage of cargo inside refrigerated space	50%
Insulation thickness	125 mm
Door opening time	3 minutes
Average time between door openings	30 minutes
Relative humidity	0.5

Table B.5: Parameters that were fixed whilst varying door opening time

Body 'K' factor	0.3 (W m^{-2} $^{o}C^{-1}$)
External height	2.8 m
External width	2.6 m
External length	13.6 m
Percentage of cargo inside refrigerated space	50%
Insulation thickness	125 mm
Temperature of refrigerated space	-20 ^{o}C
Average time between door openings	30 minutes
Relative humidity	0.5

EES code for thermodynamic modelling of VARS

```
" Fundamental thermodynamic model of Vapour Absorption Refrigeration System VARS"
"  ---------------------------------------------------------------------------------------------------------------------------------- "

" Listing of different PROCEDURES"

PROCEDURE TPQ(TC,P,Q:x,h,v,s)
"given T (temperature), P (pressure) and Q (quality) in SI units,
 this procedures returns x, h, v and s in SI units"

TK=TC+273.15
Pbar=P*.01
CALL NH3H2O(128,TK,Pbar,Q:TK,Pbar,x,h,s,u,v,Q)
END


PROCEDURE TPX(TC,P,x:Q,h,v,s)
"given T (temperature), P (pressure) and x (ammonia wt fraction) in SI
units, this procedure returns Q, h, v and s in SI units"

TK=TC+273.15
Pbar=P*.01
CALL NH3H2O(123,TK,Pbar,x:TK,Pbar,x,h,s,u,v,Q)
END


PROCEDURE PXQ(P,x,Q:TC,h,v,s)
"given P (pressure in bar), x (ammonia wt fraction) and Q, this procedure
 returns T, h, v and s in SI units"

Pbar=P*.01
CALL NH3H2O(238,Pbar,x,Q:TK,Pbar,x,h,s,u,v,Q)
TC=TK-273.15
END


PROCEDURE PHX(P,h,x:TC,Q,v,s)
"given P (pressure in bar), enthalpy (J/g), and x (ammonia wt
fraction), this procedure returns T, Q, v and s in SI units"

Pbar=P*.01
CALL NH3H2O(234,Pbar,x,h:TK,Pbar,x,h,s,u,v,Q)
TC=TK-273.15
END


PROCEDURE TXQ(TC,x,Q:P,h,v,s)
"given T (temperature in C), Q (quality) and x (ammonia wt fraction) in SI
units, this procedure returns P, h, v  and s in SI units"

TK=TC+273.15
CALL NH3H2O(138,TK,x,Q:TK,Pbar,x,h,s,u,v,Q)
P=Pbar*100
END
```

```
eshx = 0.86              { Effectiveness of solution heat exchanger }
erhx = 0.86                 { Effectiveness of refrigerant pre cooler }
epump = 0.7              { Isentropic Efficiency of pump }

" Temperatures of different points in the system (deg C)"

T[1] = 30  {Temperature at state 1, saturation temperature of strong solution leaving the Absorber,°C }
T[10] = 30   {Temperature at state 10,saturation temperature of NH3 liquid leaving the Condenser, °C }
T[13] = -20  { Temperature at state 13, Evaporation temperature, deg C }

" Pressures in the system"

P[1] = 200                    { Pressure of Absorber, kPa}
P[6] = P[1]
P[12] = P[1]
P[13] = P[1]
P[14] =P[1]

P[2] = 1500                  { Pressure of Generator, kPa}
P[3] = P[2]
P[4] = P[2]
P[5] =P[2]
P[7] = P[2]
P[8] = P[2]
P[9] =P[2]
P[10] = P[2]
P[11] = P[2]

" Mass Flows "

m[1] = 0.034                 { Mass flow of Strong solution, kg/s }

" Mass fractions "

x[8] = 1- x[7]              {Ammonia mass fraction leaving the rectifier}
x[9] = 0.99                 {mass fraction of ammonia at state 9 }
x[11] = 0.99                {mass fraction of ammonia at state 11 }
x[12] = 0.99                {mass fraction of ammonia at state 12 }
x[14] = 0.99                {mass fraction of ammonia at state 14}

" Quality of vapour at different points in the system "

q[4] = 0
q[7] = 1
q[8] = 0
q[9] = 1
q[10] =0
q[13] = 0.998

"- - - -
```

```
x[1]=Z                    { Concentration of strong solution leaving the Absorber }
x[2]=Z
x[3]=Z

" - - -
```

```
eshx = (T[3]-T[2])/(T[4]-T[2])          { Since solution coming from the pump has a lower thermal capacity compared to solution coming from the Desorber}

" - - - - - - - - - - - - - - - - - - - - - - - - - - - - - - - - "

" Mass balance at Desorber"

m[8] + m[3] = m[7] + m[4]                                   {for the total mixture}
m[8]*x[8] + m[3]*x[3] = m[7]*x[7] + m[4]*x[4]               {for ammonia }

" Energy balance at Desorber"

m[8]*h[8] +m[3]*h[3] + Qg = m[7]*h[7] +m[4]*h[4]

CALL PXQ (P[3],x[3],0: T3f,h3f,v3f,s3f)

T[7] = T3f

" - - - - - - - - - - - - - - - - - - - - - - - - - - - - - - - - "

"Mass balance at Rectifier"

m[7] = m[9] + m[8]                          { for total mixture}

"Energy balance at Rectifier"

m[7]*h[7] = m[9]*h[9] +m[8]*h[8] +Qr


" - - - - - - - - - - - - - - - - - - - - - - - - - - - - - - - - "

"Mass balance at throttle valve V1"

m[6]=m[5]

"Energy balance a throttle valve V1"

m[6]*h[6] = m[5]*h[5]

"- - - - - - - - - - - - - - - - - - - - - - - - - - - - - - - - "

" Mass balance at condenser"

m[10]=m[9]

"Energy balance at Condenser"

m[9]*h[9] = m[10]*h[10] +Qc

" - - - - - - - - - - - - - - - - - - - - - - - - - - - - - - - - "

" Mass balance at Refrigerant pre cooler"

m[11] = m[10]
m[14] = m[13]

" Energy balance at Refrigerant pre cooler"
```

```
Qrhx_liq = m[10]*(h[10]-h[11])          {Heat lost by hot liquid refrigerant coming from Condenser}
Qrhx_vap = m[13]*(h[14]-h[13])          {Heat gained by cold refrigerant vapour coming from Evaporator}

Qrhx_liq = Qrhx_vap                                  { Heat lost by hot (soln from Condenser) saturated
ammonia liquid is equal to the heat gained by cold ammonia vapour (coming from Evaporator)}

" Effectiveness of Refrigerant pre cooler"

erhx = (T[14] - T[13])/ (T[10] - T[13])              { Since the stream coming out from Evaporator has a
lower thermal capacity compared to the stream coming from Condenser}

"- - - - - - - - - - - - - - - - - - - - - - - - - - -"

" Mass balance at throttle valve V2"

m[12] =m[11]

" Energy balance at throttle valve V2"

m[11]*h[11] = m[12]*h[12]

" - - - - - - - - - - - - - - - - - - - - - - - - - - -"

" Mass balance at Evaporator"

{m[13]=m[12]}

" Energy balance at Evaporator"

m[13]*h[13] = m[12]*h[12] +Qe

" - - - - - - - - - - - - - - - - - - - - - - - - - - -"
"Coefficient of performance of VARS system"

COP = Qe/(Qg+Wp)                                     {Overall Coefficient of Performance}
COP_th = Qe/Qg                                       {Thermal Coefficient of Performance}
checkQ = Qg+Qe+Wp-(Qc+Qr+Qa)

" - - - - - - - - - - - - - - - - - - - - - - - - - - -"

" Different CALL functions "

CALL TPX (T[1],P[1],x[1]: Q[1],h[1],v[1],s[1])
CALL PHX (P[2],h[2],x[2]: T[2],Q[2],v[2],s[2])
CALL TPX (T[3],P[3],x[3]: Q[3],h[3],v[3],s[3])
CALL PXQ (P[4],x[4],q[4]: T[4],h[4],v[4],s[4])
CALL PHX (P[5],h[5],x[5]: T[5],Q[5],v[5],s[5])
CALL PHX (P[6],h[6],x[6]: T[6],Q[6],v[6],s[6])
CALL TPQ (T[7],P[7],q[7]: x[7],h[7],v[7],s[7])
CALL PXQ (P[8],x[8],q[8]: T[8],h[8],v[8],s[8])
CALL PXQ (P[9],x[9],q[9]: T[9],h[9],v[9],s[9])
CALL TPQ (T[10], P[10], q[10]: x[10],h[10],v[10],s[10])
CALL PHX (P[11],h[11],x[11]: T[11],Q[11],v[11],s[11])
CALL PHX (P[12],h[12],x[12]: T[12],q[12],v[12],s[12])
CALL TPQ (T[13],P[13],Q[13]: x[13],h[13],v[13],s[13])
CALL TPX (T[14],P[14],x[14]: Q[14],h[14],v[14],s[14])
```

Appendix C

The functional parameters of SOFC single cell used in the model described in *Chapter 4* are given in Table C.1

Table C.1: Functional parameters of SOFC single cell used in the model

Functional parameters			
Single cell dimensions	Thickness of electrolyte, T_e	$5*10^{-5}$ (m)	Design parameter
	Thickness of anode, T_a	$1020*10^{-6}$ (m)	[1]
	Thickness of cathode, T_c	$5*10^{-5}$ (m)	Design parameter
	Thickness of bipolar plate, T_{BP}	$1.5*10^{-3}$ (m)	Design parameter
	Width of channel, $W_{channel}$	$1*10^{-3}$ (m)	Design parameter
	Active area of cell	100 (cm^2)	Design parameter
Parameters needed for calculation of cell voltage	Anode proportionality coefficient	$1.344*10^9$ (mA cm^{-2})	[2]
	Anode activation energy	10^5 (J mol^{-1})	[2]
	Cathode proportionality coefficient	$2.051*10^8$ (mA cm^{-2})	[2]
	Cathode activation energy	$1.2*10^5$ (J mol^{-1})	[2]
	Porosity of anode	0.48	[2]
	Tortuosity of anode	5.4	[2]
	Porosity of cathode	0.4	Design parameter
	Tortuosity of cathode	4	Design parameter
	Effective pore radius	$3*10^{-6}$ (m)	[2]
	Electrolyte constant	$3.44*10^8$ (S K m^{-1})	[3]
	Electrolyte activation energy	10^5 (J mol^{-1})	[4]

Algorithm followed by the MATLAB code for calculating the thermal energy generated within the SOFC stack.

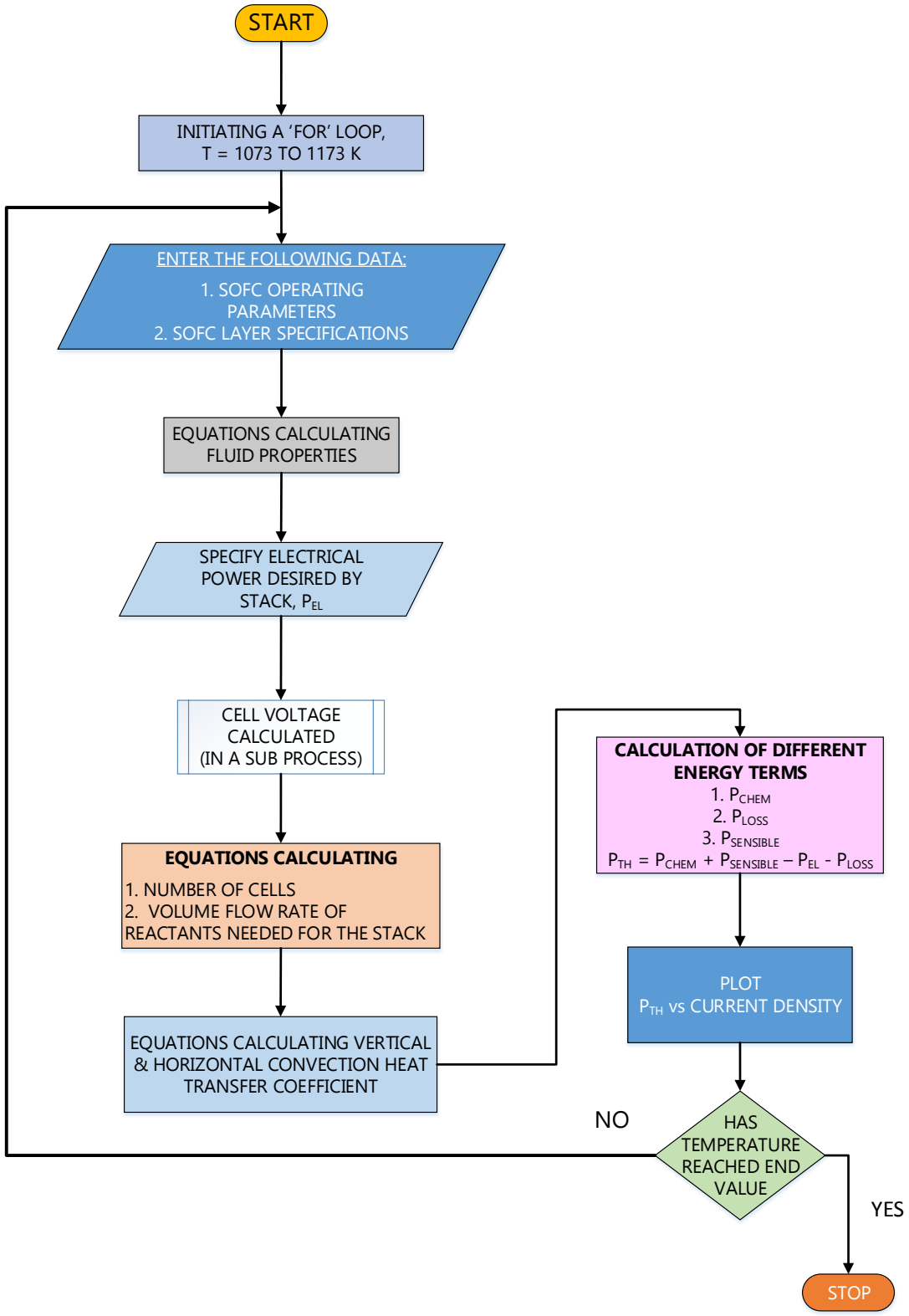

Figure C.1: Algorithm followed for thermal model of SOFC

Equations relating to fluid properties

1) Temperature dependent density of hydrogen (kg m^{-3})

$$\rho_{H_2} = \left(\frac{2}{1000}\right) * \left(P * \frac{10^5}{8.314 * T}\right) \quad \textbf{Eq. C.1}$$

2) Temperature dependent density of air (kg m^{-3})

$$\rho_{AIR} = \left(\frac{28.97}{1000}\right) * \left(P * \frac{10^5}{8.314 * T}\right) \quad \textbf{Eq. C.2}$$

3) Temperature dependent specific heat capacity of hydrogen (kJ kg^{-1} K^{-1})

$$C_{p,H_2} = (-1 * 10^{-11} * T^4) + (4 * 10^{-8} * T^3) - (5 * 10^{-5} * T^2) + (0.0247 * T) + 10.33 \quad \textbf{Eq. C.3}$$

This equation was formed from the trend line fitted to the graph depicting variation of C_p with temperature and is valid for 175 < T < 1300 K.

4) The change in enthalpy of hydrogen (kJ kg^{-1}) is given by

$$\Delta H_{H_2} = C_{p,H_2} * \Delta T \quad \textbf{Eq. C.4}$$

5) Temperature dependent specific heat capacity of air (kJ kg^{-1} K^{-1})

$$C_{p,air} = (0.0002 * T) + 0.9435 \quad \textbf{Eq. C.5}$$

This equation was also formed from the trend line fitted to the graph depicting the variation of C_p with temperature and is valid for 250 < T < 1500 K.

6) The change in enthalpy of air (kJ kg^{-1}) is given by

$$\Delta H_{Air} = C_{p,Air} * \Delta T \quad \textbf{Eq. C.6}$$

7) The temperature dependent thermal conductivity of air (W m^{-1} K^{-1}) is given by

$$k_{Air} = \left(1.5207 * 10^{-11} * T_f^3\right) - \left(4.8574 * 10^{-8} * T_f^2\right) + \left(1.0184 * 10^{-4} * T_f\right) - 3.93 * 10^{-4} \quad \textbf{Eq. C.7}$$

The above equation is valid for 100 < T_f < 1600 K. T_f is the mean fluid temperature which is the average of outer insulation temperature of the stack and the ambient temperature.

8) The temperature dependent dynamic viscosity of air (kg m^{-1} s^{-1}) is given by

$$\mu_{Air} = \left(\left(-1 * 10^{-6} * T_f^2\right) + \left(0.0049 * T_f\right) + 0.4065\right) * 10^{-5} \quad \textbf{Eq. C.8}$$

The above equation is valid for 100 < T_f < 1600 K

Equations related to diffusion

1) Binary diffusion coefficient of hydrogen (cm^2 s^{-1})

$$D_{H_2-H_2O} = 1.9562 * 10^{-5} * T^{1.75} \quad \textbf{Eq. C.9}$$

2) Knudsen diffusion coefficient of hydrogen (cm^2 s^{-1})

$$D_{H_{2,k}} = \left(\frac{2}{3}\right) * r_p * \sqrt{\left(\frac{8RT}{\pi\, m_{H2}}\right)} * 10000 \quad \textbf{Eq. C.10}$$

3) Binary diffusion coefficient of oxygen (cm^2 s^{-1})

$$D_{O_2-N_2} = 3.4549 * 10^{-6} * T^{1.75} \quad \textbf{Eq. C.11}$$

4) Knudsen diffusion coefficient of oxygen (cm^2 s^{-1})

$$D_{O_{2,k}} = \left(\frac{2}{3}\right) * r_p * \sqrt{\left(\frac{8RT}{\pi\, m_{O2}}\right)} * 10000 \quad \textbf{Eq. C.12}$$

References

1. Zeng M., et al., *Investigation of thermal radiation effects on solid oxide fuel cell performance by a comprehensive model.* **Journal of Power Sources**, 2012. **206**: p. 185-196.
2. Ni M, M.K.H. Leung, and D.Y.C. Leung, *Parametric study of solid oxide fuel cell performance.* **Energy Conversion and Management**, 2007. **48**(5): p. 1525-1535.
3. Kakaç S, A. Pramuanjaroenkij, and X.Y. Zhou, *A review of numerical modeling of solid oxide fuel cells.* **International Journal of Hydrogen Energy**, 2007. **32**(7): p. 761-786.
4. Ryan O' Hayre, S.W.C., Whitney Colella, Fritz B. Prinz, *Fuel Cell Fundamentals*. Second Edition ed. 2009: John Wiley & Sons.

Appendix D

CFD plots of temperature distribution, pressure and velocity profiles of the fluids are shown here for different combinations of cathode exhaust flow rate and thermal oil flow rates

V_{air} = 4.46 L s^{-1}, Cathode exhaust flow rate

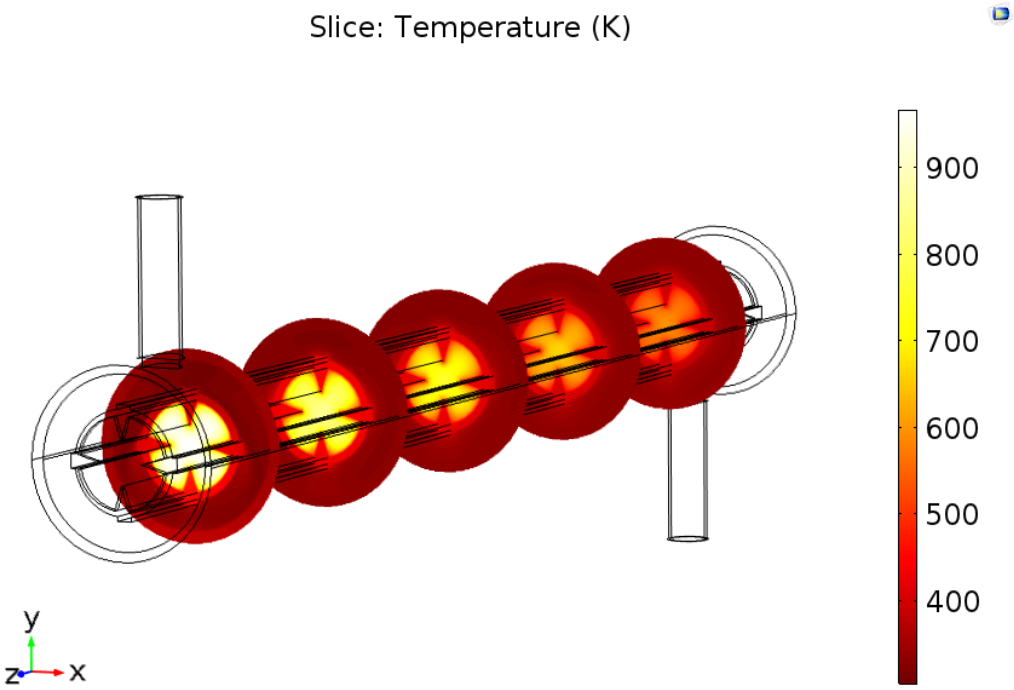

Figure D.1: Temperature profile development through oil and air domains
($T_{Air,In}$ = 973.15 K, $T_{Oil,In}$ = 300.15 K, v_{Air} = 4.46 L s^{-1}, m_{Oil} = 0.02 kg s^{-1})

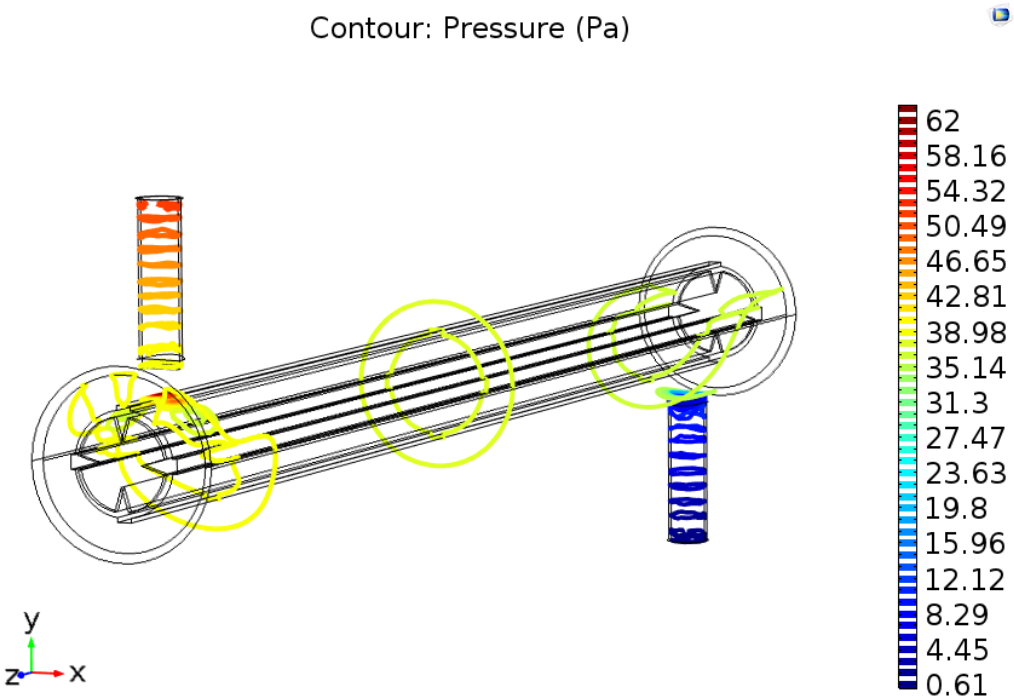

Figure D.2: Pressured drop for thermal oil
($T_{Air,In}$ = 973.15 K, $T_{Oil,In}$ = 300.15 K, v_{Air} = 4.46 L s^{-1}, m_{Oil} = 0.02 kg s^{-1})

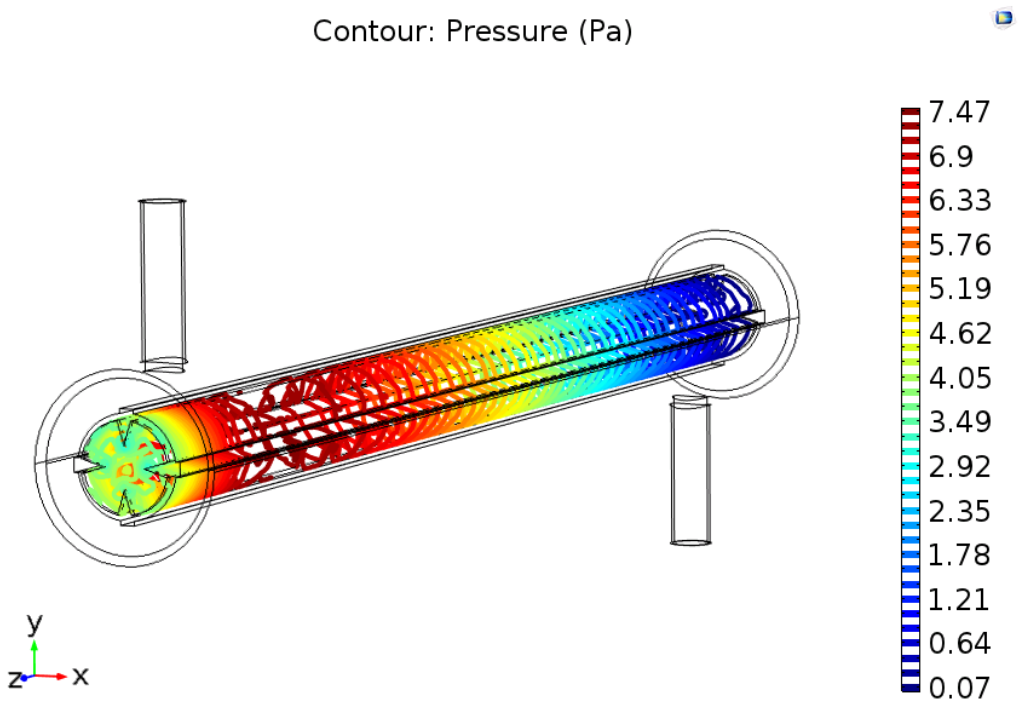

Figure D.3: Pressured drop for air side
($T_{Air,In}$ = 973.15 K, $T_{Oil,In}$ = 300.15 K, v_{Air} = 4.46 L s^{-1}, m_{Oil} = 0.02 kg s^{-1})

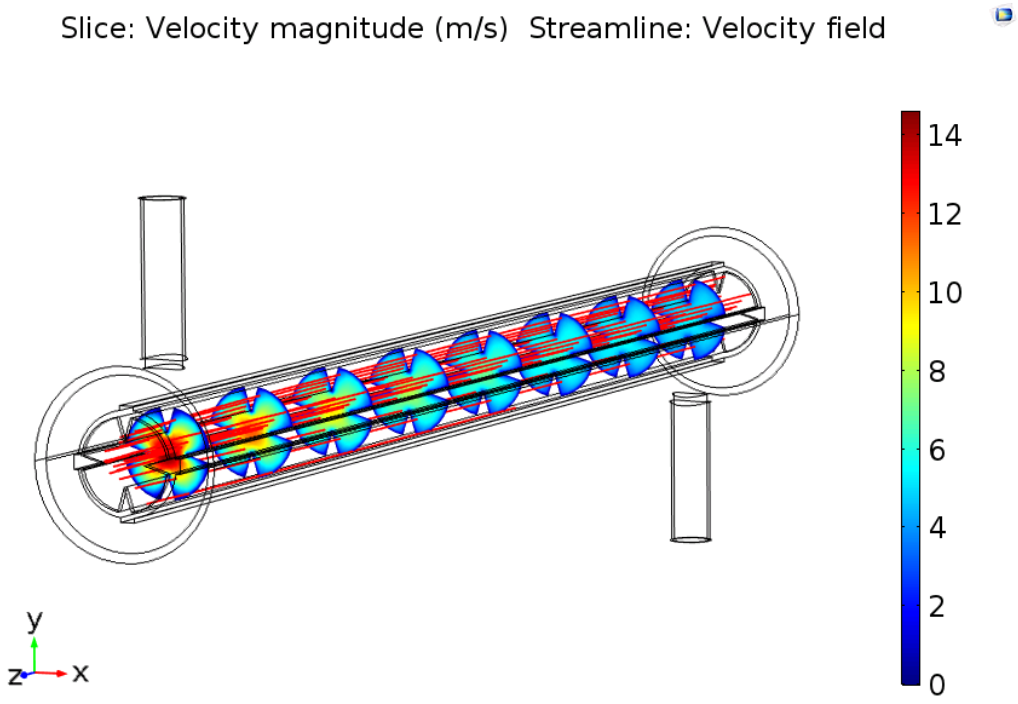

Figure D.4: Velocity stream lines and velocity profile for air
($T_{Air,In}$ = 973.15 K, $T_{Oil,In}$ = 300.15 K, v_{Air} = 4.46 L s^{-1}, m_{Oil} = 0.02 kg s^{-1})

V_{air} = 3.55 L s^{-1}, Cathode exhaust flow rate

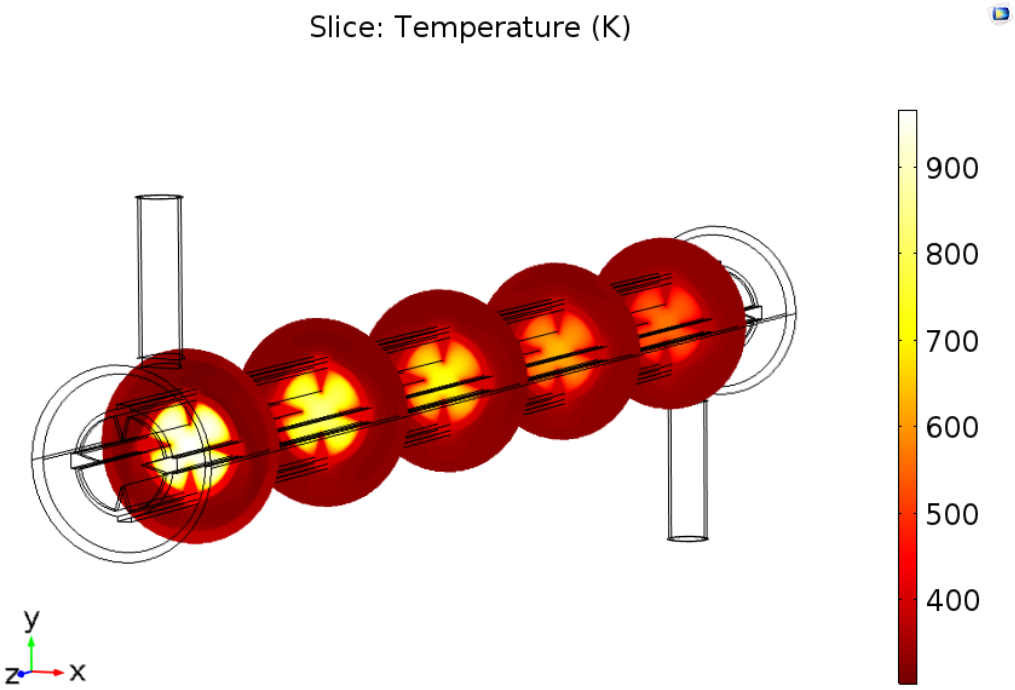

Figure D.5: Temperature profile development through oil and air domains
($T_{Air,In}$ = 973.15 K, $T_{Oil,In}$ = 300.15 K, v_{Air} = 3.55 L s^{-1}, m_{Oil} = 0.02 kg s^{-1})

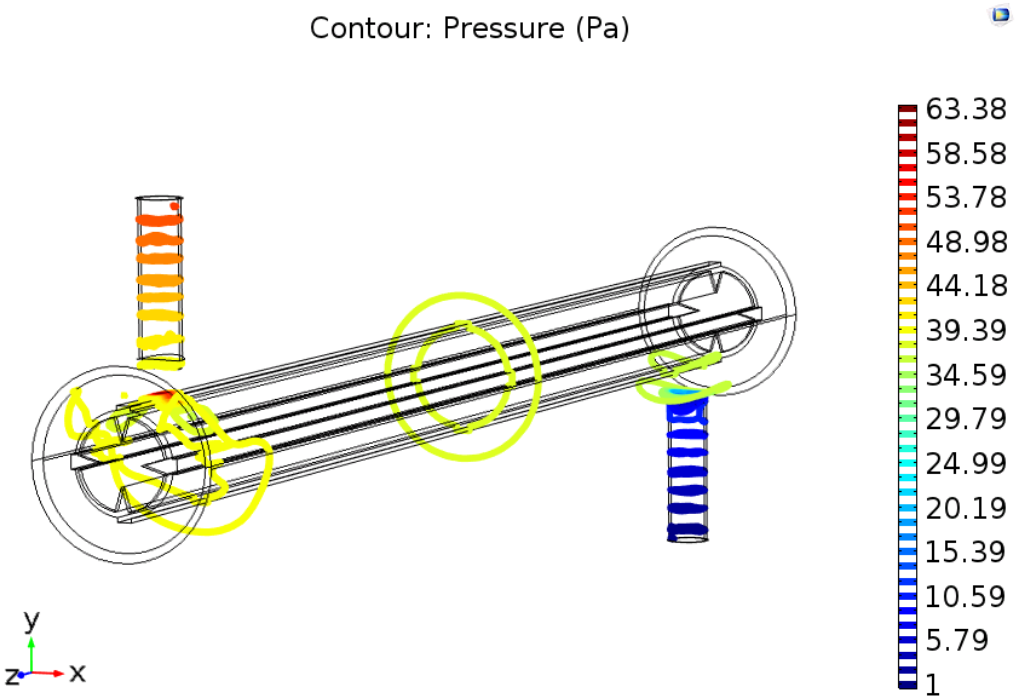

Figure D.6: Pressure drop for thermal oil
($T_{Air,In}$ = 973.15 K, $T_{Oil,In}$ = 300.15 K, v_{Air} = 3.55 L s^{-1}, m_{Oil} = 0.02 kg s^{-1})

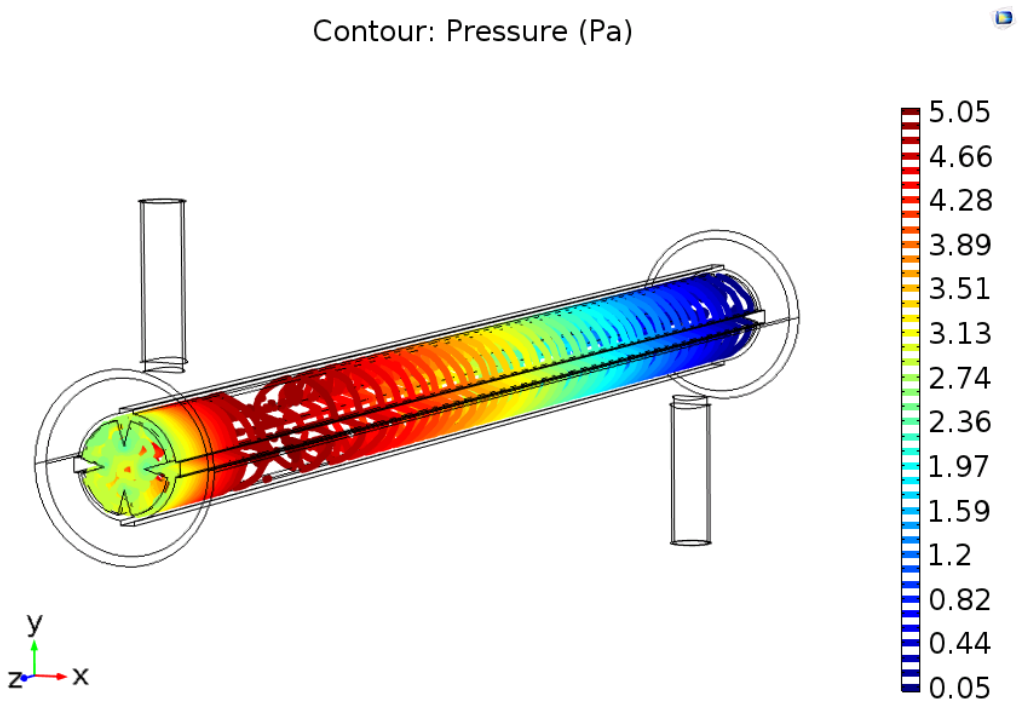

Figure D.7: Pressured drop for air side
($T_{Air,In}$ = 973.15 K, $T_{Oil,In}$ = 300.15 K, v_{Air} = 3.55 L s^{-1}, m_{Oil} = 0.02 kg s^{-1})

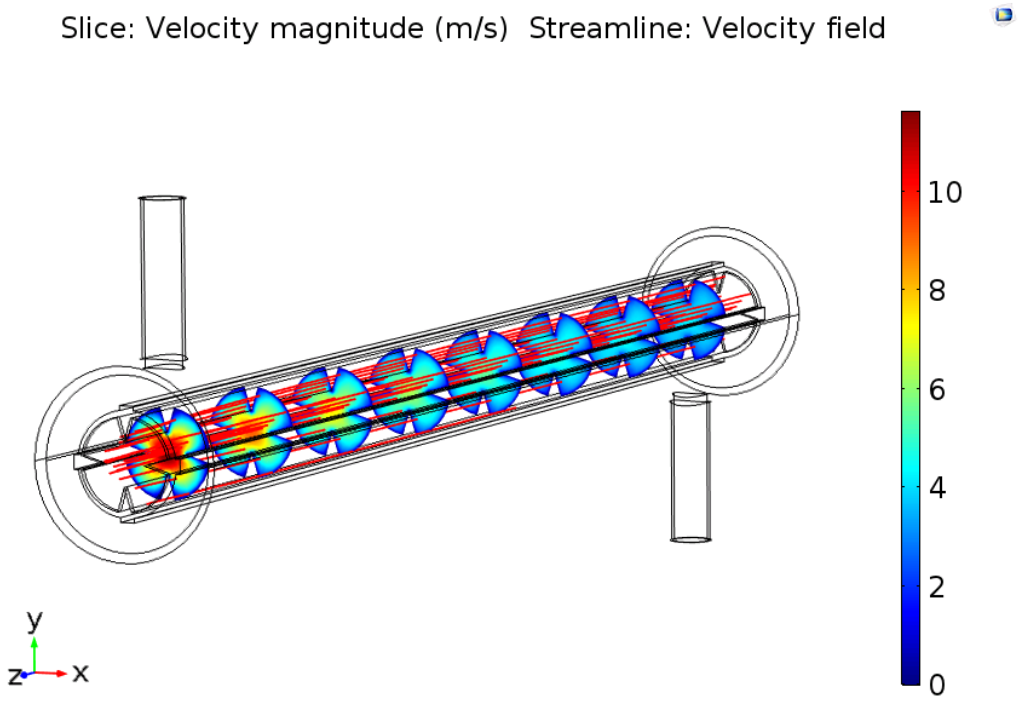

Figure D.8: Velocity stream lines and velocity profile for air
($T_{Air,In}$ = 973.15 K, $T_{Oil,In}$ = 300.15 K, v_{Air} = 3.55 L s^{-1}, m_{Oil} = 0.02 kg s^{-1})

V_{air} = 11.06 L s^{-1}, Cathode exhaust flow rate

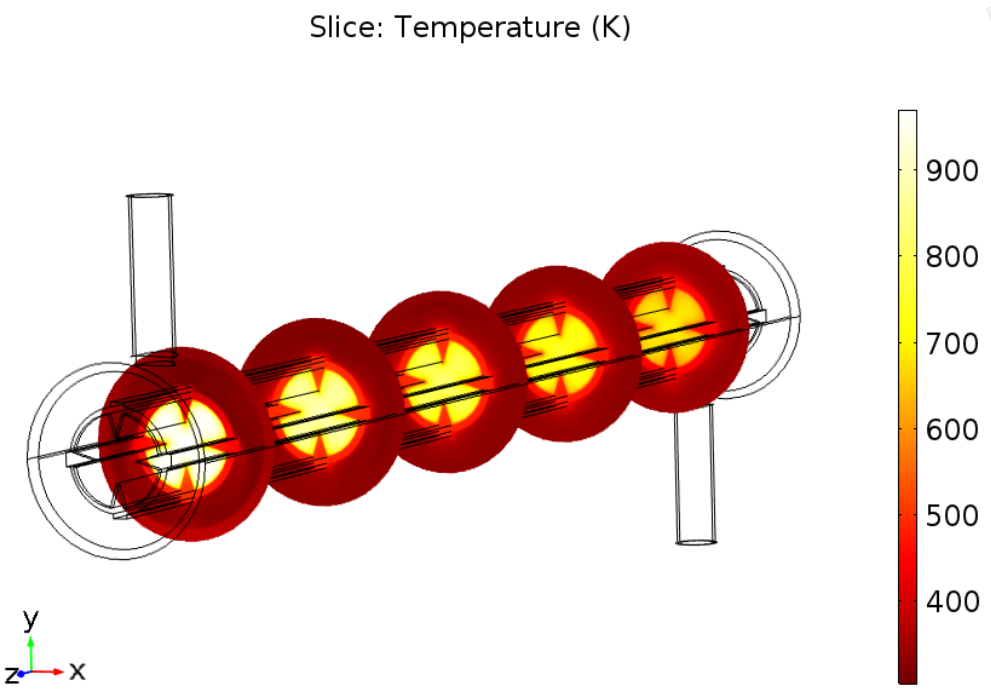

Figure D.9: Temperature profile development though oil and air domains
($T_{Air,In}$ = 973.15 K, $T_{Oil,In}$ = 300.15 K, v_{Air} = 11.06 L s^{-1}, m_{Oil} = 0.02 kg s^{-1})

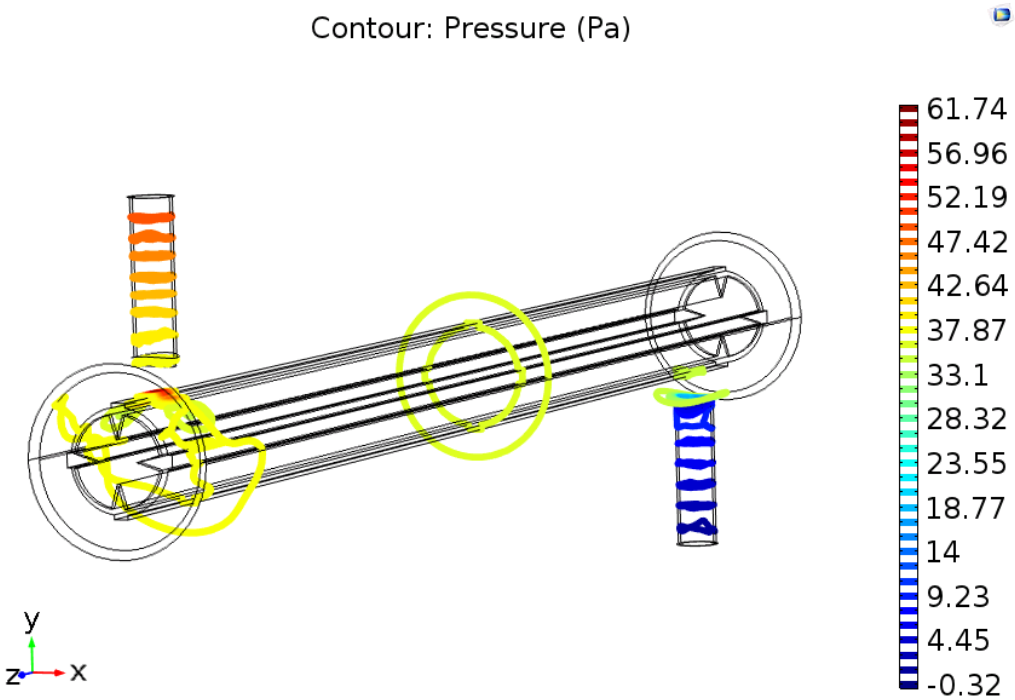

Figure D.10: Pressure drop for thermal oil
($T_{Air,In}$ = 973.15 K, $T_{Oil,In}$ = 300.15 K, v_{Air} = 11.06 L s^{-1}, m_{Oil} = 0.02 kg s^{-1})

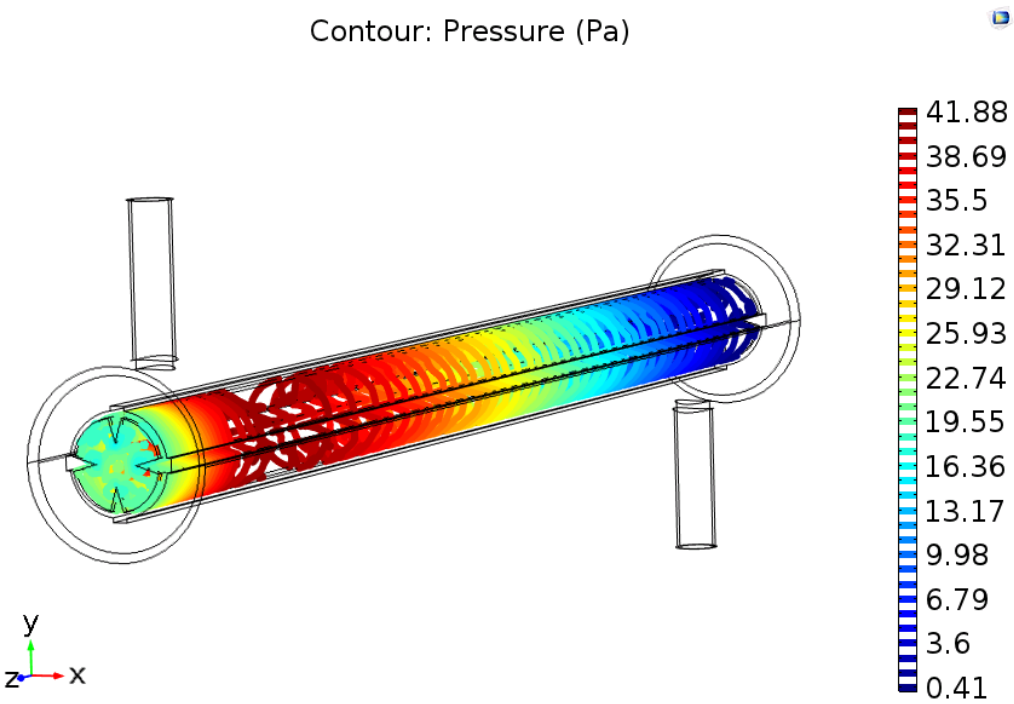

Figure D.11: Pressure drop for air side
($T_{Air,In}$ = 973.15 K, $T_{Oil,In}$ = 300.15 K, v_{Air} = 11.06 L s^{-1}, m_{Oil} = 0.02 kg s^{-1})

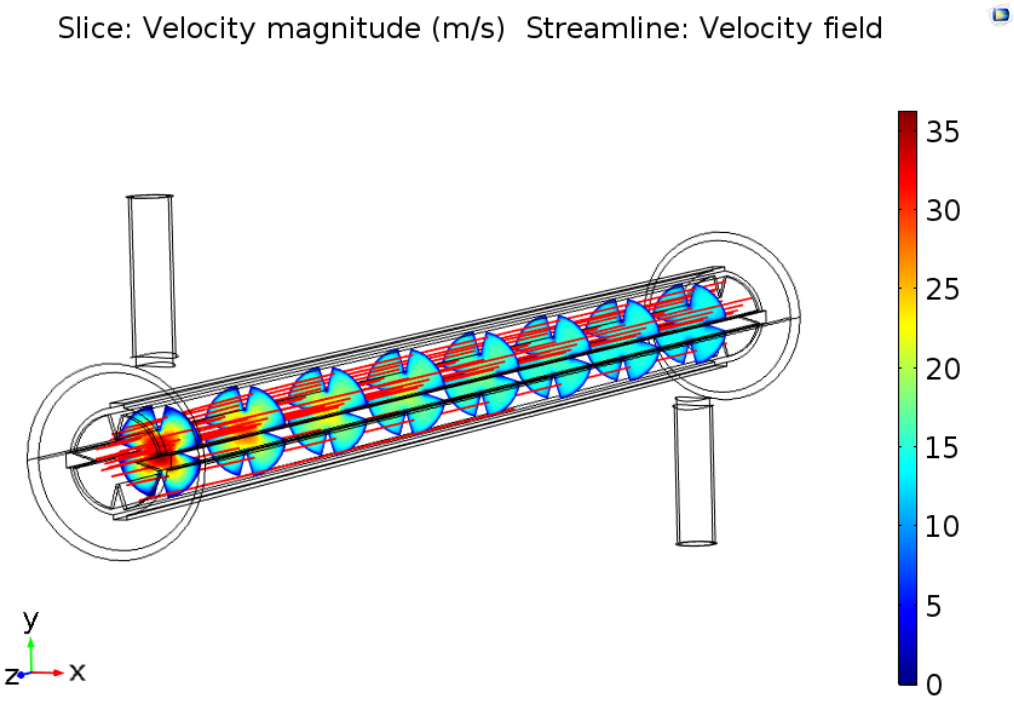

Figure D.12: Velocity stream lines and velocity profile for air
($T_{Air,In}$ = 973.15 K, $T_{Oil,In}$ = 300.15 K, v_{Air} = 11.06 L s^{-1}, m_{Oil} = 0.02 kg s^{-1})

V_{air} = 8.61 L s^{-1}, Cathode exhaust flow rate

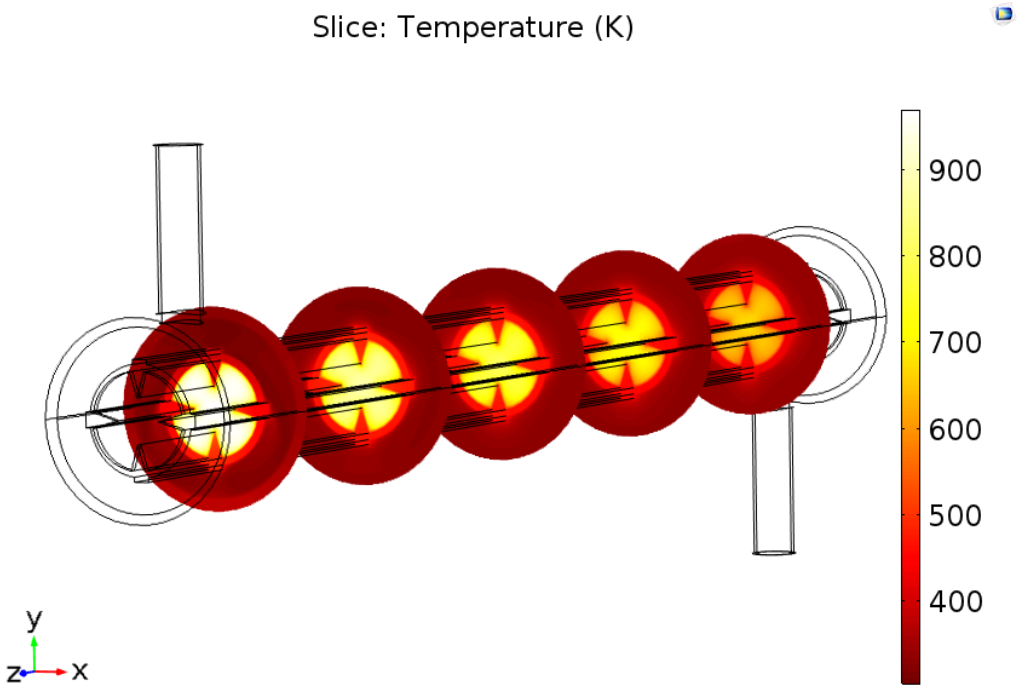

Figure D.13: Temperature profile development through oil and air domains
($T_{Air,In}$ = 973.15 K, $T_{Oil,In}$ = 300.15 K, v_{Air} = 8.61 L s^{-1}, m_{Oil} = 0.02 kg s^{-1})

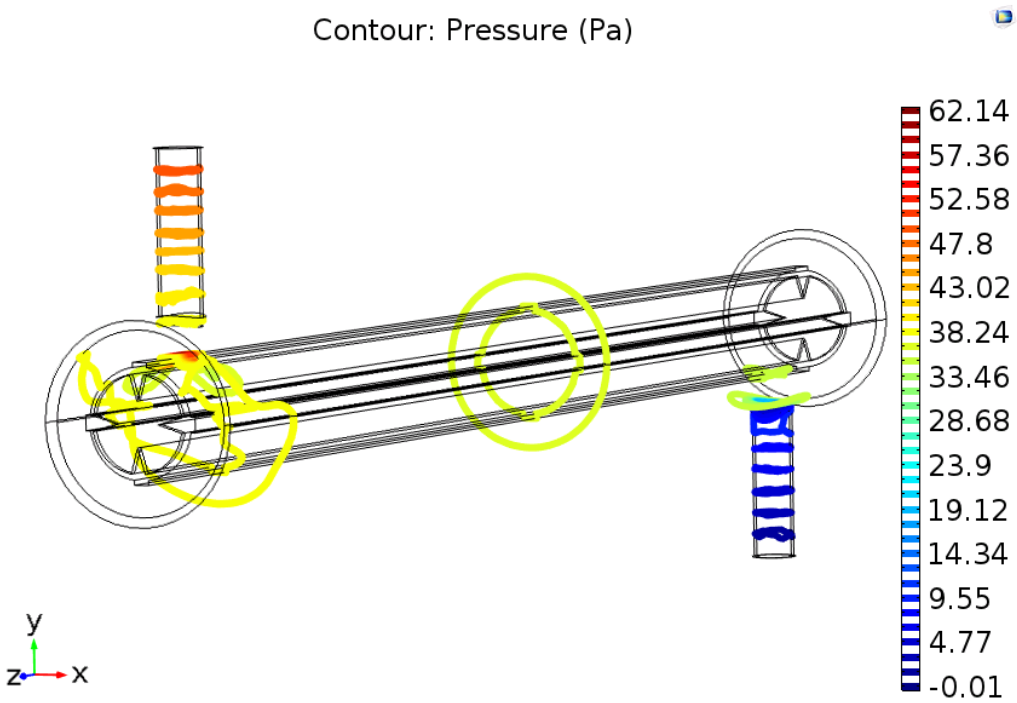

Figure D.14: Pressure drop for thermal oil
($T_{Air,In}$ = 973.15 K, $T_{Oil,In}$ = 300.15 K, v_{Air} = 8.61 L s^{-1}, m_{Oil} = 0.02 kg s^{-1})

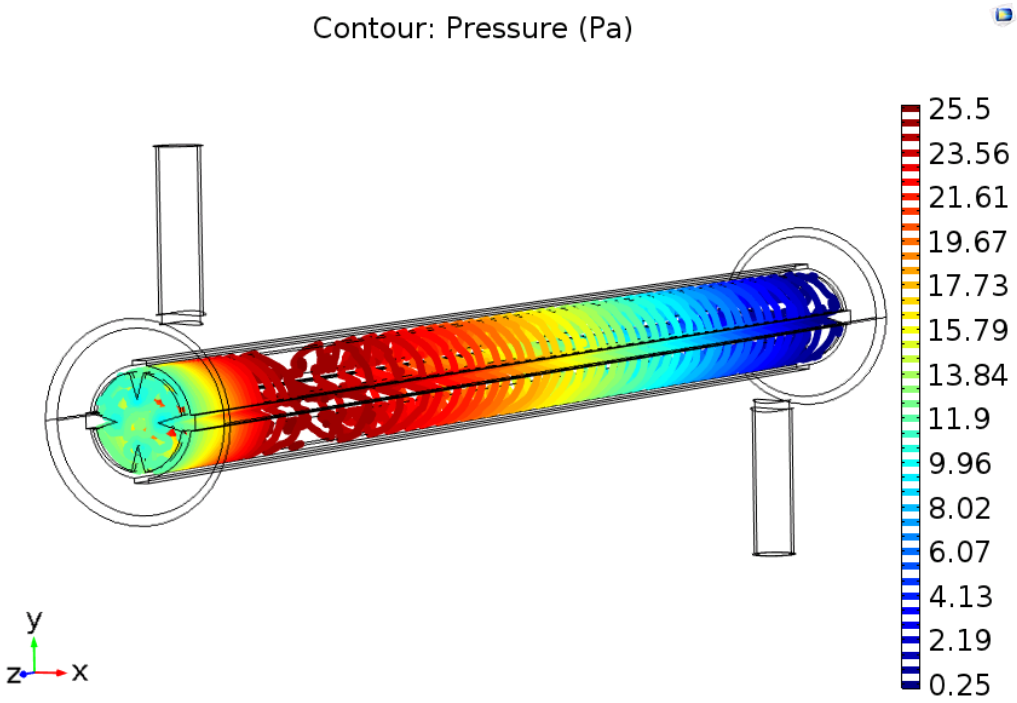

Figure D.15: Pressure drop for air side
($T_{Air,In}$ = 973.15 K, $T_{Oil,In}$ = 300.15 K, v_{Air} = 8.61 L s^{-1}, m_{Oil} = 0.02 kg s^{-1})

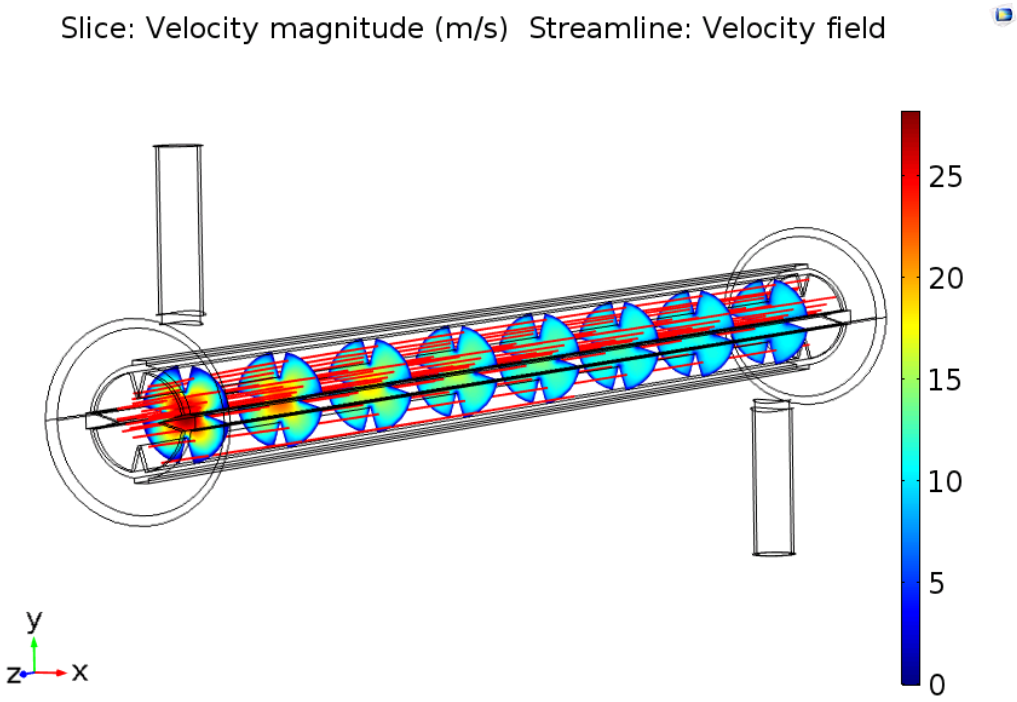

Figure D.16: Velocity stream lines and velocity profile for air
($T_{Air,In}$ = 973.15 K, $T_{Oil,In}$ = 300.15 K, v_{Air} = 8.61 L s^{-1}, m_{Oil} = 0.02 kg s^{-1})

V_{air} = 6.85 L s^{-1}, Cathode exhaust flow rate

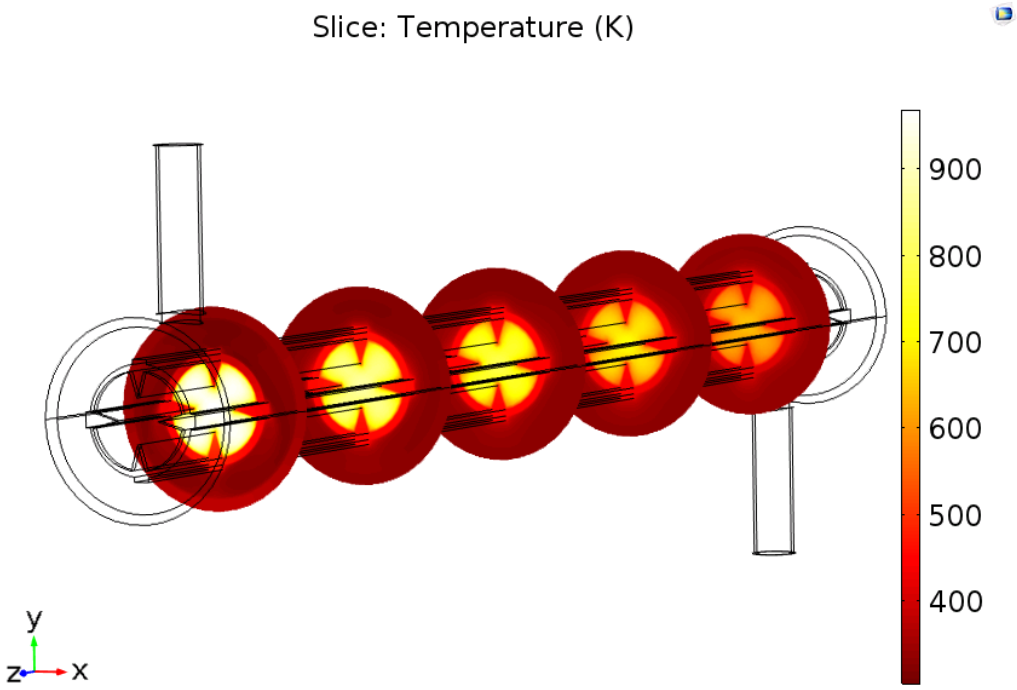

Figure D.17: Temperature profile development through oil and air domains
($T_{Air,In}$ = 973.15 K, $T_{Oil,In}$ = 300.15 K, v_{Air} = 6.85 L s^{-1}, m_{Oil} = 0.02 kg s^{-1})

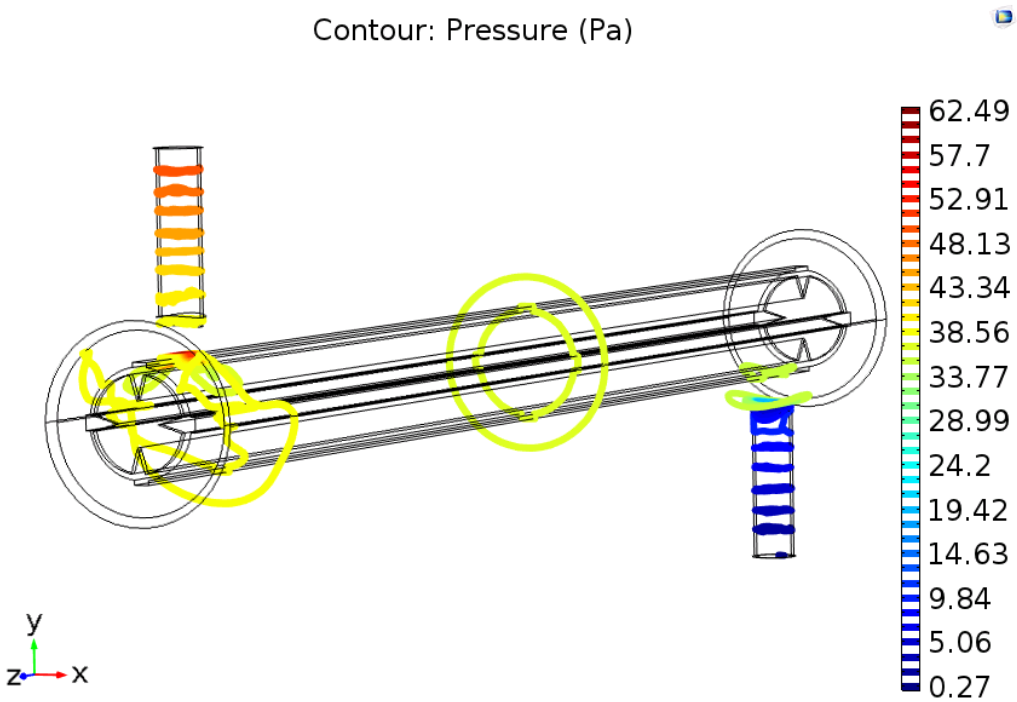

Figure D.18: Pressure drop for thermal oil
($T_{Air,In}$ = 973.15 K, $T_{Oil,In}$ = 300.15 K, v_{Air} = 6.85 L s^{-1}, m_{Oil} = 0.02 kg s^{-1})

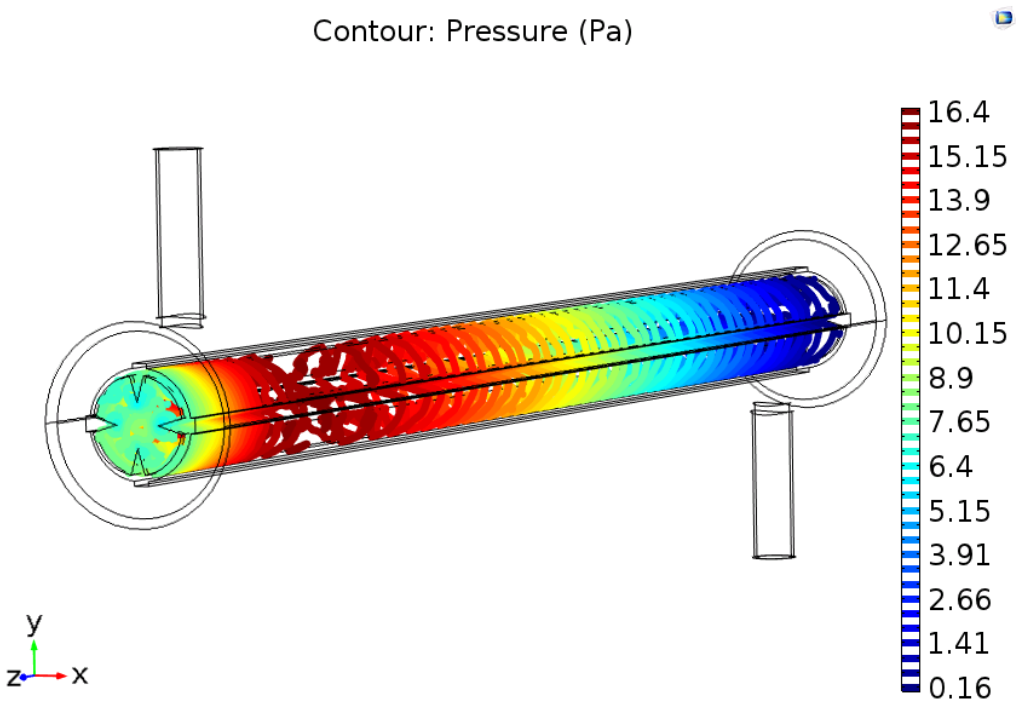

Figure D.19: Pressure drop for air side
($T_{Air,In}$ = 973.15 K, $T_{Oil,In}$ = 300.15 K, v_{Air} = 6.85 L s^{-1}, m_{Oil} = 0.02 kg s^{-1})

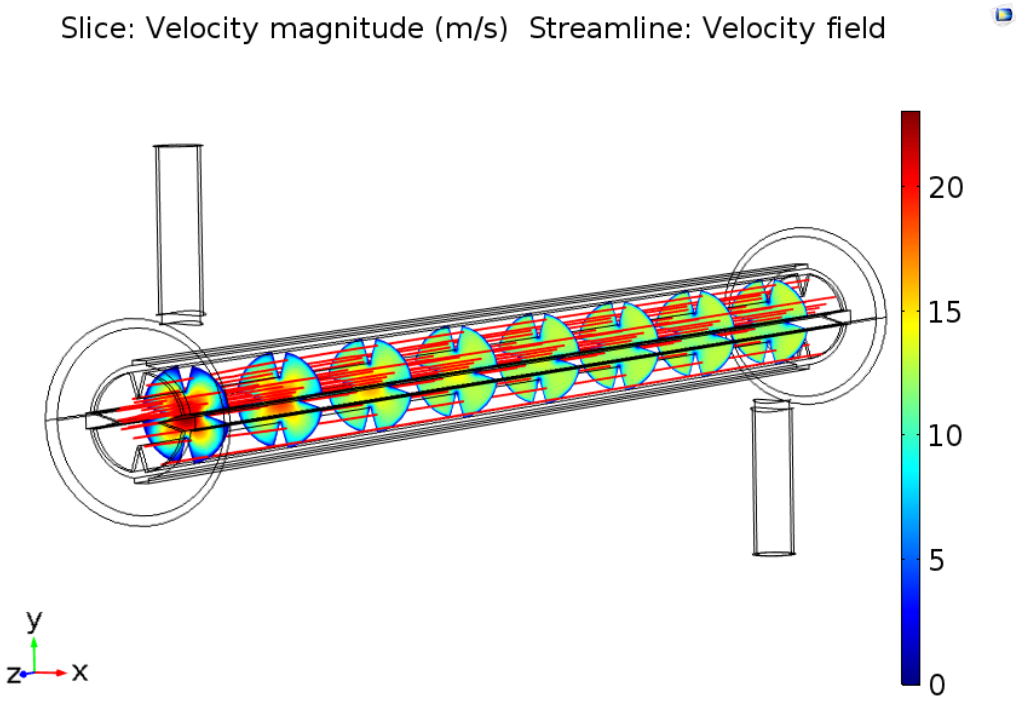

Figure D.20: Velocity stream lines and velocity profile for air
($T_{Air,In}$ = 973.15 K, $T_{Oil,In}$ = 300.15 K, v_{Air} = 6.85 L s^{-1}, m_{Oil} = 0.02 kg s^{-1})

Thermo-physical properties of Paratherm HR

Temperature (K)	Specific heat (J kg^{-1} K^{-1})	Density (kg m^{-3})	Thermal conductivity (W m^{-1} K^{-1})	Dynamic viscosity (Pa s)
255.2222	1842.192	993.24	0.1176876	0.544
269.1111	1884.06	977.22	0.1176876	0.134
283	1925.928	977.22	0.1176876	0.05
296.8889	1925.928	961.2	0.1176876	0.021
310.7778	1967.796	945.18	0.1176876	0.012
324.6667	2009.664	945.18	0.1176876	0.0071
338.5556	2051.532	929.16	0.1159569	0.0047
352.4444	2051.532	913.14	0.1159569	0.0033
366.3333	2093.4	913.14	0.1142262	0.0025
380.2222	2135.268	897.12	0.1142262	0.0019
394.1111	2177.136	897.12	0.1124955	0.0015
408	2177.136	881.1	0.1124955	0.0013
421.8889	2219.004	865.08	0.1107648	0.0011
435.7778	2260.872	865.08	0.1107648	0.00095
449.6667	2302.74	849.06	0.1090341	0.00082
463.5556	2302.74	833.04	0.1073034	0.00072
477.4444	2344.608	833.04	0.1055727	0.00064
491.3333	2386.476	817.02	0.103842	0.00057
505.2222	2428.344	817.02	0.1021113	0.00051
519.1111	2428.344	801	0.1021113	0.00046
533	2470.212	784.98	0.0986499	0.00042
546.8889	2512.08	784.98	0.0969192	0.00038
560.7778	2553.948	768.96	0.0951885	0.00035
574.6667	2553.948	752.94	0.0934578	0.00032
588.5556	2595.816	752.94	0.0917271	0.0003
602.4444	2637.684	736.92	0.0899964	0.00028
616.3333	2679.552	736.92	0.086535	0.00026
630.2222	2679.552	720.9	0.0848043	0.00024
644.1111	2721.42	704.88	0.0813429	0.00022

(Source: www.paratherm.com)

Appendix E

The concentration and mass flow rates of the refrigerant desorbed for both cases of geometry G3 and G4 and for case 2 of geometry G2 is shown here.

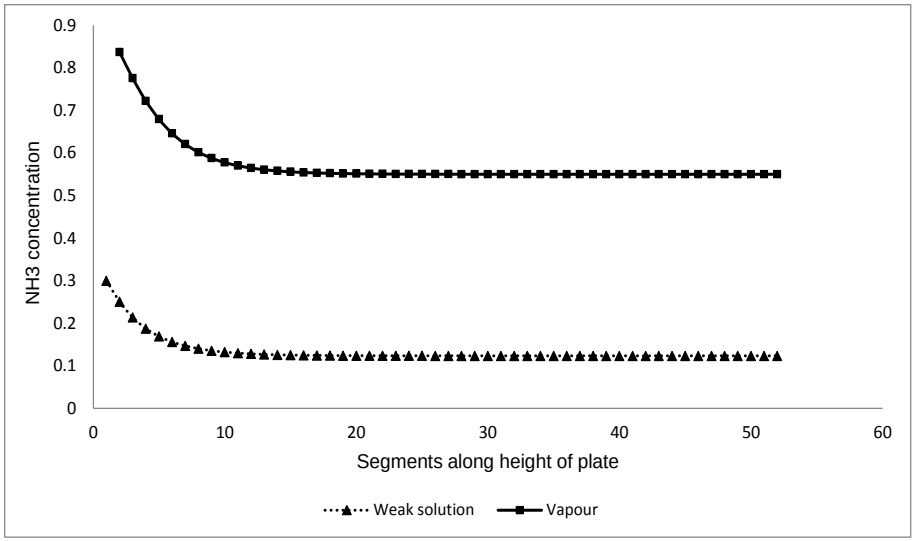

a) Case 2 – Middle channels: concentration

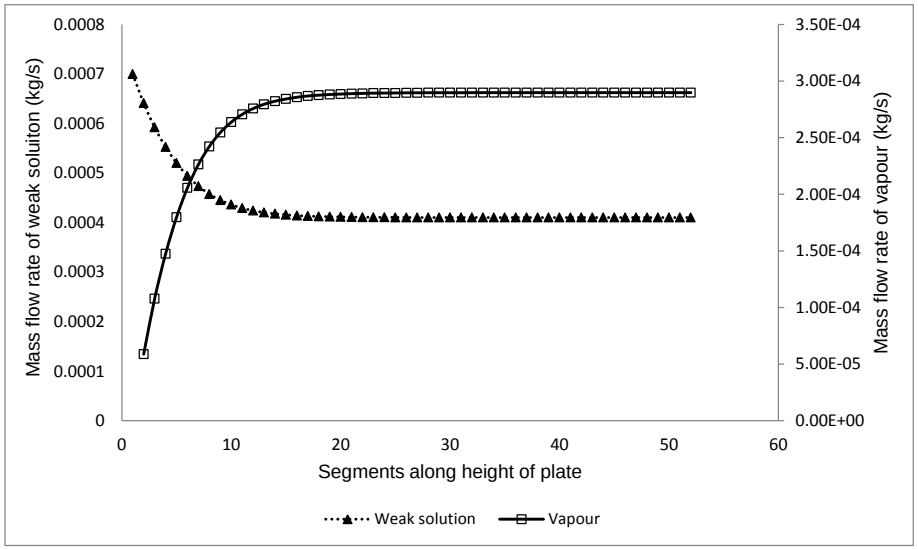

b) Case 2 – Middle channels: mass flow rate

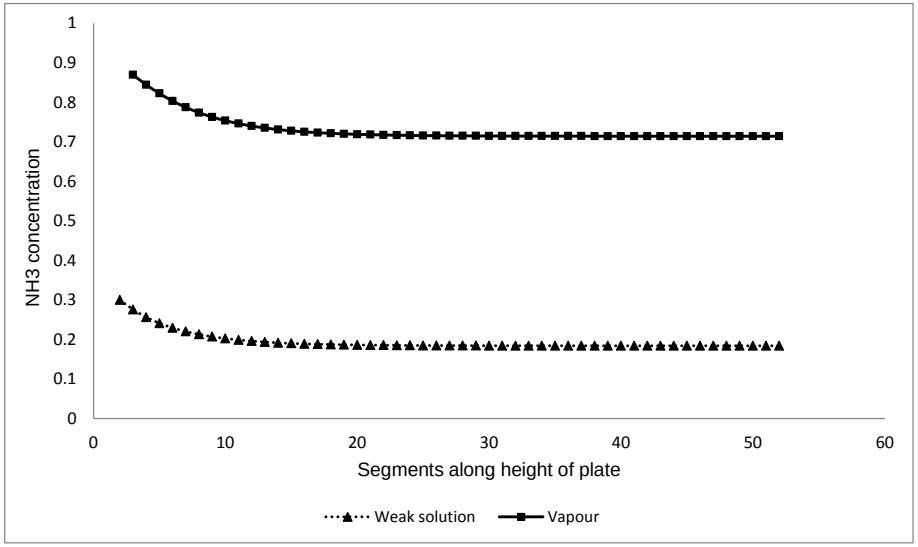

c) Case 2 – End channels: concentration

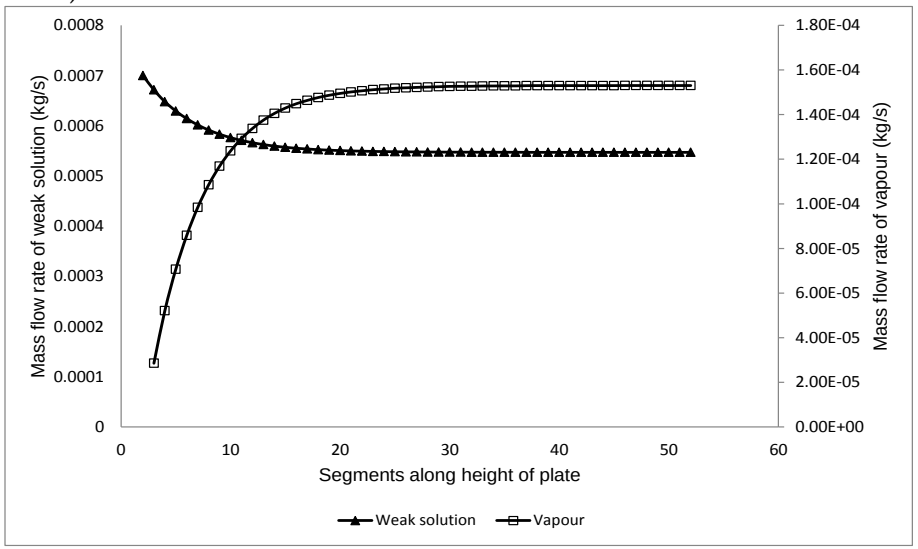

d) Case 2 – End channels: mass flow rate

Figure E.1: Concentration and mass flow rate of weak solution and vapour along middle & end channels – Case 2, Geometry G2 (T_{SOLN} = 110^{o}C)

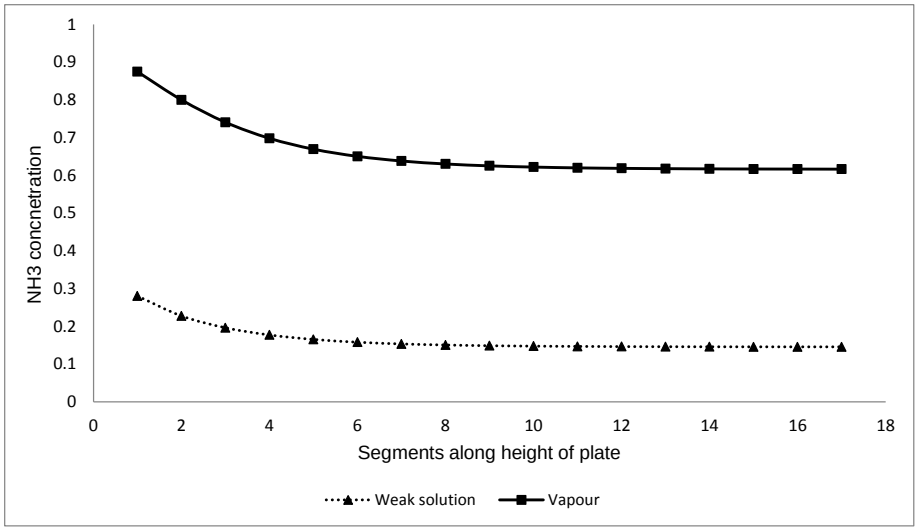

a) Case 1 – Central middle channels: concentration

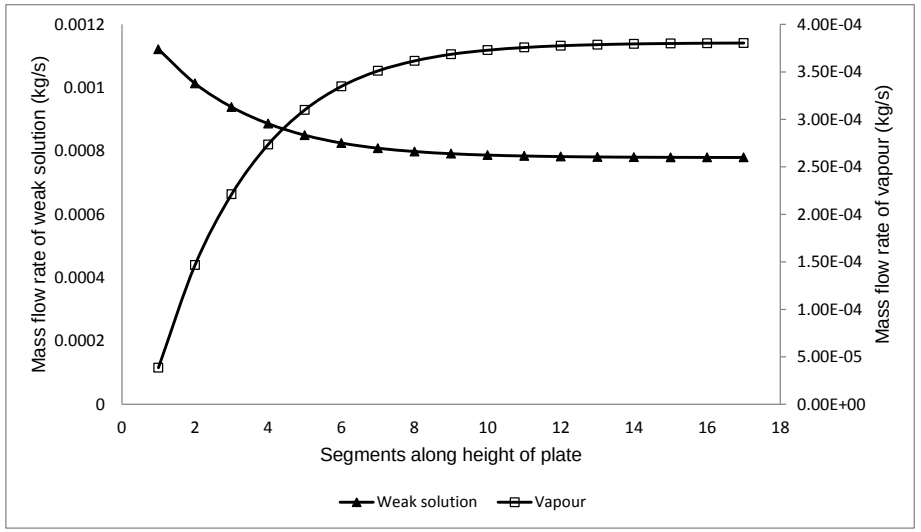

b) Case 1 – Central middle channels: mass flow rate

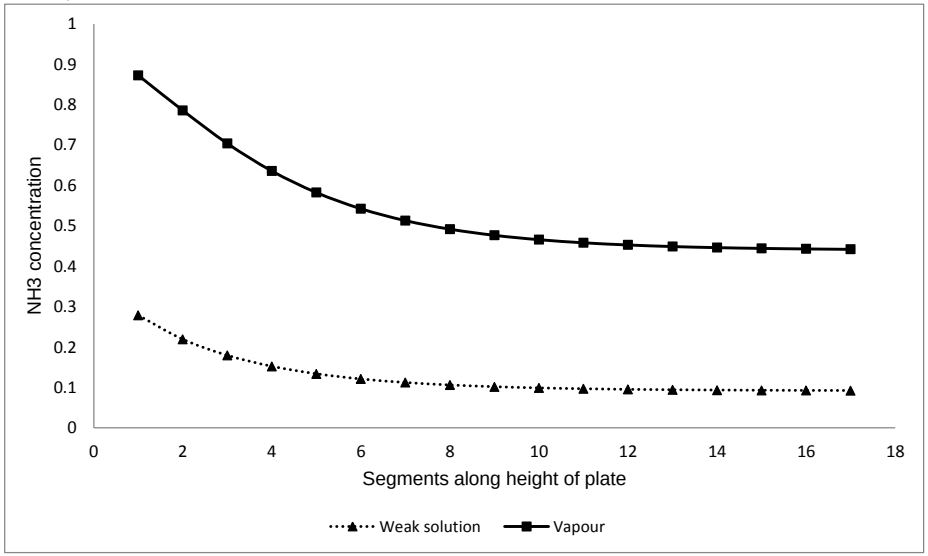

c) Case 1 – Peripheral middle channels: concentration

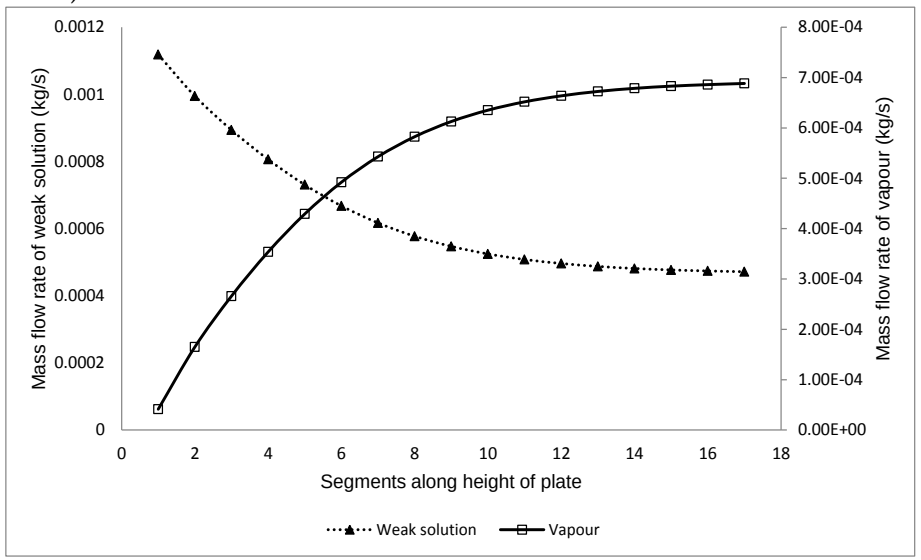

d) Case 1 – Peripheral middle channels: mass flow rate

Figure E.2: *Concentration and mass flow rate of weak solution and vapour along central & peripheral middle channels – Case 1, Geometry G3 (T_{SOLN} = 110^{o} C)*

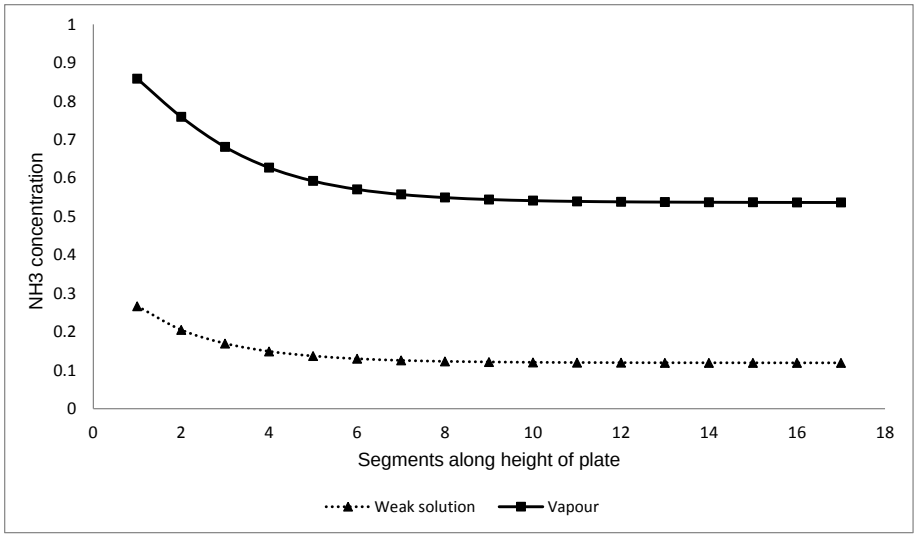

a) Case 2 – Middle channels: concentration

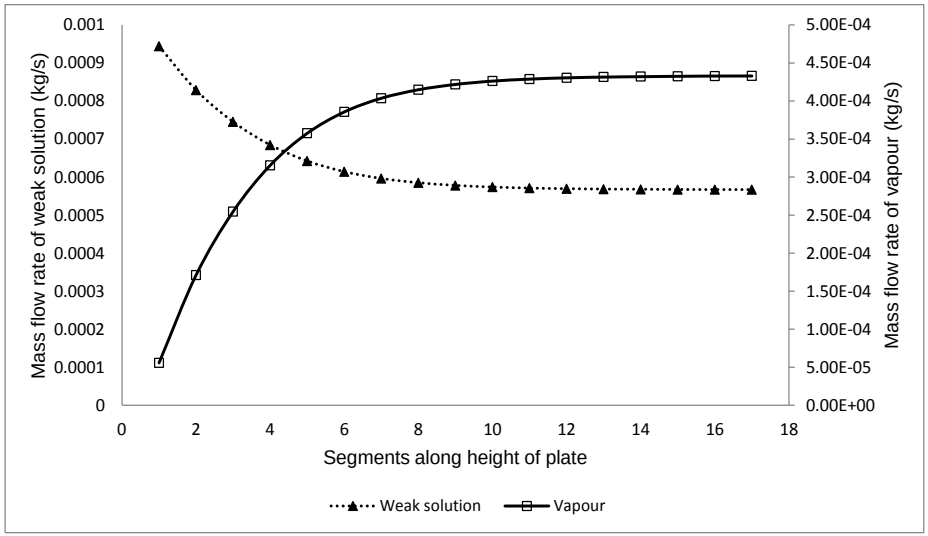

b) Case 2 – Middle channels: mass flow rate

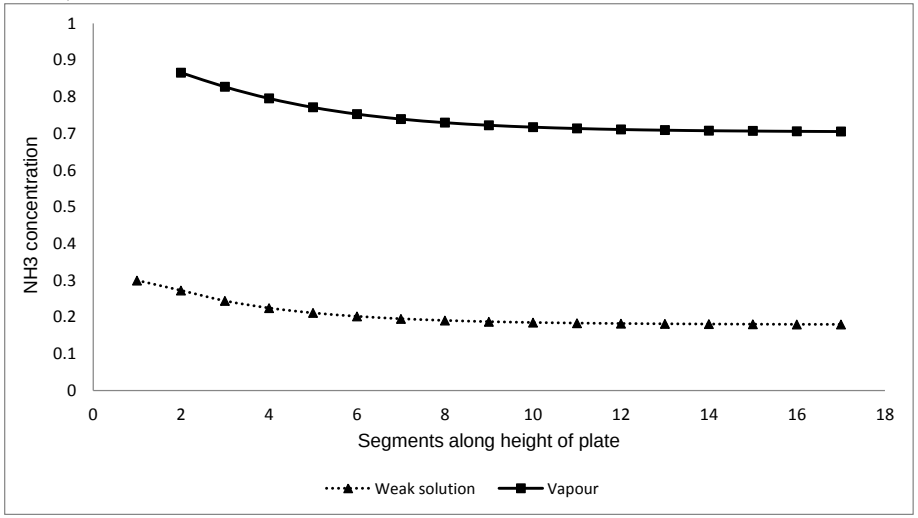

c) Case 2 – End channels: concentration

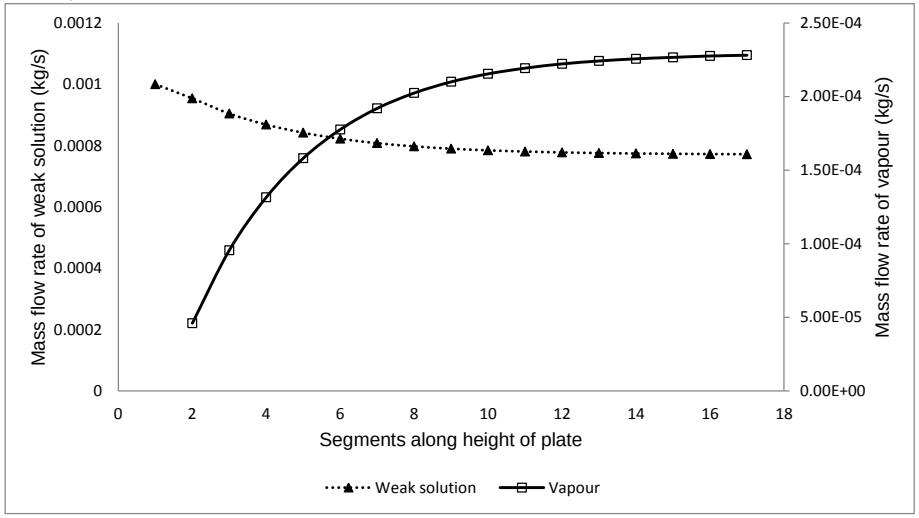

d) Case 2 – End channels: mass flow rate

Figure E.3: Concentration and mass flow rate of weak solution and vapour along middle and end channels – Case 2, Geometry G3 (T_{SOLN} = 110^{o}C)

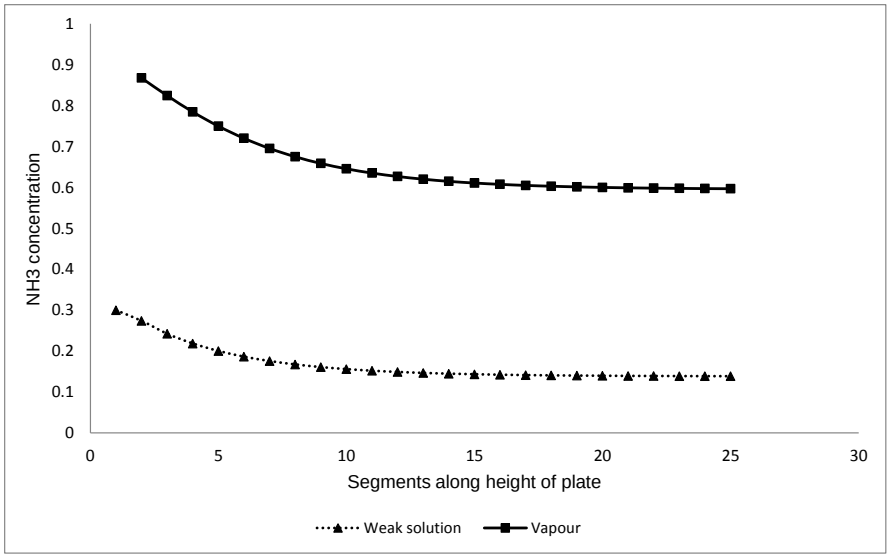

a) Case 1 – Central middle channels: concentration

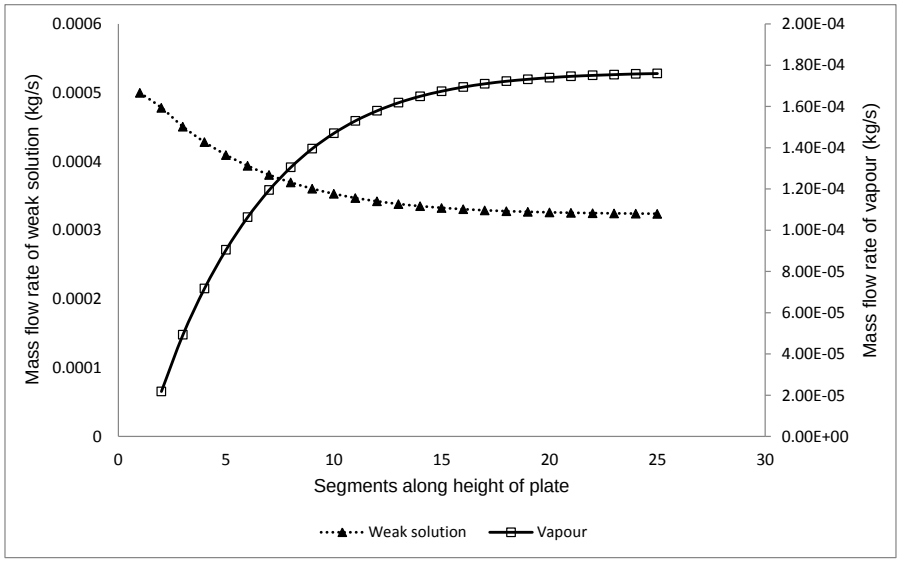

b) Case 1 – Central middle channels: mass flow rate

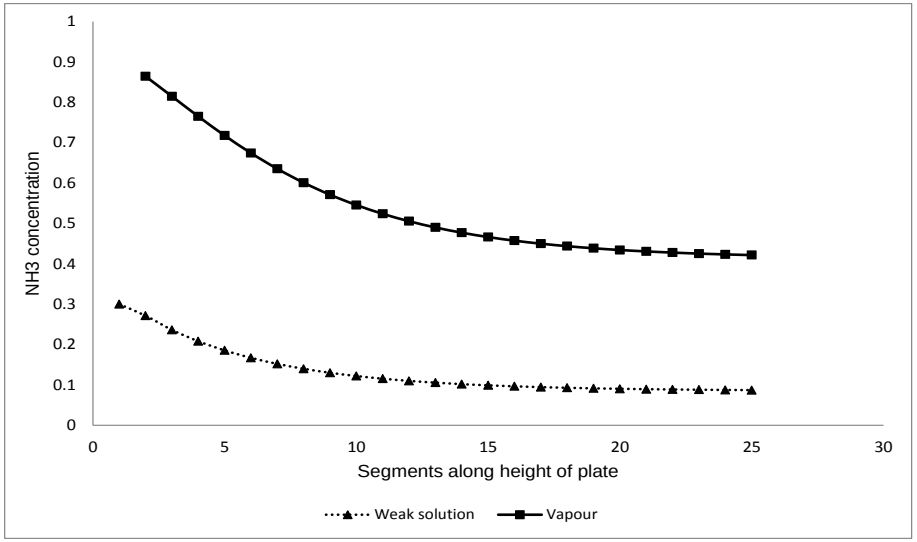

c) Case 1 – Peripheral middle channels: concentration

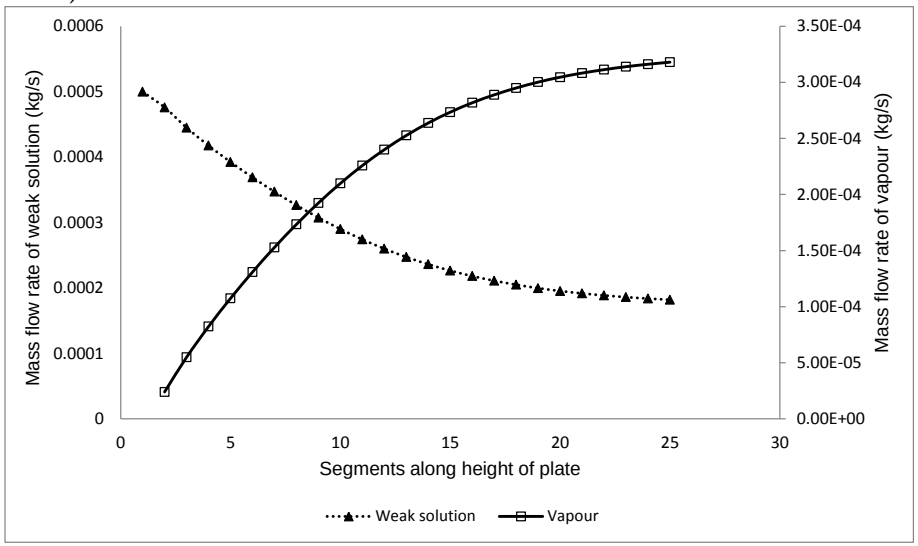

d) Case 1 – Peripheral middle channels: mass flow rate

Figure E.4: *Concentration and mass flow rate of weak solution and vapour along central & peripheral middle channels – Case 1, Geometry G4 (T_{SOLN} = 110^{o}C)*

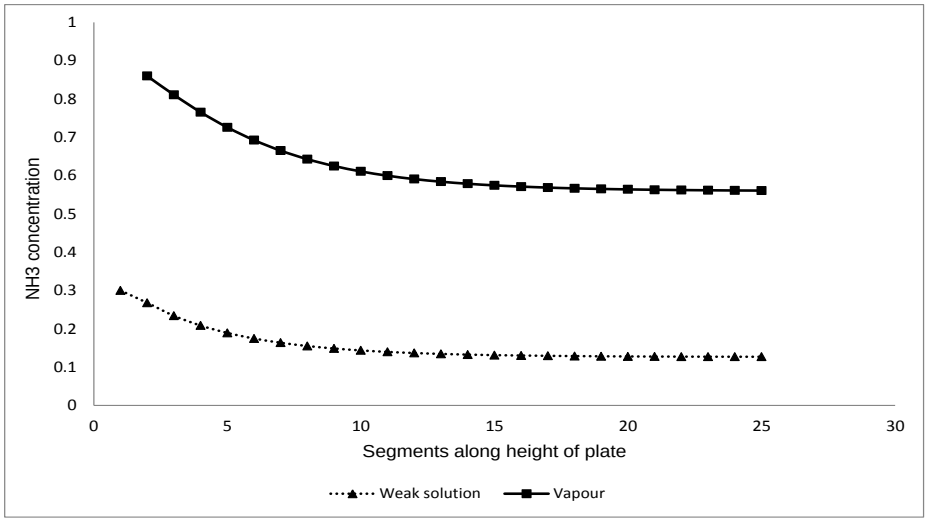

a) Case 2 –Middle channels: concentration

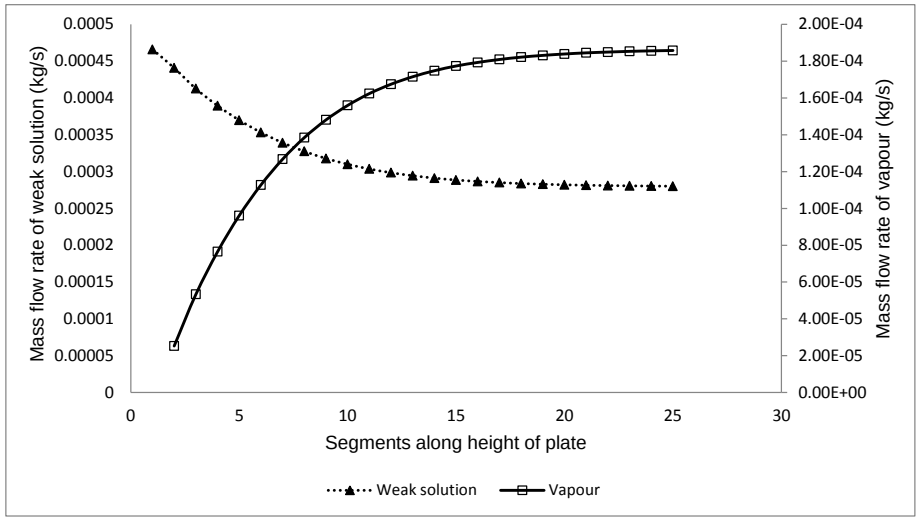

b) Case 2 – Middle channels: mass flow rate

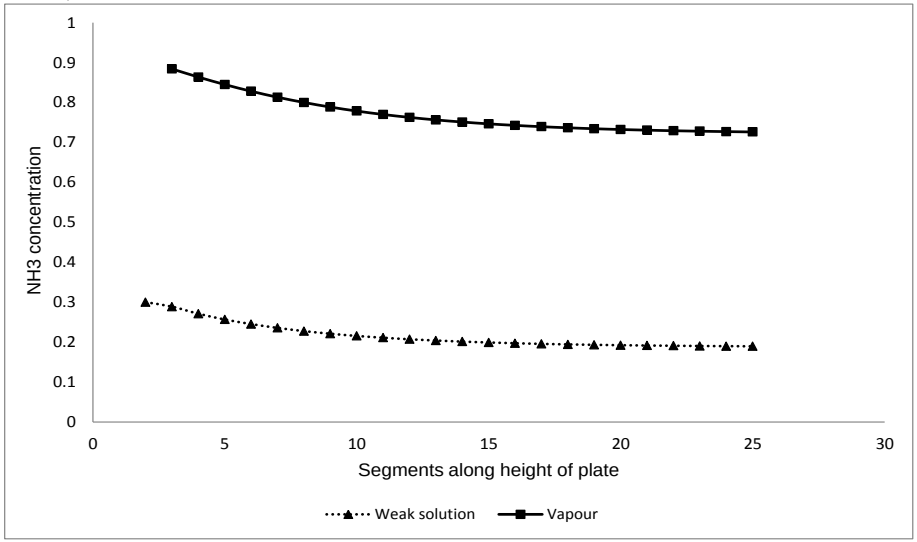

c) Case 2 – End channels: concentration

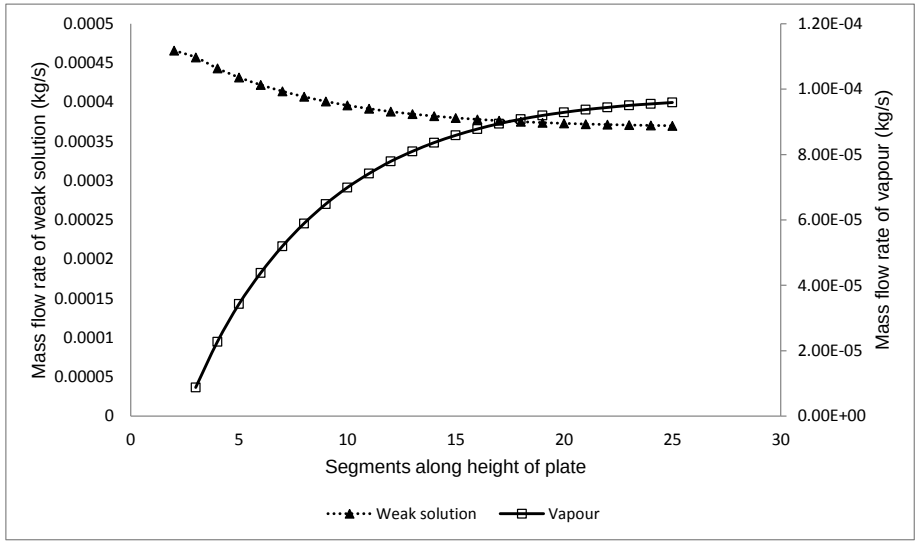

d) Case 2 – End channels: mass flow rate

Figure E.5: Concentration and mass flow rate of weak solution and vapour along middle and end channels – Case 2, Geometry G4 (T_{SOLN} = 110^{o}C)

Appendix F

Thermal resistance network of heat pipe

The heat pipe can be considered to be built of a thermal resistance network and is shown in Figure F.1.

The above resistance network can be simplified by omitting certain terms. A general rule of thumb in electrical circuit theory is that resistance with large values in parallel may be treated as open circuits and resistance with small values in series may be treated as short circuit.

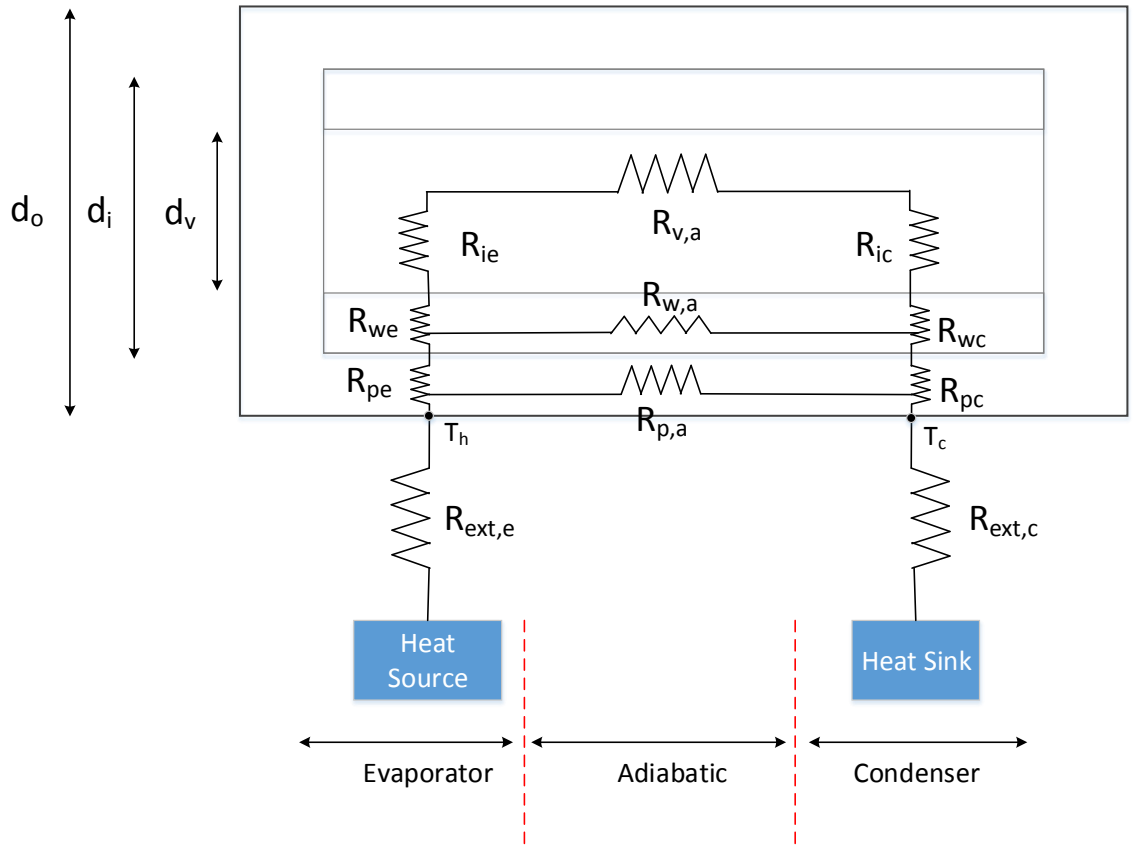

Figure F.1: Thermal resistance network of heat pipe

$R_{p,e}$ & $R_{p,c}$ = Radial conduction resistance of the heat pipe wall at the evaporator and condenser

$R_{w,e}$ & $R_{w,c}$ = Resistance of the liquid-wick combination at the evaporator and condenser

$R_{i,e}$ & $R_{i,c}$ = Resistance of the liquid-vapour interface at the evaporator and condenser

$R_{v,a}$ = Resistance of the vapour section in the adiabatic region

$R_{p,a}$ = Axial conduction resistance of the heat pipe wall at the adiabatic section

$R_{w,a}$ = Resistance of the liquid-wick combination at the adiabatic section

$R_{ext,e}$ = Contact resistance between heat source and evaporator

$R_{ext.c}$ = Contact resistance between heat sink and condenser

The indicative value for different resistance terms is given in Table F.1 [1]

Table F.1: Indicative value for different thermal resistances

Resistance	°C/W
$R_{p,e}$ & $R_{p,c}$	10^{-1}
$R_{w,e}$ & $R_{w,c}$	10^{1}
$R_{i,e}$ & $R_{i,c}$	10^{-5}
$R_{v,a}$	10^{-8}
$R_{p,a}$	10^{2}
$R_{w,a}$	10^{4}

One can see that $R_{w,a}$ and $R_{p,a}$ have very large values and $R_{v,a}$, $R_{i,e}$ & $R_{i,c}$ have very small values. Hence the total effective resistance can be written as

$$R_{tot} = R_{pe} + R_{we} + R_{wc} + R_{pc}$$

The thermal resistance network comes in handy in calculating the temperature drop across and along the heat pipe. The total radial thermal resistance across the evaporator is $R_{pe} + R_{we}$ and has a value of 0.0849 K W^{-1} and the total radial thermal resistance across the condenser is $R_{wc} + R_{pc}$ and has a value of 0.136 K W^{-1}. These values are for the heat pipe design specified in *Chapter 6*. So the total thermal resistance of the entire heat pipe is

0.2216 K W^{-1}. With 250 W of heat being transported along the heat pipe, the temperature on the outer surface of the heat pipe on the condenser end can be calculated using

$$T_e - T_c = R_{tot}\, Q$$

This gives a temperature drop of 55.4 K between the outer surfaces of the evaporator and condenser. The outer surface at the evaporator end was calculated to be 180 ^{o}C. Hence the outer surface of the condenser will be at a temperature of 397.6 K or 124.5 ^{o}C.

Air duct design

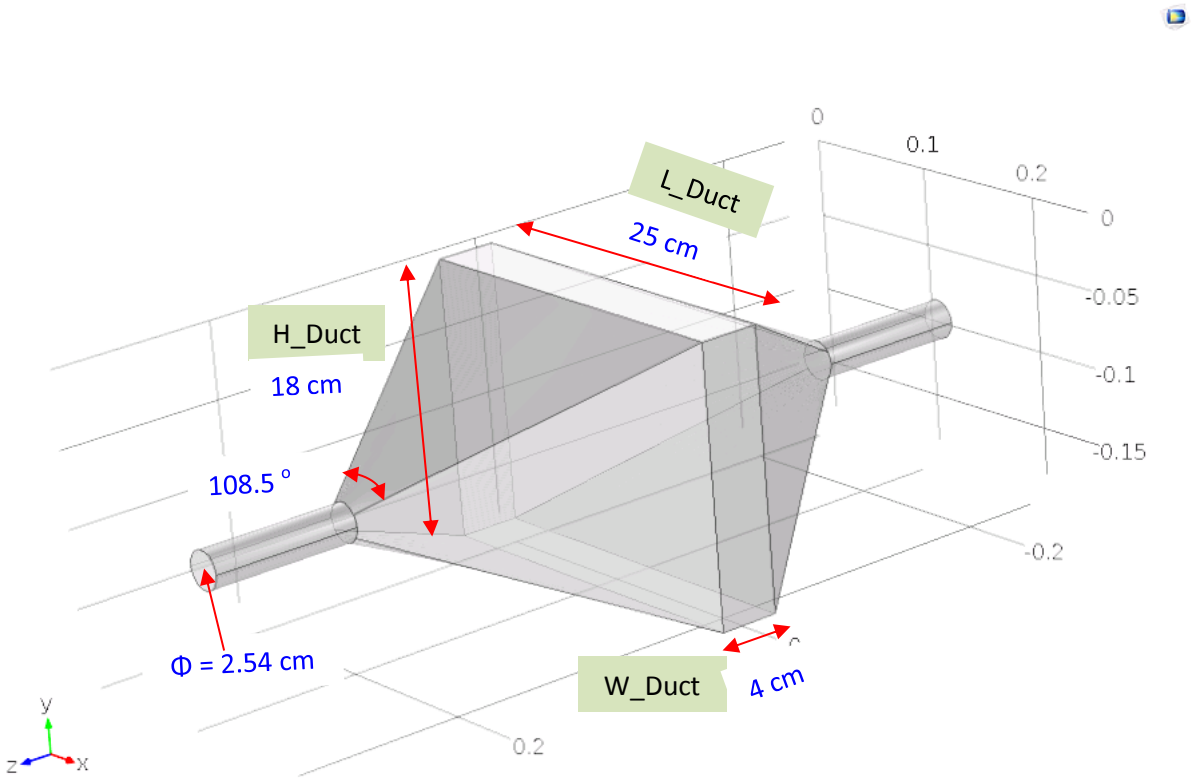

Figure F.2: Air duct design for evaporator chamber

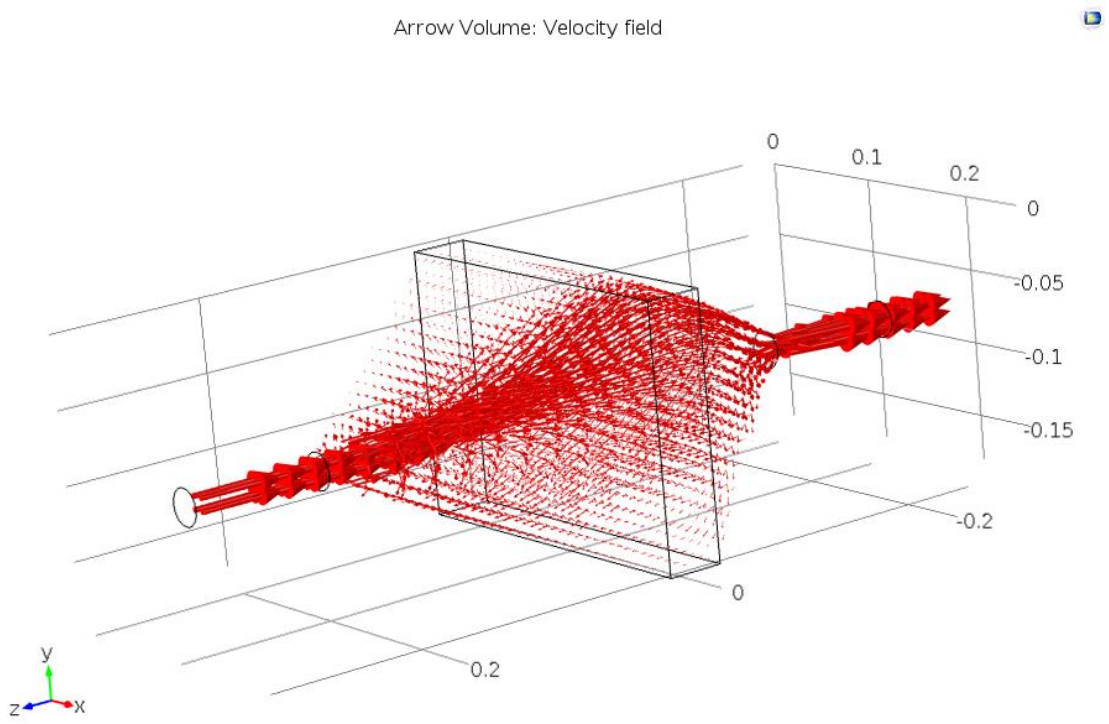

Figure F.3: Velocity flow through the heat pipe duct

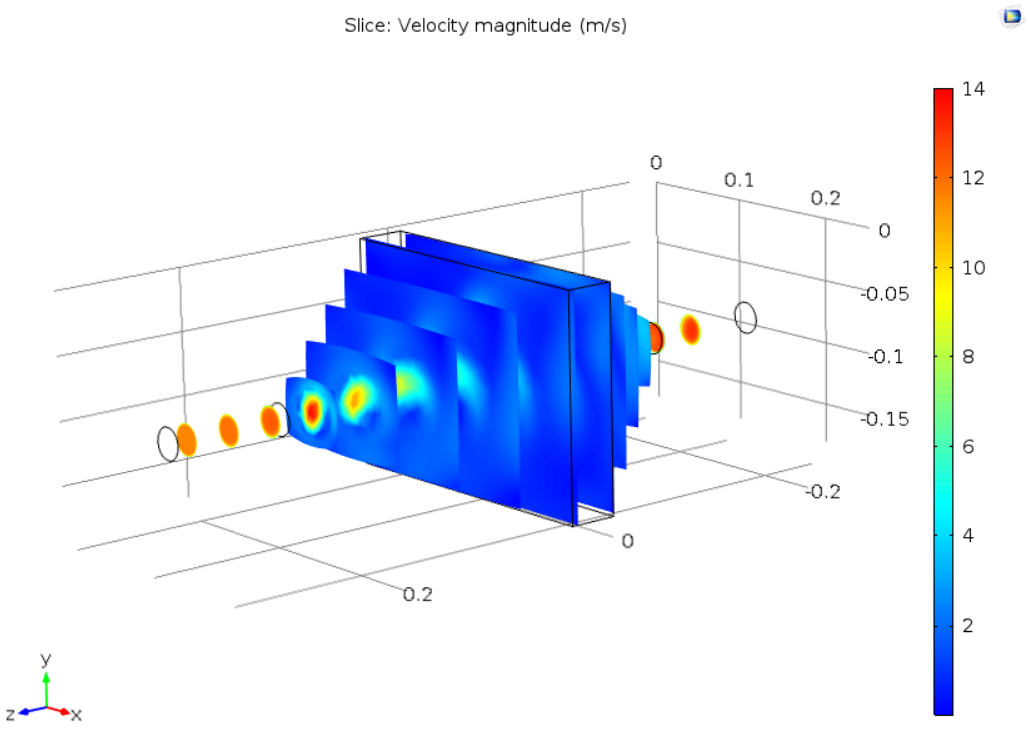

Figure F.4: Velocity magnitude through the heat pipe duct

Evaporator surface area

The evaporator surface area needs to be increased in order to achieve the desired heat input and the way to achieve this is to add fins on the evaporator side. The geometry of the fin and the spacing of the fins along the evaporator section are shown in Figure F.5 and Figure F.6 respectively.

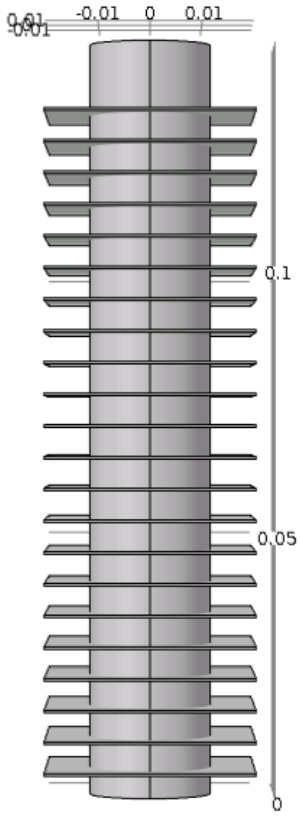

Figure F.5: A heat pipe evaporator section with fins

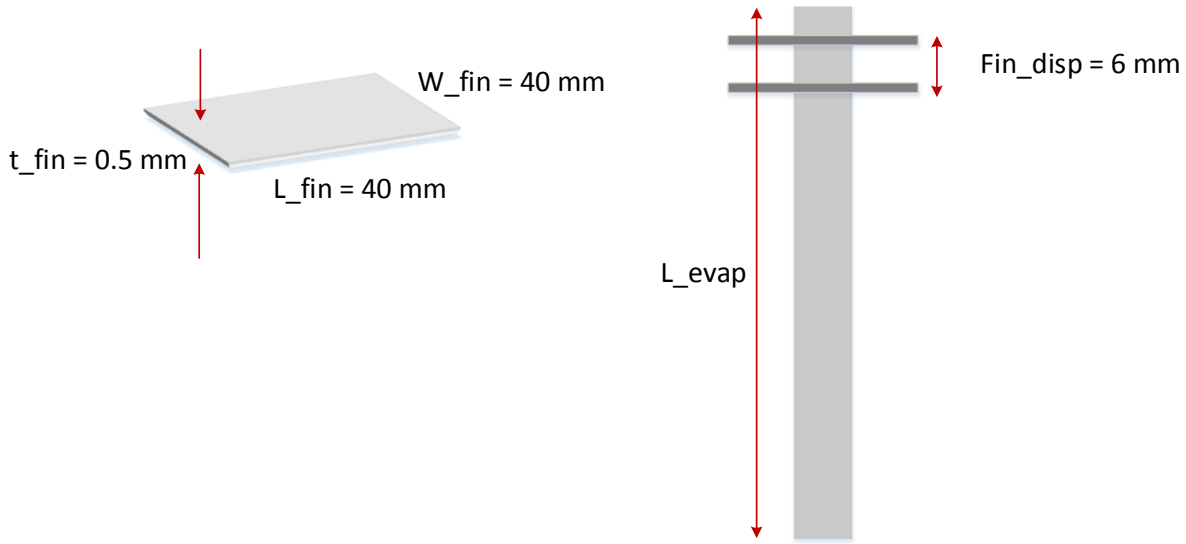

Figure F.6: Fin dimensions and fin spacing along the evaporator section of heat pipe

References

1. Lee, H.S., *Thermal Design: Heat Sinks, Thermoelectrics, heat Pipes, Compact Heat Exchangers and Solar cells*. 2010: Wiley. 180-237.

Centre for Fuel Cell & Hydrogen Research
School of Chemical Engineering
University of Birmingham, UK